UNIVERSITÀ DEGLI STUDI DI NAPOLI FEDERICO II

DIPARTIMENTO DI SCIENZE CHIMICHE

Dottorato di Ricerca in Scienze Chimiche – XXXV Ciclo

PhD THESIS

Energetic valorisation of sludges from civil and industrial sources

Scientific Committee (Tutors):
Prof. Fabio Montagnaro
Prof. Piero Salatino (DICMaPI)
Dott. Ing. Roberto Solimene (STEMS-CNR)
Dott. Marco Balsamo

PhD Student:
Francesca Di Lauro

Supervisor:
Prof. Gerardino D’Errico

PhD Course Coordinator:
Prof. Angela Lombardi

Abstract

Technological and economic development, population growth and the progressive urbanization of vast areas of the planet have caused an increase in global energy demand. The aim of this PhD Thesis is the energetic valorisation of a particular type of biomass, i.e., sludges from civil and industrial sources, aiming at the reduction of the material destined to disposal, and for their reuse as energetic vector. In particular, two types of sewage sludge were selected for these studies: i) a sludge from tannery industry, ii) a municipal sludge.

Among the thermochemical valorisation paths, the energy recovery of this waste has been first investigated through fluidised bed (FB) gasification, where the target product is syngas. In fact, there is a limited literature concerning the FB gasification of sludges, in particular when they come from specific industrial sources. Then, the innovative process known as hydrothermal liquefaction (HTL), where the target product is a bio-oil, has been applied to sludges. Both represent "StE" technologies ("sludge-to-energy").

For the gasification tests, the tannery sludge was considered. With its 34% C-content (dry basis), the material is appropriate for energetic valorisation. Since the sludge came from the tannery industry, particularly relevant was its chromium content. In the parent material, we did not observe the harmful hexavalent Cr species. Under the best conditions, a syngas with 42% H_2 (dry and N_2-free basis) and a lower heating value of 12 MJ/kg was obtained (in line with values commonly reported for syngas for energetic purposes), with a limited tar concentration and the production of bottom ash whose gasification degree was, for all practical purposes, complete. The Cr(VI) concentration in bottom and fly ashes was not higher than 10 mg/kg, while the Cr(total) concentration was 3−4 orders of magnitude greater, showing the right choice of operating conditions that did not promote the oxidation of Cr(III) to Cr(VI). Degrees of chromium oxidation in ash ranged, as a function of the operating conditions, from 0.008% to 0.120%.

For HTL, activities were conducted to limit thermal transients, to reduce the extent of collateral reactions that could lead to the increased formation of co-products. In addition, the effect of separation method of products, reaction time and temperature on products yield (Y) was assessed. Results showed that the upgrades to the heating system allowed to attain an average heating rate of about 8°C/min, determining improved performances vs. configurations characterized by lower heating rates. The centrifugation method was more effective, with respect to liquid-liquid extraction, yielding a bio-crude recovery up to 5.2% greater. The analysis of the effect of time and temperature on products yield has showed that higher temperatures, coupled with short reaction times, favour the distribution of products towards bio-oil formation. At 10 min and 350°C, an optimal value of both $Y_{bio\text{-}crude}$=43% and energy recovery of 59% was obtained (higher heating value HHV=30 MJ/kg) for the municipal sludge ($Y_{bio\text{-}crude}$=29.5% and energy recovery of 44% was observed for the tannery sludge, HHV=36 MJ/kg). The results obtained show that both processes are promising for the energy valorisation of sludge from both civil and industrial sources, and in the specific case of tannery sludge it is possible to limit the formation of hexavalent Cr in the reaction products.

The product of interest obtained is in the case of gasification a syngas useful both as an energy carrier and as chemicals, while in the case of hydrothermal liquefaction a liquid fuel, easily integrated into the production chain of liquid fuels in the transport sector.

Nomenclature 1

Chapter 1 – State of the art 2

1.1 Overview of the world energetic panorama 2

1.2 Energy from biomass 3

1.2.1 Types of biomass 3

Sewage sludge 4

Tannery sludge 6

1.2.2 Biomass conversion technologies 8

Aerobic/anaerobic digestion 9

Combustion 10

Pyrolysis 10

Gasification 11

Hydrothermal processes 12

1.3 Gasification process 14

1.3.1 Role of main operating parameters 15

Feedstock type and inherent moisture content 16

Particle size 16

Temperature 17

Gasifying mediums 17

Air equivalence ratio (AER) and steam-to-biomass ratio (S/B) 18

1.3.2 Types of gasifiers 18

1.4 Hydrothermal liquefaction process 20

1.4.1 Role of main operating parameters 21

Role of water 21

Effect of temperature 23

Effect of reaction time 24

1.4.2 Effect of macro-components 25

Cellulose, hemicellulose and lignin 25

Protein 26

Lipid and fat 27

Prediction models for bio-oil yield 27

1.4.3 Effects of catalyst 27

1.4.4 Types of reactor configurations for HTL 28

1.4.4.1 Batch reactors 28

Phase separation after the HTL process 29

1.4.4.2 Continuous reactors 30

1.5 Objectives of the research – Aim of the PhD Thesis 30

Chapter 2 – Materials and methods 33

2.1 Characterisation of municipal and tannery sludges and reaction products 33

2.1.1 Proximate analysis...34

2.1.2 Ultimate analysis...35

2.1.3 Determination of the higher heating value (HHV) and chlorine content 36

2.1.4 Determination of metal content by inductively coupled plasma-mass spectrometry (ICP-MS) 37

2.1.5 Speciation of chromium in tannery sludge by spectrophotometric method 38

2.1.6 Determination of the macro-compounds in the starting sludges..40

Analysis of lipids content 40

Analysis of carbohydrates content 41

Analysis of proteins content 41

2.1.7 Speciation of tar and incondensable gas through gas chromatography and mass spectrometry techniques...41

2.1.8 Infrared spectroscopy analysis for syngas speciation 43

2.1.9 Qualitative characterisation of bio-oil and aqueous phase by H-nuclear magnetic resonance (H-NMR) 44

2.1.10 Qualitative characterization of biocrude and aqueous phase by liquid chromatography-mass spectrometry (LC-MS) 45

2.2 Experimental apparatus (fluidised bed) for gasification tests 45

2.2.1 Experimental procedure for gasification tests 46

2.2.2 Operating conditions for gasification tests on tannery sludge 47

2.3 Experimental apparatus for HTL tests 48

2.3.1 Set-up of HTL apparatus...49

2.3.2 Experimental procedure for HTL tests 50

2.3.3 Protocol for the separation of HTL products..51

2.3.4 Matrix of experimental tests..55

Chapter 3 – Characterisation of tannery and municipal sludges 57

3.1 Proximate analysis 57

3.2 Ultimate analysis 57

3.3 Higher heating value and chlorine content 58

3.4 Metal concentration by ICP-MS...59

3.5 Total and hexavalent chromium 61

3.6 Determination of the biochemical components in the starting sludges 61

Chapter 4 – Fluidized bed gasification on tannery sludge: results 63

4.1 Outcomes of fluidized bed gasification tests 63

4.3 Bottom and fly ash characterization with chromium speciation 71

Chapter 5 – Hydrothermal liquefaction process on sewage sludges: results 75

5.1 Choice of steel for reactor construction 75

5.2 Set-up of the experimental apparatus and test protocols 78

5.2.1 Analysis of the water thermodynamic state..78

5.2.2 Comparison of reactor configurations 79

5.2.3 Effect of separation protocol on bio-crude recovery 81

5.3 Effect of reaction time/temperature on product distribution 83

5.3.1 Preliminary study on the effect of TS-MS mixtures on biocrude yield..............................88

5.4 Biocrude characterisation 90

5.4.1 Determination of the metal content by ICP-MS in the biocrude and co-products...............91

Chromium speciation 93

5.4.2 Qualitative chemical composition analysis of biocrude and aqueous phase 94

Chapter 6 – Comparison of gasification and hydrothermal liquefaction processes 103

Chapter 7 – Final remarks and future developments 107

References published by the PhD Student 109

References 110

Collection of papers published by the Ph.D. Candidate 125

Nomenclature

AAS	- Atomic Absorption Spectroscopy
AER	- Air Equivalence ratio
AP	- Aqueous Phase
BC	- Biocrude
CC	- Carbon Efficiency
Cen	- Centrifugation
CGE	- Cold Gas Efficiency
DCM	- Dichloromethane
EF	- Entrained flow gasifiers
ER	- Equivalence Ratios
FB	- Fluidized bed gasifier
FXB	- Fixed bed gasifiers
GC-MS	- Gas Chromatography-Mass Spectrometry
HHV	- Higher Heating Value
H-NMR	- H-Nuclear Magnetic Resonance
HTC	- Hydrothermal Carbonisation
HTG	- Hydrothermal Gasification
HTL	- Hydrothermal Liquefaction
HTP	- Hydrothermal Processing
ICP-MS	- Inductively Coupled Plasma-Mass Spectrometry
ID	- Internal Diameter
L-L	- Liquid-Liquid extraction
LC-MS	- Liquid Chromatography-Mass Spectrometry
LHV	- Lower Heating Value
MS	- Municipal Sludge
P	- Pressure
PAH	- Polycyclic Aromatic Hydrocarbons
PID	- Proportional-Integral-Derivative
S/B	- Steam-to-biomass ratio
SCW	- Supercritical water
SF	- Separating Funnel
SI	- Severity Index
SR	- Solid Residue
SS	- Sewage Sludge
StE	- Sludge-to-Energy
STP	- Standard Temperature and Pressure
T	- Temperature
t	- Time
TCD	- Thermal Conductivity Detector
TS	- Tannery Sludge
UV-Vis	- UV-visible
V	- Volume
W	- Weight
WPS	- Water-soluble products
Y	- Yield

Subscript:

db	- Dry basis
dafb	- Dry ash-free basis

Chapter 1 – State of the art

1.1 Overview of the world energetic panorama

From data published by the United Nations in the "World Population Perspective" of 2022 (DESA - UN, 2022), the current world population amounts to 7.9 billion individuals, and it is projected to grow over the next 80 years, reaching 8.5 billion in 2030 and 9.7 billion in 2050 (Table 1.1). The direct consequence of this is the growing demand for energy in large areas of the planet with a total world energy supply in 2020 exceeding 600000 PJ, mainly satisfied by fossil fuels (International Energy Agency, Key World Energy Statistics 2021), distributed in a heterogeneous way on the Earth's surface in form of:

1. oil,
2. coal,
3. natural gas.

Table 1.1 – Population of the world in the year 2022, 2030 and 2050 (DESA - UN, 2022).

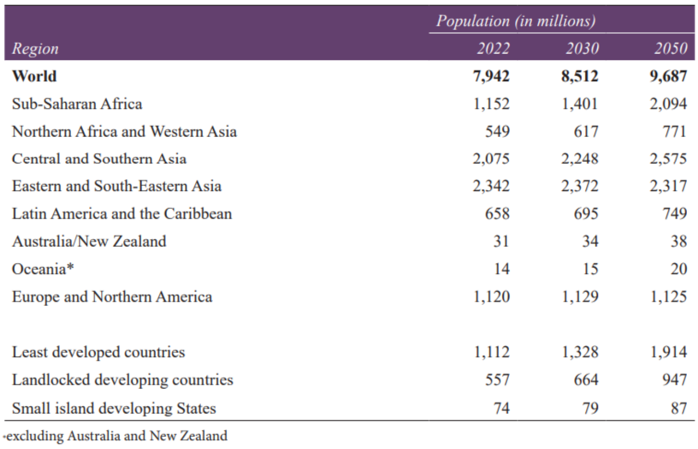

	Population (in millions)		
Region	*2022*	*2030*	*2050*
World	**7,942**	**8,512**	**9,687**
Sub-Saharan Africa	1,152	1,401	2,094
Northern Africa and Western Asia	549	617	771
Central and Southern Asia	2,075	2,248	2,575
Eastern and South-Eastern Asia	2,342	2,372	2,317
Latin America and the Caribbean	658	695	749
Australia/New Zealand	31	34	38
Oceania*	14	15	20
Europe and Northern America	1,120	1,129	1,125
Least developed countries	1,112	1,328	1,914
Landlocked developing countries	557	664	947
Small island developing States	74	79	87

*excluding Australia and New Zealand

Fossil (from the Latin "fodere"="to dig") fuels represent hydrocarbons that have been stored over a period of millions of years deep within the Earth. When we combust these sources of carbon for our energy needs, we create an imbalance in carbon content in the atmosphere. Majority of the anthropogenic increase in carbon dioxide has been due to the burning of fossil fuels, which is claimed as one of the biggest drivers of global warming (Balsamo et al., 2023). Phenomena such as climate change as a result of greenhouse emissions are encouraging a divert towards the development of alternative energy, to diverse the current energy portfolio and eventually replace fossil fuel usage (Fernando et al., 2006). In this perspective, there is an increasing interest in renewable energy, which are clean energy sources available to all, whose main feature lies in the ability not to run out at the end of the cycle (Tregambi et al., 2019; Di Lauro et al., 2021; Bhuiyan et al., 2022). They are the alternative to fossil fuels and can contribute to the diversification of energy supply, the reduction of greenhouse gas emissions and the reduction of dependence on volatile and unreliable markets for fossil fuels, in particular for oil and gas (a matter that is tragically topical at the time this note is being drafted) with the prospect of greater energy independence of Countries where there are no deposits.

However, fossil fuels remain today the main source of energy livelihood, as shown in Figure 1.1 published by the U.S. Energy Information Administration in the 2022 Monthly Energy Review (EIA MER, 2022), which traces, with annual periodicity from 1950 to 2020, the energy production (in quadrillions of Btu) related to the different sources.

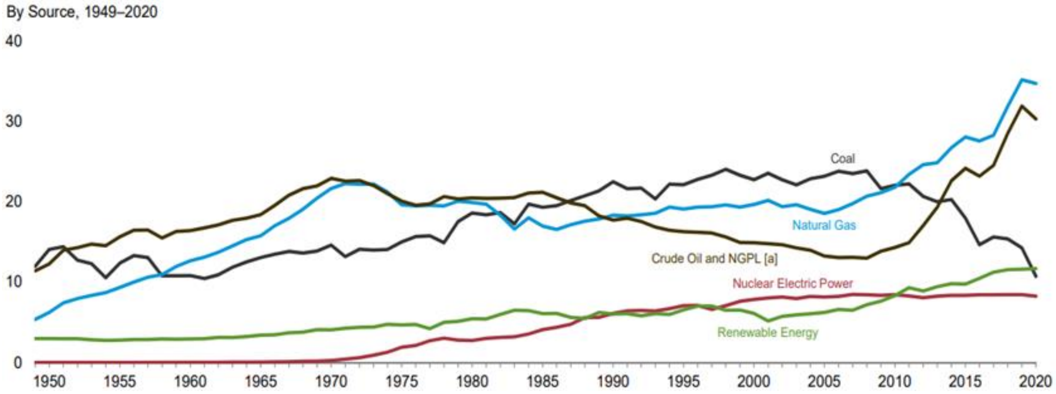

Figure 1.1 – Annual primary energy production from 1950 to 2020 (EIA MER, 2022).

In this context, biomass can represent a promising option to meet the need of diminishing the dependence on fossil fuels, as there is so much biomass being generated everyday – naturally and through human intervention. Biomass includes everything we grow and the tons of waste including agricultural residues, food waste, sewage sludge etc. These are rich sources of carbon and hydrogen which can be concentrated to produce energy vectors. These cheap, renewable and do not polluting alternative energy resources are highly needed to meet current energy demand and represent one of the most important issues closely related to sustainable human society development in 21st century.

1.2 Energy from biomass

Biomass is a solid carbon neutral product generated by natural as well as anthropogenic processes, that can reduce CO_2 emissions and atmospheric pollution. Biomass is a material of biological origin, and can be converted into solid, liquid, and gaseous fuels through different conversion processes (Nussbaumer, 2003; Babu, 2008; Sikarwar et al., 2016). Biomass resources mainly include wood and forestry residues/by-products (sawdust, bark, treetops, lignin), agricultural crops and crop residues (wheat/rice straws, corn stover), marine products, municipal solid wastes (MSW), sewage sludge, waste streams from animal farms (manure) and food processing (Xu and Etcheverry, 2008; Yang et al., 2009; Yang et al., 2011).

1.2.1 Types of biomass

The term biomass may be used to indicate any organic material derived from plants, animals, or human source. Irrespective of the source, all types of biomasses are composed by a combination of biochemical components: cellulose, lignin, carbohydrates, proteins, and lipids. However, the proportion of these components varies significantly depending on the matrix. Agricultural waste can refer to any residue produced by agri-food industries such as corn stover, rice, roots, bagasse, straw residues, coconut etc., while forest woody material mainly consists of residues or by-products from manufacturing processes, biomass plantation and tree residues (Forster-Carneiro et al., 2013).

Lignocellulosic biomass is the most abundant organic material on the Earth and differs to other alternative energy sources because the resource is varying and their utilisation to energetic carrier takes place through many conversion processes (Rambo et al., 2015). It is also sometimes referred to as fibre and can be divided in three major polymers: cellulose, hemicellulose, and lignin. Moreover, its use is not in contrast with the availability of food. On the other hand, compared with agricultural biomass, forest woody biomass as a feedstock has many advantages in terms of production, storage, and transportation biomass for conversion (Zhu and Pan, 2010). For example, due to high lignin content and low ash composition, forest biomass represents a valuable feedstock for energy utilisation (Achinas and Euverink, 2016; Yu et al., 2021).

Municipal and industrial wastes is also another interesting source to produce biofuel (Barampouti et al., 2019). These materials can originate either from residential or non-residential sources, and the utilisation of this waste limits environmental problems associated with the disposal of household waste, food processing by-products, processing papers and black liquors (Limayem and Ricke, 2012). A significant volume of the municipal/industrial waste is, in fact, discharged into public sewers, streams, lakes, landfills, and other sinks, at great cost to the industry and/or the community that accepts these effluents.

Another type of biomass that attracts great interest as a means of energy production is represented by algae (Bhattacharya and Medlin, 1998). From their size, algae can be distinguished as microalgae and macroalgae. Generally, a macroalga is referred to when considering large aquatic photosynthetic plants that can be seen with the naked eyes. They usually have higher cellulose and ash content but lower lipid and protein content than microalgae. Microalgae refer to the algae that can only be seen with the aid of a microscope and they are often cultivated in extensive or intensive artificial environments – the latter being of more interest with regard to biofuels. Intensive autotrophic microalgal biomass cultivation requires substantial resources to achieve high rates of conversion and productivity yields (Biller et al., 2015). The two most common cultivation methods are through open-pond systems or some variant of photo-bioreactors (PBR) (Chisti, 2007). Research in the intensive cultivation of microalgae has been conducted since the 1950s (Spoehr and Milner, 1949). Subsequent researches into intensive cultivation was found in reviews by Goldman (Goldman, 1979), and Tapie and Bernard (Tapie and Bernard, 1988). Algae are often promoted as an ideal “next generation” biofuel feedstock because they can produce intracellular lipid droplets, which are high-density energy storage molecules that can be readily converted into biodiesel. For a traditional algae-to-biodiesel technology, lipid content was the only criterion for screening suitable algal species (Williams and Laurens, 2010).

Sewage sludge

Sewage sludge (SS) is the main waste from wastewater treatment, containing high percentage of water (usually in the range of 80–90%$_{vol.}$). It is generally the solid residue obtained from the wastewater treatment and can be produced in two steps during the process. The wastewater treatment and the generation of sewage sludge is shown in Figure 1.2.

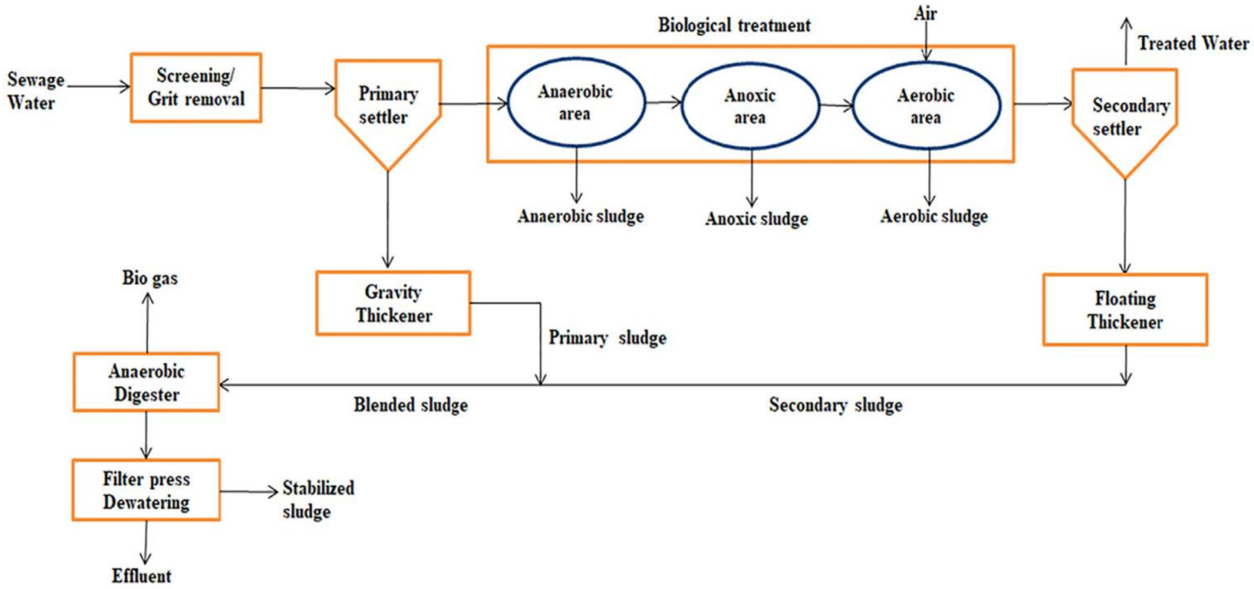

Figure 1.2 – The schematic of a typical wastewater treatment plant (Bora et al., 2020).

Primary sludge is generated during the removal of insoluble matters such as granular materials, grease, and scum from wastewater by screening followed by coagulation, oil separation, sand removing and sedimentation (Rushdi et al., 2013). The settled primary sludge contains mainly water (between 97% and 99%) and highly putrescible organic matters (Appels et al., 2008). Secondary sludge is generated as a result of biological treatment (also called activated sludge process) of primary treatment effluents. The activated sludge is rich in dissolved organic substances and consists of a complex flake structure that settles on the bottom of the tank, then collected and sent to the drying section.

More generally, sludge is a mixture of organic or volatile matters (such as proteins, carbohydrates, and lipids), inorganic matters (ash, metal, metal oxides) and associated water (Tyagi and Lo, 2013). The main components of the sludge that are technically and economically feasible to recover are nutrients such as primary nitrogen and phosphorous, and energy that can be obtained from organic carbon compounds.

The management of SS is a growing issue around the world. The remarkable production of sludges from civil and industrial sources and the expensive operating costs associated with their landfilling (ca. 80–140 €/ton) pose serious environmental concerns. In fact, level of pathogens in sludge is unsuitable for human contact, so it must be processed and/or disposed of with more complex and expensive methods than normal waste products (Xu and Lancaster, 2008; Cieślik et al., 2015).

Mostly of sludge is disposed of using expensive, unsustainable methods such as incineration and landfilling. In addition, these disposal methods become increasingly complex when associated with industrial sludges that have characteristics, in terms of pathogens or heavy metals, that do not always allow landfilling or complete combustion if not pre-treated with specific pathogen removal techniques. Nowadays, one of the primary goals of wastewater treatment plants is to develop more environmentally friendly processes to reduce the volume of sludge for disposal and to convert sludge into bio-energy. This has shifted the view to sewage sludge from a waste to be treated and disposed of, to a renewable resource for energy recovery. It is expected, therefore, that the upcoming sludge management efforts will concentrate on the recovery and reuse of value-added products from sludge (Judex et al., 2012; Kokalj et al., 2017; Prestigiacomo et al., 2019; Ghodke et al., 2021).

Being the sludge reuse in agriculture limited by the presence of heavy metals, organic micro-pollutants and pathogens (but also dangerous compounds, e.g. heavy metals, hormones, pharmaceuticals or pathogens). The most optimal alternative solutions for sludge purification are methods based on elevated temperatures, which eliminate pathogens (Carraturo et al., 2020). These methods include: sludge incineration, co-incineration, gasification, pyrolysis, wet oxidation, plasma technologies, or hydrothermal treatment (HTT). Among the different forms in which sewage sludge can be converted (syngas, biochar, bio-oil), research in recent decades is placing a strong emphasis on liquid fuels to be included in the production chain for the transport sector, that currently covers a good share of global energy demand. The conversion of sludges into bio-oils (high energy density liquids candidate to produce advanced “drop in” biofuels) can represent a promising route to limit the risks of soil/groundwater pollution associated with sludges disposal, and a way to obtain an added-value product (Lyu et al., 2015; Oladejo et al., 2019), thus increasing the sustainability of wastewater treatment plants and contributing to the needs of developing credible/sustainable biofuel production processes. However, the biomass as it exists cannot be directly used in the refineries, thus the role of a biomass-to-fuel conversion process is to transform the biomass to energy dense fuel that can be used in the existing infrastructure. Biomass-derived fuels are converted to a highly viscous liquid energy source referred to as biocrude (or bio-oil), which has similarities to the fossil fuel crude oil visually and in composition. The obtained biocrude is a mixture of hydrocarbons, oxygenates and nitrogenates, which can be refined to petroleum products and valuable chemicals in the existing petroleum refineries (Zhu et al., 2013). Before using the sewage sludge for energy recovery by thermochemical processes, usually, this moisture content must be reduced to minimum levels using several available drying techniques. Much of this water can be removed via drainage, thickening, or mechanical dewatering, obtaining a dewatered sewage sludge that contains about 73–84% of moisture (Chan and Wang, 2016). The removal of the remaining moisture content can only be achieved through thermal drying, which can bring the moisture content down to about 6%. The need to dry the SS before its use involves an energy expenditure that penalises the efficiency of the thermochemical processes.

Tannery sludge

The Italian leather industry comprises about 1200 companies. Italy, in 2019, produced 128 million of m^2 of finished leathers for a production value of 4.9 billion euros, of which 3.6 billion euros account for export. The tannery districts are nowadays using advanced treatment plants that are reaching high levels of specialisation for tannery discharges (UNIC Sustainability Report 2020). The obtained sludge is rich in chromium (the removal of chromium by wastewater is greater than 99.4%). The huge volume of sludges generated by the leather industry, with a yearly global production of solid wastes derived from the tanning process estimated to be on the order of 1 ton per ton of raw leather, poses economic and environmental issues associated with their landfilling, mainly due to the relevant amount of chemicals adopted in the tanning process; on average, 2 kg of chemicals are used to produce 1 m^2 of leather (Montagnaro and Caracciolo, 2022). In the circular economy perspective, the valorisation of the organic content of tannery sludge (TS) to produce energy vectors is a promising strategy to overcome the abovementioned issues ("sludge-to-energy (StE)" strategy).

The tanning sludge, deriving from the purification treatment of the relative wastewater, has a composition that can vary within very wide limits, depending on the production cycle, the type of treated leather hides and treatments. Table 1.2 shows the typical composition ranges of dehydrated sludge obtained from the effluent purification of some Italian tanneries.

Interestingly, although the values refer to a generic centrifuged sludge, the moisture content is still relatively high. Usually, a sludge coming out of the purification treatment has a moisture content of 70–90%, and this value must be reduced not only for landfilling, but also and especially if thermo-conversion treatments are provided (Mao et al., 2016), otherwise not effective with so high humidity levels to be removed. In fact, dehydration operations are energetically expensive, posing an economic, environmental, and procedural problem. Therefore, such consumptions will very much affect the global energy balance, and therefore the efficiency, of any sludge thermo-conversion process. Among the pollutants present in consortia sludge, particular attention should be paid to the high levels of Cr. This amount of Cr is attributable to the tanning process, in which Cr(III) basic salts are used. In a conventional tanning process, about one third of the chromium adopted is not fixed to the leather and therefore flows into the wastewater to be treated through the consortium sewage plants; it is then separated by precipitation from the effluent, in the form of chromium hydroxide ($Cr(OH)_3$), and it is found at the end of the purification process in tannery sludge.

Among currently available StE technologies, the thermochemical treatments such as combustion, pyrolysis, and gasification appear to be particularly promising due to both the possibility of fixing harmful metals in the solid residues and the high conversion efficiency of organic compounds, the latter being generally greater than 80% (Zhou et al., 2021). Thermochemical processing of sludges has also the advantage of characteristic reaction times (from seconds to minutes) much shorter than those required in biochemical conversion routes such as anaerobic digestion (in the order of days/weeks), where the converted organic fraction does not exceed 60% (Oladejo et al., 2019). While the direct combustion of several types of sludges is a common practice, gasification and pyrolysis processes are still limitedly explored for the valorisation of this residue (Eurostat 2015). Among the abovementioned thermal processes, the direct combustion of a tannery sludge suffers critical environmental issues that limit its applicability, as the full oxidising conditions that are realized in the combustion chamber would unavoidably lead to the oxidation of Cr(III) (typically found in tannery sludges) to the more harmful Cr(VI) state (Kavouras et al., 2015). Several studies have been carried out to limit undesired chromium release from sludge combustion, such as pre-treatment with hydroxyapatite to reduce heavy-metal volatilisation along incineration, or post-combustion stabilization of Cr-rich ashes through vitrification with SiO_2, Na_2O, and CaO (Tang et al., 2013; Varitis et al., 2017).

Table 1.2 – Composition of centrifuged sludge obtained by purification of tannery wastewater (Abou Elmagd and Mahmoud 2014, Wystalska and Sobik-Szołtysek, 2019).

Composition (wt.%)	
Moisture	55–75
Organic matter	40–75
Inorganic matter	25–60
Organic carbon	21–38
Ammonium nitrogen	0.1–1.6
Organic nitrogen	1.3–7.0
Phosphorus	0.01–0.06
Chromium (III)	0.8–5.0
Aluminium	0–5.0
Iron	0.6–12
Calcium	1.0–15
Sulphur (total)	0.7–7.0

1.2.2 Biomass conversion technologies

There are multiple processes to convert biomass to energy: combustion, pyrolysis, gasification, torrefaction, etc. All these technologies have different chemicals or energy carriers as their objective, also each of them has specific needs for the feedstock and the kind of output energy they can provide (Sharma et al., 2014). For example, direct combustion of biomass may be promising in power plants to produce electricity but not in internal combustion engines where there is a need for liquid fuel. Instead, pyrolysis can produce liquid fuels but requires a feedstock that have a low moisture content, as the preventive drying of the raw material makes this process less energy efficient and more expensive. The choice of the conversion process depends on different factors: i) biomass feedstock type and properties, ii) end-used requirements, iii) environmental standards, iv) economic condition. In general, as the reader can see in Figure 1.3, the conversion of biomass can be divided into two main technologies: i) biochemical technologies which degrades biomass with enzymes and microorganisms, ii) thermochemical conversion technologies which use heat to breakdown the biomass polymer.

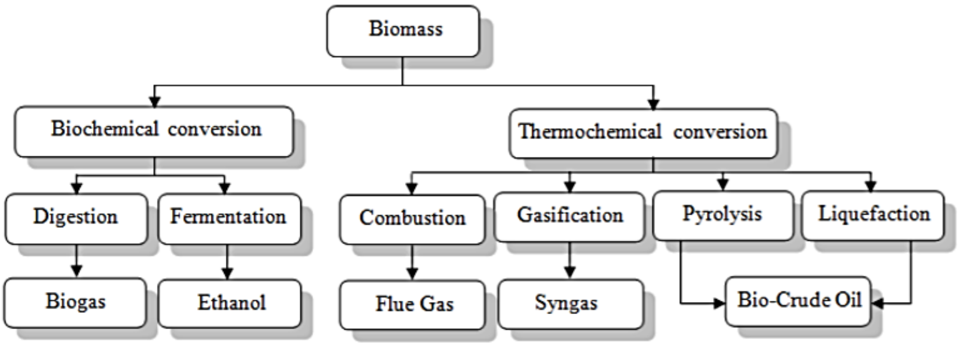

Figure 1.3 – Biomass conversion technologies (Nazari et al., 2018).

The degradation of biomass through biochemical processes occurs naturally. Biochemical conversion is the process by which biomass is converted into gas (CO_2/CH_4), waste (compost or fertilizer) and water or ethanol (C_2H_5OH), using microorganisms. This processes mainly refer to: i. aerobic fermentation producing compost, carbon dioxide and water, ii. anaerobic fermentation producing fertilizer and gas (CH_4/CO_2), and iii. alcoholic fermentation producing ethanol (C_2H_5OH), carbon dioxide (CO_2) and waste.

Thermochemical conversion technologies are based on the thermal breakdown of biomass to produce valuable chemicals and fuel. These processes do not necessarily produce useful energy directly; under controlled temperature and oxygen content conditions, the original biomass feedstock may be converted into more convenient forms of energy carriers, such as producer gas (based on hydrogen), oils or methanol (Sharma et al., 2014). Thermochemical conversion technologies include combustion, gasification, pyrolysis, hydrothermal processing, with generation of biogas, biocrude and/or biochar.

Aerobic/anaerobic digestion

In recent years, several biochemical methods have been studied, with low environmental impact, characterised by limited energy consumption, mainly with regard to obtaining biogas, ethyl alcohol, compost and proteins from waste biomass (Saxena et al., 2009; Ward et al., 2014; Sawatdeenarunat et al., 2015). Biochemical systems are among the most promising and environmentally sustainable alternatives to reducing carbon dioxide levels in the atmosphere, as biomass can act as a carbon reservoir, to support or directly replace fossil fuels without any net contribution to atmospheric CO_2, if produced and used sustainably.

Anaerobic fermentation is used to produce biogas: the waste is kept without oxygen for about 2–8 weeks at about 40 °C, producing a gas of general composition: 65–70% methane, 35–30% carbon dioxide and traces of other gases (e.g., H_2S and H_2); it has an approximate calorific value of about 26 MJ/m^3 (White and Plaskett, 1981). The anaerobic bioconversion of lignocellulosic materials into CH_4 and CO_2 is performed by a number of microorganisms in several stages: hydrolytic, acidogenic, acetogenic and methanogenic. The last stage is very important and plays a significant role in bioconversion. The activity of methanogenic bacteria, which are able to convert organic acids into methane and carbon dioxide, depends on temperature, pH and concentration of substrates and minerals. However, the anaerobic digestion of cellulosic materials in digesters is a slow process, mainly due to lignin.

Some natural anaerobic ecosystems, however, are efficient in degrading lignocellulosic materials. Typical examples are the anterior stomachs of ruminants: these microorganisms have been shown to be able to convert a wide range of lignocellulosic material into biogas, with efficiencies between 50 and 60% (Kivaisi and Eliapenda, 1992). Another method is to produce landfill gas (a mixture of methane and other gases). The degradation of the organic component of waste in landfills is a process carried out by a succession of microbial populations: the bacteria present in the waste and in the soils act as the initial inoculum for the degradation of waste. Initially, this degradation is aerobic: C and H is converted into CO_2 and water through a phase in which strongly exothermic reactions are exploited, and the increase in waste temperature increases the biochemical activity. After that, once the amount of oxygen available is exhausted, the methanogenic microbes start their anaerobic metabolic activity and produce CH_4. However, if the aerobic phase continues for a prolonged period, the final methane yield may decrease as valuable carbon is consumed. Typically, it is estimated that 1% of biodegradable C is lost at this stage in CO_2, and a further 1% is lost in leachate (Richards et al., 1992).

Combustion

Biomass combustion is one of the earliest and fastest method for energy use. This process has been adapted to produce liquid transportation fuels and chemical feedstocks. Currently, the direct combustion of biomass continues to be the predominant pathway for bioenergy worldwide (Bridgwater, 2003). During biomass combustion, hot gases are produced at temperatures around 800–1000 ºC. Meanwhile, for complete combustion, heat is produced as a result of the oxidation of carbon- and hydrogen-rich biomass to CO_2 and H_2O, respectively. Any type of biomass can be burned, however, in practice, only biomasses with a moisture content of less than 50% are applicable for a feasible combustion process (McKendry, 2002). Due to this condition, the biomass with high moisture content need to go for pre-dried process before being introduced to the process, with related energy disadvantages. Moreover, the pre-treatment of biomass includes also palletisation and briquetting, torrefaction and slow pyrolysis. The two latter determine an improves of biodegradability and reduce the volume and bulk density. Details on kinetics of combustion process are complex and imperfect combustion will result in the release of intermediate compounds. These intermediates may result in environmental air pollutants such as CH_4, CO, while sulphur and nitrogen contents cause the emission of SO_x and NO_x, respectively (Tanger et al., 2013).

Pyrolysis

Pyrolysis is the thermochemical decomposition of dry organic biomass, in the complete absence of oxygen, into bio-oil, biochar, and syngas at temperatures between 300–600 °C. Based on thermogravimetric analysis (TGA) of biomass, there are three steps characterizing a typical pyrolysis process. The first stage, the pre-pyrolysis, occurs between 120 and 200 °C with a slight weight loss observed when some transformations occur, such as the breakdown of part of the chemical bonds constituting the biomass, the appearance of free radicals and the formation of carbonyl groups, with a corresponding release of small amounts of water, CO, and CO_2. The second stage is the main pyrolysis process, during which solid decomposition takes place, accompanied by significant weight loss from the biomass initially fed. The last stage is the continuous devolatilisation of the char, caused by the further splitting of the bonds C-H and C-O (Maschio et al., 1992). Depending on the reaction temperature, heating rate and residence time, pyrolysis can be divided into flash, fast, and slow.

Flash pyrolysis also referred to as ultra-fast pyrolysis is characterised by high heating rates (10^3–10^4 °C/s) and temperature (900–1300 °C), short residence time (less than one second), and rapid cooling of the pyrolysis vapour as well as rapid removal of char from the system (Amutio et al., 2012), so due to the reduction in secondary cracking reactions in fash pyrolysis, the yield of the liquid fraction of the products (bio-oil) is maximised to about 60–75 wt% of the total products.

Fast pyrolysis is a process with a high heating rate (up to hundreds of °C/min) and a short residence time. Short reaction times combined with a high temperature generally result in a higher yield of liquid product. Typically, fast pyrolysis is associated with an extremely short residence time (~1 s) and the reaction temperature is about 100 ºC higher than that of slow pyrolysis (500 ºC vs. 400 ºC) (Yanik et al., 2007). Liquid products consist of an aqueous phase containing several low molecular weight compounds and a non-aqueous phase (tar) comprising a variety of insoluble high molecular weight organic aromatic compounds. The bio-oil, the main product of rapid pyrolysis, is a potential liquid fuel that can be easily stored and transported. Compared to heavy petroleum fuel oil, bio-oil has a high water content (15–30 wt.%), a low pH (<3), a much higher oxygen content (35–40 wt.%), as well as a lower heating value (higher heating value (HHV) of 16–19 MJ/kg) (Czernik and Bridgewater, 2004).

Several factors must be considered to maximise the yield of the liquid in a rapid pyrolysis process. These may include: fine grain size (less than 1 mm), carefully controlled temperature (between 450 ºC and 550 ºC), high heating rate (>200 ºC/s), short hot steam residence time and rapid vapour cooling (Yanik et al., 2007). In addition to bio-oil production, fast pyrolysis generates H_2 at high temperatures (700–1000 °C).

In contrast, slow pyrolysis with relatively lower reaction temperatures and longer residence times would produce similar amounts of liquid, solid and gaseous products. A moderate or slow pyrolysis process, with a relatively long steam residence time and a low heating rate, has been used to produce coal for thousands of years. The solid product, the char, can be used in a wide range of industries, from domestic use, metallurgical or chemical use as raw material for the production of chemicals, activated carbon, adsorbents, soil improvers and pharmaceuticals. Higher char yield can be obtained from biomass with higher lignin content and lower hemicellulose content.

Gasification

Gasification has also been named as indirect liquefaction since its product, “syngas” or “producer gas”, could be further converted into liquid fuel through the “Fischer-Tropsch (FT)” reaction. Gasification is the exothermic partial oxidation (typically 35% of the demand for O_2 required for complete combustion) of biomass with optimised process conditions for high yields of CO, H_2, CH_4, and CO_2.

It is considered a partial combustion process. In general, combustion focuses on heat generation, while the purpose of gasification is to create gaseous products that can be used directly for combustion or stored for other applications. In addition, gasification offers many advantages as it is considered to have a lower environmental impact than combustion due to lower emissions of toxic gases into the atmosphere and more versatile use of solid by-products, the use of compact equipment with a relatively small footprint, accurate control of the oxidation process and high thermal efficiency.

Syngas (heating value ~ 4–6 MJ/m^3) also finds applications, ranging from steam or heat generation to hydrogen/natural gas production, as fuel cell feed, and for the synthesis of several chemical compounds. For example, high quality cleaned syngas can also be used as feedstock to produce methanol and other important chemical building blocks (McKendry, 2002).

Hydrothermal processes

Biomass conversion through hydrothermal processes is one of the promising techniques to produce solid, liquid, or gaseous fuels. On the most fundamental level, the goal of the hydrothermal process is to replicate and enhance the extreme environmental conditions which transformed ancient biomass into petroleum crude. This process is carried out under elevated temperatures, between 200–500 °C, with suitable pressures (40–200 bar), to keep the aqueous slurry in a single liquid state. Eliminating the liquid-to-gas phase change results in considerable energetic savings that cannot be achieved using other thermochemical conversion processes, which require dry biomass. Additionally, the special properties of water under hydrothermal conditions can significantly enhance biomass reforming into energy dense products.

The main advantage of hydrothermal processing (HTP) is that wet biomass, typically with a moisture content in the range of 70–90%, can be directly processed without need for the drying process, which requires high energy costs. In fact, HTL conditions improves the dewaterability of sewage sludge. Moreover, HTP, with its wide range of temperature and pressure, has the capacity to process many kinds of biomass for the conversion into products like biochar, biocrude or gases as fuels, and useful chemicals. A basic representation of HTP is shown in Figure 1.4.

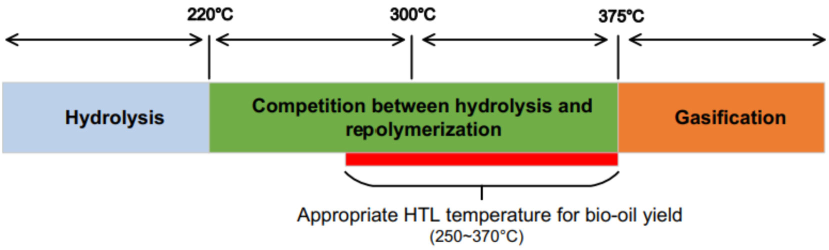

Figure 1.4 – Process types in the temperature range of HTP (Guo et al., 2015).

Depending on the processing temperature and pressure, hydrothermal processing can be divided into three main regions, namely: hydrothermal carbonisation (HTC), hydrothermal liquefaction (HTL) and hydrothermal gasification (HTG). To understand the behaviour of biomass in hydrothermal conditions, Figure 1.5 gives a phase diagram for water, also reporting values for the dielectric constant.

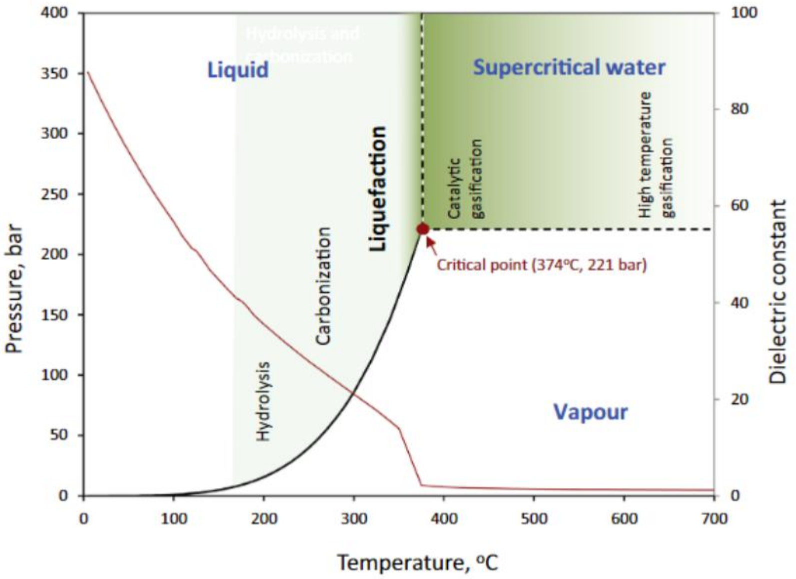

Figure 1.5 – Pressure-temperature phase diagram for water, and static dielectric constant for water at 200 bar as a function of temperature (Tran, 2016).

This figure represents the pressure-temperature phase diagram of water in sub-/super-critical conditions. Water is considered an environmentally friendly medium for most organic reactions. Supercritical water (SCW) can act both as a reagent and as a catalyst for these processes. Under this condition, water properties such as ionic product, density, viscosity, and dielectric constant, show rapid changes. SCW is an excellent solvent for most homogeneous organic reactions due to the high miscibility and absence of any phase boundary. It acts as a "non-polar" solvent capable of reacting with different compounds. The dielectric constant, an indicator of the effectiveness of the hydrogen bond, is 80 at normal temperature and pressure, and it is substantially reduced to 5 at the critical point, typical of a non-polar solvent. This is usually due to the reduction of the number of hydrogen bonds with increasing temperature. As a result, the affinity of water to hydrophilic molecules increases (Archer and Wang, 1990; Kumar et al., 2018).

In general, HTC takes place at relatively low temperature and pressure (<250 °C and 20–100 bar) for several hours (Nizamuddin et al., 2017) and converts biomass into a solid fuel together with the by products including a large amount of liquid phase (process water) and a little gas (mainly CO_2 and traces of CH_4) (Tekin et al., 2014; Alvarez-Murillo et al., 2016; Wang et al., 2019). The main goals during HTC is the conversion of lignocellulosic components in biochar (Wang et al., 2018; Sharma et al., 2020; Wilk et al., 2022).

Increasing the temperature and pressure in the ranges of 250–400 °C and 40–200 bar, respectively, reactive processes that come into play lead mainly to the production of a liquid fuel, and the process is called hydrothermal liquefaction. The HTL process (Montagnaro et al., 2021) allows to obtain a bio-oil with lower oxygen content and higher heating value compared to other thermochemical processes, such as pyrolysis. Nevertheless, the biocrude contains a higher oxygen content than crude oil, which causes negative effects including instability (Czernik and Bridgwater, 2004). The possibility of obtaining a liquid fuel – to provide a drop-in-fuel replacement for petroleum – is very important in a historical period where crude oil is the principal energy resource for the world's transportation sector.

At higher temperature and pressure than those characteristic for HTL (i.e., after critical point of water), the free-radical reaction pathway dominates; this condition is favourable for hydrothermal gasification which takes place at supercritical water condition (Kruse, 2009). Under pressurised hot water, biomass macro-components fragment into their liquid components and, then, into their gaseous components (mainly CO_2, CH_4 and H_2).

1.3 Gasification process

Gasification is a key process for the thermochemical conversion of biomass. Biomass gasification has a high potential for application in waste processing compared to other existing techniques such as landfilling, incineration, etc., because it can accept a wide variety of inputs and multiple useful products can be produced. In the presence of a gasifying agent, biomass is converted to a multifunctional gaseous mixture, usually defined syngas (or synthesis gas), which can be used to produce energy (heat and/or electricity generation), chemicals (i.e., ammonia), and biofuels. Furthermore, a solid residue after biomass conversion (char) is generally found (Bridgwater, 2003; Sikarwar et al., 2017; Molino et al., 2018). Syngas consists of a mixture of CO, H_2, CO_2, CH_4, that represent the primary components, and H_2O, H_2S, NH_3, tar, and other trace species, with a composition dependent on feedstock type and characteristics, operating conditions, such as gasifier temperature and pressure, type of bed materials and gasifying agent, and gasification technology (Molino et al., 2013, Rodríguez-Olalde et al., 2015).

Usually, gasification is divided into three steps: drying (endothermic step) and pyrolysis (endothermic step), oxidation (exothermic stage), and reduction (endothermic stage). Pyrolysis (1.1) is the first stage of biomass gasification. During this phase, raw materials are decomposed into tar and volatile hydrocarbon gases containing certain amounts of hydrogen before gasification reactions begin. Subsequently, a series of homogeneous and heterogeneous reactions takes place in the gasifier:

$$C_nH_mO_k \rightarrow CO + H_2O + CH_4 + CO_2 + H_2 + (C_2\text{-}C_5) \qquad \text{Endothermic} \qquad (1.1)$$

$$C + O_2 \rightarrow CO_2 \qquad \Delta H = -406\ kJ/mol \qquad (1.2)$$

$$C + \frac{1}{2}O_2 \rightarrow CO \qquad \Delta H = -111\ kJ/mol \qquad (1.3)$$

$$H_2 + \frac{1}{2}O_2 \rightarrow H_2O \qquad \Delta H = -242\ kJ/mol \qquad (1.4)$$

$$C + H_2O \rightarrow H_2 + CO \qquad \Delta H = 131\ kJ/mol \qquad (1.5)$$

$$C + 2H_2O \rightarrow 2H_2 + CO_2 \qquad \Delta H = 90\ kJ/mol \qquad (1.6)$$

$$C + CO_2 \rightarrow 2CO \qquad \Delta H = 172\ kJ/mol \qquad (1.7)$$

$$C + 2H_2 \rightarrow CH_4 \qquad \Delta H = -75\ kJ/mol \qquad (1.8)$$

$$CO + H_2O \rightleftarrows H_2 + CO_2 \qquad \Delta H = -42\ kJ/mol \qquad (1.9)$$

$$CO + 3H_2 \rightleftarrows CH_4 + H_2O \qquad \Delta H = -206\ kJ/mol \qquad (1.10)$$

$$Tar + H_2O \rightarrow H_2 + CO_2 + CO + C_nH_m \qquad \text{Exothermic} \qquad (1.11)$$

Reactions (1.2), (1.3), (1.4) are oxidation reactions that occur in the presence of oxygen. Since the reactions (1.2) and (1.3) are exothermic, sufficient heat is generated to dry the raw material, break the chemical bonds (biomass pyrolysis) and maintain a high temperature to guide the gasification reactions. Among these reactions, the reaction (1.2) has the greatest release of energy. In contrast, the heat generation capacity of the reaction (1.3) is only 65% of that of (1.2). Reactions (1.5)–(1.7) are the main gasification reactions. The reaction (1.8) is the methanation reaction, it proceeds slowly at low temperatures and in the absence of catalysts. In addition, the water-gas shift (1.9) reaction is also of great importance as it plays a significant role in hydrogen generation. Reactions (1.9) and (1.10) take place in both directions depending on temperature, pressure, and specific reagent concentrations in the system. Tar-reforming (1.11) can also be added as a step to produce light hydrocarbons from large tar molecules.

When the dry gas composition is known, it is also possible to estimate the heating value of the producer gas, the carbon conversion (CC) during the gasification process and the cold gas efficiency (CGE) (Del Grosso et al., 2020; Di Carlo et al., 2022).

The lower heating value (LHV) of the producer gas depends on the composition of the gas and heating value of flammable gas such as H_2, CO, CH_4, C_nH_m. The expression to calculate the LHV of the gas mixture can be expressed as:

$$LHV_{products} = LHV_{H_2} \cdot y_{H_2} + LHV_{CO} \cdot y_{CO} + LHV_{CH_4} \cdot y_{CH_4} + LHV_{C_nH_m} \cdot y_{C_nH_m} \tag{1.12}$$

where y is the molar fraction of flammable gases, and LHV for each of them is listed in handbooks.

The cold gas efficiency can be now identified:

$$CGE = \frac{LHV_{products} \cdot \sum \dot{n}_i \cdot 22.4}{LHV_{biomass}} \tag{1.13}$$

where $\sum \dot{n}_i$ is the amount of product gas for kg of inlet fuel [kmol/kg_{fuel}].

Finally, the carbon conversion is determined by the ratio (db, dry basis) of C in syngas to C in the biomass (from ultimate analysis, referred as $m_{C,biomass}$):

$$CC = \frac{\sum_i m_{C_i\,(db)}}{m_{C,biomass\,(db)}} \cdot 100 \tag{1.14}$$

where m_{C_i} is the carbon mass of the syngas component i.

1.3.1 Role of main operating parameters

There are many parameters which have a significant impact on the syngas quality/yield. The main variables include (Delgado et al., 1997; Rapagnà et al., 2000; Sikarwar et al., 2016):

- Feedstock type and inherent moisture content
- Particle size
- Temperature
- Gasifying mediums
- Air equivalence ratio (AER) and steam-to-biomass ratio (S/B)

Feedstock type and inherent moisture content

Biomass contains biopolymers such as lignin (10–25 wt.%), cellulose (35–55 wt.%), and hemicellulose (20–40 wt.%) (Okolie et al., 2019). Cellulose, hemicellulose, and lignin are the three main elements of biomass. In the gasification of a biomass, the higher the ratio of cellulose/hemicellulose to lignin in a given biomass, the higher the gasification efficiency. The amount of cellulose and hemicellulose is directly related to the syngas yield, while the lignin content determines the oil formation in the product. Normally, in a typical biomass, the cellulose-lignin ratio varies from 0.5 to 2.7, and the hemicellulose-lignin ratio varies from 0.5 to 2.0 (Mishra and Upadhyay, 2021). Another important parameter in the gasification of biomass is the moisture content. The total moisture content of some biomass can be as high as 90%. Moisture drains much of the deliverable energy from a gasification plant, as the energy used in evaporation (at least 2260 kJ/kg of moisture in biomass) is not recovered (Basu, 2010). This important input design parameter must be known for the assessment of the cost, or energy penalty, in drying the biomass. Consideration is mainly given to two types of moisture contents, namely intrinsic moisture, which is the water content of the material without taking into account the impact of weather, and extrinsic moisture, incorporating the influence of weather conditions. The syngas characteristics and the optimal operation of the gasifier depend on the moisture content to a significant extent. Woody and low-moisture herbaceous biomasses contain less than 15 wt.% moisture. This makes them more suitable for thermal conversion since most gasifiers are designed to accommodate biomass feedstock with a moisture content of 15–30 wt.%.

Particle size

Another important variable in the gasification process is the particle size (Acharya et al., 2010). Temperature and heating rate of particles have a fundamental influence on the reactivity of biomass during gasification. In fact, more controlled gasification is achieved if temperatures remain uniform throughout the particle, and it is known that fluid-particle heat transfer is excellent for finer particles. In addition, the rate of gasification increases exponentially, according to the Arrhenius law, with the increase in temperature, and this is relevant when kinetics controls the gasification process (de Lasa et al., 2011). Literature data show that an increase in carbon conversion and in the amount of H_2 produced is observed when particle size is reduced. Finally, a decrease in particle size improves syngas yield and decreases tar yields (Rapagnà and de Celso, 2008; Hernández et al., 2010). In contrast, the residual coal yield is higher when coarser particles are used in the process. This is due to incomplete pyrolysis resulting from the increased heat transfer resistance offered by larger particles (Lv et al., 2004). However, it should be noted that, when choosing the optimum particle dimensions for biomass gasification, while fixed bed gasifiers are less sensitive to particle size, fluidised bed reactors have a lower tolerance (Basu, 2010).

Temperature

Temperature and partial pressure of the gasifying agent are other crucial parameters which have the potential to influence the syngas yield and overall biomass conversion (Farid et al., 2015). Several experimental and modelling studies have reported the effects of temperature on char conversion, gas yield and composition, and tar production. Higher temperature can lead to an increase in the degradation of the tars by transforming them to syngas species. This is caused by the volatilisation of the active components of tar. The Boudouard reaction and the thermal cracking reaction effectively degrade residual char and tar when the temperature is increased (He et al., 2009). Therefore, maintaining a high temperature can contribute productively for biomass gasification. A temperature greater than 800 °C results in higher char transformation and lower tar yield on account of higher conversion of carbon, volatile species, and high molecular weight hydrocarbons into gaseous products (Skoulou et al., 2009). From this point of view, it is desirable to have a higher gasification temperature. Optimal ranges of temperatures were reported between 750 and 850 °C for gasification of agricultural waste fuels, and 850–950 °C for woody biomass (in comparison to temperatures well higher than 1000 °C for coal) (Devi et al., 2003; Hanping et al., 2008; Gao et al., 2009). However, the desire for lower ash agglomeration/melting necessitates lower temperatures which practically restrict the operating temperature range (Salaices et al., 2010). Moreover, it is found that H_2 yield at equilibrium initially increases to a limit, then decreases, with a rise in temperature, given the complex network of reactions that governs the gasification process (Mahishi and Goswami, 2007).

Gasifying mediums

The choice here depends on the type of gasifier and the desired quality of the syngas. The main gasifying agents are, alone or in mixture (sometimes, CO_2 is used as well):

- Oxygen
- Steam
- Air

If oxygen is used as a gasifying agent, the conversion path shifts to the production of oxygenated compounds, mainly CO for low oxygen and CO_2 for high oxygen contents, while the H_2 content in the syngas is reduced. When the amount of oxygen exceeds a certain amount, the process moves from gasification to combustion. If steam is used as a gasification agent, the gas produced contains more hydrogen per unit of carbon, resulting in a higher H/C ratio. Some of the intermediate reaction products, like CO and H_2, help to gasify solid carbon. If air (cheaper) is used instead of oxygen, the nitrogen contained in it greatly dilutes the product (Basu, 2010). This can be a problem if the syngas is intended for energy purposes, while for other applications (e.g., ammonia synthesis), the presence of nitrogen in the syngas is even desired. The choice of the gasifying agent affects the heating value of the gas produced. Usually, oxygen gasification has the highest heating value followed by gasification of steam and air (Rapagnà et al., 2000; Coll et al., 2001).

Air equivalence ratio (AER) and steam-to-biomass ratio (S/B)

The equivalence ratio is an important gasifier design parameter. It is the ratio of the actual air–fuel ratio to the stoichiometric air–fuel ratio needed for complete conversion. The equivalence ratio dictates the performance of the gasifier. For example, pyrolysis takes place in the absence of air and hence AER=0; for gasification of biomass, it lies between 0.2 and 0.3. Higher AER results in lower H_2 and CO yields, with an increase in CO_2, which in turn decreases the LHV of the syngas. By contrast, a higher AER improves tar cracking due to higher O_2 availability for volatile species to react with. The syngas quality strongly depends on the AER value, which must be significantly below 1.0 to ensure that the fuel is gasified rather than combusted. However, an excessively low ER value (<0.2) results in several problems, including incomplete gasification (and excessive tar production, as demonstrated in Montagnaro and Zaccariello, 2022), excessive char formation, and a low heating value of the product gas. On the other hand, too high AER (>0.4) results in excessive formation of products of complete combustion, such as CO_2 and H_2O, at the expense of desirable products, such as CO and H_2 (Basu, 2010; Haro et al., 2013; Migliaccio et al., 2021; Di Lauro et al., 2022), although the syngas specific mass yield turns to be higher (Montagnaro and Zaccariello, 2022).

The ratio of steam to biomass (S/B) is another influential parameter that affects the input energy requirements, syngas quality and yield. Usually, lower S/B ratios result in higher amounts of char and CH_4 formations, whereas increasing S/B positively enhances the reforming reactions by providing an oxidative environment, thereby raising the oxidised product gas yield. While, increasing S/B results in a higher H_2 yield and therefore the syngas has high calorific content. The process also produces a low amount of tar (Parthasarathy and Narayanan, 2014; Sharma and Sheth, 2016).

1.3.2 Types of gasifiers

Gasifiers are mainly classified based on their gas–solid contacting mode (Figure 1.6):

- Fixed bed gasifiers (FXB)
- Fluidized bed gasifiers (FB)
- Entrained flow gasifiers (EF)

In a FXB, the fuel is supported on a grate. This type is also called moving bed because the fuel moves down in the gasifier as a plug. Both mixing and heat transfer within the fixed bed are rather poor, which makes it difficult to achieve uniform distribution of fuel, temperature, and gas composition across the cross-section of the gasifier. Thus, fuels that are prone to agglomeration are not suitable in this case. Therefore, FXB gasifiers are not very effective for biomass fuels or coal with a high caking index in large-capacity units. A FXB gasifier can be either updraft, when the fuel enters from the top, gasifying agent from the bottom, or downdraft, where both fuel and gasification agent enter from the top, with the fuel coming in from a lock-hopper. In a typical updraft gasifier (Figure 1.6a), fuel is fed from the top; the product gas leaves from the top as well. The gasifying agent is slightly preheated and enters the gasifier through a grid at the bottom. The gas then rises through a bed of descending fuel or ash in the gasifier chamber while the air, as it enters the bottom of the bed, meets hot ash and unconverted char descending from the top. In updraft gasification, the char at the bottom of the bed meets the gasifying agent first, and complete combustion occurs, producing H_2O and CO_2 and raising the temperature to 1000 °C. The hot gases percolate upwards through the bed, driving endothermic reactions with unreacted char to form H_2 and CO, with consequent cooling to 750 °C. The gases pyrolyze the dry biomass which is descending and dry the incoming biomass. Contrary to updraft gasifiers, in a downdraft gasifier the gasifying agent is fed at the combustion zone, middle section, as shown in Figure 1.6b. Biomass flows from the top to the drying section, where the moisture is removed and then further into the pyrolysis zone, where the solid fuel is converted into char and gases. Now, as the motion continues, the gasifying agent is fed, and the gases are combusted. The principal purpose of maintaining the gasification temperature is met at this zone, and then the biomass further moves into the reduction zone.

FB gasifiers (Montagnaro and Zaccariello, 2022) offer uniform temperature distribution that varies from a minimum of 700 °C to a maximum of 900 °C, and a well-mixing platform for gas and solid. That, in turn, reduces the risk of fuel agglomeration. Silica, sand and dolomite are commonly used as bed material for FB gasifiers. The excellent gas-solid mixing and the large thermal inertia of the bed make this type of gasifier relatively insensitive to the fuel's quality (Molino et al., 2018). The FB design has proved to be particularly advantageous for gasification of biomass. Its tar production lies between that for updraft (~50 g/Nm^3) and downdraft gasifiers (~1 g/Nm^3), with an average value of around 10 g/Nm^3. FB gasifiers are further divided into two main categories based on the velocity of the gasifying medium: i. Bubbling bed gasifier, ii. Circulating bed gasifier (Figure 1.6c). In a bubbling FB, the biomass is fed from the side, and/or below the bottom of the bed, and the gasifying agent's velocity is controlled so that it is just greater than the minimum fluidization velocity of the bed material. The producer gas exits from the top of the gasifier, and ash is either removed from the bottom or from the producer gas using a cyclone (Migliaccio et al., 2021; Di Lauro et al., 2022). While, in a circulating FB, two integrated units are present. In the first unit, the riser, the bed material is kept fluidized by the gasifying agent, with a higher velocity than that found in a bubbling bed gasifier. This allows the bed material to be fluidized to a greater extent and the overall residence time is longer, due to the circulation, which is affected by passing the syngas and entrained bed material through a cyclone which separates the syngas from the bed material which is recirculated back to the riser.

Finally, EF reactors (Troiano et al., 2017) operate at a 20–70 bar pressure Figure 1.6d. Carbon conversion efficiency of almost 100% is achievable in an EF reactor. They are essentially co-current plug-flow reactors, where gas and fuel travel. The solid fuel is ground in a pulverizing mill to sizes below 80 μm, and then conveyed by part of the combustion air to a set of burners suitably located around the furnace. The gasification temperature generally well exceeds 1000 °C. This allows production of a gas that is nearly tar-free and has a very low methane content. The syngas, being very hot, must be cooled in downstream heat exchangers that produce the superheated steam required for gasification. However, operability at the high creates problems for material selection and ash melting (Troiano et al., 2017; Mishra and Upadhyay, 2021). For example, this apparatus is not much suitable for biomass as, due to the short residence time (of about few seconds) in EF reactors, the fuel needs to be very fine, and grinding fibrous biomass into such fine particles is difficult.

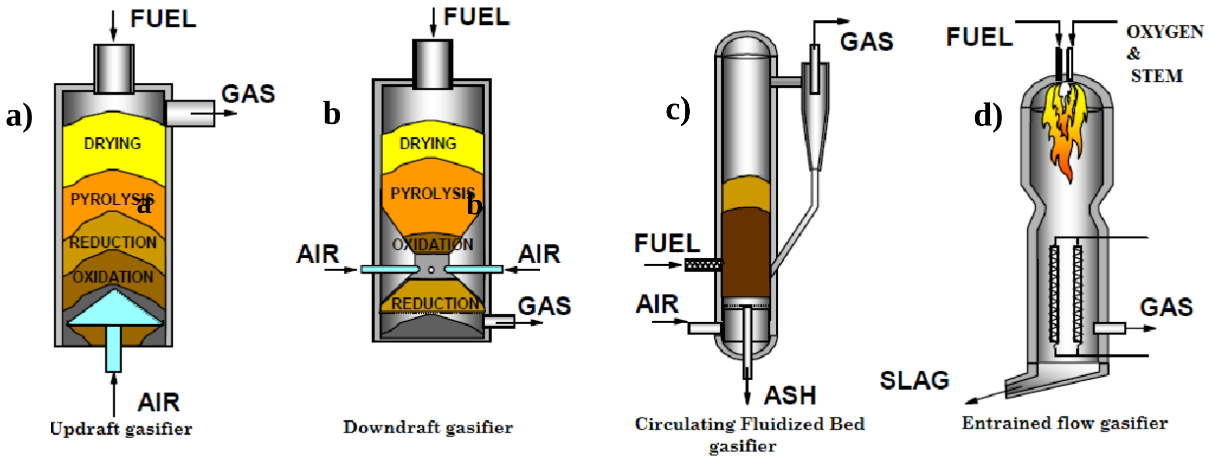

Figure 1.6 – Schematic of different types of gasifiers: a) Updraft gasifier (FXB), b) Downdraft gasifier (FXB), c) Fluidized bed gasifier (FB), d) Entrained flow gasifier (EF) (adapted from Budhathoki, 2013).

1.4 Hydrothermal liquefaction process

Hydrothermal liquefaction (HTL) is one of the promising techniques for conversion of biomass, in particular wet biomass, into liquid fuels by processing it in a hot, pressurised water environment for sufficient time to break down the solid biopolymeric structure to mainly liquid components. This process operates at high pressure (40–200 bar) and relatively low temperature (< 360 °C) and uses water as the main solvent, mostly in subcritical or near critical conditions. The main products of HTL are bio-oil, water-soluble products, char, and gas (Toor et al., 2011; Vardon et al., 2011; Fan et al., 2022).

HTL, as pyrolysis, is a thermochemical conversion technology to convert biomass feedstocks to biofuels (Kruse and Dahmen, 2015). However, compared with bio-oil from fast pyrolysis, biocrude obtained from HTL have better properties, i.e., lower moisture content, lower oxygen/carbon and consequently higher heating value of about 30–36 MJ/kg (Demirbas, 2011). In addition, the HTL process allows to exploit the biomass water content for biocrude production, thus avoiding the high-energy demanding dewatering step commonly associated with other competitive processes of energy conversion (e.g.: oxy-pyrolysis, gasification). This is very important for biomasses that present high moisture content, such as sewage sludge, because the dewatering treatment is a bottleneck in the biomass conversation (Tyagi and Lo, 2013).

Although biomass is subject to a series of complicated reactions during the liquefaction process, the basic reaction mechanism proposed by researchers can be summarised as follows (Behrendt et al., 2008; Theegala and Midgett, 2012):

1. Biomass hydrolysis and depolymerisation to monomers and unit structures;
2. Decomposition/degradation of the produced monomers (thermally and chemically) to form intermediates through reactions of dehydration, dehydrogenation, deoxygenation, cleavage, deamination, decarboxylation, cracking/fragmentation, etc.;
3. Rearrangement of the reactive fragments/intermediates through re-polymerization, condensation, and cyclization, to form products.

In a nutshell, in a first phase, parameters such as temperature and pressure modify the structure of long chain polymers consisting of hydrogen, oxygen and carbon, to obtain shorter chain hydrocarbons. Then, there is the phase of decomposition of the biomass monomers by cleavage, dehydration, decarboxylation, and deamination. This step involves the loss of water molecule (dehydration), loss of CO_2 molecule (decarboxylation) and removal of amino acid content (deamination). The dehydration and decarboxylation facilitate the removal of oxygen from the biomass in the form of H_2O and CO_2, respectively. Biomass comprising macromolecules are hydrolysed to form polar oligomers and monomers. Most of the degradation products such as polar organic molecules, furfurals, glycoaldehydes, phenols and organic acids are highly soluble in water. The last step is the recombination and repolymerisation of reactive fragments in which the inversion occurs with respect to the initial phases. Free radicals without hydrogen are recombined or repolymerised to form high molecular weight carbonyl compounds through processes of condensation, cyclization and polymerization (Gollakota et al., 2018). A basic reaction pathway for the liquefaction of biomass is represented in Figure 1.7.

Figure 1.7 – The basic reaction pathways for the liquefaction process of biomass (Huang and Yuan, 2015).

HTL product yields and properties vary significantly according to the feedstock processed as well as the reaction conditions employed (Jazrawi et al., 2015). Although the product distribution in bio-oil varies with the composition of the raw material and process conditions, the same groups of compounds are detected in almost all HTL bio-oils (Pavlovič et al., 2013). The liquid oils contain a range of chemicals including carboxylic acids, alcohols, aldehydes, esters, ketones, sugars, lignin-derived phenols, furans, etc. (Stöcker, 2008).

It is important to underline that, since the HTL process is applied to different types of biomasses and these are made up of very complex matrices, at present there is a limited understanding of the reaction mechanisms behind the process. In addition, these reactions are influenced by many factors, such as temperature, heating time, reaction time, use of catalysts etc. (Di Lauro et al., 2020; Fan et al., 2022).

1.4.1 Role of main operating parameters

<u>*Role of water*</u>

As can be seen from Table 1.3 and Figure 1.8, the properties of water in normal conditions change drastically when water is at sub- and super-critical conditions, and beyond the critical point; the properties of water can be changed without any phase transition (Kumar et al., 2018; Wang et al., 2019).

Under near-critical conditions at 350 °C, the density and viscosity are greatly reduced from 0.997 g/cm^3 and 0.89 mPa s at ambient conditions to 0.80 g/cm^3 and 0.11 mPa s at subcritical conditions. This leads to enhanced rate of reaction. The ionic product decreases first and then increases by five orders of magnitude close to the critical point, which supports acid/base catalysed reactions without the need to add any external catalyst (Biller and Ross, 2016). Another important change that happens to water at near-critical conditions is the significant reduction in its dielectric constant.

Table 1.3 – Properties of water in standard, subcritical and supercritical conditions.

Properties of water	**Standard**	**Subcritical**	**Supercritical**
Temperature (°C)	25	250–350	350–400
Pressure (bar)	1	50–200	200–250
Density, ρ (g cm^{-3})	0.997	0.80	0.17
Dynamic viscosity, η (mPa s)	0.89	0.11	0.03
Heat capacity, C_P (kJ kg^{-1} K^{-1})	4.22	4.86	13.0
Dielectric constant, ε	78.5	27.1	5.9
Ionic product, pK_W	14.0	11.2	19.4
Heat conductivity, λ (mW m^{-1} K^{-1})	608	620	160

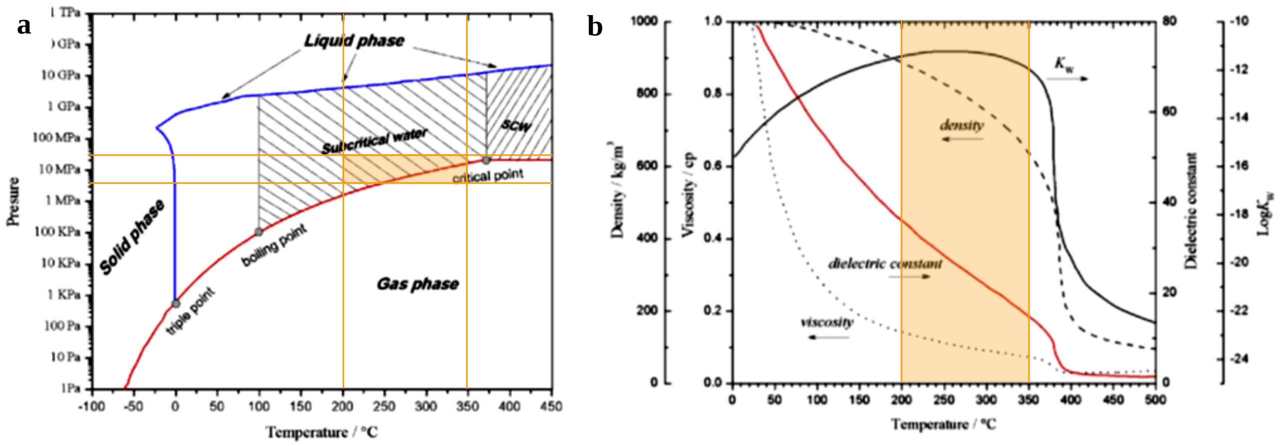

Figure 1.8 – Phase diagram (a) and properties of water at 25 MPa (b) as a function of temperature (Wang et al., 2019).

With increase in temperature, oxygen and hydrogen start to have a more shared distribution of electrons and thus reduced electronegativity of oxygen occurs. The dielectric constant decreases from 78.5 at 25 °C to 5.9 at 400 °C, which makes water closer to a non-polar solvent thereby more affine to organic hydrocarbons which is important for the HTL process (Zhang, 2010). In detail, during HTL, water is heated and pressurised, weakening the hydrogen bonds and bringing about vast changes to its properties, particularly the dielectric constant and ionic product, which can increase opportunities for the water to take part in reactions (Biller and Ross, 2012). With higher temperatures, it can be seen that the dielectric constant is decreased. This means that the water molecule becomes less polar, principally due to the more evenly shared electrons between the oxygen and hydrogen atoms. At the same time, the ionic product rises under subcritical conditions. As a result, the dissociation of water into H_3O^+ and OH^- increases, suggesting that the hot-compressed water is a good medium for acid- or base- catalysed reactions (Toor et al., 2011). These dramatic changes, relative to ambient conditions, make the solvent properties (hot compressed water) roughly equivalent to those of acetone at room temperature, allowing nonpolar hydrophobic compounds to be more miscible. With the increased solubility in water, ionic reactions of organics present in the biomass are favoured as the possibilities of contact with the dissociated H_3O^+ and OH^- ions are amplified (Peterson et al., 2008; Zhang, 2010).

Thus, these unique properties for subcritical water allow it to depolymerise biomass (a combination of complex macromolecules) into smaller fragments and then, these small molecules recombine with each other to form a mixture of new compounds including short carbon-chain compounds like hydrocarbons, thus producing the liquid fuel product known as biocrude. When the product comes to Standard Temperature and Pressure (STP) conditions, the formed oil products separate from water-soluble compounds due to difference in polarity.

On the other hand, high energy is required to reach sub- and super- critical conditions. So, several studies have investigated various solvents for different feedstocks. Recently, organic solvents started to draw attention due to their lower critical points compared with water. Generally, various organic solvents (such as ethanol, acetone, or propanol) were studied to increase both conversion rate and chemical composition of the biocrude oil (Heitz et al., 1994; Yuan et al., 2007, Liu and Zhang, 2008, Chumpoo and Prasassarakich, 2010). For instance, Liu and co-workers studied the effect of three different organic solvents on biocrude oil yield for pinewood liquefaction, and the results revealed high conversion rate with acetone, whereas biocrude yield was maximised with ethanol. Yuan et al. focused on solvent mixtures (addition of water to alcohol), to enhance liquefaction efficiency. The effect of various ethanol/water concentrations on product yields from liquefaction of bagasse was investigated, for example by Chumpoo and co-workers, to improve the yield and quality of biocrude. Tong et al., 2021 demonstrate that for HTL applied to sewage sludge, when methanol is used in mixture with water, an improvement in the yield and quality of bio-oil is achieved, while Huang and co-workers (Huang et al., 2013) always for sewage sludge have obtained a yield of about 40% when ethanol is used as a reaction medium in the process. Although there are reports in the literature of beneficial effects in the use of organic solvents in the HTL process, their use implies side effects for both the associated cost and their disposal. Moreover, the removal of water present in the biomass, and its replacement with another solvent, implies the drying of the parent biomass, eliminating one of the main advantages of hydrothermal liquefaction compared to other thermal conversion processes.

Effect of temperature

Reaction temperature is a key parameter in thermochemical conversion of biomass and strongly influences both yield and quality of the biocrude. The final temperature not only defines the solvation properties of the hydrothermal media, but it also plays a direct role in biomass degradation. Elevated temperatures favour biomass depolymerization. This not only increases the concentration of free radicals, but also the probability of repolymerization of the fragmented species. The recombination of small molecular reactive species after depolymerization is what primarily leads to bio-oil formation (Xu et al., 2018; Di Lauro et al., 2021).

Low temperatures (<280 °C) inhibit biomass depolymerization resulting in poor bio-oil yields. Most often, low temperature thermochemical conversion coupled with longer residence times leads to significant char formation. This process is widely known as hydrothermal carbonization and can be useful for producing biochar with reduced oxygen and nitrogen content (Wilk et al., 2021). Conversely, high temperature environments (> 350 °C) promote increased gas and aqueous phase products. At these elevated temperatures, secondary decomposition reactions take place which significantly reduce the production of bio-oil. In an analysis of various biomass feedstocks including microalgae, macroalgae, cattle manure, grassland perennials and eucalyptus, optimal bio-oil yields were observed in the range of 300–360 °C (Akhtar and Amin, 2011). Each study revealed an ideal conversion temperature for each feedstock. Unsurprisingly, previous studies have shown a strong correlation between initial feedstock composition and the optimal temperature for bio-oil production. Compact biomass feedstocks such as microalgae are better reformed under higher temperature (~350 °C) conditions (Biller and Ross, 2011). HTL processes which convert mixed feedstocks that contain a multitude of diverse organic compounds must find a compromise between the ideal bio-oil forming temperatures for each component. Zhou and co-workers (Zhou et al., 2010) reported maximum bio-crude yield at 300 °C from HTL of macroalgae, whereas Yin et al., (2010), as well as Zhang et al. (2011), found 310 °C and 340 °C as the most beneficial temperatures, using cattle manure and newspaper as a feedstock, respectively. Zhong and Wei (2004) studied HTL of woody biomass at different temperatures, 280, 300, 320, 340 and 360 °C. They reported that the bio-oil yield increased with increasing reaction temperature up to 320–340 °C. Further increasing the temperature resulted in a decline in bio-oil yield, as described previously. The maximum bio-oil yield of 32.2% and lowest solid residue yield of 10.34% were obtained at 340 °C and in the presence of K_2CO_3 catalyst.

Effect of reaction time

To date, most of the research into the HTL of biomass has been conducted using batch reactors. Most of these are operated under isothermal conditions, where a constant reaction temperature is maintained for a prolonged period of time. Residence time is a parameter which may significantly affect the composition of the products and the overall conversion of biomass. It is necessary to optimise reaction time, for the adequate destruction of the structural components in the feedstock (Sasaki et al., 2003). It was observed that longer residence times lead to decrease the bio-crude oil yield, whereas shorter times are beneficial (Zhang et al., 2011). Residence time can play a major role in optimizing bio-oil quantity and quality. In general, longer residence times have been shown to decrease the overall bio-oil yields. Residence times can also influence the final bio-oil quality. Various residence times studied over two temperature profiles of 180 and 250 °C indicated that the reaction products were significantly different. In addition, longer reaction times were shown to significantly increase the degradation of biomass into lighter products, which increased the amount of aqueous organic and gas phase products (Lai et al., 2018; Di Lauro et al., 2021). Residence times that maximise the saturation of bio-oil within the HTL media will result in optimal bio-oil yields. Longer residence times will likely promote the increased formation of gas and char products (Wilk et al., 2019).

Yin et al. (2010) observed a decrease in bio-oil yield from HTL of cattle manure at 310 °C, and in the presence of NaOH as catalyst, while increasing reaction time. Increasing the reaction time from 15 to 40 min resulted in a decrease in bio-oil yield from 39.57% to 12.95%, which was attributed to the decomposition and condensation of bio-oil products to form residual solids. A different trend was however observed by Xu and Lancaster (2008). The authors observed an increase in bio-oil yield at longer reaction times from 15 to 120 min, which might be due to the conversion of water-soluble products (WSP) to bio-oils.

Temperature and reaction time are the most commonly studied parameters. Temperature controls the properties that water exhibits and is the key in determining the components degradation. Reaction time is the time period for which the sample is subjected to a specified temperature. The combination of temperature and reaction time are the deciding factors for the rate of hydrolysis of the component and the further degradation of products. Hemicellulose from wood biomass was shown to completely hydrolyse at 230 °C and 2 min (Mok and Antal, 1992). Starch from sweet potato was 100% hydrolysed at 180 °C, 10 min, but the maximum glucose yield was obtained at 200 °C, 30 min, and 220 °C, 10 min (Nagamori and Funazukuri, 2004). Hemicellulose and starch both begin to hydrolyse at 180 °C; nevertheless, the optimized conversion requires the right combination of temperature and reaction time.

1.4.2 Effect of macro-components

As previously mentioned, biomass consists of different components such as carbohydrates, lignin, proteins, and lipids. The breakdown of the different macrostructures initiates under different temperatures, depending on the chemical structure of the particular macromolecule. Each of these components, when subjected to hydrothermal conditions, can undergo different conversion pathways, as described below.

Cellulose, hemicellulose and lignin

Carbohydrate is a collective name for individual sugars and their polymers, which generally includes monosaccharides, oligosaccharides, and polysaccharides. The name carbohydrate is derived from the empirical formula of hydrated carbon, $C_n(H_2O)_n$. All carbohydrates, including sugars, starches, cellulose, hemicellulose, and chitin, are fundamentally polymers of monosaccharides.

Cellulose is normally the largest fraction of plant biomass (40–50 wt.%), followed by hemicellulose and lignin (Akhtar and Amin, 2011). It is a linear polysaccharide with an average molecular weight of around 100000 g mol^{-1}, made of D-glucose units and with crystalline structure, making it water insoluble; however, subcritical water with high ionic product can break its crystallinity. Decomposition of cellulose increases with increasing temperature. Hemicellulose makes up 20–40% of plant biomass. It is a branched polymer with an average molecular weight of <30000 g/mol with non-crystalline and random structure, which makes it easily hydrolysable. In hydrothermal processing, hemicellulose is hydrolysed easily at temperatures above 180 °C and, at 220 °C, hemicelluloses could completely dissolve in water. Lignin is a high molecular weight aromatic heteropolymer with chemical formulas $C_9H_{10}O_2$, $C_{10}H_{12}O_3$ and $C_{11}H_{14}O_4$. It consists of *p*-hydroxy phenylpropanoid units, which are held together with C-C or C-O-C ether bonds. Lignin is commonly associated with hemicellulose both physically and chemically through covalent bonds (Ruiz et al., 2013). It is relatively resistant to chemical or enzymatic degradation; however, in hydrothermal processing, many phenol and methoxyphenol compounds are formed through hydrolysis of ether bonds. The degradation of carbohydrates in hot-compressed water has been comprehensively reviewed by several researchers (Sasaki et al., 1998; Gao et al., 2012). Due to the difference in the structures of cellulose and starch, the rates of hydrolysis vary significantly. Rogalinski et al. (2008) report the full conversion of cellulose at 280 °C within 2 min residence time in a continuous flow reactor. It was also observed that the hydrolysis rate substantially increased from 240 °C to 310 °C at 250 bar for cellulose. At the same time, starch hydrolysis was shown to be considerably faster at the same reaction conditions. These authors claim that a rapid heating rate of the reactor is important so that to avoid further product degradation prior to reaching the set-point temperature. The importance of this observation becomes apparent when comparing their results to those carried out in batch type reactors with slow heating capabilities, in which significant depolymerisation was reported at lower temperatures of <260 °C (Kamio et al., 2008).

The produced saccharides, mainly glucose in the case of cellulose and starch hydrolysis, have also been vastly investigated, and their degradation mechanisms have been proposed by numerous researchers (Srokol et al., 2004; Klingler and Vogel, 2010; Promdej and Matsumura, 2011). A general pathway emerges in which glucose and fructose, which co-exist according to the Lobry de Bruyn–Alberda van Ekenstein transformation, degrade to form a range of products including furans, acids and aldehydes via isomerization, dehydration, defragmentation, re-arrangement, and recombination reactions (Antal et al., 1990). However, during HTL, it is believed that various side-chain reactions simultaneously occur, affecting the course of the subsequent reaction pathways (Peterson et al., 2008).

<u>Protein</u>

Proteins are polymers of amino acids mostly found in animal or microbial type of biomass. Proteins are made up of amino acid building blocks which are structurally bound together through peptide bonds and contain a large fraction of nitrogen that can affect the bio-oil properties such as smelling and combustion properties, so the degradation of proteins is also of great importance to HTL of biomass. The long chains of proteins can be slightly hydrolysed at temperatures below 230 °C while, at temperatures above 250 °C, proteins are completely hydrolysed to amino acids, which will then be degraded fast to hydrocarbons, amines, aldehydes and acids through decarboxylation and deamination reactions (Toor et al., 2011).

The process has been reported to produce low amino acid yields (>10 wt.%), mainly due to their rapid degradation rates (Zhu et al., 2008). Klingler et al. (2007) conclude that the primary amino acid degradation mechanisms are decarboxylation and deamination. However, during the HTL of biomass, the degradation products from protein have been observed to react with the sugars present from the other components of the feedstock, through Maillard-type reactions. This results in the formation of N-containing cyclic organic compounds such as pyridines and pyrroles, which are commonly found in the biocrude derived from HTL.

Lipid and fat

Lipids and fat are non-polar molecules and are chemically similar to hydrocarbons; they can be extracted via the use of solvents. Numerous reports have been published which aim solely at maximising the lipid production and extraction for the biodiesel industry (Halim and Danquah, 2012; Frank et al., 2013), while neglecting the carbohydrate and protein components. In this respect algae, with their high lipid content, are the most promising biomass for the HTL process. In fact, there are several works on HTL process that studied the bio-oil conversion of algae with good results in terms of yield and HHV. The majority of researchers dealing with the HTL process opt to directly convert the algae without applying any preceding lipid extraction techniques. During HTL, the lipids become increasingly soluble in the water as its dielectric constant drops with higher temperatures and pressures. Above ~300 °C, the main constituent of the lipids, triacylglycerides, have been shown to completely decompose into free fatty acids and glycerol (Holliday et al., 1997). At these conditions, the fatty acids are relatively stable and thus it can be expected that the biocrudes produced from the HTL of high-lipid feedstocks will retain substantial levels of free fatty acids derived from the lipid component (Biller and Ross, 2011; Hietala and Savage, 2021).

Prediction models for bio-oil yield

A few models have been developed to predict the yield and properties of bio-oil during the HTL process. A linear model has been built to calculate the bio-oil yield of HTL from the biochemical composition, including proteins, lipids, and carbohydrates, which established the relationship between bio-oil yield and biochemical composition. Reaction time and temperature are kinetic factors that were added to the above component additivity model for proposing a new model to predict bio-oil yield, enabling the prediction of bio-oil yield from HTL of biomass under a wide range of operating conditions. But these models still have relatively low accuracy, and they lack enough broad data and, therefore, have limited credibility. Currently, there are different literature works that study the interaction of macro-components using model compounds, to bridge the gaps between input variables and the output bio-oil yield and properties. Moreover, the synergistic/antagonist effect of different organic fraction is evaluated through different predictive models (Yang et al., 2019; Li et al., 2021; Kumar, 2022; Katoungtung and Tippayawong, 2022), but with limited advances in post-experiment guidance to accelerate the engineered HTL bio-oil production.

1.4.3 Effects of catalyst

During HTL tests, another important subset of chemical reactions are reduction reactions. Since one of the main purposes of liquefaction is the removal of hetero-atoms, especially oxygen, reduction reactions bring the biocrude closer to more chemically-desirable properties. Unfortunately, these reactions have not been shown very selective under non-catalytic conditions, which is most likely why the majority of experimental HTL tests is carried out in the presence of a catalyst. The use of homogeneous and heterogeneous catalysts in HTL of biomass has been widely studied for their promoting effects on both yield and quality of the biocrude (Nagappan et al., 2021; Prestigiacomo et al., 2022). Different kinds of homogeneous and heterogeneous catalysts have been employed in hydrothermal liquefaction process, but the most common catalysts used were alkali metal compounds, e.g., Na_2CO_3, NaOH, K_2CO_3, KOH, LiOH, RbOH, and CsOH (Xu and Etcheverry, 2008; Wang et al., 2018).

A previous work from Zhang et al. (2011) studied the effects of both homogeneous and heterogeneous catalysts (i.e., formic acid (HCO_2H), KOH and FeS) on HTL of mixtures of secondary pulp/paper mill sludge and waste newspaper, a common municipal solid waste that contains a high fraction of volatile material and lignin. Effects of using hydrogen as a reducing gas were also investigated. The study concluded that the presence of H_2 had no significant effects on bio-oil yield. In terms of oil yield, the performance of catalysts was: FeS > KOH > HCO_2H and, in terms of conversion of biomass, the order of the catalysts was KOH > FeS > HCO_2H. The highest oil yield obtained was 29.9 wt.% with FeS catalyst at 300 °C and 2 MPa initial pressure of nitrogen, with 20 min residence time.

Ross et al. (2010) studied the effects of different alkali and organic acid catalysts on HTL of microalgae in a 75 mL batch reactor and concluded that the catalytic activities for bio-oil yields increased in the order of HCOOH < KOH < CH_3COOH < Na_2CO_3. With Na_2CO_3, the bio-oil yield attained 27.3 wt.% at 350 °C and 60 min residence time, and the oil has an HHV of 39.9 MJ/kg. Similar results were reported by many other researchers, demonstrating good catalytic activities of Na_2CO_3 for HTL of various biomass feedstocks, such as microalgae and municipal sludge (Hammerschmidt et al., 2011; Theegala and Midgett, 2012).

Prestigiacomo et al. (2021) also studied the effect of organic acids on sewage sludge, by demonstrating how the use of formic acid as green hydrogen donor in the HTL can significantly increase both biocrude yield and quality.

1.4.4 Types of reactor configurations for HTL

There are two types of reactors generally used in research of HTL processes – batch and continuous reactors. Batch reactors are mostly used in labs due to simplicity and versatility in handling the feedstock, especially with high solid load (Peterson et al., 2008; Prestigiacomo et al., 2020). In case of a continuous HTL system, the sample is directly subjected to the desired temperature and for the required time. The retention time is controlled by the length of the reactor and by the flowrate of the feedstock slurry. Continuous systems have limitations on the solid load of the feedstock as, if it exceeds a certain percentage, it becomes hard to pump the slurry in the system (Elliott et al., 2015).

1.4.4.1 Batch reactors

In most of the studies, the reactor is heated with the sample inside, from room temperature to the desired temperature. This forces the sample to go through all the temperature range until the desired temperature is achieved, instead of subjecting the sample directly to the desired temperature. The same issue is encountered during the cooling part of the process, as the reactor is shut down after the desired retention time is completed, and it is left to cool down to room temperature without any intervention, resulting in additional time of reaction than the selected retention time. To take this parameter into account, the yield of the biocrude is often defined based on a process severity index (*SI*) defined by Overend and Chornet (1987), in which the combined effect of time (*t*) and reaction temperature (T_r, expressed in °C) can be expressed through a single variable (Ruiz et al., 2021; Prestigiacomo et al., 2022):

$$SI = \int_0^t e^{\frac{T_r - 100}{14.75}} \, \mathrm{d}t \tag{1.16}$$

Faeth et al. (2013) demonstrated a method they called as fast HTL, which might be closer to conditions in the continuous system, that used fast heating rates and short retention time in a batch experiment and obtained significantly higher bio-oil yields in comparison to conventional method. However, to achieve such high heating rate, the use of a batch reactor of a few mL is suggested, drastically limiting considerations on the products generated by the process.

Another limitation of the batch reactors is scalability. The progressive goal for HTL systems is to produce biofuel and chemicals commercially, on a large scale. It might be possible to use large-scale batch reactors for high-value compounds of limited quantity but, for huge production of fuels, continuous systems are needed, to achieve industrial-scale economical and energy efficient systems (Castello et al., 2018). Batch experiments give a good idea of products and conditions of the HTL process, thus providing a good starting point for understanding the HTL mechanism. However, for progression to commercial scale, it is important to move towards testing in continuous systems, to experience the issues that are specific to them (Elliot et al., 2015). The construction of continuous systems is faced with some technical problems, like the need for the systems to be resistant to high temperatures, up to 400 °C, and high pressure, up to 200 bar.

Phase separation after the HTL process

Although the literature on batch reactors in the HTL process is extensive, little attention has been paid to the development of an efficient separation method to effectively recover the bio-oil produced. After the biomass liquefaction reaction, hydrophilic solvents (such as acetone, ethanol) are mainly used to extract the bio-oil from the product mixture obtained through liquid-liquid extraction (Jena et al., 2011; Li et al., 2018; Xi et al., 2018). In the choice of solvent, they are most often preferred with negligible water solubility and low boiling point, to facilitate subsequent separation of the solvent from the biocrude by evaporation of the hydrophobic solvent (Yin et al., 2010; Brand et al., 2014; Chan et al., 2014; Leng et al., 2018; Remón et al., 2019). The use of a low boiling point extraction solvent can, in fact, allow us to develop an economic distillation to recover the bio-oil produced. However, to ensure a high recovery of the bio-oil produced, a huge amount of highly toxic hydrophobic solvent should be used in the liquid-liquid separation phase that should subsequently be evaporated, condensed, and eventually recycled. This makes this method difficult to implement on a real scale. Moreover, from the point of view of recovery efficiency, an accurate choice of the evaporation conditions of the solvent is essential to efficiently determine the yield of the bio-oil. Yield determination is highly dependent on the product separation protocol and the evaporation conditions of the solvent. High vacuums, high boiling temperatures and too long evaporation times can in fact lead to the loss of low-pressure behaviour in the biocrude product, underestimating the performance of the process (Jo et al., 2017). Furthermore, it should not be overlooked that, when an organic solvent is added to an aqueous mixture, water as a solvent change its characteristics, becoming less hydrophilic than pure water, because part of the organic solvent is solubilised in it. For example, the solubility of dichloromethane in water is 13.8 g/L at 20 ºC; therefore, some slightly polar species present in bio-oil may be solubilised in the aqueous phase during liquid-liquid extraction (Mujahid et al., 2020).

1.4.4.2 Continuous reactors

Most of the HTL studies were performed in batch reactors. However, continuous flow reactors are desirable for large-scale applications of the HTL technologies, to promote the energy utilisation efficiency and make the process economically feasible. With batch reactors, it is almost not possible to have very short residence time for better oil yields, as discussed in the previous section. Thus, the advantage of using continuous flow reactor with controllable residence time, is that maximum higher bio-oil yield could be achieved in a shorter reaction time (Castello et al., 2018). Jazrawi et al. (2013) studied hydrothermal liquefaction of Chlorella and Spirulina microalgae in a continuous flow reactor of 2 L volume at 250–350 °C and 150–200 bar, for a residence time of 3–5 min. The best operating conditions were 350 °C and 3 min residence time, giving 41.7 wt.% bio-oil yield. Hammerschmidt et al. (2011) also performed HTL of three types of sludge, two food industry sludge samples with 12 and 6.7 wt.% solids concentration, respectively, and one wastewater sludge with 7.7 wt.% solid concentration, in a 127 mL continuous flow reactor. The reactor was operated at 300–350 °C and 250 bar with a feed rate of 5.2 and 10.5 g/min, respectively. The feed was first mixed with K_2CO_3 as a homogeneous catalyst, and then the mixture was pumped to the reactor filled with ZrO_2 as a heterogeneous catalyst. Although the residence time in the catalytic bed was controlled to be 10 minutes in most runs, a longer residence time and higher catalyst concentration resulted in greater bio-oil yields.

1.5 Objectives of the research – Aim of the PhD Thesis

Technological and economic development, population growth and the progressive urbanization of vast areas of the planet have caused an increase in global energy demand. At the same time, the use of renewable energies and the energy enhancement of residual biomass have become prominent issues within the sphere of sustainable development goals (in particular, those illustrated in Figure 1.9). Over the past decades, the use of biomass in renewable fuel production technologies has been seen as a promising way to reduce the environmental impact of fossil fuels. In a circular economy, among the different types of biomasses, those defined as “waste” like agricultural residues, food waste, sewage sludge etc., are of particular interest since a significant volume of the municipal/industrial waste is discharged into public sewers, streams, lakes, landfills, and other sinks, at great cost to the industry and/or the community that accepts these effluents.

Figure 1.9 – Main United Nations SDG (sustainable development goals) to which this PhD Thesis gives its contribution.

The aim of this PhD Thesis is the energetic valorisation of a particular type of waste, sewage sludges, from civil and industrial sources, aiming at the reduction of the material destined to disposal, and for their reuse as energetic vector (SDG=7, 11, 13 as in Figure 1.9). Literature references show, in fact, serious environmental and economic concerns related to the remarkable production of sludges from civil and industrial sources, with the expensive environmental and operating costs associated with their landfilling. In this context, among the thermochemical valorisation paths, the energy recovery of this waste will be first investigated through fluidised bed gasification, where the target product is syngas. In fact, there is a limited literature concerning the fluidised bed gasification of sludges, in particular when they come from specific industrial sources. Then, the innovative process known as hydrothermal liquefaction (HTL), where the target product is bio-oil, will be applied to sludges. Both represent "StE" technologies ("sludge-to-energy"), which aim at the production of energy carriers while allowing to reduce the volume of sludge to be disposed of, save natural resources (e.g., land in which to dispose of sludge) and generate by-products of potential value (e.g., ash for use in the field of building materials, or as adsorbents in wastewater decontamination processes). Two types of sewage sludge were selected for these studies: i) an industrial sludge from the tannery industry, ii) a municipal sludge. While Chapter 2 of this Thesis reports on materials and methods, a specific section (Chapter 3) is devoted to the characterisation of the two sludges.

Chapter 4 is focused on the gasification process. In this case the process has been studied only on the tannery sludge, as this process has already been investigated by the research group in the case of municipal sludge (Migliaccio et al., 2021). In particular, when using tannery sludge, special attention must be paid to the high levels of Cr(III) in the sludge. This amount of Cr is attributable to the tanning process, in which Cr(III) basic salts are used. In this case we aimed at,:

i. a careful choice of operating conditions, in order to avoid/limit the oxidation of Cr(III) to the most toxic and environmental dangerous Cr(VI); in this regard, the choice of a fluidized bed reactor plant was made following the need to ensure an excellent contact between the gas phase and solid during the heterogeneous process.

ii. The chemical characterization of products (syngas) and residues (bottom ash, fly ash and tar), of the gasification process, also in order to verify the distribution and oxidation state of Cr at the end of the process.

The innovative hydrothermal liquefaction process has been applied to both types of sludge in a 500 mL batch reactor (purposely designed by the PhD Candidate), to investigate the effect of the main operating parameters on the process. In particular, the study of this process concerned (Chapter 5):

i. Set-up of a lab-scale plant based on a 500 mL batch autoclave reactor for HTL test on a sewage sludge. This study is of particular interest, because most of the literature is based on studies of small-scale batch reactors (10–100 mL) and, consequently, the effect of thermal transients on product yields is little investigated in the literature.

ii. Determination of the reactor configuration characterised by the highest heating and cooling rates.

iii. Study of the bio-oil recovery with different separation techniques applied to the liquid fraction produced by the HTL process.

iv. Determination of the yield of the products and properties of the bio-oil obtained at different HTL temperature and process times for the two different sludges.

v. In the specific case of tannery sludge, the distribution and oxidation state of chromium in the different phases produced by the HTL process.

vi. Preliminary study on synergistic/antagonistic effects during the HTL process applied to mixtures of two types of sludge, that have different composition in terms of lipids, proteins, carbohydrates, and ash.

Chapter 6 provides an analysis of the advantages and disadvantages of the two technologies investigated and a comparison between them, in terms of energy recovery of the process, quality and yield of the energy vector produced. Conclusions and future developments are reported as well.

The final part of this PhD Thesis reports a complete list of all the papers authored by the PhD Candidate in the PhD time-frame, with the corresponding full documents.

Chapter 2 – Materials and methods

This chapter describes the characterisation techniques used to obtain an "ID card" of the two selected sludges and for reaction products obtained by gasification and hydrothermal liquefaction. Moreover, a detailed description of the experimental apparatus used for the gasification tests will be presented. Finally, for the HTL process, it will be described: i) the 500 mL lab-scale batch reactor set-up; ii) the experimental procedure for liquefaction tests; iii) the separation protocols used for products recovery.

2.1 Characterisation of municipal and tannery sludges and reaction products

The tannery (TS) and municipal sludges (MS) were supplied in powder and pellet form, respectively. Both sludges are characterised by an earthy odour and visually appear of a brown (TS) or dark-brown (MS) colour. A summary of the characterisations carried out for the starting sludge and the products obtained from the two thermoconversion processes is given in Table 2.1.

Table 2.1 – Description of the main characterisation techniques.

Stream	Description	Characterisation technique
Tannery sludge	The industrial tannery sludge (TS), coming from a plant located in southern Italy, was kindly provided by the Italian Leather Research Institute ("Stazione Pelli" – SSIP)	• Proximate analysis • Ultimate analysis • Evaluation of the higher heating value (HHV) followed by determination of the chlorine content by Mahler bomb • Determination of metal content by inductively coupled plasma-mass spectrometry (ICP-MS) • Determination of the content of Cr(total) and Cr(VI) and, by difference, Cr(III) • Determination of macro-components in terms of lipids, proteins, and carbohydrates
Municipal sludge	The sewage sludge taken as a reference material was a municipal sludge (MS) deriving from a wastewater treatment plant located in Milano (Italy).	• All as above, except for chromium analyses
Syngas	It represents the target product obtained from the gasification process.	• Infrared spectroscopy analysis for syngas speciation
Fly-ash **Bottom-ash**	They represent a residue resulting from the gasification process.	• Proximate analysis • Ultimate analysis • Determination of metal content by ICP-MS • Determination of the content of Cr(total) and Cr(VI) and, by difference, Cr(III), for ashes from tannery sludge gasification
Tar	It represents a by-product resulting from the gasification process.	• Chemical speciation by gas chromatography-mass spectrometry (GC-MS)

Bio-oil	It represents the target product obtain from the hydrothermal liquefaction process.	• Evaluation of HHV followed by determination of the chlorine content by Mahler bomb • Determination of metal content by ICP-MS • Determination of the content of Cr(total) and Cr(VI) and, by difference, Cr(III), for bio-oil from tannery sludge HTL • Speciation of bio-oil by liquid chromatography-mass spectrometry (LC-MS) and H-nuclear magnetic resonance (H-NMR)
Aqueous phase	It represents a by-product resulting from the gasification process	• Determination of metal content by ICP-MS • Determination of the content of Cr(total) and Cr(VI) and, by difference, Cr(III), for bio-oil from tannery sludge HTL • Speciation of water soluble compounds by LC-MS and H-NMR

2.1.1 Proximate analysis

The proximate analysis was carried out on both the parent sludges and the by-products of the gasification process, namely bottom ash, and fly ash, by reference to UNI 9903/ASTM D5142 standards and using a TGA701 LECO thermobalance (Figure 2.1). This instrumentation consists of a balance, a furnace, a supply system and a gas purge system, and a computer for system control, data acquisition and processing. The procedure followed for the analysis is described below:

1. the thermobalance proceeds with the tare weight of the crucible into which the sample to be analysed is to be placed, determining the weight of the empty crucible; at the end of this operation, the sample is to be entered in quantities typically close to 1 g; the exact weight of the introduced sample is determined directly with the thermobalance, and will constitute the reference value for the next steps;
2. the first stage of the analysis consists in the determination of the moisture content; the sample is heated at a rate of 6 °C/min to 107 °C in an inert environment (N_2 atmosphere) and the loaded crucible shall be subjected to cyclic weighing at intervals of 1 s. The final temperature shall be maintained until changes in the weight of the sample are no longer recorded. Under these conditions, the sample loses its moisture content, which is evaluated as the ratio of the recorded weight loss to the initial weight of the sample;
3. the second stage consists in determining the content of volatile matter; the crucible - closed by a refractory cover to prevent loss of material during the devolatilization phase - is heated at a rate of 50 °C/min to 950 °C in an inert environment (N_2 atmosphere). The system is then kept at this temperature for 7 min, and then cooled down to 600 °C. Under these conditions, the sample loses its volatile content. At this temperature, the lid is removed manually from the crucible and the instrument proceeds

to reassess the weight of the sample: the content of volatile substances initially present in the sample is determined as the ratio of weight loss (vs. the previous stage) to the initial weight of the sample;

4. the last stage of the analysis consists in the determination of the fixed carbon and ash content; the crucible is heated at a rate of 15 ºC/min from 600 ºC to 750 ºC in an oxidizing medium (pure O_2 atmosphere), and is subjected to cyclic weighing at intervals of 1 s. Under these conditions, C present in the sample burns. The final temperature is maintained until changes in the weight of the sample are no longer recorded: the fixed carbon content is assessed as the ratio of the weight loss (vs. the previous weighing) to the initial weight of the sample. The ratio of the final weight to the initial weight of the sample is the ash content, that is, the inert residue in the combustion process.

Figure 2.1 – TGA701 LECO thermobalance.

2.1.2 Ultimate analysis

The ultimate analysis (or elemental analysis) aims to determine the mass percentages of carbon, hydrogen and nitrogen present in the analysed sample. The elemental analysis was performed on both parent sludges and bottom ash and fly ash deriving from the gasification process. The principle on which this analysis is based is to measure the composition of the gases produced by the complete combustion, using an excess of oxygen, of a fixed mass of a sample inside a furnace. This determination is carried out on small portions of dried and ground material (in quantities of the order of 0.02–0.03 g), as reported by the ASTM reference standard D5373 and using an element analyser, in our case LECO CHN628 (Figure 2.2a). The percentage by weight of the elements in the sample is measured from the detection of the respective combustion products in pure oxygen at a temperature of 950 ºC, i.e., carbon dioxide (for C), water (for H) and nitrogen oxides (for N). The combustion gases are sent to infrared absorption detectors to measure CO_2 and H_2O concentrations. An aliquot of the gases is transported by a stream of He and passed through a copper catalyst at high temperature (700 ºC) for the removal of oxygen and the reduction of nitrogen oxides to elemental nitrogen, and finally conveyed to other filters to remove CO_2 and H_2O. The nitrogen content is then measured with a thermal conductivity detector (TCD), which is based on the difference in thermal conductivity of various gaseous species. The TCD consists of two filaments, one crossed by the pure carrier gas (He), and the other by the carrier gas containing the gas to be analysed. By varying the conductivity of the gas, the amount of heat exchanged by the filament with the gas varies, and then the temperature of the filament itself varies. This change in temperature involves a change in the electrical conductivity of the filament, and therefore an alteration in the flow of current passing through it.

The analysis was accompanied by the determination of the sulphur content in the sludge. An elementary LECO SC-144DR analyser was used for this purpose (Figure 2.2b). The analysis makes it possible to measure the content of S which is released during combustion of the sample in pure oxygen (producing SO_2), and is conducted at a temperature of 1350 °C, sufficiently high to cause combustion not only of organic sulphur, but also of any pyrolytic sulphur present.

Figure 2.2 – LECO CHN628 (a-left) and LECO SC-144DR (b-right) analysers.

2.1.3 Determination of the higher heating value (HHV) and chlorine content

HHV is the amount of heat produced by the complete combustion of a unit mass of fuel (sludge or bio-crude in the case under consideration), when the combustion products are brought back to the initial temperature, and therefore also including the latent heat for condensation of water vapour produced during combustion. HHV was determined using a Parr 6200 calorimeter (Figure 2.3). In this analysis, the sample, bio-oil, or sludge (in this case, previously dried and ground), is placed in a calibrated crucible, in quantities not exceeding 1 g, inside a “Mahler bomb”: a cylindrical steel container with a screw cover, which contains two iron rods for casing the crucible and inserting a tungsten filament in contact with the sample. The cover is equipped with two holes for the connection of the electrodes, and a valve for the supply of pure oxygen (20 bar). Once the calorimetric bomb is prepared, it is placed in a basket containing 1 kg of distilled water and allocated in the calorimeter. The electrodes are then connected to the bomb cover, and the calorimeter cover is closed. The measure is conducted under adiabatic conditions. The analysis begins when the temperature inside the bomb and that of the water contained in the basket are equal; at this point the combustion is triggered by a spark, produced by passing a current through the tungsten filament. The heat produced by combustion is transferred to water, which is therefore affected by an increase in temperature, from which the calorific value of the sample is assessed by energy balance. The reference standard for the determination of the higher heating value is ASTM D5865.

Starting from the higher heating value, it is possible to calculate the lower heating value (LHV) according to the relation:

$$\text{LHV} = \text{HHV} - n\,\Delta H \tag{2.1}$$

where n represents the kg of water produced on kg of fuel, while ΔH is the latent heat of evaporation of H_2O, approx. 2.5 MJ/kg. The value for n can be calculated from the hydrogen content of the starting biomass, as obtained by elemental analysis. LHV can therefore be understood as the "net calorific value" of the material, naturally in the hypothesis of complete combustion.

The chlorine content has been measured downstream of the higher heating value. Chlorine is indirectly evaluated by introducing 5 mL of 2% sodium carbonate aqueous solution into the calorimetric bomb, which absorbs the chlorine compounds released during combustion. At the end of the HHV measurement, the obtained solution is collected and diluted to a volume of 50 mL by adding distilled water; the solution is then analysed using an ion chromatograph (883 Basic IC plus from Metrohm), allowing the determination of the chlorine content of the sample. The reference standard for the determination of the chlorine content is UNI 9903.

Figure 2.3 – Parr 6200 calorimeter (a-left) and sealed calorimeter bomb (b-right).

2.1.4 Determination of metal content by inductively coupled plasma-mass spectrometry (ICP-MS)

Metal determination was performed by ICP-MS, following the reference standard EPA 3052 and using an Agilent technologies 7500ce instrument (Figure 2.4). This technique makes it possible to determine different metal and non-metallic species at concentrations of up to one part per billion (ppb). ICP-MS analyses were conducted on samples after pre-treatment of grinding and acid digestion, to verify the concentration of the metals present. The acid digestion was carried out using HNO_3 and H_2O_2 in a hermetically sealed system, to reach temperatures higher than those of boiling acids at room temperature, with increased solubilizing and oxidizing properties of the reagents used. The choice of these reagents has been made in order not to add interfering species to the ICP-MS, as H, N and O are not determinable elements.

Figure 2.4 – Agilent technologies 7500ce instrument for ICP-MS analysis.

2.1.5 Speciation of chromium in tannery sludge by spectrophotometric method

Since chromium is the main metal in tannery sludge, the total Cr content in samples was determined by atomic absorption spectroscopy (AAS), to validate the determination obtained by ICP-MS. The analytical methods used for the determination of Cr(total) and Cr(VI) (and, by difference, Cr(III)) are present in "Analytical methods for sludge. Chemical-physical parameters", Quaderni IRSA-CNR n. 64.

AAS is widely used for both qualitative and quantitative determinations of trace inorganic species (0.1 ppm–0.1 ppb), especially metals in matrices. The analysis was performed with a Varian SpectrAA 220 atomic absorption spectrometer (Figure 2.5).

Figure 2.5 – Varian SpectrAA 220 atomic absorption spectrometer.

For the measurement of Cr(total), the following solutions were prepared:

1. a reference solution (standard) with known chromium salt(VI). We started from 0.0721 g of $K_2Cr_2O_7$ dissolved in 0.5 L of water. After dilution with a ratio of 1:10, the calculated Cr concentration is 5.0977 mg/L;
2. a solution containing the solid to be analysed. For this purpose, 0.5 g of solid dissolved with 10 mL of 65% concentrated nitric acid and 5 mL of pure H_2O_2 were taken. The solution was then brought to volume with a 15 wt.% solution of HNO_3;
3. solutions for the construction of the calibration line from the reference solution "point 1". In particular, 7 solutions were prepared (6 at a known concentration of Cr, and 1 "black" at zero Cr concentration), then brought to volume (25 mL) with a solution of 15 wt.% of HNO_3.

From Cr solutions of know concentration, by atomic absorption it was possible to determine the absorbance for each of them and, consequently, to build the calibration line. By interpolation, it was subsequently possible to determine the concentration of Cr(total) present in the solutions containing the sample under investigation. For the determination of Cr(VI), the spectrophotometric method was used for measurements in the field of UV-visible (UV-Vis). The reference method used is EPA 3060A and the tests were performed with an Agilent UV–vis Cary 5000 instrument (Figure 2.6).

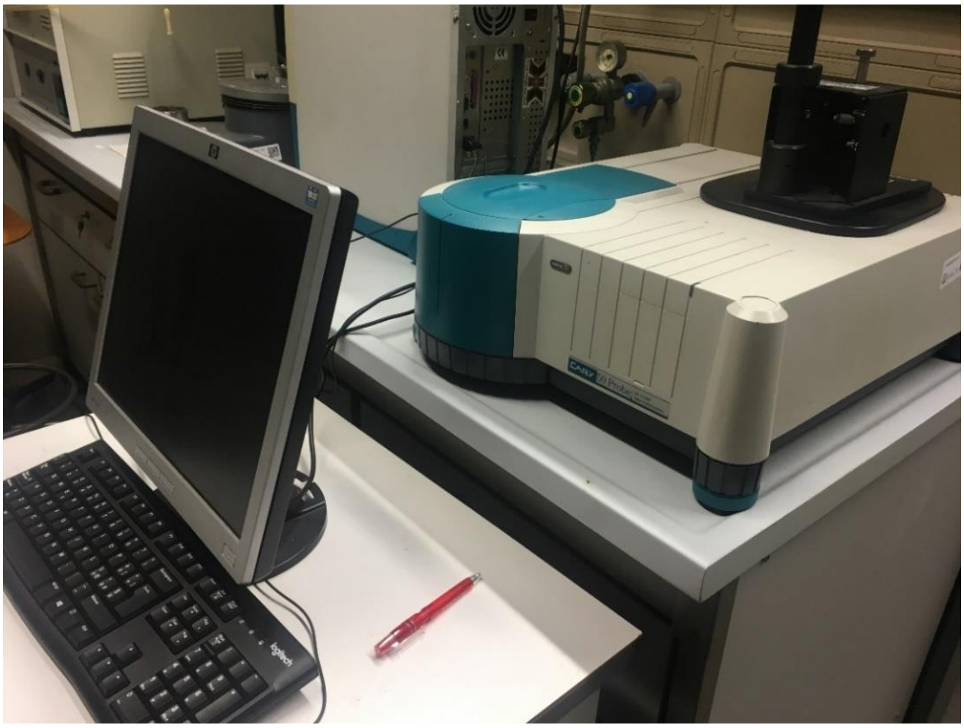

Figure 2.6 – Agilent UV–vis Cary 5000 instrument for Cr(VI) determination.

The determination of the Cr(VI) concentration was made by solubilising the sample in an acid medium, and its concentration was determined on the solution filtered by colorimetric reaction with diphenylcarbazide.

In a first step, the sample to be analysed was stirred in water for 30 min, after which the solution was alkalized by adding NaOH, to obtain the precipitation of Fe. The filtrate was subsequently subjected to the determination of hexavalent chromium, this time acidifying the solution for the determination of Cr(VI) in H_2SO_4. This first phase of the procedure was carried out because ICP-MS analysis of tannery sludge showed a high amount of iron which, if present as Fe^{2+}, in acid solution reacts with dichromate interfering in the determination of Cr(VI). Subsequently, they were prepared:

1. a reference solution with known chromium salt (as in the previous case);
2. a diphenylcarbazide solution, interacting with Cr(VI) resulting in a change in the colour of the starting solution from transparent to pink. The solution was prepared by dissolving 0.0207 g of the reagent in 10 mL of ethyl alcohol and 40 mL of a 1:10 solution of 98 wt.% concentrated H_2SO_4 and water;
3. a solution containing the solid to be analysed - 0.5 g of solid was hot dissolved in a solution consisting of 5 mL of 98 wt.% of H_2SO_4 and 5 mL of water and subsequently brought to volume (25 mL) with water;
4. solutions for the construction of the calibration line from the reference solution "point 1". In particular, 5 solutions were prepared (4 at a known concentration of Cr(VI), and 1 "blank" at zero chromium concentration), 2 drops of phosphoric acid and 0.5 mL of the "point 2" solution were added, and the volume was brought to 25 mL with water.

From the known Cr solutions, the absorbance for each of them could be determined using UV-vis spectrophotometry and the calibration line could be built accordingly. The concentration of chromium(VI) in the two solutions containing the sample under analysis could subsequently be determined by interpolation.

2.1.6 Determination of the macro-compounds in the starting sludges

Despite the potential of lipids, proteins, and carbohydrates in influencing the hydrothermal liquefaction process of sewage sludge, there is a gap in the literature concerning a detailed characterization of their content in substrates intended for HTL. This may be partly due to the lack of established standard methods for analysing these parameters in sewage sludge. In this paragraph, the characterization protocols that have produced consistent results for the determination of macro-components in sludges will be defined.

Analysis of lipids content

The Bligh and Dyer (Bligh and Dyer, 1959) method, with slight modification (as reported below), was used for lipids analysis: 0.5 g of the standard (i.e., palmitic acid) or sample (municipal or tannery sludges) was used in all analyses conducted in triplicates. To this, 3.75 mL (1:2 v/v) chloroform:methanol was added and vortexed for 2 min. Then, 1.25 mL of chloroform was added and vortexed for another 2 min. Finally, 1.25 mL of deionized water was added and vortexed for 1 min. The sample was then centrifuged to enable separation of the organic and aqueous layer. A known volume of the bottom organic layer (chloroform extract) was recovered carefully using a Pasteur pipette. Following extraction, a known volume of the chloroform extract (aliquot) was placed into a pre-weighed (W_1) aluminium pan (Fisher Scientific). The extract was allowed to dry at room temperature until a constant weight (W_2) was obtained. Lipids content (then expressed as %) was calculated as:

$$\%\text{Lipids} = \frac{(W_2 - W_1)\cdot V}{V_{aliq.}\cdot m_{sludge}} \qquad (2.2)$$

where V is the volume of organic layer, $V_{aliq.}$ is the volume of the chloroform extract, m_{sludge} is the sludge weight.

Analysis of carbohydrates content

For the determination of carbohydrates, we used the phenol-sulfuric acid method proposed by Albalasmeh et al. (2013), based on light absorption in the visible and UV range. However, this method has been re-adapted to solid samples by solubilising 5 mg sludge in 8 mL solvent. Then, a 2 mL aliquot of a carbohydrate solution is mixed with 1 mL of 5% aqueous solution of phenol in a test tube. Subsequently, 5 mL of concentrated sulfuric acid is added rapidly to the mixture. After allowing the test tubes to stand for 10 min, they are centrifugated for 30 s and placed for 20 min in a water bath at room temperature for colour development. Then, light absorption at 490 nm is recorded on a spectrophotometer. Reference solutions are prepared in identical manner as above, except that the 2 mL aliquot of carbohydrate is replaced by Millipore double-treated water.

Analysis of proteins content

The modified Lowry test was used for proteins determination (Hartree, 1972), again adapted to solid samples by solubilising 50 mg sludge in 7.4 mL solvent. The analysis involved the preparation of 3 solutions:

1. a solution where 2 mg of potassium sodium tartrate and 100 mg of $NaCO_3$ are dissolved in 500 mL 1 N NaOH and diluted with water to 1 L.
2. a solution where 2 mg of potassium sodium tartrate and 1 g of $CuSO_4\cdot 5H_2O$ are dissolved in 90 mL of water and 10 mL of NaOH 1 N are added.
3. a solution where the Folin-Ciocâlteu reagent is diluted with water with a ratio of 1:10 in vol.

Protein samples are diluted to 1 mL with water and treated with 0.9 mL of solution “1”. A blank and a standard are set up in the same way. The tubes are placed in a water bath at 50 °C for 10 min, cooled to room temperature (21–25 °C), and treated with 0.1 mL of solution “2”. The solutions are left at room temperature for at least 10 min, then 3 mL of solution “3” is forced in rapidly to ensure mixing within 1 s. The tubes are again heated at 50 °C for 10 min and cooled to room temperature. Solutions absorbance are read in 1 cm cuvettes at 650 nm.

2.1.7 Speciation of tar and incondensable gas through gas chromatography and mass spectrometry techniques

GC-MS is one of the most widely used analytical techniques, since it constitutes one of the most advanced methods and allows the identification and semi-quantification of organic substances in a variety of matrices, even if the mixture is particularly heterogeneous (as in the case of tar). The tar obtained by the sludge gasification process was recovered from the collecting flasks, which form part of the condensers set downstream of the fluidised bed gasification reactor (*vide infra*), by solubilising in acetone, and this stream was subsequently subjected to a qualitative and semi-quantitative analysis, to determine the spectrum of the organic compounds present. The analysis was conducted using GC-MS. The incondensable gases, which leave the condensers train, deprived of the liquid component, have been analysed with a microgc Agilent 3000A instrument (Figure 2.7) that allows to determine the concentration of numerous light hydrocarbons (C_1–C_6), in addition to the main gases generated by gasification on a dry and N_2-free basis (CO, CO_2, CH_4, H_2, O_2), with concentrations up to the order of parts per million (the instrument available is equipped with four modules with TCD detector).

Figure 2.7 – Microgc Agilent 3000A instrument.

As far as the condensable species (tar) are concerned, their analysis was carried out with an Agilent 7890A gas chromatograph which is associated an HP-35 phenyl-ethyl-methyl siloxane column (length 30 m, thickness 0.25 mm), accompanied by a 5975C VL MSD mass spectrometer acting as a detector (Figure 2.8). Tar and acetone solution is loaded in GC vials, which are placed in the autosampler. By means of a syringe, a very small aliquot of the solution is taken and injected into the column, which is kept at 50 °C for five minutes, then heated to 200 °C at a rate of 5 °C/min, then to 270 °C at a heating rate of 10 °C/min, and finally it reaches 310 °C with a rate of 5 °C/min. During this programmed temperature ramp, the various organic compounds are adsorbed, and the retention time is measured. The final stage consists of a period of 15 minutes, in which the column is kept at a constant temperature of 310 °C, to allow the analysis of species with longer retention times. The identification takes place by comparison of the spectrum under examination with reference databases (in our case, NIST 11 database). In this way, by comparing the TIC chromatogram (total ion current) obtained by gas chromatography with the mass spectra associated with each chromatographic peak, it is possible to obtain information from both a semi-quantitative and a qualitative point of view.

Figure 2.8 – Agilent 7890A gas chromatograph - 5975C VL MSD mass spectrometer.

2.1.8 Infrared spectroscopy analysis for syngas speciation

Syngas is the target product of gasification, and its characterization is necessary to estimate the efficiency of the process. In particular, the main process output gases are, on a dry and N_2-free basis: CO, CO_2, CH_4, O_2 and H_2, and analysers (H&B series, Hartmann & Braun) are used to monitor their concentration. They perform the measurement by exploiting the absorption in the infrared spectrum (NDIR sensor: non-dispersive infrared), except for the O_2 analyser which uses a magneto-mechanical sensor. They are specific for continuous analysis and they are connected in series, to allow the simultaneous measurement of the gases under analysis. Instruments automatically select one of the available calibration ranges to deliver the best possible accuracy. The analysers used are (Figure 2.9):

- H&B CO and CO_2 analyser Uras 10 E (0–0.1% vol./0–0.5% vol. for CO and 0–20% vol./0–50% vol. for CO_2);
- CO H&B Advance Optima Uras 14 analyser (0–0.05% vol./0–0.2% vol./0–2% vol./0–20% vol.);
- Analyser for CH_4, C_2H_4 and C_2H_6, H&B Uras 10 P (0–2% vol./0–10% vol.);
- H&B Magnos 6G O_2 analyser (0–10% vol./0–25% vol.);
- Analyser for H_2 in N_2, H&B Caldos 5G (0–10% vol./0–50% vol.).

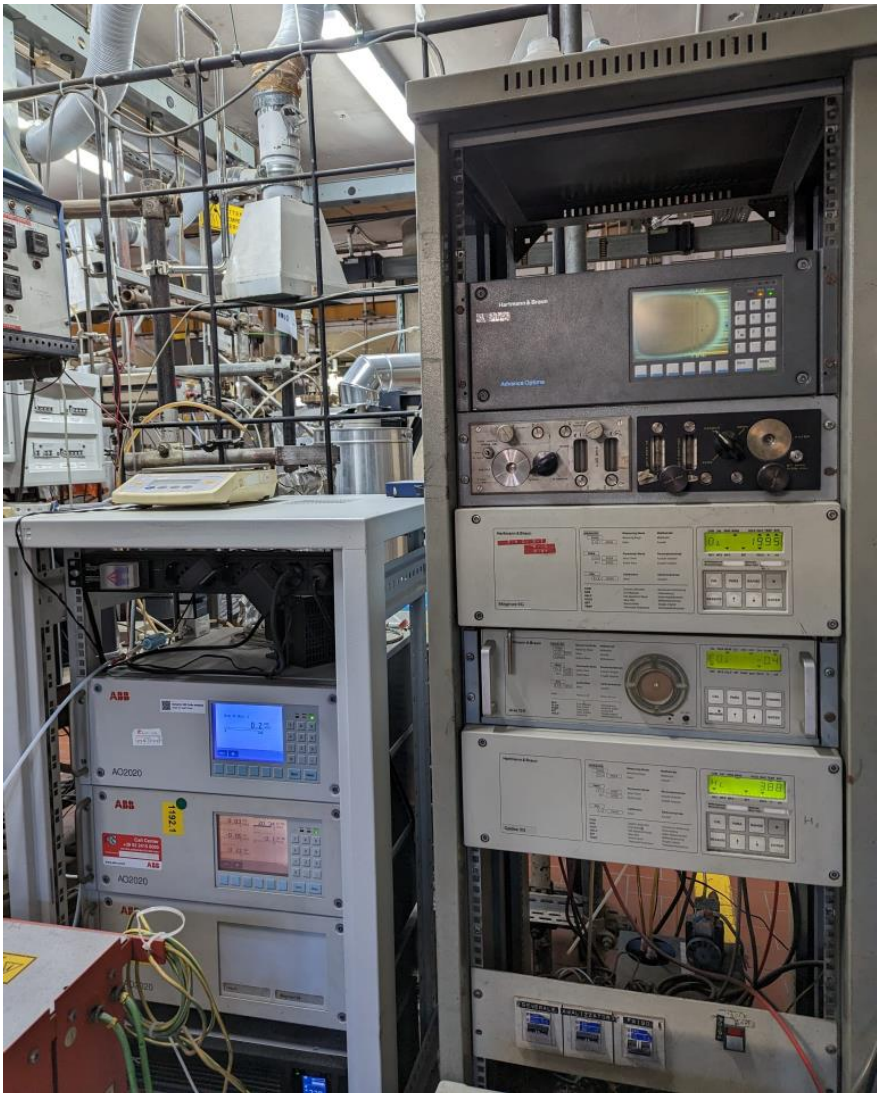

Figure 2.9 – IR analysers for syngas characterisation.

The gas is collected inside the reactor by means of a stainless-steel probe (external/internal diameter 6/4 mm), inserted approximately for 0.1 m inside the FB. This probe is connected to a calibrated suction pump, to suck a flow of 50–60 Ndm^3/h. To prevent fine solid particles from reaching the analysers, a glass wool filter is placed between the probe and the analysers themselves.

2.1.9 Qualitative characterisation of bio-oil and aqueous phase by H-nuclear magnetic resonance (H-NMR)

To obtain a qualitative analysis of biocrude obtained, the samples of bio-oil was subjected to H-nuclear magnetic resonance spectroscopy. From this analysis it was possible to acquire the one-dimensional ^{1}H-NMR spectra and the two-dimensional ^{1}H, ^{1}H-COSY and ^{1}H,^{13}C-HSQC spectra.

^{1}H NMR spectra were recorded in DMSO-d_6 (biooil samples) or in D_2O (water samples) at 400 MHz on a Bruker 400 MHz spectrometer. ^{1}H,^{1}H COSY and ^{1}H,^{13}C HSQC were run at 400 MHz using Bruker standard pulse programs. Chemical shifts are given in ppm. The aqueous phases were exchanged with D_2O before running the spectra.

2.1.10 Qualitative characterization of biocrude and aqueous phase by liquid chromatography-mass spectrometry (LC-MS)

To get an overview of the species present in the biocrude and in the aqueous phase obtained from the HTL process, the samples achieved from the process were also subjected to LC-MS analysis. LC / MS analyses were performed in positive ion mode using an Agilent 1260 / 6230DA ESI-TOF instrument under the following conditions: 35 psi nebulizer pressure; drying gas (nitrogen) flushed at 8 L / min at a temperature of 325 ° C; capillary voltage 3500 V; fragmenter voltage 175 V. An Eclipse Plus C18 column (150 × 4.6 mm, 5 µm) at a flow rate of 0.4 mL / min was used.

Eluent system: 0.1% formic acid in water (solvent A) /0.1% formic acid and 2% water in acetonitrile (solvent B): 0-1.50 min from 1 to 13% of B, 1.50-7.50 min from 13 to 15% of B, 7.50-12.50 min from 15 to 20% of B, 12.50-27.50 min from 20 to 40% of B, 27.50-37.50 min from 40 to 60% of B, 37.50-45.0 min from 60 to 85% of B, 45.0-52.5 min from 85 to 95% of B, 52.5-65.1 100% of B.

Sludge samples were dissolved in DMSO/MeOH (1:4 v/v) filtered through nylon membranes (13 mm, 0.45 µm) and injected for LC-MS analyses.

2.2 Experimental apparatus (fluidised bed) for gasification tests

The experimental apparatus used for the gasification process is depicted in Figure 2.10. The primary gas is fed from the bottom of the reactor, and initially passes through a windbox that also acts as a preheater, of 41 mm of internal diameter and 600 mm high, made of steel for high temperatures. This section is filled with ceramic rings both to promote the thermal exchange between the gas entering from below and the heated surfaces, and to uniform the gas flow into the reactor. The windbox ends with a flange in which a zone has been created to house the metal nets, that serve both as a distributor of the fluidisation gas, and as a support for the material inside the reactor. Above the windbox there is the fluidisation column, 41 mm of internal diameter, and 1 m of height, made of steel resistant to high temperatures. It is equipped at both ends with flanges, one to be coupled at the bottom with the preheater and then with the distribution plate, and the other at the top with the reactor head, consisting of a conical truncated duct, at the exit of which there is a cyclone. To reach and maintain the operating temperatures necessary for conducting the experimental tests, both the preheater and the reactor are immersed in an oven, consisting of electrical heaters, placed inside two low-density ceramic fibre half-shells, providing a total power of 5 kW. The furnaces are connected to a PID temperature controller, which ensures that the operating temperature is reached and maintained by a type K thermocouple in contact with the bed and positioned immediately above the gas distributor. The thermal insulation of the furnace-column system is achieved using a ceramic insulator, and an outer envelope made of aluminium foil. At the reactor head outlet, an aliquot of the gases is sampled to be sent to the series of online analysers described above; another aliquot is sampled for the collection of gasification oils; the remainder is sent to the extraction hood. Before arriving at the analysers, the hot gases pass through a filter to remove the elutriated solid material and then through a refrigeration system to condense the water in the gases, which could produce interference in the IR detection cells inside the analysers. As regards the sludge feeding system in the reactor, it is of a mechanical-pneumatic type. The combined action of a screw and a secondary gas flow, necessary for the sludge to enter the reactor, is used. This system is connected to the fluidisation column by means of a cylindrical duct of 4 mm ID, made of stainless steel, positioned laterally at the base of the bed (in particular, 5 mm high from the distributor of the fluidisation gas). Specifically, the feeding system consists of a hopper for the accumulation of the material to be fed, and a worm screw, which transports the material to a cylindrical container, equipped with an inlet for the secondary gas flow necessary to move the material and to pneumatically enter it at the base of the FB. The worm screw is driven by a low voltage (24 V) electric motor of 500 W, connected to a speed variator.

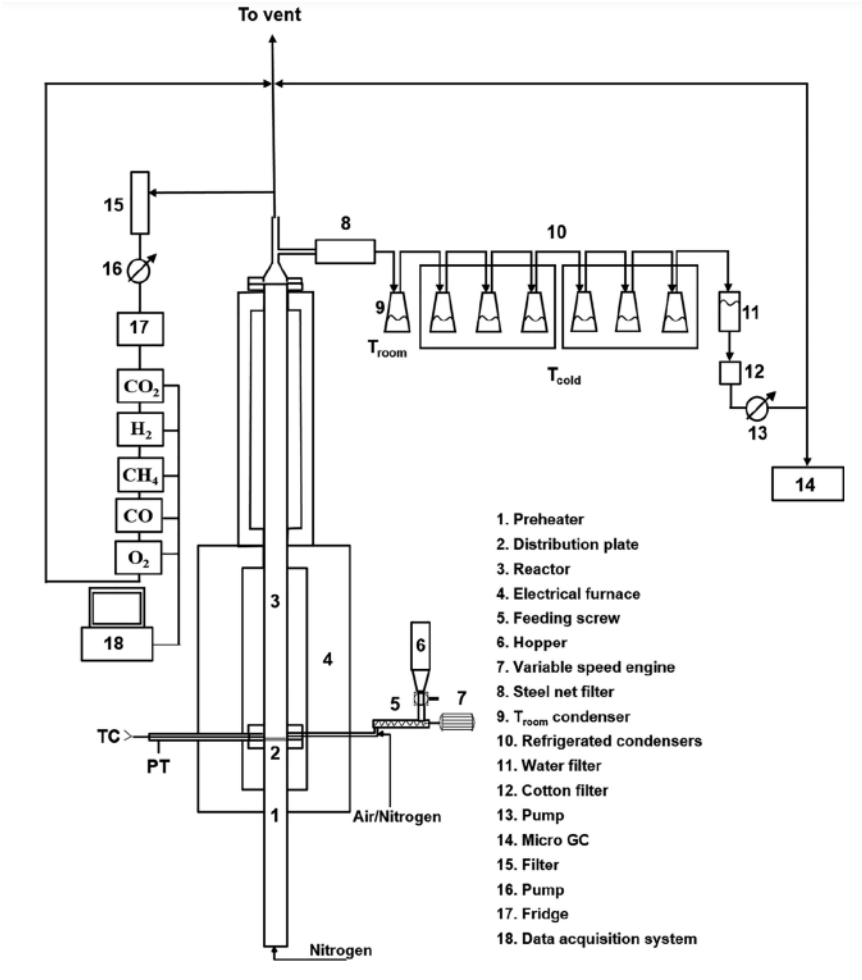

Figure 2.10 – Scheme of the fluidised bed apparatus for gasification tests.

2.2.1 Experimental procedure for gasification tests

During a typical gasification test:

1. After heating the FB gasifier to the desired temperature (with inert material), the sludge is fed from the top of the hopper until it is filled (as received);

2. After starting the sludge feed, the process parameters, monitored in real time by the control PC, allow to evaluate the achievement of stationary conditions and system stability, and to properly schedule the start of sampling of process outputs. Continuous analysis of the gas composition is carried out, recording the concentrations throughout the whole gasification test, using an IR analyser;
3. Another part of the gas is drawn from the main current coming out of the reactor by a high precision pump and sent to the metal filter for the removal of fly ash. The filter is heated to a temperature of 180 °C with an electric band, to avoid tar condensation;
4. The gases coming out of the filter are sent to a condensation train (composed of one flask at room temperature and six flasks at −12 °C) to collect the produced tar compounds, then measured and analysed by means of GC-MS. The gases leaving the condensation train, deprived of the liquid component, are analysed by a micro-gas chromatograph determining the concentration of incondensable gases and numerous light hydrocarbons (C_1–C_6), with concentrations up to the order of the ppm;
5. At the end of the gasification test, the sludge supply is stopped, and the system is "shut-down", the electric heaters are shut down and the reactor is allowed to cool down to room temperature, in nitrogen flow;
6. Once the reactor has been cooled, the bed material is discharged, and the inert fluidisation material (sand) is separated from the solid gasification residue (bottom ash) through a combination of sieving and density-based procedures. In this way, the ash from the process can then be subjected to the required characterisation;
7. After the plant shut-down phase, the flasks constituting the condensation train are removed and weighed to determine the amount of liquid collected. The condensation train consists of a series of conical flasks of the same volume (250 mL), connected together. The first flask is collected at room temperature, while the other six flasks are kept at −12 °C by means of a saturated solution of water and sodium chloride. The analysis phase involves weighing the flasks before and after sampling, to determine the amount of tar collected;
8. The reaction products obtained (syngas, tar, and ashes) are then be subjected to the subsequent characterisation analyses.

2.2.2 Operating conditions for gasification tests on tannery sludge

The operating conditions of the gasification tests are illustrated in Table 2.2. The bed inert material was silica sand, 300−400 μm (inventory=180 g). The fluidising gas was composed by the sum of a stream of 300 NL/h of N_2 and a stream of 50 NL/h of air (85.7% of N_2 and 14.3% of air). Therefore, the gas fed can be seen as an oxygen-nitrogen mixture, very poor (compared to air) in oxygen, whose content in the supply is in fact about 3% (rest N_2). The tests were conducted at 850 °C, fluidising the system at a fluidisation velocity (expressed at 850 °C) of 0.30 m/s (expressed at 850 °C; the minimum fluidisation velocity for this system was 0.04 m/s). After sieving the sludge to a size finer than 1 mm, two tests were carried out: “test 1” and “test 2”, with sludge flow rates of 99 and 63 g/h, respectively. The tannery sludge was used as received, with a total moisture content of 18.5%$_{wt.}$.

Once the characteristics of the sludge were known, these two flow rates values resulted in air/fuel equivalence ratios of 15 and 24% of the stoichiometric value for tests 1 and 2, respectively (values calculated based on the chemical composition of the sludge), ensuring that operating conditions were well far from A*ER*=100%. These A*ER* levels have been selected also in order to operate in such a way as to avoid the complete oxidation of the material, to favour instead the kinetic patterns of gasification (A*ER*<1; please remember that A*ER*=1 would guarantee all the stoichiometric oxygen for the combustion of the solid), while aiming to limit the undesired oxidation of Cr(III) towards the most toxic hexavalent species. These A*ER* values were in line with literature reviews on the topic (Molino et al., 2018).

Table 2.2 – Operating conditions of FB gasification tests of industrial tannery sludge.

	Test 1	Test 2
Bed inert material	Silica sand, 300–400 μm, *inventory*=180 g, *H*/*D*=3	
Gasification temperature	850 °C	
Minimum fluidisation velocity	0.04 m/s (850 °C)	
Fluidising gas	300 NL/h N_2 + 50 NL/h air (3% O_2; 97% N_2)	
Fluidisation velocity	0.30 m/s (850 °C)	
Flow rate of <1 mm sludge	99 g/h	63 g/h
Reaction time	61 min	92 min
air-to-fuel A*ER*	0.15	0.24

2.3 Experimental apparatus for HTL tests

As part of the energy enhancement of municipal and industrial sludge used in the hydrothermal liquefaction process, an important preliminary phase involved the choice of a suitable reaction system. In fact, the HTL process is carried out at 40–200 bar and 200–350 °C to improve the water solubility of hydrophobic organic compounds (such as free fatty acids), to guide the reactive path towards the bio-oil target. On the other hand, under the above conditions, the water solubility of inorganic salts decreases considerably, potentially leading to the precipitation of crystalline salts, which in turn can easily attach to the walls of both the reactor and its components (as mixer, heat exchanger, etc.). This can cause fouling or even blockages and problems associated with the proper functioning of the system. In addition, corrosion, and in particular the pitting phenomena, can occur rapidly in subcritical environment, characteristic of the HTL process. Literature data report studies on different materials tested under subcritical conditions, but only a few have sufficient corrosion resistance, especially when considering a wide pH range. Accordingly, as a material for the construction of the HTL

reactor, a nickel-chromium-molybdenum alloy (Hastelloy C-276) was chosen. This alloy is particularly resistant to pitting and crevice corrosion in reducing environments in the pH 1–14 range, allowing HTL testing even in the presence of different acid and basic catalysts. In addition, the presence of Cr gives good resistance to oxidizing and reducing environments. Details on the choice of material are given in Paragraph 5.1.
Following the selection of the best material for the HTL reactor, a study was made with the aim of establishing the layout of the experimental apparatus, based on the selected conditions and the experimental procedure. Figure 2.11 represents the laboratory scale plant adopted in this PhD project for HTL tests. It is underlined that the full design of the HTL reactor has been originally developed in this PhD Thesis, and its realisation represents a part of the work carried out under the PhD Thesis period.

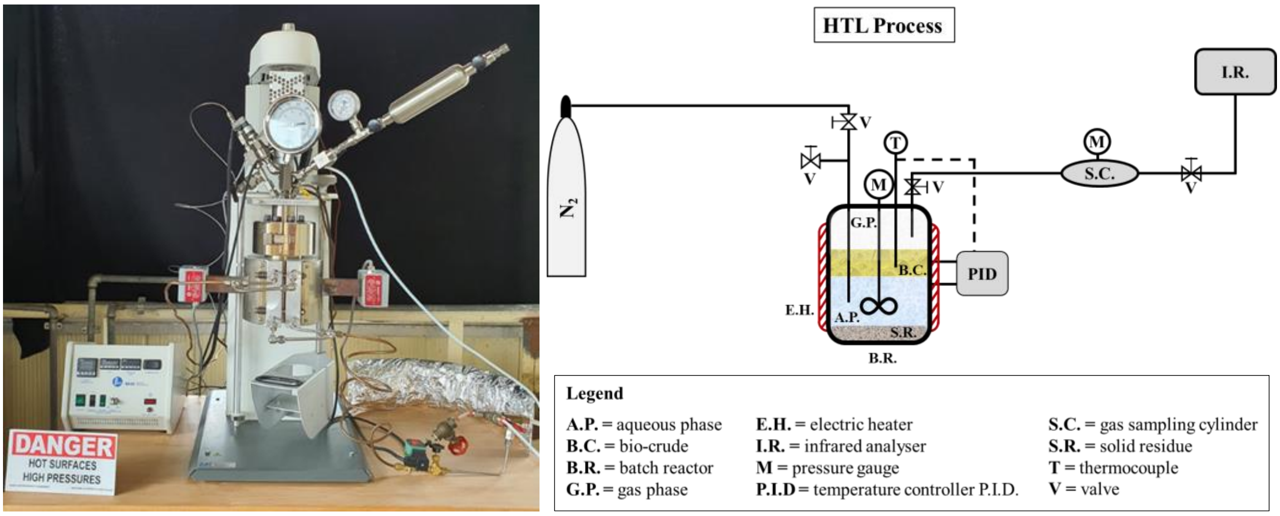

Figure 2.11 – Batch autoclave reactor of 500 mL, picture (on the left) and layout (on the right) of the lab-scale apparatus.

The lab-scale apparatus consists of a 500 mL batch reactor (Parr Instruments, series PA 4575A) equipped with:

1. digital pressure transducer coupled with a needle valve for pressure measurement and control;
2. tubular electric heater coupled with thermocouples and PID system for temperature setting, measurement, and heating rate control;
3. magnetic stirrer with maximum torque of 1.76 Nm and variable speed motor 1/8 hp, suitable for matrices with high viscosity as sludge (10^2–10^4 cP);
4. single loop cooling coil;
5. inlet and outlet ports for gas injection and liquid/gas withdrawal;
6. gas sampling cylinder.

2.3.1 Set-up of HTL apparatus

The set-up of the specifically designed and commissioned HTL plant has been performed through blank tests, loading only distillated water inside the vessel and monitoring the evolution of pressure P and temperature T

in heating processes conducted at different initial pressures, analysing the thermodynamic state of the water under different test conditions.

In addition, during these tests, strategies were evaluated to increase the heating rate and reduce the heat losses occurred at the head and base of the reactor (areas not affected by the heating aluminium blocks). Consequently, to optimize the operation of the HTL process, the different configurations of the experimental apparatus have been studied, aimed at minimizing the thermal transients related to the heating of the vessel content from ambient temperature to the chosen reaction temperature. Starting from a configuration defined "A", corresponding to the system as described in the previous paragraph (where it is possible to obtain a heating rate of about 4 °C/min), it was possible to define two additional configurations, "B" and "C", which report some upgrades (Figure 2.12):

1. Configuration B: the heating stage was carried out also with the support of a 1000 W heating plate of 145 mm diameter located on the bottom of the vessel, and the top of the reactor was insulated with a layer of rock wool;
2. Configuration C: with respect to B configuration, it was added a band heater of 114.3 mm internal diameter and 63.5 mm height (Watlow Series MI band) with a power of 1250 W, coupled with a cylindrical steel block located between the reactor and the heating plate. Temperature control of this system is guaranteed by coupling the heating band with a PID controller, series PXU21A20.

Figure 2.12 – Left) configuration B and Right) configuration C of the experimental apparatus for HTL tests; 1) rock wool insulation, 2) heating plate 3) insulated heating bands.

2.3.2 Experimental procedure for HTL tests

Following the set-up of experimental apparatus, an experimental procedure protocol for a typical HTL test was originally defined. The steps are listed below:

1. Biomass is mechanically sieved, reducing sludge pellets to powder with a grain size of <400 μm;
2. The solid thus obtained is dried in an oven at 105 ºC for 4 h, to remove the moisture content therein, and a sufficient is taken, to obtain a 10 wt.% solid mixture in water; for all the HTL experimental tests carried out in this PhD work, 30 g of dry sludge is mixed with 270 g of distilled water, reproducing the characteristic percentage of solid content present in a sludge resulting from a wastewater treatment plant, in case it has not undergone the energy-intensive dehumidification step; the choice to dry the sewage sludge and then add distilled water comes from the need to know the real percentage by weight of moisture and not add further components to the sludge that would be derived from running water;
3. After loading the slurry (sludge/water) into the vessel, the reactor is sealed through the steel flanges, and subsequently insulated with rock wool;
4. Parallel to step “3”, the heating plate (B configuration) or the heating plate-heating band system (C configuration) is heated;
5. The two aluminium heating blocks are closed around the reactor walls, and the atmosphere inside the vessel is made inert by a pressure purging procedure, which involves sending a quantity of N_2 such as to bring the molar fraction of oxygen into the gas phase very close to zero. The removal of O_2 present in the reactor is performed to avoid the undesired oxidative phenomena that could alter the reactive networks, and therefore the products of the HTL process;
6. At the end of inertization, the system, at room *T*, is pressurised to a value calculated to determine that a pressure of approximately 200 bar is reached at the set-point temperature chosen for the reaction (considering the contribution due to the increase in endogenous pressure generated by the heating of the system). In the determination of this *P*-value, it is ensured that the water preferentially persists in the liquid state throughout the duration of the test.
7. The stirrer inside the reactor is activated at a speed of 600 rpm, the heating plate/band heater under the base of the vessel are placed, and the heating blocks are turned on. At this point, the HTL test begins.
8. Once the heating ramp has been completed and the time *t* for which the reaction is to be conducted has elapsed (isothermal stage), a fast cooling of the reactor is carried out, so to "freeze" chemical reactions, thus avoiding products re-distribution during thermal transients. Cooling takes place by a water flow through the internal coils of the aluminium block.
9. At the end of the process, the system returns at ambient *T*. In the reactor, there is an overpressure compared to the initial one, which allows us to quantify the gas produced during the process; the system is depressurized, and we proceed with the withdrawal of the phases present inside the vessel, using small quantities of dichloromethane (about 30 g), necessary to remove the organic residue attached to the reactor walls, thermocouple, cooling loop and stirrer.

2.3.3 Protocol for the separation of HTL products

The separation protocol consists of a series of operations aimed at an effective recovery of the solid residue, the aqueous phase and bio-oil, to define their quantitative yields. For this purpose, after the HTL test, the liquid and solid phases were recovered from the vessel with a spatula, and 30 g of dichloromethane (DCM) were added to maximize the products recovery. At this point the procedure splits into two paths, one concerning the solid and one concerning the water/oil phase:

1. The slurry was filtered on a Büchner under vacuum at 0.4 bar. After filtration, the solid phase was subjected to a Soxhlet extraction with DCM to recover the bio-oil from the solid pores, using about 150 g of DCM as the extracting solvent. At the end of this operation, it is possible to take and dry the solid residue in the oven at 105 °C for 24 h, to remove DCM and traces of water. In the collecting flask it is, instead, present the soluble fraction in DCM, that is then subjected to vacuum distillation at 0.4 bar aimed at evaporating DCM and recovering the bio-oil extracted through Soxhlet (Figure 2.13).

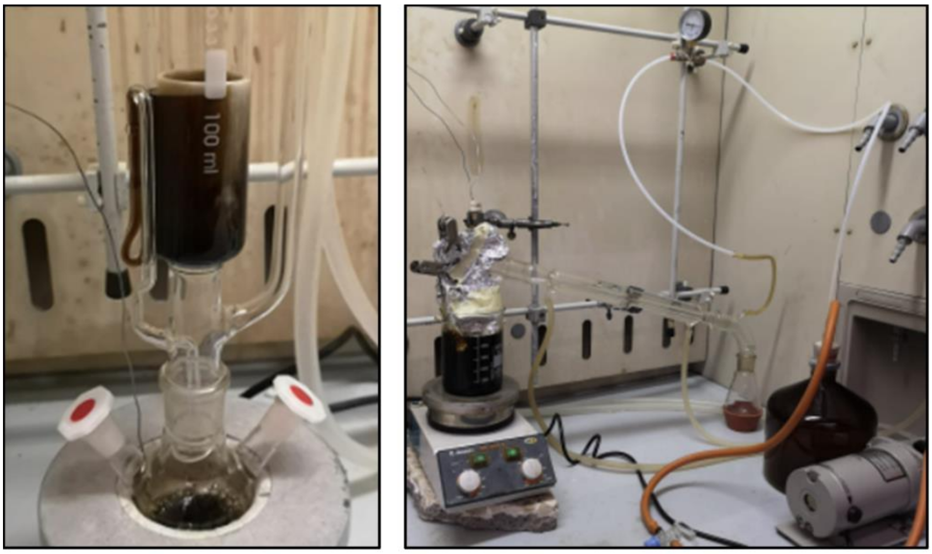

Figure 2.13 – Left) Soxhlet extractor and Right) vacuum distillation apparatus.

2. The liquid phase was separated into biocrude and aqueous phase according to two different separation techniques. The first one is liquid-liquid (L-L) extraction performed with DCM in a separating funnel, followed by vacuum distillation for bio-oil recovery. L-L extraction is carried out by adding to the solution 200 g of DCM which, after manual vigorous stirring, extracts the organic component soluble in it from the aqueous phase, by stratifying on the bottom of the separating funnel (DCM density=1.33 g/cm^3 at 20 °C). It is thus possible to recover the soluble component in DCM, which is subjected to vacuum distillation aimed at the evaporation of the solvent and the consequent recovery of bio-oil. In a different method, the water-biocrude mixture was separated by centrifugation. The separation by centrifuge is carried out in a NEYA 8 BASIC ventilated apparatus (Figure 2.14), inside which there are 4 tubes of 175 mL each. The liquid phase is distributed equally among the containers and centrifuged for 10 min at 4000 rpm, obtaining the stratification between the aqueous and the oily phase: the supernatant aqueous phase was taken by means of Pasteur pipettes, while the underlying bio-crude was recovered with the aid of 20 g of DCM and finally distilled under vacuum.

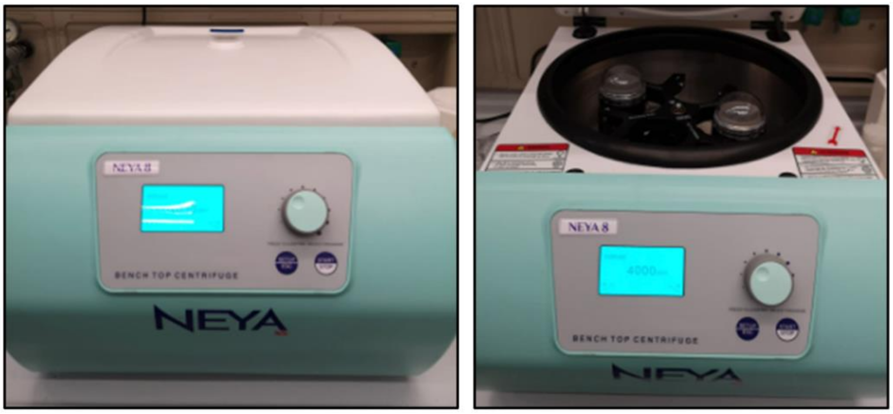

Figure 2.14 – NEYA 8 BASIC ventilated centrifuge used for the separation of bio-oil from the aqueous phase.

The separation phases described above can be summarized as in Figure 2.15.

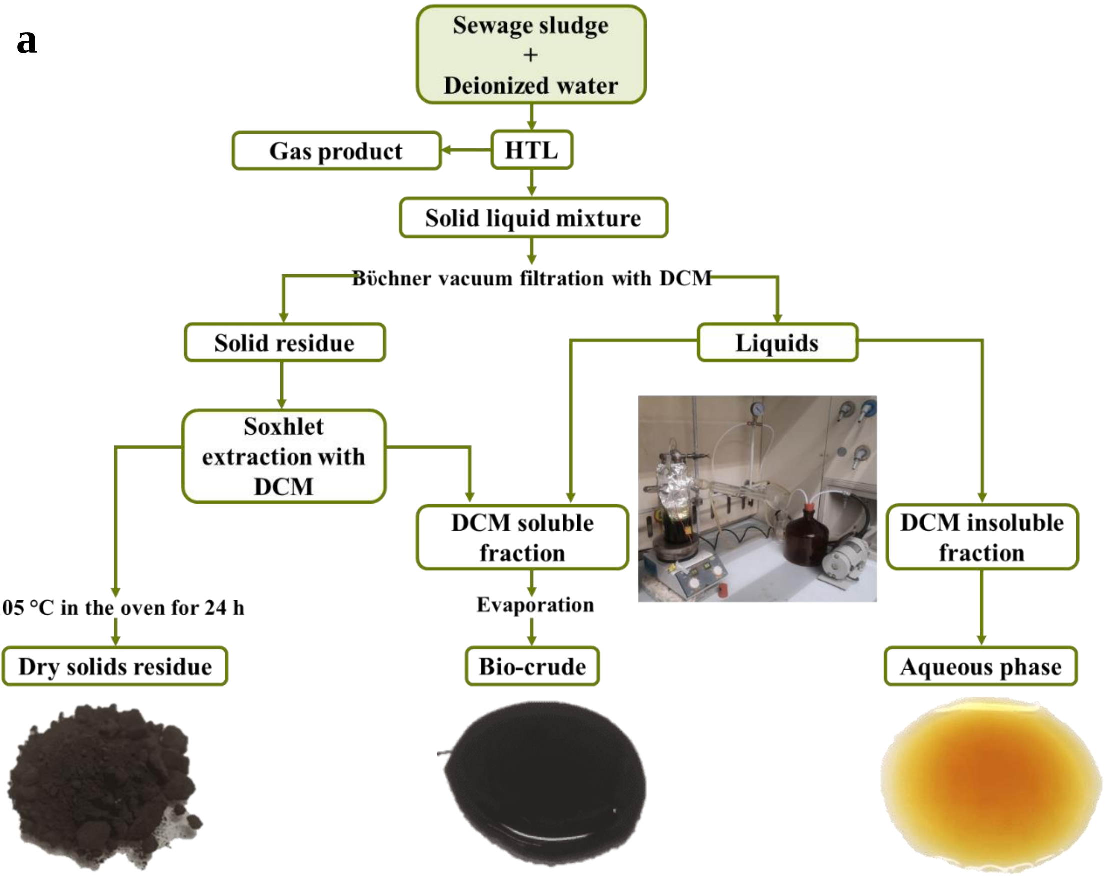

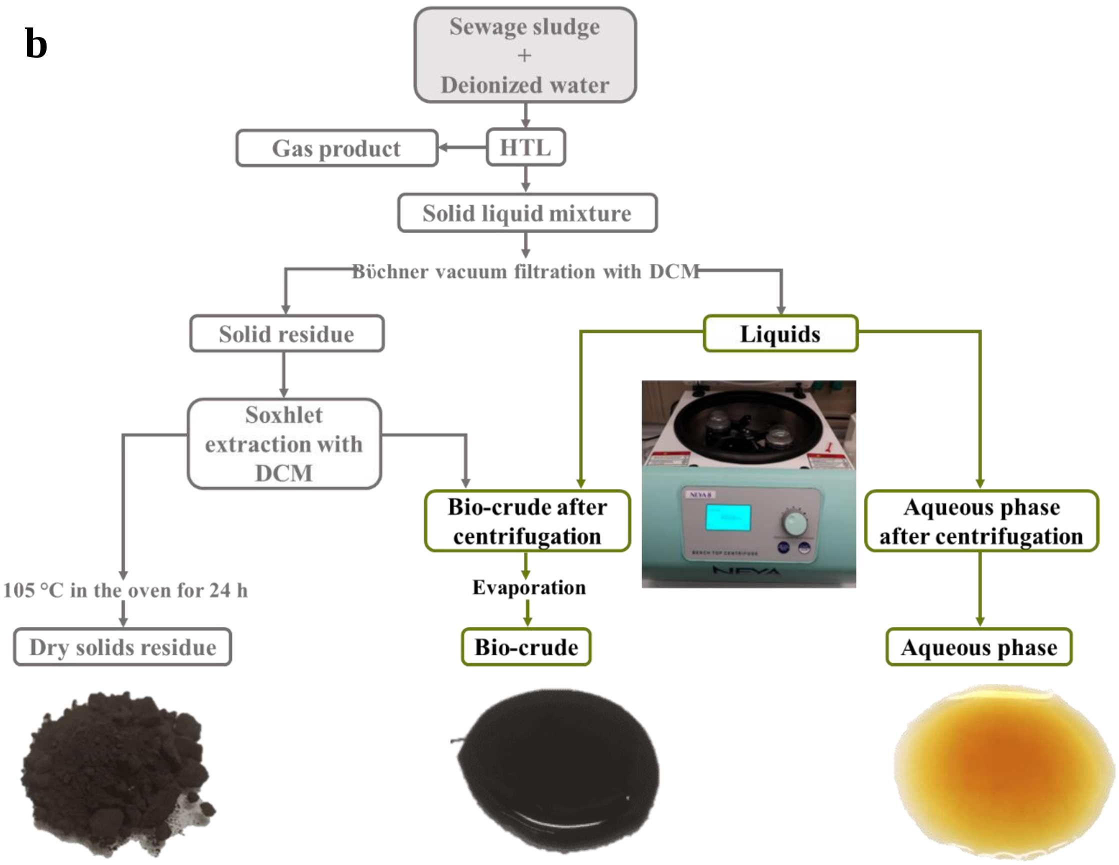

Figure 2.15 – Diagrams of HTL separation processes: a) L-L extraction b) centrifugation method (protocols originally proposed in this PhD work).

After the separation processes, the gas, solid residue, and biocrude yields (*Y*) were calculated according to Eqs. (2.3–2.5), respectively:

$$Y_{gas} = \frac{m_{CO_2}}{m_{biomass,dafb}} \text{ or } Y_{gas} = \frac{m_{CO_2}}{m_{biomass,db}} \tag{2.3}$$

$$Y_{solid\ residue} = \frac{m_{solid,db}}{m_{biomass,db}} \tag{2.4}$$

$$Y_{biocrude} = \frac{m_{biocrude}}{m_{biomass,dafb}} \text{ or } Y_{biocrude} = \frac{m_{biocrude}}{m_{biomass,db}} \tag{2.5}$$

where m_{CO_2}, m_{solid}, $m_{biocrude}$ and $m_{biomass}$ represent the mass of gas, solid residue, biocrude and starting biomass, respectively. The subscript "*db*" refers to dry basis, while "*dafb*" refers to dry ash-free basis.

It is important to note that, for the bio-oil and gas phases the yields can be reported on a dry basis or on dry and ash-free basis (considering therefore only the reactive fraction of the starting biomass) while the solid residue yield can be reported only on a dry basis, not being able to discriminate in the solid the contribution of ashes and bio-char. In fact, during the HTL process, the ash in the starting sludge may be partly dissolved in the aqueous phase and partly remain in the solid residue.

Regarding the gas phase, only CO_2 formation is taken into account, justified by the fact that it is the majority component in the mixture of gases produced (about 85%) (Basar et al., 2021). It is therefore considered that the pressure inside the system is generated by a mixture of nitrogen, already present inside the reactor, and carbon dioxide generated by the process. To determine the mass of CO_2 produced, the van der Waals non-ideal gas status law is used:

$$(P' + \frac{a_m n^2}{V^2})(V - nb_m) = nRT' \tag{2.6}$$

where *n* are the total moles, sum of the two gases present in the reactor, *T'* is the system temperature at the end of cooling phase, which corresponds to the initial test temperature, *P'* is the final pressure recorded at the end of the reaction and at *T'*, *V* is the reactor head space not occupied by the condensed phases (equal to 0.2 L), *R* is the gas constant; a_m and b_m are the constants of van der Waals of the mixture (CO_2-N_2 in this case), calculated according to Eqs. (2.7) and (2.8), respectively (Valderrama, 2003):

$$a_m = \sum_{i=1}^{N} \sum_{j=1}^{N} x_i x_j \sqrt{a_i a_j}\,(1 - k_{ij}) \tag{2.7}$$

$$b_m = \sum_{i=1}^{N} x_i b_i \tag{2.8}$$

where *N* represents the number of components of the mixture, x_i and x_j are the molar fractions of the two components, a_i, a_j and b_i are the van der Waals constants of the pure components, while k_{ij} is a binary interaction parameter, usually calculated by regression analysis of experimental data of phase equilibrium.

Using Eqs. (2.6), (2.7) and (2.8) it is possible to determine the number of moles of CO_2 and, consequently, the mass of the latter, through which the gas yield is determined as in Eq. (2.3).

In addition, on each bio-crude was determined the energy recovery as the ratio of the higher heating value of the bio-oil and the starting sludge, multiplied by the mass yield of bio-oil.

$$ER = \frac{HHV_{biocrude} \cdot Y_{biocrude}}{HHV_{biomass}} \tag{2.9}$$

2.3.4 Matrix of experimental tests

Table 2.3 shows the matrix of the HTL tests, depending on the type of sludge used, the temperature, the reaction time, the reactor configuration (hence, a different heating rate) and the method of separation of the bio-oil and water phases. The influence of these variables on the HTL process has been assessed both quantitatively and qualitatively. Each test has been associated with an acronym in which the first letters define the type of sludge used (MS=municipal sludge; TS=tannery sludge), the second are associated with the type of reactor configuration (B-C), while the third describe the separation protocol used for biocrude recovery (SF for separating funnel; Cen for centrifugation). Finally, the two numbers represent, in the order shown in the Table 2.3, the setpoint temperature used during the HTL test and the reaction time in the isotherm phase.

Table 2.3 – Overview of the HTL experimental tests.

Test	Configuration	*T* [°C]	*t* [min]	Separation method	Designation
1	B	300	20	Separatory funnel	MS-B-SF-300-20
2	B	300	20	Centrifuge	MS-B-Cen-300-20
3	B	350	20	Separatory funnel	MS-B-SF-350-20
4	B	350	20	Centrifuge	MS-B-Cen-350-20

5	C	300	0	Centrifuge	MS-C-Cen-300-0
6	C	300	10	Centrifuge	MS-C-Cen-300-10
7	C	300	20	Centrifuge	MS-C-Cen-300-20
8	C	300	30	Centrifuge	MS-C-Cen-300-30
9	C	300	40	Centrifuge	MS-C-Cen-300-40
10	C	300	50	Centrifuge	MS-C-Cen-300-50
11	C	300	60	Centrifuge	MS-C-Cen-300-60
10	C	350	0	Centrifuge	MS-C-Cen-350-0
11	C	350	10	Centrifuge	MS-C-Cen-350-10
12	C	350	20	Centrifuge	MS-C-Cen-350-20
13	C	350	30	Centrifuge	MS-C-Cen-350-30
14	C	350	40	Centrifuge	MS-C-Cen-350-40
15	C	350	50	Centrifuge	MS-C-Cen-350-50
16	C	360	60	Centrifuge	MS-C-Cen-350-60
17	C	300	0	Centrifuge	TS-C-Cen-300-0
18	C	300	10	Centrifuge	TS-C-Cen-300-10
19	C	300	20	Centrifuge	TS-C-Cen-300-20
20	C	300	30	Centrifuge	TS-C-Cen-300-30
21	C	300	40	Centrifuge	TS-C-Cen-300-40
22	C	300	50	Centrifuge	TS-C-Cen-300-50
23	C	300	60	Centrifuge	TS-C-Cen-300-60
24	C	350	0	Centrifuge	TS-C-Cen-350-0
25	C	350	10	Centrifuge	TS-C-Cen-350-10
26	C	350	20	Centrifuge	TS-C-Cen-350-20
27	C	350	30	Centrifuge	TS-C-Cen-350-30
28	C	350	40	Centrifuge	TS-C-Cen-350-40
29	C	350	50	Centrifuge	TS-C-Cen-350-50
30	C	360	60	Centrifuge	TS-C-Cen-350-60

Chapter 5 was devoted to the study of the best reactor configuration, separation protocol, and analysed the best operating conditions (in terms of temperatures and reaction times) for the two sludges under investigation. Finally, a comparison in terms of yields and quality of the biocrude produced by the two types of sludges are reported and critically discussed.

Chapter 3 – Characterisation of tannery and municipal sludges

This chapter is devoted to highlight differences and/or similarities between the two sewage sludges under investigation in this PhD work. The compositional differences will allow to discriminate dissimilarities in the products obtained by the biomass thermoconversion processes.

3.1 Proximate analysis

Table 3.1 shows the results obtained by immediate analysis of the tannery and municipal sludge (as received). Three repetitions were carried out for each of the two sludges; analyses showed an excellent reproducibility of the data.

Table 3.1 - Proximate analysis for the parent sludges as received (percentages by weight).

		Test 1	***Test 2***	***Test 3***	***Mean value***
Tannery sludge	Moisture	18.51	18.12	18.74	18.46 ± 0.31
	Volatiles	50.13	50.07	50.19	50.13 ± 0.06
	Fixed carbon	n.d.	n.d.	n.d.	n.d.
	Ash	31.36	31.07	31.07	31.41 ± 0.43
Municipal sludge	Moisture	12.69	12.67	12.70	12.68 ± 0.01
	Volatiles	56.39	56.32	56.35	56.36 ± 0.03
	Fixed carbon	9.65	9.44	9.53	9.54 ± 0.11
	Ash	21.27	21.57	21.45	21.43 ± 0.15

For the tannery sludge (TS), moisture and volatiles accounted for, respectively, 18.46 and 50.13%. The ash is present in an average value of 31.41% while no fixed carbon was detected ("not detected", n.d.). Carbon is therefore to be sought in combination with other species, and its overall content has been demonstrated by elemental analysis, as reported below. The municipal sludge (MS) has, instead, an average moisture content of 12.68%; the rest is composed of volatiles (56.36%), ash (21.43%) and fixed carbon (9.54%). It is important to note that, the higher presence of volatile and fixed carbon (the latter absent in TS), and the lower ash content, make MS a biomass with a greater energy potential than TS, and therefore more attractive in thermochemical valorisation processes.

3.2 Ultimate analysis

Table 3.2 shows the results obtained by elemental analysis, carried out on dried and ground sewage sludges (<400 μm). In this case, too, three repetitions were performed, which showed an excellent reproducibility of the obtained data. The percentages given are calculated on a moisture-free basis. For TS, a total C content of 33.61% was revealed by ultimate analysis, together with 5.10% H, 2.44% N, and 4.07% S. While, MS has the following composition values: 34.55% (C), 4.87% (H), 5.90% (N), 0.77% (S). The emphasis here is on the fraction of C, which makes the sludges suitable for energy enhancement processes.

Table 3.2 - Ultimate analysis for the parent sludges (percentages by weight, dry basis).

		Test 1	***Test 2***	***Test 3***	***Mean value***
Tannery sludge	C	33.52	33.53	33.78	33.61 ± 0.14
	H	5.33	4.99	4.97	5.10 ± 0.19
	N	2.49	2.38	2.45	2.44 ± 0.05
	S	4.10	4.05	4.06	4.07 ± 0.03
Municipal sludge	C	34.20	34.82	34.63	34.55 ± 0.32
	H	5.09	4.98	4.53	4.87 ± 0.24
	N	5.92	5.98	5.81	5.90 ± 0.07
	S	0.76	0.83	0.72	0.77 ± 0.04

3.3 Higher heating value and chlorine content

Table 3.3 shows the results obtained from the analysis for the determination of the higher heating value (*HHV*). Three replicas were made for each sludge.

Table 3.3 – Higher heating value of the two sludges (dry basis).

		Test 1	***Test 2***	***Test 3***	***Mean value***
Tannery sludge	*HHV* [MJ/kg]	15.26	14.66	14.79	14.90 ± 0.31
	LHV [MJ/kg]	value calculated from *HHV*			13.62
Municipal sludge	*HHV* [MJ/kg]	16.52	16.39	17.15	16.67 ± 0.40
	LHV [MJ/kg]	value calculated from *HHV*			15.57

On a dry basis, the mean value of *HHV* for TS is 14.90 MJ/kg, while it is 16.67 MJ/kg for MS. Moreover, the data obtained from the elemental analysis, in particular, the percentage by weight of hydrogen, allowed to calculate the lower heating value (*LHV*). On a moisture-free basis, it was possible to calculate the kg of H_2O theoretically produced by the combustion of 1 kg of sludge. By subtracting, from *HHV*, the product between kg H_2O/kg sludge and the enthalpy of H_2O vaporisation (2.5 MJ/kg), *LHV* of 13.62 and 15.57 MJ/kg were obtained for tannery and municipal sludge, respectively. The values of *HHV* and *LHV* are in line, in order of magnitude, with the commonly reported data for sludge (Jiang et al., 2010; Dong et al., 2015).

Once again, it is highlighted, that more volatiles and carbon (C), and the less ash content for MS resulted in higher heating values vs. TS.

Measurements of the chlorine content, made downstream of the calorific value measurements, produced the results given in Table 3.4. The repetitions were two, and with a good agreement between the results obtained. Finally, Table 3.5 synoptically illustrates the contents of the main elements (including O, calculated by difference), along with those of ashes and moisture, both on a dry and wet basis, for the two sludges.

Table 3.4 – Chlorine content of sludges (percentages by weight, dry basis).

		Test 1	*Test 2*	*Mean value*
Tannery sludge	Cl	0.33	0.37	0.35 ± 0.03
Municipal sludge	Cl	0.59	0.62	0.61 ± 0.02

Table 3.5 – Synoptic list of main sludges properties (average % by weight).

	Tannery sludge		*Municipal sludge*	
	dry basis	*wet basis*	*dry basis*	*wet basis*
C	33.61	27.41	34.55	30.66
H	5.10	4.16	4.87	4.32
N	2.44	1.99	5.90	5.24
S	4.07	3.32	0.77	0.68
Cl	0.35	0.29	0.61	0.54
Ash	38.52	31.41	24.54	21.43
Moisture	---	18.46	---	12.68
O (by difference)	15.91	12.96	28.66	25.03

MS is much richer in chlorine than TS. The content of Cl can be ascribed to the possible use of household detergents that usually contain sodium hypochlorite, known to be an effective disinfectant, which ends up in the sewage water body and subsequently in the sludge originating from the purification of these wastewater. If the gasification process is considered, the higher Cl content in MS is very critical not only in terms of emission levels of hydrochloric acid (HCl) at the exit of the gasifier, but also because of the impact it can have on the portioning of the other elements in ash and, consequently, on its further utilization. Similar problems could occur for hydrothermal liquefaction biochar (Ronda et al., 2019).

On contrary, TS has a much higher S content than MS (about five times greater on dry basis), due to the high amount of sulphates used in the tanning process. During the gasification process, the sulphur in the biomass feedstock is mainly converted to hydrogen sulphide (H_2S), sulphur dioxide (SO_2) and some amounts of carbonyl sulphide (COS), with related problems on gasifier corrosion, poisoning of catalysts, and SO_2 and H_2S emission (Hongrapipat et al., 2015). While, if the HTL process is considered, high concentrations of sulphur originally present in TS could be found in the biocrude obtained by the process, making necessary a further *up-grade* for S removal from the liquid fuel. Similar considerations to those made for sulphur can also carried out for nitrogen, whose content is higher in MS.

3.4 Metal concentration by ICP-MS

Table 3.6 shows the results for the concentration of metals obtained by ICP-MS for the two sludges under investigation. The results are reported as mean values of triplicate analyses.

For TS, the most abundant metal was Ca, with a concentration equal to 49.64 g/kg. Then, in concentration descending order, the most abundant metals were Fe, Cr, Si, Al, Na, Zn and Mg. All of them, including Ca, are at least one order of magnitude higher in concentration than all other metals. As expected, the chromium concentration is extremely high (22.5 g/kg), especially when compared to common sludge from urban wastewater purification processes (about 0.08 g/kg for MS). Regarding MS, the more abundant elements are Fe, Ca, P and Al. The Ca, Fe, and Al concentration is probably associated to the stabilization and flocculation stages of sewage sludge, whereas P is commonly found in such sludges. A large amount of Mg and K is also present.

Table 3.6 – Results of the ICP-MS analysis performed on sludges (dry basis).

Metal	Tannery sludge [g/kg]	Municipal sludge [g/kg]
B	0.035 ± 0.09	0.055 ± 0.06
Na	4.32 ± 0.06	0.42 ± 0.07
Mg	1.01 ± 0.03	3.60 ± 0.04
Al	4.77 ± 0.17	6.93 ± 0.21
Si	8.74 ± 0.22	2.54 ± 0.16
P	0.46 ± 0.02	14.96 ± 0.7
Ca	49.64 ± 1.89	13.78 ± 0.56
K	0.46 ± 0.02	2.02 ± 0.08
Ti	0.72 ± 0.07	0.20 ± 0.03
V	0.021 ± 0.001	0.015 ± 0.003
Cr	22.52 ± 0.12	0.081 ± 0.004
Mn	0.081 ± 0.001	0.25 ± 0.02
Fe	24.77 ± 0.06	26.71 ± 0.09
Co	0.010 ± 0.001	0.0043 ± 0.0002
Ni	0.010 ± 0.001	0.07 ± 0.01
Cu	0.072 ± 0.002	0.29 ± 0.03
Zn	1.16 ± 0.03	0.59 ± 0.02
As	0.0022 ± 0.0001	0.0031 ± 0.0001
Zr	0.31 ± 0.01	0.0034 ± 0.0001
Mo	0.003 ± 0.001	0.006 ± 0.002
Sn	0.0031 ± 0.0001	0.018 ± 0.001
Sb	0.001 ± 0.001	n.d.

Ba	0.044 ± 0.002	0.13 ± 0.02
Hg	n.d.	0.0030 ± 0.0002
Pb	0.024 ± 0.001	0.069 ± 0.004

3.5 Total and hexavalent chromium

The high Cr content is a critical point in the energy valorisation of TS; for this reason, the total Cr content and the contribution of Cr(VI) to the latter was evaluated. Table 3.7 gives the total Cr concentration data (on wet and dry basis), obtained by AAS, for the tannery sludge. Two replicas were conducted, and the results show excellent reproducibility.

Table 3.7 – Total Cr content in tannery sludge.

	Wet basis [g/kg]	**Dry basis [g/kg]**
Test 1	20.60	25.28
Test 2	20.70	25.49
Mean value	20.65 ± 0.07	25.38 ± 0.15

As regards the determination of Cr(VI) by UV-Vis spectrophotometry, the solution containing the sludge did not change from transparent to pink (as compared to the test for the reference solution) after the addition of diphenylcarbazide solution, an indicator of the absence of Cr(VI) in solution. This could also be attributed to the limit of detection of the technique used, which is equal to a concentration of Cr(VI) in solution of 0.05 mg/L (equivalent to a Cr(VI) content in the starting sludge of 2 ppm). Therefore, if present, the Cr(VI) content in the starting sludge would not exceed 2 ppm.

3.6 Determination of the biochemical components in the starting sludges

In the field of the energy valorisation of biomass a fundamental role is represented by the amount of organic matter, as well as the type of macro-components that make up biomass. Table 3.8 shows the percentage by weight of lipid, proteins and carbohydrates present in the sludges. The analyses were carried out on a dry basis and are reported as mean values of triplicate analyses. TS has a lipid concentration more than twice that of MS; on the contrary, the TS carbohydrate content is about half that of MS. The protein content is instead slightly greater for TS. The higher lipid and protein content of TS can be ascribed to the nature of the latter. It, in fact, resulting from a process of processing animal leather presents many residues of lipids and proteins.

Table 3.8 – Composition of macro-components in the sewage sludges (percentages by weight, dry basis).

	Lipids	**Proteins**	**Carbohydrates**
Tannery sludge	5.3 ± 0.2	29.4 ± 0.9	21.0 ± 0.02
Municipal sludge	2.4 ± 0.1	25.0 ± 0.1	59.0 ± 0.03

It is important to emphasize that, looking at the lipid content, the value is particularly lower if compared to the other two macro-components. This result is of particular interest considering that, in the energy valorisation of biomass, the lipid, together with carbohydrates component plays a fundamental role in the production of fuels with high energy value. These compositions are however in line with those commonly reported in the literature for sewage sludge (Li et al., 2021).

Chapter 4 – Fluidized bed gasification on tannery sludge: results

The valorisation process of the sewage sludge through gasification in fluidized bed was carried out on TS. The choice to use this type of sludge comes from a lacking literature on this specific topic (Ongen et al., 2013), compared to the gasification of municipal sludge (Nipattummakul et al., 2010; Werle, 2013; Migliaccio et al., 2021). Given the lack of data on TS gasification, the possibility of obtaining a high added-value syngas using reducing conditions has been explored in this work. Moreover, the possible formation of SO_2 and Cr(VI) has been evaluated, considering that this sludge is rich in chromium and sulphides, as described in Chapter 3. The results presented in this chapter are reported in a paper authored by the PhD candidate (Di Lauro et al., 2022).

4.1 Outcomes of fluidized bed gasification tests

The syngas obtained from the sludge gasification process was analysed downstream of the condensation/filtration stages. Table 4.1 reports the main outcomes of the FB gasification tests. On a dry and N_2-free basis, for test 1 (A*ER*=0.15), syngas was mostly composed of CO (35.49%), H_2 (41.58%), CH_4 (3.67%), and C_2H_4 (2.89%), the rest being CO_2. The concentration of SO_2 in the syngas was 193 ppm, while H_2/CO and CH_4/H_2 ratios of 1.17 and 0.09, respectively, were obtained. The tar concentration in syngas was 26.4 g/Nm^3, and a fly ash flow rate of 7.57 g/h was collected. For test 2 (less reducing conditions, *ER*=0.24), syngas was mostly composed of H_2 (32.69%), CO (27.05%), CH_4 (5.15%), and C_2H_4 (4.66%), the rest being CO_2. In this case, the concentration of SO_2 in the syngas was found to be 137 ppm, while H_2/CO and CH_4/H_2 ratios of 1.21 and 0.16, respectively, were obtained. The tar concentration in syngas was 22.3 g/Nm^3, and a fly ash flow rate of 4.24 g/h was collected.

The more severe reducing conditions of test 1 allowed to obtain an amount of the two main gasification species (CO+H_2) of 77.07%, which is 22% more than what we observed during test 2 (CO+H_2=59.74%). Correspondingly, the CO_2 content obtained in the syngas from test 1 (16.16%) was far lower than what was observed in test 2 (CO_2=30.10%). It is here obviously recalled that CO_2 does not contribute to the syngas heating value, and that its formation is favoured by less reducing conditions as those experienced in test 2. The evaluation of heating values of the syngas was carried out based on its chemical composition: in test 1, it had *LHV*=12.0 and *HHV*=13.1 MJ/Nm^3, while values were lower in test 2 (*LHV*=11.6 and *HHV*=12.6 MJ/Nm^3). They fall within the ranges reported by NETLDOE, USA, where data from industrial gasifiers to produce syngas as an energetic vector are reported (*LHV*=8.3−13.0 MJ/Nm^3 on a dry and N_2-free basis). Regarding the production of sulphur dioxide, its values are not negligible but remain within the legal limits. Finally, the cold gas efficiency for test 1 and test 2 are respectively equal to 65% and 46%, confirming the best quality of syngas obtained from test 1.

Table 4.1 – Main outcomes of the FB gasification tests.

Syngas composition (dry and N_2-free basis)	***Test 1 (AER = 0.15)***	***Test 2 (AER = 0.24)***
CO [% vol.]	35.49	27.05
H_2 [% vol.]	41.58	32.69
CH_4 [% vol.]	3.67	5.15
C_2H_4 [% vol.]	2.89	4.66
C_2H_6 [% vol.]	0.09	0.09
CO_2 [% vol.]	16.16	30.10
Total [% vol.]	99.88	99.74
SO_2 [ppm]	193	137
H_2/CO [vol./vol.]	1.17	1.21
CH_4/H_2 [vol./vol.]	0.09	0.16
***HHV* [MJ/Nm^3]**	13.1	12.6
***LHV* [MJ/Nm^3]**	12.0	11.6
Tar concentration in syngas [g/Nm^3]	26.4	22.3
Elutriated stream flow rate (fly ash) [g/h]	7.57	4.24
Cold gas efficiency	0.65	0.46

4.2 Tar characterization

Tar concentration values, when not lower (ENEA Report, 2015), are in line with values listed in literature for the gasification of coal, biomass, and sludges (Phuphuakrat et al., 2010). Table 4.2 shows the results obtained for the condensation stage at room temperature, and the first and second condensation stages at -12 °C, for the gasification test with *AER*=0.15. Similarly, the test results with *AER*=0.24 are reported in Table 4.3. The identified compounds were listed in order of relevance of the normalized peak area, as obtained from the chromatograms. The database used for the recognition of chromatographic peaks is NIST 11, which refers to the mass spectra characteristic of each analyte. In this regard, the table also shows the values of "match quality", which indicate the degree of similarity of the mass spectrum of the sample in question with that reported in the database.

Table 4.2 – GC−MS results on the characterization of tar compounds collected during gasification test 1 (*AER*=0.15), at room temperature and at -12 °C.

Retention time	Peak normalised area, %	Compound	CAS#	Match quality
Test 1 – tar collected at room temperature				
65.848	35.85	Anthracene ($C_{14}H_{10}$)	120-12-7	95
39.402	13.20	Naphthalene ($C_{10}H_8$)	91-20-3	95
64.776	12.74	Dibenzothiophene ($C_{12}H_8S$)	132-65-0	97
66.212	5.97	Phenanthrene ($C_{14}H_{10}$)	85-01-8	96
52.47	5.54	Acenaphthylene ($C_{12}H_8$)	208-96-8	90
78.942	5.07	Fluoranthene ($C_{16}H_{10}$)	206-44-0	94
48.485	4.43	Biphenyl ($C_{12}H_{10}$)	92-52-4	95
57.826	4.43	Fluorene ($C_{13}H_{10}$)	86-73-7	94
82.346	3.31	Pyrene ($C_{16}H_{10}$)	129-00-0	94
55.015	2.98	Dibenzofuran ($C_{12}H_8O$)	132-64-9	91
45.655	1.53	1-Methylnaphthalene ($C_{11}H_{10}$)	90-12-0	94
44.826	1.16	2-Methylnaphthalene ($C_{11}H_{10}$)	91-57-6	93
72.930	0.97	2-Phenylnaphthalene ($C_{16}H_{12}$)	612-94-2	93
72.948	0.80	1-Phenylnaphthalene ($C_{16}H_{12}$)	605-02-7	90
47.937	0.61	Indole (C_8H_7N)	120-72-9	94
32.478	0.57	Phenol (C_6H_6O)	108-95-2	87
13.994	0.48	Pyridine (C_5H_5N)	110-86-1	94
67.685	0.37	Dibenzo[*a*,*e*]cyclooctene ($C_{16}H_{12}$)	262-89-5	94
Test 1 – tar collected at -12 °C (stage I)				
39.413	80.00	Naphthalene ($C_{10}H_8$)	91-20-3	95
39.945	3.00	Benzo[*c*]thiophane (C_8H_6S)	270-82-6	97
65.864	2.93	Phenanthrene ($C_{14}H_{10}$)	85-01-8	96
52.470	1.90	Acenaphthylene ($C_{12}H_8$)	208-96-8	90
13.956	1.89	Pyridine (C_5H_5N)	110-86-1	97
32.474	1.71	Phenol (C_6H_6O)	108-95-2	94
48.485	1.40	Biphenyl ($C_{12}H_{10}$)	92-52-4	95
44.830	1.19	1-Methylnaphthalene ($C_{11}H_{10}$)	90-12-0	95
64.788	0.90	Dibenzothiophene ($C_{12}H_8S$)	132-65-0	96
55.022	0.87	Dibenzofuran ($C_{12}H_8O$)	132-64-9	93

57.838	0.79	Fluorene ($C_{13}H_{10}$)	86-73-7	90
29.584	0.78	Aniline (C_6H_7N)	62-53-3	94
47.945	0.60	Indole (C_8H_7N)	120-72-9	95
31.399	0.44	Indene (C_9H_8)	95-13-6	91
8.734	0.36	Benzene (C_6H_6)	71-43-2	94
66.238	0.34	Anthracene ($C_{14}H_{10}$)	120-12-7	76
51.131	0.30	2-Vinylnaphthalene ($C_{12}H_{10}$)	827-54-3	81
45.662	0.26	2-Methylnaphthalene ($C_{11}H_{10}$)	91-57-6	97
42.761	0.14	Quinoline (C_9H_7N)	91-22-5	94
29.798	0.12	Benzonitrile (C_7H_5N)	100-47-0	87
42.712	0.07	Isoquinoline (C_9H_7N)	119-65-3	81
Test 1 – tar collected at -12 °C (stage II)				
8.742	54.40	Benzene (C_6H_6)	71-43-2	90
6.178	45.60	2-Methylfuran (C_5H_6O)	534-22-5	81

Table 4.3 – GC−MS results on the characterization of tar compounds collected during gasification test 2 (*AER*=0.24), at room temperature and at -12 °C.

Retention time	**Peak normalised area, %**	**Compound**	**CAS#**	**Match quality**
Test 2 – tar collected at room temperature				
65.834	53.87	Phenanthrene ($C_{14}H_{10}$)	85-01-8	96
64.761	12.30	Dibenzothiophene($C_{12}H_8S$)	132-65-0	97
66.205	8.95	Anthracene ($C_{14}H_{10}$)	120-12-7	93
78.916	8.58	Fluoranthene ($C_{16}H_{10}$)	206-44-0	96
82.316	4.87	Pyrene ($C_{16}H_{10}$)	129-00-0	93
52.458	2.43	Acenaphthylene ($C_{12}H_8$)	208-96-8	91
57.823	2.38	Fluorene ($C_{13}H_{10}$)	86-73-7	93
72.911	2.31	2-Phenylnaphthalene ($C_{16}H_{12}$)	612-94-2	92
48.466	1.38	Biphenyl ($C_{12}H_{10}$)	92-52-4	94
55.004	1.22	Dibenzofuran ($C_{12}H_8O$)	132-64-9	81
39.394	0.85	Naphthalene ($C_{10}H_8$)	91-20-3	94
70.272	0.50	2-Methylanthracene ($C_{15}H_{12}$)	613-12-7	83
51.109	0.35	2-Vinylnaphthalene ($C_{12}H_{10}$)	827-54-3	86
Test 2 – tar collected at -12 °C (stage I)				
39.394	91.75	Naphthalene ($C_{10}H_8$)	91-20-3	95
39.934	2.03	Benzo[*c*]thiophane (C_8H_6S)	270-82-6	97
32.474	1.07	Phenol (C_6H_6O)	108-95-2	91

65.860	0.95	Phenanthrene ($C_{14}H_{10}$)	85-01-8	95
13.967	0.92	Pyridine (C_5H_5N)	110-86-1	97
52.466	0.71	Acenaphthylene ($C_{12}H_8$)	208-96-8	91
48.470	0.55	Biphenyl ($C_{12}H_{10}$)	92-52-4	91
29.580	0.46	Aniline (C_6H_7N)	62-53-3	93
44.815	0.44	1-Methylnaphthalene ($C_{11}H_{10}$)	90-12-0	83
54.985	0.27	Dibenzofuran ($C_{12}H_8O$)	132-64-9	76
8.730	0.24	Benzene (C_6H_6)	71-43-2	94
47.937	0.21	Indole (C_8H_7N)	120-72-9	76
31.372	0.17	3-Ethynyltoluene (C_9H_8)	766-82-5	91
64.761	0.16	Dibenzothiophene ($C_{12}H_8S$)	132-65-0	70
57.819	0.05	Fluorene ($C_{13}H_{10}$)	86-73-7	90
Test 2 – tar collected at -12 °C (stage II)				
65.841	49.98	Phenanthrene ($C_{14}H_{10}$)	85-01-8	94
8.738	13.64	Benzene (C_6H_6)	71-43-2	94
6.174	10.44	2-Methylfuran (C_5H_6O)	534-22-5	81
64.776	9.40	Naphtho[1,2-*b*]thiophane ($C_{12}H_8S$)	234-41-3	81
52.447	8.75	Acenaphthylene ($C_{12}H_8$)	208-96-8	74
66.205	4.33	9-Methylidenefluorene ($C_{14}H_{10}$)	4425-82-5	76
52.477	3.45	Biphenylene ($C_{12}H_8$)	259-79-0	70

In both cases, tar species were mostly made up of polycyclic aromatic hydrocarbons (PAH), with the number of C atoms variable between 5 and 16, and in some cases also in the presence of heteroatoms (N, S, and O). More oxidizing conditions (test 2) determined a larger relative contribution of 2-, 3-, and 4-ring PAH not containing heteroatoms. Moreover, the following compounds were also identified:

- compounds with a simple structure (benzene);
- PAH without heteroatoms, having 2 (naphthalene, methylnaphthalene, indene, biphenyl, and vinylnaphthalene), 3 (anthracene, fluorene, phenanthrene, acenaphthylene, phenylnaphthalene, and methylanthracene), and 4 (fluoranthene and pyrene) rings;
- compounds containing N, with a simple structure (pyridine, aniline, and benzonitrile) or having 2 rings (indole and quinoline);
- compounds containing S, with 2 (benzothiophene) and 3 (dibenzothiophene and naphthothiophene) rings;
- compounds containing O, with a simple structure (phenol and methylfuran) or having 3 rings (dibenzofuran).

In Figure 4.1 and 4.2 (tar obtained in all stages of condensation in the test with *AER*=0.15 and *AER*=0.24, respectively), we can see the "abundance" of each class of compounds mentioned above, considering that the data obtained are based on semi-quantitative and not quantitative analyses, since reference is made to the normalized area of peaks.

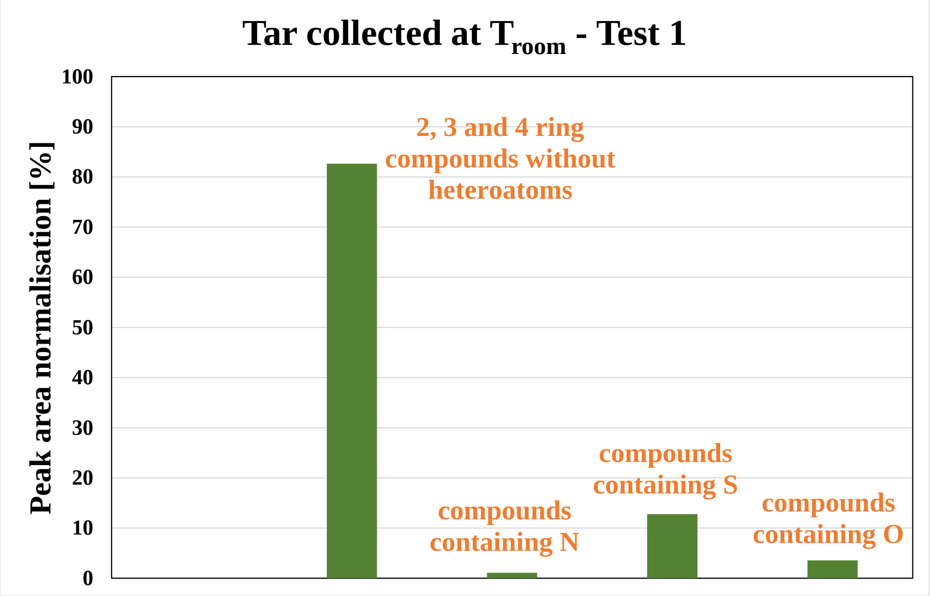

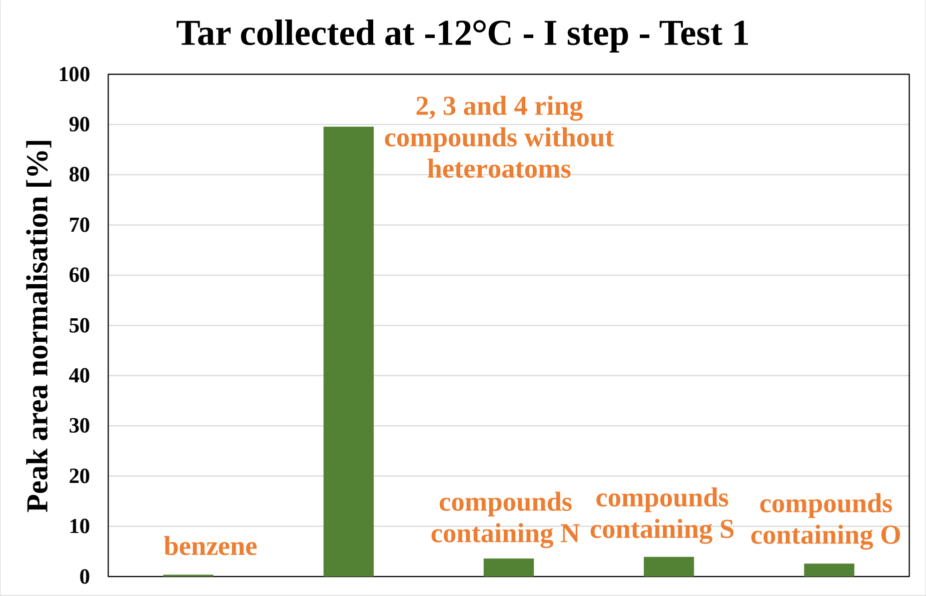

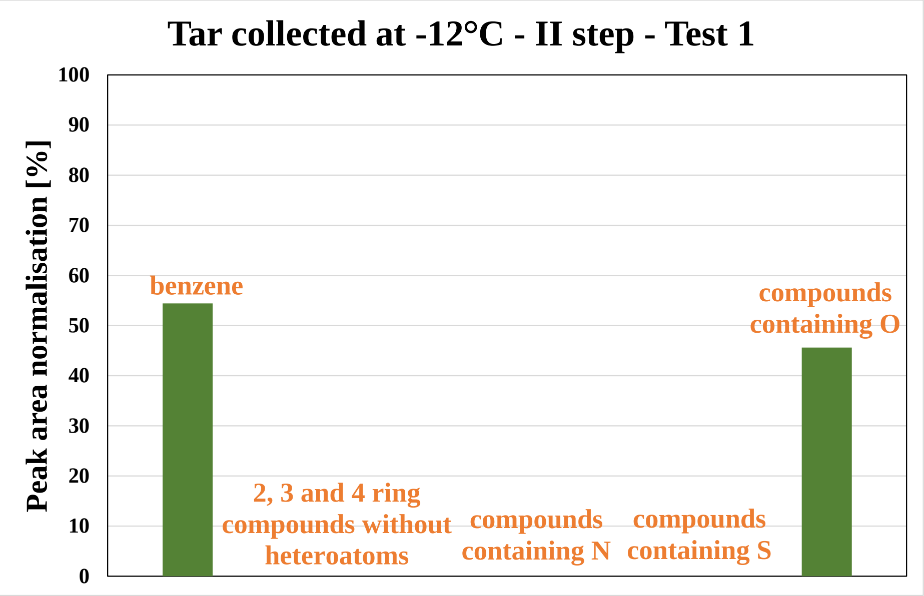

Figure 4.1 – Speciation of tar collected from gasification test 1 (*AER*=0.15) based on the peak-normalized area.

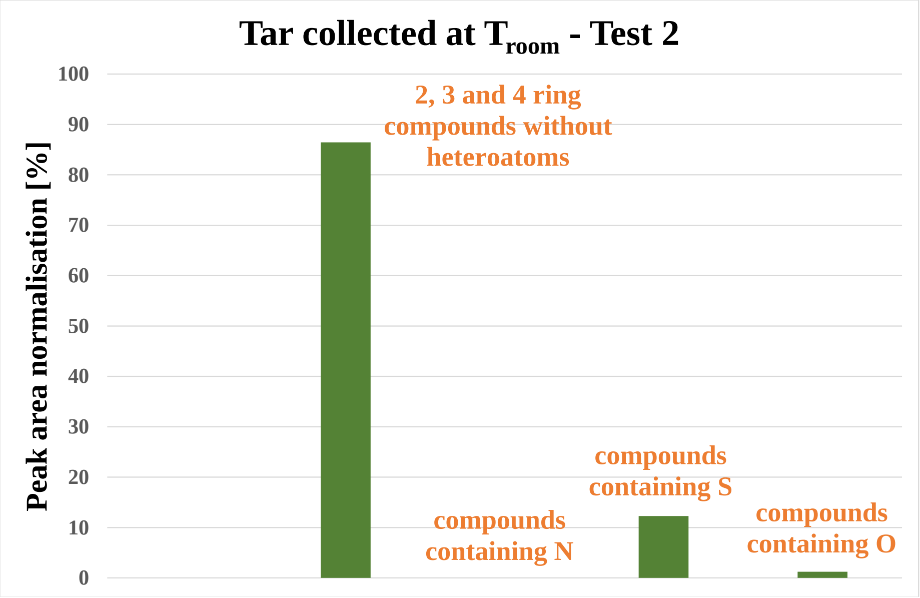

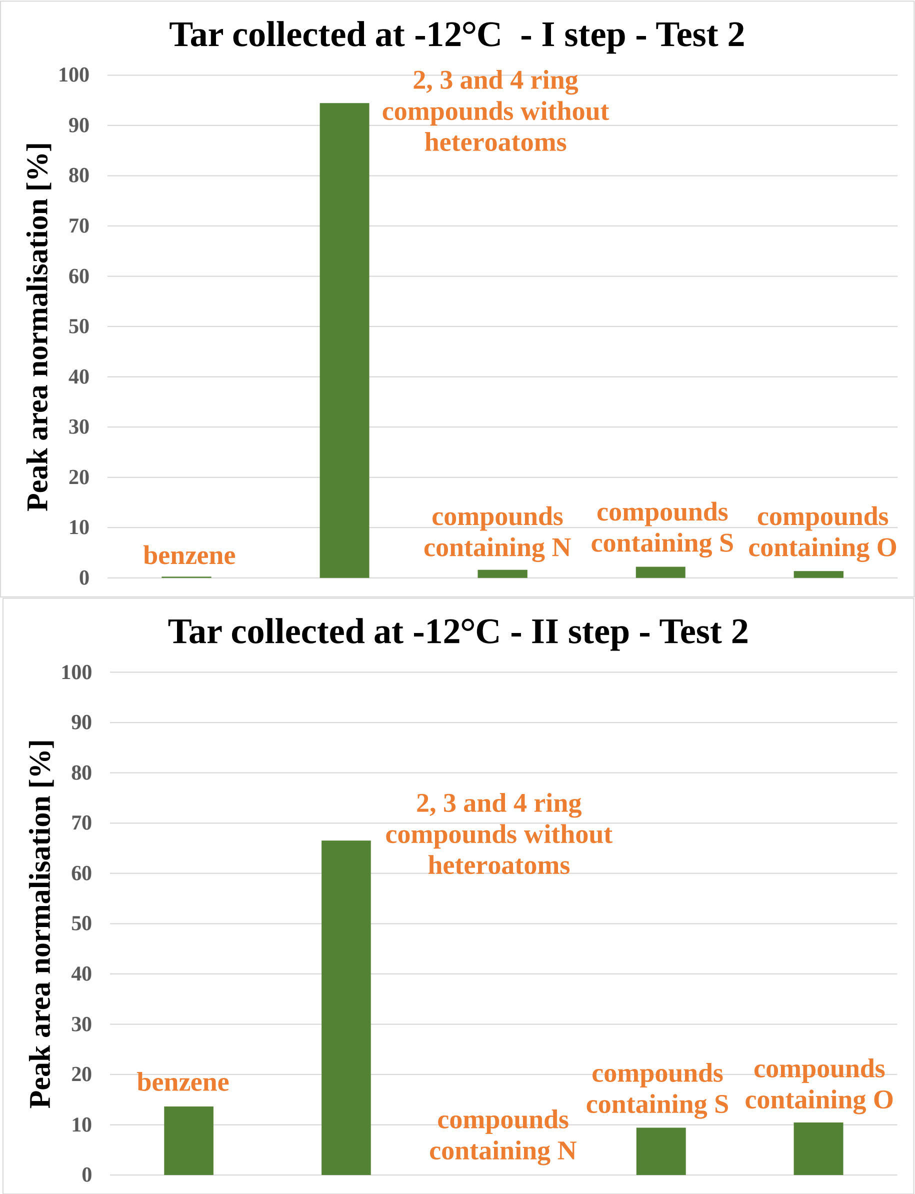

Figure 4.2 – Speciation of tar collected from gasification test 2 (*AER*=0.24) based on the peak-normalized area.

Tar collected at room temperature are rich in PAHs without heteroatoms, with a presence of two, three and four rings. This is followed by compounds containing S, O and, if present, N. For tar collected at -12 °C, the most abundant compounds are, again, PAHs (except for stage II in the *AER*=0.15 test, where they are absent) but in stage I, unlike the stage at room temperature, there is a greater relevance of nitrogen compounds than oxygenated ones, and a small amount of benzene. The latter is much more abundant in tar collected in stage II, to which compounds containing O and, in the *AER*=0.24 test, compounds containing S are added.

The composition of tar produced by gasification depends on the operating conditions and the composition of the starting material. It is possible to observe that, compared to the use of a civil sewage sludge (Migliaccio et al., 2021), the sludge analysed in this work produces tar containing S, due to the significant presence of S in the sludge under investigation (about 4% by weight on dry basis, Table 3.5). The chemical nature of the detected tar species is consistent with literature indications for sludges, at least from the qualitative viewpoint (a quantitative comparison cannot be performed, as data specifically referred to tannery sludge are hard to be found). For example, Phuphuakrat and colleagues (2010) detected, as main tar compounds from sewage sludge fixed bed gasification, benzene, phenol, indene, and naphthalene. Among biomass tar species discussed by Pio et al. (2020), naphthalene, heterocyclic compounds, and two-/three-/four-ring aromatic hydrocarbons were present.

4.3 Bottom and fly ash characterization with chromium speciation

Bottom ash from both FB gasification tests 1 and 2 was mostly composed by inorganic ash (Table 4.4), to confirm the almost complete conversion of volatiles and C under both *AER* values. As a matter of fact, from ultimate analysis, C contents not higher than 0.2% were observed. On the other hand (Table 4.5), the elutriated fly ash, having experienced a mean residence time in the FB gasifier that is much shorter than for the case of bottom ash, contained about 14−17% of volatiles and 3−4% of fixed carbon (i.e., the gasification burn-off degree for this stream is lower than 1). Carbon content amounts to about 8–9.5% (on a dry basis), while "ashes", properly, have an amount around 80%.

In both bottom and fly ash, the concentration of the harmful Cr(VI) species was, as expected, higher when a higher *AER* value was adopted (9.6 vs 8.2 ppm in bottom ash, 7.1 vs 4.1 ppm in fly ash; more oxygen favours the conversion to Cr(VI)), but the gasifier operating conditions indeed guarantee that these values are 3−4 orders of magnitude lower than the concentration of total chromium, which remains in the preferred form of Cr(III) and tends to concentrate in elutriated fly rather than bottom ash. While the (although) limited oxygen presence in the FB gasifier was able to promote the chromium oxidation to Cr(VI), the degree of conversion in bottom ash was 0.069 (AER=0.15) and 0.12% (AER=0.24) only. The shorter mean residence time of fly ash in the gasifier has, in this respect, a positive consequence, i.e., chromium has less time to enter in contact with oxygen. As a matter of fact, the degree of chromium oxidation to Cr(VI) was 0.008 (AER=0.15) and 0.013% (AER=0.24), i.e., 1.6−1.7 times smaller than for bottom ash.

In the circular economy perspective, an interesting route lies on the possibility of chromium removal (in particular, in its trivalent state) from ashes, in order to recirculate the metal in the tanning process. Contextually, possible options could include leaching with acid solutions or extraction with solvents followed by chemical precipitation for selective recovery of Cr in the form of basic chromium sulphate, a valuable product for the tanning material essential to produce ferro-chromium, the substrate for the manufacture of stainless steel. In fact, chromium is the main element that provides the high corrosion resistance of stainless steel. To this end, the possibility of recycling Cr contained in the ash resulting from thermal processes on the leather residues was studied by reduction in carbon at a temperature of 1600 °C, to produce a commercial high-carbon ferrochrome alloy (Alves et al., 2012). This process is particularly suitable for tannery ashes that contain high concentrations of both chromium and iron, which also have a role in leather production. In Tables 4.6 and 4.7, the results of the ICP-MS analysis, respectively on bottom and fly ash, are listed. In particular, it is seen that the mean value concentration of Fe is around 19 g/kg in bottom ash, and 74 g/kg in fly ash. These high concentration values can be attributed to the high Fe and Ca content in the starting sludge, as these metals take part in the tannery process from which the sludge derives.

Table 4.4 – Results of the analyses on bottom ash from FB gasification of tannery sludge.

Proximate analysis (% by weight)		
	Test 1 *AER*=0.15	***Test 2*** *AER*=0.24
Moisture	n.d.	n.d.
Volatiles	n.d.	n.d.
Fixed carbon	n.d.	n.d.
Ash	100	100
Ultimate analysis (% by weight; dry basis)		
	Test 1 *AER*=0.15	***Test 2*** *AER*=0.24
C	0.18	0.12
H	n.d.	n.d.
N	0.29	0.30
Chromium speciation		
	Test 1 *AER*=0.15	***Test 2*** *AER*=0.24
Cr(total) [g/kg]	11.8	8.0
Cr(VI) [g/kg]	8.2	9.6
Conversion to Cr(VI) [%]	0.069	0.120

Table 4.5 – Results of the analyses on fly ash from FB gasification of tannery sludge.

Proximate analysis (% by weight)		
	Test 1 *AER*=0.15	***Test 2*** *AER*=0.24
Moisture	1.54	1.31
Volatiles	13.84	17.10
Fixed carbon	3.17	3.97
Ash	81.45	77.62
Ultimate analysis (% by weight; dry basis)		
	Test 1 *AER*=0.15	***Test 2*** *AER*=0.24
C	9.54	7.99
H	n.d.	n.d.
N	0.68	0.62
Chromium speciation		
	Test 1 *AER*=0.15	***Test 2*** *AER*=0.24
Cr(total) [g/kg]	53.3	56.4
Cr(VI) [g/kg]	4.1	7.1
Conversion to Cr(VI) [%]	0.008	0.013

Table 4.6 – ICP-MS analysis for bottom ash obtained in TS gasification tests.

Metal [g/kg]	***Test 1*** ***AER*=0.15**	***Test 2*** ***AER*=0.24**
Sb	0.008	0.007
As	0.017	0.035

B	0.460	0.557
Cd	< 0.0001	< 0.0001
Co	< 0.0001	< 0.0001
Hg	0.0015	0.002
Na	4.80	11.20
Mg	3.025	6.30
Si	239.50	234.72
K	7.30	10.39
Ca	30.70	29.0
V	0.028	0.044
Mn	0.103	0.24
Zn	0.478	0.411
Se	< 0.0001	< 0.0001
Mo	0.045	0.025
Tl	< 0.0001	< 0.0001
Ni	0.426	0.088
Pb	< 0.0001	< 0.0001
Cu	0.101	< 0.0001
Sn	0.016	0.017
Al	17.84	29.62
Cr	11.78	7.97
Fe	17.80	19.82
Ti	2.36	2.34
Zr	0.216	0.172

Table 4.7 – ICP-MS analysis for fly ash obtained in TS gasification tests.

Metal [g/kg]	***Test 1*** ***AER*=0.15**	***Test 2*** ***AER*=0.24**
Sb	0.013	0.010
As	< 0.0001	0.032
B	0.180	0.208
Cd	0.287	< 0.0001
Co	0.017	0.016
Hg	0.001	0.001
Na	5.27	3.66

Mg	3.36	3.83
Si	28.97	27.41
K	6.83	2.83
Ca	132.20	132.76
V	0.062	0.064
Mn	0.334	0.312
Zn	3.90	2.89
Se	< 0.0001	< 0.0001
Mo	0.113	0.085
Tl	0.001	0.001
Ni	2.72	3.64
Pb	0.050	0.014
Cu	0.811	0.445
Sn	0.040	0.033
Al	35.35	28.43
Cr	53.39	56.38
Fe	72.11	75.45
Ti	10.19	9.90
Zr	0.758	0.754

Chapter 5 – Hydrothermal liquefaction process on sewage sludges: results

5.1 Choice of steel for reactor construction

The first part of the PhD work concerned the choice of an appropriate steel for the reactor system designed for HTL tests which, conducted under sub-critical conditions, present some problems related to the lower solubility of salts in water that causing corrosion phenomena and in particular pitting phenomena.

Among the different steels on the market were considered two types, whose chemical composition characteristics are given in Table 5.1:

1. AISI 316 L
2. Hastelloy C-276

The first with a cost that corresponds to half of the second.

Table 5.1 – Chemical compositions of alloys 316 and C-276.

Grade	C	Mn	Si	P	S	Cr	Ni	Cu	Mo	Fe	Co	W
316	0.03	2	0.75–1	0.045	0.030	16–18	10–14	/	2–3	Rest	/	/
C-276	0.01	1	/	/	/	16	57	/	16	5	2.5	4

The corrosion resistance of a particular alloy is a function of the ability of the material to withstand the depassivation phenomena.

Depassivation: The presence of chromium alloy ensures the possibility of forming on the steel surface a very thin film (also called passive film), consisting mainly of oxides and hydroxides of chromium (Cr_2O_3 and $Cr(OH)_3$): this film is insoluble, compact, and adherent to the substrate and is protective for the material on which it forms. The film of oxide/chromium hydroxide, being very thin – the thickness is a few nanometers – and transparent to the light radiation, gives the stainless steel the typical metallic gray-silvery colour. All the properties described above are the consequence of the rapid reaction of the chromium present in the alloy with the oxygen of the atmosphere. The oxidation of stainless steel, also called passivation, occurs naturally and spontaneously in neutral oxidizing environments, such as in contact with air, or, as is customary in the manufacturing processes of semi-finished products, is induced artificially by immersing the semi-finished product in a diluted solution of nitric acid: the protective film of oxide and/or chromium hydroxide acts to seal and establish a barrier between the material and the external environment. The passive chrome oxide/hydroxide film also has another important feature: if it is scratched, abraded, or mechanically damaged, it will spontaneously reform on the surface of the component, again hindering the corrosive action. The depassivation pH allows us to determine the pH below which the passive film breaks (Table 5.2).

Table 5.2 – Depassivation pH of alloys 316 and C-276.

	316	C-276
Depassivation pH	≈ 2	n.d.

(Stainless steel in 2M solution of Cl- at T environment)	In the case of these alloys the operating pH range varies from 1 to 14. Literature data show that pH values close to 1 are the only materials capable of withstanding 0.1% Cl concentrations.

Another important parameter for in the choice of alloy is the PREN (Pitting Resistance Equivalent Number).

PREN: Based on the percentage of chromium and molybdenum in the alloy, from which corrosion resistance directly depends, it is possible to derive the value of a parameter, the PREN, which provides a rough indication of the ability of a stainless steel to withstand pitting or, more generally, localized corrosion. The formulae for deriving the values of these indicators are:

PREN = %Cr + 3.3 (%Mo) for ferritic types

PREN = %Cr + 3.3 (%Mo) + 16 (%N) for austenitic types

PREN = %Cr + 3.3 (%Mo) + 16 (or 30) (%N) for austenitic-ferritic types (duplex)

the higher this index, the greater the resistance to pitting that is probably the most known corrosive phenomenon on stainless steels. This is caused by a local tear of the passive layer, resulting from the action of strongly activating elements such as chloride (Cl^{-}) or fluoride (Fl^{-}) ions. On the surface are created dots or smallpox, characterized by a crater (anodic area) surrounded by a halo (cathodic area). To avoid this form of corrosion it is necessary to choose alloys with high quantities of chromium, nickel and molybdenum that have a more resistant passive layer. PREN classification is used because it is easy to determine, but it should be remembered that it does not provide a complete and exhaustive description of the corrosion resistance properties of stainless steels (Table 5.3).

Table 5.3 – PREN range of alloys 316 and C-276.

	316	**C-276**
PREN	≈ 24–29	≈ 64–69

Pitting corrosion can be considered negligible for PREN > 40.

The considerations made in this paragraph show better corrosion resistance than Hastelloy C-276 compared to AISI 316. However, given the costs associated with Hastelloy C-276, an estimate of the corrosion rates of AISI 316 was made from literature data on corrosion of steels in both acid and caustic environments. These estimates are given below for some case studies (Grgur 2020; Monteiro et al., 2020; Hren et al., 2021; Yuan et al., 2021).

Calculation of the corrosion rate for the less performing material (AISI 316)

Dimensions of the Parr reactor

V= 500 cm^3

Internal diameter = 6.35 cm

Height = 16.8 cm

Lateral surface = $\pi \cdot d_i \cdot h = \pi \cdot 6.35 \cdot 16.8 = 335.1\ cm^2$

$S_b = \pi r^2 = 31.6\ cm^2$

Sludges contact surface = 366.7 cm^2

1. Experimental studies conducted at room temperature, to test the corrosion resistance of various steels in different environments, report for an aqueous solution containing 10% of H_2SO_4 and 5% of NaCl, a corrosion rate, for AISI 316, of 17.4 mm/y (0.0019 mm/h).

Determination of Cr and Ni release in solution for AISI 316

%Cr = 18%

%Ni= 14%

ρ = 7.98 g/cm^3

$$Release_{Cr} = 7.98\frac{g}{cm^3}\cdot 1.74\frac{cm}{y}\cdot 0.18 = 2.5\frac{g}{cm^2 y} = 0.27\frac{mg}{cm^2 h}$$

$$Release_{Ni} = 7.98\frac{g}{cm^3}\cdot 1.74\frac{cm}{y}\cdot 0.14 = 1.94\frac{g}{cm^2 y} = 0.21\frac{mg}{cm^2 h}$$

$$Release_{Cr} = 0.27\frac{mg}{cm^2 h}\cdot 366.7\ cm^2 = 99.0\frac{mg}{h}$$

$$Release_{Ni} = 0.21\frac{mg}{cm^2 h}\cdot 366.7\ cm^2 = 77.0\frac{mg}{h}$$

2. By referring instead to experimental studies conducted in a caustic environment, for AISI 316L a maximum critical corrosion rate of about 18 mm/y (0.0020 mm/h) is obtained in a solution of NaOH at 50% by weight at 90 °C (deaerated environment). While this corrosion rate in the same open-circuit environment shows a maximum corrosion rate of 0.5 mm/y (0.000057 mm/h).

Critical corrosion rate

$$Release_{Cr} = 7.98\frac{g}{cm^3}\cdot 1.8\frac{cm}{y}\cdot 0.18 = 2.6\frac{g}{cm^2 y} = 0.29\frac{mg}{cm^2 h}\cdot 366.7 cm^2 = 106.3\ \frac{mg}{h}$$

$$Release_{Ni} = 7.98\frac{g}{cm^3}\cdot 1.8\frac{cm}{y}\cdot 0.14 = 2.0\frac{g}{cm^2 y} = 0.23\frac{mg}{cm^2 h}\cdot 366.7 cm^2 = 84\frac{mg}{h}$$

Corrosion rate in open circuit

$$Release_{Cr} = 7.98\frac{g}{cm^3}\cdot 0.05\frac{cm}{y}\cdot 0.18 = 0.072\frac{g}{cm^2 y} = 0.0.0082\frac{mg}{cm^2 h}\cdot 366.7 cm^2 = 3.0\ \frac{mg}{h}$$

$$Release_{Ni} = 7.98\frac{g}{cm^3}\cdot 0.05\frac{cm}{y}\cdot 0.14 = 0.056\frac{g}{cm^2 y} = 0.0064\ \frac{mg}{cm^2 h}\cdot 366.7 cm^2 = 2.3\ \frac{mg}{h}$$

These calculations are negligible for Hastelloy C-276, which has no corrosive effects over time for these H_2SO_4 concentrations and NaCl.

It should also be noted that the released amount of Cr and Ni was calculated by considering a corrosion rate in a pressure and ambient temperature system. Higher values of pressure and temperature will lead to a lower solubility of salts in solution and an increase in the corrosive phenomena. On the other hand, for precautionary reasons, reference is made to the worst conditions found in the several work. The systems in question have, in one case, high percentages of SO^{4-} and Cl^{-}, and in the other, high percentages of NaOH, which could be higher than those of our system.

However, this study led, both for precautionary reasons and for the possibility of working in a wider pH range, to choose Hastelloy C-276 as the steel for the construction of the reactor purposely designed for the HTL process.

5.2 Set-up of the experimental apparatus and test protocols

An important part of the PhD work related to the HTL process applied to different types of sewage sludge, has involved a detailed study on the performance of the plant to optimize the experimental apparatus and obtain the best operating conditions for the hydrothermal liquefaction. Moreover, two different separation protocols of the liquid phase produced during HTL process were compared to select the better in terms of yield and quality of the bio-oil produced. The results obtained by these studies have allowed to select the test protocols and phase separation technique used for the experimental campaign carried out in this PhD work, the results of which are reported from paragraph 5.3.

5.2.1 Analysis of the water thermodynamic state

The first study carried out concerned the identification of the initial pressure value to be subjected to the reactive mixture so that, at the chosen reaction temperature, the system is at a final pressure between 180 and 220 bar (characteristic values for conducting the HTL process). This is possible considering the liquid-vapour balance that is established between water, HTL reaction medium, and nitrogen, an inert gas used in the pre-pressurization step of the system. Combining the Antoine and the van der Waals equations gives the initial pressures (P_0) for the temperatures of interest in this PhD work (300 and 350 °C) which are 56 and 28 bar, respectively. Figure 5.1 shows the evolution of the thermodynamic profile of the blank tests (loading only distilled water) conducted in the batch reactor. This profile is useful to verify that the water, in the tests with set-point temperature (T^{set}) of 300 and 350 °C and determined initial pressure of the equations described above, is preferentially in the liquid state for the duration of the experiment.

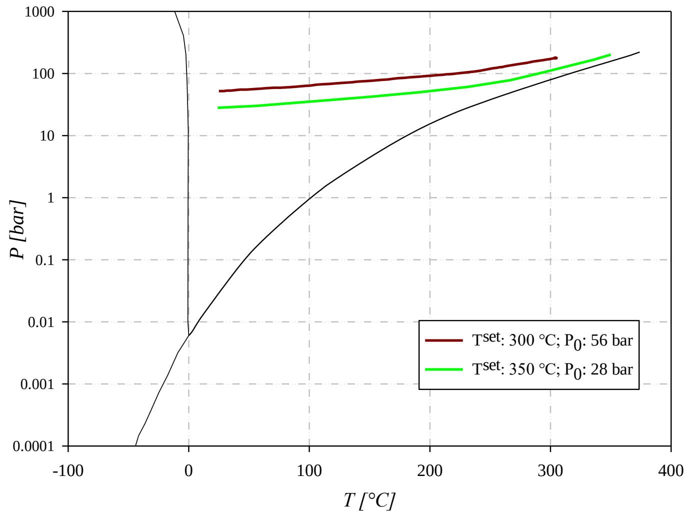

Figure 5.1 – Evolution of the thermodynamic state of distilled water during heating tests at different initial pressures. The curves in black delimit the zones of water existence in the different states of aggregation.

5.2.2 Comparison of reactor configurations

Once established the initial pressure of the HTL tests, new blank tests were carried out to determine the system response during the heating and cooling stages, by varying the reactor configuration. Three configurations were investigated, A, B and C (*vide* Chapter 2), and the respective thermal profiles were analysed: the objective of the upgrades made to the system to be found in the intention to enhance the heating ramp and limit the formation of undesirable products along the HTL process.

Figure 5.2 shows the time trend of the reactor temperature for the different configurations investigated, when 300 mL of distilled water were heated at a set point temperature of 350 °C. It can be observed that in configuration A (absence of insulation and auxiliary heating systems), B (presence of insulation and heating with plate at the base of the reactor) and C (addition of a band heater compared to configuration B) the system requires, respectively, 90, 55 and 48 min to reach the temperature of 350 °C. For all three systems, the cooling stage is very fast and in the order of 5 min, thus achieving a "*quench*" of the system to avoid the occurrence of secondary reactions that could lead to a redistribution of products during the cooling phase.

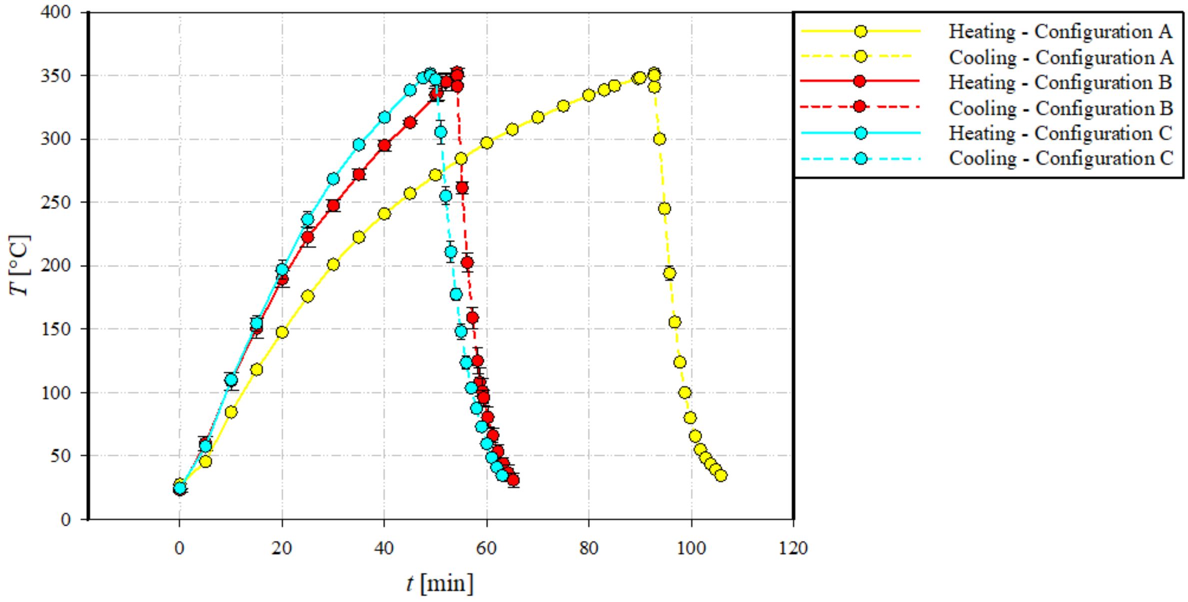

Figure 5.2 – Set-up of the purposely designed batch autoclave reactor for HTL. Results of the heating/cooling test for configurations A, B and C, using distilled water.

Then, to complete the set-up phase of the experimental apparatus, it was investigated the influence that the presence of sludge could have on the *T*-*P* couple during a typical HTL test, compared to the non-reactive case. Figure 5.3 shows the temperature and pressure pattern for an HTL test conducted at 350 °C for 20 min in configuration C, which is overlapping on the blank curve (distilled water only). This trend is like that obtained at different temperatures and times; therefore, similar considerations can be extended to all the temperature-pressure couples considered in this PhD project.

The sludge does not significantly influence the temperature-pressure curve due to the low concentration of the sludge in the reactive system (about 10% by weight), that do not determine a significant effect on the thermal properties of the aqueous phase. Only at T^{sets} the reactive system has slightly higher pressure values, which is due to gas generation during the HTL process of the sludge (e.g., by decarboxylation reactions with CO_2 development).

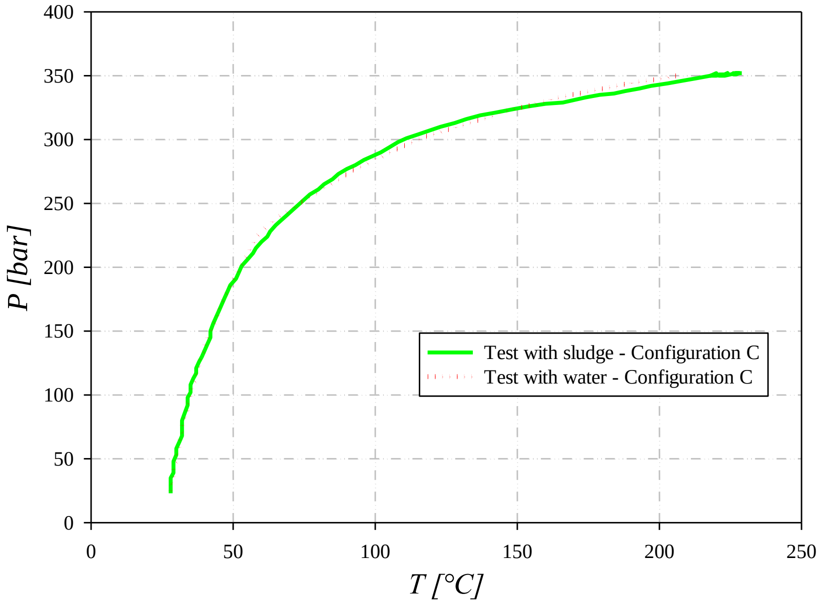

Figure 5.3 – Comparison of temperature vs. pressure profile between blank test and sludge test, configuration C.

Based on data obtained for the system with distilled water, HTL tests of the influence of the reactor configuration on the bio-oil yields were carried out. Configuration A was discarded due to the too long heating times. Figure 5.4 shows the yields of the bio-crude, solid and gaseous phases produced with a different heating ramp at temperatures of 300 and 350 °C and for an isothermal stage of 20 min. It is possible to observe that, for both temperatures, there are no relevant variations in the gas and solid yields when the heating rate changes (case B vs. C), while, for the tests carried out at 300 °C (MS-B-Cen-300-20 vs. MS-C-Cen-300-20), an increase of $Y_{biocrude}$ of 2% is observed for configuration C with respect to the B case; on the contrary, for the tests carried out at a temperature of 350 °C, a decrease in the biocrude yield for configuration C of about 10% can be noted. However, it is important to highlight that, at 350 °C for configuration B, the reaction time in the non-isothermal stage, is greater than for configuration C, so the system is subjected to a reaction time that is globally longer (of about 8 min). In addition, comparing the higher heating value of the two bio-oils obtained in the tests at 350 °C and 20 minutes for the two configurations, for case C the *HHV* is 31.4 MJ/kg, a value 3.7% greater than that obtained for the configuration B (Table 5.4). It should be noted that it has not been possible to quantify the yield in HTL soluble products in the aqueous phase in the present experimental campaign.

Based on these results, configuration C was selected for a deeper experimental campaign, to study the effect of temperature and time of the HTL process on yields and properties of the resulting phases.

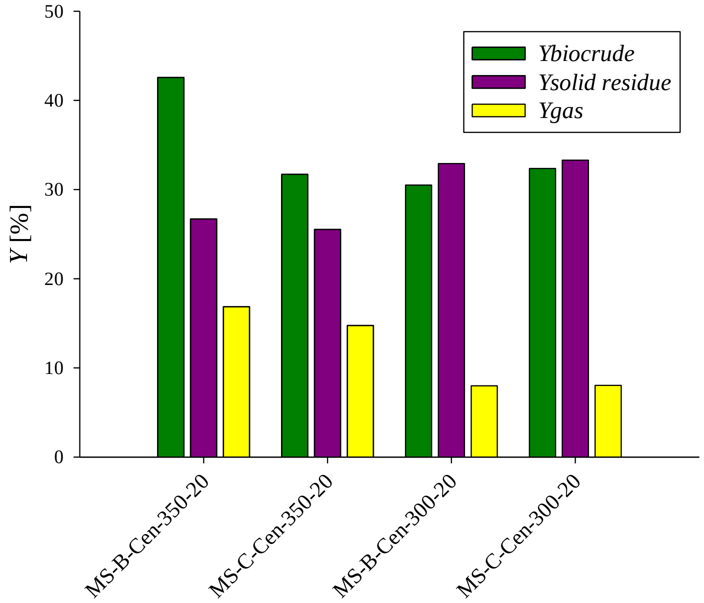

Figure 5.4 – Yields of biocrude, solid and gas phase for HTL tests performed on municipal sludge for configurations B and C (temperatures of 300 and 350 °C, isothermal stage of 20 min).

Table 5.4 – Higher heating value of biocrude obtained for different heating rate.

Test	***HHV [MJ/kg]***
MS-B-Cen-350-20	30.33
MS-C-Cen-350-20	31.44

5.2.3 Effect of separation protocol on bio-crude recovery

In parallel line with the study of the best reactor configuration, a survey was carried out on the effect of the separation protocol on the recovery of biocrude produced by HTL.

In the liquefaction of several types of biomass (lignocellulosic biomass, sewage sludge, macroalgae and microalgae), the most widely used separation method for the recovery of bio-oil from the reaction mixture produced via HTL consists of two phases: i) filtration of the reaction mixture to remove the solid from the liquid water/bio-oil mixture and ii) liquid-liquid extraction (L-L) of the oil phase from the aqueous phase, using solvents that are poorly miscible with water, such as dichloromethane (Malins et al., 2015). To recover the bio-oil that is soluble in water and that deposited on the solid residue, a large amount of solvent is generally used during filtration and extraction.

In this study, to minimise the amount of extracting solvent used in the filtration and L-L extraction phases, an alternative method of separating the oil and water phases was evaluated, using the centrifugation of liquid products in order to obtain the stratification of the oily phase on the bottom of the tube subjected to a centrifuge (Mujahid et al., 2020).

Figure 5.5 shows the yields of biocrude, on a dry and ash-free basis, obtained from HTL tests under the same reaction conditions: "SF" refers to a separation by solvent extraction (DCM) in a separating funnel, while

"Cen" refers to a separation obtained by centrifugation. The tests were conducted in duplicate at set point temperatures of 300 °C and 350 °C and for a reaction time of the isothermal stage of 20 minute.

It is noted that the yield of bio-oil, that is produced under identical reaction conditions, is different when different separation methods are used. For both temperatures the use of the centrifuge is more effective in the extraction of the biocrude from the aqueous phase. In fact, the use of centrifugation led to a recovery of bio-oil of 3% and 6% greater than liquid-liquid extraction, at 300 °C and 350 °C, respectively. As an example, at 350 °C, $Y_{bio\text{-}crude}$ is 44% in the case of centrifugation vs. 38% in the case of extraction.

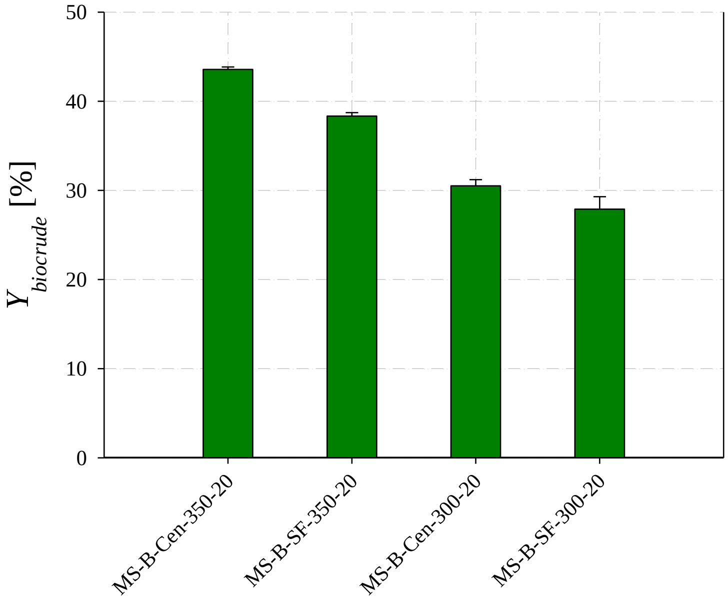

Figure 5.5 – $Y_{bio\text{-}crude}$ after different liquid-liquid separation protocols at fixed reaction time/temperature. SF: separation by solvent extraction in s separatory funnel, Cen: separation by centrifugation. Starting material: municipal sludge (The tests were conducted in duplicate).

One of the problems not to be overlooked in traditional L-L separation is that an amount of bio-oil produced during HTL cannot be recovered. During the L-L extraction phase, in fact, hydrophobic species of the bio-oil are extracted in the DCM phase and stratifies on the lower part of the separatory funnel, while the hydrophilic species (or water-soluble organic substances) present in the biocrude remain in the upper part, solubilised in the aqueous phase: as a result, when water is used as a liquefaction solvent, the fraction of water-soluble organic compounds tends to remain preferentially in the aqueous phase, making their recovery in bio-oil difficult, resulting in reduction of $Y_{biocrude}$ (Prajitno et al., 2018).

On contrary, the greater quantity of biocrude recovered using the centrifugation approach can be attributed to a greater coalescence effectiveness of bio-oil drops dispersed in emulsion in water phase due to the centrifugal force, and their subsequent sedimentation on the bottom of the test tube. The greater effectiveness of the recovery of bio-oil from the aqueous phase can also be seen in Figure 5.6, through a visual inspection of the aqueous phases produced via HTL and separated in two different ways: the solution collected after centrifugation (right in the figure) is clearer than the L-L extraction method (left in the figure), suggesting that more water-soluble compounds were transferred to the bio-oil phase during centrifugation. In addition to the quantitative aspects, which lead to the preferential use of centrifugation, the use of a much lower amount of DCM also reduces the energy expenditure associated with the subsequent phase of solvent evaporation than required for the L-L, with an associated advantage of reduced environmental impact determined by the use of the halogenated DCM solvent. Therefore, the use of centrifugation is a more effective method for bio-crude separation and with an associated advantage of reduced environmental impact vs. solvent (halogenated dichloromethane) extraction.

Figure 5.6 – Aqueous phases generated by the HTL process and separated by L-L extraction (left) or centrifuge (right).

Based on these results, configuration C and the more effective centrifugation separation method for the bio-oil recovery were selected, to study the effect of temperature and time of the HTL process on yields and properties of the resulting phases.

5.3 Effect of reaction time/temperature on product distribution

HTL tests were conducted, for the two types of sludge, at two different temperatures (*T*) of 300 °C and 350 °C, and for different isothermal residence times (*t*), ranging from 0 (transient only) to 60 min. In addition, for both tannery and municipal sludge, two HTL tests were performed by stopping the heating of the system at *T* of 250 °C and 275 °C, to verify the possible products formation during thermal transients.

Figures 5.7–5.9 show, respectively, the yields of biocrude, solid residue and gas at different times and as a function of temperature on dry basis "*db*".

For $Y_{biocrude}$, it is possible to identify a non-monotonic trend which is more pronounced for MS (the sludge with a better bio-oil yield). In fact, for the latter, there is a maximum located at 30 min/300 °C ($Y_{biocrude}$=26.71%) and at 10 min for *T* of 350 °C ($Y_{biocrude}$=32.79%). After *t*=60 min, $Y_{biocrude}$ decreases at around 24% and 21%, for *T* of 350 °C and 300 °C, respectively. From tests performed during the heating transient, it can be highlighted that, even at 250 °C, the formation of biocrude is non-negligible with a value of 7.4% of $Y_{biocrude}$. For TS, the trend is less pronounced. For the tests carried out at 350 °C, there is a slight initial increase in yield at 10 min ($Y_{biocrude}$=18.2%) and then it remains almost constant up to *t*=40 min. A decrease in biocrude yield

(15.8%) is observed for *t* of 60 min. A similar trend, shifted towards longer times, was obtained for tests carried out at 300 °C. The yield of biocrude increases up to 30 min ($Y_{biocrude}$=17.1%), remains constant for *t* up to 50 min, then it slightly decreases to 60 min where $Y_{biocrude}$ is equal to 15.4%. For both sludges, higher temperatures coupled with low reaction times favour the distribution of products towards bio-oil formation; this result is more evident for MS; however, the *T*-*t* couple of 350 °C and 10 min remains the best operating condition even in the case of TS.

Concerning the solid residue from HTL of MS, $Y_{solid\ residue}$ decreases from 38% to 30% (300 °C), and from 32% to 23% (350 °C), between 0 and 30 min. The slight increase in the values of solid yield after 30 min is likely due to the decrease in $Y_{biocrude}$ and an increase in the bio-char formation. A similar trend can be observed also for TS; however, for this type of biomass, $Y_{solid\ residue}$ at the same reaction temperature is higher by about 20% compared to the civil sludge. The solid residue yield at 300 °C starts from an initial value of 61.18% (57.04% at 350 °C), passes for a minimum at reaction time of 30 min with a yield of 49.68% (53.52% at 350 °C), to increase again up to a yield of 56.77% at 60 min (52.91% at 350 °C). The higher amount of solid residue when TS was used for the HTL process, could be ascribed to a higher percentage of ash in the starting sludge (24.1% for MS vs. 38.5% for TS), which represents an unconvertible fraction likely to remain in the solid residue.

Finally, the yield of the gas phase does not follow a clear trend with *t* and Y_{gas} is smaller than 15% for all the tested operating conditions.

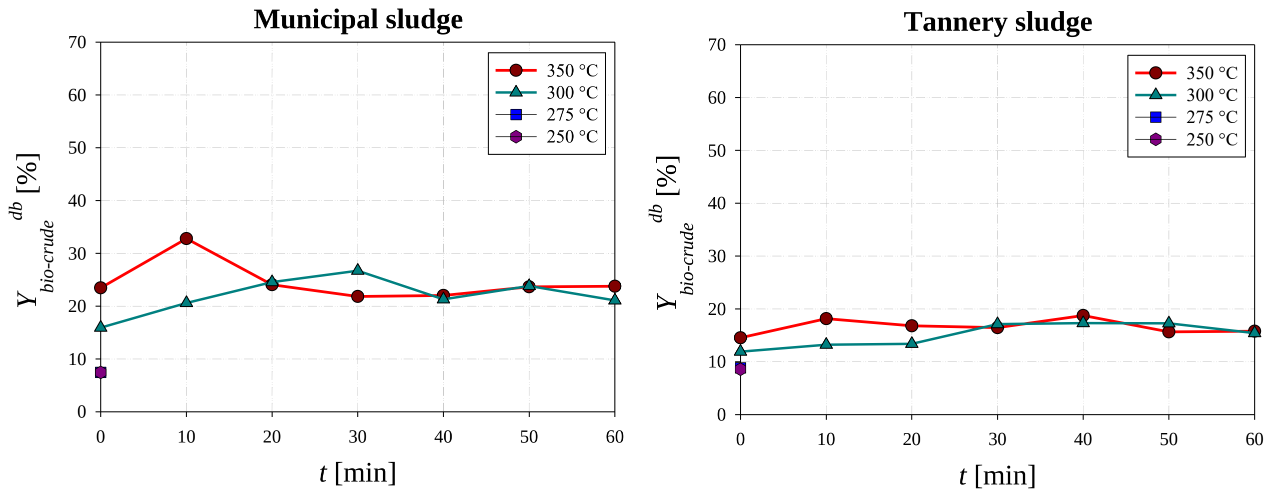

Figure 5.7 – Target biocrude yield as a function of time and for different temperature, for HTL carried out on both sewage sludges.

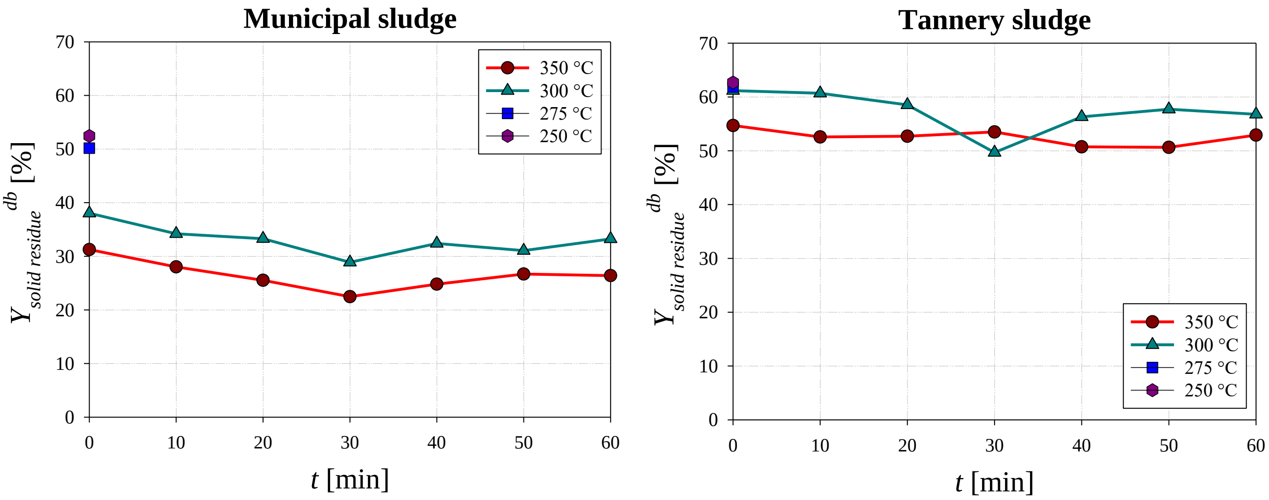

Figure 5.8 – Solid residue yield as a function of time and for different temperature, for HTL carried out on both sewage sludges.

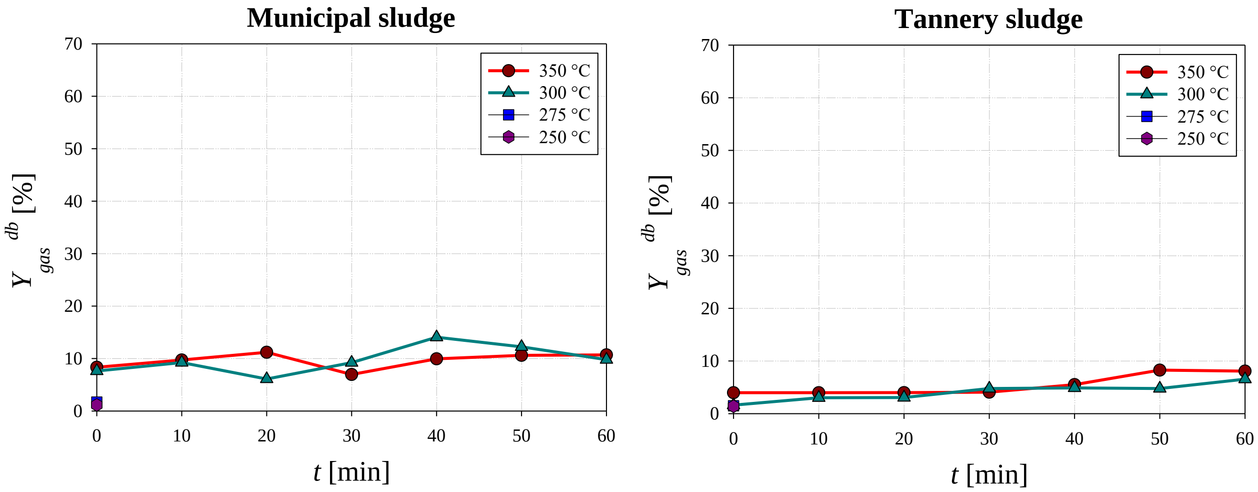

Figure 5.9 – Gas yield as a function of time and for different temperature, for HTL carried out on both sewage sludges.

The results on the biocrude yield show that, for both sludges, once the process temperature has been set, maximum yields are obtained for similar reaction time values. These maximum values are at t=10 min (for temperatures of 350 °C) and t=30 min (when the temperature during the isothermal stage is 300 °C). However, MS seems to be a better biomass than TS with a better bio-oil yield, that is about 15% greater. The differences in terms of yield, in the first instance, can be ascribed to the greater ash content present in the industrial sludge. In fact, this represents a fraction of the starting biomass that cannot be converted into bio-oil. Conversely, by reporting the yields of bio-oil on a dry and ash-free basis "*dafb*" (Figure 5.10), it is possible to observe that the differences between the two sludges are reduced, with a maximum bio-oil yield at 350 °C of about 43% and 30% for MS and TS, respectively (Figure 5.10a).

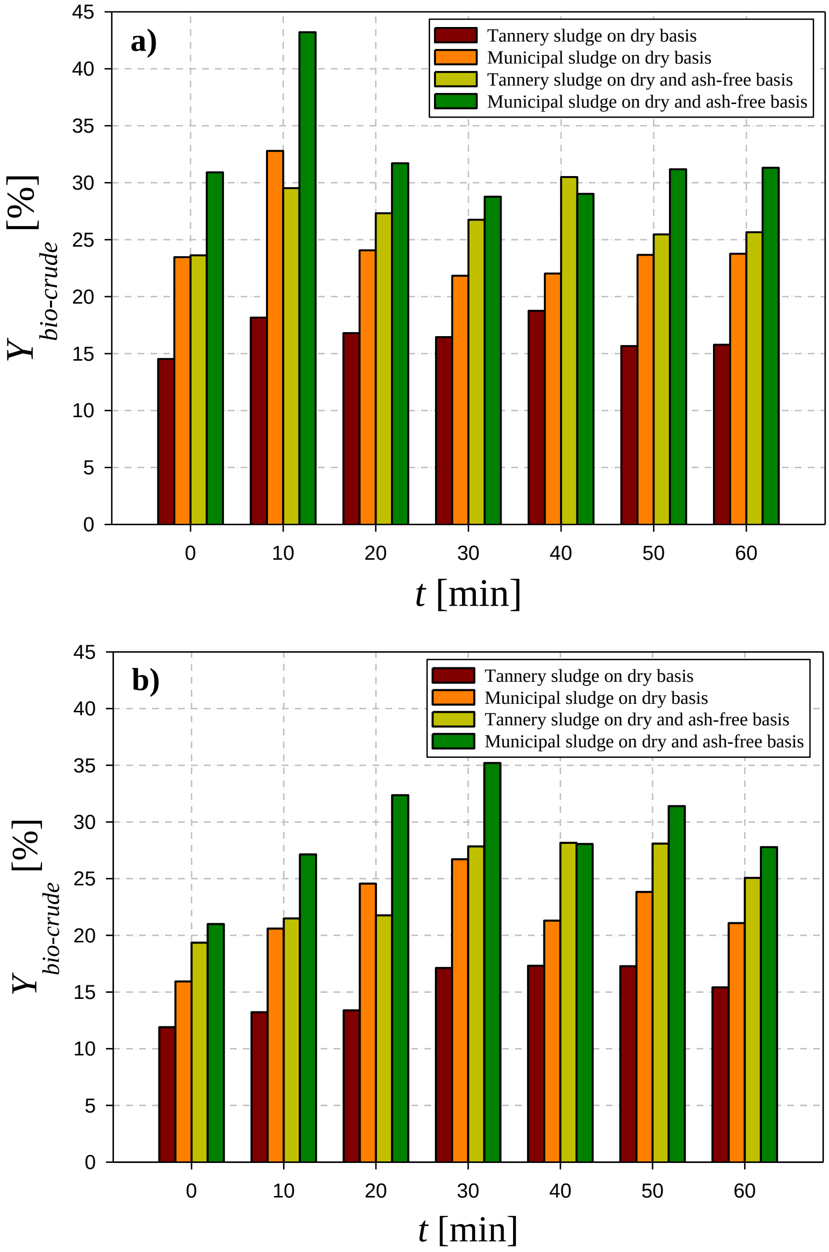

Figure 5.10 – Biocrude yield as a function of time on dry and dry and ash-free basis for sewage sludges. Reaction temperature of a) 350 °C, b) 300 °C.

The differences in biocrude yield are therefore determined by the different nature and composition of the starting biomass. For example, as noted in Chapter 3 (Table 3.6), both sludges have a high content of Ca, Fe, and Al; although with a lower relevance, Mg and K for MS and Na for TS are also present. These metals could favour the bio-oil formation thanks to their catalytic effect. Nevertheless, as reported in Table 3.8, the MS has a higher carbohydrates content than TS (59% for the municipal sludge vs 21% for tannery sludge). In the HTL process of other biomass resources (e.g., algae and lignocellulose), alkaline catalysts, such as Na_2CO_3, NaOH, K_2CO_3, and KOH, $Ca(OH)_2$ are widely used and have been proven to be effective, in particular for biomass with a higher carbohydrates content as in the case of MS (Shakya et al., 2015; Zhu et al., 2015; Castello et al., 2019; Zhu et al., 2022). In good agreement, Yokoyama et al. (1987) witnessed an increase in biocrude yield while using 2.5% sodium carbonate catalyst for the conversion of sewage sludge with 57% carbohydrates.

Moreover, the solid yield decreases with the addition of the catalyst because the alkali catalyst is an active promoter of water gas shift reaction, which forms more hydrogen that allows fragmented intermediates to stabilise and averts repolymerisation, which ultimately suppresses the formation of char (Toor et al., 2011, Biller et al., 2016). Similar consideration can be made when iron is used as a catalyst. de Caprariis et al. (2021) demonstrate that, when a lignocellulosic biomass is subjected to HTL tests performed using Fe and Zn, the absence of a carbonaceous solid residue could be explained considering the generation of active hydrogen in situ, through the redox reaction between metal and water. The sudden presence of active hydrogen assures a more reducing environment, which leads to a stabilization of the reactive intermediates derived from the degradation of cellulose, avoiding their recombination and aromatization and the consequent char formation. In the HTL of biomass, the use of Fe, as inhibitor of char formation, was studied also by Sun et al. (2011) and Miyata et al. (2017), obtaining an increase in both the liquid phase yield and its quality.

In support of the results obtained on the bio-oil yield from hydrothermal enhancement of civil and industrial sludges used in this PhD work, Figure 5.11 presents a contour plot in which data of bio-crude yield were reported to vary in time and temperature of reaction. The data are illustrated only for systems and procedures comparable to those adopted in this PhD work, in terms of reaction time, temperature and starting biomass (Qian et al., 2017; Anastasakis et al., 2018; Kapusta, 2018; Li et al., 2018; Xu et al., 2018; Badrolnizam et al., 2019; Prestigiacomo et al., 2019; Su et al., 2019; Mishra and Mohanty, 2020; Mujahid et al., 2020; Prestigiacomo et al., 2020; Qian et al., 2020). On the diagram, it was highlighted $Y_{biocrude}$ obtained for the best condition highlighted in this work, C-Cen-350-10 (triangle in orange), whose values, amounting to about 43% and 30% for MS and TS, respectively, are satisfactory when compared to the data reported in the literature. This result leads us to consider the selected starting biomass as an excellent candidate for the production of liquid bio-fuels, in particular for the case of MS.

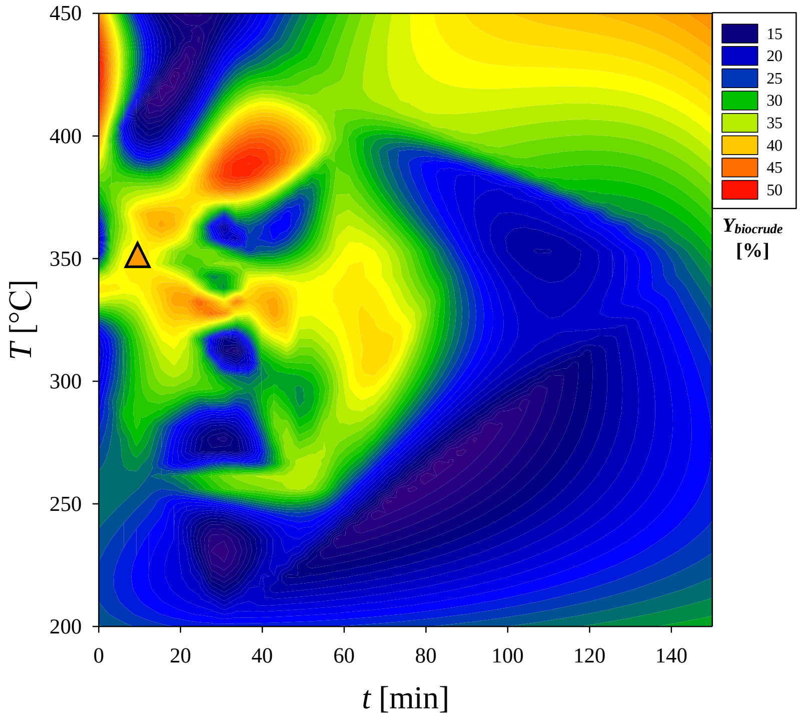

Figure 5.11 – Literature overview of biocrude yields (*dafb*) obtained via HTL, at different reaction times and temperatures. The orange triangle represents the best results obtained in this PhD work.

5.3.1 Preliminary study on the effect of TS-MS mixtures on biocrude yield

The sludges under investigation have slight differences in terms of lipids and proteins, while they differ more for their carbohydrates content (see Table 3.8). To study the effect of the concentration of the different bio-components present in the starting sludge on the biocrude yield, preliminary studies were carried out using mixtures of the two different types of sludge. For this study, in addition to MS and TS as such, three concentration ratios of tannery and municipal sludge were selected, 25:75, 50:50, 75:25. The three mixtures were subjected to the HTL process at the isothermal temperature of 350 °C and for a reaction time of 10 min (*T*-*t* pair where there is greater difference between the bio-oil yield in civil and tannery sludge, as noted in Figure 5.7) and the biocrude yields were compared to tests carried out under the same conditions when using only MS or only TS. The biocrude yield obtained for the five cases are reported in Figure 5.12 as function of the different mixtures. From a first analysis, there seems to be no synergistic/antagonistic effects in the mixtures of the two sludges, and the biocrude yield exhibits a linear dependence with the concentration of MS present in the mixture. Higher is the content of municipal sludge (or, in other terms, the content of carbohydrates), higher is the biocrude yield.

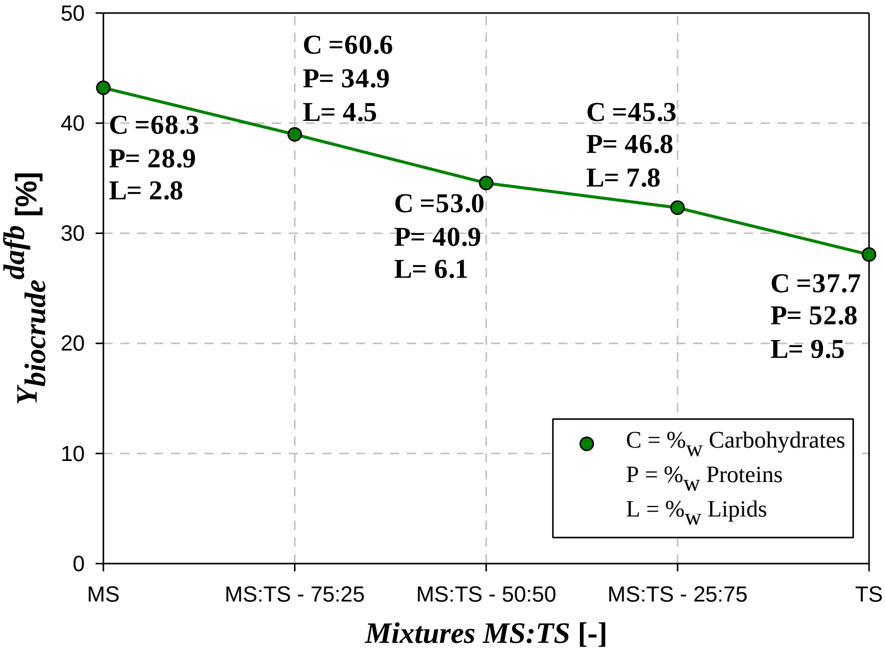

Figure 5.12 – Biocrude yield as a function of the mixture MS:TS. The carbohydrates, lipids and proteins content in the mixtures is calculated on a dry and ash-free basis.

Figure 5.13 shows a comparison between the composition in terms of lipids, proteins and carbohydrates, for sludges and mixtures under investigation in this PhD work, and the composition in terms of the same macro-components obtained from literature data on various types of biomass (Li et al., 2021). In addition, in Figure 5.13c it is reported a contour plot of bio-oil yields compared to the macro-composition of several biomasses (data on sewage sludge are not present in the latter ternary plot for lack of literature data). The chemical composition of tannery and municipal sludge (as well as their mixtures) obtained from the analysis of macro-components is confirmed by the literature data reported on sewage sludge. Furthermore, by identifying on the contour plot the region where the starting MS:TS mixtures fall (red circumscribed area), the biocrude yields on dry basis obtained from the HTL process are in line, if not slightly higher, to those that should be expected on the basis of the composition of the starting sludge.

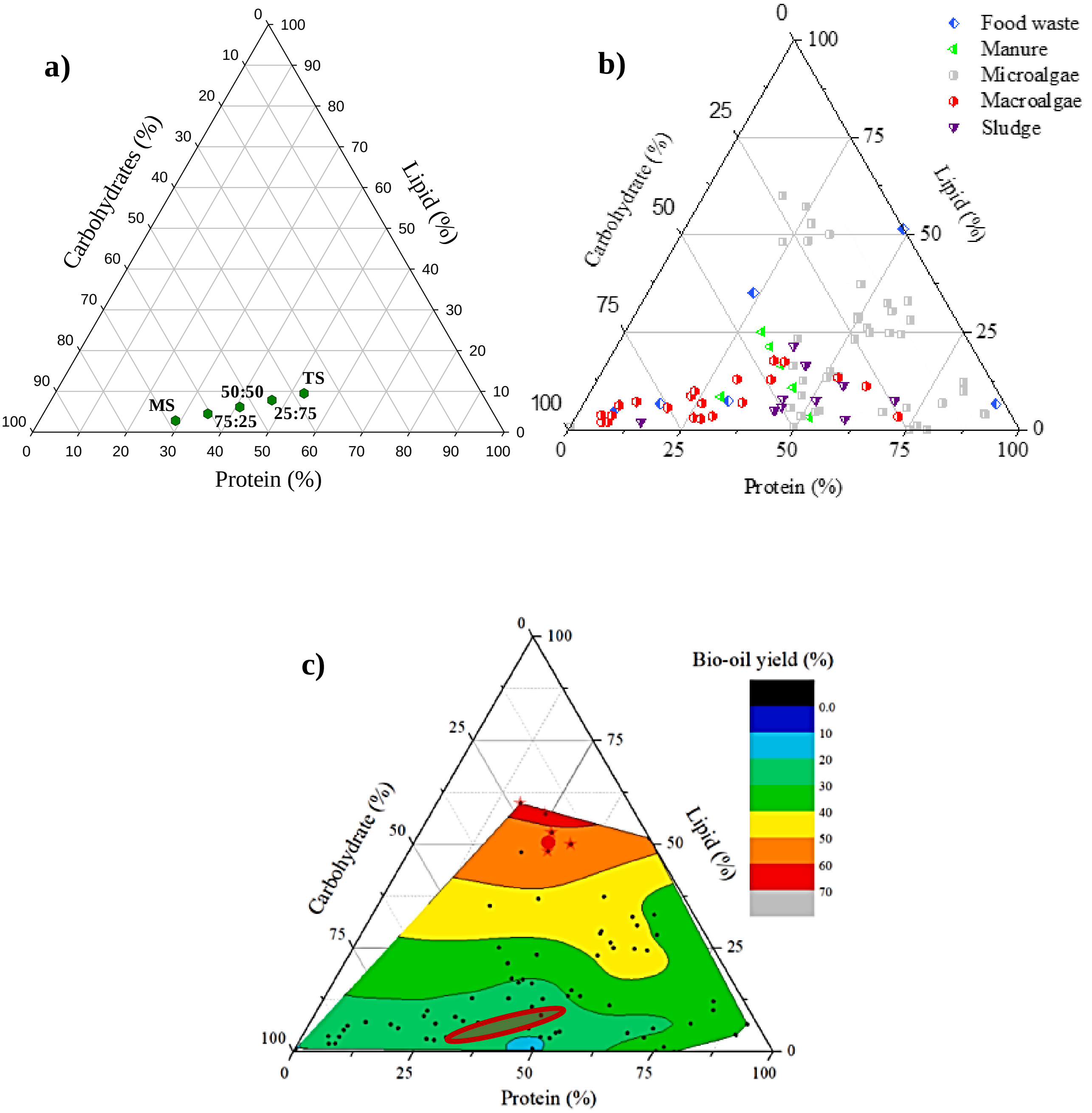

Figure 5.13 – Ternary phase diagram for a) biochemical compositions of TS, MS and mixtures MS:TS, b) biochemical compositions of different types of feedstock, c) literature overview of biocrude yields (dry basis) obtained via HTL, at different biochemical composition. Figures b and c refer to the work of Li et al. (2021).

5.4 Biocrude characterisation

Table 5.6 summarizes the biocrude yield values and the energetic properties obtained under the best operating conditions (350 °C–10 min and 300 °C–30 min) for both sludges. For the same sludge, *HHV* values are very similar, so the difference in energy recovery (*ER*) outcomes is mainly determined by the greater value of bio-crude yield obtained at 350 °C. For MS, *ER* is about 59% and 28% greater than the value retrieved at the lowest operating temperature, while, for TS, *ER* is equal to 44% and 41% for *T* of 350 °C and 300 °C, respectively.

Table 5.6 – Main properties for biocrude obtained under the best HTL process conditions.

	Test	$Y_{bio\text{-}crude}^{dafb}$ [%]	$Y_{bio\text{-}crude}^{db}$ [%]	*HHV* [MJ/kg]	*ER* [%]
Municipal sludge	**Cen-300-30**	35.2	26.7	28.8	46.0
	Cen-350-10	43.2	32.8	30.0	58.9
Tannery sludge	**Cen-300-30**	27.8	17.2	35.5	41.0
	Cen-350-10	29.5	18.2	36.1	44.1

The determination of the sulphur and chlorine content produced the results given in Table 5.7. It is possible to note that, while the Cl content in the bio-oils obtained for both sludges is one order of magnitude lower than its concentration in the starting biomass (Table 3.4), sulphur is unequally distributed between the HTL products with a total S content in the biocrude that is similar to that of the parent sludge (Table 3.2). The higher S content in the biocrude obtained from HTL of TS can be ascribed to the presence of basic chromium sulphates which are used in leather processing. The greater the presence of sulphur or other heteroatoms, the more intense will be the relative processing with higher plant operating costs. In fact, the presence of S must be limited for both environmental reasons and the protection of the most delicate parts of the plant. Therefore, bio-oil upgrade processes aimed at reducing the percentage of sulphur are necessary for both bio-oils.

Table 5.7 – Chlorine and sulphur content of the biocrude obtained (percentages by weight, dry basis).

			Test 1	*Test 2*	*Mean value*
Tannery sludge	Cen-300-30	Cl	0.010	0.009	0.010±0.001
		S	3.83	2.81	3.32±0.72
	Cen-350-10	Cl	0.026	0.030	0.028±0.003
		S	3.72	2.96	3.34±0.53
Municipal sludge	Cen-300-30	Cl	0.023	0.020	0.022±0.002
		S	1.10	1.69	1.40±0.41
	Cen-350-10	Cl	0.038	0.032	0.035±0.004
		S	1.08	0.98	1.03±0.07

5.4.1 Determination of the metal content by ICP-MS in the biocrude and co-products

Table 5.8 and 5.9 show the speciation of metals in the three phases produced by the HTL process, respectively for civil and tannery sludge. Metals after the HTL process, regardless of the sludges nature, are concentrated in the solid residue, with a high contribution from Fe, present in high concentrations in the starting sludge; while they are mostly found in traces in the bio-oil and in the aqueous phase. However, in the case of MS, the concentration of Fe (2327 ppm) and Ca (120 ppm) in biocrude and K (270 ppm) in the aqueous phase is significant. The presence of not negligible quantities of Fe (1180 ppm) is confirmed in the bio-oil resulting from the HTL process applied to TS; for this biocrude, also the Cr content is not negligible, with a concentration of about 150 ppm. So, Fe and Cr removal techniques must be evaluated among the upgrades to be made on the biocrude. In addition, Pb and Hg removal techniques (even if present in concentrations of lower order of magnitude) will need to be evaluated.

Table 5.8 – ICP-MS analysis for solid residue (SR), biocrude (BC) and aqueous phase (AP) obtained in MS liquefaction tests.

Metal	**SR-300-30 [g/kg]**	**SR-350-10 [g/kg]**	**BC-300-30 [g/kg]**	**BC-350-10 [g/kg]**	**AP-300-30 [g/kg]**	**AP-350-10 [g/kg]**
B	0.0071	n.d.	n.d.	0.027	0.0026	0.0026
Na	0.0093	n.d.	n.d.	n.d.	0.028	0.044
Mg	9.60	9.94	n.d.	n.d.	n.d.	0.0041
Al	12.67	12.57	n.d.	n.d.	n.d.	n.d.
P	54.31	56.03	n.d.	0.0045	0.095	0.050
K	1.33	1.18	n.d.	n.d.	0.22	0.27
Ca	18.71	18.79	0.12	0.10	0.020	0.060
Ti	0.43	0.47	n.d.	0.0068	0.00023	0.00022
V	0.028	0.029	0.0011	0.0014	n.d.	n.d.
Cr	0.22	0.22	n.d.	0.0023	n.d.	n.d.
Mn	0.58	0.57	n.d.	0.00030	n.d.	n.d.
Fe	102.90	103.30	2.327	1.294	0.0025	0.00032
Co	0.0080	0.0076	0.00043	0.00090	n.d.	n.d.
Ni	0.52	0.90	0.0019	0.048	n.d.	n.d.
Cu	0.95	0.87	n.d.	n.d.	n.d.	n.d.
Zn	2.53	2.38	0.025	0.029	n.d.	n.d.
As	n.d.	n.d.	n.d.	n.d.	n.d.	n.d.
Zr	0.053	0.052	0.0039	0.0019	0.000054	0.000036
Mo	0.053	0.050	0.0024	0.032	0.000011	0.000010
Sn	0.059	0.057	0.0040	0.013	0.00001	0.00002
Ba	0.45	0.47	n.d.	0.0038	0.00036	0.00059
Hg	0.0011	0.0013	0.00056	0.00050	0.00001	0.00001
Pb	0.25	0.25	n.d	0.0014	n.d.	n.d.

Table 5.9 – ICP-MS analysis for solid residue (SR), biocrude (BC) and aqueous phase (AP) obtained in TS liquefaction tests.

Metal	SR-300-30 [g/kg]	SR-350-10 [g/kg]	BC-300-30 [g/kg]	BC-350-10 [g/kg]	AP-300-30 [g/kg]	AP-350-10 [g/kg]
B	0.012	n.d.	n.d.	n.d.	n.d.	n.d.
Na	1.50	1.61	n.d.	0.041	0.84	1.06
Mg	3.71	2.70	n.d.	n.d.	n.d.	0.0058
Al	13.53	24.29	0.027	0.48	0.0017	0.00051
P	17.23	7.96	0.0027	0.012	0.021	0.0014
K	0.68	0.23	n.d.	n.d.	0.14	0.050
Ca	92.86	78.49	0.050	0.049	0.25	0.032
Ti	0.003	0.004	n.d.	n.d.	n.d.	n.d.
V	0.030	0.037	0.0062	0.0067	0.00054	0.00054
Cr	17.40	45.87	0.15	0.14	0.0040	0.00044
Mn	0.28	0.015	n.d.	n.d.	n.d.	n.d.
Fe	40.92	54.15	1.12	1.18	0.00049	n.d.
Co	0.010	0.012	0.00002	n.d.	n.d.	n.d.
Ni	0.099	0.051	0.0064	n.d.	n.d.	n.d.
Cu	0.20	0.13	n.d.	n.d.	n.d.	n.d.
Zn	1.18	3.58	n.d.	n.d.	n.d.	n.d.
As	0.054	0.012	0.0022	n.d.	0.00040	0.00012
Zr	0.0001	0.0021	n.d.	n.d.	n.d.	n.d.
Mo	0.0004	0.0032	n.d.	n.d.	n.d.	n.d.
Sn	0.00001	0.0003	n.d.	n.d.	n.d.	n.d.
Ba	0.57	0.067	0.00023	0.0012	0.00055	0.00032
Hg	0.00054	0.00045	0.00020	0.00012	0.000040	0.000010
Pb	0.043	0.045	n.d.	n.d.	n.d.	n.d.

Chromium speciation

The high Cr content is a critical point in the energy valorisation of TS by HTL process; for this reason, the total Cr content and the contribution of Cr(VI) to the latter was evaluated in the solid residue, aqueous phase and biocrude produced. Table 5.10 gives the total Cr concentration data (on wet and dry basis), obtained by AAS for our best conditions (350 °C–10 min and 300 °C–30 min). As regards the determination of Cr(VI) by UV-Vis spectrophotometry, all the solutions containing the different HTL products did not change from transparent to pink (as compared to the test for the reference solutions) after the addition of diphenylcarbazide solution, an indicator of the absence of Cr(VI) in solution. This could also be attributed to the limit of detection of the technique used, which is equal to a concentration of Cr(VI) in solution of 0.05 mg/L. Therefore, if present, the Cr(VI) content in the solid residue, biocrude and aqueous phase produced during HTL test would not exceed 0.5 ppm.

Table 5.10 – Chromium distribution in HTL products.

	SR 300-30	**SR 350-10**	**BC 300-30**	**BC 350-10**	**AP 300-30**	**AP 350-10**
Cr [g/kg]	28.52	47.35	0.22	0.23	0.0028	0.0005

5.4.2 Qualitative chemical composition analysis of biocrude and aqueous phase

The analytical technique commonly used in the literature for the study of the chemical composition of the biocrude obtained from HTL is GC-MS. However, this technique does not allow the detection of compounds with boiling temperatures higher than 300 °C. To obtain a more detailed screening, in this work a preliminary study of the chemical composition was carried out by combining ^{1}H-NMR spectroscopy with LC-MS. Figure 5.14 shows the H-NMR spectra of bio-oils obtained under the best operating conditions for municipal and civil sludge. Bio-oil samples from both sludges, obtained after treatment at 300 ºC for 30 minutes or 350 ºC for 10 minutes, were analysed:

1. ^{1}H-NMR spectra of MS-C-Cen-300-30 and MS-C-Cen-350-10 samples are very similar (Figure 5.14a and 5.14b).
2. On contrary, ^{1}H-NMR spectra of the samples TS-C-Cen-300-30 and TS-C-Cen-350-10 show some more evident differences; in particular, only in the case of TS-C-Cen-350-10 we find more intense signals related to the protons of aldehydes (i.e., derivatives of furfural) and carboxylic acids (i.e. cinnamic acid derivatives, polyunsaturated fatty acids) (Figure 5.14c and 5.14d). This confirms the tendency of aldehydes and carboxylic acids to convert into other compounds for longer times.
3. The ratio between the integration of signals in the region of aromatic protons (I_{sp^2}) and signals in the region of aliphatic protons (I_{sp^3}) shows that, in both TS and MS biocrude, there is a greater content of aromatic compounds (fraction derived from polyphenols) than aliphatic compound:

$$\frac{I_{sp^2}}{I_{sp^3}} = 0.057 \qquad \text{for MS} \tag{5.1}$$

$$\frac{I_{sp^2}}{I_{sp^3}} = 0.073 \qquad \text{for TS} \tag{5.2}$$

4. The ratio between the integration of signals in the region of the protons of alcohol groups (-CH_2OH/-CHOH) (I_{sp^3}OH) and that of the signals in the region of aliphatic protons (I_{sp^3}Al) shows that, in particular for TS but also for MS biocrude, there is a higher content of alcohols than aliphatic compound:

$$\frac{I_{sp^2 OH}}{I_{sp^3 Al}} = 0.049 \qquad \text{for MS} \tag{5.3}$$

$$\frac{I_{sp^2OH}}{I_{sp^3Al}} = 0.19 \qquad \text{for TS} \qquad (5.4)$$

5. The ^{1}H, ^{1}H-COSY analysis (spectrum not shown) revealed that some of the signals related to protons of -CH_2OH/-CHOH groups can be attributed to units of sugars.
6. In addition, ^{1}H, ^{13}C-HSQC (Figure 5.15) shows that, in the region of aromatic protons, it is possible to attribute the signals to derivatives of guaiacol (6.7/115 ppm) and derivatives of cinnamic acid or cinnamyl alcohol (6.9–7.4/130 ppm and 7.2/126 ppm). There are no significant differences between the spectral profiles of MS and TS bio-oils.
7. The presence of 3.7/55 ppm signals in the ^{1}H, ^{13}C-HSQC spectrum for -OCH_3 groups confirms that some of these phenolic/catecholic derivatives are methoxylated.
8. In both MS and TS bio-oils, there is the presence of olefin signals of unsaturated fatty acids, evident from the signal at 5.3/130 ppm in the ^{1}H, ^{13}C-HSQC spectrum and from the correlations of the latter with aliphatic protons in the ^{1}H, ^{1}H-COSY spectrum.

Spectra interpretation and peak association was supported by literature comparison with the work of Ben and Ragauskas, 2011, where mono and bi-dimensional NRM analysis was carried out on biocrude samples obtained downstream of the pyrolysis process.

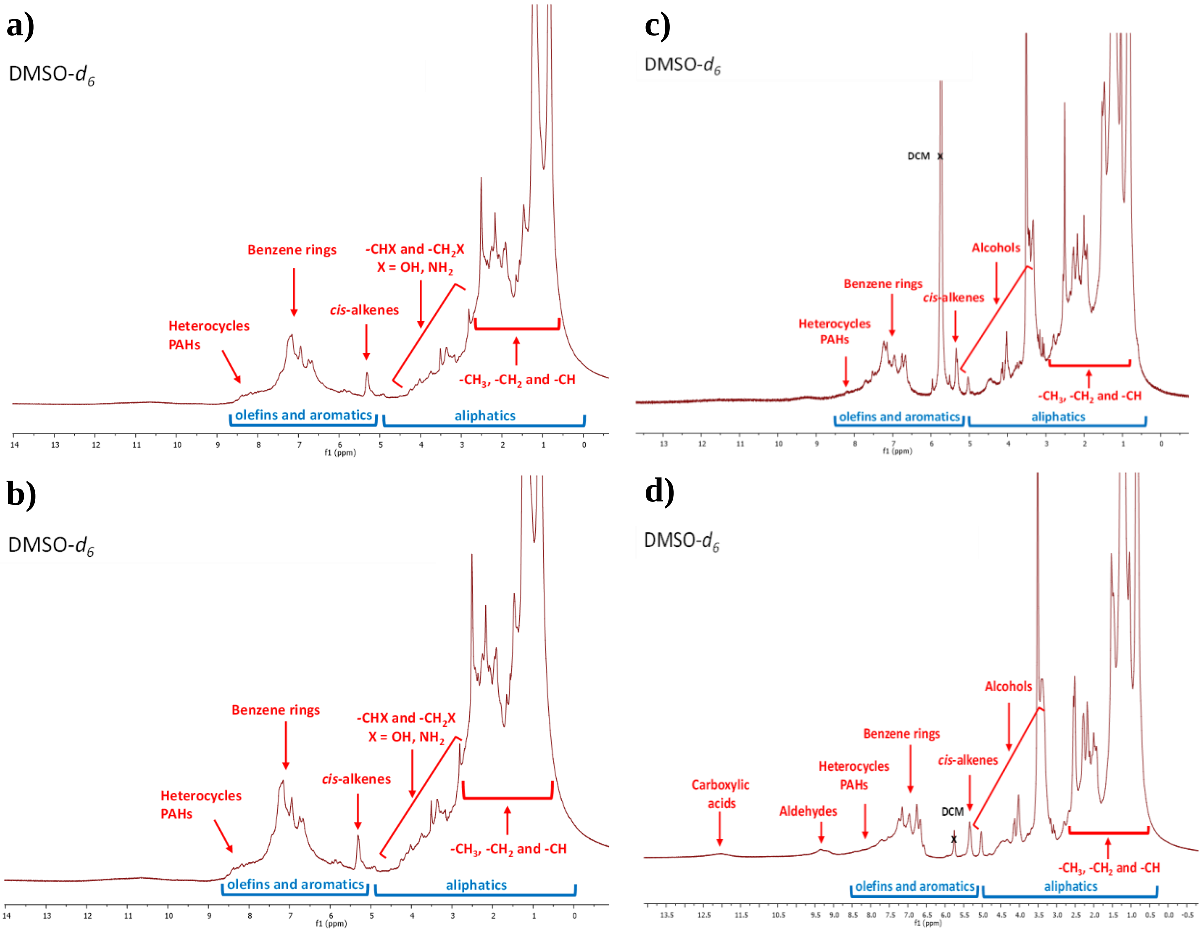

Figure 5.14 – ^{1}H-NMR spectra of bio-oils obtained for cases: a) MS-C-Cen-300-30, b) MS-C-Cen-350-10, c) TS-C-Cen-300-30, d) TS-C-Cen-350-10.

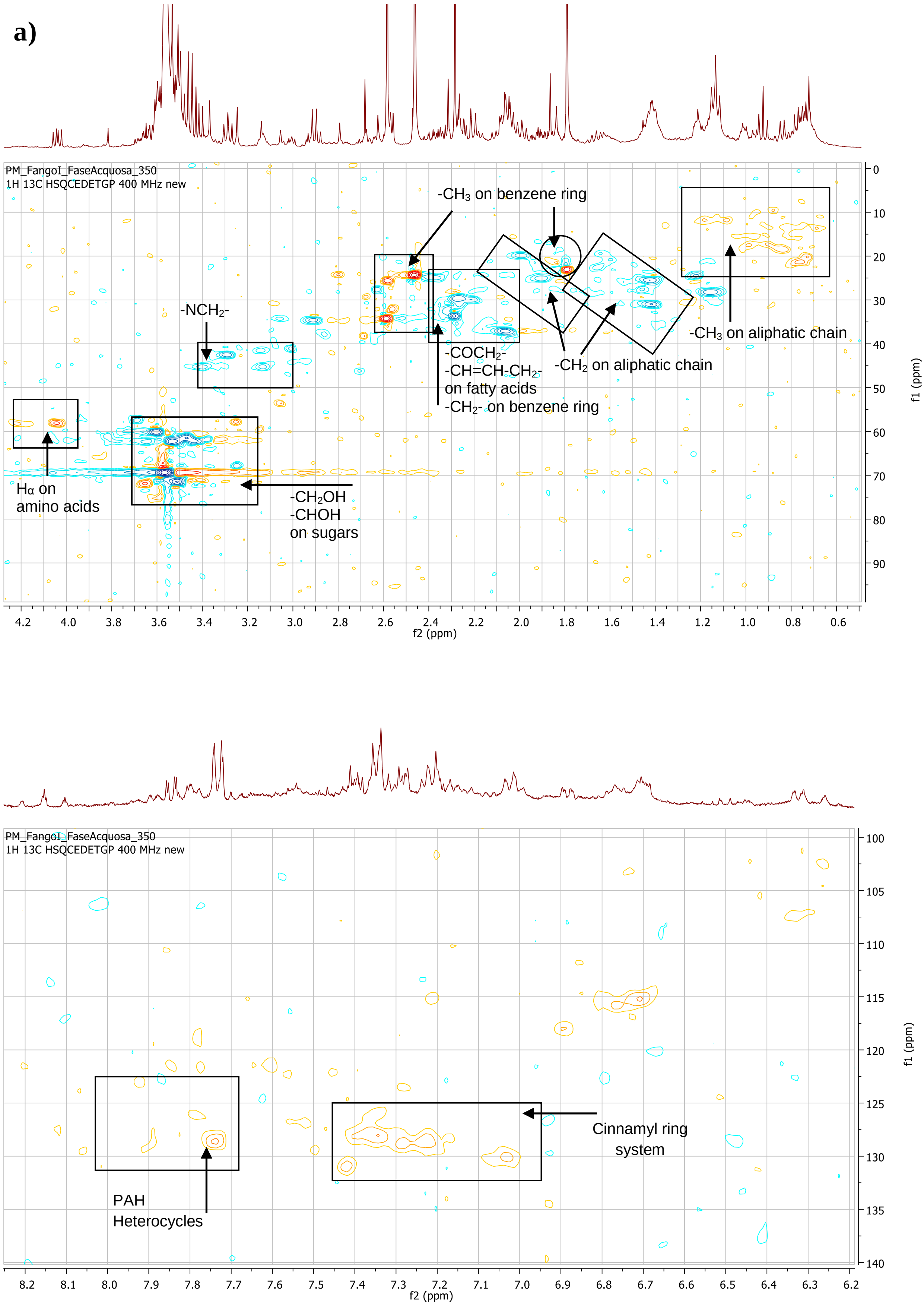
a)
PM_FangoI_FaseAcquosa_350
1H 13C HSQCEDETGTP 400 MHz new
-CH$_3$ on benzene ring
-NCH$_2$-
-COCH$_2$-
-CH=CH-CH$_2$-
on fatty acids
-CH$_2$- on benzene ring
-CH$_2$ on aliphatic chain
-CH$_3$ on aliphatic chain
Hα on
amino acids
-CH$_2$OH
-CHOH
on sugars
4.2 4.0 3.8 3.6 3.4 3.2 3.0 2.8 2.6 2.4 2.2 2.0 1.8 1.6 1.4 1.2 1.0 0.8 0.6
f2 (ppm)
0 10 20 30 40 50 60 70 80 90
f1 (ppm)
PM_FangoI_FaseAcquosa_350
1H 13C HSQCEDETGTP 400 MHz new
PAH
Heterocycles
Cinnamyl ring
system
8.2 8.1 8.0 7.9 7.8 7.7 7.6 7.5 7.4 7.3 7.2 7.1 7.0 6.9 6.8 6.7 6.6 6.5 6.4 6.3 6.2
f2 (ppm)
100 105 110 115 120 125 130 135 140
f1 (ppm)

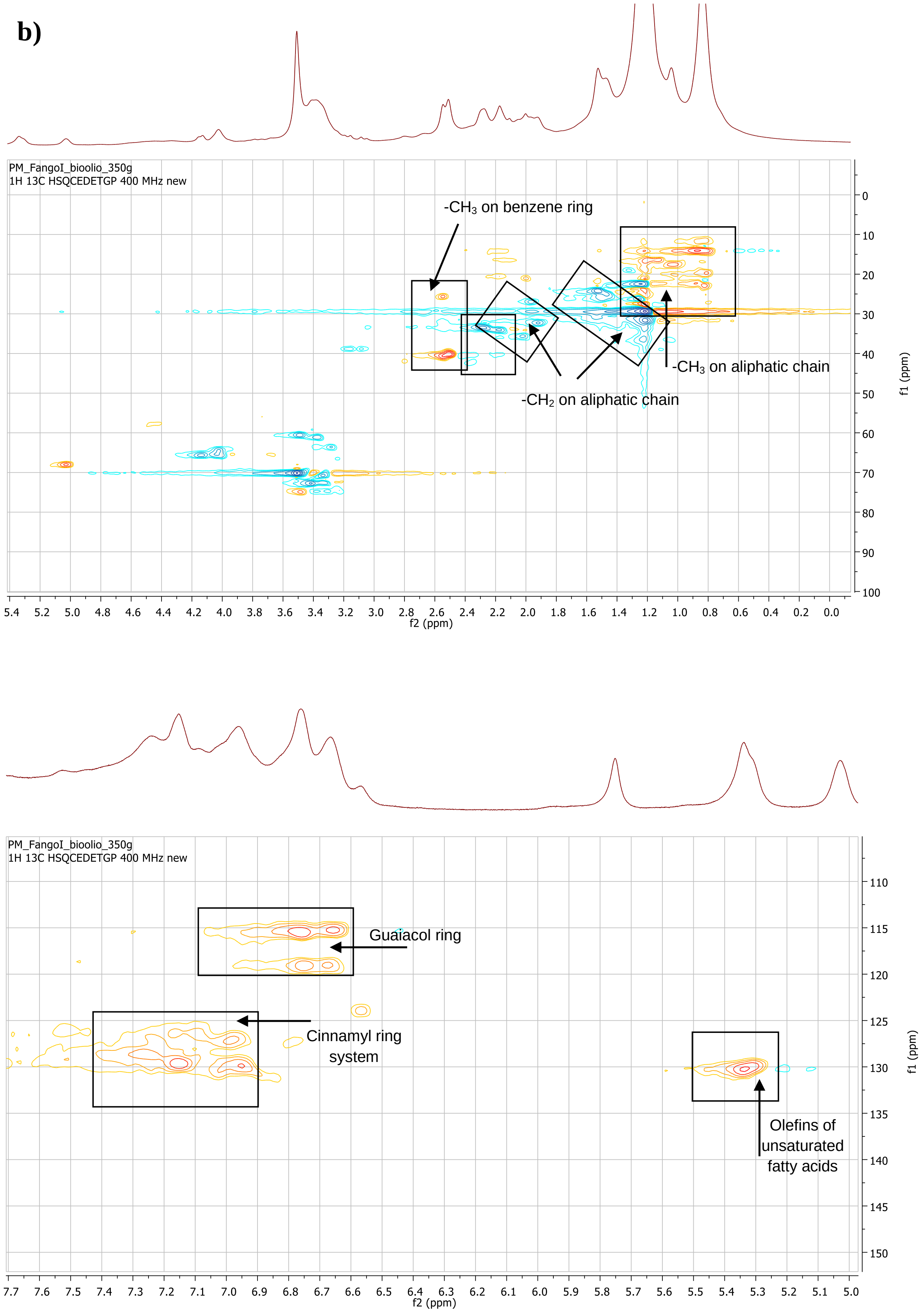

Figure 5.15 – ^{1}H, ^{13}C-HSQC spectra for biocrude obtained for cases: a) MS-C-Cen-350-10, b) TS-C-Cen-350-10.

Similar considerations can be made for the aqueous phase (Figure 5.16):

1. ^{1}H-NMR spectra of MS-C-Cen-300-30 and MS-C-Cen-350-10 samples are very similar (Figure 5.16a and 5.16b).
2. ^{1}H-NMR spectra of TS-C-Cen-300-30 and TS-C-Cen-350-10 samples are very similar (Figure 5.16c and 5.16d).
3. The ratio of signal integration in the region of aromatic protons (I_{sp^2}) to signals in the region of aliphatic protons (I_{sp3}) shows that, in both TS and MS case, there is a higher content of aromatic compounds (fraction derived from polyphenols) than aliphatic compounds:

$$\frac{I_{sp^2}}{I_{sp^3}} = 0.049 \qquad \text{for MS} \tag{5.5}$$

$$\frac{I_{sp^2}}{I_{sp^3}} = 0.080 \qquad \text{for TS} \tag{5.6}$$

4. The ratio between the integration of signals in the proton region of alcohol groups (-CH_2OH/-CHOH) ($I_{sp^3}OH$) and signals in the region of aliphatic protons ($I_{sp^3}Al$) shows that there is a slightly higher alcohol content in these groups:

$$\frac{I_{sp^2}OH}{I_{sp^3}Al} = 0.021 \qquad \text{for MS} \tag{5.7}$$

$$\frac{I_{sp^2}OH}{I_{sp^3}Al} = 0.041 \qquad \text{for TS} \tag{5.8}$$

5. The ^{1}H, ^{1}H-COSY analysis (spectrum not shown) revealed that some of the signals related to protons of -CH_2OH/-CHOH groups can be attributed to units of sugars.
6. The ^{1}H-NMR spectra of the MS and TS aqueous samples show the presence of signals between 7.5 and 9 ppm due to the protons of polycyclic aromatic hydrocarbons (PAHs), as confirmed by the ^{1}H, ^{13}C-HSQC spectra (7.7/127 ppm and 7.85/133 ppm). These signals are more intense in TS than in MS case (Figure 5.17).
7. The ^{1}H, ^{13}C-HSQC spectra show that, in the region of aromatic protons, it is possible to attribute the signals to derivatives of guaiacol (6.7/115 ppm) and derivatives of cinnamic acid or cinnamyl alcohol (6.9–7.4/130 ppm and 7.4/126 ppm). There are no significant differences between the spectral profiles for MS and TS cases.
8. The presence of 3.9/54 ppm signals in the ^{1}H, ^{13}C-HSQC spectrum for -OCH_3 groups confirms that some of these phenolic/catecholic derivatives are methoxylated.

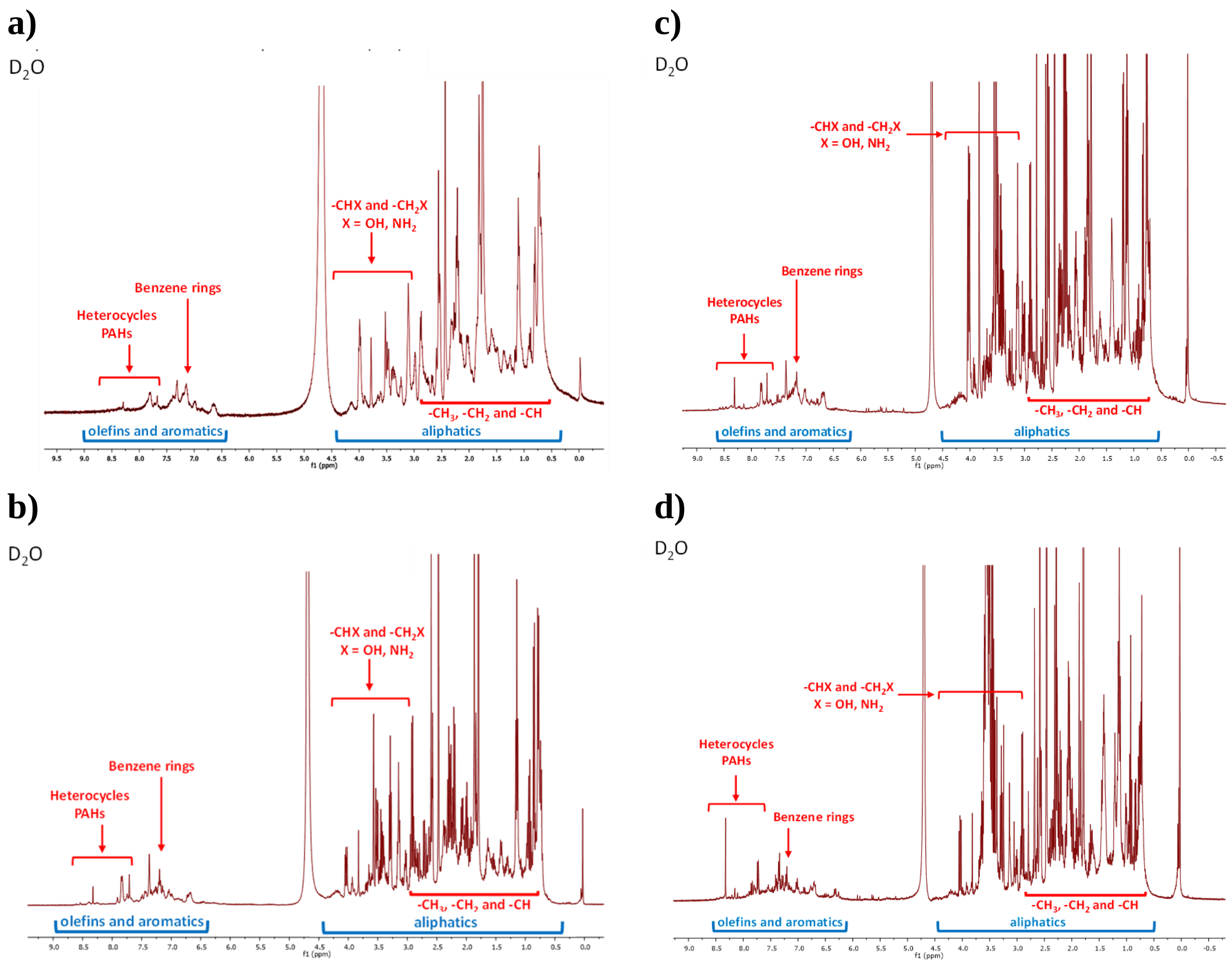

Figure 5.16 – ^{1}H-NMR spectra of aqueous phase obtained for cases: a) MS-C-Cen-300-30, b) MS-C-Cen-350-10, c) TS-C-Cen-300-30, d) TS-C-Cen-350-10.

a)

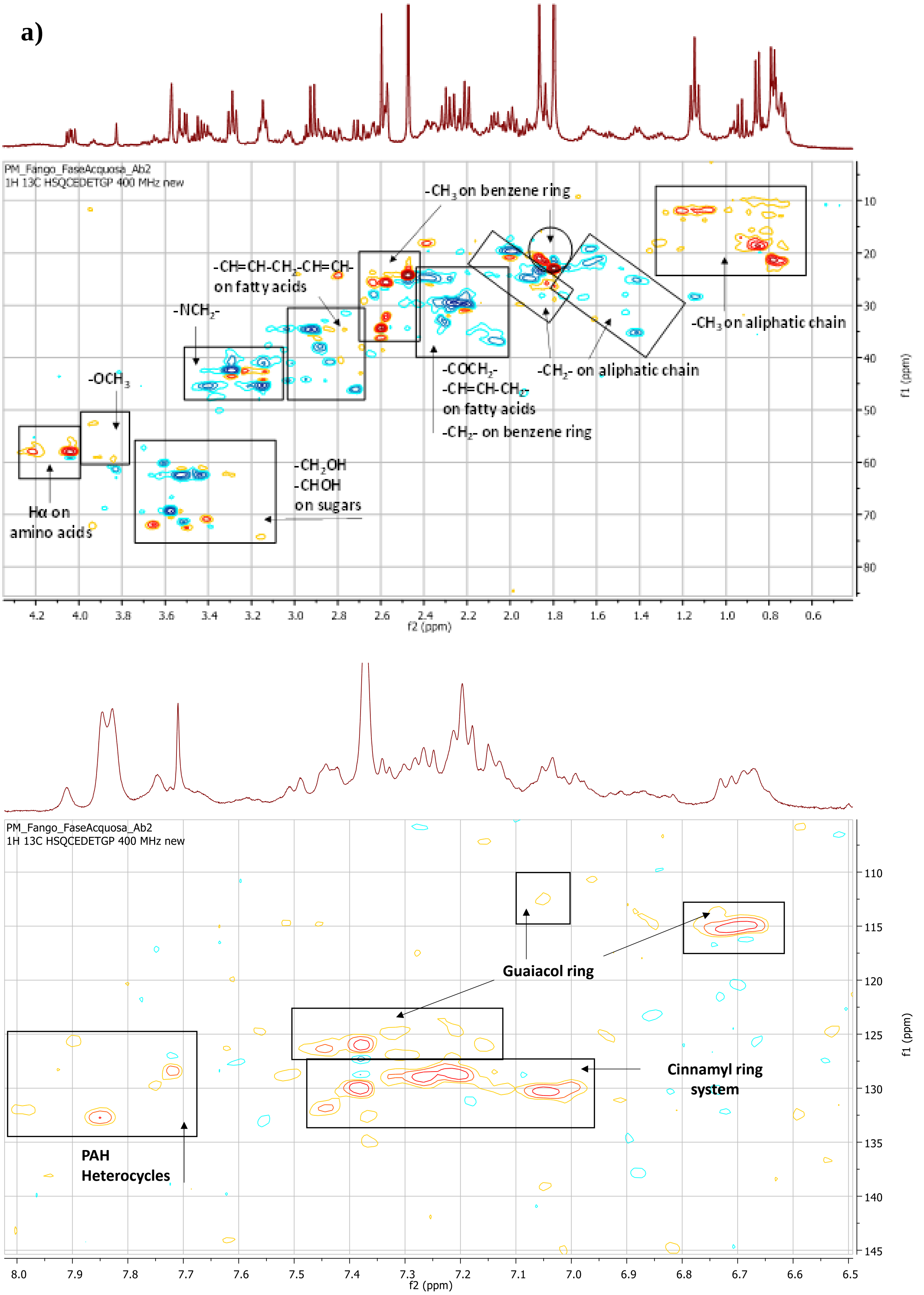
PM_Fango_FaseAcquosa_Ab2
1H 13C HSQCEDETGP 400 MHz new
-CH$_3$ on benzene ring
-CH=CH-CH$_2$-CH=CH-
on fatty acids
-NCH$_2$-
-OCH$_3$
-CH$_3$ on aliphatic chain
-COCH$_2$-
-CH=CH-CH$_2$-
on fatty acids
-CH$_2$- on benzene ring
-CH$_2$- on aliphatic chain
-CH$_2$OH
-CHOH
on sugars
Hα on
amino acids
10
20
30
40
50
60
70
80
f1 (ppm)
4.2
4.0
3.8
3.6
3.4
3.2
3.0
2.8
2.6
2.4
2.2
2.0
1.8
1.6
1.4
1.2
1.0
0.8
0.6
f2 (ppm)
PM_Fango_FaseAcquosa_Ab2
1H 13C HSQCEDETGP 400 MHz new
Guaiacol ring
Cinnamyl ring
system
PAH
Heterocycles
110
115
120
125
130
135
140
145
f1 (ppm)
8.0
7.9
7.8
7.7
7.6
7.5
7.4
7.3
7.2
7.1
7.0
6.9
6.8
6.7
6.6
6.5
f2 (ppm)

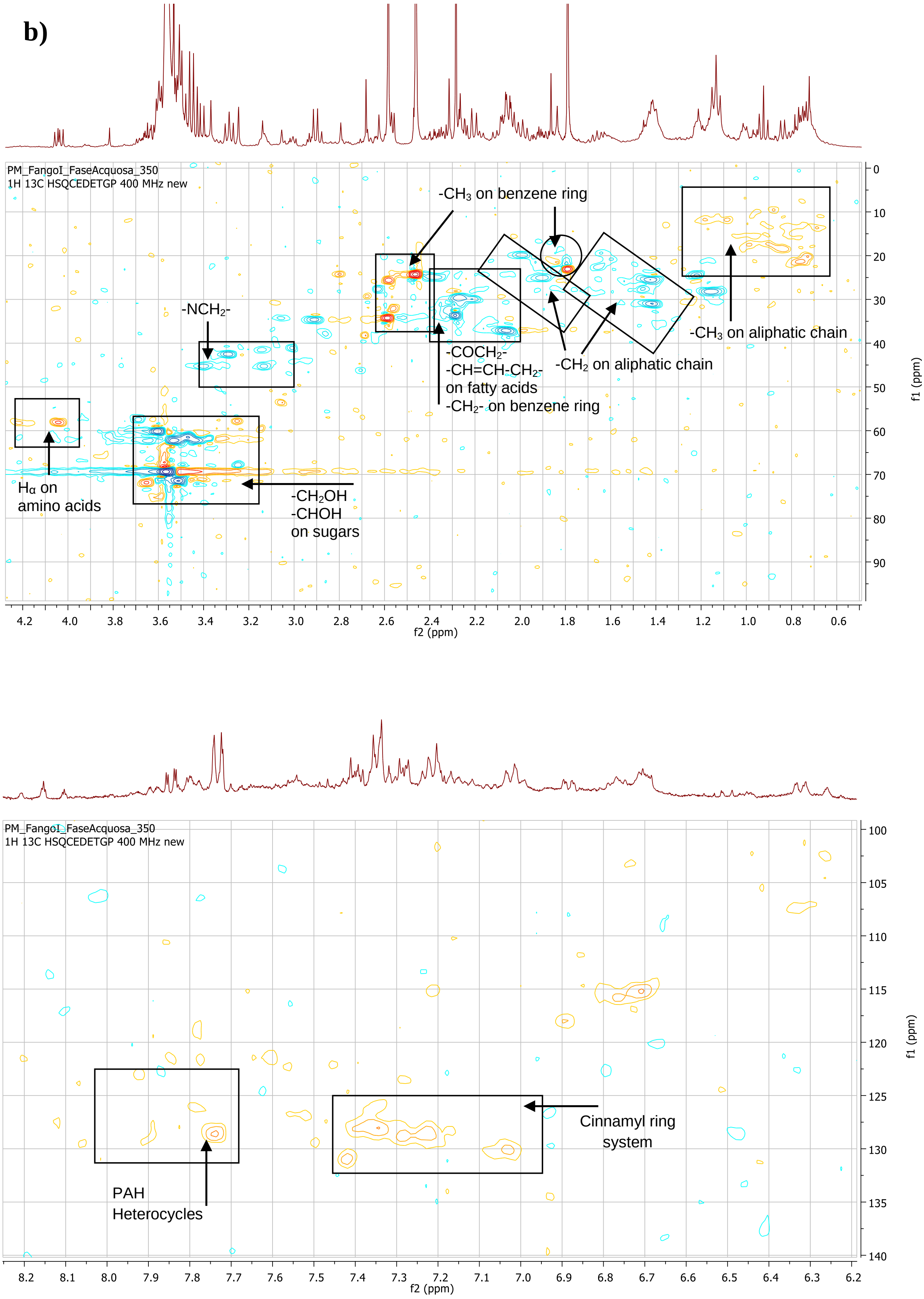

Figure 5.17 – ^{1}H,^{13}C-HSQC spectra for aqueous phase obtained for cases: a) MS-C-Cen-350-10, b) TS-C-Cen-350-10.

To support the subdivision of the results obtained from the ^{1}H-NMR spectroscopy, the main compounds identified by the LC-MS analysis, for the bio-oil and aqueous phase obtained from MS, are reported in Table 5.11.

Table 5.11 – LC−MS results on the characterization of biocrude and aqueous phase compounds attained during HTL test of municipal sludge.

#	**Time (min)**	**Compound**	**$[M+H]^+$ (*m/z*)**	**Sample**
1	3.5	*p*-aminophenol	110	Aqueous phase
2	7.1	Hydroxy-methyl-furfural	143	Aqueous phase/biocrude
3	7.2	Dimethyl indole	146	Aqueous phase
4	7.5	Methyl indole	132	Aqueous phase/biocrude
5	7.7	Quinoline	130	Aqueous phase/biocrude
6	8	Gallic acid	171	Aqueous phase
7	12	*p*-coumaric acid	165	Aqueous phase/biocrude
8	18.5	Sinapil alcohol	211	Aqueous phase/biocrude
9	19	Coniferilic alcohol	181	Aqueous phase/biocrude
10	20	*p*-cumaryl alcohol	151	Aqueous phase/biocrude
11	30.5	*p*-nitrocatechol	156	Aqueous phase/biocrude
12	31	2-phenylpyridine	156	Aqueous phase/biocrude
13	43.4	Phenanthrene	179	Aqueous phase/biocrude
14	47	Methyl palmitate	271	Biocrude
15	50.7	Pyrene	203	Aqueous phase/biocrude
16	52.2	Dibenzo-anthracene	279	Aqueous phase/biocrude
17	55	Tribenzo-coronene	425	Biocrude
18	56.5	Methyl stearate	313	Biocrude
19	57.5	Methyl oleate	297	Biocrude

Chapter 6 – Comparison of gasification and hydrothermal liquefaction processes

In this PhD project, with a view to a circular economy, the energetic valorisation of sludges from civil and industrial sources through the processes of gasification and hydrothermal liquefaction was evaluated. These processes do not solely produce useful energy from biomass directly, but they also convert biomass into more convenient, easily transportable and more energy-dense forms of energy carrier (syngas if we refer to gasification, and bio-oil when HTL is adopted). However, the choice of one technology over another is strongly influenced by parameters such as, biomass feedstock type, physicochemical properties, and the process operating conditions, target product and co-products distribution and quality. In this chapter, a preliminary comparison (also based on the obtained lab-scale results) between the two technologies will be reported, in particular when applied to sewage sludges under investigation.

Focusing on the initial biomass and the products of the two processes, the following considerations can be made:

- ***<u>Water content:</u>*** In water treatment plants, the purified water is separated out leaving the sewage sludge which resembles a slurry containing a significant content of water, that can be as high as 98%. Before using the sewage sludge for energy recovery by gasification, this moisture content has to be reduced to minimum levels using several available drying techniques. Much of this water can be removed via drainage, thickening, or mechanical dewatering, obtaining a dewatered sewage sludge that contains about 73–84% of moisture (Chan and Wang, 2016). The removal of the remaining moisture content can only be achieved through thermal drying, which can bring the moisture content down to about 6%. The need to dry the biomass before its use involves an energy expenditure that penalises the efficiency of the gasification process. On the contrary, in the process of hydrothermal liquefaction, biomass with a high moisture content such as sewage sludge is very suitable. In fact, water, being in sub-critical conditions, acts as a catalyst and a reaction medium, favouring the reactive network leading to the production of biocrude.

  To reduce the energy expenditure associated with the drying of biomass, necessary for the gasification process, a method investigated in the literature is represented by bio-drying, a new technology, which is based on a similar process as composting. The goal is different from the conventional composting process and does not aim towards a complete mineralization of the waste. In fact, the metabolic heat is used to remove water from the biomass waste at the lowest possible residence time and minimal biodegradation, hence preserving most of the gross calorific value of the biomass. During this process, the organic compounds are both substrate for microorganisms (which produce heat for drying) and the end product, thus offering a so-called "self-drying" mechanism. The end product contains a high energy value and can be used for thermal energy generation (Winkler et al., 2013).
- ***<u>Nitrogen and sulphur content:</u>*** In terms of elemental compositions, the investigated municipal sludge (MS) has a substantially higher N content (about 6 wt.%) with respect to the tannery sludge (TS). The

main sources of N-containing compounds in sewage sludge are protein and peptides. Instead, the S is higher in TS as a result of chromium sulphates present in the tanning process (about 4 wt.%). During thermochemical conversion by gasification, significant amount of sludge-bound nitrogen and sulphur are volatilised together with the volatiles emitted during pyrolysis. In a reducing environment, the presence of nitrogen compounds is likely to lead to the formation of products such as ammonia (NH_3); instead, when the S-compounds are considered, the possible formation of large amount of SO_2 shall be assessed. If the same sludge is subject to HTL, sulphur and nitrogen species can lead to the formation of organic S-compounds and N-compounds in the biocrude, which reduce its quality. During the gasification process carried out in this work, TS is subjected to reducing conditions, which do not favour the formation of SO_2 in the syngas; its values are not negligible (190 ppm) but they remain within the legal limits (part 1 of annex II to Directive 2015/2193 EU), making the gasification in fluidized bed a very promising technology for the energetic valorisation of this type of biomass. On contrary, the biocrude, target product of the HTL process, has a sulphur content of 4 wt.%; moreover, a large amount of N-compounds is found in the bio-oil, making it necessary a subsequent upgrade for the removal of these elements.

- ***<u>Metals content:</u>*** Both MS and TS also contain a high concentration of the following heavy metals: Fe, Ca, Cr, Si, Al, Na, Zn. Chemical speciation studies (Wang et al., 2005; Dąbrowska, 2014) indicate that heavy metals may exist in varying forms, for example, in organic/sulphide fraction, in hydrated iron and manganese oxide fraction or in exchangeable-carbonate fraction, depending on the kind of sludge, the properties of the metal and the technique employed in sewage sludges treatment. The potential emission of heavy metals from sewage sludge gasification has been described in a number of studies. Kistler et al. (1987) indicated that chromium and nickel were completely retained in char. The authors also reported that a substantial fraction of lead, and some of the zinc, were also mobilised in the gasifier, while barium was mobilised from only specific types of sludge. In addition, Elled et al. (2008) have observed that more reducing conditions promote the volatility of As, Cd, Pb, Sb, Se, Tl and Zn, while the volatility of Cu and Ni is reduced.

  In our studies, particular attention has been paid to the speciation of the Cr contained in TS. In both bottom and fly ash, obtained from the gasification process, the concentration of the more harmful Cr(VI) was, as expected, higher when a higher equivalence ratio (*AER*) value was adopted, but the gasifier operating conditions indeed guarantee that these values are 3−4 orders of magnitude lower than the concentration of total chromium, which remains in the preferred form of Cr(III) and tends to concentrate in elutriated fly rather than bottom ash. While the (although) limited oxygen presence in the gasifier was able to promote the chromium oxidation to Cr(VI), the degree of conversion in bottom ash was 0.069% (AER=0.15) and 0.12% (AER=0.24) only. The shorter mean residence time of fly ash in the gasifier has, in this respect, a positive consequence, i.e., chromium has less time to enter in contact with oxygen. As a matter of fact, the degree of chromium oxidation to Cr(VI) was 0.008% (AER=0.15) and 0.013% (AER=0.24). If we shift the attention to the hydrothermal liquefaction process, in this case not aiming at the complete oxidation of the organic component, it is possible to neglect the oxidation of Cr in its hexavalent form. In fact, downstream of the HTL process, chromium, which is mainly found in the solid residue and only in small traces in the biocrude, is present exclusively as trivalent chromium. In this case, not producing Cr(VI), the HTL process is the most convenient for biomass with high concentrations of this metal.

- ***Energy recovery:*** Both gasification and HTL processes result in an energy recovery that is in line with the data reported in the literature. In the case of gasification applied to TS, an energy recovery of 65% is obtained for AER=0.15 (on a dry and N_2-free basis); while a recovery of 44% is obtained by the liquefaction process carried out at 350 °C and 10 min for the same type of sludge.

  Despite the higher energy recovery achieved by the gasification process, it is necessary to underline that in this case it is necessary to consider the energy consumption necessary to dry the sludge and that the gas is diluted in nitrogen with a decrease in the calorific value of the gas obtained downstream of the process.
- ***Co-products generated by processes:*** Biomass gasification for power generation produces mainly flue gases and unwanted by-products such as ashes and tar (gasification bottleneck) which are often left unutilised, especially tar, despite its rich fuel and chemical potentials. During the gasification on TS, tar concentration values, when not lower (ENEA Report, 2015), are in line with values listed in literature for the gasification of coal, biomass, and sludges. In particular, tar species were mostly made up of polycyclic aromatic hydrocarbons (PAH), with number of C atoms variable between 5 and 16, and in some cases also in the presence of heteroatoms (N, S, and O). To reduce the tar formation, the addition of catalytic materials is reported in the literature. de Andrés et al. (2011) found that dolomite has the highest activity in tar elimination, followed by alumina and olivine. Meanwhile, Cao et al. (2014) indicated that lignite char-loaded nickel catalyst is quite active not only for tar reduction, but also for the elimination of NO_x precursors.

  A co-product that, instead, deserves particular attention in HTL is represented by the aqueous phase generated downstream of the process, that presents a particularly high total organic content (TOC), usually in the range of 10000–25000 (Watson et al., 2020, Matayeva and Biller, 2021). Therefore, it cannot be discharged into a water body without a proper purification treatment. In particular, after the HTL test performed on the sewage sludge, in the aqueous phase are present, at lower concentration due to their slight solubility in water, the same components found in the biocrude, while a suite of organic acids was also found. Because of the significant content of organic material into the aqueous by-product stream, recovery or reuse of this product is essential for economical processing by HTL. A possible reuse of the aqueous phase can be represented by its recycling in the HTL reactor to increase the yield of biocrude. Another option being developed is the use of catalytic hydrothermal gasification (Watson et al., 2020). By this process, the organic material in the aqueous by-product can be converted to methane (which can be easily separated from water) and carbon dioxide gas. Together with the aqueous phase, another co-product of the HTL process is represented by the solid residue where, as also observed by the results presented in this PhD thesis, all the metals present in the starting biomass are concentrated. In this case can be evaluated ways of reuse of this material as an adsorbent material, or as an additional cementitious material.

Chapter 7 – Final remarks and future developments

Aim of this PhD Thesis in Chemical Sciences (years 2019–2023) has been to investigate the energetic valorisation of a particular type of biomass, i.e., sludges from civil and industrial sources, for the reduction of the material destined to disposal, and for their reuse as energetic vector. In fact, the increasing levels of sewage sludge production demands research and development to introduce more commercially feasible options for limiting socio-economic and environmental problems associated with its current treatment. The properties of sewage sludge, however, are highly variable, because each sewage sludge has specific origin and unique production conditions. In particular, two types of sewage sludge were selected for these studies: i) a sludge from tannery industry, ii) a municipal sludge.

Among the thermochemical valorisation paths, the energy recovery of this waste has been first investigated through fluidised bed gasification, where the target product is syngas. In fact, there is a limited literature concerning the FB gasification of sludges, in particular when they come from specific industrial sources. Then, the innovative process known as hydrothermal liquefaction, where the target product is a bio-oil, has been applied to sludges. This process is advantageous in that it uses wet biomass which does not require drying, uses water which is a unique and environmentally friendly solvent. Both represent "StE" technologies ("sludge-to-energy").

The following main results have been obtained:

- Both processes result in a reduction of the material placed in landfill obtaining two energy carriers (syngas and biocrude). In the case of gasification as a by-product, bottom and fly ashes are obtained with a total yield of about $50\%_{wt}$, thus halving the starting mass. In the case of hydrothermal liquefaction, the best operating conditions experienced (350 °C–10 min) lead instead to a reduction of the solid residue up to about 30% compared to the starting biomass. In the case of HTL, however, it should be noted that in addition to a solid residue as a co-product of the process, an aqueous phase with a particularly high organic content, is generated, resulting in its treatment before being released into a water body. For both solid residues obtained from a circular economy perspective, the alternative to landfilling can be their re-use as adsorbent materials.
- Gasification of the tannery sludge has made it possible to obtain, under the best adopted operating conditions (850 °C, AER=0.15) a syngas with 42% H_2 (dry and N_2-free basis) and a lower heating value of 12 MJ/kg, with a limited tar concentration and the production of bottom ash whose gasification degree was, for all practical purposes, complete. The Cr(VI) concentration in bottom and fly ashes was not higher than 10 mg/kg, while the Cr(total) concentration was 3−4 orders of magnitude greater, showing the right choice of operating conditions that did not promote the oxidation of Cr(III) to Cr(VI) at a relevant extent.
- The study of the HTL process in a purposely designed 500 mL batch reactor allowed to study the effect of the thermal transients, and the effect of separation method, that are little investigated in literature when reactor sizes are comparable to those used in this PhD project. Results show that the upgrades

to the heating system allowed to attain an average heating rate of about 8 °C/min, generally determining improved performances compared to configurations characterised by lower heating rates. Moreover, the centrifugation method was more effective with respect to the more common liquid-liquid extraction with dichloromethane, with a bio-crude recovery up to 5.2% greater. The analysis of the effect of time and temperature on products yield has showed that, at fixed time, a higher bio-crude yield was obtained at 350 °C with respect to 300 °C. At 10 min, an optimal value of both $Y_{bio\text{-}crude}$=43% and energy recovery of 59% was observed (HHV=30 MJ/kg) for the municipal sludge, while, for the tannery sludge, lower yields are obtained with a maximum of 29.5% (energy recovery of 44%). However, for both sludges, the yield values are in line with those reported in the literature, confirming that this biomass is very promising for energy purposes, transforming what represents a waste into a high added-value product. The bio-crude obtained has the chemical characteristics of a mixture rich in esters, O- and N-heterocycles, and aromatic compounds. Future upgrades treatment (e.g., catalytic hydrotreatment) will be required to improve the quality and properties of the obtained bio-crude, for its application in the transport sector.

The processes of gasification and hydrothermal liquefaction seem, therefore, to be viable for the conversion of civil and industrial sludge into biofuels with high added value. Future developments could be aimed at:

- an evaluation of the energetic yield of the gasification process, that, along with the investigation of possible recycle routes for gasification ash (f.i.: as an adsorbent material, or in the materials construction industry), will help to increase the circularity of the proposed process, with clear financial and environmental advantages accompanying the production of an energy vector from an industrial residue;
- investigating the possibility of chromium removal (in particular, in its trivalent state) from ashes and solid residues arising from both technologies, in order to recirculate the metal in the tanning process. Contextually, possible options could include leaching with acid solutions or extraction with solvents, followed by chemical precipitation for selective recovery of Cr in the form of basic chromium sulfate, a valuable product for the tanning process. Moreover, Cr present in the solid residue could represent a substitute for the chromite ore, which is a raw material essential to produce ferro-chromium, the substrate for the manufacture of stainless steel;
- evaluating, in the HTL process, possible synergistic/antagonist effects by varying the composition of the biological components in the starting biomass, for example through the mixing of the sewage sludges investigated in this PhD project;
- studying possible techniques for removing metals from the starting sludge before carrying out the HTL process, in order to "quantify" the contribution due to the catalytic effect of ash in bio-oil yield;
- verifying the effect of hydrogen donors on the yield/quality of the biocrude obtained from HTL.

References published by the PhD Student

a. Di Lauro F., Balsamo M., Solimene R., Montagnaro F., Salatino P., *Hydrothermal liquefaction for the production of energetic vectors from residual materials: Literature analysis and characterisation of a tannery sludge*, Proceedings of the 8th International Symposium on Energy from Biomass and Waste, "Venice 2020", virtual Conference, 2020, Venezia (Italy).

b. Di Lauro F., Balsamo M., Solimene R., Migliaccio R., Caracciolo D., Salatino P., Montagnaro F., *Outline of a process for the hydrothermal liquefaction of a tannery sludge for biofuel production*, Proceedings of the 10th European Combustion Meeting 330, 2021, Naples, Italy.

c. Di Lauro F., Tregambi C., Montagnaro F., Salatino P., Chirone R., Solimene R., *Improving the performance of calcium looping for solar thermochemical energy storage and* CO_2 *capture*, Fuel 298, 2021, 120791.

d. Di Lauro F., Migliaccio R., Ruoppolo G., Balsamo M., Montagnaro F., Imperiale E., Caracciolo D., Urciuolo M., *Tannery sludge gasification in a fluidized bed for its energetic valorization*, Industrial & Engineering Chemistry Research 61, 2022, 16972–16979.

e. Tregambi C., Di Lauro F., Montagnaro F., Salatino P., Solimene R., *110th anniversary: Calcium looping with concentrated solar power for carbon capture and thermochemical energy storage*, Industrial & Engineering Chemistry Research 58, 2019, 21262–21272.

f. Montagnaro F., Di Lauro F., Balsamo M., Caracciolo D., *Hydrothermal liquefaction as an emerging route to produce bio-liquids for energetic application starting from tannery sludge – Role of operating parameters*, Italian Leather Research Magazine XCVII (2), 2021, 37–40.

References

1. Amutio M., Lopez G., Aguado R., Bilbao J., Olazar M., *Biomass oxidative fash pyrolysis: autothermal operation, yields and product properties*, Energy Fuels 26, 2012, 1353–1362.
2. Abou Elmagd A.M., Mahmoud M.S., *Tannery wastewater treatment using activated sludge process system (Lab Scale Modeling)*, International Journal of Engineering and Technical Research (IJETR) 2, 2014, 21–28.
3. Acharya B., Dutta A., Basu P., *An investigation into steam gasification of biomass for hydrogen enriched gas production in presence of CaO*, International Journal of Hydrogen Energy 35, 2010, 1582–1589.
4. Achinas S., Euverink G.J.W., *Theoretical analysis of biogas potential prediction from agricultural waste*, Resource-Efficient Technologies 2, 2016, 143–147.
5. Akhtar J., Amin N.A.S., *A review on process conditions for optimum bio-oil yield in hydrothermal liquefaction of biomass*, Renewable and Sustainable Energy Reviews 15, 2011, 1615–1624.
6. Albalasmeh A.A., Berhe A.A., Ghezzehei T.A., *A new method for rapid determination of carbohydrate and total carbon concentrations using UV spectrophotometry*, Carbohydrate Polymers 97, 2013, 253–261.
7. Alves C.R., Keglevich de Buzin P.J.W., Heck N.C., Schneider I.A.H., *Utilization of ashes obtained from leather shaving incineration as a source of chromium for the production of HC-FeCr alloy*, Minerals Engineering 29, 2012, 124−126.
8. Alvarez-Murillo A., Sabio E., Ledesma B., Román S., González-García C.M., *Generation of biofuel from hydrothermal carbonization of cellulose. Kinetics modelling*, Energy 94, 2016, 600–608.
9. Anastasakis K., Biller P., Madsen R.B., Glasius M., Johannsen I., *Continuous hydrothermal liquefaction of biomass in a novel pilot plant with heat recovery and hydraulic oscillation*, Energies 11, 2018, 2695.
10. Antal Jr M.J., Mok W.S.L., Richards G.N., *Mechanism of formation of 5- (hydroxymethyl)-2-furaldehyde from d-fructose and sucrose*, Carbohydrate Research 199, 1990, 91–109.
11. Appels L., Baeyens J., Degrève J., Dewil R., *Principles and potential of the anaerobic digestion of waste-activated sludge*, Progress in Energy and Combustion Science 34, 2008, 755–781.
12. Archer D.G., Wang P., *The dielectric constant of water and Debye-Hückel limiting law slopes*, Journal of Physical and Chemical Reference Data 19, 1990, 371.
13. Babu B.V., *Biomass pyrolysis: a state-of-the-art review*, Biofuels Bioproducts & Biorefining 2, 2008, 393–414.
14. Badrolnizam R.S., Elham O.S.J., Hadzifah S.N., Husain M.H.N., Hidayu A.R., Mohammad N.F., Mohamad Daud A.R., *Sewage sludge conversion via hydrothermal liquefaction (HTL) – A preliminary study*, Journal of Physics: Conference Series 1349, 2019, 012108.
15. Balsamo M., Montagnaro F., Anthony E.J., *Socio-economic parameters affect CO_2 emissions and energy consumption – An analysis over the United Nations Countries*, Current Opinion in Green and Sustainable Chemistry 40, 2023, 100740.

16. Barampouti E.M., Mai S., Malamis D., Moustakas K., Loizidou M., *Liquid biofuels from the organic fraction of municipal solid waste: A review*, Renewable and Sustainable Energy Reviews 110, 2019, 298–314.
17. Basar I.A., Liu H., Carrere H., Trably E., Eskicioglu C., *A review on key design and operational parameters to optimize and develop hydrothermal liquefaction of biomass for biorefinery applications*, Green Chemistry 23, 2021, 1404–1446.
18. Basu P., *Biomass Gasification and Pyrolysis*, Elsevier, Oxford, 2010.
19. Behrendt F., Neubauer Y., Oevermann M., Wilmes B., Zobel N., *direct liquefaction of biomass*, Chemical Engineering & Technology 31, 2008, 667–677.
20. Ben H., Ragauskas A.J., *Heteronuclear Single-Quantum Correlation–Nuclear Magnetic Resonance (HSQC-NMR) Fingerprint Analysis of Pyrolysis Oils*, Energy Fuels 25, 2011, 5791–5801.
21. Bhattacharya D., Medlin L., *Algal phylogeny and the origin of land plants*, Plant Physiology 116, 1998, 9–15.
22. Bhuiyan M.A., Zhang Q., Khare V., Mikhaylov A., Pinter G., Huang X., *Renewable energy consumption and economic growth nexus — A systematic literature review*, Frontiers in Environmental Science 10, 2022, 878394.
23. Biller P., Ross A.B., *Potential yields and properties of oil from the hydrothermal liquefaction of microalgae with different biochemical content*, Bioresource Technology 102, 2011, 215–225.
24. Biller P., Ross A.B., *Hydrothermal processing of algal biomass for the production of biofuels and chemicals*, Biofuels 3, 2012, 603–623.
25. Biller P., Sharma B.K., Kunwar B., Ross A.B., *Hydroprocessing of bio-crude from continuous hydrothermal liquefaction of microalgae*, Fuel 159, 2015, 197–205.
26. Biller P., Ross A.B., *Production of biofuels via hydrothermal conversion*, in Handbook of Biofuels Production: Processes and Technologies: Second Edition, 2016.
27. Biller P., Madsen R.B., Klemmer M., Becker J., Iversen B.B., Glasius M., *Effect of hydrothermal liquefaction aqueous phase recycling on bio-crude yields and composition*, Bioresource Technologies 220, 2016, 190–199.
28. Bligh E.G., Dyer W.J., *A rapid method of total lipid extraction and purification*, Canadian Journal of Biochemistry and Physiology 37, 1959, 911–917.
29. Bora A.P., Gupta D.P., Durbha S.K., *Sewage sludge to bio-fuel: a review on the sustainable approach of transforming sewage waste to alternative fuel*, Fuel 259, 2020, 116262.
30. Brand S., Hardi F., Kim J., Suh D.J., *Effect of heating rate on biomass liquefaction: Differences between subcritical water and supercritical ethanol*, Energy 68, 2014, 420–427.
31. Bridgwater A.V., *Renewable fuels and chemicals by thermal processing of biomass*, Chemical Engineering Journal 91, 2003, 87–102.

32. Budhathoki R., *Three zone modeling of downdraft biomass gasification: Equilibrium and finite kinetic approach*, Master's thesis, Master's Degree Program in Renewable Energy Department of Chemistry, University of Jyväskylä, March 11, 2013.
33. Carraturo F., Del Giudice C., Morelli M., Cerullo V., Libralato G., Galdiero E., Guida M., *Persistence of SARS-CoV-2 in the environment and COVID-19 transmission risk from environmental matrices and surfaces*, Environmental Pollution 265, 2020, 115010.
34. Castello D., Pedersen T.H., Rosendahl L.A., *Continuous hydrothermal liquefaction of biomass: A critical review*, Energies 11, 2018, 3156.
35. Castello D., Haider M.S., Rosendahl L.A., *Catalytic upgrading of hydrothermal liquefaction biocrudes: Different challenges for different feedstocks*, Renewable Energy 141, 2019, 42.
36. Chan Y.H., Yusup S., Quitain A.T., Uemura Y., Sasaki M., *Bio-oil production from oil palm biomass via subcritical and supercritical hydrothermal liquefaction*, The Journal of Supercritical Fluids 95, 2014, 407–412.
37. Chan W.P., Wang J.-Y., *Comprehensive characterisation of sewage sludge for thermochemical conversion 1 processes – Based on Singapore survey*, Waste Management 54, 2016, 131–142.
38. Chisti Y., *Biodiesel from microalgae*, Biotechnology Advances 25, 2007, 294–306.
39. Chumpoo J., Prasassarakich P., *Bio-oil from hydro-liquefaction of bagasse in supercritical ethanol*, Energy & Fuels 24, 2010, 2071–2077.
40. Cieślik B.M., Namieśnik J., Konieczka P., *Review of sewage sludge management: standards, regulations and analytical methods*, Journal of Cleaner Production 90, 2015, 1–15.
41. Coll R., Salvadó J., Farriol X., Montané D., *Steam reforming model compounds of biomass gasification tars: conversion at different operating conditions and tendency towards coke formation*, Fuel Processing Technology 74, 2001, 19–31.
42. Czernik S., Bridgewater A.V., *Overview of applications of biomass fast pyrolysis oil*, Energy & Fuels 18, 2004, 590–598.
43. de Caprariis B., Scarsella M., Bavasso I., Bracciale M., Tai L., De Filippis P., *Effect of Ni, Zn and Fe on hydrothermal liquefaction of cellulose: Impact on bio-crude yield and composition*, Journal of Analytical and Applied Pyrolysis 157, 2021, 105225.
44. de Lasa H., Salaices E., Mazumder J., Lucky R., *Catalytic steam gasification of biomass: Catalysts, thermodynamics and kinetics*, Chemical Reviews 111, 2011, 5404–5433.
45. Del Grosso M., Sridharan B., Tsekos C., Klein S., de Jong W., *A modelling based study on the integration of 10 MWth indirect torrefied biomass gasification, methanol and power production*, Biomass and Bioenergy 136, 2020, 105529.
46. Delgado J., Aznar M.P., Corella J., *Biomass gasification with steam in fluidized bed: Effectiveness of CaO, MgO, and CaO−MgO for hot raw gas cleaning*, Industrial & Engineering Chemistry Research 36, 1997, 1535–1543.
47. Demirbas A., *Competitive liquid biofuels from biomass*, Applied Energy 88, 2011, 17–28.

48. Devi L., Ptasinski K.J., Janssen F.J.J.G., *A review of the primary measures for tar elimination in biomass gasification processes*, Biomass and Bioenergy 24, 2003, 125–140.
49. Di Carlo A., Savuto E., Foscolo P.U., Papa A.A., Tacconi A., Del Zotto L., Aydin B., Bocci E., *Preliminary results of biomass gasification obtained at pilot scale with an innovative 100 kwth dual bubbling fluidized bed gasifier,* Energies 15, 2022, 4369.
50. Dong H., Jiang X., Lv G., Chi Y., Yan J., *Co-combustion of tannery sludge in a commercial circulating fluidized bed boiler,* Waste Management 46, 2015, 227–233.
51. Eurostat, https://ec.europa.eu/eurostat/statistics-explained/index.php?title=File:Sewage_sludge_disposal_from_urban_wastewater_treatment,_by_type_of_treatment,_2015_(%25_of_total_mass)_V2.png&oldid=349285#filelinks (accessed December 12, 2022).
52. Elliott D.C., Biller P., Ross A.B., Schmidt A.J., Jones S.B., *Hydrothermal liquefaction of biomass: Developments from batch to continuous process*, Bioresource Technology 178, 2015, 147–156.
53. Fan Y., Hornung U., Dahmen N., *Hydrothermal liquefaction of sewage sludge for biofuel application: A review on fundamentals, current challenges and strategies*, Biomass and Bioenergy 165, 2022, 106570.
54. Farid M.M., Jeong H.J., Hwang J., *Kinetic study on coal–biomass mixed char co-gasification with* H_2O *in the presence of* H_2, Fuel 162, 2015, 234–238.
55. Fernando S., Adhikari S., Chandrapal C., Murali N., *Biorefineries: current status, challenges, and future direction*, Energy & Fuels 20, 2006, 1727–1737.
56. Faeth J.L., Valdez P.J., Savage P.E., *Fast hydrothermal liquefaction of nannochloropsis sp. to produce biocrude*, Energy and Fuels 27, 2013, 1391– 1398.
57. Forster-Carneiro T., Berni M.D., Dorileo I.L., Rostagno M.A., *Biorefinery study of availability of agriculture residues and wastes for integrated biorefineries in Brazil*, Resources, Conservation and Recycling 77, 2013, 78–88.
58. Frank E.D., Elgowainy A., Han J., Wang Z., *Life cycle comparison of hydrothermal liquefaction and lipid extraction pathways to renewable diesel from algae*, Mitigation and Adaptation Strategies for Global Change 18, 2013, 137–158.
59. Gao N., Li A., Quan C., *A novel reforming method for hydrogen production from biomass steam gasification*, Bioresource Technology 100, 2009, 4271–4277.
60. Gao Y., Wang X.H., Yang H.P., Chen H.P., *Characterization of products from hydrothermal treatments of cellulose*, Energy 42, 2012, 457–465.
61. Ghodke P.K., Sharma A.K., Pandey J.K., Chen W.H., Patel A., Ashokkumar V., *Pyrolysis of sewage sludge for sustainable biofuels and value-added biochar production*, Journal of Environmental Management 298, 2021, 113450.
62. Gollakota A.R.K., Kishore N., Gu S., *A review on hydrothermal liquefaction of biomass*, Renewable and Sustainable Energy Reviews 81, 2018, 1378–1392.
63. Goldman J.C., *Outdoor algal mass cultures – I applications*, Water Research 13, 1979, 1–19.

64. Grgur B.N., *Corrosion of the stainless steel 316Ti in 10% hydrochloric and sulfuric acid*, Zaštita materijala 61, 2020, 339–345.
65. Guo Y., Yeh T., Song W., Xu D., Wang S., *A review of bio-oil production from hydrothermal liquefaction of algae*, Renewable and Sustainable Energy Reviews 48, 2015, 776–790.
66. Halim R., Danquah M.K., *Bioprocess development for chlorophyll extraction from microalgae,* Lee, J. (eds) Advanced Biofuels and Bioproducts. Springer, New York, NY, 2013, 4614–3348.
67. Hammerschmidt A., Boukis N., Hauer E., Galla U., Dinjus E., Hitzmann B., Larsen T., Nygaard S.D., *Catalytic conversion of waste biomass by hydrothermal treatment*, Fuel 90, 2011, 555–562.
68. Hanping C., Bin L., Haiping Y., Guolai Y., Shihong Z., *Experimental investigation of biomass gasification in a fluidized bed reactor*, Energy & Fuels 22, 2008, 3493–3498.
69. Haro P., Trippe F., Stahl R., Henrich E., *Bio-syngas to gasoline and olefins via DME – A comprehensive techno-economic assessment*, Applied Energy 108, 2013, 54–65.
70. Hartree E.F., *Determination of protein: A modification of the lowry method that gives a linear photometric response*, Analytical Biochemistry 48, 1972, 422–427.
71. He M., Hu Z., Xiao B., Li J., Guo X., Luo S., Yang F., Feng Y., Yang G., Liu S., *Hydrogen-rich gas from catalytic steam gasification of municipal solid waste (MSW): Influence of catalyst and temperature on yield and product composition,* International Journal of Hydrogen Energy 34, 2009, 195–203.
72. Heitz M., Brown A., Chornet E., *Solvent effects on liquefaction: Solubilization profiles of a Canadian prototype wood, Populus deltoides, in the presence of different solvents,* The Canadian Journal of Chemical Engineering 72, 1994, 1021–1027.
73. Hernández J.J., Aranda-Almansa G., Bula A., *Gasification of biomass wastes in an entrained flow gasifier: Effect of the particle size and the residence time*, Fuel Processing Technology 91, 2010 681–692.
74. Hietala D.C., Savage P.E., *A molecular, elemental, and multiphase kinetic model for the hydrothermal liquefaction of microalgae*, Chemical Engineering Journal 407, 2021, 127007.
75. Holliday R.L., King J.W., List G.R., *Hydrolysis of vegetable oils in sub- and supercritical water,* Industrial & Engineering Chemistry Research 36, 1997, 932–935.
76. Hongrapipat J., Saw W.L., Pang S., *Co-gasification of blended lignite and wood pellets in a dual fluidized bed steam gasifier: The influence of lignite to fuel ratio on* NH_3 *and* H_2S *concentrations in the producer gas,* Fuel 139, 2015, 494–501.
77. Hren M., Kosec T., Lindgren M., Huttunen-Saarivirta E., Legat A., *Sensor development for corrosion monitoring of stainless steels in* H_2SO_4 *solutions*, Sensors 21, 2021, 1449.
78. Huang H., Yuan X., Zhu H., Li H., Liu Y., Wang X., Zeng G., *Comparative studies of thermochemical liquefaction characteristics of microalgae, lignocellulosic biomass and sewage sludge*, Energy 56, 2013, 52–60.
79. Huang H., Yuan X., *Recent progress in the direct liquefaction of typical biomass,* Science 49, 2015, 59–80.

80. International Energy Agency, Key World Energy Statistics 2021, WorldEnergyBalancesHighlights2021.xlsx (live.com) (accessed December 12, 2022).
81. Jazrawi C., Biller P., Ross A.B., Montoya A., Maschmeyer T., Haynes B.S., *Pilot plant testing of continuous hydrothermal liquefaction of microalgae*, Algal Research 2, 2013, 268–277.
82. Jazrawi C., Biller P., He Y., Montoya A., Ross A.B., Maschmeyer T., Haynes B.S., *Two-stage hydrothermal liquefaction of a high-protein microalga*, Algal Research 8, 2015, 15–22.
83. Jena U., Vaidyanathan N., Chinnasamy S., Das K.C., *Evaluation of microalgae cultivation using recovered aqueous co-product from thermochemical liquefaction of algal biomass*, Bioresource Technology 102, 2011, 3380–3387.
84. Jiang X., Li C., Fei Z., Chi Y., Yan J., *Combustion characteristics of tannery sludge and volatilization of heavy metals in combustion*, Journal of Zhejiang University-Science A 11, 2010, 530–537.
85. Jo H., Prajitno H., Zeb H., Kim J., *Upgrading low-boiling-fraction fast pyrolysis bio-oil using supercritical alcohol: Understanding alcohol participation, chemical composition, and energy efficiency*, Energy Conversion and Management 148, 2017, 197–209.
86. Judex J.W., Gaiffi M., Burgbacher H.C., *Gasification of dried sewage sludge: status of the demonstration and the pilot plant*, Waste Management 32, 2012, 719–723.
87. Kamio E., Takahashi S., Noda H., Fukuhara C., Okamura T., *Effect of heating rate on liquefaction of cellulose by hot compressed water*, Chemical Engineering Journal 137, 2008, 328–338.
88. Kapusta K., *Effect of ultrasound pretreatment of municipal sewage sludge on characteristics of bio-oil from hydrothermal liquefaction process*, Waste Management 78, 2018, 183–190.
89. Katongtung T., Tippayawong N., *Machine learning prediction of biocrude yields and higher heating values from hydrothermal liquefaction of wet biomass and wastes*, Bioresource Technology 344, 2022, 126278.
90. Kavouras P., Pantazopoulou E., Varitis S., Vourlias G., Chrissafis K., Dimitrakopulos G.P., Mitrakas M., Zouboulis A.I., Karakostas T., Xenidis A., *Incineration of tannery sludge under oxic and anoxic conditions: Study of chromium speciation*, Journal of Hazardous Materials 283, 2015, 672−679.
91. Kivaisi A.K., Eliapenda S., *Conversion of some agro-industrial residues into volatile fatty acids and methane by rumen microorganisms*, Ed. Pergamon Press 3, 1992.
92. Klingler D., Berg J., Vogel H., *Hydrothermal reactions of alanine and glycine in sub and supercritical water*, The Journal of Supercritical Fluids 43, 2007, 112–119.
93. Klingler D., Vogel H., *Influence of process parameters on the hydrothermal decomposition and oxidation of glucose in sub- and supercritical water*, The Journal of Supercritical Fluids 55, 2010, 259–270.
94. Kokalj F., Arbiter B., Samec N., *Sewage sludge gasification as an alternative energy storage model*, Energy Conversion and Management 149, 2017, 738–747.
95. Kruse A., *Hydrothermal biomass gasification*, The Journal of Supercritical Fluids 47, 2009, 391–399.
96. Kruse A., Dahmen N., *Water – A magic solvent for biomass conversion*, The Journal of Supercritical Fluids 96, 2015, 36–45.

97. Kumar M., Oyedun A.O., Kumar A., *A review on the current status of various hydrothermal technologies on biomass feedstock*, Renewable and Sustainable Energy Reviews 81, 2018, 1742–1770.

98. Kumar R., *A review on the modelling of hydrothermal liquefaction of biomass and waste feedstocks*, Energy Nexus 5, 2022, 100042.

99. Lai F., Chang Y., Huang H., Wu G., Xiong J., Pan Z., Zhou C., *Liquefaction of sewage sludge in ethanol-water mixed solvents for bio-oil and biochar products* 148, Energy, 2018, 629–641.

100. Leng L., Li J., Yuan X., Li J., Han P., Hong Y., Wei F., Zhou W., *Beneficial synergistic effect on bio oil production from co-liquefaction of sewage sludge and lignocellulosic biomass*, Bioresource Technology 251, 2018, 49–56.

101. Li Q., Liu D., Song L., Hou X., Wu C., Yan Z., *Efficient hydro-liquefaction of woody biomass over ionic liquid nickel based catalyst*, Industrial Crops and Products 113, 2018, 157–166.

102. Li R., Ma Z., Yang T., Li B., Wei L., Sun Y., *Sub–supercritical liquefaction of municipal wet sewage sludge to produce bio-oil: Effect of different organic–water mixed solvents*, The Journal of Supercritical Fluids 138, 2018, 115–123.

103. Li J., Zhang W., Liu T., Yang L., Li H., Peng H., Jiang S., Wang X., Leng L., *Machine learning aided bio-oil production with high energy recovery and low nitrogen content from hydrothermal liquefaction of biomass with experiment verification*, Chemical Engineering Journal 425, 2021, 130649.

104. Limayem A., Ricke S.C., *Lignocellulosic biomass for bioethanol production: current perspectives, potential issues and future prospects*, Progress in Energy and Combustion Science 38, 2012, 449–467.

105. Liu Z., Zhang F.S., *Effects of various solvents on the liquefaction of biomass to produce fuels and chemical feedstocks*, Energy Conversion and Management 49, 2008, 3498–3504.

106. Lv P., Xiong Z., Chang J., Wu C., Chen Y., Zhu J., *An experimental study on biomass air-steam gasification in a fluidized bed*, Bioresource Technology 95, 2004, 95–101.

107. Lyu G., Wu S., Zhang H., *Estimation and comparison of bio-oil components from different pyrolysis conditions*, Frontiers in Energy Research 3, 2015, 28.

108. Mahishi M.R., Goswami D., *Thermodynamic optimization of biomass gasifier for hydrogen production*, International Journal of Hydrogen Energy 32, 2007, 3831–3840.

109. Malins K., Kampars V., Brinks J., Neibolte I., Murnieks R., Kampare R., *Bio-oil from thermo-chemical hydro-liquefaction of wet sewage sludge*, Bioresource Technology 187, 2015, 23–29.

110. Mao L., Gao B., Deng N., Liu L., Cui H., *Oxidation behaviour of Cr(III) during thermal treatment of chromium hydroxide in the presence of alkali and alkaline earth metal chlorides*, Chemosphere 145, 2016, 1–9.

111. Maschio G., Koufopanos C., Lucchesi A., *Pyrolysis, a promising route for biomass utilization*, Bioresource Technology 42, 1992, 219–231.

112. Matayeva A., Biller P., *Hydrothermal liquefaction aqueous phase treatment and hydrogen production using electro-oxidation*, Energy Conversion and Management 244, 2021, 114462.

113. McKendry P., *Energy production from biomass (part 2): conversion technologies*, Bioresource Technology 83, 2002, 47–54.

114. Migliaccio R., Brachi P., Montagnaro F., Papa S., Tavano A., Montesarchio P., Ruoppolo G., Urciuolo M., *Sewage sludge gasification in a fluidized bed: Experimental investigation and modelling*, Industrial & Engineering Chemistry Research 60, 2021, 5034−5047.

115. Mishra S., Mohanty K., *Co-HTL of domestic sewage sludge and wastewater treatment derived microalgal biomass – An integrated biorefinery approach for sustainable biocrude production*, Energy Conversion and Management 204, 2020, 112312.

116. Mishra S., Upadhyay R.K., *Review on biomass gasification: Gasifiers, gasifying mediums, and operational parameters*, Materials Science for Energy Technologies 4, 2021, 329–340.

117. Miyata Y., Sagata K., Hirose M., Yamazaki Y., Nishimura A., Okuda N., Arita Y., Hirano Y., Kita Y., *Fe-assisted hydrothermal liquefaction of lignocellulosic biomass for producing high-grade bio-oil*, ACS Sustainable Chemistry & Engineering 5, 2017, 3562−3569.

118. Mok W.S.L., Antal M.J., *Uncatalyzed solvolysis of whole biomass hemicellulose by hot compressed liquid water*, Industrial & Engineering Chemistry Research 31, 1992, 1157–1161.

119. Molino A., Iovane P., Donatelli A., Braccio G., Chianese S., Musmarra D., *Steam gasification of refuse-derived fuel in a rotary kiln pilot plant: Experimental tests*, Chemical Engineering Transactions 32, 2013, 337–342.

120. Molino A., Larocca V., Chianese S., Musmarra D., *Biofuels production by biomass gasification: A review*, Energies 11, 2018, 811.

121. Montagnaro F., Caracciolo D., *The potential role of tannery industry for a sustainable use of energy sources*, Italian Leather Research Magazine XCVIII (3), 2022, 36–41.

122. Montagnaro F., Zaccariello L., *Gasification of spruce wood chips in a 1.5 MW_{th} fluidised bed reactor*, Energies 15, 2022, 5883.

123. Monteiro R.D., van de Wetering J., Krawczyk B., Engelberg D.L., *Corrosion behaviour of type 316L stainless steel in hot caustic aqueous environments*, Metals and Materials International 26, 2020, 630–640.

124. Mujahid R., Riaz A., Insyani R., Kim J., *A centrifugation-first approach for recovering high-yield bio-oil with high calorific values in biomass liquefaction: A case study of sewage sludge*, Fuel 262, 2020, 116628.

125. Nagamori M., Funazukuri T., *Glucose production by hydrolysis of starch under hydrothermal conditions* 233, 2004, 229–233.

126. Nagappan S., Bhosale R.R, Nguyen D.D., Chi N.T.L, Ponnusamy V.K., Woong C.S., Kumar G., *Catalytic hydrothermal liquefaction of biomass into bio-oils and other value-added products – A review*, Fuel 285, 2021, 119053.

127. Nazari L., Sarathy S., Santoro D., Ho D., Ray M.B., Xu C.C., *3 - Recent advances in energy recovery from wastewater sludge*, Direct Thermochemical Liquefaction for Energy Applications 2018, 67–100.

128. NETL DOE, https://netl.doe.gov/research/coal/energy-systems/gasification/gasifipedia/syngas-composition (accessed January 7, 2023).

129. Nipattummakul N., Ahmed I.I., Kerdsuwan S., Gupta A.K., *Hydrogen and syngas production from sewage sludge via steam gasification*, International Journal of Hydrogen Energy 35, 2010, 11738–11745.

130. Nizamuddin S., Baloch H.A., Griffin G.J., Mubarak N.M., Bhutto A.W., Abro R., Mazari S.A, Ali B.S., *An overview of effect of process parameters on hydrothermal carbonization of biomass*, Renewable and Sustainable Energy Reviews 73, 2017, 1289–1299.

131. Nussbaumer T., *Combustion and co-combustion of biomass: Fundamentals, technologies, and primary measures for emission reduction*, Energy & Fuels 17, 2003, 1510–1521.

132. Okolie J.A., Rana R., Nanda S., Dalai A.K., Kozinskic J.A., *Supercritical water gasification of biomass: A state-of-the-art review of process parameters, reaction mechanisms and catalysis*, Sustainable Energy & Fuels 3, 2019, 578–598.

133. Oladejo J., Shi K., Luo X., Yang G., Wu T., *A review of sludge-to-energy recovery methods*, Energies 12, 2019, 60.

134. Ongen A., Ozcan H.K., Arayici S., *An evaluation of tannery industry wastewater treatment sludge gasification by artificial neural network modeling*, Journal of Hazardous Materials 263, 2013, 361−366.

135. Overend R.P., Chornet E., *Fractionation of lignocellulosics by steam-aqueous pretreatments*, Philosophical Transactions of the Royal Society of London. Series A, Mathematical and Physical Sciences 321, 1987, 523–536.

136. Pavlovič I., Knez Ž., Škerget M., *Hydrothermal reactions of agricultural and food processing wastes in sub- and supercritical water: A review of fundamentals, mechanisms, and state of research*, Journal of Agricultural and Food Chemistry 61, 2013, 8003–8025.

137. Parthasarathy P., Narayanan K.S., *Hydrogen production from steam gasification of biomass: Influence of process parameters on hydrogen yield – A review*, Renewable Energy 66, 2014, 570–579.

138. Peterson A.A., Vogel F., Lachance R.P., Fröling M., Antal Jr M.J., Tester J.W., *Thermochemical biofuel production in hydrothermal media: A review of sub-and supercritical water technologies*, Energy & Environmental Science 1, 2008, 32–65.

139. Phuphuakrat T., Nipattummakul N., Namioka T., Kerdsuwan S., Yoshikawa K., *Characterization of tar content in the syngas produced in a downdraft type fixed bed gasification system from dried sewage sludge*, Fuel 89, 2010, 2278−2284.

140. Pio D.T., Tarelho L.A.C., Pinto P.C.R., *Gasification-based biorefinery integration in the pulp and paper industry: A critical review*, Renewable and Sustainable Energy Reviews 133, 2020, 110210.

141. Prajitno H., Park J., Ryu C., Park H.Y., Lim H.S., Kim J., *Effects of solvent participation and controlled product separation on biomass liquefaction: A case study of sewage sludge*, Applied Energy 218, 2018, 402–416.

142. Prestigiacomo C., Costa P., Pinto F., Schiavo B., Siragusa A., Scialdone O., Galia A., *Sewage sludge as cheap alternative to microalgae as feedstock of catalytic hydrothermal liquefaction processes*, The Journal of Supercritical Fluids 143, 2019, 251–258.

143. Prestigiacomo C., Laudicina V.A., Siragusa A., Scialdone O., Galia A., *Hydrothermal liquefaction of waste biomass in stirred reactors: One step forward to the integral valorization of municipal sludge*, Energy 201, 2020, 117606.

144. Prestigiacomo C., Proietto F., Laudicina V.A., Siragusa A., Scialdone O., Galia A., *Catalytic hydrothermal liquefaction of municipal sludge assisted by formic acid for the production of next-generation fuels*, Energy 232, 2021, 121086.

145. Prestigiacomo C., Zimmermann J., Hornung U., Raffelt K., Dahmen N., Scialdone O., Galia A., *Effect of transition metals and homogeneous hydrogen producers in the hydrothermal liquefaction of sewage sludge*, Fuel Processing Technology 237, 2022, 107452.

146. Prestigiacomo C., Scialdone O., Galia A., *Hydrothermal liquefaction of wet biomass in batch reactors: critical assessment of the role of operating parameters as a function of the nature of the feedstock*, The Journal of Supercritical Fluids 189, 2022, 105689.

147. Promdej C., Matsumura Y., *Temperature effect on hydrothermal decomposition of glucose in sub- and supercritical water*, Industrial & Engineering Chemistry Research 50, 2011, 8492–8497.

148. Qian L., Wang S., Savage P.E., *Hydrothermal liquefaction of sewage sludge under isothermal and fast conditions*, Bioresource Technology 232, 2017, 27–34.

149. Qian L., Wang S., Savage P.E., *Fast and isothermal hydrothermal liquefaction of sludge at different severities: Reaction products, pathways, and kinetics*, Applied Energy 260, 2020, 114312.

150. Rambo M.K.D., Schmidt F.L., Ferreira M.M.C., *Analysis of the lignocellulosic components of biomass residues for biorefinery opportunities*, Talanta 144, 2015, 696–703.

151. Rapagnà S., Jand N., Kiennemann A., Foscolo P.U., *Steam-gasification of biomass in a fluidised-bed of olivine particles*, Biomass and Bioenergy 19, 2000, 187–197.

152. Rapagnà S., di Celso G.M., *Devolatilization of wood particles in a hot fluidized bed: Product yields and conversion rates*, Biomass and Bioenergy 32, 2008, 1123–1129.

153. Remón J., Randall J., Budarin V.L., Clark H.J., *Production of bio-fuels and chemicals by microwave-assisted, catalytic, hydrothermal liquefaction (MAC-HTL) of a mixture of pine and spruce biomass*, Green Chemistry 21, 2019, 284–299.

154. Report ENEA, 2015 https://www.enea.it/it/Ricerca_sviluppo/documenti/ricerca-di-sistema-elettrico/adp-mise-enea-2015-2017/combustibili-fossili-e-ccs/rds_par2015-252.pdf/view.

155. Ronda A., Gómez-Barea A., Haro P., de Almeida V.F., Salinero J, *Elements partitioning during thermal conversion of sewage sludge*, Fuel Processing Technology 186, 2019, 156−166.

156. Richards K.M., Maunder D.H., Gorman J.F., *Landfill gas: the energy environment paradox*, Ed. Pergamon Press 3, 1992.

157. Rodríguez-Olalde N.E., Mendoza-Chávez E., Castro-Montoya A.J., Saucedo-Luna J., Maya-Yescas R., Rutiaga-Quiñones J.G., Ponce Ortega J.M., *Simulation of syngas production from lignin using guaiacol as a model compound*, Energies 8, 2015, 6705–6714.

158. Rogalinski T., Ingram T., Brunner G., *Hydrolysis of lignocellulosic biomass in water under elevated temperatures and pressures*, The Journal of Supercritical Fluids 47, 2008, 54–63.

159. Ross A.B., Biller P., Kubacki M.L., Li H., Lea-Langton A., Jones J.M., *Hydrothermal processing of microalgae using alkali and organic acids*, Fuel 89, 2010, 2234–2243.

160. Ruiz H.A., Rodríguez-Jasso R.M., Fernandes B.D., Vicente A.A., Teixeira, J.A., *Hydrothermal processing, as an alternative for upgrading agriculture residues and marine biomass according to the biorefinery concept: A review*, Renewable and Sustainable Energy Reviews 21, 2013, 35–51.

161. Ruiz H.A., Galbe M., Garrote G., Ramirez-Gutierrez D.M., Ximenes E., Sun S.N., Lachos-Perez D., Rodríguez-Jasso R.M., Sun R.C., Yang B., Ladisch M.R., *Severity factor kinetic model as a strategic parameter of hydrothermal processing (steam explosion and liquid hot water) for biomass fractionation under biorefinery concept*, Bioresource Technology 342, 2021, 125961.

162. Rushdi A.I., Al-Mutlaq K.F., Sasmal S.K., Simoneit B.R.T., *Alteration of sewage sludge biomass into oil-like products by hydrous pyrolysis methods*, Fuel 103, 2013, 970–979.

163. Salaices E., Serrano B., de Lasa H., *Biomass catalytic steam gasification thermodynamics analysis and reaction experiments in a CREC riser simulator*, Industrial & Engineering Chemistry Research 49, 2010 6834–6844.

164. Sasaki M., Kabyemela B., Malaluan R., Hirose S., Takeda N., Adschiri T., Arai K., *Cellulose hydrolysis in subcritical and supercritical water*, The Journal of Supercritical Fluids 13, 1998, 261–268.

165. Sasaki M., Adschiri T., Arai K., *Production of cellulose II from native cellulose by near-and supercritical water solubilisation*, Journal of Agricultural and Food Chemistry 51, 2003, 5376–5381.

166. Saxena R.C., Adhikari D.K., Goyal H.B., *Biomass-based energy fuel through biochemical routes: A review*, Renewable and Sustainable Energy Reviews 13, 2009, 167–178.

167. Sawatdeenarunat C., Surendra K.C., Takara D., Oechsner H., Khanal S.K., *Anaerobic digestion of lignocellulosic biomass: challenges and opportunities*, Bioresource Technology 178, 2015, 178–186.

168. Shakya R., Whelen J., Adhikari S., Mahadevan R., Neupane S., *Effect of temperature and* Na_2CO_3 *catalyst on hydrothermal liquefaction of algae*, Algal Resource 12, 2015, 80–90.

169. Sharma S., Meena R., Sharma A., Goyal P.K., *Biomass conversion technologies for renewable energy and fuels: a review note*, IOSR Journal of Mechanical and Civil Engineering 11, 2014, 28–35.

170. Sharma S., Sheth P.N., *Air–steam biomass gasification: Experiments, modelling and simulation*, Energy Conversion and Management 110, 2016, 307–318.

171. Sharma R., Jasrotia K., Singh N., Ghosh P., Srivastava S., Sharma N.R., Singh J., Kanwar R., Kumar A., *A comprehensive review on hydrothermal carbonization of biomass and its applications*, Chemistry Africa 3, 2020, 1–19.

172. Sikarwar V.S., Zhao M., Clough P., Yao J., Zhong X., Memon M.Z., Shah N., Anthony E.J., Fennell P.S., *An overview of advances in biomass gasification*, Energy & Environmental Science 9, 2016, 2927–3304.

173. Sikarwar V.S., Zhao M., Fennell P.S., Shah N., Anthony E.J., *Progress in biofuel production from gasification*, Progress in Energy and Combustion Science 61, 2017, 189–248.

174. Skoulou V., Swiderski A., Yang W., Zabaniotou A., *Process characteristics and products of olive kernel high temperature steam gasification (HTSG)*, Bioresource Technology 100, 2009, 2444–2451.

175. Spoehr H., Milner H.W., *The chemical composition of chlorella; effect of environmental conditions*, Plant Physiology 24, 1949, 120–149.

176. Srokol Z., Bouche A.G., van Estrik A., Strik R.C.J., Maschmeyer T., Peters J.A., *Hydrothermal upgrading of biomass to biofuel; studies on some monosaccharide model compounds*, Carbohydrate Research 339, 2004, 1717–1726.

177. Stöcker M., *Biofuels and biomass-to-liquid fuels in the biorefinery: Catalytic conversion of lignocellulosic biomass using porous materials*, Angewandte Chemie International Edition 47, 2008, 9200–9211.

178. Su Y., Liu D., Gong M., Zhu W., Yu Y., Gu H., *Investigation on the decomposition of chemical compositions during hydrothermal conversion of dewatered sewage sludge*, International Journal of Hydrogen Energy 44, 2019, 26933–26942.

179. Sun P., Heng M., Sun S.H., Chen J., *Analysis of liquid and solid products from liquefaction of paulownia in hot-compressed water*, Energy Conversion and Management 52, 2011, 924–933.

180. Tang P., Zhou Y., Xie Z., *Effects of hydroxyapatite addition on heavy metal volatility during tannery sludge incineration*, Environmental Science and Pollution Research 20, 2013, 4405−4413.

181. Tanger P., Field J.L., Jahn C.E., DeFoort M.W., Leach J.E., *Biomass for thermochemical conversion: Targets and challenges*, Frontiers in Plant Science 4, 2013, 218.

182. Tapie P., Bernard A., *Microalgae production: technical and economic evaluations*, Biotechnology and Bioengineering 32, 1988, 873–885.

183. Tekin K., Karagöz S., Bektaş S., *A review of hydrothermal biomass processing*, Renewable and Sustainable Energy Reviews 40, 2014, 673–687.

184. Theegala C.S., Midgett J.S., *Hydrothermal liquefaction of separated dairy manure for production of bio-oils with simultaneous waste treatment*, Bioresource Technologies 107, 2012 456–463.

185. Tong Y., Yang T., Li B., Kai X., Li R., *Two-stage liquefaction of sewage sludge in methanol-water mixed solvents with low-medium temperature*, The Journal of Supercritical Fluids 168, 2021, 105094.

186. Toor S.S., Rosendahl L., Rudolf A., *Hydrothermal liquefaction of biomass: A review of subcritical water technologies*, Energy 36, 2011, 2328–2342.

187. Tran K.Q., *Fast hydrothermal liquefaction for production of chemicals and biofuels from wet biomass – The need to develop a plug-flow reactor*, Bioresource Technology 213, 2016, 327–332.

188. Troiano M., Montagnaro F., Salatino P., Solimene R., *Experimental characterization of particle-wall interaction relevant to entrained-flow gasification of biomass*, Fuel 209, 2017, 674–684.
189. Tyagi V.K., Lo S.L., *Sludge: A waste or renewable source for energy and resources recovery*, Renewable and Sustainable Energy Reviews 25, 2013, 708–728.
190. United Nations, Department of Economic and Social Affairs, Population Division, World Population Prospects 2022 Summary of Results, https://www.un.org/development/desa/pd/sites/www.un.org.development.desa.pd/files/wpp2022_summary_of_results.pdf (accessed December 12, 2022).
191. UNIC Sustainability Report 2020, https://unic.it/storage/Rapporto%20sostenibilità%202020/Report_Sostenibilità_2020_ENG_online.pdf (accessed December 12, 2022).
192. U.S. Energy Information Administration, Office of Energy Statistics, U.S. Department of Energy, Monthly Energy Review 2022, https://www.eia.gov/totalenergy/data/monthly/pdf/mer.pdf, (accessed December 12, 2022).
193. Valderrama J.O., *The state of the cubic equations of state*, Industrial & Engineering Chemistry Research 42, 2003, 1603–1618.
194. Varitis S., Kavouras P., Pavlidou E., Pantazopoulou E., Vourlias G., Chrissafis K., Zouboulis A.I., Karakostas T., Komninou P., *Vitrification of incinerated tannery sludge in silicate matrices for chromium stabilization*, Waste Management 59, 2017, 237−246.
195. Vardon D.R., Sharma B.K., Scott J., Yu G., Wang Z., Schideman L., Zhang Y., Strathmann T.J., *Chemical properties of biocrude oil from the hydrothermal liquefaction of spirulina algae, swine manure, and digested anaerobic sludge*, Bioresource Technology 102, 2011, 8295–8303.
196. Wang T., Zhai Y., Zhu Y., Li C., Zeng G., *A review of the hydrothermal carbonization of biomass waste for hydrochar formation: process conditions, fundamentals, and physicochemical properties*, Renewable and Sustainable Energy Reviews 90, 2018, 223–247.
197. Wang W., Yu Q., Meng H., Han W., Li J., Zhang J., *Catalytic liquefaction of municipal sewage sludge over transition metal catalysts in ethanol-water co-solvent*, Bioresource Technology 249, 2018, 361–367.
198. Wang L., Chang Y., Li A., *Hydrothermal carbonization for energy-efficient processing of sewage sludge: A review*, Renewable and Sustainable Energy Reviews 108, 2019, 423–440.
199. Ward A.J., Lewis D.M., Green F.B., *Anaerobic digestion of algae biomass: A review*, Algal Research 5, 2014, 204–214.
200. Watson J., Wang T., Si B., Chen W.-T. Aierzhati A., Zhang Y., *Valorization of hydrothermal liquefaction aqueous phase: Pathways towards commercial viability*, Progress in Energy and Combustion Science 77, 2020, 100819.
201. Werle S., *Sewage sludge gasification: Theoretical and experimental investigation*, Environment Protection Engineering 39, 2013.
202. White L.P., Plaskett L.G., *Biomass as Fuel*, Ed. Academic Press 1, 1981.

203. Williams P.J.B., Laurens L.M.L., *Microalgae as biodiesel & biomass feedstocks: Review & analysis of the biochemistry, energetics & economics*, Energy & Environmental Science 3, 2010, 554–590.

204. Wilk M., Magdziarz A., Jayaraman K., Szymańska-Chargot M., Gökalp I., *Hydrothermal carbonization characteristics of sewage sludge and lignocellulosic biomass. A comparative study*, Biomass and Bioenergy 120, 2019, 166–175.

205. Wilk M., Śliz M., Gajek M., *The effects of hydrothermal carbonization operating parameters on high-value hydrochar derived from beet pulp*, Renewable Energy 177, 2021, 216–228.

206. Wilk M., Gajek M., Śliz M., Czerwińska K., Lombardi L., *Hydrothermal carbonization process of digestate from sewage sludge: Chemical and physical properties of hydrochar in terms of energy application*, Energies 15, 2022, 6499.

207. Winkler M.-K.H., Bennenbroek M.H., Horstink F.H., van Loosdrecht M.C.M., van de Pol G.-J., *The biodrying concept: An innovative technology creating energy from sewage sludge*, Bioresource Technology 147, 2013, 124–129.

208. Wystalska K., Sobik-Szołtysek J., *2 - Sludge from tannery industries*, Industrial and Municipal Sludge, 2019, 31–46.

209. Xi D., Jiang C., Zhou R., Fang Z., Zhang X., Liu Y., Luan B., Feng Z., Chen G., Chen Z., Liu Q., Yang S., *The universality of lignocellulosic biomass liquefaction by plasma electrolysis under acidic conditions*, Bioresource Technology 268, 2018, 531–538.

210. Xu C., Etcheverry T., *Hydro-liquefaction of woody biomass in sub- and supercritical ethanol with iron-based catalysts*, Fuel 87, 2008, 335–345.

211. Xu C., Lancaster J., *Conversion of secondary pulp/paper sludge powder to liquid oil products for energy recovery by direct liquefaction in hotcompressed water*, Water Research 42, 2008, 1571–1582.

212. Xu D., Lin G., Liu L., Wang Y., Jing Z., Wang S., *Comprehensive evaluation on product characteristics of fast hydrothermal liquefaction of sewage sludge at different temperatures*, Energy 159, 2018, 686–695.

213. Yang Y., Gilbert A., Xu C., *Production of bio-crude from forestry waste by hydro-liquefaction in sub-/super-critical methanol*, AIChE Journal 55, 2009, 807–819.

214. Yang C., Jia L., Chen C., Liu G., Fang, W., *Bio-oil from hydro-liquefaction of Dunaliella Salina over Ni/REHY catalyst*, Bioresource Technology 102, 2011, 4580–4584.

215. Yang J., He Q.S., Corscadden K., Niu H., Lin J., Astatkie T., *Advanced models for the prediction of product yield in hydrothermal liquefaction via a mixture design of biomass model components coupled with process variables*, Applied Energy 233–234, 2019, 906–915.

216. Yanik J., Kornmayer C., Saglam M., Yüksel M., *Fast pyrolysis of agricultural wastes: Characterization of pyrolysis products*, Fuel Processing Technology 88, 2007, 942–947.

217. Yin S., Dolan R., Harris M., Tan Z., *Subcritical hydrothermal liquefaction of cattle manure to bio-oil: Effects of conversion parameters on bio-oil yield and characterization of bio-oil*, Bioresource Technology 101, 2010, 3657–3664.

218. Yokoyama S., Suzuki A., Murakami M., Ogi T., Koguchi K., Nakamura E., *Liquid fuel production from sewage sludge by catalytic conversion using sodium carbonate*, Fuel 66, 1987, 1150–1155.

219. Yu Q., Wang Y., Le Q.V., Yang H., Hosseinzadeh-Bandbafha H., Yang Y., Sonne C., Tabatabaei M., Lam S.S., Peng W., *An overview on the conversion of forest biomass into bioenergy*, Frontiers in Energy Research 9, 2021, 684234.

220. Yuan B., Yan C., Li Z., Li L., Wang C., *Dynamic pitting processes of 316 stainless steel in NaCl +* Na_2CO_3 *solution with digital holography*, Corrosion Communications 4, 2021, 57–67.

221. Yuan X., Li H., Zeng G., Tong J., Xie W., *Sub-and supercritical liquefaction of rice straw in the presence of ethanol–water and 2-propanol–water mixture*, Energy 32, 2007, 2081–2088.

222. Zhang Y., *Hydrothermal liquefaction to convert biomass into crude oil*, Biofuels from Agricultural Wastes and Byproducts, Chapter 10, 2010.

223. Zhang L., Champagne P., Xu C.C., Bio-*crude production from secondary pulp/paper-mill sludge and waste newspaper via co-liquefaction in hot-compressed water*, Energy 36, 2011, 2142–2150.

224. Zhong C., Wei X., *A comparative experimental study on the liquefaction of wood*, Energy 29, 2004, 1731–1741.

225. Zhou D., Zhang L., Zhang S., Fu H., Chen J., *Hydrothermal liquefaction of macroalgae Enteromorpha prolifera to bio-oil*, Energy & Fuels 24, 2010, 4054–4061.

226. Zhou Y., Chen Z., Gong H., Yang Z., *Chromium speciation in tannery sludge residues after different thermal decomposition processes*, Journal of Cleaner Production 314, 2021, 128071.

227. Zhu X., Zhu C., Zhao L., Cheng H., *Amino acids production from fish proteins hydrolysis in subcritical water*, Chinese Journal of Chemical Engineering 16, 2008 456–460.

228. Zhu J.Y., Pan X.J., *Woody biomass pretreatment for cellulosic ethanol production: Technology and energy consumption evaluation*, Bioresource Technology 101, 2010, 4992–5002.

229. Zhu Y., Albrecht K.O., Elliott D.C., Hallen R.T., Jones S.B., *Development of hydrothermal liquefaction and upgrading technologies for lipid-extracted algae conversion to liquid fuels*, Algal Research 2, 2013, 455–464.

230. Zhu Z., Toor S.S., Rosendahl L., Yu D., Chen G., *Influence of alkali catalyst on product yield and properties via hydrothermal liquefaction of barley straw*, Energy 80, 2015, 284–292.

231. Zhu Y., Zhao Y., Tian S., Zhang X., Wei X., *Catalytic hydrothermal liquefaction of sewage sludge: Effect of metal support heterogeneous catalysts on products distribution*, Journal of the Energy Institute 103, 2022, 154–159.

Collection of papers published by the Ph.D. Candidate

1. Tregambi C., Di Lauro F, F. Montagnaro, P. Salatino, R. Solimene, *110th anniversary: Calcium looping with concentrated solar power for carbon capture and thermochemical energy storage*, Industrial & Engineering Chemistry Research 58, 2019, 21262–21272.
2. Tregambi C., Di Lauro F., Montagnaro F., Salatino P., Solimene R., *Limestone calcination-carbonation in a fluidized bed reactor/receiver for thermochemical energy storage applications*, Proceedings of the 24th SolarPACES International Conference on Solar Power and Chemical Energy Systems, 2018, Casablanca, Morocco (then published on AIP Conference Proceedings, 210008, 2019).
3. Tregambi C., Di Lauro F., Montagnaro F., Chirone R., Solimene R, Salatino P., *Improving the performances of Calcium Looping for solar thermochemical energy storage and* CO_2 *capture*, Proceedings of the 15th Conference on Sustainable Development of Energy, Water and Environment Systems, 2020, 447, Cologne, Germany (virtual Conference).
4. Di Lauro F., Tregambi C., Montagnaro F., Salatino P., Chirone R., Solimene R., *Improving the performance of calcium looping for solar thermochemical energy storage and* CO_2 *capture*, Fuel 298, 2021, 120791.
5. Di Lauro F., Balsamo M., Solimene R., Migliaccio R., Caracciolo D., Salatino P., Montagnaro F., *Outline of a process for the hydrothermal liquefaction of a tannery sludge for biofuel production*, Proceedings of the 10th European Combustion Meeting, 2021, 274, Naples, Italy (virtual Conference).
6. Pascual S., Di Lauro F., Lisbona P., Romeo L.M., Tregambi C., Montagnaro F., Solimene R., Salatino P., *Improvement of performance of fluidized bed calcium looping for thermochemical solar energy storage: Modelling and experiments*, Proceedings of the 10th European Combustion Meeting, 2021, 330, Naples, Italy (virtual Conference).
7. Di Lauro F., Migliaccio R., Ruoppolo G., Balsamo M., Montagnaro F., Imperiale E., Caracciolo D., Urciuolo M., *Tannery sludge gasification in a fluidized bed for its energetic valorization*, Industrial & Engineering Chemistry Research 61, 2022, 16972–16979.
8. Marroccoli M., Ibris N., Telesca A., Tregambi C., Solimene R., Di Lauro F., Ruiz de Ballesteros O., Salatino P., Montagnaro F., *Dolomite-based binders manufactured using concentrated solar energy in a fluidised bed reactor*, Solar Energy 232, 2022, 471–482.
9. Di Lauro F., Balsamo M., Solimene R., Salatino P., Montagnaro F., *Hydrothermal liquefaction process to obtain sludge-derived bio-fuels: Setup of the experimental apparatus and preliminary tests*, Proceedings of the International Conference on Biomass (published on Chemical Engineering Transactions), 92, 2022, 174, Naples, Italy.
10. Di Lauro F., Balsamo M., Solimene R., Salatino P., Montagnaro F., *Hydrothermal liquefaction of a sewage sludge for the production of biofuels: optimization of the experimental apparatus and effect of operating parameters on the process performance*, Proceedings of the 17th Conference on Sustainable Development of Energy, Water and Environment Systems, 2022, 223, Paphos, Cyprus.

11. Urciuolo M., Migliaccio R., Ruoppolo G., Di Lauro F., Balsamo M., Montagnaro F., Imperiale E., Caracciolo D., *Energetic valorisation of tannery sludge by gasification in fluidised bed*, Proceedings of the 13th European Conference on Industrial Furnaces and Boilers, 2022, 651, Albufeira, Portugal.

I&EC research
Industrial & Engineering Chemistry Research

Article

Cite This: *Ind. Eng. Chem. Res.* 2019, 58, 21262−21272

pubs.acs.org/IECR

110th Anniversary: Calcium Looping Coupled with Concentrated Solar Power for Carbon Capture and Thermochemical Energy Storage

Claudio Tregambi,[†] Francesca Di Lauro,[‡] Fabio Montagnaro,[§] Piero Salatino,[*,†] and Roberto Solimene[‡]

[†]Dipartimento di Ingegneria Chimica, dei Materiali e della Produzione Industriale, Università degli Studi di Napoli Federico II, Piazzale Vincenzo Tecchio 80, 80125 Napoli, Italy

[‡]Istituto di Ricerche sulla Combustione (IRC), Consiglio Nazionale delle Ricerche (CNR), Piazzale Vincenzo Tecchio 80, 80125 Napoli, Italy

[§]Dipartimento di Scienze Chimiche, Università degli Studi di Napoli Federico II, Complesso Universitario di Monte Sant'Angelo, 80126, Napoli, Italy

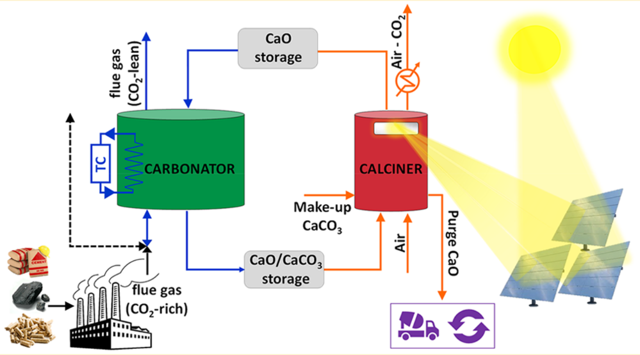

ABSTRACT: Concentrating solar power (CSP) technologies with energy storage can greatly enhance the dispatchability and the exploitation of solar energy in different applications. In this context, the present study addresses coupling CSP with calcium looping (CaL) along the 2-fold perspective of accomplishing: (a) carbon capture and sequestration or utilization (CCSU); (b) thermochemical energy storage (TCES). The experimental campaign, aimed at assessing limestone performances over extended cycling under realistic operating conditions, was performed in a fluidized bed reactor directly irradiated by a simulator of concentrated solar radiation. Infrared thermography was used to map the fluidized bed surface during "solar-driven" calcination. Experimental results indicated that TCES operating conditions yield a more reactive material due to the development of better microstructural properties, as inferred from N_2- and Hg-intrusion porosimetry, which reflect the different thermal history experienced by sorbent material. Working out of process variables in terms of density of energy storage revealed that the CSP-CaL integrated process can represent an attractive alternative option to commercial technologies based on molten salts.

1. INTRODUCTION

Reduction of greenhouse gas release to the atmosphere is challenging the energy world toward decreasing CO_2 emissions and increasing the share of renewable energies. Concentrating solar power (CSP) technologies may play a key role in the rich and diversified portfolio of renewable energy sources in view of some distinctive features. CSP implies concentration, by means of optical sun tracking mirrors (heliostats), of solar radiation onto a solar receiver, whence it can be exploited to drive power cycles, to supply process heat, or to sustain solar-driven chemical processes. The current installed capacity of CSP systems is far smaller than that of photovoltaic power plants. However, CSP is characterized by a few remarkable and unique features that make it a valuable option for selected applications: (a) CSP has the potential of achieving much higher thermal efficiencies, as the whole solar spectrum, rather than selected spectral ranges, may be exploited; (b) coupling of CSP with relatively inexpensive thermal energy storage (TES) systems makes CSP a "dispatchable" energy source over the hour-to-day time scale;[1] (c) CSP may be a source of valuable high-temperature thermal energy, which can be exploited as process heat or in hybrid schemes where CSP is coupled with endothermal physical or chemical processes. The current benchmark of CSP technologies is represented by the solar tower-top receiver coupled with molten salts acting as heat transfer fluid and heat storage medium at the same time. In the very next future, thermochemical energy storage (TCES) is bound to play a major role as it enables a larger storage density and virtually unlimited time scale of energy storage and dispatchability.[2,3] TCES is based on the storage of concentrated solar energy in the noble and stable form of chemical bonds[4−6] by sustaining a reversible chemical reaction characterized by large latent heat. Along the endothermic step, solar energy is collected, and reaction products are stored separately. Retrieval of stored energy is eventually accomplished by promoting, under proper operating conditions, the course of the reverse exothermic reaction.

Received: June 8, 2019
Revised: September 19, 2019
Accepted: October 24, 2019
Published: October 24, 2019

DOI: 10.1021/acs.iecr.9b03083

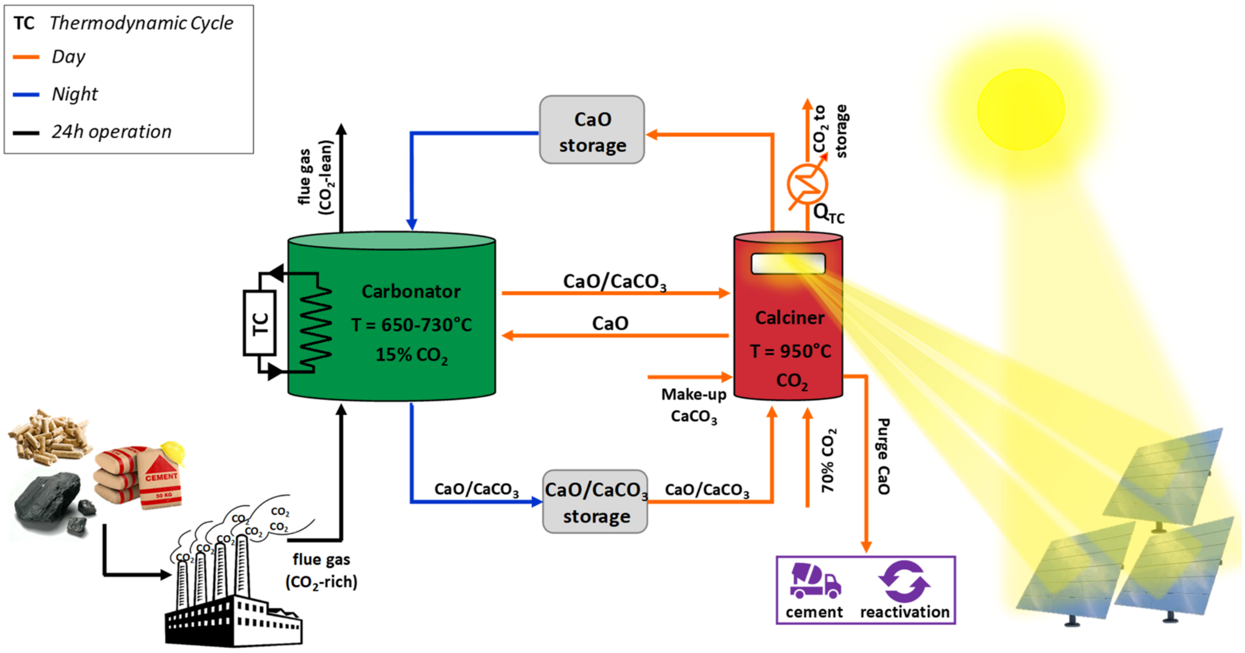

Figure 1. Outline of the integrated CaL-CSP process for CCSU.

Many perspective TCES processes involve gas/solid chemical reactions, and this is challenging chemical reaction engineers in the effort of designing multiphase chemical reactors that can be effectively coupled with CSP. The use of a dense suspension of solid particles as solar receiver media in CSP is gaining widespread consideration, as the dense suspension can simultaneously work as receiver, heat transfer fluid, and heat storage medium.[7−13] Fluidized bed (FB) reactors represent a well-known, affordable, and reliable system to exploit the remarkable properties of particle receivers. Fluidized beds are characterized by large heat transfer coefficients and thermal diffusivities[14−17] and can provide an ideal environment to sustain heterogeneous or solid-catalyzed chemical processes required for TCES. The interaction of the incident radiative flux with the fluidized bed may be indirect or direct. Indirect heating of the FB may be accomplished by concentrating the solar radiation onto a cavity or an exposed surface, whence heat is eventually transferred to the solid suspension by convection/conduction.[14,18] Direct heating of the FB may be accomplished by concentrating solar radiation directly onto the fluidized suspension, via openings or optically accessible windows and transparent walls.[19−21] Direct heating enables higher process temperature, as bed solid is directly heated by the concentrated radiation (i.e., no heat flux limitations due to cavity/walls are foreseen). However, axial/radial gradients inside the bed can be established owing to the highly concentrated and uneven incident solar radiation with a potential impact on the performance of reactive materials.[20−22] The use of an uneven and unsteady fluidization strategy to enhance the bed thermal diffusivity and limit the time/spatial temperature nonhomogeneity is currently being pursued.[15,23,24]

Limestone calcination is a reversible reaction with a fairly large latent heat of reaction (ΔH° = 183 kJ mol^{-1}) whose coupling with CSP has already been considered for different applications: (i) solar-driven production of cement;[25−30] (ii) TCES of solar energy via reversible calcium looping (CaL); (iii) carbon capture and sequestration or utilization (CCSU) via reversible CaL. Integration of renewable energies into carbon capture technologies is currently pursued in the literature to reduce the energy penalty and increase the overall process efficiency.[31−34] In the present study, integration of CSP with reversible CaL (CSP-CaL) is addressed with reference to both CCSU and TCES applications.

When CSP-CaL integration is primarily targeted to CCSU, operating conditions during calcination, namely, process temperature and reaction environment, reflect those of conventional combustion-driven CaL cycles ($T \cong 940$ °C, 70%$_v$ CO_2).[35] Integration between CaL and CSP for CCSU, where CSP supplies the energy required to the calciner, has received much attention over the past decade.[36−40] This integration was experimentally investigated by this group,[21] with a focus on the effect of the overheating of the FB upper surface, due to the incident solar radiation, on the sorbent reactivity.

When CSP-CaL integration is targeted to TCES, different process schemes can be considered. This kind of integration has also been scrutinized in the recent literature.[41−44] Sarrion et al.[45] and Benitez-Guerrero et al.[46,47] investigated the use of natural sorbents in a CaL-TCES process in which calcination is performed at low temperature (725 °C) using He as gas carrier, whereas the carbonation is performed at high temperature (850 °C) using a stream of pure CO_2. The use of composite materials by mechanical blending of natural sorbents with inert compounds,[48,49] as well as by synthesis involving acetate precursors[50] or biotemplates,[51] has been investigated with the aim of improving sorbent reactivity for both TCES and CCSU.

The present study addresses the experimental characterization of CSP-CaL integration in a solar-driven directly irradiated FB reactor, using limestone as a sorbent. The lab-scale FB reactor is heated with simulated solar radiation emitted by an array of three short-arc Xe-lamps coupled with an elliptical reflector, producing a concentrated beam on the FB surface having a peak flux of 3 MW m^{-2} and a total irradiated power of 3 kW$_{th}$. Operating conditions of the tests were selected taking into account both process options recalled above, corresponding to either CCSU or TCES as the prevailing target. For the purpose of comparison, the CaL-TCES cycle analyzed in this study is

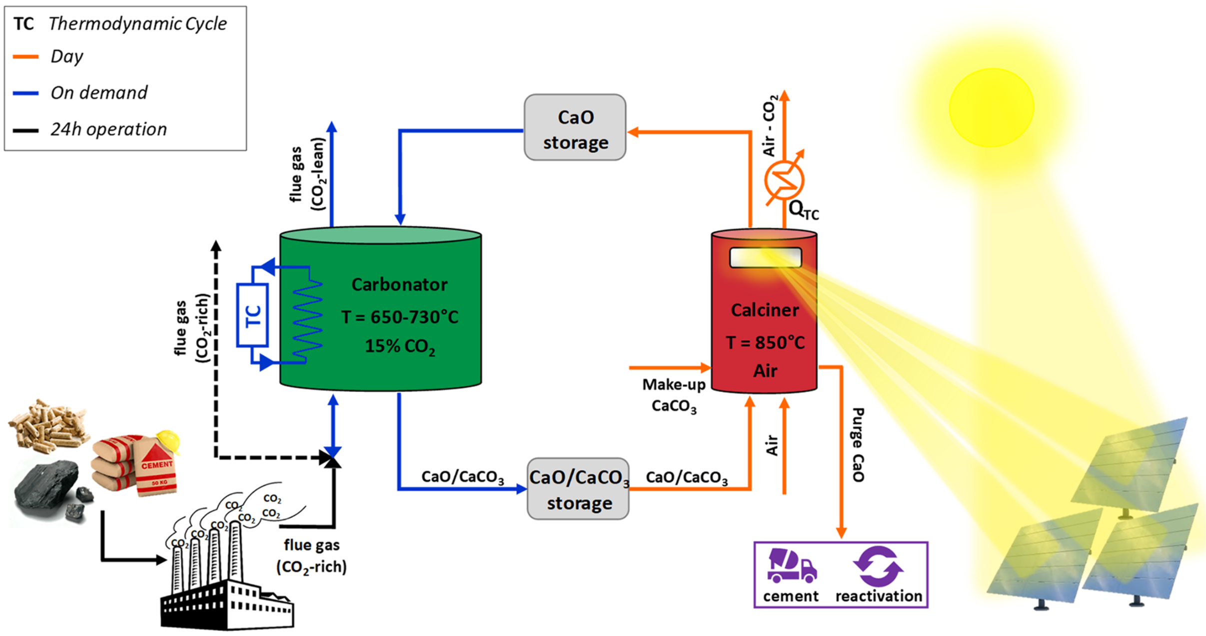

Figure 2. Outline of the integrated CaL-CSP process for TCES.

based on an open loop configuration with respect to CO_2, differently from the CaL-CCSU scheme. Exothermic sorbent carbonation is accomplished using effluents typical of those from CO_2 emitting industries, such as power plants or cement/steel production plants. Sorbent calcination is accomplished in air, hence at much lower CO_2 partial pressure, a feature that enables operation at lower calcination temperature and less severe sintering of the sorbent. The sorbent was iteratively looped between carbonation and calcination up to 20 reaction cycles. Mapping of bed temperature during operation of the fluidized bed reactor was accomplished by infrared thermography. The reactivity of the sorbent was characterized upon iterated cycling under either CCSU or TCES process conditions. Moreover, sorbent samples retrieved at different stages of CaL were characterized from the standpoint of microstructural properties. Sorbent deactivation and microstructural modifications upon cycling are correlated with the time−temperature history experienced by sorbent particles. Finally, CO_2 uptake upon iterated cycles is worked out to assess the density of energy storage that can be accomplished by CSP-CaL integration in either option.

2. COMPARISON BETWEEN ALTERNATIVE LAYOUTS FOR CSP AND CAL INTEGRATION

Two alternative process layouts have been taken into account and compared, depending on whether CCSU or TCES is assumed as the primary target of CSP-CaL integration.

The integrated process targeted to CCSU is outlined in Figure 1. It has already been analyzed in previous studies[21,38] that provide a detailed description of the process and a comparison with combustion-driven CaL. The process is designed to work on a 24 h time basis, and its operation is briefly recalled here:

(i) During the daytime, a classical CaL is performed between the carbonator and calciner, with the peculiarity that solar energy is used to sustain calcination. In addition to the recirculated Ca-based sorbent, the calciner processes an additional stream of carbonated material coming from the $CaO/CaCO_3$ storage vessel which, after calcination, is stored in a CaO storage vessel for night-time operation. Accordingly, the $CaO/CaCO_3$ storage vessel is emptied during the daytime, whereas the CaO storage is filled up. The maximum inventory of the storage vessels is designed so as to guarantee the operation of the system over the whole night.

(ii) During the night-time, the calciner is not in operation. CaO storage supplies the sorbent required for CO_2 capture to the carbonator, whence the carbonated material is sent to the $CaO/CaCO_3$ storage vessel.

Altogether, the cycle is closed with respect to CO_2. CO_2 leaving the calciner is collected for further sequestration and/or utilization. Calcination is performed in a CO_2-rich environment and, due to thermodynamic constraints, requires a higher reaction temperature than in the TCES case.

When TCES is the primary goal, CaL-CSP integration is accomplished according to the scheme outlined in Figure 2. Operation of the system is as follows:

(i) During the daytime, harvesting of solar energy takes place in the calciner by converting a stream of carbonated material from the $CaO/CaCO_3$ storage vessel and accumulating the calcined material in the CaO storage vessel. Accordingly, the $CaO/CaCO_3$ storage vessel is emptied during the daytime, whereas the CaO storage vessel is filled up.

(ii) During the night-time, the calciner is not operated due to the absence of solar energy.

(iii) Retrieval of collected solar energy occurs on demand, during both the daytime and night-time, as long as CaO is available from the storage. Accordingly, the carbonator is fed with CaO from the storage vessel, while spent carbonated material is sent to the $CaO/CaCO_3$ storage. Vessels for storage of both calcined/regenerated and carbonated sorbent are thus used to buffer the operation of the loop.

Overall, the cycle operates “once through” with respect to CO_2 in this case. Carbonation is accomplished using exhaust gas from CO_2-intensive industries, such as power plants based on fossil fuels or cement/steel production plants. Calcination, sustained by concentrated solar energy, is performed using air as gas carrier/fluidizing gas, under CO_2-lean conditions. Accordingly, calcination may be carried out at lower temperature, a feature that moderates the severity of sorbent sintering and reduces the degree of sorbent deactivation upon extended cycling.

It is recalled that, in both integrated processes, the regenerated sorbent consists of nearly pure CaO, whereas the carbonated material is a mixture of CaO and $CaCO_3$, as the heterogeneous carbonation reaction is almost never complete. In both processes, a makeup of fresh limestone and a purge of exhausted material must be accomplished to compensate for the accumulation of deactivated sorbent over time. Typical makeup values are of about 5% of the looping streams,[52] so that particles experience an average life of 20 reaction cycles. Spent limestone leaving the looping cycles can be used as raw material for the cement industry in the manufacture of, e.g., Portland cements.[53] Alternative strategies could contemplate reactivation of the spent limestone by means of water/steam hydration or other regeneration techniques.[54,55]

3. EXPERIMENTAL SECTION

3.1. Experimental Apparatus. The FB reactor used in the experimental campaign is outlined in Figure 3. It consists of three sections. The lower section, acting as a wind-box, is a cylinder of 0.15 m height and of 0.102 m internal diameter. The second section is a cylinder of 0.102 m internal diameter and of 0.1 m height. This section hosts the fluidized bed, resting on a gas distributor consisting of a metallic porous plate with 0.5 mm holes drilled on a triangular pitch. The aspect ratio (internal diameter/height ratio) of the bed is close to unity to promote the establishment of "gulfstreaming" patterns that enhance mixing of bed solids at the bed scale.[56] The upper section of the reactor, 0.4 m high, is conically shaped and acts as the freeboard. The top of this section is confined by a ceramic glass optical window through which the bed may be irradiated by simulated solar radiation. The window has a thickness of 4 mm and a maximum operating temperature of 700 °C. The transmittance of the window is about 0.9 in the spectral range between 340 and 2350 μm. The conical shape of the freeboard ensures that there is no restriction to the incident radiative flux. Moreover, it promotes disengagement of the particles ejected by bubble eruptions so that the transparent window could be kept clean very effectively. The gas discharge port is located at midlevel in the freeboard conical section, so that the entrainment of solid particles ejected by bubble bursting and the impact of finer particles with the upper transparent window are minimized. The reactor is thermally insulated with multiple layers of rock wool blanket.

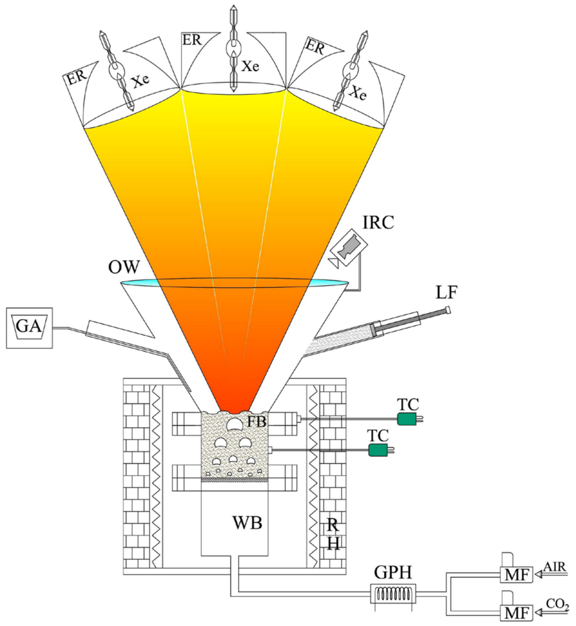

Figure 3. Outline of the fluidized bed reactor and its ancillary equipment. ER: elliptical reflector; FB: fluidized bed; GPH: gas preheater; IRC: infrared camera; TC: thermocouple; WB: wind-box; Xe: short-arc Xe-lamp; GA: gas analyzer; LF: limestone feeder; MF: mass flow controller; OW: optical window; RH: radiant heater.

Gas feeding is controlled by two electronic mass flow meters, one calibrated for air and the other, for CO_2. The reactor is heated by a combination of devices. Direct irradiation of the bed is accomplished with an array of three short-arc Xe lamps of 4 kW_{el} each, coupled with elliptical reflectors. The use of Xe lamps to simulate the solar spectrum is well established in the literature as they approach the spectral features of solar radiation, especially in the visible range. The distribution of the simulated radiation on the FB surface has been characterized and is reported by Tregambi et al.[21] The peak flux and total irradiated power are of about 3 MW m^{-2} and 3.2 kW_{th}, respectively. Additional heating could be provided, especially during the reactor start-up, by two semicylindrical radiant heaters surrounding the bed and the wind-box sections, being partly overlapped with the conical section. The heaters are driven by an ON/OFF PID controller connected to a K-type thermocouple located inside the FB. Moreover, fluidizing gas preheating up to a maximum temperature of 750 °C could be accomplished in a stainless-steel heat exchanger equipped with a serpentine-coil element as electric heater, regulated by means of a rheostat.

The reactor is equipped with an array of K-type thermocouples located immediately downstream of the gas preheater, in the wind-box section and in the FB reactor. The latter were located both (i) 0.05 m above the gas distributor and 0.05 m from the reactor wall ("middle" location) and (ii) 0.08 m above the gas distributor and 0.01 m from the reactor wall ("upper" location).

A thermal infrared camera (Optris PI-400, 7.5−13 μm, 382 × 288 pixels, maximum frame rate 80 Hz) was used to map the surface temperature of the FB. Noteworthy, since the IR camera is blind when the optical window is mounted on the reactor (as the window material absorbs the IR radiation in the 7.5−13 μm spectral range), bed surface temperature mapping could only be accomplished after removing the glass enclosure.

CO_2 concentration at the exhaust was continuously monitored during the tests using an Advance Optima ABB AO2020 (Uras 14, 0−100%$_v$) analyzer. Gas was sampled via a 6 mm stainless steel (ID 4 mm) probe, inserted in the reactor through one of the four outlet pipes and located at a level of 0.15−0.20 m above the bed surface. A suction pump is calibrated to sample at a rate of 0.050−0.060 N m^3 h^{-1}. A steel wool filter was interposed between the pump and the reactor to avoid fine solid particles from reaching the analyzer.

3.2. Materials. The bed material consisted of mixtures of sorbent (active bed material) and silica sand (inert bed material).

The sorbent was an Italian natural limestone (termed “Sardo”), ground and sieved in the 420−590 μm range. The $CaCO_3$ content of the limestone was experimentally evaluated by heating a sample (1−2 g mass) in a muffle furnace at 950 °C for 1 h and measuring the weight change with an analytical balance (0.1 mg precision). The measure was repeated three times. The purity of the sample, in terms of $CaCO_3$, turned out to be 98.5$\%_{wt}$.

The silica sand, derived from Ticino river (Italy), is of alluvial origin, naturally rounded and polychrome in color, with excellent thermo-mechanical resistance up to 1700 °C. The sand was ground and sieved in the 850−1000 μm range. The inert bed material is mainly used as a thermal flywheel, to mitigate temperature variations during the occurrence of the chemical reactions. Size ranges of the two bed components were intentionally different so as to enable easy separation by sieving. The main properties of the materials are summarized in Table 1, together with the theoretical value of minimum fluidization velocity (u^t_{mf}) evaluated according to the Wen and Yu equation.

Table 1. Selected Properties of the Sorbent and Bed Inert Materials

material	particle density [kg m^{-3}]	size range [μm]	u^t_{mf} at 650−950 °C [m s^{-1}]
Sardo limestone	2400	420−590	0.09−0.08
Ticino sand	2600	850−1000	0.32−0.27

3.3. Experimental Procedure and Operating Conditions.

The experimental campaign was focused on the assessment of the Sardo limestone reactivity over cycling, under reactive conditions relevant to either CaL-CCSU or CaL-TCES, for the integration of the CaL cycle with CSP systems. Accordingly, the limestone was iteratively looped between carbonation and calcination stages until completion of 20 reaction cycles. Three sets of tests were performed for each of the two process conditions, and the experimental results were statistically analyzed to obtain mean values and standard deviations of relevant variables for each cycle stage.

The experimental protocol is represented in the CO_2 partial pressure (P_{CO_2}) vs temperature (T) map reported in Figure 4.

In both reactive conditions (TCES and CCSU), carbonation was performed during a heating step from about 650 to 730 °C in an atmosphere containing CO_2 at concentration of 15$\%_v$, a typical value of flue gases in coal-fired power plants. The CO_2 concentration level and the presence in the flue gases of other gaseous species, like H_2O and SO_2, can be relevant to the performance of the CaL cycle,[57,58] but the analysis of their effect is beyond the scope of this study. Different calcination conditions were established depending on whether TCES or CCSU was the target. In CCSU experiments, calcination was performed during a heating step from 850 °C to 940−950 °C by fluidizing the bed with a stream with an inlet CO_2 concentration of 70$\%_v$. In TCES experiments, calcination was performed during a heating step from 750 °C to 850−860 °C while fluidizing the bed with a gas stream consisting of atmospheric air. The temperature of 850−860 °C (estimated by separate kinetic measurements in a different FB reactor, results not reported) is the temperature at which the calcination rate in air is comparable with that recorded at 940−950 °C in a CO_2-rich stream at 70$\%_v$ CO_2. The gas superficial velocity of the fluidizing gas was kept at 0.6 m s^{-1} during both carbonation and calcination, corresponding to nearly twice the minimum fluidization velocity of the inert sand. Under these conditions, the FB behaves as a bubbling fluidized bed reactor. The bed inventory was 850 g, consisting in 730 g of inert sand and 120 g of active limestone. It is worth noting that the addition of inert sand (that would not be required in industrial applications) as a ballast to the reactive sorbent was accomplished with the only purpose of moderating bed temperature changes induced by CO_2 uptake and release. Carbonation and calcination were sequentially performed in the same FB reactor (Figure 3) by alternating operating conditions relevant to each stage. To better simulate realistic CaL-CSP coupling (Figures 1 and 2), only the calcination step was sustained by simulated solar heating. In the other stages of the cycles, the reactor was thermally sustained by the radiant heaters and the gas preheater. Due to the small size (i.e., large surface-to-volume ratio) of the reactor and the limited amount of Ca sorbent (about 15$\%_{wt}$ of the bed), the bed temperature turned out to be efficiently controlled by the heaters even during the exothermic carbonation stage.

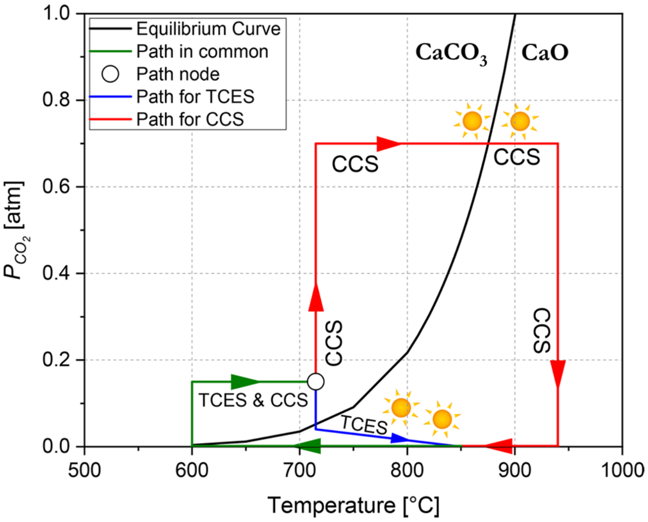

Figure 4. Representation of the experimental path followed during CaL-CCSU and CaL-TCES cycles, plotted in CO_2 partial pressure (P_{CO_2}) vs temperature (T) map. The equilibrium curve for $CaCO_3$ decomposition is reported.

During a typical CaL-TCES test, the bed was initially loaded with about 730 g of inert sand and heated up to 730−750 °C with both radiant heaters and a gas preheater. Atmospheric air was used as fluidizing gas. Once the set temperature was approached, a sample of 120 g of limestone was fed to the reactor through one of the gas discharge ports. At the same time, the solar simulator was turned on and the radiant heaters were powered off. The first calcination step lasted 20 min. Eventually, all the heaters were powered off and the reactor was cooled down to 650 °C. Then, the reactor was heated up again to 730 °C with both radiant and gas heaters. During this step, a gas stream with an inlet CO_2 concentration of 15$\%_v$ was used as fluidizing gas to perform the carbonation reaction (carbonation step). Input thermal power was tuned to make the carbonation step last 20−25 min. Once 730 °C was reached, radiant heaters were powered off; simultaneously, the inlet gas stream was switched to atmospheric air, and the solar simulator was powered on for 20 min to perform the calcination reaction and complete the reaction cycle (calcination step). Finally, the

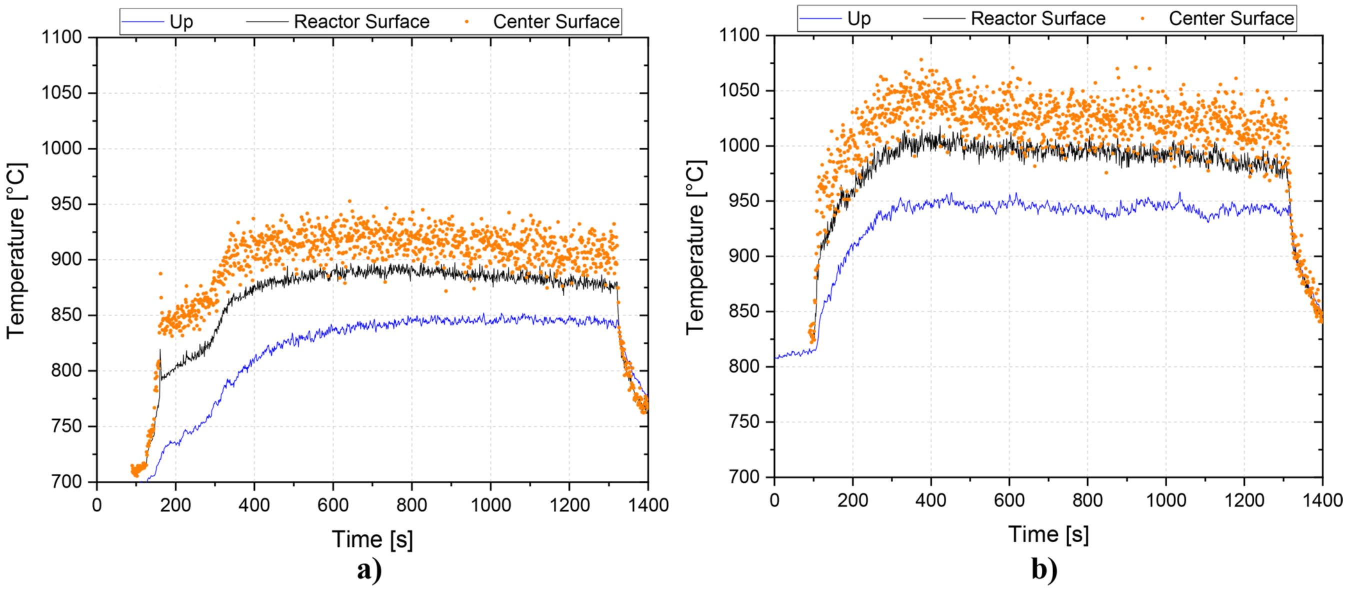

Figure 5. In-bed and surface temperature vs time profiles during a typical calcination driven by concentrated solar radiation in CaL-TCES (a) and CaL-CCSU (b) experiments.

reactor was then cooled down to 650 °C to eventually start a new carbonation/calcination loop.

The experimental procedure followed during CaL-CCSU tests differs from that followed in the CaL-TCES tests. Apart from the different operating conditions established during the calcination step, previously discussed, during the first calcination step limestone was fed when the bed temperature reached 875 °C. Moreover, between each carbonation and the subsequent calcination step, the reactor was rapidly heated from 730 to 850 °C, using the radiant heaters and the gas preheater, while the sorbent was exposed to the gas stream with an inlet CO_2 concentration of $70\%_v$. This intermediate step ensured that solar irradiation during the calcination extended for the same time interval as in TCES experiments (20 min). Notably, no significant chemical reactions took place during this intermediate step, as the material was already carbonated and the temperature was not high enough to promote calcination.

During the experimental tests, time-resolved profiles of bed temperature and of CO_2 concentration at the exhaust were continuously recorded at a sampling frequency of 1 Hz by a data logging system, using data acquisition and postprocessing protocols developed in the LabVIEW environment. The CO_2 concentration data were worked out to calculate the carbonation degree of the material after each carbonation step.

Some experiments, according to either the CaL-TCES or the CaL-CCSU test protocol, were performed after the transparent window at the top of the reactor had been removed, in order to obtain IR thermographic maps of the temperature distribution on the exposed surface of the FB during solar-assisted calcination.

Finally, sorbent samples were retrieved from the bed after selected calcination steps in both CaL-CCSU and CaL-TCES tests. These samples, carefully separated from the inert silica sand by sieving, were subjected to N_2- and Hg-intrusion porosimetric analyses to investigate the evolution of the material specific surface area and pore size distribution upon iterated cycles. Samples were degassed at 200 °C for 12 h before N_2-intrusion porosimetry. Data of N_2-intrusion were postprocessed with the Brunauer–Emmett–Teller (BET) theory to obtain the specific surface area and with the Barrett–Joyner–Halenda (BJH) theory on the desorption curve to obtain the pore size distribution.

4. RESULTS AND DISCUSSION

4.1. Temperature Distribution during Solar-Driven Calcination. A reference temperature distribution in the bed was characterized by keeping the reactor at the set temperature by means of the radiant heaters and of the gas preheater only, that is, without radiative contribution from the array of Xe lamps. Under these conditions, bed temperatures were fairly uniform and no appreciable temperature gradient could be detected. On the contrary, irradiation of the bed surface gives rise to measurable axial/radial temperature gradients that may affect the time–temperature history of the sorbent particles. Highly concentrated radiative fluxes induce local overheating of the FB surface, whose extent decreases with increasing fluidization gas velocity and as the collection of the incident radiation changes from a surface-receiver to a volumetric-receiver pattern.[23] Bed surface overheating also has a detrimental effect on the reactivity of solid particles, similar to that of higher temperature on increased sintering phenomena.[20,21] The temperature time series recorded during selected calcination stages according to either the TCES or the CCSU test protocols are reported in Figure 5. Temperature profiles refer to bed and surface temperatures recorded during a typical calcination step.

Both diagrams refer to the fourth calcination step, that was fully representative of other calcination steps, and report: (a) the temperature measured in the "up" location (i.e., just below the bed surface) by means of the K-type thermocouple (blue curve); (b) the temperature measured by the IR camera and averaged over the whole FB surface (reactor surface; black curve); (c) the temperature measured by the IR camera and averaged over a circular region of about 25 mm centered on the FB surface (center surface; orange dots). The solar simulator is powered on after about 100 s and powered off after about 1300 s (total time of 20 min). It is recalled that tests aimed at characterizing the bed surface temperature by thermography were performed after removing the upper transparent enclosure of the reactor. Accordingly, it was not possible to record the exhaust CO_2 concentration, as the measure was affected by contamination of air from the environment. Temperature profiles recorded under CaL-TCES conditions (Figure 5a) display an apparent endotherm in the 180 s < t < 300 s range, presumably associated with the rapid course of calcination under CO_2-lean conditions, that is not observed under CaL-CCSU conditions (Figure 5b). Table 2 reports time-averaged temperatures in the range of 200 s < t < 1200 s.

Table 2. Time-Averaged Temperatures in the 200−1200 s Time Interval Recorded Inside the FB and on the FB Surface during a Typical Calcination Step in the CaL-TCES and CaL-CCSU Tests

position	mean temperature [°C] CaL-TCES	mean temperature [°C] CaL-CCSU
"up" thermocouple	826 ± 30	943 ± 6
whole FB surface	876 ± 23	993 ± 11
center of FB surface	907 ± 22	1026 ± 20

In both operating conditions, the average bed surface temperature exceeds that measured inside the bed by nearly 50 °C due to the high concentrated radiation incident on the FB surface. Overheating may become as large as 80 °C in the central area of the bed surface due to uneven surface distribution of the incident flux. Data obtained in CCSU conditions agree with those reported in a previous study.[21]

4.2. CO_2 Uptake and Sorbent Carbonation Degree.

Figure 6 reports the carbonation degree of the limestone sorbent after the carbonation stage for the 20 reaction cycles. Data points refer to both CaL-TCES and CaL-CCSU operating conditions. Each point of the graph is an average value of three independent experimental tests. Reproducibility of experimental data is confirmed by the relatively small values of standard deviations.

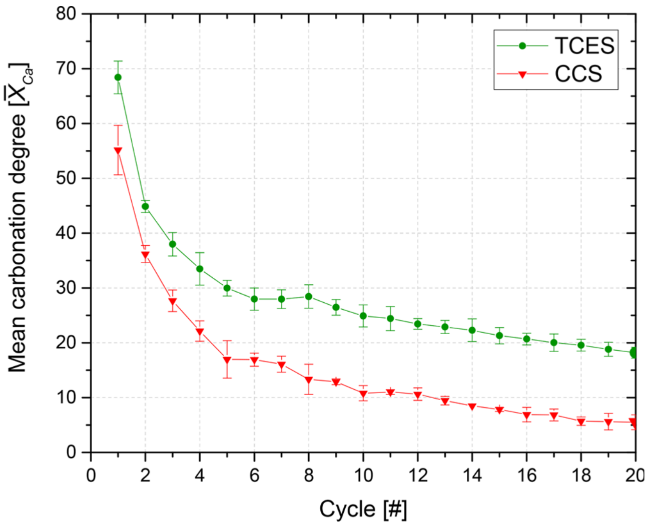

Figure 6. Mean carbonation degree ($\bar{X}_{Ca}$) as a function of the loop cycle for all the tests performed under CaL-TCES and CaL-CCSU conditions.

As expected, the degree of sorbent carbonation, hence CO_2 uptake, declines upon iterated calcination−carbonation cycles. The decrease is very pronounced at first and becomes moderate during the last reaction cycles. A remarkable difference of CO_2 uptake is observed when comparing results obtained under CaL-TCES and CaL-CCSU operating conditions. The value of $\bar{X}_{Ca}$ obtained in CaL-TCES tests is larger than that achieved under CaL-CCSU conditions at the same reaction step. $\bar{X}_{Ca}$ is 33%, 23%, and 18%, respectively, during the fourth, twelfth, and twentieth reaction cycles in CaL-TCES tests. As a comparison, the corresponding values recorded in CaL-CCSU tests were 22%, 11%, and 6%. Altogether, the difference in the mean carbonation degree averaged over all the 20 cycles is about 13%.

Porosimetric characterization of sorbent samples at different stages along with conversion was accomplished using N_2- and Hg-intrusion porosimetry. This analysis is helpful to scrutinize sorbent deactivation over iterated cycling, as well as the different behavior of the sorbent in the two reactive conditions. Figure 7 reports the data of the differential intrusion vs pore diameter, as obtained from N_2 (Figure 7a) and Hg (Figure 7b) porosimetry, for samples processed in both TCES and CCSU conditions.

The inspection of Figure 7a,b suggests that

(i) In TCES samples, the porosity is mostly developed around a characteristic pore diameter of 20−30 nm.

(ii) In CCSU samples, the porosity is shifted toward larger values as compared with results obtained in TCES samples. The mode of the pore size distribution is equal to about 70−80 nm.

(iii) For both TCES and CCS samples, the cumulative pore volume decreases over repeated cycling, as a result of thermal sintering effects that cause the loss in sorbent reactivity (see Figure 6).

Values of sorbent specific surface area, as obtained from BET postprocessing of N_2-intrusion porosimetry data, are shown in Figure 8 as a function of the reaction cycle.

A progressive decrease of the specific surface area with increasing reaction cycles is observed for both TCES and CCSU samples. The decrease is more pronounced during the first reaction cycles and much milder during the last reaction cycles, which recalls in a certain way the trend of the mean carbonation degree over cycling (Figure 6). Moreover, the specific surface area of the samples obtained from the CCSU experiments is always quite lower than that of the corresponding TCES samples.

Both the higher values of the specific surface area and the lower values of the characteristic pore sizes contribute to explain the higher reactivity of samples looped in TCES conditions. The higher temperature and the larger concentrations of CO_2 experienced by the sorbent during calcination in CCSU conditions should induce, since the first reaction cycle, the formation of a more sintered and compact structure that hinders CO_2 diffusion and reduces sorbent uptake.

4.3. Density of Energy Storage.

Data on sorbent carbonation degree and CO_2 uptake can be processed to assess the energy storage density of sorbents looped in both TCES and CCSU conditions. The energy storage density cumulates contributions from the accumulation of latent and sensible heats of the carrier. The first contribution comes from the calcined core of the material that, reacting with CO_2, releases the chemical energy stored. The latter contribution is due to the excess sensible enthalpy of the material with respect to that at the discharge temperature (650 °C in both the process layouts). It is now worth noting that, under TCES conditions, higher mean carbonation degrees are achieved, which lead to higher latent

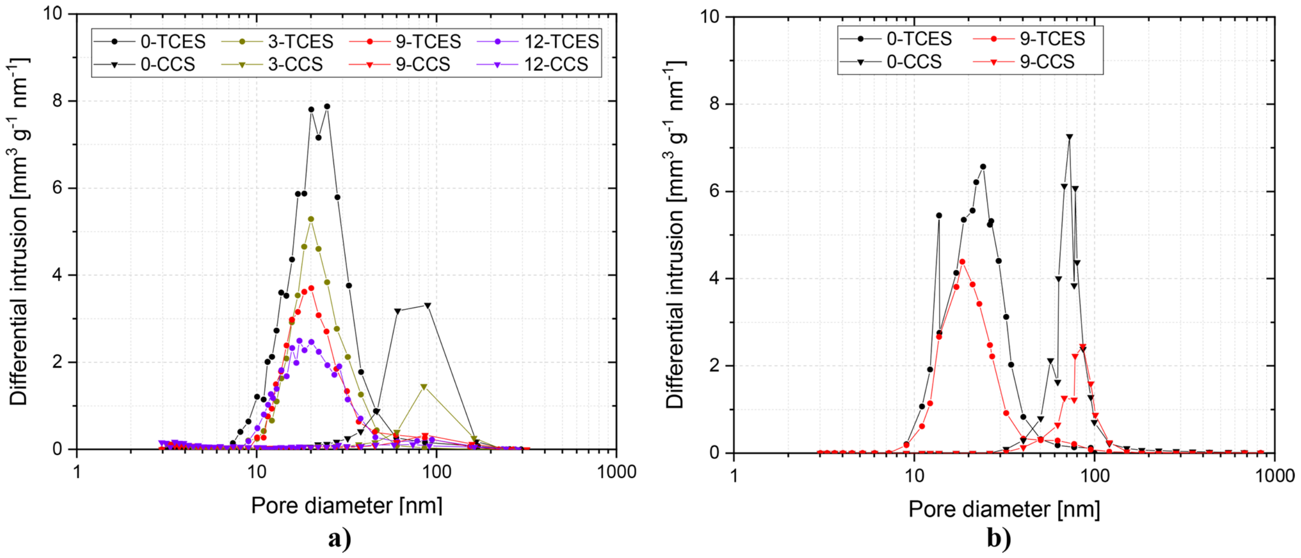

Figure 7. Differential intrusion vs pore diameter from N_2-intrusion porosimetric data elaborated with BJH theory (a) and Hg-intrusion porosimetric data (b). Data refer to samples calcined after different cycle numbers.

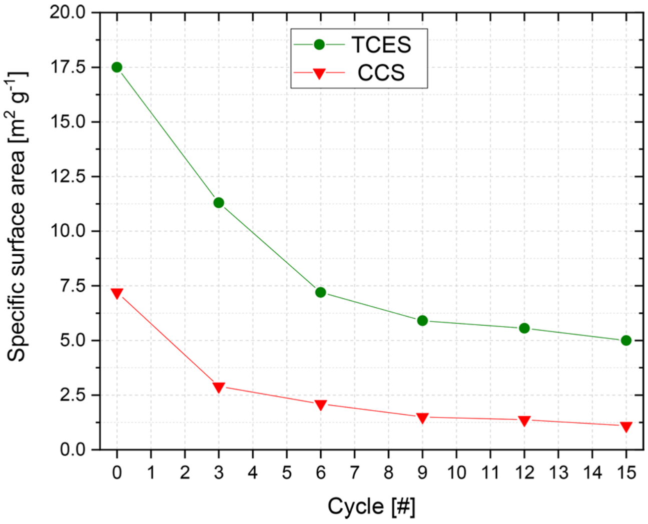

Figure 8. BET specific surface area of calcined samples vs reaction cycle for both TCES and CCSU experiments.

heat contributions. On the other side, under CCSU conditions, the higher temperatures employed during calcination produce a greater contribution of sensible energy storage.

Figure 9 reports the energy storage density of the sorbent subjected to prescribed reaction cycles. Contributions to energy storage due to the latent heat of reaction and sensible heat are separately shown. The energy storage density at a given cycle is computed considering the average sorbent carbonation degree up to that reaction cycle. Data reported in the chart have been calculated using, as input data, a latent heat of reaction at 650 °C of 178 kJ mol^{-1}, an average specific heat of 1 kJ kg^{-1} °C^{-1}, a bulk density of 1400 kg m^{-3}, and a $CaCO_3$ purity for the limestone of 98.5%$_{wt}$.

The inspection of the diagram suggests the following conclusions:

(i) The energy storage density decreases over repeated cycling. This effect is more pronounced during the first reaction cycles and becomes milder upon further cycling. The decrease is related to the loss of CO_2 uptake sorbent capacity upon repeated cycles due to sorbent sintering and resembles the trends of mean carbonation degree.

(ii) The energy storage density of samples looped in TCES conditions is always larger than that of the corresponding CCSU samples.

(iii) TCES samples feature a larger share of latent heat storage, which is the most stable form of energy storage, than CCSU samples. For instance, in the first and twentieth TCES cycle, the latent heat contributes 87% and 73%, respectively, compared with 78% and 50% in the corresponding CCSU cycles.

By considering a sorbent with a mean average life of 10 and 20 cycles, the energy storage density, including contributions of latent and sensible heat, is about 1130 and 962 MJ m^{-3}, respectively, under TCES operating conditions. It is 960 and 777 MJ m^{-3} under CCSU conditions. These figures are slightly higher than the sensible heat storage capacity obtained with molten salts, whose value ranges between 730 and 900 MJ m^{-3} according to different sources.[1,59,60] It should also be considered that, in the CaL-TCES process, thermal energy is released at a much higher and constant temperature (650 °C), a feature that positively affects the thermodynamics of thermal energy conversion to power.[61] Moreover, a relevant share of the stored energy is retained as chemical energy, which is inherently more stable than sensible heat over time.

Altogether, TCES of solar energy via the proposed CSP-CaL integration appears to be feasible and characterized by remarkable peculiarities with respect to the molten salt technology. The mean average life cycle of the particles is a key parameter for the success of the technology. The average life of 20 reaction cycles considered here, obtained by taking into account a makeup of fresh limestone and a purge of exhaust material equal to about 5% of the looping streams, guarantees a successful integration. Extrapolation of experimental data, performed by considering the last decay of sorbent reactivity, indicates that, after 30 reaction cycles, the mean energy storage density is about 850 MJ m^{-3} for the TCES operating condition, thus still slightly higher than that of the molten salts. It is recalled that, as described in Section 2, purged spent limestone can be exploited in the cement industry as raw material for Portland

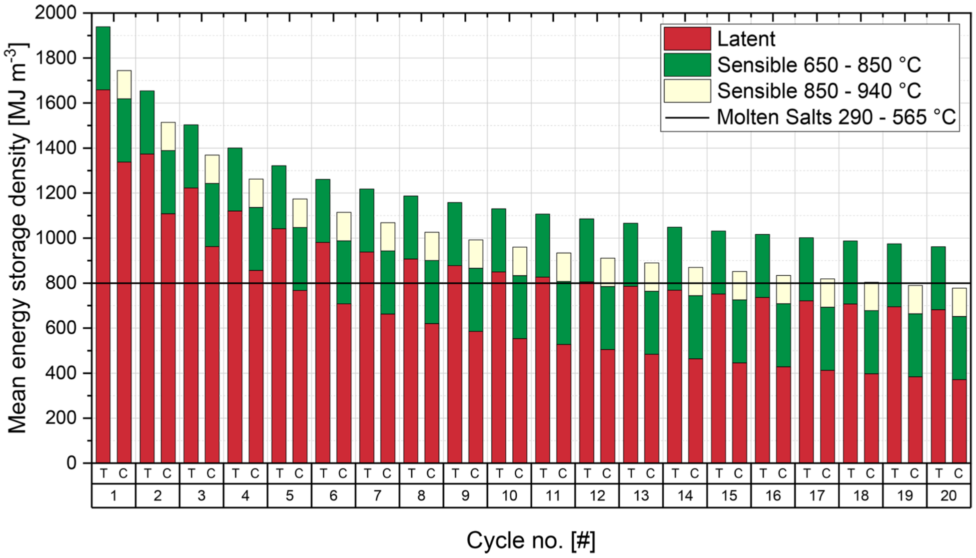

Figure 9. Energy storage density as a function of the reaction cycle for both CaL-TCES (T) and CaL-CCSU (C) processes.

cement production[53] or physically/chemically reactivated[54,55] and reintroduced into the looping cycle.

5. CONCLUSIONS

Integration between concentrated solar power (CSP) and calcium looping (CaL) has been experimentally characterized in a lab-scale FB reactor heated by direct concentrated radiation from a simulated solar source. Two different sets of process conditions were scrutinized, the first one consistent with a prevailing thermochemical energy storage (TCES) target and the second consistent with a prevailing carbon capture and sequestration or utilization (CCSU) target.

The experimental campaign aimed at characterizing the CO_2 uptake capacity of the sorbent over multiple iterated CaL cycles. Experimental results indicated that CaL under TCES conditions gives rise to a more reactive sorbent, characterized by larger carbonation degrees, larger specific surface area, and smaller values of characteristic pore size diameter, as inferred by the N_2- and Hg-intrusion porosimetry, as compared with CCSU. The better performance of the sorbent under TCES conditions was ascribed to the lower temperature experienced by the sorbent during calcination. On the contrary, the higher temperature and CO_2 concentration experienced by the sorbent during calcination in CaL-CCSU mode gives rise, since the early stages, to the formation of a more sintered and compact structure that hinders CO_2 diffusion and reduces the sorbent reactivity.

Temperature mapping of the FB during solar-assisted calcination in either CaL-TCES or CaL-CCSU modes indicated that overheating of the bed surface with respect to the bulk of the bed by about 50 °C occurred. The excess temperature was about 80 °C in the central area of the bed surface, where radiative flux was maximum.

The density of solar energy storage associated with CSP-CaL integration was assessed by working out the measured CO_2 sorbent uptake. Energy storage densities in the range of 960−1130 MJ m^{-3} were obtained under CaL-TCES conditions (by considering sorbent uptake after 10−20 cycles). Correspondingly, the energy storage density under CCSU conditions was of the order of 780−960 MJ m^{-3}. These figures are slightly higher than those obtained by sensible heat storage of solar energy with molten salts in the range of 290−565 °C. Moreover, compared with molten salts, the CaL option features better stability of the storage in the long term and higher temperature level at which the stored energy may be exchanged.

The comparison between alternative CaL-TCES and CaL-CCSU schemes for CSP-CaL integration suggests that CaL-TCES warrants the largest energy storage density, especially as far as the more stable storage by latent heat of reaction is considered. On the other hand, the CaL-CCSU option takes full advantage of the overall reduction of the carbon footprint of the integrated process, through capture of concentrated CO_2, though at the expense of a moderate reduction of the energy storage density. Whether the CaL-TCES or the CaL-CCSU alternative pathways should be undertaken is critically dependent on the process background and, in particular, on the feasibility of the CO_2 sequestration or reuse options if a concentrated stream of CO_2 is generated by CSP-CaL integration.

■ AUTHOR INFORMATION

Corresponding Author

*E-mail: piero.salatino@unina.it.

ORCID

Fabio Montagnaro: 0000-0002-6377-3989
Piero Salatino: 0000-0002-0002-1691

Notes

The authors declare no competing financial interest.

■ ACKNOWLEDGMENTS

The support of Mr. Luciano Cortese (IRC CNR) in Hg porosimetry analyses and of Dr. Paola Giudicianni (IRC CNR) in N_2 porosimetry analyses is gratefully acknowledged.

■ REFERENCES

(1) Gil, A.; Medrano, M.; Martorell, I.; Lázaro, A.; Dolado, P.; Zalba, B.; Cabeza, L. F. State of the art on high temperature thermal energy storage for power generation. Part 1−Concepts, materials and modellization. *Renewable Sustainable Energy Rev.* **2010**, *14*, 31−55.

(2) Chen, X.; Zhang, Z.; Qi, C.; Ling, X.; Peng, H. State of the art on the high-temperature thermochemical energy storage systems. *Energy Convers. Manage.* **2018**, *177*, 792−815.

(3) Sunku Prasad, J.; Muthukumar, P.; Desai, F.; Basu, D. N.; Rahman, M. M. A critical review of high-temperature reversible thermochemical energy storage systems. *Appl. Energy* **2019**, *254*, 113733.

(4) André, L.; Abanades, S.; Flamant, G. Screening of thermochemical systems based on solid-gas reversible reactions for high temperature solar thermal energy storage. *Renewable Sustainable Energy Rev.* **2016**, *64*, 703−715.

(5) Bayon, A.; Bader, R.; Jafarian, M.; Fedunik-Hofman, L.; Sun, Y.; Hinkley, J.; Miller, S.; Lipiński, W. Techno-economic assessment of solid−gas thermochemical energy storage systems for solar thermal power applications. *Energy* **2018**, *149*, 473−484.

(6) Carrillo, A. J.; González-Aguilar, J.; Romero, M.; Coronado, J. M. Solar energy on demand: a review on high temperature thermochemical heat storage systems and materials. *Chem. Rev.* **2019**, *119* (7), 4777−4816.

(7) Alonso, E.; Romero, M. Review of experimental investigation on directly irradiated particles solar reactors. *Renewable Sustainable Energy Rev.* **2015**, *41*, 53−67.

(8) Ho, C. K. A review of high-temperature particle receivers for concentrating solar power. *Appl. Therm. Eng.* **2016**, *109*, 958−969.

(9) Ho, C. K. Advances in central receivers for concentrating solar applications. *Sol. Energy* **2017**, *152*, 38−56.

(10) Kang, Q.; Dewil, R.; Degrève, J.; Baeyens, J.; Zhang, H. Energy analysis of a particle suspension solar combined cycle power plant. *Energy Convers. Manage.* **2018**, *163*, 292−303.

(11) Kang, Q.; Flamant, G.; Dewil, R.; Baeyens, J.; Zhang, H. L.; Deng, Y. M. Particles in a circulation loop for solar energy capture and storage. *Particuology* **2019**, *43*, 149−156.

(12) Reed, S.; Sugo, H.; Kisi, E. High temperature thermal storage materials with high energy density and conductivity. *Sol. Energy* **2018**, *163*, 307−314.

(13) Zhang, H.; Benoit, H.; Perez-Lopèz, I.; Flamant, G.; Tan, T.; Baeyens, J. High-efficiency solar power towers using particle suspensions as heat carrier in the receiver and in the thermal energy storage. *Renewable Energy* **2017**, *111*, 438−446.

(14) Chirone, R.; Salatino, P.; Ammendola, P.; Solimene, R.; Magaldi, M.; Sorrenti, R.; De Michele, G.; Donatini, F. Development of a novel concept of solar receiver/thermal energy storage system based on compartmented dense gas fluidized beds. In *Proceedings of the 14th International Conference on Fluidization − from fundamentals to products*; Engineering Conferences International: New York, 2013; pp 95−102.

(15) Salatino, P.; Ammendola, P.; Bareschino, P.; Chirone, R.; Solimene, R. Improving the thermal performance of fluidized beds for concentrated solar power and thermal energy storage. *Powder Technol.* **2016**, *290*, 97−101.

(16) Almendros-Ibáñez, J. A.; Fernández-Torrijos, M.; Díaz-Heras, M.; Belmonte, J. F.; Sobrino, C. A review of solar thermal energy storage in beds of particles: Packed and fluidized beds. *Sol. Energy* **2019**, *192*, 193.

(17) Briongos, J. V.; Gómez-Hernández, J.; González-Gómez, P. A.; Serrano, D. Two-phase heat transfer model of a beam-down gas-solid fluidized bed solar particle receiver. *Sol. Energy* **2018**, *171*, 740−750.

(18) Benoit, H.; Pérez López, I.; Gauthier, D.; Sans, J. L.; Flamant, G. On-sun demonstration of a 750°C heat transfer fluid for concentrating solar systems: Dense particle suspension in tube. *Sol. Energy* **2015**, *118*, 622−633.

(19) Bellan, S.; Matsubara, K.; Seok Cho, H.; Gokon, N.; Kodama, T. A CFD-DEM study of hydrodynamics with heat transfer in a gas-solid fluidized bed reactor for solar thermal applications. *Int. J. Heat Mass Transfer* **2018**, *116*, 377−392.

(20) Tregambi, C.; Montagnaro, F.; Salatino, P.; Solimene, R. Directly irradiated fluidized bed reactors for thermochemical processing and energy storage: Application to calcium looping. *AIP Conf. Proc.* **2016**, *1850*, 090007-1−090007-8.

(21) Tregambi, C.; Montagnaro, F.; Salatino, P.; Solimene, R. An experimental characterization of Calcium Looping integrated with concentrated solar power. *Chem. Eng. J.* **2018**, *331*, 794−802.

(22) Tregambi, C.; Montagnaro, F.; Salatino, P.; Solimene, R. Solar-driven torrefaction of a lignin-rich biomass residue in a directly irradiated fluidized bed reactor. *Combust. Sci. Technol.* **2019**, *191* (9), 1609−1627.

(23) Tregambi, C.; Chirone, R.; Montagnaro, F.; Salatino, P.; Solimene, R. Heat transfer in directly irradiated fluidized beds. *Sol. Energy* **2016**, *129*, 85−100.

(24) Migliozzi, S.; Paulillo, A.; Chirone, R.; Salatino, P.; Solimene, R. Hydrodynamics of compartmented fluidized beds under uneven fluidization conditions. *Powder Technol.* **2017**, *316*, 476−491.

(25) Abanades, S.; André, L. Design and demonstration of a high temperature solar heated rotary tube for continuous particles calcination. *Appl. Energy* **2018**, *212*, 1310−1320.

(26) Sebastian Gonzalez, R.; Flamant, G. Technical and economic feasibility analysis of using concentrated solar thermal technology in the cement production process: hybrid approach − a case study. *J. Sol. Energy Eng.* **2014**, *136*, 025001-1−025001-12.

(27) Meier, A.; Bonaldi, E.; Cella, G. M.; Lipinski, W.; Wuillemin, D. Solar chemical reactor technology for industrial production of lime. *Sol. Energy* **2006**, *80*, 1355−1362.

(28) Tregambi, C.; Solimene, R.; Montagnaro, F.; Salatino, P.; Marroccoli, M.; Ibris, N.; Telesca, A. Solar-driven production of lime for ordinary Portland cement formulation. *Sol. Energy* **2018**, *173*, 759−768.

(29) Moumin, G.; Tescari, S.; Sundarraj, P.; de Oliveira, L.; Roeb, M.; Sattler, C. Solar treatment of cohesive particles in a directly irradiated rotary kiln. *Sol. Energy* **2019**, *182*, 480−490.

(30) Oliveira, F. A. C.; Fernandes, J. C.; Galindo, J.; Rodríguez, J.; Cañadas, I.; Vermelhudo, V.; Nunes, A.; Rosa, L. G. Portland cement clinker production using concentrated solar energy − A proof-of-concept approach. *Sol. Energy* **2019**, *183*, 677−688.

(31) Jordán, P. S.; Eduardo, A. M. J.; Zdzislaw, M. C.; Martín, Z. G. A.; Liborio, H. P.; Antonio, F. Z. J.; Román, D. G. M. Techno-economic analysis of solar-assisted post-combustion carbon capture to a pilot cogeneration system in Mexico. *Energy* **2019**, *167*, 1107−1119.

(32) Wang, F.; Deng, S.; Zhao, J.; Wang, J.; Sun, T.; Yan, J. Performance and economic assessments of integrating geothermal energy into coal-fired power plant with CO_2 capture. *Energy* **2017**, *119*, 278−287.

(33) Parvareh, F.; Sharma, M.; Qadir, A.; Milani, D.; Khalilpour, R.; Chiesa, M.; Abbas, A. Integration of solar energy in coal-fired power plants retrofitted with carbon capture: A review. *Renewable Sustainable Energy Rev.* **2014**, *38*, 1029−1044.

(34) Liu, Y.; Deng, S.; Zhao, R.; He, J.; Zhao, L. Energy-saving pathway exploration of CCS integrated with solar energy: A review of innovative concepts. *Renewable Sustainable Energy Rev.* **2017**, *77*, 652−669.

(35) Coppola, A.; Scala, F.; Salatino, P. Characterization of calcium looping sorbents with a novel twin bed reactor. *Fuel Process. Technol.* **2018**, *172*, 49−54.

(36) Matthews, L.; Lipiński, W. Thermodynamic analysis of solar thermochemical CO_2 capture via carbonation/calcination cycle with heat recovery. *Energy* **2012**, *45*, 900−907.

(37) Reich, L.; Yue, L.; Bader, R.; Lipiński, W. Towards solar thermochemical carbon dioxide capture via calcium oxide looping: a review. *Aerosol Air Qual. Res.* **2014**, *14*, 500−514.

(38) Tregambi, C.; Montagnaro, F.; Salatino, P.; Solimene, R. A model of integrated calcium looping for CO_2 capture and concentrated solar power. *Sol. Energy* **2015**, *120*, 208−220.

(39) Zhai, R.; Li, C.; Qi, J.; Yang, Y. Thermodynamic analysis of CO_2 capture by calcium looping process driven by coal and concentrated solar power. *Energy Convers. Manage.* **2016**, *117*, 251−263.

(40) Zhang, X.; Liu, Y. Performance assessment of CO_2 capture with calcination carbonation reaction process driven by coal and concentrated solar power. *Appl. Therm. Eng.* **2014**, *70*, 13−24.

(41) Alovisio, A.; Chacartegui, R.; Ortiz, C.; Valverde, J. M.; Verda, V. Optimizing the CSP-calcium looping integration for thermochemical energy storage. *Energy Convers. Manage.* **2017**, *136*, 85−98.

(42) Chacartegui, R.; Alovisio, A.; Ortiz, C.; Valverde, J. M.; Verda, V.; Becerra, J. A. Thermochemical energy storage of concentrated solar

power by integration of the calcium looping process and a CO_2 power cycle. *Appl. Energy* **2016**, *173*, 589−605.

(43) Edwards, S. E. B.; Materić, V. Calcium looping in solar power generation plants. *Sol. Energy* **2012**, *86*, 2494−2503.

(44) Ortiz, C.; Romano, M. C.; Valverde, J. M.; Binotti, M.; Chacartegui, R. Process integration of Calcium-Looping thermochemical energy storage system in concentrating solar power plants. *Energy* **2018**, *155*, 535−551.

(45) Sarrion, B.; Valverde, J. M.; Perejon, A.; Perez-Maqueda, L.; Sanchez-Jimenez, P. E. On the multicycle activity of natural limestone/dolomite for thermochemical energy storage of Concentrated Solar Power. *Energy Technology* **2016**, *4*, 1013−1019.

(46) Benitez-Guerrero, M.; Valverde, J. M.; Sanchez-Jimenez, P. E.; Perejon, A.; Perez-Maqueda, L. A. Multicycle activity of natural $CaCO_3$ minerals for thermochemical energy storage in Concentrated Solar Power plants. *Sol. Energy* **2017**, *153*, 188−199.

(47) Benitez-Guerrero, M.; Sarrion, B.; Perejon, A.; Sanchez-Jimenez, P. E.; Perez-Maqueda, L. A.; Valverde, J. M. Large-scale high-temperature solar energy storage using natural minerals. *Sol. Energy Mater. Sol. Cells* **2017**, *168*, 14−21.

(48) Benitez-Guerrero, M.; Valverde, J. M.; Sanchez-Jimenez, P. E.; Perejon, A.; Perez-Maqueda, L. A. Calcium-Looping performance of mechanically modified Al_2O_3-CaO composites for energy storage and CO_2 capture. *Chem. Eng. J.* **2018**, *334*, 2343−2355.

(49) Sarrión, B.; Perejón, A.; Sánchez-Jiménez, P. E.; Pérez-Maqueda, L. A.; Valverde, J. M. Role of calcium looping conditions on the performance of natural and synthetic Ca-based materials for energy storage. *Journal of CO2 Utilization* **2018**, *28*, 374−384.

(50) Sánchez Jiménez, P. E.; Perejón, A.; Benítez Guerrero, M.; Valverde, J. M.; Ortiz, C.; Pérez Maqueda, L. A. High-performance and low-cost macroporous calcium oxide based materials for thermochemical energy storage in concentrated solar power plants. *Appl. Energy* **2019**, *235*, 543−552.

(51) Benitez-Guerrero, M.; Valverde, J. M.; Perejon, A.; Sanchez-Jimenez, P. E.; Perez-Maqueda, L. A. Low-cost Ca-based composites synthesized by biotemplate method for thermochemical energy storage of concentrated solar power. *Appl. Energy* **2018**, *210*, 108−116.

(52) Romeo, L. M.; Lara, Y.; Lisbona, P.; Escosa, J. M. Optimizing make-up flow in a CO_2 capture system using CaO. *Chem. Eng. J.* **2009**, *147*, 252−252.

(53) Telesca, A.; Calabrese, D.; Marroccoli, M.; Tomasulo, M.; Valenti, G. L.; Duelli, G.; Montagnaro, F. Spent limestone sorbent from calcium looping cycle as a raw material for the cement industry. *Fuel* **2014**, *118*, 202−205.

(54) Coppola, A.; Palladino, A.; Montagnaro, F.; Scala, F.; Salatino, P. Reactivation by steam hydration of sorbents for fluidized-bed Calcium Looping. *Energy Fuels* **2015**, *29*, 4436−4446.

(55) Erans, M.; Manovic, V.; Anthony, E. J. Calcium looping sorbents for CO_2 capture. *Appl. Energy* **2016**, *180*, 722−742.

(56) Kunii, D.; Levenspiel, O. *Fluidization Engineering*, 2nd ed.; Wiley: New York, 1991.

(57) Coppola, A.; Montagnaro, F.; Salatino, P.; Scala, F. Fluidized bed calcium looping: The effect of SO_2 on sorbent attrition and CO_2 capture capacity. *Chem. Eng. J.* **2012**, *207*−*208*, 445−449.

(58) Coppola, A.; Esposito, A.; Montagnaro, F.; Iuliano, M.; Scala, F.; Salatino, P. The combined effect of H_2O and SO_2 on CO_2 uptake and sorbent attrition during fluidised bed calcium looping. *Proc. Combust. Inst.* **2019**, *37*, 4379−4387.

(59) González-Roubaud, E.; Pérez-Osorio, D.; Prieto, C. Review of commercial thermal energy storage in concentrated solar power plants: Steam vs. molten salts. *Renewable Sustainable Energy Rev.* **2017**, *80*, 133−148.

(60) ENEA. Solar thermal energy production: guidelines and future programmes of ENEA; 2001; http://www.solaritaly.enea.it/Documentazione/Solar%20Thermal%20Energy%20Production.pdf.

(61) Ortiz, C.; Chacartegui, R.; Valverde, J. M.; Alovisio, A.; Becerra, J. A. Power cycles integration in concentrated solar power plants with energy storage based on calcium looping. *Energy Convers. Manage.* **2017**, *149*, 815−829.

AIP Conference Proceedings

Limestone calcination–carbonation in a fluidized bed reactor/receiver for thermochemical energy storage applications

Cite as: AIP Conference Proceedings **2126**, 210008 (2019); https://doi.org/10.1063/1.5117757

Claudio Tregambi, Francesca Di Lauro, Fabio Montagnaro, et al.

View Online

Export Citation

ARTICLES YOU MAY BE INTERESTED IN

Directly irradiated fluidized bed reactors for thermochemical processing and energy storage: Application to calcium looping

AIP Conference Proceedings **1850**, 090007 (2017); https://doi.org/10.1063/1.4984456

Experimental characterization of granular materials for directly irradiated fluidized bed solar receivers

AIP Conference Proceedings **2126**, 030060 (2019); https://doi.org/10.1063/1.5117572

Off-design model of concentrating solar power plant with thermochemical energy storage based on calcium-looping

AIP Conference Proceedings **2126**, 210006 (2019); https://doi.org/10.1063/1.5117755

AIP Publishing

Limestone Calcination–Carbonation in a Fluidized Bed Reactor/Receiver for Thermochemical Energy Storage Applications

Claudio Tregambi[1, a)], Francesca Di Lauro[2], Fabio Montagnaro[3], Piero Salatino[1] and Roberto Solimene[2]

[1]Dipartimento di Ingegneria Chimica, dei Materiali e della Produzione Industriale, Università degli Studi di Napoli Federico II, Piazzale Vincenzo Tecchio 80, 80125 Napoli (Italy).
[2]Istituto di Ricerche sulla Combustione, Consiglio Nazionale delle Ricerche, Piazzale Vincenzo Tecchio 80, 80125 Napoli (Italy).
[3]Dipartimento di Scienze Chimiche, Università degli Studi di Napoli Federico II, Complesso Universitario di Monte Sant'Angelo, 80126 Napoli (Italy).

[a)]Corresponding author: claudio.tregambi@unina.it

Abstract. Concentrating Solar Power (CSP) systems represent a key technology to exploit solar energy thanks to the easy integration with energy storage systems. The thermochemical energy storage (TCES) relies on reversible chemical reactions to store the solar energy in the form of chemical bonds. Limestone calcination/carbonation is an appealing reaction for TCES. This cycle has been widely studied in the Calcium Looping (CaL) process for Carbon Capture and Sequestration/Use (CCS/U), within which the calcination is usually carried out in a CO_2-rich environment at temperature of 940–950 °C. When the CaL cycle is considered for TCES, the energy required by the calciner is supplied by CSP and the whole system has to work in a closed loop, as the CO_2 released during the calcination is required for the subsequent carbonation. Therefore, the operating conditions resemble those typical of the CCS/U CaL. The novel idea of this work is to perform a CaL-TCES cycle working in an open loop configuration, by coupling the system with a CO_2 emitting industry. Calcination can then be accomplished under air atmosphere at lower temperature, thus preserving to some extent the material reactivity. In particular, the open loop CaL-TCES cycle has been experimentally investigated using a Fluidized Bed (FB) reactor directly heated by a solar simulator (3 MW m^{-2} peak flux, 3 kW_{th} total power). Several looping cycles have been carried out on a commercial limestone sample to estimate the sorbent reactivity over cycling. The properties of calcined sorbents have been investigated by chemical physical analyses. A comparison with results obtained under CCS/U CaL conditions has also been performed, to scrutinize the potential advantages of working in an open loop configuration.

INTRODUCTION

Extensive R&D is in progress to exploit the huge amount of solar energy falling on Earth. Concentrating Solar Power (CSP) is a fast-growing renewable technology in which the solar energy, upon concentration, is focused onto a receiver whence it is converted to electricity or industrial process heat. With respect to photovoltaic, CSP can exploit the whole solar spectrum. Moreover, CSP can be easily integrated with energy storage systems relying on sensible, latent and thermochemical energy storage (TCES) [1]. TCES is a quite complex technology, but rewards with high density of energy storage and improved stability over long time-scales, as the incident energy is stored in the noble form of chemical bonds [2–3]. Several kinds of processes for TCES are currently worldwide investigated, and most of them involve gas/solid chemical reactions. Therefore, a system able to work both as solar receiver and chemical reactor could provide unquestionable advantages in the economy of the process. Dense gas–solid Fluidized Beds (FBs) fit well the requirements of solar receiver in CSP systems thanks to their large heat transfer and thermal diffusivities coefficients [4–6], and can also provide an ideal environment to carry out the heterogeneous gas/solid reactions

SolarPACES 2018
AIP Conf. Proc. 2126, 210008-1–210008-8; https://doi.org/10.1063/1.5117757
Published by AIP Publishing. 978-0-7354-1866-0/$30.00

required for TCES. In solar FB, the interaction between the incident radiative flux and the FB can occur in an indirect or direct way. The direct heating configuration permits higher operating temperatures as the high concentrated solar radiation directly heats the dense suspension, but care must be paid to avoid the bed surface overheating [7–9]. Uneven and unsteady fluidization are currently investigated to limit the time and spatial temperature non-homogeneity and to avoid the thermo mechanical stresses to the reactor wall or to the ancillary equipment [7,9–11].

Limestone calcination/carbonation is an appealing reaction for TCES due to the cheapness of the raw material and the interesting reaction enthalpy at fairly high process temperatures. This cycle has been widely studied in the Calcium Looping (CaL) process for Carbon Capture and Sequestration/Use (CCS/U), within which the calcination is usually carried out in a CO_2-rich environment at temperature of 940–950 °C. In last years, a possible integration between a CaL cycle for CCS/U with a CSP system has been investigated by several research groups [12–16]. When the CaL cycle is considered for TCES, the whole system has to work in a closed loop as the CO_2 released during the calcination is required for the subsequent carbonation: the operating conditions resemble those typical of the CCS/U CaL and compressors/tanks are needed to store both $CaO/CaCO_3$ and CO_2. Integration between CSP and the CaL cycle for TCES is widely investigated in recent literature [17–22]. Sarrion et al. [19] and Benitez Guerrero et al. [20] are investigating a CaL-TCES process in which the calcination is performed at low temperature (725 °C) using He as gas carrier, whereas the carbonation is performed at high temperature (850 °C) using a pure CO_2 stream. Our idea is to perform a CaL-TCES cycle without recovering the CO_2 released, working in an open loop configuration. Calcination can then be accomplished under air atmosphere at lower temperature, thus preserving the material reactivity over cycling. Moreover, compressors/tanks for CO_2 are no longer necessary. In our proposed process scheme, CO_2 required for the carbonation is provided by coupling the CaL-TCES cycle with CO_2 emitting industries (combustion power plants, cement production plants). In a previous work [9], we experimentally investigated the integration of CSP with the CaL cycle in reactive conditions relevant to CCS/U. Particular attention was paid on the effect that the overheating of the FB upper surface – induced by the impinging concentrated solar radiation – has on the material reactivity. Instead, in this work, the open loop CaL-TCES cycle has been experimentally investigated using a FB reactor directly heated by a solar simulator (3 MW m^{-2} peak flux, 3 kW$_{th}$ total power). Reactive conditions during calcination are much milder than those applied in [9]. Several looping cycles have been performed on a commercial limestone to evaluate the evolution of the sorbent reactivity over cycling. Chemical physical analyses have been also performed to investigate the properties of the calcined sorbents. The results obtained have been eventually compared with those obtained under CCS/U CaL calcination conditions (940 °C, 70%$_v$ CO_2 atmosphere), to scrutinize the advantage, mostly in terms of sorbent reactivity, of performing the CaL-TCES cycle in an open loop configuration.

EXPERIMENTAL

Experimental Apparatus and Materials

The experimental apparatus used in the present work is reported in Fig. 1-a.

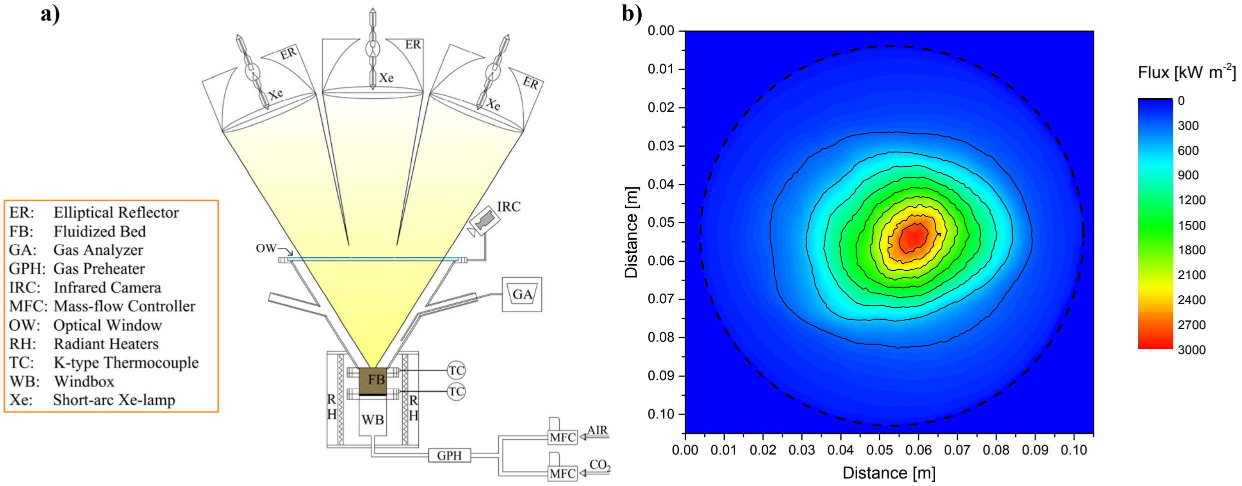

FIGURE 1. a) Outline of the experimental apparatus and its ancillary equipment; b) Distribution of the radiative flux incident onto the bed surface. The dashed circle represents the internal boundary of the reactor.

It consists of a FB reactor with an internal bed diameter of 0.102 m and a height of 0.1 m. The wind-box section is 0.15 m high. The upper part of the FB reactor is connected to a conically-shaped section, 0.4 m high, which represents the freeboard. The upper section of the freeboard is confined by a ceramic glass optical window through which the simulated solar radiation enters the bed. The window has a thickness of 4 mm and a maximum operating temperature of 700 °C. The transmittance of this glass is about 0.9 in the spectral range between 340 μm and 2350 μm. The conical shape of the upper freeboard ensures that there is no restriction to the radiative flux. Moreover, it promotes effective settlement of the particles ejected by bubble eruptions so that the transparent window can be kept clean. The gas discharge port is located at mid-level in the freeboard conical section so that entrainment of solid particles ejected by bubble bursting and impact of finer particles with the upper transparent window are minimized. The solar concentrated radiation is simulated by an array of three short arc Xe lamps of 4 kW_{el} each, coupled with elliptical reflectors. The spatial distribution of the incident radiative flux, measured following an experimental procedure detailed in a previous work [9], is shown in Fig. 1-b. The peak flux is of approximately 3000 kW m^{-2}, a value typical of research-oriented applications of CSP to high-temperature thermochemical energy storage, whereas the total irradiated power over the whole FB surface is of about 3.2 kW_{th}. The reactor is also surrounded by two semi cylindrical radiant heaters which accomplish two main tasks: i) heating of the reaction chamber, and ii) insulation of the internal chamber from the environment. A gas preheater may also be used to heat up the inlet gas stream up to 750 °C depending on the experimental requirements. The semi cylindrical heaters are driven by an ON/OFF PID controller connected to a K-type thermocouple located inside the bed, whereas gas preheating was regulated by acting on the applied voltage by means of a rheostat. Preheating of the fluidizing gas was used for better control and fine tuning of bed temperature. Finally, two electronic mass flow controllers were used to supply air and CO_2 to the reactor.

The reactor is equipped with two K-type thermocouples: one, termed "middle", located 0.05 m above the gas distributor and 0.05 m distant from the reactor wall; the second, termed "up", located 0.08 m above the gas distributor and 0.01 m from the reactor wall. Two Advance Optima ABB AO2020 (Uras 14 0–20$\%_v$ and Uras 14 0–100$\%_v$) analyzers were used to monitor the CO_2 concentration at the exhaust. Gas sampling is accomplished via a 6 mm stainless steel (ID 4 mm) probe, inserted in the reactor through one of the four outlet pipes and located at a level of 0.15–0.20 m above the bed surface. A suction pump is calibrated to sample at a rate of 0.050–0.060 Nm^3 h^{-1}. A steel wool filter is interposed between the pump and the reactor to avoid that fine solid particles reach the analyzer. The fluidized bed material consisted of a mixture of a Ca-based sorbent and of an inert granular material, sieved in the size range 420–590 μm and 850–1000 μm, respectively. The main properties of the materials are reported in Table 1, together with the theoretical value of minimum fluidization velocity (u_{mf}^{t}) evaluated according to the classical Wen and Yu equation. The inert material was silica sand from Ticino river (Italy), an alluvial origin sand, naturally rounded, polychrome in colour, which displays high thermo mechanical resistance up to 1700 °C. The sorbent was an Italian limestone (termed "Sardo") with a high $CaCO_3$ content, equal to about 98.5$\%_{wt}$.

TABLE 1. Selected properties of the sorbent and bed inert materials.

Material	Particle density [kg m^{-3}]	Size range [μm]	u_{mf}^{t} @ 650–950 °C [m s^{-1}]
Sardo limestone	2200	420–590	0.09–0.07
Ticino sand	2600	850–1000	0.32–0.27

Experimental Procedure and Operating Conditions

The experimental tests consisted of several consecutive calcination and carbonation cycles of the Sardo limestone. Tests were performed under different operating conditions, relevant to either CaL-CCS or CaL-TCES applications. In both cases, the carbonation was performed during a heating step from about 600 °C to 715 °C and using a gas stream with a CO_2 concentration of 15 $\%_v$. Concerning the calcination, a bulk bed temperature of 940–950 °C and an inlet CO_2 concentration of 70$\%_v$ were used for the CaL-CCS experiments, whereas a bulk bed temperature of 850–860 °C and a gas stream consisting of atmospheric air were used for the CaL-TCES tests. The temperature of 850–860 °C is the temperature required to have a calcination rate, under an air stream, comparable to that experienced at 940–950 °C under a gas stream with a CO_2 concentration of about 70$\%_v$. This temperature value was estimated by ad hoc performed kinetic measurements in a small FB reactor on the Sardo limestone. In each experimental test, a bed inventory of 850 g was used, consisting in 730 g of inert sand (served as thermal flywheel) and 120 g of reactive limestone. The fluidizing velocity was always set at 0.6 m s^{-1} during carbonation and calcination, a value approximately twice the minimum fluidization velocity of the inert sand. Both reactions were performed in the same FB reactor previously described (Fig. 1-a) by alternating the operating conditions between that of carbonation and that of calcination. In all the tests, consistently with realistic conditions of CaL-CSP coupling, only the calcination step was performed under radiative flux. Thermal supply in the other stages of the experiments was ensured by the radiant heaters and the gas preheater. It is worth noting that the use of radiant heaters during carbonation is here required only because of the laboratory scale of the experimental facility, and because of the dilution of the bed inventory with an 85%$_{wt}$ of inert silica sand. In an industrial-scale plant, the system would be completely autothermal and energy would have to be extracted with an internal heat exchanger during occurrence of the carbonation reaction. During a typical CaL-TCES test, the bed was charged with about 730 g of inert sand and heated up to 730–750 °C by using both the radiant heaters and the gas preheater. Atmospheric air was used as fluidizing gas. Once the pre-set temperature was reached, the radiant heaters were powered off and, simultaneously, a sample of 120 g of limestone was fed to the reactor and the solar simulator was powered on. A time of 15 min was waited to perform the calcination reaction (calcination zero), after which the solar simulator was powered off and the reactor cooled down to 600 °C. Once reached the pre-set temperature, the reactor was heated up again to 715 °C by using the radiant heaters and the gas preheater. During this step, the reactor was fluidized using a gas stream with an inlet CO_2 concentration of 15 %$_v$ to perform the carbonation reaction (carbonation step). Then, once the 715 °C was reached, the radiant heaters were powered off and, simultaneously, the inlet gas stream was switched to atmospheric air and the solar simulator was powered on for 20 min to perform the calcination reaction and complete the reaction cycle (calcination step). The reactor was then cooled down to 600 °C to eventually start a new carbonation/calcination loop. The experimental procedure applied during a typical CaL-CCS tests only slightly differs from the one just described for the CaL-TCES tests. The main relevant differences, besides the different operating conditions applied for the calcination reaction which have been already detailed above, are the following: i) to perform the calcination zero, the reactor was heated up to 875 °C prior to the limestone feeding; ii) after the carbonation step and prior to the calcination step, the reactor was rapidly heated from 750 °C to 850 °C by using the radiant heaters and the gas preheater under a gas stream with an inlet CO_2 concentration of 70%$_v$. During this intermediate step, no significant chemical reactions take place as the material is already carbonated and the temperature level are not sufficiently high to promote the calcination reaction. A sketch of the experimental procedure in the partial pressure of CO_2 (P_{CO_2}) vs. temperature diagram is reported in Fig. 2.

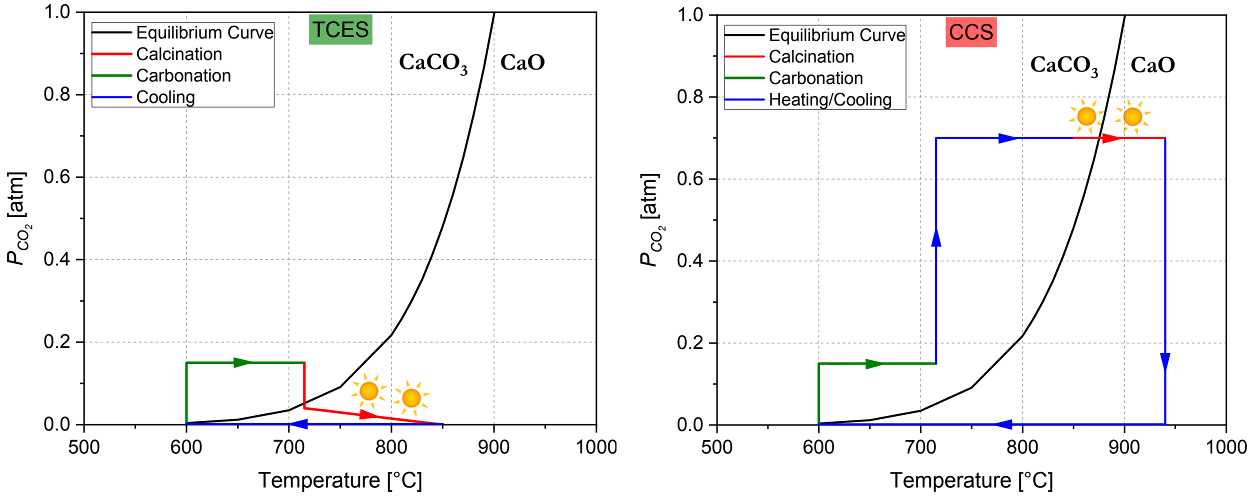

FIGURE 2. Path of experimental procedure applied during CaL-TCES (left) and CaL-CSS (right) cycles, viewed in the partial pressure of CO_2 (P_{CO_2}) vs. temperature diagram. The figures report also the equilibrium curve of $CaCO_3$ decomposition.

During the experimental tests, time-resolved profiles of in-bed temperatures and CO_2 concentration of the exhaust gas were continuously acquired at a sampling frequency of 1 Hz by a data logging system and an ad hoc procedure developed in the LabVIEW environment. The CO_2 concentration data were post processed to evaluate the carbonation degree of the material after each carbonation step. In order to process the data, a first carbonation/calcination loop was performed without charging the limestone material to measure the response in time domain of the reactor under blank conditions. Through this data it was eventually possible to disclose the time profile of the reacted CO_2, and evaluate the overall CO_2 reacted or released, according to the following equation:

$$Reacted\ or\ Released\ CO_2 = \pm \int_{t=t_0}^{t=t_F} (F_{CO_2,IN} - F_{CO_2,OUT})dt = \pm \int_{t=t_0}^{t=t_F} \Delta F_{CO_2}\, dt \tag{1}$$

where $F_{CO_2,IN}$ and $F_{CO_2,OUT}$ are the molar flow of CO_2 at reactor inlet and outlet, respectively, ΔF_{CO_2} is their difference, and t_0 and t_F are the time instant at which reactions begin and end, respectively.

Moreover, sorbent samples were recovered after selected calcination step in both CaL-CCS and CaL-TCES tests. These samples, carefully separated from the inert silica sand by sieving and manual inspection, were subjected to N_2 porosimetric analyses to investigate the evolution of the material specific surface area/pore size distribution and scrutinize potential differences between CaL-CCS and CaL-TCES samples.

RESULTS AND DISCUSSION

A Complete Calcination-Carbonation Cycle

Figure 3 reports the chart plot of the calcination zero followed by a typical carbonation and calcination cycle for the CaL-TCES tests. The red curve refers to the temperature read by the "up" thermocouple, while the black curve refers to the CO_2 concentration of the exhaust gas. The limestone is fed to the reactor at about 500 s, and its injection is easily recognized by the steep temperature decrease, whose value reaches approximately 650 °C. Subsequently, immediately after the limestone feeding, the temperature of the system rapidly increases to about 860 °C due to the ignition of the solar simulator. The calcination reaction begins as soon as the material is fed to the system, as highlighted by the sharp increase of the CO_2 concentration in the exhaust gas. It can also be observed that the calcination reaction hampers the temperature increase, whose growth is slowed down especially between 775 °C and 820 °C. The solar simulator is powered off at about 1500 s, and the reactor is cooled down to approximately 600 °C in 2000 s. Then, at about 3500 s, the reactor is heated again up to 715 °C using the radiant heaters and the gas preheater while being fluidized with a gas stream containing an inlet CO_2 concentration of $15\%_v$. During this step the carbonation reaction occurs, as clearly highlighted by the sharp increase of the temperature value due to the exothermic reaction. The time profile of the CO_2 concentration does not show clearly the carbonation reaction, whose effects are hidden in the relatively slow increase of the CO_2 concentration towards the stationary $15\%_v$ value. At about 4800 s, the gas stream is switched to atmospheric air and the solar simulator is powered on, so as to start the calcination reaction. The CO_2 concentration profile obtained, showing a decreasing-increasing-decreasing trend, is the result of two opposite effects, namely the decrease induced by the different composition of the gas stream fed to the reactor and the increase caused by the calcination of the carbonated material. On the other side, the ignition of the solar simulator is highlighted by the sharp temperature increase, whose value reaches about 850 °C in 10 min. Again, it is also possible to observe a slowdown in the temperature increase between 750 °C and 775 °C which can be attributed to the course of the fast step of the calcination reaction. A full carbonation calcination cycle has then an overall duration of about 75 min.

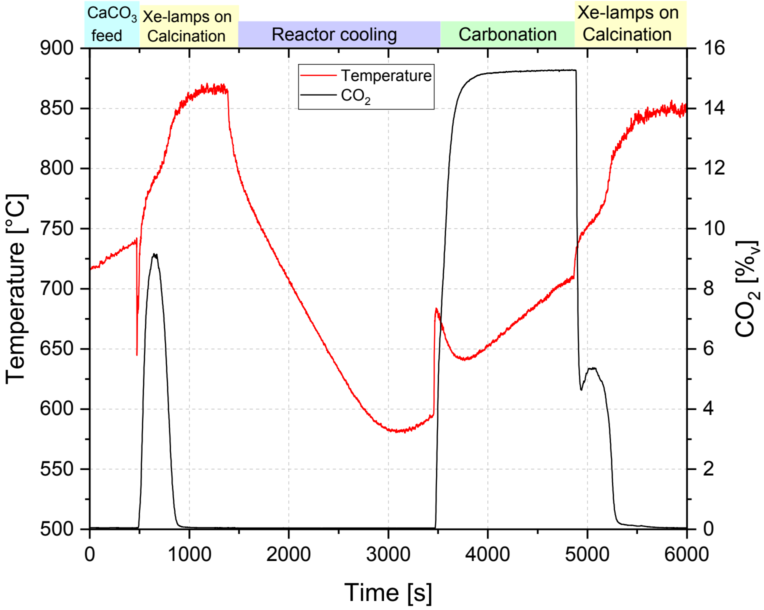

FIGURE 3. Plot of in-bed temperature and CO_2 concentration at the exhaust during a complete calcination-carbonation cycle.

The chart plot of the CaL-CCS tests shows no relevant differences with respect to the one shown in Fig. 3 for the CaL-TCES tests. The main differences are related to the calcination step, that is performed at higher temperature (940-950 °C) and with a CO_2 inlet concentration of $70\%_v$. Moreover, a heating step from 750 to 850 °C is performed after the carbonation step and before the solar simulator ignition, as described before. This step is performed to keep the solar simulator on for the same 20 min time adopted in the tests performed under the CaL-TCES conditions. In the CaL-CCS tests a full carbonation calcination cycle has then a slightly longer duration, equal to about 100 min.

Detailed Analysis of a Typical Carbonation and Calcination Reaction

Figure 4-a shows the data related to the first carbonation reaction, after synchronization and subtraction of the CO_2 profile of the blank test. The time scale on the abscissa is the same of Fig. 3. It is possible to observe that the carbonation reaction starts as soon as the gas stream containing the CO_2 enters the reactor. The reaction is characterized by a first fast carbonation followed by a slower reaction step. Using the same approach (synchronization-subtraction of the blank test), it is also possible to disclose the data related to the calcination reaction, which are shown in Fig. 4-b. Again, the time scale on the abscissa is the same of Fig. 3. The overall CO_2 reacted/released, which can be estimated using Eq. (1), is highlighted in green in Fig. 4-a and in red in Fig. 4-b.

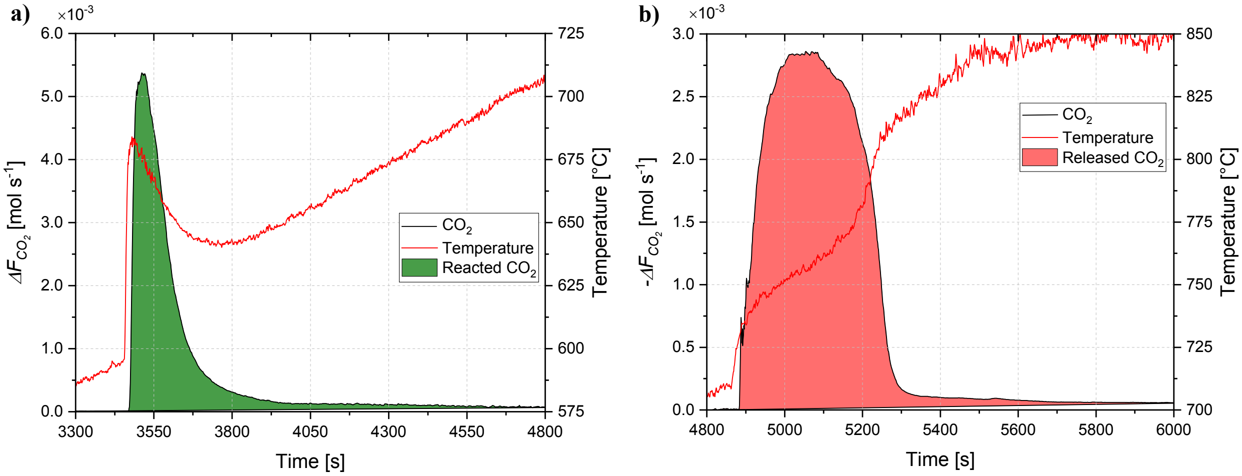

FIGURE 4. a) Time profile of CO_2 during the first carbonation (a) and calcination (b) reaction after data post-processing.

Evolution of the Mean Carbonation Degree

Figure 5 reports the mean carbonation degree ($\bar{X}_{Ca}$) as a function of the loop cycle for all the tests performed under CaL-TCES and CaL-CCS operating conditions. It can be observed that, as expected, the sorbent reactivity decreases with the progress of the reaction cycles. The decrease is very high during the first cycles and much less pronounced during last reaction cycles, thus suggesting a stabilization of the chemical physical properties of the reactive material. The gradual reduction of the reactivity can be correlated to the progressive thermal/chemical sintering to which the material undergoes, as documented in Fig. 6-a where the evolution of the material porosity for samples recovered after the calcination zero and four, for the test performed under CaL-TCES and CaL-CCS conditions, can be viewed. The plots highlight that, with the progress of the reaction cycles, the cumulative porosity of the material is progressively reduced, especially in the mesoporous range (Fig. 6-b).

The most interesting result is however related to the difference in the carbonation degree between the test performed under CaL-TCES and CaL-CCS operating conditions. The carbonation degree obtained under CaL-TCES is always remarkably higher than that achieved under CaL-CCS conditions. During the second and eighth carbonation, for example, the difference between the tests performed under the different conditions is equal to about 16% and 15%, respectively. This increased reactivity is probably the result of a less severe thermal sintering of the material looped under CaL-TCES conditions, due to the lower calcination temperature experienced. This explanation is strengthened by comparing the results of the porosimetric analyses of samples obtained under CaL-TCES and CaL-CCS at the same calcination stage (Fig. 6-a and 6-b). Indeed, it can be observed that the cumulative pore volume of the samples looped under CaL-TCES is always higher than that of the corresponding samples looped under CaL-CCS at the same cycle. These results should be considered only preliminary and further investigations will be carried out by collecting samples at different calcination stages and performing analyses also with the Hg-intrusion porosimetry technique to support the data of pore size distribution and evolution just discussed.

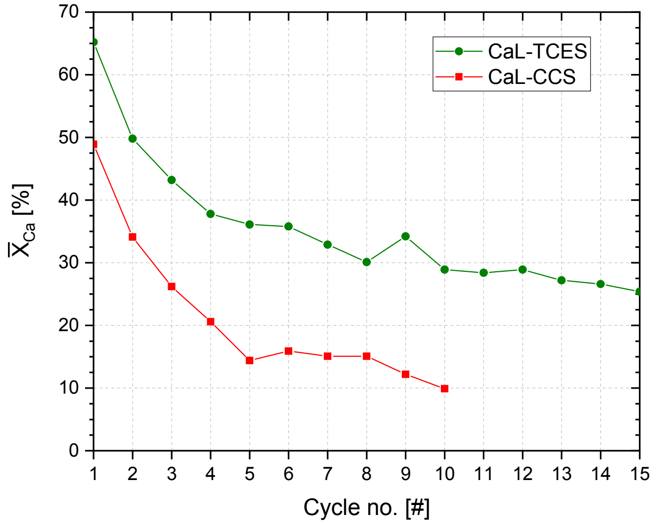

FIGURE 5. Mean carbonation degree vs. loop cycle for all the tests performed under CaL-TCES and CaL-CCS conditions.

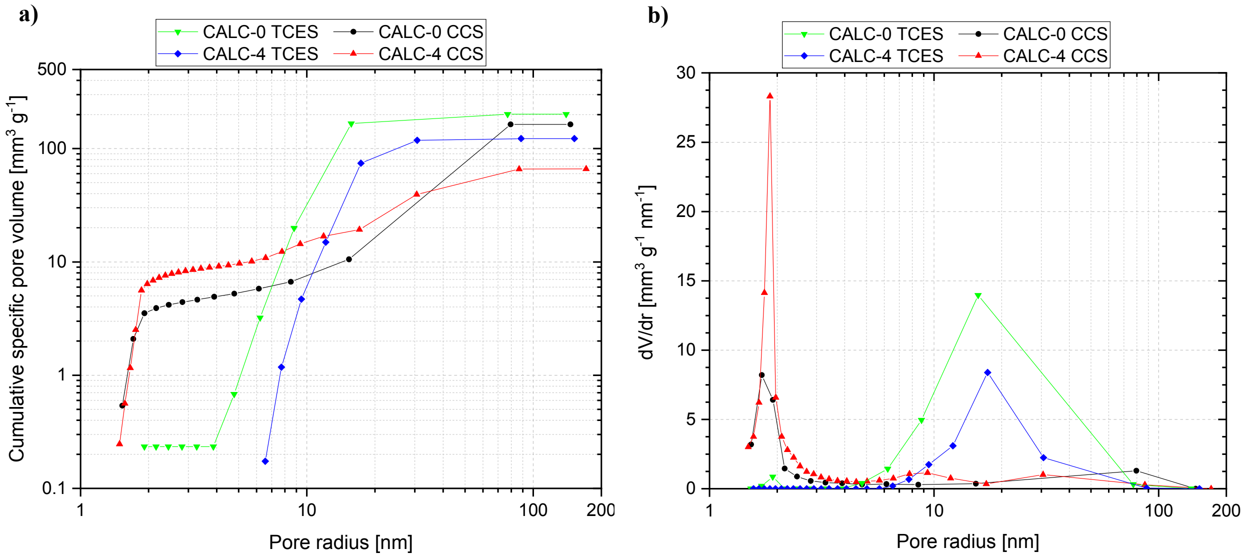

FIGURE 6. a) Cumulative distribution of pore volume vs. the pore radius for the test performed under both CaL-CCS and CaL-TCES conditions; b) First derivative of the data shown in a).

Overall, the increased reactivity of the limestone is an important result concerning the thermochemical storage of solar energy, as higher mean carbonation degree involves correspondingly higher density of energy storage. More into detail, the mean carbonation degree averaged over the 15 cycles performed is equal to about 35%. This corresponds to a density of energy storage of about 0.62 MJ $\mathrm{kg}_{\mathrm{CaCO_3}}^{-1}$ or 750 MJ $\mathrm{m}_{\mathrm{CaCO_3}}^{-3}$ (considering a bulk bed density of 1200 kg m^{-3}), if only the latent heat of the chemical reaction is considered. The value is increased up to 0.83 MJ $\mathrm{kg}_{\mathrm{CaCO_3}}^{-1}$ or 1000 MJ $\mathrm{m}_{\mathrm{CaCO_3}}^{-3}$ if also a contribution of sensible heat from 850 °C to 650 °C is contemplated. The density of energy storage obtained is comparable with that of a sensible heat storage system based on molten salts between 565 °C and 265 °C, which values about 900 MJ m^{-3} [1]. However, with the TCES system based on

$CaO/CaCO_3$, the energy is released at a much higher and constant temperature, and thus the efficiency of the inherent thermodynamic cycles for energy production can be accordingly higher [23].

CONCLUSIONS

In this work, the open loop CaL-TCES cycle has been experimentally investigated under realistic process conditions using a directly irradiated FB reactor. A $CaCO_3$ rich Italian natural limestone was used for the experimental tests. The carbonation reaction was carried out at a bulk bed temperature of 650 °C and using an inlet CO_2 concentration of 15%$_v$. Sorbent regeneration was instead performed heating the reactor through the solar simulator at a bulk bed temperature of 850 °C and using atmospheric air as fluidizing gas. Operating conditions relevant to CCS/U (940-950 °C and 70%$_v$ inlet CO_2 concentration) were also investigated for comparison purposes. Results obtained show that the mean carbonation degree of the sorbent looped under CaL-TCES conditions is always higher than that of the sorbent looped under CaL-CCS conditions. For example, taking as reference the 1st and 6th cycles, mean carbonation degree of 65% and 30% were obtained in TCES conditions and of 48% and 15% in CCS conditions. This difference in reactivity is probably ascribed to the milder calcination conditions experienced in the CaL-TCES tests. Porosimetric analyses performed on calcined samples support this explanation, as the sorbent looped in TCES conditions showed a higher cumulative specific pore volume, which is also more developed in the mesoporous region. For the TCES tests, the mean carbonation degree averaged over the 15 cycles performed is equal to 35%, which corresponds to a mean density of energy storage of about 1 GJ $m^{-3}_{CaCO_3}$. This value is comparable to that of the molten salts, but when exploiting the $CaO/CaCO_3$ cycle the energy can be released at a much higher temperature, with a corresponding increased efficiency of the thermodynamic cycle for energy production.

REFERENCES

1. A. Gil, M. Medrano, I. Martorell, A. Lázaro, P. Dolado, B. Zalba and L. F. Cabeza, Renew. Sust. Energ. Rev. **14**, 31–55 (2010).
2. L. André, S. Abanades and G. Flamant, Renew. Sust. Energ. Rev. **64**, 703–715 (2016).
3. A. Bayon, R. Bader, M. Jafarian, L. Fedunik-Hofman, Y. Sun, J. Hinkley, S. Miller and W. Lipiński, Energy **149**, 473–484 (2018).
4. J. A. Almendros-Ibáñez, M. Fernández-Torrijos, M. Díaz-Heras, J. F. Belmonte and C. Sobrino, Sol. Energy **In Press**.
5. J. V. Briongos, J. Gómez-Hernández, P. A. González-Gómez and D. Serrano, Sol. Energy **171**, 740–750 (2018).
6. S. Bellan, K. Matsubara, H. Seok Cho, N. Gokon and T. Kodama, Int. J. Heat Mass Tran. **116**, 377–392 (2018).
7. C. Tregambi, R. Chirone, F. Montagnaro, P. Salatino and R. Solimene, Sol. Energy **129**, 85–100 (2016).
8. C. Tregambi, F. Montagnaro, P. Salatino and R. Solimene, AIP Conf. Proc. **1850**, 090007-1–090007-8 (2017).
9. C. Tregambi, F. Montagnaro, P. Salatino and Solimene R., Chem. Eng. J. **331**, 794–802 (2018).
10. P. Salatino, P. Ammendola, P. Bareschino, R. Chirone and R. Solimene, Powder Technol. **290**, 97–101 (2016).
11. S. Migliozzi, A. Paulillo, R. Chirone, P. Salatino and R. Solimene, Powder Technol. **316**, 476–491 (2017).
12. L. Matthews and W. Lipiński, Energy **45**, 900–907 (2012).
13. L. Reich, L. Yue, R. Bader and W. Lipiński, Aerosol Air Qual. Res. **14**, 500–514 (2014).
14. C. Tregambi, F. Montagnaro, P. Salatino and R. Solimene, Sol. Energy **120**, 208–220 (2015).
15. R. Zhai, C. Li, J. Qi and Y. Yang, Energ. Convers. Manage. **117**, 251–263 (2016).
16. X. Zhang and Y. Liu, Appl. Therm. Eng. **70**, 13–24 (2014).
17. S. E. B. Edwards and V. Materić, Sol. Energy **86**, 2494–2503 (2012).
18. R. Chacartegui, A. Alovisio, C. Ortiz, J. M. Valverde, V. Verda and J. A. Becerra, Appl. Energ. **173**, 589–605 (2016).
19. B. Sarrion, J. M. Valverde, A. Perejon, L. Perez-Maqueda and P. E. Sanchez-Jimenez, Energy Technol. **4**, 1013–1019 (2016).
20. M. Benitez-Guerrero, J. M. Valverde, P. E. Sanchez-Jimenez, A. Perejon, L. A. Perez-Maqueda, Sol. Energy **153**, 188–199 (2017).
21. A. Alovisio, R. Chacartegui, C. Ortiz, J. M. Valverde and V. Verda, Energ. Convers. Manage. **136**, 85–98 (2017).
22. C. Ortiz, M. C. Romano, J. M. Valverde, M. Binotti and R. Chacartegui, Energy **155**, 535–551 (2018).
23. C. Ortiz, R. Chacartegui, J. M. Valverde, A. Alovisio and J. A. Becerra, Energ. Convers. Manage. **149**, 815–829 (2017).

Improving the Performances of Calcium Looping for Solar Thermochemical Energy Storage and CO_2 Capture

C. Tregambi
Dipartimento di Ingegneria
Università degli Studi del Sannio, Benevento, Italy
e–mail: claudio.tregambi@unisannio.it

F. Di Lauro, F. Montagnaro
Dipartimento di Scienze Chimiche
Università degli Studi di Napoli Federico II, Napoli, Italy
e–mail: francesca.dilauro2@unina.it, fabio.montagnaro@unina.it

R. Chirone, R. Solimene*
Istituto di Ricerche sulla Combustione
Consiglio Nazionale delle Ricerche, Napoli, Italy
e–mail: chirone@irc.cnr.it, roberto.solimene@cnr.it

P. Salatino
Dipartimento di Ingegneria Chimica, dei Materiali e della Produzione Industriale
Università degli Studi di Napoli Federico II, Napoli, Italy
e–mail: piero.salatino@unina.it

ABSTRACT

Concentrating solar thermal (CST) technologies for power production can play a key role in the future portfolio of renewable energies. Integration of CST with thermochemical energy storage (TCES) allows the achievement of high densities of energy storage and largely increases the dispatchability of solar energy. Limestone iterative calcination/carbonation, also known as Calcium Looping (CaL), is an appealing reaction for TCES, widely investigated in the scientific literature and with proven benefits with respect to current commercial technologies in terms of energy storage density. In this work, three different techniques aimed at improving the performances of CaL for integration with concentrated solar power (CSP) systems were investigated: i) lowering of calcination temperature; ii) precalcination; iii) use of a dolomite sorbent. Experimental tests were carried out in a lab-scale directly irradiated fluidized bed reactor, under realistic process conditions relevant to either TCES or carbon capture and storage/utilization (CCSU). Data were compared with those achieved in a previous study (reference case). Experimental results revealed that all the strategies investigated can increase the potentialities of the system in terms of energy storage density at least to some extent. Best results are obtained with the use of the dolomite sorbent, with an average increase of about 20% with respect to the reference case. N_2-physisorption analyses revealed that the increased reactivity arises from better microstructural properties in terms of specific surface. Lowering of calcination temperature and precalcination also produce benefits but with a lower extent. Optimal choice among the different strategies should take into account the intrinsic peculiarities of each investigated technique.

KEYWORDS

Calcination; Concentrated solar power; Concentrated solar thermal; Dolomite and limestone; Fluidized bed; Particle receiver; Precalcination; Solar energy.

INTRODUCTION

Current trends in European policy foresee an increasing share of renewables. Among them, solar energy displays a huge potentiality, as the amount of thermal radiation investing the Earth is far larger than the current world energy demand. Concentrating solar thermal (CST) systems represent an attractive technology for power production. In CST, solar energy is concentrated by means of optical sun tracking mirrors, called heliostats, and focused onto a receiver. Here, the concentrated solar energy is absorbed by a heat transfer medium and thus converted into medium-to-high temperature heat. This heat can be eventually used to drive a thermodynamic cycle for power production, or to sustain energy intensive physical and/or chemical processes. A key feature of CST systems is the integration with technologies for energy storage, which allow to decouple the two steps of solar energy collection and exploitation, thus greatly enhancing the dispatchability of the technology. Thanks to this feature, energy production by means of CST technologies can occur on demand, and CST can even be compared to base load power plants. The current benchmark in CST systems for power production is represented by the solar tower receiver with molten salts as heat transfer and energy storage media. The molten salts currently used are a binary mixture of $NaNO_3$ and KNO_3, capable of working within the 290−565 °C temperature range. Use of temperature values outside the range causes the salt solidification/thermal degradation and is thus ruled out. The relatively low upper temperature of the molten salts strongly impacts the overall efficiency of the technology. Moreover, since storage of energy is performed as sensible heat, the densities achieved are not very high, and the storage period is limited as well.

Research currently focuses on the development of alternative heat transfer media, capable of exceeding the temperature limit imposed by molten salts. Use of dense solid suspensions is widely investigated in the literature for this purpose. Several kinds of solid media can be safely used at steady-state temperatures even higher than 1000 °C, and have no limitations with regards to the lower temperature limit [1]. On the other side, research on more efficient technologies for energy storage is pursued. Thermochemical energy storage (TCES) is a promising technology relying on reversible chemical reactions to store the energy in the form of chemical bonds. Along the endothermic step, solar energy is collected, and reaction products are stored separately. Retrieval of stored energy is eventually accomplished by promoting, under proper operating conditions, the course of the reverse exothermic reaction. TCES is a more complex technology, but rewards with improved densities of energy storage and virtually unlimited time scale of energy storage and dispatchability. Chemical reactions frequently considered are hydration/dehydration [2], calcination/carbonation [3–6], oxidation/reduction [6,7] of metal hydroxides, carbonates and oxides. Alternative approaches are instead devoted to the production of solar fuels by means of coal/biomass torrefaction, pyrolysis [8], gasification processes [9] or H_2/CO production via H_2O/CO_2 splitting cycles and/or solar CH_4 reforming [10]. As many perspective TCES processes involve gas/solid chemical reactions, fluidized bed (FB) reactors represent a well-known, affordable and reliable system to exploit the remarkable properties of particle receivers while providing an ideal environment to sustain the heterogeneous chemical processes required for TCES [11,12].

Limestone iterative calcination/carbonation, also known as Calcium Looping (CaL), is an appealing reaction for TCES of solar energy. It features a high heat of reaction ($\Delta_r H° = 183\ \mathrm{kJ\ mol^{-1}}$), as requested for the achievement of large values of energy storage densities. Moreover, the raw material is cheap and widely available in nature. Coupling of CaL with concentrated solar power (CSP) systems is largely investigated in the literature for both TCES [3,5,13,14] and carbon capture and sequestration/utilization (CCSU) [5,15–17]. In this study, integration between CSP and CaL, aimed at both TCES and CCSU, was experimentally investigated in a directly irradiated 0.1 m ID FB reactor. This process was already tested in a previous study in which the performances of limestone over 20 reaction cycles, in terms of reactivity and attainable energy storage densities, were disclosed. In this work, the focus was the investigation of different measures to limit the loss of reactivity over cycling and maximize the densities of energy storage attainable within the CaL-CSP system. A different reactive material (Dolomite) was tested. Moreover, for limestone, use of both lower calcination temperatures and precalcination were investigated. Experimental results in terms of mean carbonation degree and attainable densities of energy storage over 20 iterated reaction cycles were obtained under realistic process conditions for the CSP-CaL integration. Finally, sorbent samples retrieved at different calcination stages were characterized with N_2-porosimetry analysis to further deepen correlation between material reactivity and microstructural properties.

EXPERIMENTAL

Experimental apparatus

The experimental apparatus used in the present work is depicted in Figure 1. It consists of a FB reactor with internal diameter and height equal to about 0.1 m. The bed aspect ratio is thus close to the unity value, a choice made to achieve the establishment of a single vortex ring that promotes mixing of bed solids at the bed scale. The lower section of the reactor, acting as wind-box, is 0.15 m high. The gas distributor, located at the upper end of the wind-box section, consists of a metallic porous plate with 0.5 mm holes drilled on a triangular pitch. The freeboard of the reactor is instead made of a conical section with a height of 0.4 m and an internal cone angle of about 30 °. A ceramic glass optical window, located at the upper end of the freeboard, seals the reactor environment. The conical shape of the freeboard is crucial to reduce the gas velocity and to allow disengagement of the solid particles transported by the fluidizing gas. In this way, it is possible to preserve the bed inventory and reduce scratches and fouling on the optical window. The gas discharge ports are located at midlevel in the freeboard conical section. Gases are fed to the reactor by means of dedicated electronic mass flow controllers, carefully calibrated for the specific gas.

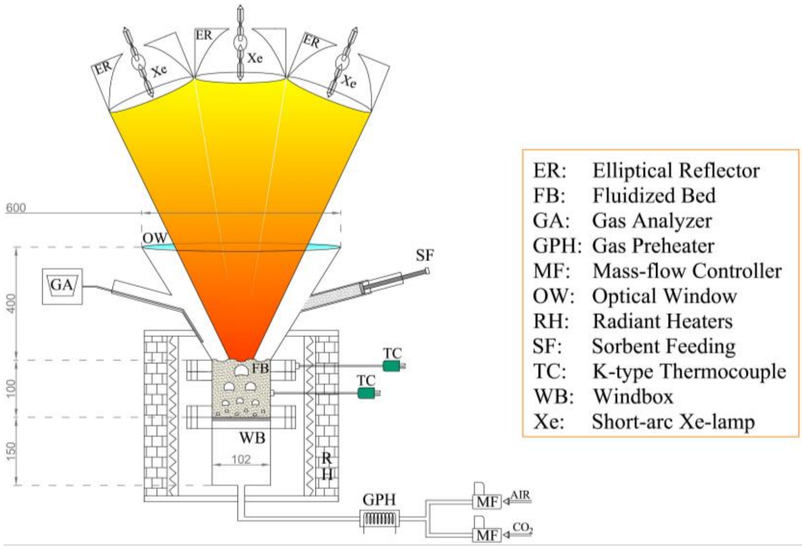

Figure 1. Experimental apparatus used in the present work. Dimensions in mm

Heating of the reactor is accomplished by means of:

i) preheating of the fluidizing gas, up to a maximum temperature of 750 °C, in a stainless-steel heat exchanger equipped with a serpentine-coil element as electric heater and regulated by means of a rheostat;

ii) two semicylindrical radiant heaters, which completely surround the wind-box and fluidized bed sections, and part of the conical section. The heaters are driven by an ON/OFF PID controller connected to a K-type thermocouple located inside the FB;

iii) a concentrated solar radiation, focused on the upper surface of the FB. The radiation is simulated by means of three short-arc Xe lamps, 4 kW_e each, carefully located in the focal point of the elliptical reflectors. Characterization of the simulated radiation on the FB surface was performed in a previous work [16]. The peak flux and total irradiated power are of about 3 MW m^{-2} and 3.2 kW_{th}, respectively.

The whole reactor is thermally insulated with multiple layers of rock wool blanket. The reactor is equipped with an array of K-type thermocouples, 1 mm diameter, located downstream of the gas preheater, in the wind-box section and in the FB reactor, to obtain measurements in the different key points. Moreover, CO_2 concentration at the exhaust was continuously monitored during the tests using an Advance Optima ABB AO2020 (Uras 14, 0−100$\%_v$) analyzer.

Materials

The bed material consisted of a mixture of silica sand and reactive sorbent. The silica sand represents an inert material within the process, and acts as a thermal flywheel to mitigate temperature variations during the occurrence of the chemical reactions. It features an excellent thermo-mechanical resistance up to 1700 °C and is naturally rounded and polychrome in color. It is of alluvial origin and comes from the Ticino river (Italy). The sand was ground and sieved in the 850−1000 μm range. Reactive materials consisted instead of:

i) an Italian natural limestone (termed “Sardo”), featuring a $CaCO_3$ content of 98.5$\%_{wt}$. This limestone was already used and characterized in a previous work [5];

ii) a dolomite sorbent, obtained from a mine close to the city of Caserta (Italy). The $CaCO_3$ content of this material is of 58.0$\%_{wt}$.

Both reactive materials were ground and sieved in the 420−590 μm range. Material properties are summarized in Table 1.

Table 1. Selected properties of the sorbent and bed inert materials

Material	Bulk density [kg m^{-3}]	Size range [μm]	u^t_{mf} @ 650–950 °C [m s^{-1}]	$CaCO_3$ content [$\%_{wt}$]
Limestone	1400	420–590	0.09–0.07	98.5
Dolomite	1400	420–590	0.09–0.07	57.5
Ticino sand	1500	850–1000	0.32–0.27	0

Experimental conditions and procedure

Experiments were aimed at testing different techniques to enhance the performances of the CSP-CaL integration. Operating conditions relevant to two different process schemes – “open loop” and “closed loop” – developed and extensively described in a previous study [5], were investigated. The open loop targets TCES. Calcination is performed using an air stream, and CO_2 leaving the calciner is released to the atmosphere. Integration with CO_2 emitting plants is mandatory to retrieve the stored energy at the exothermal stage. The closed loop targets both CCSU and TCES. Calcination is performed in a CO_2-rich environment and thus requires higher temperature with respect to the open loop. CO_2 leaving the calciner is stored. When used for TCES, closed loop does not require integration with CO_2 emitting plants. Data obtained in the same study [5], using limestone and a calcination temperature of 850 °C in air for the open loop, and of 940 °C in 70$\%_v$ CO_2 for the closed loop, set the reference baseline which results obtained in this work are compared to. Here, the following improvements were assessed for the open loop scheme:

i) using limestone, lowering of the calcination temperature in all reaction stages from 850 °C to 750 °C, to limit the effects of thermal sintering;
ii) using limestone, precalcination at 750 °C, followed by calcination stages at 850 °C. Precalcination was prolonged for either 25 min or 60 min;
iii) use of dolomite instead of limestone, with calcination stages at 850 °C.

With regards to the closed loop scheme:

i) using limestone, precalcination at 750 °C for 25 min, followed by calcination stages at 940 °C (reactive atmosphere of 70%$_v$ CO_2, as for the reference case);
ii) use of dolomite instead of limestone, with calcination stages at 940 °C (reactive atmosphere of 70%$_v$ CO_2).

Carbonation was always performed at about 650 °C and using a gas with an inlet CO_2 concentration of 15%$_v$, for both open and closed loop schemes, as in the reference study [5]. Enhancement techniques here investigated thus only act on the calcination step.

In all the tests performed, the fluidizing gas velocity was kept at 0.6 m s^{-1} during both carbonation and calcination, corresponding to nearly twice the minimum fluidization velocity of the inert sand. Under these conditions, the FB behaves as a bubbling fluidized bed reactor. A bed inventory of 850 g was used, consisting in 730 g of inert sand and 120 g of reactive sorbent. Carbonation and calcination were sequentially performed by alternating operating conditions relevant to each stage, until completion of 20 reaction cycles. To better simulate realistic CaL-CSP coupling, only the calcination step was sustained by simulated solar heating. In the other stages of the cycles, the reactor was thermally sustained by the radiant heaters and the gas preheater.

During a typical test for open loop configuration – case i), the bed was initially loaded with 730 g of inert sand and preheated up to 700 °C with both radiant and gas heaters. Atmospheric air was used as fluidizing gas. Once approached the set temperature, a sample of 120 g of sorbent was fed to the reactor through one of the gas discharge ports. At the same time, the solar simulator was turned on and the radiant heaters powered off. The calcination step was prolonged for 25 min. Eventually, all the heaters were powered off and the reactor was cooled down to 650 °C. Then, the reactor was heated up again to 700 °C with both radiant and gas heaters. During this step, a gas stream with an inlet CO_2 concentration of 15%$_v$ was used as fluidizing gas, so to perform the carbonation reaction. Input thermal power was tuned to make the carbonation step last 20 min. Then, radiant heaters were powered off and, simultaneously, the inlet gas stream was switched to atmospheric air and the solar simulator was powered on for 25 min, to perform the calcination reaction and complete the reaction cycle. Finally, the reactor was then cooled down to 650 °C to eventually start a new loop.

During tests for open loop configuration – case ii), the same experimental procedure was used, but the initial calcination was prolonged for 25 or 60 min according to the specific test. Subsequent solar calcination steps were performed at 850 °C and prolonged for 20 min.

For open loop configuration – case iii), initial preheating was stopped at 750 °C instead of 700 °C. All the calcination steps, initial one included, were performed at 850 °C and prolonged for 20 min.

Finally, for closed loop configuration, the experimental procedure only slightly differs. When precalcination was not performed (case ii)), initial preheating was arrested at 875 °C. For both cases, calcination steps (except the initial one for case i)) were performed at 940 °C in a reactive atmosphere of 70%$_v$ CO_2 and prolonged for 20 min. Moreover, between each carbonation and the subsequent calcination step, the reactor was rapidly heated from 700 °C to 850 °C, using the radiant heaters and the gas preheater, while the sorbent was exposed to the gas stream with an inlet CO_2 concentration of 70%$_v$. This intermediate step ensured that solar irradiation during the calcination extended for the same time interval of 20 min.

During each experimental test, time-resolved profiles of bed temperature and of CO_2 concentration at the exhaust were continuously recorded at a sampling frequency of 1 Hz by a data logging system, using data acquisition and postprocessing protocols developed in the LabVIEW environment. Sorbent samples were retrieved from the bed after selected calcination steps. These samples, carefully separated from the inert silica sand by sieving, were subjected to N_2-porosimetry analysis to investigate the evolution of the material specific surface area and pore size distribution. Samples were degassed at 200 °C for 12 h before porosimetry analyses. Data were post-processed with the Brunauer–Emmett–Teller (BET) theory to obtain the specific surface area, and with the Barrett–Joyner–Halenda (BJH) theory on the desorption curve to obtain the pore size distribution.

Data analysis

CO_2 concentration data were worked out to calculate the mean carbonation degree ($\bar{X}_{Ca}$) of the material after each carbonation step (*N*), as:

$$\bar{X}_{Ca}(N) = \frac{\int_{t_0}^{t_F}\left(F_{CO_2}^{IN} - F_{CO_2}^{OUT}\right)\mathrm{d}t}{\frac{m_0 x_{CaCO_3}}{PM_{CaCO_3}}} \qquad (1)$$

where $F_{CO_2}^{IN}$ and $F_{CO_2}^{OUT}$ is the molar flowrate of CO_2 at reactor inlet and outlet, respectively, t_0 and t_F are the time instant at which reaction begins and ends, respectively, m_0 is the initial mass of sorbent fed to the system, x_{CaCO_3} is the $CaCO_3$ mass fraction of the sorbent (see Table 1), PM_{CaCO_3} is the molecular weight of $CaCO_3$. Further details on the data analysis procedure can be found in a previous work [13]. Data of mean carbonation degree were eventually processed to assess the average density of energy storage (E_{SD}) vs the reaction step as:

$$E_{SD} = \Delta_r H\, \overline{X_{Ca,N}}\, \frac{\rho_{bulk}\, x_{CaCO_3}}{PM_{CaCO_3}} + \frac{\rho_{bulk}\overline{C_p}\left(T_{1st,CAL} - T_{CARB}\right) + \rho_{bulk}\overline{C_p}\left(T_{CAL} - T_{CARB}\right)(N-1)}{N} \qquad (2)$$

where $\Delta_r H$ is the latent heat of reaction at 650 °C (178 kJ mol^{-1}), ρ_{bulk} is the sorbent bulk density as in Table 1, $\overline{C_p}$ is the sorbent average specific heat (1 kJ kg^{-1} $°C^{-1}$), $T_{1st,CAL}$ and T_{CAL} are the temperature during the first and subsequent calcination steps, T_{CARB} is the temperature during the carbonation step (650 °C), and $\overline{X_{Ca,N}}$ is the average sorbent carbonation degree up to the reaction cycle considered, computed as:

$$\overline{X_{Ca,N}} = \frac{\sum_{N=1}^{N} \bar{X}_{Ca}(N)}{N} \qquad (3)$$

Values of energy storage density embody contributions from latent and sensible heats of the carrier. The first contribution arises from the calcined core of the material that, reacting with CO_2, releases the chemical energy previously stored upon calcination. The latter contribution is due to the excess sensible enthalpy of the material with respect to that at the discharge temperature.

RESULTS

Sorbent carbonation degree

Figure 2 shows the data of mean carbonation degree vs reaction stage, for the tests performed under operating conditions relevant to the open loop configuration. It appears that all the strategies provide some degree of advantage with respect to the reference case. For tests with limestone, the best performances are obtained when lowering the calcination temperature down to 750 °C. Under these conditions, the increase of $\overline{X_{Ca,N}}$ is remarkable and equals about 11.5% and 9.0% if N is 10 and 20, respectively.

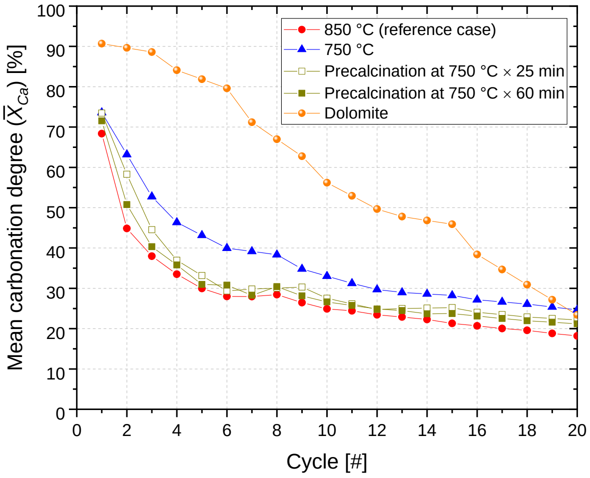

Figure 2. Mean carbonation degree vs reaction stage, open loop configuration

The higher reactivity is probably induced by a lower extent of the sintering phenomena that progressively deteriorate the micro- and meso- porosity of the material. Data of N_2-physisorption analysis post processed with BET (Table 2) support this claim. When calcined at lower temperature, limestone exhibits a larger specific surface after both the initial and third calcination step. Reactivity is thus increased, allowing the achievement of higher values of mean carbonation degree.

Table 2. Specific surface as obtained from BET post process of N_2-physisoprtion data

Calcination step [–]	**Specific surface [m^2 g^{-1}]**		
	850 °C (reference)	750 °C	Dolomite
0	17.5	29.3	37.0
3	11.3	16.3	23.6

Working at 750 °C is however not free from drawbacks, as it comes at the expense of a longer residence time in the calciner, induced by the inevitably lower kinetic rates. This is the reason for which limestone precalcination at 750 °C temperature, followed by standard looping cycles at 850 °C, was assessed. The rationale behind this approach is that of inducing the formation of a highly porous structure by first calcining the material at lower temperature, to then benefit of this structure even during the subsequent cycles at higher temperature. Data with a precalcination step of 25 and 60 min are shown in Figure 2 as well. The increase in the mean carbonation degree with respect to the reference case is more limited. Precalcination has an effect especially during the first cycles whereas, for higher numbers of looping stage, the values of mean carbonation degree mostly approach those obtained in the reference case. When precalcination is prolonged for 25 min, the increase of $\overline{X_{Ca,N}}$, which is of about 8.4% when the first 3 cycles are considered, decrease to 4.3% and 3.6% when 10 and 20 reaction cycles are, respectively, used. On the other side, when precalcination is prolonged for 60 min, the values become 3.8% (3 cycles), 2.3% (10 cycles) and 2.2% (20 cycles). Thus, prolonging of the precalcination step does not provide additional benefits into hardening/stabilization of the material microstructure and even brings to a worse reactivity. Finally, Figure 2 shows data obtained using the dolomite as reactive material, at the calcination temperature of 850 °C.

Values of carbonation degree achieved are far larger than any other case. A value of 90% is obtained during the first cycle, and the material appears to have a better resistance toward sintering phenomena, as the decay in reactivity over cycling is less severe. Altogether, the increase in carbonation degree with respect to the reference case is of 42% and 30% when data are averaged over 10 and 20 reaction cycles, respectively. The larger values of mean carbonation degree arise again from better microstructural properties (Table 2). Specific surface of calcined samples of dolomite is more than twice that of limestone samples processed under the same experimental conditions. It is believed that MgO crystals, which are inert within the given process conditions, inhibit the sintering phenomena and preserve the material reactivity over cycling [14,18]. Physisorption data were also post processed with BJH theory to assess if the limestone calcined at lower temperature, or the calcined samples of dolomite, developed a different characteristic dimension of pore diameter when compared to limestone calcined at 850 °C. Data of the differential intrusion vs pore diameter are shown in Figure 3 for samples retrieved after the initial calcination step. It appears that no remarkably differences are obtained in terms of pore dimensions. A characteristic pore diameter of about 20–30 nm is indeed observed for all samples.

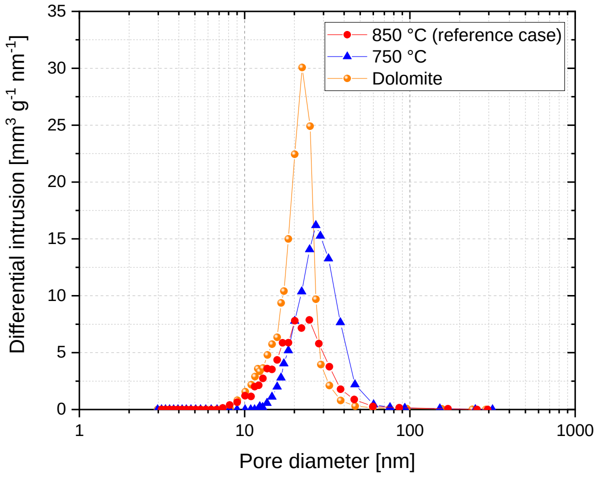

Figure 3. Differential intrusion vs pore diameter from N_2-physisorption data post processed with BJH theory. Data refer to samples after the initial calcination step

Figure 4 shows the data of mean carbonation degree vs reaction stage, for the tests performed in closed loop configuration.

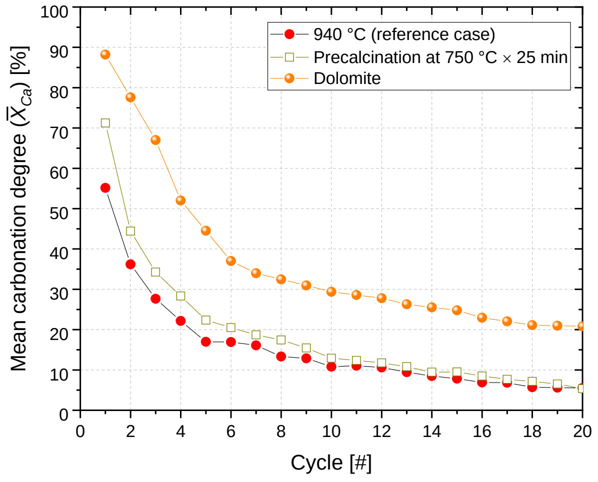

Figure 4. Mean carbonation degree vs reaction stage, closed loop configuration

Results are somewhat similar to those previously discussed for the open loop scheme. Indeed, both the use of a precalcination step and of a natural dolomite sorbent brings to the achievement of higher carbonation degrees. With precalcination, the microstructure formed during the initial calcination gives appreciable advantages up to about the 10th reaction stage. From the 11th reaction cycle on, the enhancement is lower than 2%, and at the 20th reaction cycle there is no more difference between the carbonation degree for the two samples. Altogether, the increase in the values of mean carbonation degree is of about 5.7% and 3.4% when averaged over 10 and 20 reaction cycles, respectively. The enhancement values are comparable to those achieved for the open loop scheme, meaning that the precalcination technique has a similar positive impact in both operating conditions. Use of the dolomite sorbent has a much stronger effect. Altogether, the enhancement with respect to the reference case is of 26.3% and 21.3% when averaged over 10 and 20 reaction cycles, respectively.

Table 3 summarizes the average carbonation degrees obtained after 10 and 20 reaction cycles, as obtained from Eq. (3), for all the tests performed. The values of 10 and 20 reaction stages correspond to the average life of a sorbent processed in a CaL scheme featuring a make-up (and purge) fraction of 10% and 5% of the looping stream, respectively for 10 and 20 cycles, calcium-basis, as typically considered in literature [15].

Table 3. Average carbonation degrees (values in %) after 10 and 20 reaction cycles

	Open loop configuration					**Closed loop configuration**		
	850 °C	**750 °C**	**Precalcination**		**Dolomite**	**950 °C**	**Precalc. 20 min**	**Dolomite**
			20 min	**60 min**				
$\overline{X}_{Ca,10}$ [–]	35.0	46.4	39.3	37.4	76.9	22.8	28.6	49.2
$\overline{X}_{Ca,20}$ [–]	28.1	37.1	31.7	32.5	61.9	15.3	18.7	36.6

Density of energy storage

Data of mean carbonation degree were post processed with Eqs. (2)–(3) to estimate the average density of energy storage. Figure 5 shows data related to the open loop configuration.

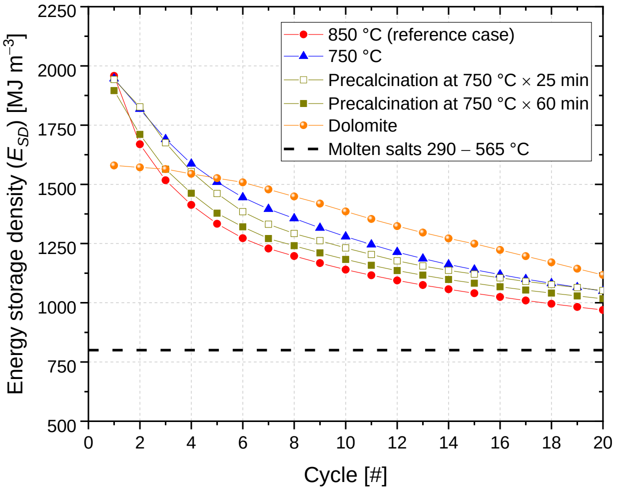

Figure 5. Average density of energy storage vs reaction stage, open loop configuration

The dashed line refers to the storage density of the molten salts system, which represents the current benchmark in the CSP technology for power production. In any of the investigated cases, the values of energy storage density are larger than that of the molten salts. Moreover, all the techniques improve the energy storage density of the reference case. With regards to an average sorbent life of 10 and 20 reaction cycles, the best performances are obtained when using dolomite instead of limestone. The enhancement is however much more limited than one would have expected from the $\bar{X}_{Ca}$ values shown in Figure 2, due to the relatively low $CaCO_3$ content of dolomite (see Table 1). Indeed, once formed, MgO is not recarbonated under the operating conditions experienced, and represents an inert fraction that does not contribute to thermochemical energy storage. Altogether, using dolomite as reactive material, E_{SD} is equal to 1385 MJ m^{-3} and 1118 MJ m^{-3}, for an average sorbent life of 10 and 20 cycles, respectively. These figures are 22% and 15% higher than those achieved in the reference case. The corresponding E_{SD} values when performing calcination at 750 °C are 1280 MJ m^{-3} and 1050 MJ m^{-3}, 12% and 8% higher than for the reference case. Finally, when carrying out a short (25 min) precalcination at 750 °C, the values become 1230 MJ m^{-3} and 1050 MJ m^{-3}, with an average increase of 8% with respect to the reference case. The difference between precalcination and calcination at 750 °C is quite feeble or almost null, because the increase in the latent heat storage, driven by the higher values of $\bar{X}_{Ca}$ (see Figure 2), is mostly compensated by the decrease in the sensible heat storage, arising from the lower calcination temperature. It is indeed observed that the share of latent heat storage over the total value increases when lowering the calcination temperature. To give an example, it values about 87% at 750 °C vs 75% at 850 °C, for an average sorbent life of 20 cycles.

Finally, Figure 6 shows the average values of E_{SD} for tests related to closed loop. Similar considerations with respect to those inferred for tests in open loop configuration here apply. Higher values of E_{SD} are again obtained when using dolomite instead of limestone as reactive material. With dolomite, E_{SD} for an average sorbent life of 10 and 20 cycles are equal to, respectively, 1126 MJ m^{-3} and 946 MJ m^{-3}. These figures are respectively 15% and 19% higher than those for the reference case. Precalcination has a weaker effect. Energy storage densities are now indeed of 1090 MJ m^{-3} and 865 MJ m^{-3}, 12% and 9% higher than those achieved in the reference case, for an average sorbent life of 10 and 20 cycles, respectively.

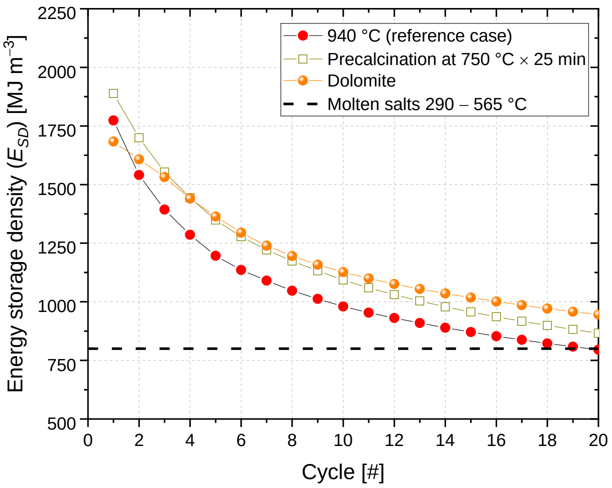

Figure 6. Average density of energy storage vs reaction stage, closed loop configuration

Discussion

An overall analysis of the experimental results suggests that a short precalcination, lowering of the calcination temperature, and use of dolomite sorbent, can increase the performances of the CSP-CaL technology in terms of mean carbonation degree and density of energy storage. Each technique owns specific advantages and drawbacks that must be considered in a global analysis:

- use of dolomite allows the highest gain in performances. However, the price of dolomite is higher than that of limestone. Moreover, dolomite is a more friable material, meaning that the production of fine particles is increased during the looping cycles. This means that higher values of make-up streams will be required to compensate for the material loss [15]. Further, very fine particles can decrease the performance of directly irradiated FB receivers due to increased scattering phenomena, and significantly contribute to fouling and scratching of optical windows;
- lowering of the calcination temperature moderately increases the performances. Even if the upgrade is similar to that obtained with precalcination, especially for longer sorbent life cycles, a higher share of energy is thermochemically stored. This technique however slowdowns the calcination kinetics, requiring increased residence times in the calciner;
- precalcination has the weaker effect over the techniques investigated. As only the first step is performed at lower temperature, kinetics is mostly unaffected. Moreover, unlike the other strategies, an additional unit specifically designed for material pretreatment is here required.

Given the intrinsic peculiarities of each technique, the optimal choice among the different strategies should arise from a detailed techno-economic analysis, which considers the specific advantages and drawbacks of each solution.

CONCLUSIONS

Assessment of different techniques aimed at improving the performances of the Calcium Looping (CaL) cycle for integration with concentrated solar power (CSP) systems was performed. Experimental tests were carried out in a directly irradiated fluidized bed reactor, under realistic process conditions relevant to either thermochemical energy storage (TCES) or carbon capture and storage/utilization (CCSU). Three different approaches were tested: lowering of calcination temperature, precalcination, use of a dolomite sorbent instead of limestone. Results were compared with reference data obtained in a previous study.

Experimental results under open loop conditions revealed that the best performances in terms of energy storage densities are obtained using dolomite as reactive material. Energy storage densities increase of about 19% with respect to the use of limestone, when considering an average life for the sorbent of 10–20 cycles. The upgrade arises from higher values of mean carbonation degree. Investigation of material microstructure with N_2-porosimetry revealed that the calcined samples of dolomite feature considerably larger values of specific surface. On the other side, characteristic values of pore size diameter are similar to those of calcined limestone samples. Lowering of the calcination temperature and precalcination also produce benefits, but to a minor extent. The effect in terms of overall energy storage density is similar for the two techniques, with an enhancement of about 10% with respect to the reference case. However, lowering of the calcination temperature also brings to a higher share of latent thermochemical energy storage over the total. Experimental tests under closed loop conditions disclosed similar results. Use of dolomite as reactive material brings to best results, with an average increase in energy storage densities of 17% (10–20 cycles). Precalcination has indeed weaker effects, with enhancement in energy storage densities of about 10%. Altogether, given the intrinsic peculiarities of each technique, the optimal choice among the different strategies should arise from a detailed techno-economic analysis which takes into account the specific advantages and drawbacks of each solution.

REFERENCES

1. Zhang, H., Benoit, H., Perez-Lopèz, I., Flamant, G., Tan, T., Baeyens, J., High-efficiency solar power towers using particle suspensions as heat carrier in the receiver and in the thermal energy storage, *Renew. Energy.*, Vol. 111, pp 438-446, 2017.
2. Angerer, M., Becker, M., Härzschel, S., Kröper, K., Gleis, S., Vandersickel, A., Spliethoff, H., Design of a MW-scale thermo-chemical energy storage reactor, *Energy Reports*, Vol. 4, pp 507-519, 2018.
3. Ortiz, C., Valverde, J.M., Chacartegui, R., Perez-Maqueda, L.A., Giménez, P., The Calcium-Looping ($CaCO_3$/CaO) process for thermochemical energy storage in Concentrating Solar Power plants, *Renew. Sustain. Energy Rev.*, Vol. 113, pp 109252, 2019.
4. André, L., Abanades, S., Evaluation and performances comparison of calcium, strontium and barium carbonates during calcination/carbonation reactions for solar thermochemical energy storage, *J. Energy Storage*, Vol. 13, pp 193-205, 2017.
5. Tregambi, C., Di Lauro, F., Montagnaro, F., Salatino, P., Solimene, R., 110th Anniversary: Calcium Looping Coupled with Concentrated Solar Power for Carbon Capture and Thermochemical Energy Storage, *Ind. Eng. Chem. Res.*, Vol. 58, pp 21262-21272, 2019.
6. Yan, Y., Wang, K., Clough, P.T., Anthony, E.J., Developments in calcium/chemical looping and metal oxide redox cycles for high-temperature thermochemical energy storage: A review, *Fuel Process. Technol.*, Vol. 199, pp 106280, 2020.
7. Singh, A., Tescari, S., Lantin, G., Agrafiotis, C., Roeb, M., Sattler, C., Solar thermochemical heat storage via the Co_3O_4/CoO looping cycle: Storage reactor modelling and experimental validation, *Sol. Energy*, Vol. 144, pp 453-465, 2017.
8. Zeng, K., Gauthier, D., Minh, D.P., Weiss-Hortala, E., Nzihou, A., Flamant, G., Characterization of solar fuels obtained from beech wood solar pyrolysis, *Fuel*, Vol. 188, pp 285-293, 2017.
9. Bellouard, Q., Abanades, S., Rodat, S., Dupassieux, N., Solar thermochemical gasification of wood biomass for syngas production in a high-temperature continuously-fed tubular reactor, *Int. J. Hydrogen Energy*, Vol. 42, 13486-13497, 2017.
10. Agrafiotis, C., Roeb, M., Sattler, C., A review on solar thermal syngas production via redox pair-based water/carbon dioxide splitting thermochemical cycles, *Renew. Sustain. Energy Rev.*, Vol. 42, pp. 254–285, 2015.
11. Almendros-Ibáñez, J.A., Fernández-Torrijos, M., Díaz-Heras, M., Belmonte, J.F., Sobrino, C., A review of solar thermal energy storage in beds of particles: Packed and fluidized beds, *Sol. Energy*, Vol. 192, pp 193–237, 2019.
12. Zsembinszki, G., Solé, A., Barreneche, C., Prieto, C., Fernández, A.I., Cabeza, L.F., Review of reactors with potential use in thermochemical energy storage in concentrated solar power plants, *Energies*, Vol. 11, 2358, 2018.
13. Tregambi, C., Di Lauro, F., Montagnaro, F., Salatino, P., Solimene, R., Limestone Calcination – Carbonation in a Fluidized Bed Reactor / Receiver for Thermochemical Energy Storage Applications, *AIP Conf. Proc.*, Vol. 2126, pp. 210008, 2019.
14. Sarrion, B., Valverde, J.M., Perejon, A., Perez-Maqueda, L., Sanchez-Jimenez, P.E., On the Multicycle Activity of Natural Limestone/Dolomite for Thermochemical Energy Storage of Concentrated Solar Power, *Energy Technol.*, Vol. 4, pp 1013-1019, 2016.
15. Tregambi, C., Montagnaro, F., Salatino, P., Solimene, R., A model of integrated calcium looping for CO_2 capture and concentrated solar power. *Sol. Energy*, Vol. 120, pp 208-220, 2015.
16. Tregambi, C., Salatino, P., Solimene, R., Montagnaro, F., An experimental characterization of Calcium Looping integrated with concentrated solar power, *Chem. Eng. J.*, Vol. 331, pp 797-802, 2018.

17. Yang, N., Zhou, Y., Ge, X., A flexible CO_2 capture operation scheme design and evaluation of a coal-fired power plant integrated with a novel DCP and retrofitted solar system, *Energy*, Vol. 170, pp 73-84, 2019.
18. Coppola, A., Scala, F., Salatino, P., Montagnaro, F., Fluidized bed calcium looping cycles for CO_2 capture under oxy-firing calcination conditions: Part 2. Assesment of dolomite vs. limestone, *Chem. Eng. J.*, Vol. 231, pp 544-549, 2013.

Fuel 298 (2021) 120791

Contents lists available at ScienceDirect

Fuel

journal homepage: www.elsevier.com/locate/fuel

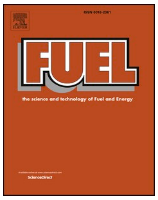

Full Length Article

Improving the performance of calcium looping for solar thermochemical energy storage and CO_2 capture

Francesca Di Lauro [a], Claudio Tregambi [b,*], Fabio Montagnaro [a], Piero Salatino [c], Riccardo Chirone [d], Roberto Solimene [d]

[a] Dipartimento di Scienze Chimiche, Università degli Studi di Napoli Federico II, Complesso Universitario di Monte Sant'Angelo, 80126 Napoli, Italy
[b] Dipartimento di Ingegneria, Università degli Studi del Sannio, Piazza Roma 21, 82100 Benevento, Italy
[c] Dipartimento di Ingegneria Chimica, dei Materiali e della Produzione Industriale, Università degli Studi di Napoli Federico II, Piazzale Tecchio 80, 80125 Napoli, Italy
[d] Istituto di Scienze e Tecnologie per l'Energia e la Mobilità Sostenibili, Consiglio Nazionale delle Ricerche, Piazzale Tecchio 80, 80125 Napoli, Italy

ARTICLE INFO

Keywords:
Concentrated solar power (CSP)
Dolomite and limestone calcination
Fluidized bed
Particle receiver
Precalcination
Solar energy

ABSTRACT

Concentrating solar thermal (CST) technologies for power production can play a major role in the future portfolio of renewable energies. Limestone calcination/carbonation (Calcium Looping (CaL)), is an appealing reaction whose integration with CST is widely investigated for thermochemical energy storage (TCES) and carbon capture and storage/utilization (CCSU). Experimental data under realistic CST conditions/reactors currently lacks, since most of the experimental activities have been performed in thermogravimetric analyzers. In this study, CaL-CST integration was investigated in a lab-scale directly irradiated fluidized bed reactor, able to mimic the operating conditions required for industrial implementation of the technology. Three different techniques to improve the performance of CaL-CST for TCES and CCSU were investigated: i) lowering of calcination temperature; ii) pre-calcination; iii) use of dolomite instead of limestone. Experimental results revealed that all the strategies moderately improve system performance. After 20 cycles, depending on the technique applied, the mean carbonation degree ranges within 28.1–37.1% (TCES) and 15.3–18.7% (CCSU) with limestone, and values 61.5% (TCES) and 36.7% (CCSU) with dolomite. Figures of energy storage density are less sensitive to the different techniques, as pay for the lower calcination temperature (limestone), or for the presence of an inert MgO fraction (dolomite). Corresponding values range within 941–1065 MJ m^{-3} (TCES) and 777–872 MJ m^{-3} (CCSU), for loose-packed conditions. N_2-physisorption analyses revealed that the increased reactivity arises from better microstructural properties in terms of specific surface. Optimal choice among the different strategies should consider the intrinsic peculiarities of each investigated technique.

1. Introduction

Current trends in European policy foresee an increasing share of renewables. Among them, solar energy displays a huge potentiality, as the amount of thermal radiation investing the Earth is far larger than the current world energy demand. Concentrating solar thermal (CST) systems represent an attractive technology for power production. In CST, solar energy is concentrated by means of optical sun tracking mirrors, called heliostats, and focused onto a receiver. Here, the concentrated solar energy is absorbed by a heat transfer medium and thus converted into medium-to-high temperature heat. This heat can be eventually used to drive a thermodynamic cycle for power production, or to sustain energy intensive physical and/or chemical processes. A key feature of CST systems is the integration with technologies for energy storage, which allow to decouple the two steps of solar energy collection and exploitation, greatly enhancing energy dispatchability. Thanks to this feature, energy production by means of CST technologies can occur on demand, and CST can even be compared to base load power plants. The current benchmark in CST systems for power production is represented by the solar tower receiver with molten salts acting as heat transfer fluid and energy storage medium. The molten salts currently used are a binary mixture of $NaNO_3$ and KNO_3, capable of working within the 290–565 °C temperature range. Use of temperature values outside the range causes the salt solidification/thermal degradation and is thus ruled out. The relatively low upper temperature limit of the molten salts strongly impacts the overall process efficiency. Moreover, since storage of energy is

---

* Corresponding author.
E-mail address: claudio.tregambi@unisannio.it (C. Tregambi).

https://doi.org/10.1016/j.fuel.2021.120791
Received 23 November 2020; Received in revised form 17 February 2021; Accepted 29 March 2021

performed as sensible heat, the densities achieved are not very high, and the storage period is limited as well.

Research currently focuses on the development of alternative heat transfer media, capable of exceeding the temperature limit imposed by molten salts. Use of solid particles is widely investigated in the literature for this purpose. Several kinds of granular solid media can be safely used at steady-state temperatures even higher than 1000 °C and have no limitations with regard to the lower temperature limit [1–3]. On the other side, research on more efficient systems for energy storage is pursued. Thermochemical energy storage (TCES) is a promising technology relying on reversible chemical reactions. Collection of solar energy occurs through the endothermal step, while reversal of the chemical reaction allows subsequent release and exploitation of the stored energy. Though more complex, TCES pays with improved densities of energy storage and virtually unlimited time scale of energy storage and dispatchability. Chemical reactions frequently considered are hydration/dehydration [4], calcination/carbonation [5–8], oxidation/reduction [8–11] of metal hydroxides, carbonates and oxides [12]. Alternative approaches are instead devoted to the production of solar fuels by means of coal/biomass torrefaction [13], pyrolysis [14], gasification [15], or by H_2O/CO_2 thermochemical splitting cycles and/or CH_4 reforming for H_2/CO production [16]. Literature review highlights that most of the processes considered for TCES deal with solid/gas chemical reactions. Therefore, fluidized bed (FB) systems may be used in the context of CST technologies to benefit of the peculiarities of particle receivers, while simultaneously exploiting their intrinsic nature as multiphase chemical reactors [17–20]. Moreover, as research in the field progresses, unconventional schemes of solar FB reactors/receivers are developed [20], such as the directly irradiated fluidized bed autothermal reactor (DIFBAR) designed and investigated in Naples, whose integration with TCES system has been modelled [21] and demonstrated at lab scale [2,22]. Limestone calcination is an attractive reaction to be performed with CST technologies. Featuring a high heat of reaction ($\Delta_r H^\circ = 178\ \mathrm{kJ\ mol^{-1}}$), it has been largely investigated as model reaction for solar energy collection and lime production within the cement industry [23–26]. Moreover, iterative cycles of limestone calcination/carbonation, also known as Calcium Looping (CaL), represent an appealing process for TCES of solar energy, as very large values of energy storage densities may be achieved. Cheapness and availability of the raw material further increase its potentiality. Coupling of CaL with concentrated solar power (CSP) systems is largely investigated in the literature for both TCES [5,7,27–30] and carbon capture and sequestration/utilization (CCSU) [7,31–35].

A significant drawback that penalizes the CaL process is the progressive deactivation (i.e. loss of material reactivity) along cycling, induced by sintering of the CaO grains that occurs at the high temperature and high CO_2 partial pressure required [36–38]. Deactivation reduces the maximum achievable carbonation degree, lowering the overall energy storage density and CO_2 capture efficiency. Several techniques have been proposed to enhance the performance and cycling stability of Ca-based materials. Many researchers have developed different synthesis methods to introduce inert stabilizers in the structure of CaO [39–43], such as Al_2O_3 [44,45], SiO_2 [46,47], TiO_2 [48] ZrO_2 [49,50], or doped CaO with binary metallic compounds of Mg and Fe through the sol–gel method [51]. Han et al. [52] studied the performances of CaO-based composites synthesized with inert stabilizers. Best results were obtained with the Al-stabilized material, for which a storage density of 1.5 GJ ton^{-1} is estimated upon 50 reaction cycles in a thermogravimetric analyzer (TGA). Antzara et al. [53] developed a synthetic Zr-promoted CaO-based sorbent and tested its performance in a fluidized bed reactor for CO_2 capture. Carbonation was performed with a CO_2 concentration of $10\%_v$ at 650–680 °C, while calcination at temperature within 750–920 °C according to the CO_2 concentration (0 or $80\%_v$). Effect of steam during carbonation/calcination was also evaluated in wet tests ($20\%_v$ H_2O concentration). The synthetic sorbent showed better performance than natural limestone in all the investigated conditions. Under severe calcination atmosphere, 70% of the initial sorption capacity was retained after 20 looping cycles. Sánchez Jiménez et al. [42] prepared $CaCO_3$ and $CaCO_3$-MgO composites for application in TCES. A very porous structure was formed upon thermal calcination of acetate precursors, obtained by treatment of calcined samples of natural minerals (limestone and dolomite) with acetic acid. Tests in a TGA showed increased values of carbonation degree with respect to the raw materials, which were attributed to the very porous structure formed and to the presence of MgO crystals which increased the stability of the material. Incorporation of even multiple additives to obtain bi- and tri-metallic configurations was investigated by Heidari and coworkers with positive outcomes [54]. Other techniques investigated in literature to increase the performances of Ca-based materials are mechanical activation [55] and thermal pre-treatments [56,57]. Grinding has been studied by Benitez-Guerrero et al. [58] to understand the effects of milling on the CO_2 capture performance of limestone. Several grinding mechanisms have been examined, obtaining an increase in porosity and specific surface of CaO particles which led to an increase in the CO_2 capture efficiency. Teixeira et al. [59] investigated milling of limestone together with industrial wastes (coal fly ash and spent fluid catalytic cracking catalyst) as inert materials. Inerts acted as spacers of CaO particles, increasing their separation and reducing their coalescence and sintering at high temperatures. An increase in the material reactivity was observed from experiments in both TGA and fixed bed. Thermal pretreatment consists in performing the initial calcination of the reactive material under different conditions with respect to those of the subsequent looping cycles. The idea behind this approach is that the initial calcination dictates the formation of the material skeleton/microstructure which is most responsible for the subsequent reactivity. Thermal pretreatment has been studied by several Authors using different temperatures and reaction times [56,60–62]. Manovic et al. [63] studied the effect of precalcination at temperature between 900 and 1100 °C for 6, 24 and 64 h in an atmosphere of pure CO_2. Subsequent reactive tests were performed isothermally at 800 °C in either a TGA or a tubular furnace. Carrier gas was N_2 during carbonation and $100\%_v$ (tubular furnace) or $50\%_v$ CO_2 for the calcination. Overall, a CO_2 capture capacity of 5–10% higher with respect to that of the raw limestone was observed. Valverde et al. [64] investigated precalcination of limestone and dolomite in a stream of either air at 850 °C or $70\%_v$ CO_2 at 950 °C, using a reaction time of 20 min. Subsequent carbonation/calcination cycles were performed in typical CaL conditions (carbonation at 650 °C and $15\%_v$ CO_2, calcination at 950 °C and $70\%_v$ CO_2), obtaining a higher capture capacity with respect to untreated samples. On the other hand, Alonso et al. [57] performed precalcination at temperatures between 900 and 1100 °C using a gas stream of either air or $10\%_v$ CO_2 in air, for time intervals between 10 and 60 min. Reactive tests were then performed in a TGA using a gas stream with a CO_2 concentration of $10\%_v$ (rest air) at a temperature of 650 °C for the carbonation and 950 °C for the calcination. A decline in the CO_2 capture capacity similar to that of the untreated materials was found by these Authors, in contrast to what has been reported in other research papers.

Survey of literature showed that integration between CaL and CSP is a widely investigated topic, but experimental data under realistic CSP conditions/reactors currently lack, since most of the experimental campaigns have been performed in TGA. In this study, CSP–CaL aimed at both TCES and CCSU, was experimentally investigated in a directly irradiated FB reactor operated under realistic process conditions for the CaL-CSP integration. This process was already tested in a previous research paper by the same Authors in which the performance of limestone over 20 reaction cycles, in terms of reactivity and attainable energy storage densities, were disclosed [7]. The system is conceived to be implemented in a beam-down tower CSP plant. With respect to the more demonstrated tower top system, this layout allows the solar receiver/reactor to be located on the ground level, strongly facilitating its construction and operation, at the expense of a lower overall efficiency of the heliostatic field because of the double reflection path. In this study, the focus was the investigation of different measures to limit the loss of reactivity over cycling and maximize the densities of energy storage attainable within the CaL-CSP system. A different reactive material (dolomite) was tested. Moreover, for limestone, use of both lower calcination temperatures and precalcination were investigated. Experimental tests on precalcination were aimed to disclose the potentiality of this technique, since the analysis of literature showed controversial data. In this study, the experimental tests are performed in a directly irradiated FB reactor with a 0.1 m internal diameter, able to mimic the operating conditions required for industrial implementation of the technology. Experimental results in terms of mean carbonation degree and attainable densities of energy storage over 20 iterated reaction cycles were obtained. Samples of the calcined sorbent were collected at different stages and characterized with N_2-porosimetry analysis to further deepen correlation between material reactivity and microstructural properties.

2. Experimental

2.1. Experimental apparatus

Fig. 1 depicts the experimental rig used in this work. It consists of a FB reactor with internal diameter and height equal to about 0.1 m. The bed aspect ratio is thus close to the unity value, a choice made to achieve the establishment of a single vortex ring that promotes mixing of bed solids at the bed scale. The lower section of the reactor, acting as wind-box, is 0.15 m high. The gas distributor, located at the upper end of the wind-box section, consists of a metallic porous plate with 0.5 mm holes drilled on a triangular pitch. The freeboard of the reactor is instead made of a conical section with a height of 0.4 m and an internal cone angle of about 30°. A ceramic glass optical window, located at the upper end of the freeboard, seals the reactor environment. The conical shape of the freeboard is crucial to reduce the gas velocity and to allow disengagement of the solid particles transported by the fluidizing gas. In this way, it is possible to preserve the bed inventory and reduce scratches and fouling on the optical window. The gas discharge ports are at middle height of the freeboard section. Gases are fed to the reactor by means of dedicated electronic mass flow controllers, carefully calibrated for the specific gas.

Heating of the reactor is accomplished by means of:

i) preheating of the inlet gas stream, up to 750 °C, through a resistive heater. A rheostat is used to finely control the power fed to the heater;
ii) two semicylindrical radiant heaters, which completely surround the wind-box and fluidized bed sections, and part of the conical section. A proportional-integrative-derivative controller drives the radiant heaters, using temperature data from the inside of the FB;
iii) a concentrated solar radiation, focused on the upper surface of the FB. The radiation is simulated by means of three short-arc Xe lamps, 4 kW_e each, carefully located in the focal point of the elliptical reflectors. The solar simulator features a peak flux of about 3 MW m^{-2} and a total irradiated power of about 3.2 kW_{th} [32];

Several layers of rock wools thermally insulate the reactor. K-type thermocouples, 1 mm diameter, are located in different key points of the system (e.g. downstream of gas preheating, within the wind-box and inside the FB). Finally, an online gas analyzer measures the CO_2 concentration of the outlet gas stream (Advance Optima ABB AO2020 – Uras 14, 0–100%$_v$).

2.2. Materials

The bed material consisted of a mixture of silica sand and reactive sorbent. The silica sand, sieved to have particles with a diameter within 850–1000 µm, represents an inert material for the process and simply serves as thermal flywheel. Reactive materials consisted instead of:

i) an Italian natural limestone (termed “Sardo”), featuring a $CaCO_3$ content of 98.5%$_{wt}$. This limestone was already used and characterized in a previous work [7];
ii) a dolomite sorbent, obtained from a mine close to the city of Caserta (Italy). The $CaCO_3$ content of this material is of 57.5%$_{wt}$.

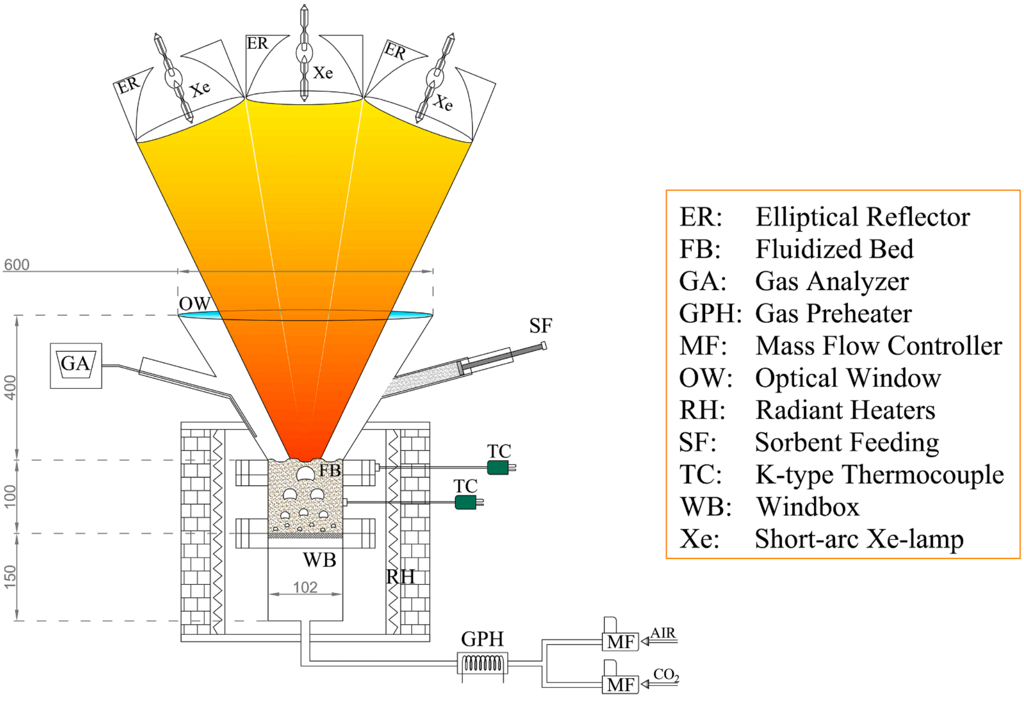

Fig. 1. Experimental apparatus used in the present work. Dimensions in mm.

Table 1
Selected properties of the raw and calcined sorbent, and of the inert bed material.

Material	Bulk density [kg m^{-3}]		Size range [μm]	u^t_{mf}(650–950 °C) [m s^{-1}]	$CaCO_3$ content (raw sorbent) [%$_{wt}$]	CaO content (calcined sorbent) [%$_{wt}$]	Decomposition temperature*** [°C]
	loose *	tapped**					
Limestone	1385	1590	420–590	0.09–0.07	98.5	97.4	825
Dolomite	1311	1514	420–590	0.09–0.07	57.5	61.3	730 – 760
Ticino sand	1269	1489	850–1000	0.32–0.27	0	0	–

[*] Experimentally measured in a FB reactor after gently settling the material from fluidized conditions
[**] Experimentally measured in a graduated cylinder by pouring the material layer by layer and tapping the cylinder
[***] Data from Green and Perry [65]

Both reactive materials were sieved to obtain particles with a diameter within 420–590 μm. Material properties are summarized in Table 1. Data of decomposition temperature are obtained from Green and Perry [65].

2.3. Experimental conditions and procedure

Experiments were aimed at testing different techniques to enhance the performance of the CSP-CaL integration. Operating conditions relevant to two different process schemes – "open loop" and "closed loop" – developed and extensively described in a previous study [7], were investigated. The open loop targets TCES. Calcination is performed using an air stream, and CO_2 leaving the calciner is released to the atmosphere since it is too diluted to be economically stored. As a consequence, integration with CO_2 emitting plants is mandatory to retrieve the stored energy in the exothermic carbonation stage. The closed loop is intended for either CCSU or TCES. Calcination occurs in a CO_2-rich atmosphere and thus the CO_2 leaving the calciner can be stored for subsequent sequestration, or reutilization in the exothermic carbonation step. With reference to TCES, the open loop scheme can benefit of lower calcination temperatures, hence of improved material reactivity, but pays this advantage with the need of a source of CO_2.

It is important to underline that the lower calcination temperature exploited in the open loop scheme does not induce a reduction in the efficiency of the thermodynamic cycle for power production, since in both schemes retrieval of energy is performed during the exothermic carbonation stage. Data obtained in the same previous study [7], using limestone and a calcination temperature of 850 °C in air for the open loop, and of 950 °C in 70%$_v$ CO_2 for the closed loop, are used as reference to discuss the results obtained in this work. Here, for both open and closed loop schemes, carbonation was performed at about 650 °C and using as reactive gas a mixture of CO_2 (15%$_v$) in air, as in the reference study [7]. On the other side, for the open loop scheme, the following techniques were assessed:

i) using limestone, lowering of the calcination temperature in all reaction stages from 850 °C to 750 °C, to reduce the extent of thermal sintering without excessively penalizing the kinetics;
ii) using limestone, first calcination at 750 °C (precalcination), followed by calcination stages at 850 °C. Precalcination was prolonged for either 25 min or 60 min;
iii) use of dolomite instead of limestone, with calcination stages at 850 °C.

With regard to the closed loop scheme:

i) using limestone, precalcination at 750 °C for 25 min, followed by calcination stages at 950 °C (reactive atmosphere of 70%$_v$ CO_2, as for the reference case);
ii) use of dolomite instead of limestone, with calcination stages at 950 °C (reactive atmosphere of 70%$_v$ CO_2).

All the experimental conditions are detailed and summarized in Table 2.

In all the tests an inlet gas velocity of nearly 0.6 m s^{-1} was used, so as to operate the reactor under bubbling conditions. The bed inventory was of 850 g, with a mass fraction of reactive material ranging within 14–18%$_{wt}$. The inert sand (not required for industrial applications) was used in this study to act as thermal ballast to the reactive sorbent, with the only purpose of moderating bed temperature changes induced by exothermic and endothermic chemical reactions. During the tests, operating conditions were sequentially and iteratively switched to favour the course of the carbonation and calcination reactions, until fulfilment of 20 looping cycles. To better mimic CaL-CSP coupling, the solar simulator was used to heat the system only during sorbent calcination. In the other stages, the system was thermally controlled by gas preheating and external radiative heaters. Due to the relatively small size of the experimental rig (i.e., large surface-to-volume ratio), and of the small amount of reactive material (14–18%$_{wt}$ of the whole inventory), operation of the reactor was not completely autothermal even during the exothermal carbonation stage. During a typical test for open loop configuration – case i) the sand was initially loaded within the bed, and the reactor preheated up to 700 °C using air as fluidizing gas. Once approached the scheduled temperature, the reactive material was fed to the system. Simultaneously, the solar simulator was powered on to drive the calcination process and increase the temperature of the FB up to 750 °C. Calcination was prolonged for 25 min, then the FB was cooled down to 650 °C by shutting down all the heaters. Once approached this temperature, both radiant and gas heaters were powered back on to heat up the FB to 700 °C, while using as fluidizing agent a gas mixture of CO_2 (15%$_v$) in air, so as to perform carbonation. Input power was finely controlled to make this stage last 20 min. After this step, the fluidizing gas was switched to air, and the solar simulator was turned on for 25 min to reach 750 °C and promote the course of calcination, thus completing a

Table 2
Summary of experimental conditions investigated.

Technique	Open loop		Closed loop	
	Carbonation (15%$_v$ CO_2)	Calcination (Air)*	Carbonation (15%$_v$ CO_2)	Calcination (70%$_v$ CO_2)**
Limestone (reference)	650 °C	850 °C	650 °C	950 °C
Limestone (750 °C)	650 °C	750 °C	–	–
Limestone, precalc. (25 min)	650 °C	750 °C (1st) 850 °C (2nd–20th)	650 °C	750 °C (1st, air) 950 °C (2nd–20th)
Limestone, precalc. (60 min)	650 °C	750 °C (1st) 850 °C (2nd–20th)	–	–
Dolomite	650 °C	850 °C	650 °C	950 °C

[*] For calcination in ambient air (410 ppm of CO_2), the equilibrium temperature is about 521 °C.
[**] For calcination in 70%$_v$ CO_2, the equilibrium temperature is about 875 °C.

first looping cycle. Finally, the FB was cooled down to 650 °C and a new cycle was started.

During tests for open loop configuration – case ii), the same experimental procedure was used, but the initial calcination was prolonged for 25 or 60 min according to the specific test. Subsequent solar calcination steps were performed at 850 °C and prolonged for 20 min.

For open loop configuration – case iii), initial preheating was stopped at 750 °C instead of 700 °C. All the calcination steps, initial one included, were performed at 850 °C and prolonged for 20 min.

Finally, for closed loop configuration, the experimental procedure only slightly differs. When precalcination was not performed (case ii)), initial preheating was arrested at 875 °C. For both cases, calcination steps (except the initial one for case i)) were performed at 950 °C in a reactive atmosphere of 70%$_v$ CO_2 and prolonged for 20 min. Moreover, after each carbonation, a fast heating step up to 850 °C was performed using only the radiant and gas heaters, while fluidizing the reactor with a gas mixture of 70%$_v$ CO_2 in air. This intermediate heating stage was required to not extend the subsequent solar calcination beyond the scheduled time of 20 min.

During each experimental test, data of temperature and of outlet CO_2 concentration were logged with a 1 Hz occurrence using a home-built LabVIEW protocol. Small samples (about 1 g) of sorbent were collected after each carbonation step and after selected calcination stages. Inert sand particles were carefully removed by mechanical sieving. Carbonated samples were heated for 1 h in a muffle furnace at 950 °C under an air stream, and their weight change was measured with an analytical balance (0.1 mg precision). Calcined samples were instead analyzed by N_2-porosimetry: the adsorption isotherm was post-processed with the Brunauer–Emmett–Teller (BET) equation to estimate the specific surface area, whereas the desorption isotherm was post-processed with the Barrett–Joyner–Halenda (BJH) theory to deduce the pore size distribution.

2.4. Data analysis

The mean carbonation degree ($\overline{X}_{Ca}$) of the material was estimated after each carbonation step (N), by using data of weight change of the samples heated in the muffle furnace:

$$\overline{X}_{Ca}(N) = \frac{\left(m_0^N - m_F^N\right)}{m_F^N x_{CaO}}\frac{PM_{CaO}}{PM_{CO_2}} \qquad (1)$$

where m_0^N and m_F^N are, respectively, the initial and final mass of the sample heated in the muffle furnace with reference to cycle N, PM_{CaO} and PM_{CO_2} are the molecular weight of CaO and CO_2, respectively, and x_{CaO} is the CaO mass fraction in the calcined sorbent (see Table 1). Data of mean carbonation degree were eventually processed to assess the average density of energy storage (E_{SD} [MJ m^{-3}]) vs the reaction step as:

$$E_{SD} = \Delta_r H \overline{X}_{Ca,N}\frac{\rho_{bulk}x_{CaCO_3}}{PM_{CaCO_3}} + \frac{\rho_{bulk}\overline{C_p}\left(T_{1st,CAL} - T_{CARB}\right) + \rho_{bulk}\overline{C_p}\left(T_{CAL} - T_{CARB}\right)(N-1)}{N} \qquad (2)$$

where $\Delta_r H$ is the enthalpy of reaction at 650 °C (0.173 MJ mol^{-1}), ρ_{bulk} is the raw sorbent bulk density (see Table 1), which is taken as reference for the design of the vessel containing the sorbent, x_{CaCO_3} is the $CaCO_3$ mass fraction of the raw sorbent (see Table 1), PM_{CaCO_3} is the molecular weight of $CaCO_3$ (100.09×10^{-3} kg mol^{-1}), $\overline{C_p}$ is the sorbent average specific heat (1×10^{-3} MJ kg^{-1} °C^{-1}), $T_{1st,CAL}$ and T_{CAL} are the temperature during the first and subsequent calcination steps, T_{CARB} is the temperature during the carbonation step (650 °C), and $\overline{X}_{Ca,N}$ is the average sorbent carbonation degree up to the reaction cycle considered, computed as:

$$\overline{X}_{Ca,N} = \frac{\sum_{N=1}^{N}\overline{X}_{Ca}(N)}{N} \qquad (3)$$

Values of E_{SD} computed by Eq. (2) gather contributions of both chemical and sensible heat storage. The chemical heat contribution, first term on right-hand side of Eq. (2), springs from the calcined core of the material able to react with CO_2 according to exothermic carbonation. The sensible heat contribution, second term on right-hand side of Eq. (2), originates from the excess sensible enthalpy owned by the sorbent with respect to that at the discharge (i.e. carbonation) temperature. This term considers that the first calcination step is performed at a different temperature with respect to that of subsequent calcination stages, when precalcination is exploited.

Choice of the density value is crucial for a correct estimation of the energy storage density, and which value should be used depends on the degree of packing of the material achieved in the storage vessel. In this study, the energy storage density was computed by referring to the two extreme values of density achievable, a loose value and a tapped value. Tapped density is a favourable scenario, because the material is more densely packed, and thus values of E_{SD} are larger. Loose density is a worst (i.e., conservative) scenario, as the material is more loosely packed, with correspondingly smaller values of E_{SD}. It should be noted that ratio between loose and tapped density is roughly the same for limestone and dolomite and equals 0.87. The same ratio also holds for the values of E_{SD}, as easily inferable from Eq. (2).

3. Results

3.1.

Fig. 2 shows the data of mean carbonation degree vs reaction stage, for the tests performed under operating conditions relevant to the open loop configuration.

It appears that all the strategies provide some degree of advantage with respect to the reference case. For tests with limestone, the best performance is obtained when lowering the calcination temperature down to 750 °C. Under these conditions, the increase of $\overline{X}_{Ca,N}$ is remarkable and equals about 11.4% and 9.0% if N is 10 and 20, respectively. The higher reactivity is probably induced by a lower extent of the sintering phenomena that progressively deteriorate the micro– and meso– porosity of the material. Data of N_2–physisorption analysis post processed with BET (Table 3) support this claim. When calcined at lower temperature, limestone exhibits a larger specific surface after both the initial and third calcination step. Reactivity is thus increased, allowing the achievement of higher values of mean carbonation degree.

Working at 750 °C is however not free from drawbacks, as it comes at the expense of a longer residence time in the calciner, induced by the

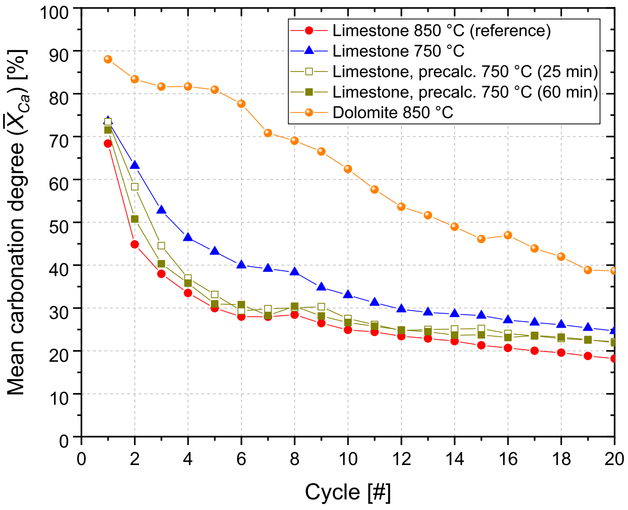

Fig. 2. Mean carbonation degree vs reaction stage, open loop configuration.

Table 3
Values of specific surface as obtained from post process of N_2-physisoprtion data.

Calcination step [–]	Specific surface [$m^2\ g^{-1}$]		
	Limestone (reference)*	Limestone (750 °C)	Dolomite (850 °C)
0	17.5	29.3	37.0
3	11.3	16.3	23.6

* Data from Tregambi et al. [7], for calcination in air at 850 °C.

inevitably lower kinetic rates. This is the reason for which limestone precalcination at 750 °C temperature, followed by standard looping cycles at 850 °C, was assessed. The rationale behind this approach is that of inducing the formation of a highly porous structure by first calcining the material at lower temperature, to then benefit of this structure even during the subsequent cycles at higher temperature. Data with a precalcination step of 25 and 60 min are shown in Fig. 2 as well. The increase in the mean carbonation degree with respect to the reference case is more limited. Precalcination has an effect especially during the first cycles whereas, for higher numbers of looping stage, the values of mean carbonation degree mostly approach those obtained in the reference case. When precalcination is prolonged for 25 min, the increase of $\overline{X}_{Ca,N}$, which is of about 8.4% when the first 3 cycles are considered, decrease to 4.3% and 3.6% when 10 and 20 reaction cycles are, respectively, used. On the other side, when precalcination is prolonged for 60 min, the values become 3.8% (3 cycles), 2.3% (10 cycles) and 2.4% (20 cycles). Thus, prolonging of the precalcination step does not provide additional benefits into hardening/stabilization of the material microstructure and even brings to a worse reactivity. On the basis of the obtained results, it is advised to prolong the precalcination step only until the complete material calcination is achieved. Finally, Fig. 2 shows data obtained using the dolomite as reactive material, at the calcination temperature of 850 °C. Values of carbonation degree achieved are far larger than any other case. A value of 88.0% is obtained during the first cycle, and the material appears to have a better resistance toward sintering phenomena, as the decay in reactivity over cycling is less severe. Altogether, the increase in carbonation degree with respect to the reference case is of 41.2% and 33.4% when data are averaged over 10 and 20 reaction cycles, respectively. The larger values of mean carbonation degree arise again from better microstructural properties (Table 3). Specific surface of calcined samples of dolomite is more than twice that of limestone samples processed under the same experimental conditions. It is believed that MgO crystals, which are inert within the given process conditions, inhibit the sintering phenomena and preserve the material reactivity over cycling [66,67]. Physisorption data were also post processed with BJH theory to assess if the limestone calcined at lower temperature, or the calcined samples of dolomite, developed a different characteristic dimension of pore diameter when compared to limestone calcined at 850 °C. Data of differential intrusion vs pore diameter are shown in Fig. 3 for samples retrieved after the initial calcination step. It appears that no remarkably differences are obtained in terms of pore dimensions. A characteristic pore diameter of about 20–30 nm is indeed observed for all samples.

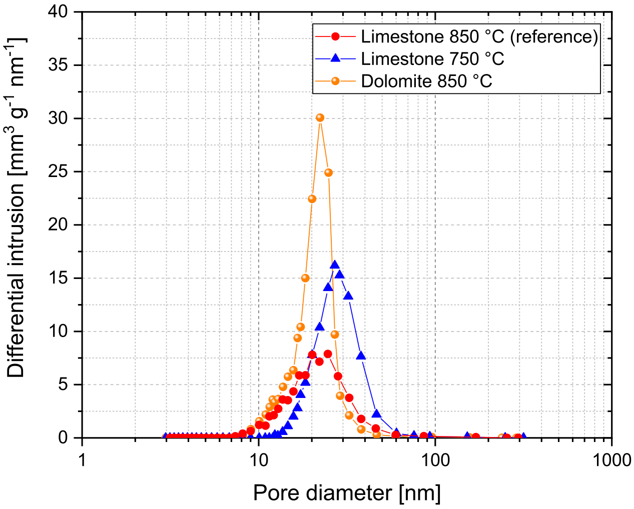

Fig. 3. Differential intrusion vs pore diameter from N_2-physisorption data post processed with BJH theory. Data refer to samples after the initial calcination step.

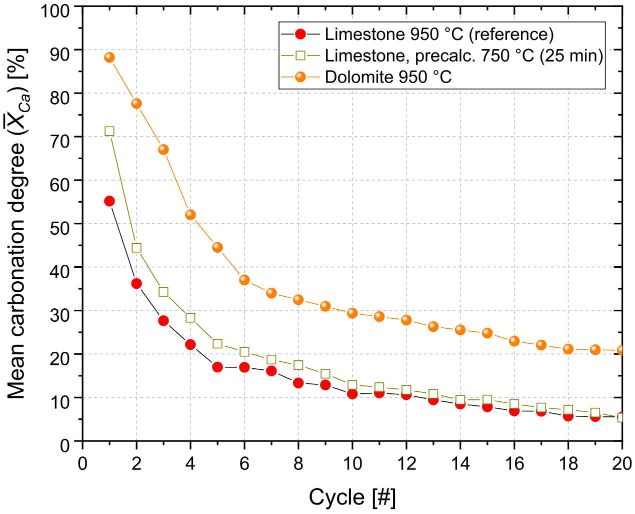

Fig. 4. Mean carbonation degree vs reaction stage, closed loop configuration.

Fig. 4 shows the data of mean carbonation degree vs reaction stage, for the tests performed in closed loop configuration. Results are somewhat similar to those previously discussed for the open loop scheme. Indeed, both the use of a precalcination step and of the natural dolomite sorbent brings to the achievement of higher carbonation degrees. With precalcination, the microstructure formed during the initial calcination gives appreciable advantages up to about the 10th reaction stage. From the 11th reaction cycle on, the enhancement is lower than 2%, and at the 20th reaction cycle there is no more difference between the carbonation degree for the two samples. Altogether, the increase in the values of mean carbonation degree is of about 5.7% and 3.4% when averaged over 10 and 20 reaction cycles, respectively. The enhancement values are comparable to those achieved for the open loop scheme, meaning that the precalcination technique has a similar positive impact in both operating conditions. Use of the dolomite sorbent has a much stronger effect. Altogether, the enhancement with respect to the reference case is of 26.5% and 21.4% when averaged over 10 and 20 reaction cycles, respectively.

Table 4 summarizes the average carbonation degrees obtained after 10 and 20 reaction cycles, as obtained from Eq. (3), for all the tests performed. The values of 10 and 20 reaction stages correspond to the

Table 4
Average carbonation degrees (values in %) after 10 and 20 reaction cycles.

Technique	Open loop configuration		Closed loop configuration	
	$\overline{X}_{Ca,10}$ [–]	$\overline{X}_{Ca,20}$ [–]	$\overline{X}_{Ca,10}$ [–]	$\overline{X}_{Ca,20}$ [–]
Limestone (reference)*	35.0	28.1	22.8	15.3
Limestone (750 °C)	46.4	37.1	–	–
Limestone, precalc. (25 min)	39.3	31.7	28.6	18.7
Limestone, precalc. (60 min)	37.4	30.5	–	–
Dolomite	76.2	61.5	49.3	36.7

* Data from Tregambi et al. [7].

average life of a sorbent processed in a CaL scheme featuring a make-up (and purge) fraction of 10% and 5% of the looping stream (calcium basis), respectively [31,35].

3.2. Density of energy storage

Data of mean carbonation degree were post processed with Eqs. (2)–(3) to estimate the average density of energy storage. Fig. 5 shows data related to the open loop configuration. The dashed line refers to the storage density of the molten salts system, which represents the current benchmark in the CSP technology for power production. In any of the investigated cases, the values of energy storage density are larger than that of the molten salts. Moreover, all the techniques improve the energy storage density of the reference case. With regard to an average sorbent life of 10 and 20 reaction cycles, the best performance is obtained when using dolomite instead of limestone. The enhancement is however much more limited than one would have expected from the $\overline{X}_{Ca}$ values shown in Fig. 2, due to the relatively low $CaCO_3$ content of dolomite (see Table 1). Indeed, once formed, MgO is not recarbonated under the operating conditions experienced, and represents an inert fraction that does not contribute to thermochemical energy storage.

Altogether, when using dolomite as reactive material, E_{SD} (loose density) is equal to 1257 MJ m^{-3} and 1065 MJ m^{-3}, for an average sorbent life of 10 and 20 cycles, respectively. These figures are 14% and 13% higher than those achieved in the reference case. The corresponding E_{SD} values when performing calcination at 750 °C are 1236 MJ m^{-3} and 1014 MJ m^{-3}, respectively 12% and 8% higher than for the reference case. Finally, when carrying out a short (25 min) precalcination at 750 °C, the values become 1193 MJ m^{-3} and 1020 MJ m^{-3}, both 8% larger with respect to the reference case. The difference between precalcination and calcination at 750 °C is quite feeble or almost null, because the increase in the chemical heat storage, driven by the higher values of $\overline{X}_{Ca}$ (see Fig. 2), is mostly compensated by the decrease in the sensible heat storage, arising from the lower calcination temperature. It is indeed observed that the share of chemical heat storage over the total value increases when lowering the calcination temperature. To give an example, it values about 86% at 750 °C vs 74% at 850 °C, for an average sorbent life of 20 cycles.

Finally, Fig. 6 shows the average values of E_{SD} for tests related to closed loop. Both the investigated techniques improve the energy storage density with respect to the reference case. Precalcination gives the best results up to the 13th cycle, then the trend reverts, and performance of the dolomite slightly exceeds that of precalcination. As a matter of fact, when using dolomite, E_{SD} (loose density) for an average sorbent life of 10 and 20 cycles are equal to, respectively, 1037 MJ m^{-3} and 872 MJ m^{-3}, 9% and 12% higher than those of the reference case. When using precalcination, energy storage densities are of 1063 MJ m^{-3} and 844 MJ m^{-3}, 11% and 9% higher than those achieved in the reference case, for an average sorbent life of 10 and 20 cycles, respectively.

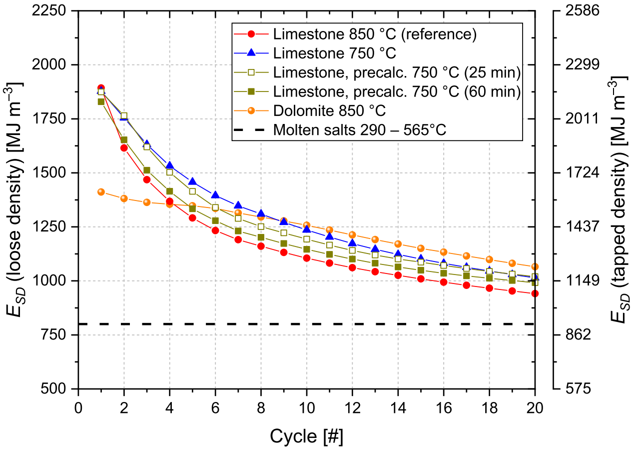

Fig. 5. Average density of energy storage vs reaction stage, open loop configuration.

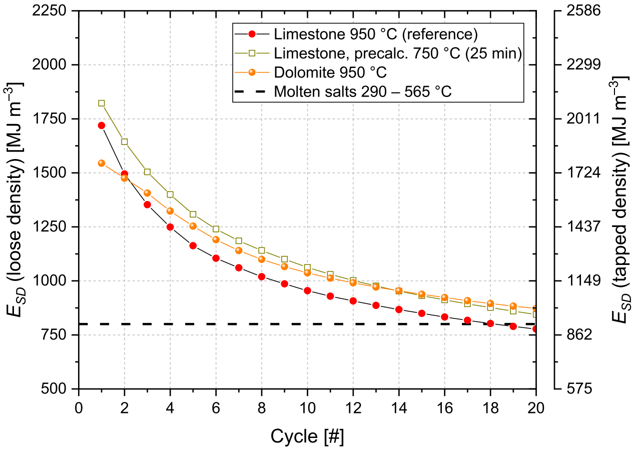

Fig. 6. Average density of energy storage vs reaction stage, closed loop configuration.

Table 5 summarizes the values of energy storage density obtained after 10 and 20 reaction cycles, as inferred from Eq. (2), for all the tests performed. Data computed with both values of density are shown. Figures estimated with tapped density are about 15% larger than those related to loose density, and present an even more appealing scenario for the use of CaL as thermochemical energy storage system when compared to molten salts. Exact values to be used for the design of the storage vessels should be considered upon evaluation of the bulk bed density effectively experienced in the reservoirs.

3.3. Discussion

An overall analysis of the experimental results suggests that a short precalcination, lowering of the calcination temperature, and use of a dolomite sorbent, can increase the performance of the CSP-CaL technology in terms of mean carbonation degree and density of energy storage. With respect to the reference data [7], the increase in performance is within 8–14% depending on the technique and process condition considered. Though not very high, the gain is not negligible if considering that only cost-effective techniques and natural sorbents were considered in this study. Each technique owns specific advantages and drawbacks that must be considered in a global analysis:

Table 5
Average values of energy storage density for calcium looping after 10 and 20 reaction cycles, and for molten salts.

Technique	N [–]	E_{SD} (open loop) [MJ m^{-3}]		E_{SD} (closed loop) [MJ m^{-3}]	
		loose density	tapped density	loose density	tapped density
Molten salts (290 – 565 °C)	–	800 (only sensible heat storage)			
Limestone (reference)*	10	1105	1269	955	1096
	20	941	1081	777	892
Limestone 750 °C	10	1236	1419	–	–
	20	1014	1165	–	–
Precalcination 750 °C, 25 min	10	1193	1370	1063	1220
	20	1020	1171	844	970
Precalcination 750 °C, 60 min	10	1146	1316	–	–
	20	991	1139	–	–
Dolomite	10	1257	1452	1037	1198
	20	1065	1231	872	1008

* Data from Tregambi et al. [7].

- use of dolomite allows the highest gain in performance for the open loop configuration whereas, for the closed loop configuration, it performs better only beyond the 13th looping cycle. However, the price of dolomite is higher than that of limestone. Moreover, dolomite is a more friable material, meaning that the production of fine particles increases during the looping cycles. As a consequence, larger values of make–up streams will be required to compensate for the material loss [31]. Further, very fine particles can decrease the performance of directly irradiated FB receivers due to increased scattering phenomena, and significantly contribute to fouling and scratching of optical windows;
- lowering of the calcination temperature moderately increases the system performance. Even if the upgrade is similar to that obtained with precalcination, especially for longer sorbent life cycles, a higher share of energy is thermochemically stored. This technique however slowdowns the calcination kinetics, requiring increased residence times in the calciner;
- precalcination has initially the weaker effect for the open loop configuration, whereas it levels off with that of lower calcination temperature from the 17th looping cycle. For the closed loop configuration, it is preferable up to the 13th reaction cycle. As only the first step is performed at lower temperature, kinetics is mostly unaffected. Moreover, unlike the other strategies, an additional unit specifically designed for material pretreatment is here required.

Given the intrinsic peculiarities of each technique, the optimal choice among the different strategies should arise from a detailed techno–economic analysis, which considers the specific advantages and drawbacks of each solution.

4. Conclusions

Assessment of different techniques aimed at improving the performance of the Calcium Looping (CaL) cycle for integration with concentrated solar power (CSP) systems was performed. Experimental tests were carried out in a directly irradiated fluidized bed reactor, under realistic process conditions relevant to either thermochemical energy storage (TCES) or carbon capture and storage/utilization (CCSU). Three different approaches were tested: lowering of calcination temperature, precalcination, use of a dolomite sorbent instead of limestone. Results were compared with reference data obtained in a previous study. Experimental results under open loop conditions revealed that all the three different techniques allow to improve the process performance when compared with the reference conditions. Depending on the applied technique, the energy storage densities increase of about 8–14% when considering an average life for the sorbent of 10–20 cycles. Investigation of material microstructure with N_2 porosimetry revealed that the calcined samples of dolomite feature considerably larger values of specific surface. On the other side, characteristic values of pore size diameter are similar to those of calcined limestone samples. Experimental tests under closed loop conditions disclosed similar results, with an average increase in energy storage densities of 9–12% according to the applied technique.

Overall, the three techniques improve only moderately the process performance. Though not very high, the gain is not negligible if considering that only cost-effective techniques and natural sorbents were considered in this study. Altogether, given the intrinsic peculiarities of each technique, the optimal choice among the different strategies should arise from a detailed techno economic analysis which considers the specific advantages and drawbacks of each solution. Future studies will be aimed at investigating the use of synthetic carbonates, that could further increase the system performance, at the expense of higher material costs.

CRediT authorship contribution statement

Francesca Di Lauro: Methodology, Investigation, Writing - review & editing, Visualization. **Claudio Tregambi:** Conceptualization, Methodology, Investigation, Writing - original draft, Writing - review & editing, Visualization. **Fabio Montagnaro:** Conceptualization, Writing - review & editing. **Piero Salatino:** Conceptualization, Writing - review & editing. **Riccardo Chirone:** Conceptualization, Writing - review & editing. **Roberto Solimene:** Conceptualization, Methodology, Writing - review & editing, Visualization.

Declaration of Competing Interest

The authors declare that they have no known competing financial interests or personal relationships that could have appeared to influence the work reported in this paper.

Acknowledgements

Claudio Tregambi wishes to thank the Italian Ministry of Education, University and Research (MIUR), for funding his research position within the “PON Ricerca e Innovazione 2014-2020, Asse I Investimenti in Capitale Umano” – AIM 1823125-1, CUP: F84I19000010001.

Ca.ve. Dolomitica S.r.l. (Ailano – Caserta, Italy) is gratefully acknowledged for providing samples of the dolomite sorbent used within the present experimental campaign.

References

[1] Zhang H, Benoit H, Perez-Lopèz I, Flamant G, Tan T, Baeyens J. High-efficiency solar power towers using particle suspensions as heat carrier in the receiver and in the thermal energy storage. Renew Energy 2017;111:438–46. https://doi.org/10.1016/j.renene.2017.03.101.

[2] Tregambi C, Padula S, Galbusieri M, Coppola G, Montagnaro F, Salatino P, et al. Directly irradiated fluidized bed reactor for thermochemical energy storage and solar fuels production. Powder Technol 2020;366:460–9. https://doi.org/10.1016/j.powtec.2020.02.045.

[3] Tregambi C, Bevilacqua C, Cammarota A, Chirone R, Salatino P, Solimene R, et al. Experimental characterization of granular materials for directly irradiated fluidized bed solar receivers. AIP Conf Proc 2019;2126:030060. https://doi.org/10.1063/1.5117572.

[4] Angerer M, Becker M, Härzschel S, Kröper K, Gleis S, Vandersickel A, et al. Design of a MW-scale thermo-chemical energy storage reactor. Energy Rep 2018;4:507–19. https://doi.org/10.1016/j.egyr.2018.07.005.

[5] Ortiz C, Valverde JM, Chacartegui R, Perez-Maqueda LA, Giménez P. The Calcium-Looping ($CaCO_3$/CaO) process for thermochemical energy storage in Concentrating Solar Power plants. Renew Sustain Energy Rev 2019;113:109252. https://doi.org/10.1016/j.rser.2019.109252.

[6] André L, Abanades S. Evaluation and performances comparison of calcium, strontium and barium carbonates during calcination/carbonation reactions for solar thermochemical energy storage. J Energy Storage 2017;13:193–205. https://doi.org/10.1016/j.est.2017.07.014.

[7] Tregambi C, Di Lauro F, Montagnaro F, Salatino P, Solimene R. 110th anniversary: calcium looping coupled with concentrated solar power for carbon capture and thermochemical energy storage. Ind Eng Chem Res 2019;58:21262–72. https://doi.org/10.1021/acs.iecr.9b03083.

[8] Yan Y, Wang K, Clough PT, Anthony EJ. Developments in calcium/chemical looping and metal oxide redox cycles for high-temperature thermochemical energy storage: a review. Fuel Process Technol 2020;199:106280. https://doi.org/10.1016/j.fuproc.2019.106280.

[9] Liu J, Baeyens J, Deng Y, Wang X, Zhang H. High temperature Mn_2O_3/Mn_3O_4 and Co_3O_4/CoO systems for thermo-chemical energy storage. J Environ Manage 2020;267:110582. https://doi.org/10.1016/j.jenvman.2020.110582.

[10] Yilmaz D, Darwish E, Leion H. Thermochemical energy storage performance of copper oxides: Effect of support materials. J Energy Storage 2020;32:102012. https://doi.org/10.1016/j.est.2020.102012.

[11] Lucio B, Bayon A, Olivares R, Navarro ME, Ding Y, Senneca O, et al. Round robin test on enthalpies of redox materials for thermochemical heat storage: Perovskites. AIP Conf Proc 2019:210004. https://doi.org/10.1063/1.5117753.

[12] André L, Abanades S. Recent advances in thermochemical energy storage via solid – gas reversible reactions at high temperature. Energies 2020;13:5859. https://doi.org/10.3390/en13225859.

[13] Tregambi C, Montagnaro F, Salatino P, Solimene R. Solar-driven torrefaction of a lignin-rich biomass residue in a directly irradiated fluidized bed reactor. Combust Sci Technol 2019;191:1609–27. https://doi.org/10.1080/00102202.2019.1607847.

[14] Zeng K, Gauthier D, Minh DP, Weiss-Hortala E, Nzihou A, Flamant G. Characterization of solar fuels obtained from beech wood solar pyrolysis. Fuel 2017;188:285–93. https://doi.org/10.1016/j.fuel.2016.10.036.

[15] Bellouard Q, Abanades S, Rodat S, Dupassieux N. Solar thermochemical gasification of wood biomass for syngas production in a high-temperature continuously-fed tubular reactor. Int J Hydrogen Energy 2017;42:13486–97. https://doi.org/10.1016/j.ijhydene.2016.08.196.

[16] Agrafiotis C, Roeb M, Sattler C. A review on solar thermal syngas production via redox pair-based water/carbon dioxide splitting thermochemical cycles. Renew Sustain Energy Rev 2015;42:254–85. https://doi.org/10.1016/j.rser.2014.09.039.

[17] Almendros-Ibáñez JA, Fernández-Torrijos M, Díaz-Heras M, Belmonte JF, Sobrino C. A review of solar thermal energy storage in beds of particles: packed and fluidized beds. Sol Energy 2019;192:193–237. https://doi.org/10.1016/j.solener.2018.05.047.

[18] Zsembinszki G, Sole A, Barreneche C, Prieto C, Fernández AI, Cabeza LF. Review of reactors with potential use in thermochemical energy storage in concentrated solar power plants. Energies 2018;11.. https://doi.org/10.3390/en11092358.

[19] Tregambi C, Chirone R, Montagnaro F, Salatino P, Solimene R. Heat transfer in directly irradiated fluidized beds. Sol Energy 2016;129:85–100. https://doi.org/10.1016/j.solener.2016.01.057.

[20] Tregambi C, Troiano M, Montagnaro F, Solimene R, Salatino P. Beds for Concentrated Solar Thermal Technologies – A Review. Front Energy Res 2021;9:618421. https://doi.org/10.3389/fenrg.2021.618421.

[21] Padula S, Tregambi C, Solimene R, Chirone R, Troiano M, Salatino P. A novel fluidized bed battery for thermochemical energy storage in concentrated solar thermal technologies. Energy Convers Manag 2021;236:113994. https://doi.org/10.1016/j.enconman.2021.113994.

[22] Tregambi C, Bevilacqua C, Troiano M, Solimene R, Salatino P. A novel autothermal fluidized bed reactor for concentrated solar thermal applications. Chem Eng J 2020;398:125702. https://doi.org/10.1016/j.cej.2020.125702.

[23] Esence T, Guillot E, Tessonneaud M, Sans JL, Flamant G. Solar calcination at pilot scale in a continuous flow multistage horizontal fluidized bed. Sol Energy 2020;207:367–78. https://doi.org/10.1016/j.solener.2020.06.098.

[24] Tregambi C, Solimene R, Montagnaro F, Salatino P, Marroccoli M, Ibris N, et al. Solar-driven production of lime for ordinary Portland cement formulation. Sol Energy 2018;173:759–68. https://doi.org/10.1016/j.solener.2018.08.018.

[25] Tomatis M, Jeswani HK, Stamford L, Azapagic A. Assessing the environmental sustainability of an emerging energy technology: solar thermal calcination for cement production. Sci Total Environ 2020;742:140510. https://doi.org/10.1016/j.scitotenv.2020.140510.

[26] Flamant G, Hernandez D, Bonet C, Traverse JP. Experimental aspects of the thermochemical conversion of solar energy; Decarbonation of $CaCO_3$. Sol Energy 1980;24:385–95. https://doi.org/10.1016/0038-092X(80)90301-1.

[27] Tregambi C, Di Lauro F, Montagnaro F, Salatino P, Solimene R. Limestone calcination-carbonation in a fluidized bed reactor/receiver for thermochemical energy storage applications. AIP Conf Proc 2019:2126. https://doi.org/10.1063/1.5117757.

[28] Bailera M, Lisbona P, Romeo LM, Díez LI. Calcium looping as chemical energy storage in concentrated solar power plants: carbonator modelling and configuration assessment. Appl Therm Eng 2020;172:115186. https://doi.org/10.1016/j.applthermaleng.2020.115186.

[29] Karasavvas E, Panopoulos KD, Papadopoulou S, Voutetakis S. Energy and exergy analysis of the integration of concentrated solar power with calcium looping for power production and thermochemical energy storage. Renew Energy 2020;154:743–53. https://doi.org/10.1016/j.renene.2020.03.018.

[30] Chacartegui R, Alovisio A, Ortiz C, Valverde JM, Verda V, Becerra JA. Thermochemical energy storage of concentrated solar power by integration of the calcium looping process and a CO_2 power cycle. Appl Energy 2016;173:589–605. https://doi.org/10.1016/j.apenergy.2016.04.053.

[31] Tregambi C, Montagnaro F, Salatino P, Solimene R. A model of integrated calcium looping for CO_2 capture and concentrated solar power. Sol Energy 2015;120:208–20. https://doi.org/10.1016/j.solener.2015.07.017.

[32] Tregambi C, Salatino P, Solimene R, Montagnaro F. An experimental characterization of calcium looping integrated with concentrated solar power. Chem Eng J 2018;331:794–802. https://doi.org/10.1016/j.cej.2017.08.068.

[33] Yang N, Zhou Y, Ge X. A flexible CO_2 capture operation scheme design and evaluation of a coal-fired power plant integrated with a novel DCP and retrofitted solar system. Energy 2019;170:73–84. https://doi.org/10.1016/j.energy.2018.12.118.

[34] Tregambi C, Montagnaro F, Salatino P, Solimene R. Directly irradiated fluidized bed reactors for thermochemical processing and energy storage: Application to calcium looping. AIP Conf Proc 2017:1850. https://doi.org/10.1063/1.4984456.

[35] Tregambi C, Bareschino P, Mancusi E, Pepe F, Montagnaro F, Solimene R, et al. Modelling of a concentrated solar power – photovoltaics hybrid plant for carbon dioxide capture and utilization via calcium looping and methanation. Energy Convers Manag 2021;230:113792. https://doi.org/10.1016/j.enconman.2020.113792.

[36] Erans M, Manovic V, Anthony EJ. Calcium looping sorbents for CO_2 capture. Appl Energy 2016;180:722–42. https://doi.org/10.1016/j.apenergy.2016.07.074.

[37] Salaudeen SA, Acharya B, Dutta A. CaO-based CO_2 sorbents: a review on screening, enhancement, cyclic stability, regeneration and kinetics modelling. J CO_2 Util 2018;23:179–99. https://doi.org/10.1016/j.jcou.2017.11.012.

[38] Coppola A, Scala F, Salatino P. Characterization of calcium looping sorbents with a novel twin bed reactor. Fuel Process Technol 2018;172:49–54. https://doi.org/10.1016/j.fuproc.2017.11.019.

[39] Sun H, Li Y, Yan X, Wang Z, Liu W. CaO/$CaCO_3$ thermochemical heat storage performance of CaO-based micrometre-sized tubular composite. Energy Convers Manag 2020;222:113222. https://doi.org/10.1016/j.enconman.2020.113222.

[40] Guo H, Kou X, Zhao Y, Wang S, Ma X. Role of microstructure, electron transfer, and coordination state in the CO_2 capture of calcium-based sorbent by doping (Zr-Mn). Chem Eng J 2018;336:376–85. https://doi.org/10.1016/j.cej.2017.11.186.

[41] Miranda-Pizarro J, Perejón A, Valverde JM, Pérez-Maqueda LA, Sánchez-Jiménez PE. CO_2 capture performance of Ca-Mg acetates at realistic Calcium Looping conditions. Fuel 2017;196:497–507. https://doi.org/10.1016/j.fuel.2017.01.119.

[42] Sánchez Jiménez PE, Perejón A, Benítez Guerrero M, Valverde JM, Ortiz C, Pérez Maqueda LA. High-performance and low-cost macroporous calcium oxide based materials for thermochemical energy storage in concentrated solar power plants. Appl Energy 2019;235:543–52. https://doi.org/10.1016/j.apenergy.2018.10.131.

[43] Tian S, Jiang J, Yan F, Li K, Chen X, Manovic V. Highly efficient CO_2 capture with simultaneous iron and CaO recycling for the iron and steel industry. Green Chem 2016;18:4022–31. https://doi.org/10.1039/c6gc00400h.

[44] Li Y, Su M, Xie X, Wu S, Liu C. CO_2 capture performance of synthetic sorbent prepared from carbide slag and aluminum nitrate hydrate by combustion synthesis. Appl Energy 2015;145:60–8. https://doi.org/10.1016/j.apenergy.2015.01.061.

[45] Benitez-Guerrero M, Valverde JM, Sanchez-Jimenez PE, Perejon A, Perez-Maqueda LA. Calcium-Looping performance of mechanically modified Al_2O_3-CaO composites for energy storage and CO_2 capture. Chem Eng J 2018;334:2343–55. https://doi.org/10.1016/j.cej.2017.11.183.

[46] Valverde JM, Perejon A, Perez-Maqueda LA. Enhancement of fast CO_2 capture by a nano-SiO_2/CaO composite at Ca-looping conditions. Environ Sci Technol 2012;46:6401–8. https://doi.org/10.1021/es3002426.

[47] Sanchez-Jimenez PE, Perez-Maqueda LA, Valverde JM. Nanosilica supported CaO: a regenerable and mechanically hard CO_2 sorbent at Ca-looping conditions. Appl Energy 2014;118:92–9. https://doi.org/10.1016/j.apenergy.2013.12.024.

[48] Yu C, Kuo H, Chen Y. Carbon dioxide removal using calcium aluminate carbonates on titanic oxide under warm-gas conditions. Appl Energy 2016;162:1122–30. https://doi.org/10.1016/j.apenergy.2014.12.046.

[49] Guo H, Wang S, Li C, Zhao Y, Sun Q, Ma X. Incorporation of Zr into calcium oxide for CO_2 capture by a simple and facile sol-gel method. Ind Eng Chem Res 2016;55:7873–9. https://doi.org/10.1021/acs.iecr.5b04112.

[50] Antzara A, Heracleous E, Lemonidou AA. Improving the stability of synthetic CaO-based CO_2 sorbents by structural promoters. Appl Energy 2015;156:331–43. https://doi.org/10.1016/j.apenergy.2015.07.026.

[51] Da Y, Xuan Y, Teng L, Zhang K, Liu X, Ding Y. Calcium-based composites for direct solar-thermal conversion and thermochemical energy storage. Chem Eng J 2020;382:122815. https://doi.org/10.1016/j.cej.2019.122815.

[52] Han R, Gao J, Wei S, Su Y, Su C, Li J, et al. High-performance CaO-based composites synthesized using a space-confined chemical vapor deposition strategy for thermochemical energy storage. Sol Energy Mater Sol Cells 2020;206:110346. https://doi.org/10.1016/j.solmat.2019.110346.

[53] Antzara AN, Arregi A, Heracleous E, Lemonidou AA. In-depth evaluation of a ZrO_2 promoted CaO-based CO_2 sorbent in fluidized bed reactor tests. Chem Eng J 2018;333:697–711. https://doi.org/10.1016/j.cej.2017.09.192.

[54] Heidari M, Tahmasebpoor M, Antzaras A, Lemonidou AA. CO_2 capture and fluidity performance of CaO-based sorbents: effect of Zr, Al and Ce additives in tri-, bi- and mono-metallic configurations. Process Saf Environ Prot 2020;144:349–65. https://doi.org/10.1016/j.psep.2020.07.041.

[55] Sayyah M, Lu Y, Masel RI, Suslick KS. Mechanical activation of CaO-based adsorbents for CO_2 capture. ChemSusChem 2013;6:193–8. https://doi.org/10.1002/cssc.201200454.

[56] Valverde JM, Barea-López M, Perejón A, Sánchez-Jiménez PE, Pérez-Maqueda LA. Effect of thermal pretreatment and nanosilica addition on limestone performance at calcium-looping conditions for thermochemical energy storage of concentrated solar power. Energy Fuels 2017;31:4226–36. https://doi.org/10.1021/acs.energyfuels.6b03364.

[57] Alonso M, Lorenzo M, González B, Abanades JC. Precalcination of $CaCO_3$ as a method to stabilize CaO performance for CO_2 capture from combustion gases. Energy Fuels 2011;25:5521–7. https://doi.org/10.1021/ef201333e.

[58] Benitez-Guerrero M, Valverde JM, Perejon A, Sanchez-Jimenez PE, Perez-Maqueda LA. Effect of milling mechanism on the CO_2 capture performance of limestone in the Calcium Looping process. Chem Eng J 2018;346:549–56. https://doi.org/10.1016/j.cej.2018.03.146.

[59] Teixeira P, Mohamed I, Fernandes A, Silva J, Ribeiro F, Pinheiro CIC. Enhancement of sintering resistance of CaO-based sorbents using industrial waste resources for Ca-looping in the cement industry. Sep Purif Technol 2020;235:116190. https://doi.org/10.1016/j.seppur.2019.116190.

[60] Ozcan DC, Shanks BH, Wheelock TD. Improving the stability of a CaO-based sorbent for CO_2 by thermal pretreatment. Ind Eng Chem Res 2011;50:6933–42. https://doi.org/10.1021/ie102368g.

[61] Chen Z, Song HS, Portillo M, Lim CJ, Grace JR, Anthony EJ. Long-term calcination/carbonation cycling and thermal pretreatment for CO_2 capture by limestone and dolomite. Energy Fuels 2009;23:1437–44. https://doi.org/10.1021/ef800779k.

[62] Perejón A, Romeo LM, Lara Y, Lisbona P, Martínez A, Valverde JM. The Calcium-Looping technology for CO_2 capture: On the important roles of energy integration and sorbent behavior. Appl Energy 2016;162:787–807. https://doi.org/10.1016/j.apenergy.2015.10.121.

[63] Manovic V, Anthony EJ, Loncarevic D. CO_2 looping cycles with CaO-based sorbent pretreated in CO_2 at high temperature. Chem Eng Sci 2009;64:3236–45. https://doi.org/10.1016/j.ces.2009.03.051.

[64] Valverde JM, Sanchez-Jimenez PE, Perez-Maqueda LA. Ca-looping for postcombustion CO_2 capture: a comparative analysis on the performances of dolomite and limestone. Appl Energy 2015;138:202–15. https://doi.org/10.1016/j.apenergy.2014.10.087.

[65] Green DW, Perry RH. Perry's Chemical Engineers' Handbook. 8th ed. McGraw-Hill; 2008.

[66] Coppola A, Scala F, Salatino P, Montagnaro F. Fluidized bed calcium looping cycles for CO2 capture under oxy-firing calcination conditions: Part 1. Assessment of six limestones. Chem Eng J 2013;231:537–43. doi: 10.1016/j.cej.2013.07.113.

[67] Sarrion B, Valverde JM, Perejon A, Perez-Maqueda L, Sanchez-Jimenez PE. On the multicycle activity of natural limestone/dolomite for thermochemical energy storage of concentrated solar power. Energy Technol 2016;4:1013–9. https://doi.org/10.1002/ente.201600068.

Outline of a Process for the Hydrothermal Liquefaction of a Tannery Sludge for Biofuel Production

Francesca Di Lauro[1], Marco Balsamo[1], Roberto Solimene[2], Renata Migliaccio[2], Daniela Caracciolo[3], Piero Salatino[4], Fabio Montagnaro[*,1]

[1]Dipartimento di Scienze Chimiche, Università degli Studi di Napoli Federico II,
Complesso Universitario di Monte Sant'Angelo, 80126 Napoli (Italy)
[2]Istituto di Scienze e Tecnologie per l'Energia e la Mobilità Sostenibili, Consiglio Nazionale delle Ricerche,
Sede Secondaria, Piazzale V. Tecchio 80, 80125 Napoli (Italy)
[3]Stazione Sperimentale per l'Industria delle Pelli e delle Materie Concianti,
Via Campi Flegrei 34, 80078 Pozzuoli (Italy)
[4]Dipartimento di Ingegneria Chimica, dei Materiali e della Produzione Industriale,
Università degli Studi di Napoli Federico II, Piazzale V. Tecchio 80, 80125 Napoli, (Italy)

Abstract

The growing interest in renewable energies due to climate change concerns is triggering research towards liquid fuels production from renewable energy resources. The civil/industrial sludge conversion into bio-crude via hydrothermal liquefaction (HTL) can simultaneously provide a replacement to non-renewable crude-oil while dealing with waste disposal issues. In this work, a tannery sludge has been characterised by several techniques to preliminary assess the sludge composition and properties. Moreover, a lab-scale plant consisting in a batch autoclave was designed, whose exercise can allow to elucidate the reaction pathways of the HTL process so to identify optimal operating conditions for obtaining a high-yield bio-crude with more attractive energy properties. Finally, to investigate the relationships between HTL operating conditions and yield/quality of the sludge-derived bio-fuels, an original elaboration of literature data was offered.

Introduction

The modern society has experienced a rapid economic and population growth worldwide in the last 50 years, with an associated remarkable increase of the global energetic demand which is still mainly satisfied by conventional fossil fuels. According to International Energy Agency (IEA), in 2018, world total energy consumption reached 14282 Mtoe and energy generation from fossil fuels accounted for 81.3% of the total world gross energy production. Fossil fuels represent the hydrocarbons that have been stored over a period of millions of years deep within the Earth. The combustion of these carbon sources for energy production has generated an alteration of the carbon cycle balance, with an increase of the carbon dioxide concentration in the atmosphere which is claimed as one of the biggest drivers of global warming. Phenomena such as climate change and fossil fuel shortages are encouraging the development of alternative routes for energy production, to diversify the current energy portfolio and eventually replace fossil fuel usage [1]. In this context, biomasses can be a promising option to meet this need, due to the large availability of these resources in form of agricultural residues, food waste and sludges deriving from both industrial and civil wastewater treatment. In particular, the valorisation of sewage sludge as energy carrier has a twofold beneficial effect for reducing both CO_2 emissions for energy production and the economic and environmental issues related to the landfill of sewage sludge. In fact, sludges disposal costs are ca. 80–140 €/ton and they can contain high level of pathogens.

Among the different biomass conversion technologies, particularly interesting are those that lead to the production of a liquid fuel – required for many applications such as in the transport sector – including pyrolysis and hydrothermal liquefaction [2]. Hydrothermal liquefaction (HTL) is an emerging technique for conversion, in particular, of wet biomass into liquid fuels by processing it in a hot, pressurised water environment for sufficient time to break down the solid biopolymeric structure and produce a liquid bio-oil (also called bio-crude) as energy vector. The process was conceptually introduced at the beginning of the XX century by the Nobel Prize F. Bergius (German chemist, 1884–1949, Nobel in 1931) during studies on the hydrothermal carbonisation processes of cellulose. This process operates at high pressure (40–200 bar) and relatively low temperature (250–360 °C), and uses water (mostly in subcritical or near critical conditions) as solvent, catalyst and thermal flywheel [3]. Under these operating conditions, liquid water starts assuming the characteristics of a polar organic solvent, so allowing the organic molecules to take part, in water, in the desired chemical reactions. Moreover, ionic product is large enough to favour ionic reactions resulting in oil products. Besides the target bio-oil, an aqueous phase, a bio-char and a gas phase are also produced from HTL. Compared with bio-oil from pyrolysis (which operates at near-atmospheric pressure), the one obtained from HTL is generally characterised by lower contents of both moisture and oxygen/carbon, and consequently higher heating value (HHV) of about 30–40 MJ/kg [4]. In

---

[*] Corresponding author: fabio.montagnaro@unina.it

addition, the HTL process allows to exploit the sludges water content for biocrude production, thus avoiding the high-energy demanding dewatering step commonly associated with other competitive processes of energy conversion (e.g.: oxy-pyrolysis, gasification, torrefaction) [5].

HTL process is based on the following steps: i) biomass hydrolysis and depolymerisation to monomers; ii) thermo-chemical decomposition/degradation of the produced monomers to form intermediates through reactions of dehydration, dehydrogenation, deoxygenation, cleavage, deamination, decarboxylation, cracking/fragmentation, etc.; iii) rearrangement of the reactive fragments/intermediates through re-polymerisation, condensation and cyclisation to form bio-oil and bio-char. Values for the energetic ratio (i.e. the ratio between HHV of the biocrude and HHV of the starting material) around 2.8 for sewage sludge have been reported [6], to indicate that HTL is a process able to determine a significant energetic densification of the parent biomass. In addition, a biogas is produced as well, containing, besides CO_2, species of energetic value such as CH_4, H_2, CO, and, finally, the formation of an aqueous phase containing soluble organic species (e.g. alcohols, acids, phenols, ketones, N-based species) occurs.

The aim of this work is to outline a process for the hydrothermal liquefaction of an industrial sludge for bio-fuel production. In particular, a tanning sludge was characterised to determine its composition, energy properties and microstructure prior to its energetic valorisation by means of the HTL process. At the same time, a detailed design of a lab-scale plant accounting for a stirred autoclave reactor was carried out with specific technical characteristics, optimised for chemical kinetics studies. To investigate the relationships between HTL operating conditions and yields and quality of bio-fuels obtained from sludges, an original elaboration of literature data was also performed. This, in turn, can provide useful guidelines to determine optimal conditions for the execution of HTL tests in the designed experimental apparatus.

Characterisation of a tannery sludge

The biomass adopted in this work is an industrial sludge deriving from the tannery industry. The sludge sample has been characterised by means of different techniques, which also provide useful data to preliminary assess the sludge composition and properties. The proximate analysis was performed by means of a LECO TGA701 thermogravimetric analyser in compliance with the UNI 9903 standard method. The ultimate composition was determined by using a LECO CHN628 and a LECO SC-144DR analyser in accordance with the ASTM D5373 (for C, H and N determination) and the UNI 7584 (for S determination) standard methods, respectively. The results are summarised in Table 1 (% by weight). Triplicate measurements together with mean values are reported.

Table 1. Proximate/ultimate analysis for tannery sludge.

	Test 1	**Test 2**	**Test 3**	**Mean value**
Moisture	18.5%	18.1%	18.7%	18.5%
Volatile	50.1%	50.1%	50.2%	50.1%
Fixed C	n.d.	n.d.	n.d.	n.d.
Ash	31.4%	31.8%	31.1%	31.4%
C (d.b.)	33.5%	33.5%	33.8%	33.6%
H (d.b.)	5.3%	5.0%	5.0%	5.1%
N (d.b.)	2.5%	2.4%	2.4%	2.4%
S (d.b.)	4.1%	4.1%	4.1%	4.1%

The sludge has an average moisture and volatile content of 18.46% and 50.13%, respectively. The ash mass percentage is 31.41% and fixed carbon has not been detected. The carbon is then to be sought in association with other species, and its total content is evidenced by ultimate analysis (d.b.=dry basis). The sludge has the following mean values of composition: 33.61% (C), 5.10% (H), 2.44% (N), 4.07% (S). The emphasis is placed on the detected fraction of C, which allows to hypothesise subsequent studies on the energetic valorisation of the sludge via HTL due to the very nature of this material.

The heating value of the sludge was determined using a Parr 6200 calorimeter (reference standard method adopted for the determination of the HHV is ASTM D5865). Chlorine quantification in the sludge was performed downstream the HHV determination according to the UNI 9903 standard protocol, which includes absorption of chlorine (released during the sludge combustion in the calorimetric bomb) into 2% wt. sodium carbonate aqueous solution followed by ionic chromatography analysis by using a 883 Basic IC plus ion chromatograph (Metrohm).

On a dry basis, the average value of HHV (obtained from triplicate analyses) is 14.90 MJ/kg, value in accordance with those commonly reported in the literature for sludges and, in general, for biomasses. This result, together with the determined C content (Table 1), confirms the possibility of considering this sludge as an energy carrier in valorisation processes. The average chlorine content in the sludge is 0.35%.

Another important characterisation of the sludge is the determination of the metals content. In particular, the determination of the chromium content and its speciation for tanning sludge is very important, due to the high toxicity of chromium in its hexavalent state, if present. The determination of the metal content in the sludge was carried out by means of Inductively coupled plasma-mass spectrometry ICP-MS (Thermo Scientific, ICAP RQ), applied on the sample, after microwave-assisted digestion in acidic solution (HNO_3/H_2O_2). Results are summarised in Table 2.

Table 2. ICP-MS analysis on w.b. (wet basis) and d.b. (dry basis) tannery sludge.

Metal	C [mg/kg] w.b.	C [mg/kg] d.b.
Mg	826.45	1013.55
Al	3886.68	4766.60
Ca	40479.02	49643.15
Ti	587.98	721.10
Cr	18366.18	22524.13
Fe	20202.41	24776.07
Si	7128.83	8742.74
K	377.21	462.61
Na	3523.96	4321.76
Zn	945.40	1160.09
Co	5.48	7.17
Ni	10.18	12.48
Cu	56.43	69.21
As	1.85	2.27
Zr	253.86	311.33
Cd	n.d.	n.d.
Sb	0.60	0.74
Ba	31.40	38.51
Hg	0.0026	0.0032
Pb	16.32	20.01

It is interesting to note that Cr, the main tanning agent in the leather production process, is the most abundant metal after Ca and Fe, which also take part in the step of leather production. The presence of Cr poses scientific challenges for tannery sludge, and special attention should be paid to preventing oxidation of chromium from trivalent to highly harmful hexavalent state. In this case, valorisation techniques that do not aim at the complete oxidation of the organic matrix of the sludge should be preferred. Contextually, the production of a bio-fuel via HTL is potentially more attractive than the direct combustion of the sludge. With the eye on the speciation of Cr before and after the energetic valorisation tests, an important preliminary characterisation involved the determination of Cr(VI) in the parent matrix. The analytical method used for the determination of Cr(VI) is reported in "Analytical methods for sludge. Chemical-physical parameters", Quaderni IRSA-CNR n. 64. The UV-vis spectrophotometric method (using a Varian Cary 5000 spectrophotometer) was used, where Cr(VI) is solubilised in an acid medium and then its concentration determined on the solution filtered by colorimetric reaction with diphenylcarbazide. It is highlighted that, due to the high iron content determined in the sludge (cf. Table 2) which could have interfered with chromium (VI) determination, iron was previously precipitated as hydroxide by adding NaOH in the liquid sample. The solution containing the sludge did not produce, with the addition of diphenylcarbazide solution, a shift from transparent to pink (the latter color indicative of Cr(VI) presence in the sample). Consequently, Cr(VI) was not detected by the UV-vis spectrophotometer, thus confirming that its concentration in solution was lower than the lowest detection limit for this technique and equal to 0.05 mg/L (equivalent to a Cr(VI) content in the starting sludge lower than 2 mg/kg, if present).

Finally, the dried sludge was subjected to X-ray diffraction (XRD) analysis using a Bruker diffractometer (radiation Cu-Kα; range of scanned diffraction angle 2θ varying from 5 to 60 degrees; scanning rate=0.05°2θ/s). The four main crystalline phases identified from the analysis of the diffraction spectrum are calcite ($CaCO_3$), cristobalite (SiO_2), elementar sulphur and eskolaite (Cr_2O_3). It should be recalled that the XRD analysis allows to identify only phases characterised by sufficient degree of crystallinity, and therefore other phases present in the sample as amorphous or as poorly crystalline cannot be excluded. In fact, the degree of crystallinity of the sample (as determined from the diffraction spectrum) is as low as 7.90%, thus indicating the predominantly amorphous nature of the sludge being examined.

Design of a lab-scale apparatus for HTL

In the framework of valorisation via HTL of the analysed tannery sludge, an important preliminary phase involved the choice of a suitable reaction system. In fact, the HTL process is performed at ca. 40–200 bar and 200–350 °C to improve, in particular, the water solubility of hydrophobic organic compounds, such as free fatty acids, in order to drive the reactive pathway towards the target bio-oil. On the other hand, the water solubility of inorganic salts significantly decreases, thus potentially leading to the precipitation of crystalline salts, which in turn can easily attach to the walls of both the reactor and its components (such as mixer, heat exchanger and thermocouples). This can cause fouling or even blockage and associated problems of correct operation of the system. Moreover, corrosion, and in particular the pitting phenomenon, can rapidly occur in the high temperature subcritical water environment, characteristic of the HTL process. Literature data report studies of different materials tested under subcritical conditions, but only a few have sufficient corrosion resistance under harsh HTL environments. Consequently, nickel-chromium-molybdenum alloy (Hastelloy C-276) was chosen as material for the realisation of the HTL reactor. This alloy is particularly resistant to pitting and interstitial corrosion in reducing environments in the pH range 1–14, thus enabling to perform HTL tests also in presence of different acid and base catalysts. Moreover, the presence of chromium gives a good resistance to oxidizing and reducing environments.

Following the selection of the best material for the HTL reactor, a study was made with the aim of establishing the layout of the experimental apparatus, based on the selected conditions and the experimental procedure (see Figure 1).

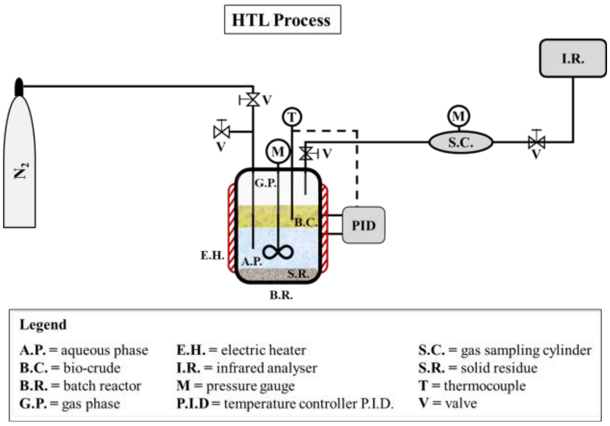

Figure 1. Layout of the lab-scale apparatus for the execution of HTL tests.

The lab-scale apparatus consists of a 500 mL batch reactor (Parr Instruments, series PA 4575A) equipped with:

i) digital pressure transducer coupled with a needle valve for pressure measurement and control;
ii) tubular electric heater coupled with thermocouples and PID system for temperature setting, measurement and heating rate control;
iii) magnetic stirrer with maximum torque of 1.76 Nm and variable speed motor 1/8 hp, suitable for matrices with high viscosity as sludge (10^2–10^4 cP);
iv) single loop cooling coil;
v) inlet and outlet ports for gas injection and liquid/gas withdrawal;
vi) gas sampling cylinder.

A typical HTL test will consist of the following stages: a) loading the slurry (wet sludge at fixed biomass concentration) into the reactor; b) first pressurization stage with N_2 fed by a gas cylinder; c) second pressurization stage by rapid heating of the system to the desired temperature level; d) running the HTL test at fixed time/temperature level; e) fast cooling of the reactor so to "freeze" chemical reactions, thus avoiding products re-distribution during thermal transients; f) depressurization of the reactor and sampling of the gas obtained from the HTL process. At the end of the test, liquid-solid phases separation will be performed by coupling filtration, liquid–liquid extraction with solvent and/or distillation.

Role of operating parameters on the performances of HTL applied to sludges

Several operating parameters can play an important role in the valorisation of sludges through HTL. The literature analysis revealed that, among them, both the reaction temperature and time affect, in particular, the energetic properties and mass yield of the obtained bio-crude [7,8]. In the following, literature data on HTL of sewage sludges have been critically elaborated to define optimal temperature and reaction time windows in which operate the hydrothermal liquefaction process for the residue under investigation.

Effect of reaction temperature

Figure 2 depicts the energy yield (Y_E) as a function of the mass yield of the bio-crude obtained after HTL (Y_{bc}). Y_E represents the ratio between the energy content of the bio-oil and the one of the parent sludge:

$$Y_E = \frac{HHV_{bc} \cdot Y_{bc}}{HHV_0} = r \cdot Y_{bc} \qquad (1)$$

where HHV_{bc} and HHV_0 are the higher heating values of bio-crude and starting biomass, respectively. In Eq. (1), r is defined as the energy ratio (i.e., the ratio between higher heating values), and iso-energy ratio lines are also reported in Figure 2 for reference.

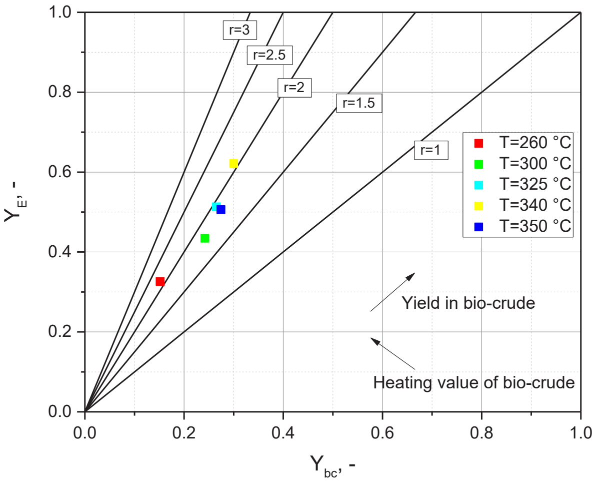

Figure 2. Energy yield as a function of bio-crude yield for HTL of sludges treated at different temperatures (data are obtained from averaged values reported in literature).

Literature data show that an increase in temperature in the range 260–340 °C (pressure range 180–250 bar; reaction time range 10–30 min) determines a monotonic increase of both Y_E and Y_{bc}. Y_E increases from 0.33 at 260 °C (Y_{bc}=0.15) to 0.62 at 340 °C (Y_{bc}=0.30). A further rise of only 10 °C in temperature can be detrimental for both energy and mass yield of bio-crude: at 350 °C, Y_E=0.51 and Y_{bc}=0.27, while r falls in the range 1.5–2 (it was >2, for instance, at both 260 and 340 °C). The above-discussed trend can be explained as follows: the rise in temperature up to 340 °C favours the reactive pathways that determine the fragmentation of organic compounds to give the desired bio-crude. Even higher temperatures are likely to promote the production of bio-gas via gasification reactions and secondary decompositions, and the formation of bio-char through the recombination of free radicals. In this context, both bio-gas and bio-char are seen as by-products that limit the productivity of the HTL process in terms of the desired bio-oil.

Effect of reaction time

Figure 3 reports Y_E vs. Y_{bc} for bio-crude obtained from the HTL process performed on sludges under different reaction times (pressure range 180–350 bar; temperature range = 260–350 °C).

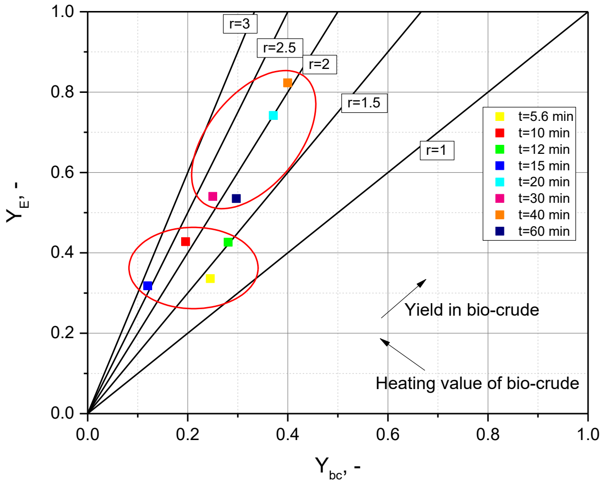

Figure 3. Energy yield as a function of bio-crude yield for HTL of sludges treated at different reactions time (data are obtained from averaged values reported in literature).

The analysis enables to identify two main "clouds" in which data do gather:

- The "short times cloud" groups data ranging from 6 to 15 min. Here Y_{bc} values vary between 0.12 and 0.28, and Y_E values belong to the interval 0.32–0.43. The experimental data lie in a wide range of r between 1.4 and 2.6;
- The "long times cloud" groups data obtained for HTL reactions times varying between 20 and 60 min. The increase in test time leads to a marked increase in energy yield, between 0.54–0.82, and in mass yield, between 0.25–0.40, with values of r of about 2.

Consequently, longer residence times generally positively influence Y_E and Y_{bc}, allowing the series/parallel reactive network characteristic of the HTL process to take place. Hence, the identified long time region seems to be optimal for achieving satisfactory values for the objective functions (Y_E and Y_{bc}). It is reasonable to expect that even longer times would lead to the decrease in process yield, given the series-parallel nature of the involved reactive network. In fact, too long residence times increase the likelihood of condensation reactions, cyclisation and repolymerisation between intermediate products, leading to the formation of bio-char at the expense of the bio-crude yield.

Conclusions

In this work, the physico/chemical properties of a tannery sludge have been studied to obtain a preliminary characterisation of the sludge for its subsequent energetic valorisation via the HTL process. The carbon content of the sludge (33.61%) together with the determined value of the higher heating value (14.90 MJ/kg) confirm the possibility of considering this sludge as a promising energy carrier in the HTL valorisation process. In addition, spectrophotometric analysis did not reveal the presence of highly toxic chromium (VI) in the tannery sludge, while the concentration of its trivalent form was 22.5 g/kg on dry basis. In this context, the HTL process appears as an attractive thermochemical route also to potentially avoid the undesired chromium oxidation, since HTL does not involve the complete oxidation of the organic matrix of the sludge (such as in the case of combustion processes). A detailed design of a lab-scale plant accounting for a stirred autoclave reactor was also carried out with specific technical characteristics, optimised for chemical kinetics studies. In particular, the harsh reaction environment that can occur during the HTL process led to the choice of a metal alloy nickel-chromium-molybdenum (Hastelloy C-276) particularly resistant to corrosion phenomena. Finally, the elaboration and critical analysis of literature data allowed to shed light on the effects of temperature and reaction time of HTL applied to sludges on the process performances. Results suggest that a temperature of ca. 340 °C and reaction times of about 20 min can provide satisfactorily values of both energy and mass yield of sludges-derived bio-crude. It should be emphasised that these considerations are based on a limited number of scientific papers available in the literature for HTL of sludges. Consequently, a deeper experimental campaign will be performed in the designed lab-scale apparatus to verify the highlighted trends and to address in detail this relatively young research process, focusing on aspects that still deserve scientific investigation.

Acknowledgements

Dr. Giovanna Ruoppolo, Dr. Massimo Urciuolo, Dr. Edoardo Imperiale and Dr. Francesco De Chiara (for useful discussion), Prof. Mauro Iuliano and Dr. Gaetano De Tommaso (for metals analyses), Dr. Rocco Di Girolamo (for XRD analyses) and the students Mr. Paolo D'Amore and Mr. Dario D'Angelo (for useful discussion) are gratefully acknowledged. This work has been carried out as part of the Italian national research project 'Biofeedstock' PONARS01_00985.

References

[1] P. Mohanty, K.K. Pant, S.N. Naik, J. Parikh, A. Hornung, J.N. Sahu, Renew. Sust. Energ. Rev. 38 (2014) 131–153. https://doi.org/10.1016/j.rser.2014.05.011.
[2] A.R.K. Gollakota, N. Kishore, S. Gu, Renew. Sust. Energ. Rev. 81 (2018) 1378–1392. https://doi.org/10.1016/j.rser.2017.05.178.
[3] S.S. Toor, L. Rosendahl, A. Rudolf, Energy 36 (2011) 2328–2342. https://doi.org/10.1016/j.energy.2011.03.013.
[4] C. Prestigiacomo, V.A. Laudicina, A. Siragusa, O. Scialdone, A. Galia, Energy 201 (2020) 117606.

https://doi.org/10.1016/j.energy.2020.117606.
[5] C.S. Theegala, J.S. Midgett, Bioresour. Technol. 107 (2012) 456–463. https://doi.org/10.1016/j.biortech.2011.12.061.
[6] D. Castello, T.H. Pedersen, L.A. Rosendahl, Energies 11 (2018) 3165. https://doi.org/10.3390/en11113165.
[7] F. Cheng, M.D. Porter, L.M. Colosi, Energ. Convers. Manage. 203 (2020) 112252. https://doi.org/10.1016/j.enconman.2019.112252.
[8] M. Déniel, G. Haarlemmer, A. Roubaud, E. Weiss-Hortala, J. Fages, Waste Biomass Valorization 8 (2017) 2087–2107. https://doi.org/10.1007/s12649-016-9726-7.

Improvement of Performance of Fluidized Bed Calcium Looping for Thermochemical Solar Energy Storage: Modelling and Experiments

S. Pascual[1], F. Di Lauro[2], P. Lisbona[3], L.M. Romeo[1], C. Tregambi[4], F. Montagnaro[2], R. Solimene[*,5], P. Salatino[6]

[1]Departamento de Ingeniería Mecánica. Escuela de Ingeniería y Arquitectura (EINA). Universidad de Zaragoza. C/ María de Luna s/n, 50018, Zaragoza, Spain
[2]Dipartimento di Scienze Chimiche, Università degli Studi di Napoli Federico II,
Complesso Universitario di Monte Sant'Angelo, 80126 Napoli, Italy
[3]Fundación Agencia Aragonesa para la Investigación y el Desarrollo (ARAID), Zaragoza, Spain
[4]Dipartimento di Ingegneria, Università degli Studi del Sannio, Piazza Roma 21, 82100 Benevento, Italy
[5]Istituto di Scienze e Tecnologie per l'Energia e la Mobilità Sostenibili,
Consiglio Nazionale delle Ricerche, Piazzale Vincenzo Tecchio 80, 80125 Napoli, Italy
[6]Dipartimento di Ingegneria Chimica, dei Materiali e della Produzione Industriale,
Università degli Studi di Napoli Federico II, Piazzale Vincenzo Tecchio 80, 80125 Napoli, Italy

Abstract

Calcium-looping (CaL) can be exploited as promising thermochemical energy storage (TCES) process in concentrated solar power (CSP) plants. The present research analyzes the influence of solids separation after carbonation in a CaL-CSP plant sizing. The results obtained from modelling and simulation of both threshold schemes (with/without solids separation) have shown a reduction of plant equipment size and energy consumption of the facility between 50 and 75% when solid separation unit is included. Based on these promising modelling results, experimental tests were performed to verify the technical feasibility of solids separation after partial carbonation, exploiting the difference of density (hence of minimum fluidization velocity) between calcined and carbonated particles. Experimental results show suitable conditions for partial separation of solids in fluidized bed for the first calcination/carbonation cycles.

Introduction

Calcium-looping process (CaL) based on the cyclic reactions of carbonation-calcination of limestone can be exploited as promising thermochemical energy storage (TCES) system in concentrated solar power (CSP) plants. Research has mainly been focused on the improvement of efficiency of different CaL integrations as TCES within power cycles [1,2], the management of the storage system [3] and the design or scaling up of the main reactors, carbonator [4–6] and calciner [7]. Fluidized beds have been identified as ideal reactors/receivers for CaL-CSP integration given the intimate gas–solid contact achieved by fluidization state and the high efficient collection of solar energy [8].

The integrated schemes presented in literature consider independent storage tanks for: i) CO_2 and lime (CaO) obtained after calcination and ii) a mixture of unconverted CaO (related to particles experiencing very short residence times) and partially carbonated lime (CL), the latter being in turn a mixture of CaO and $CaCO_3$ (because of uncomplete carbonation), obtained after carbonation step [5,6]. Under these conditions, the size of the CL storage tank will be extremely large as well as the size of the heat exchangers managing the solids flow circulating from carbonator to calciner. Up to now, the influence of the separation of the mixture of solids exiting the carbonator on the plant equipment size and the power plant consumption has not been assessed in detail. However, the analysis of a CaL-CSP operation maps under a solids separation scenario has allowed to know the behavior and power range of the heat exchangers involved in the plant [9].

The novelty of this research relies in the analysis of the CaL-TCES process including partial separation of solids at the outlet of the carbonator, in order to reduce the plant size and therefore the associated economic costs. The proposed system is a fluidized bed classifier able to separate the particles by density difference.

CaL-CSP simulation model

The CaL-CSP system consists of two main fluidized beds reactors, calciner and carbonator, with intermediate storage tanks of CO_2 and solids. The calciner is sized for 100 MW_{th} of solar input energy (E_{CL}) and working temperature is 950 ºC under CO_2 pure atmosphere to ensure a high reaction rate [10]. The endothermic calcination reaction is assumed to be complete and the limestone in the calciner is fully transformed into lime and CO_2. The CO_2 and lime formed in calciner are directed to carbonator or diverted towards their corresponding storage tanks. Since CaO quickly deactivates with the number of cycles, a stream of fresh limestone is fed in the calciner to keep a reasonable sorption activity. The $CaCO_3$ to the calciner reactor comes from: (i) the contribution of fresh limestone and (ii) the $CaCO_3$ produced after carbonation reaction. Fresh limestone counterbalances the purged solid material (f_p) which is set as a percentage of the CaO molar flow generated in calcination reaction.

The carbonator operates at 850 °C under pure CO_2 atmosphere [1]. The exothermic carbonation reaction

---

[*] Corresponding author: solimene@irc.cnr.it

(E_{CR}) is not complete with a carbonation degree decreasing upon iterated cycles. The carbonator model used to determine the deactivation of the CaO particles is tuned adjusting the kinetic model described by Grasa et al. [11] obtained for 650 ºC and an approximately CO_2 concentration between 10-15%vol. The amount of reacting CaO particles will depend on the average sorption activity of the population of particles circulating in the system [12]. Therefore, a mixture of $CaCO_3$ and CaO consisting of partially carbonated lime particles is found at carbonator outlet. Unreacted CO_2 leaving the carbonator is stored under established conditions. The CaO to CO_2 molar ratio introduced in the carbonator (R) and the average sorbent activity define the carbon capture efficiency in the carbonator reactor.

The CaL-CSP model has been evaluated under two limit scenarios after the carbonation step: (SC1) no separation and (SC2) an ideal and total separation of the mixture of $CaCO_3$ and CaO exiting the carbonator, to quantify its influence on performance, size and economics. A simplified outline of the CaL-CSP model under both scenarios is illustrated in Fig.1. The greatest influence of the solids separation unit occurs on the equipment shown in Fig.1: (i) heat exchangers with solids streams involved (*EE-CaO*, *ER-CaO*, *EE-CaCO3* and *ER-CaCO3*), (ii) fluidized bed reactors (carbonator and calciner) and (iii) mainly CaO and $CaCO_3$ storage tanks.

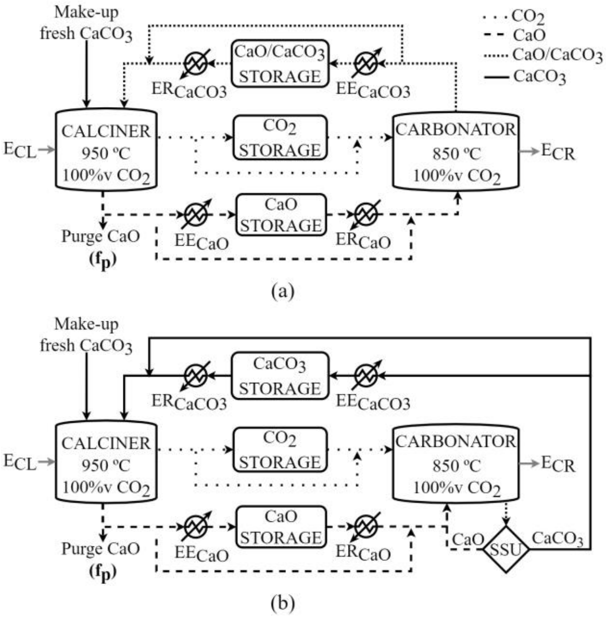

(a)

(b)

Figure 1. Simplified scheme CaL-CSP simulation model under SC1 (a) and SC2 (b).

Under scenario SC1 (Fig. 1 (a)), the solids input to the calciner (CL) is a mixture of approximately 80% lime and 20% limestone that must be heated up to 850 °C. The CL stream results from the addition of the direct flow from the carbonator at 850 °C and the discharge flow of solids stored at 200 °C. Regarding the inlet streams to the carbonator, the CaO stream discharged from the storage (200 ºC) is mixed with the direct CaO flow from calciner (950 ºC) before being introduced into carbonator at 850 ºC.

Under scenario SC2 (Fig.1 (b)), an idealized solids separation is considered assuming to be feasible the separation of the mixture of $CaCO_3$ and CaO. In particular, the separation unit (SSU) receives the mixture of $CaCO_3$ and CaO from the carbonator and separates (i) the unreacted CaO which is recirculated into the carbonator and (ii) the limestone stream sent to calciner or storage tank.

Both scenarios have been energetically compared under comparable operating conditions. A CaO purge percentage (f_p) is set in each case to keep the same constant value of R under both simulations. The molar ratio between CaO and CO_2 (R) is 4.26, whereas f_p is 3.09% and 4% for SC1 and SC2, respectively. The simulation results obtained under SC2 show a size reduction between 50 and 75% in the plant equipment influenced by solids streams compared to the CaL-CSP under SC1. Besides, the solids storage tanks size under SC2 is smaller than for scenario SC1 given the recirculation of unreacted CaO.

However, the model used under both scenarios present some limitations. First, the kinetic model used is based on the degradation of the sorption capacity of a *Piaseck* limestone in case of carbonation at 650 ºC and 10%vol of CO_2 atmosphere [11]. No experimental data of carbonation evolution under the actual operating conditions of the CaL for TCES were available in literature. Therefore, the carbonation degree should be determined experimentally under the operating conditions established in the CaL-CSP model. On the other hand, a model for solids separation has not been estimated. Only two threshold limit scenarios have been evaluated (with and without solids separation) from the energy point of view. The possible separation degree exploiting the difference in density between the unreacted CaO and the CL stream must be analyzed experimentally. Moreover, it is not possible a complete separation between CaO and $CaCO_3$ because the stream exiting the carbonator is made of partially carbonated lime particles containing both $CaCO_3$ and CaO. Thus, the separator could, in principle, separate only the more carbonated lime particles from the less converted particles.

Nevertheless, this preliminary research based on modelling allows the possibility of developing an experimental campaign to investigate the technical feasibility of, even if partial, solids separation.

Experimental tests methodology

Determination of carbonation degree. A lab-scale Directly Irradiated Fluidized Bed (DIFB) described by Tregambi et al. [13] was used to determine the carbonation degree under the CaL-CSP operating conditions described in the previous section. The experimental tests consisted of 20 consecutive calcination and carbonation cycles using an Italian natural limestone named “Sardo”, ground and sieved in the 420−590 µm range, as reactive material [13]. A bed inventory of 850 g was used, consisting in 700 g of inert sand (served as thermal flywheel but not required in industrial applications) and 150 g of reactive limestone. The fluidizing velocity was always set at 0.6 m/s during carbonation and calcination, a value approximately twice the minimum fluidization velocity of the inert sand. Both reactions took place in the same DIFB reactor by alternating the calcination-carbonation operating conditions. Consistently with realistic conditions of CaL-CSP system, only the calcination step was performed under radiative flux. Thermal supply in other stages of the experiment was ensured by radiant heaters and a gas preheater. During a typical carbonation degree test, the bed was charged with about 700 g of inert sand and heated up to 900 °C by using both the radiant heaters and the gas preheater with atmospheric air as fluidizing gas. Once the pre-set temperature was reached, the radiant heaters were powered off, the air stream was switched to CO_2 and, simultaneously, a sample of 150 g of limestone was fed to the reactor. Then, the solar simulator was powered on and its power tuned to reach a temperature of 950 °C. A time of 20 min was waited to perform the calcination reaction (calcination zero), after which the solar simulator was powered off and the reactor cooled down to 850 °C with atmospheric air stream. Once reached this temperature, the fluidizing gas was switched to CO_2 to perform the carbonation reaction (carbonation step), which was prolonged for 20 min. Finally, the solar simulator was powered on for 20 min and its power tuned to reach 950 °C so to perform the calcination reaction and complete the reaction cycle (calcination step). The reactor was then cooled down to 850 °C to eventually start a new carbonation/calcination loop.

Sorbent samples were recovered after each carbonation step to evaluate the carbonation degree of the material. These samples (1-2 g mass), carefully separated from the inert silica sand by sieving, were subjected to a calcination step in a muffle furnace at 950 °C in air for 1 h and the weight change was measured with an analytical balance (0.1 mg precision). The samples weight data were used to calculate the mean carbonation degree ($\bar{X}_{Ca}$) of the material after each carbonation step (N):

$$\bar{X}_{Ca}(N) = \frac{\frac{m_0 - m_F}{MW_{CO2}}}{\frac{m_F \cdot P_{CaCO3}}{MW_{CaO}}} \qquad (1)$$

Where m_0 is the sample mass extracted after each carbonation step, m_F is the sample mass after the calcination step in the muffle furnace, P_{CaCO3} is the purity of the Sardo limestone, MW is the molecular weight. The average sorbent capacity up to the reaction cycle considered (N) is eventually computed in Eq. (2) as:

$$\bar{X}_{Ca,N} = \frac{\sum_{N=1}^{N} \bar{X}_{Ca}(N)}{N} \qquad (2)$$

Bulk density test. The experimental tests to determine the bulk density of calcined and carbonated particles were performed in a different lab-scale Fluidized Bed (FB) without solar radiative flux simulation, described in detail in Tregambi et al. [14]. The operating conditions were the same of those used in the DIFB reactor. During a typical test, the bed was charged with about 150 g of inert sand and heated up to 900 °C by using radiant heaters and atmospheric air as fluidizing gas. Once the pre-set temperature was reached, the sand was removed from the reactor and the air flow was switched to CO_2. A sample of 150 g of limestone was then fed to the reactor, which temperature was increased to 950 ºC. When temperature reached 900 ºC, the calcination started. The calcination zero was prolonged for 20 min. The CO_2 flow was switched to air after the calcination zero (20 min). The calcined material with the inert sand was then removed from the reactor after 2 min of air atmosphere by exploiting a vacuum system. The material extraction after calcination was performed in air atmosphere to prevent material carbonation as a consequence of the temperature reduction during extraction. The inert sand was separated from the calcined material by sieving and put back into the reactor, which temperature was set at 850 ºC. Once the pre-set temperature was reached, the calcined material was introduced into the reactor to perform the carbonation reaction after changing the gas stream from air to CO_2. The carbonated material with the inert sand was removed from the reactor after 20 min with the same procedure as calcination step. Once the inert sand was separated from the carbonated material by sieving, it was put back into the reactor. The reactor was heated up to 900 ºC using air as fluidizing stream. Once the pre-set temperature was reached, the air flow was switched to CO_2 and carbonated material was introduced to start the next calcination step.

The reactive material recovered after each carbonation and calcination step was analyzed to evaluate the bulk density and the granulometric distribution. The bulk density was determined by measuring the weight and volume of the reactive material in a 50 mL graduated cylinder. The reactive material was slowly and manually poured within the cylinder up to a certain volume mark. The material bulk density was calculated as the weight divided by the volume reached in the glass cylinder. On the other hand, the reactive material was sieved considering the following particle diameter ranges: 420–590 µm, 300–420 µm, 200–300 µm, 100–200 µm, <100 µm. The weight of material collected in each of the sieve ranges described was measured to know the particle size distribution of the carbonated (CL) and calcined (unreacted CaO) material after each cycle.

Development and validation of a density model

A simple and theoretical model (TM) at particle scale during iterated cycles of calcination and calcination was developed based on the experimental test results obtained. The assumptions taken for the model were the following: (i) no attrition and fragmentation phenomena, (ii) sintering only takes place during calcination causing porosity and size reduction, (iii) particles do not change volume during carbonation step and (iv) bed porosity remains the same for calcination and carbonation and is assumed constantly equal to 0.45.

Based on this model, the bulk density experimental results for carbonated and calcined particles can be related to the carbonation degree according to the following equation:

$$X_{carb_i} = \frac{MW_{CaO}}{MW_{CO_2}}\left(\frac{\rho_{carb_i}}{\rho_{calc_{i-1}}} - 1\right) \qquad (4)$$

where $\rho_{carb,i}$ is the bulk density of carbonated particles (CL) at carbonation number i, $\rho_{calc,i\text{-}1}$ is the bulk density of calcined particles (unreacted CaO) at calcination step i-1 and $X_{carb,i}$ is the carbonation degree after i carbonation step.

In parallel, the model can be used to calculate (i) the effective particle density and (ii) the particle diameter after each calcination and carbonation step. The effective particle density is computed by Eq. (5) for carbonated particles and by Eq. (6) for calcined particles:

$$\rho_p^{carb_i} = \frac{\rho_{carb_i}}{(1-\varepsilon_{bed})} \qquad (5)$$

$$\rho_p^{calc_i} = \frac{\rho_{calc_i}}{(1-\varepsilon_{bed})} \qquad (6)$$

where $\rho_p^{carb_i}$ and $\rho_p^{calc_i}$ are the carbonated and calcined particle density at cycle i, while ρ_{carb_i} and ρ_{calc_i} are the bulk density obtained after carbonation and calcination step (i) from the experimental test. The void fraction assumed (ε_{bed}) was 0.45 for both carbonated and calcined material. The void fraction value is typically of the fluidized bed state and is similar to the value obtained considering the bulk density of the fresh limestone (1590 kg/m^3) and the calcium carbonate density (2930 kg/m^3).

The particle diameter is computed by Eq. (7) for carbonated particles at step i+1 and for calcined particles at step i:

$$\frac{d_p^{carb_{i+1}}}{d_p} = \frac{d_p^{calc_i}}{d_p} = \left(\frac{\rho_0 \cdot MW_{CaO}}{\rho_{calc_i} \cdot MW_{CaCO_3}}\right)^{1/3} \qquad (7)$$

where $d_p^{calc_i}$ is the diameter of the calcined particle at cycle i, which matches the diameter of the carbonated particle at cycle i+1 ($d_p^{carb_{i+1}}$). Whereas d_p is the initial particle diameter, taking as reference the mean particle diameter of Sardo limestone (505 μm) used as raw material. Finally, ρ_0 is the experimental bulk density of the fresh limestone. The relationship between $d_p^{carb_{i+1}}$ and $d_p^{calc_i}$ was justified by analyzing the particle diameter after each carbonation and calcination step obtained from the experimental test. The mean particle size after calcination i was practically similar to the mean particle size obtained after carbonation i+1.

Results from model computations were used to determine the theoretical minimum fluidization velocity by applying the Wen & Yu model [15]. The particle diameter and effective particle density values from the experimental model developed were used to obtain the theoretical minimum fluidization velocity for each calcination (unreacted CaO) and carbonation (CL) step.

Results and discussion

The mean carbonation degree for each of the 20 carbonation-calcination cycles is shown in Fig.2. The black dots curve corresponds to the average carbonation degree for the 20 cycles performed in the DIFB. The grey and white points curves are related to the mean carbonation degree value obtained within the FB reactor and by the Theoretical Model (TM) developed applying Eq. (4), respectively.

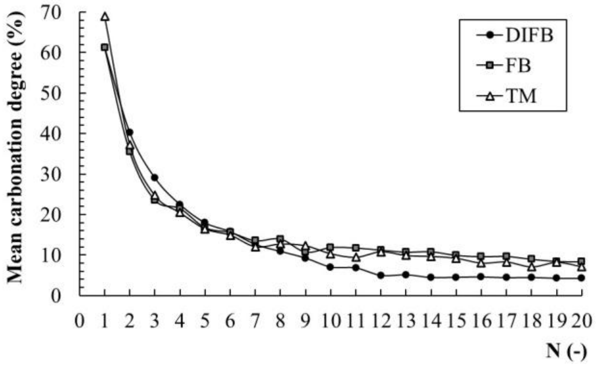

Figure 2. Mean carbonation degree results under DIFB, FB and TM conditions.

Experimental data obtained using the DIFB and FB show similar results. Values of carbonation degree obtained within DIFB are slightly lower, probably because of a more severe sintering induced by the concentrated solar radiation [8,13]. The experimental carbonation degree results under the second test conditions (FB) are used to validate the theoretical carbonation degree model (TM). Both curves show practically the same trend.

The average sorbent capacity in the reaction cycle number 20, computed by Eq. (2), is 13.72% under DIFB conditions, and around 16% under FB or TM assumptions. Direct irradiation has a weak negative effect on the carbonation, mainly from cycle 10th to 20th, favoring the sintering of the material.

The effective bulk density of particles for carbonated and calcined particles after each cycle is illustrated in Fig.3. The black squares curve represents the carbonated particles density applying Eq. (5), while the white rhombs curve is obtained through Eq. (6) for the calcined particles density.

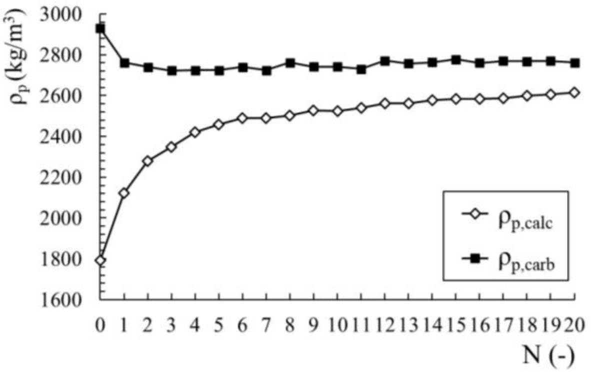

Figure 3. Effective particle density of carbonated and calcined particles.

The particle density after each carbonation (black dots curve) remains practically unchanged (about 2750 kg/m^3). The first value of the black dots curve (N = 0) corresponds to the effective particle density of the raw material (fresh limestone). The carbonated particle density value may be governed by the $CaCO_3$ compact structure. On the other hand, the calcined particles density increases rapidly until 6th and more slowly for the further steps. Thus, the effect of sintering on calcined particle density is clearer than carbonated particles density. Therefore, the particles density after each calcination increases proportionally to the reduction in the carbonation degree step by step.

The particle diameter results for carbonated and calcined material after each cycle is shown in Fig.4. The black squares curve represents the carbonated particles diameter, while the white rhombs curve is obtained for the calcined particles size, both applying Eq. (7).

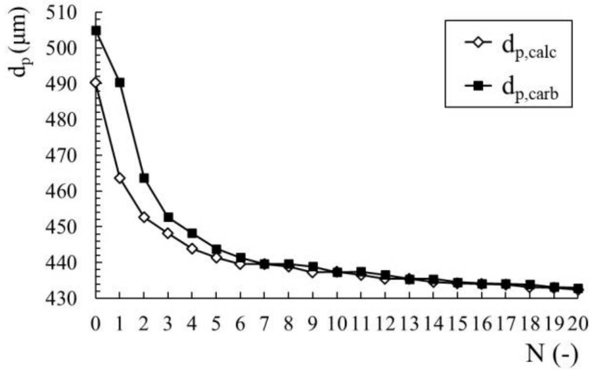

Figure 4. Theoretical particle diameter for carbonated and calcined material.

The particles size is reduced step by step in the calcination reaction for both carbonated and calcined particles. The size is kept in the range between 430 and 440 µm from cycle 6th to 20th. The smaller the particles size with number of carbonation-calcination cycles, the greater the sintering phenomenon influence and therefore an increase of the calcined particles density is produced. The mean particle size up to 20 cycles from the theoretical model amounts to 449 µm, whereas the average particle diameter obtained from the experimental data is 453 µm. Therefore, the theoretical model developed from the bulk density data collected approaches the experimentally determined particle size.

The theoretical minimum fluidization velocity (u_{mf}) for carbonated and calcined particles after each cycle is illustrated in Fig.5. The white rhombs curve represents the u_{mf} of the calcined particles or unconverted CaO, while the black squares curve shows the u_{mf} of carbonated particles or CL stream. Both were calculated considering air as fluidizing gas at ambient temperature (25 ºC) to compare the theoretical results with the experimental data. The comparison between theoretical and experimental u_{mf} will be performed in future studies.

Nevertheless, as can be seen in Fig.5, the minimum velocity required for fluidization of carbonated particles during the first 5 cycles is between 27 and 11% higher than that of calcined particles. Since cycle 6th, the difference of u_{mf} between carbonated and calcined particles remains practically constant (u_{mf} of carbonated material is 7% more over u_{mf} of calcined material).

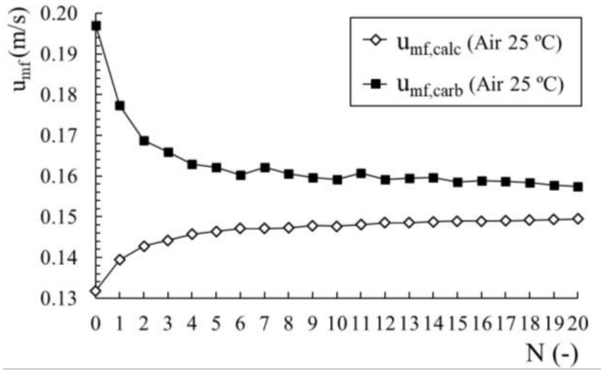

Figure 5. Theoretical minimum fluidization velocity of calcined and carbonated particles under experimental conditions (air 25 ºC).

Fig.6 illustrated the theoretical minimum fluidization velocity using CO_2 as fluidizing gas at 850 ºC. In the same way, the white rhombs curve represents the u_{mf} of the calcined particles or unconverted CaO, while the black squares curve shows the u_{mf} of carbonated particles or CL stream.

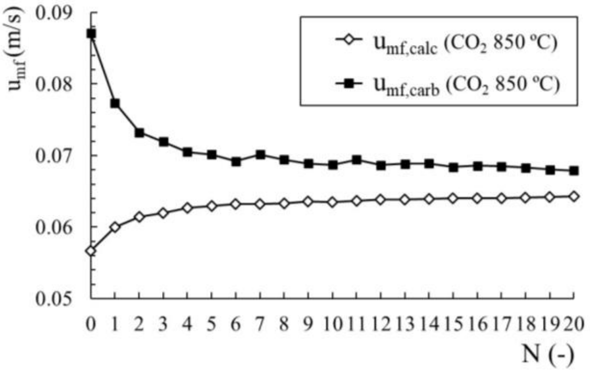

Figure 6. Theoretical minimum fluidization velocity of calcined and carbonated particles under real operating conditions (CO_2 850 ºC).

The minimum velocity required for fluidization of the partially carbonated lime during the first 5 cycles is between 29 and 11% higher than that of unconverted CaO particles. Since cycle 6th, the difference of u_{mf} between carbonated and calcined particles remains practically constant (u_{mf} of CaO and $CaCO_3$ mixture is 8% more over u_{mf} of unconverted CaO).

Results show suitable conditions for partial separation of solids in a fluidized bed for particles subjected to few carbonation-calcination cycles. For future work, the experimental measurement of the minimum fluidization velocity must be performed to compare and validate the results obtained through the experimental model developed. In the same way, a sensitivity study of the sorbent purge percentage variation on the carbonation degree may be analyzed to improve the CaO average sorption capacity under the operating conditions selected in the CaL-CSP model.

Conclusions

In the present work, the partial separation of solids after carbonation reaction has been experimentally investigated under a CaL-CSP model operating conditions using fluidized bed reactors (850 °C and 950 °C for carbonation and calcination, respectively, reacting atmosphere always of 100% CO_2). A potential reduction in equipment size and energy flows between 50 and 75 % can be achieved when going from a system without solids separation to one with total separation of solids after carbonation step.

Results obtained show that the density of carbonated and calcined particles are related to the mean carbonation degree of the sorbent and the particle size. A model developed from experimental data is used to determine the particle density and diameter after each carbonation and calcination step. The theoretical minimum fluidization velocity calculated of calcined material (unreacted CaO) is lower than the carbonated material (partially carbonated lime) for the first cycles. A partial separation of solids may be technically feasible for particles with few cycles operated.

Acknowledgements

The FPU Programme and the mobility grant for FPU beneficiaries of the Spanish Ministry of Science, Innovation and Universities (FPU2017/03902 and EST19/00144) provided financial support for S.P. PhD studies.

References

[1] R. Chacartegui, A. Alovisio, C. Ortiz, J.M. Valverde, V. Verda, J.A. Becerra, Thermochemical energy storage of concentrated solar power by integration of the calcium looping process and a CO_2 power cycle, Appl. Energy. 173 (2016) 589–605. https://doi.org/10.1016/j.apenergy.2016.04.053.

[2] U. Tesio, E. Guelpa, V. Verda, Integration of ThermoChemical Energy Storage in Concentrated Solar Power. Part 2: comprehensive optimization of supercritical CO_2 power block, Energy Convers. Manag. X. 6 (2020) 100038. https://doi.org/10.1016/j.ecmx.2020.100038.

[3] R. Bravo, C. Ortiz, R. Chacartegui, D. Friedrich, Hybrid solar power plant with thermochemical energy storage: A multi-objective operational optimisation, Energy Convers. Manag. 205 (2020) 112421. https://doi.org/10.1016/j.enconman.2019.112421.

[4] M. Bailera, P. Lisbona, L.M. Romeo, L.I. Díez, Calcium looping as chemical energy storage in concentrated solar power plants: Carbonator modelling and configuration assessment, Appl. Therm. Eng. (2020) 115186. https://doi.org/10.1016/j.applthermaleng.2020.115186.

[5] S. Pascual, M. Bailera, P. Lisbona, L.I. Díez, L.M. Romeo, Solar calcium looping energy storage: Preliminary comparison between pilot and large scale, ECOS 2020 - Proc. 33rd Int. Conf. Effic. Cost, Optim. Simul. Environ. Impact Energy Syst. (2020) 1511–1522.

[6] M. Bailera, S. Pascual, P. Lisbona, L.M. Romeo, Modelling calcium looping at industrial scale for energy storage in concentrating solar power plants, Energy. (2021) 120306. https://doi.org/10.1016/j.energy.2021.120306.

[7] P. Lisbona, M. Bailera, T. Hills, M. Sceats, L.I. Díez, L.M. Romeo, Energy consumption minimization for a solar lime calciner operating in a concentrated solar power plant for thermal energy storage, Renew. Energy. 156 (2020) 1019–1027. https://doi.org/10.1016/j.renene.2020.04.129.

[8] C. Tregambi, F. Di Lauro, F. Montagnaro, P. Salatino, R. Solimene, Limestone calcination-carbonation in a fluidized bed reactor/receiver for thermochemical energy storage applications, AIP Conf. Proc. 2126 (2019). https://doi.org/10.1063/1.5117757.

[9] S. Pascual, P. Lisbona, M. Bailera, L.M. Romeo, Design and operational performance maps of calcium looping thermochemical energy storage for concentrating solar power plants, Energy. 220 (2021). https://doi.org/10.1016/j.energy.2020.119715.

[10] V. Manovic, J.P. Charland, J. Blamey, P.S. Fennell, D.Y. Lu, E.J. Anthony, Influence of calcination conditions on carrying capacity of CaO-based sorbent in CO_2 looping cycles, Fuel. 88 (2009) 1893–1900. https://doi.org/10.1016/j.fuel.2009.04.012.

[11] G.S. Grasa, J.C. Abanades, CO_2 Capture Capacity of CaO in Long Series of Carbonation/Calcination Cycles, Ind. Eng. Chem. Res. 45 (2006) 8846–8851. https://doi.org/10.1021/ie0606946.

[12] N. Rodriguez, M. Alonso, G. Grasa, J.C. Abanades, Heat requirements in a calciner of $CaCO_3$ integrated in a CO_2 capture system using CaO, Chem. Eng. J. 138 (2008) 148–154. https://doi.org/10.1016/j.cej.2007.06.005.

[13] C. Tregambi, F. Di Lauro, F. Montagnaro, P. Salatino, R. Solimene, 110th anniversary: Calcium looping coupled with concentrated solar power for carbon capture and thermochemical energy storage, Ind. Eng. Chem. Res. 58 (2019) 21262–21272. https://doi.org/10.1021/acs.iecr.9b03083.

[14] C. Tregambi, F. Montagnaro, P. Salatino, R. Solimene, Solar-Driven Torrefaction of a Lignin-Rich Biomass Residue in a Directly Irradiated Fluidized Bed Reactor, Combust. Sci. Technol. 191 (2019) 1609–1627. https://doi.org/10.1080/00102202.2019.1607847.

[15] C.Y. Wen, Y.H. Yu, A Generalized Method for Predicting the Minimum Fluidization Velocity, A.I.Ch.E. J. (1966) 610–612.

I&EC research
Industrial & Engineering Chemistry Research

pubs.acs.org/IECR

Article

Tannery Sludge Gasification in a Fluidized Bed for Its Energetic Valorization

Francesca Di Lauro, Renata Migliaccio, Giovanna Ruoppolo, Marco Balsamo, Fabio Montagnaro,* Edoardo Imperiale, Daniela Caracciolo, and Massimo Urciuolo

Cite This: *Ind. Eng. Chem. Res.* 2022, 61, 16972−16979

Read Online

ACCESS | Metrics & More | Article Recommendations

ABSTRACT: The present article deals with the valorization of the organic content of tannery sludges to produce energy vectors. In this scenario, gasification is a viable option to obtain a flexible gaseous stream (syngas) of interesting energetic value, under operating conditions that do not favor the oxidation of Cr(III) (typically found in tannery sludges) to the more harmful Cr(VI) state. To this end, an industrial tannery sludge was characterized through proximate/ultimate analyses and determination of the heating value, showing its capability to act as a solid fuel in a gasification process, and metal analyses, showing that its Cr(VI) content was below the detection limit (2 ppm). The material was subjected to gasification tests in a lab-scale fluidized bed (FB) reactor. The reactor, with a 41 mm inside diameter and a 1 m height, was electrically kept at an operating temperature of 850 °C. The fluidization velocity was 0.30 m/s at 850 °C, i.e., 7.5 times the value of the minimum fluidization velocity. The gasifying stream was composed by O_2 (3% vol.) diluted in N_2. The adopted oxidant equivalence ratio (ER) levels were 0.15 and 0.24, to ensure substoichiometric (i.e., reducing) conditions in the FB atmosphere. Under the most reducing operating conditions, it was possible to produce syngas with a lower heating value of 12.0 MJ/N m^3 (dry and N_2-free basis). It contained, under these conditions, about 42% H_2, 36% CO, and 4% CH_4, plus 16% CO_2 and other components. The tar produced from the process, fully characterized by gas chromatography−mass spectrometry, showed a favorably low concentration of about 25 g/N m^3. FB bottom and fly ashes were analyzed for their carbon and metal contents. In bottom ash, the total Cr concentration resulted in the range of 8−12 g/kg, with a Cr(VI) concentration between 8 and 10 ppm. In the elutriated stream, the total Cr concentration was about 55 g/kg, with a Cr(VI) concentration between 4 and 7 ppm. The Cr(VI) concentration was higher when higher values of the ER were used, but it resulted in 3−4 orders of magnitude lower than the total Cr concentration, showing the appropriateness of the process to produce syngas with very limited oxidation of chromium in the solid residues.

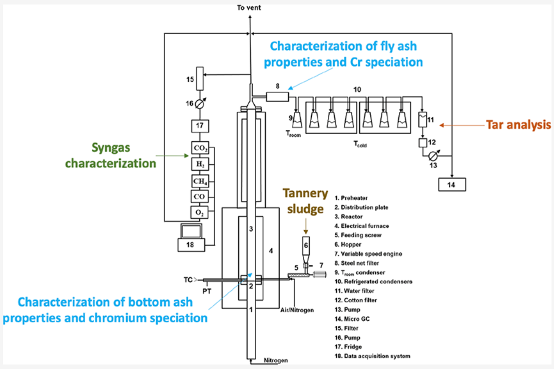

1. INTRODUCTION

The Italian leather industry comprises about 1200 companies. Italy, in 2019, produced 128 millions of m^2 of finished leathers for a production value of 4.9 billion euros, of which 3.6 billion euros account for export. The tannery districts are nowadays using advanced treatment plants that are reaching high levels of specialization for tannery discharges.[1] The obtained sludge is rich in chromium (the removal of chromium by wastewater is greater than 99.4%). The huge volume of sludges generated by the leather industry, with a yearly global production of solid wastes derived from the tanning process estimated to be on the order of 1 ton per ton of raw leather, poses economic and environmental issues associated with their landfilling, mainly due to the relevant amount of chemicals adopted in the tanning process (on average, 2 kg of chemicals are used to produce 1 m^2 of leather). In the circular economy perspective, the valorization of the organic content of tannery sludge to produce energy vectors is a promising strategy to overcome the abovementioned issues ("sludge-to-energy (StE)" strategy).[2]

Among currently available StE technologies, the thermochemical treatments such as combustion, pyrolysis, and gasification appear to be particularly promising due to both the possibility of fixing harmful metals in the solid residues and the high conversion efficiency of organic compounds, the latter being generally greater than 80%.[3] Thermochemical processing of sludges has also the advantage of characteristic reaction times (from seconds to minutes) much shorter than those required in

Received: September 6, 2022
Revised: October 22, 2022
Accepted: October 28, 2022
Published: November 10, 2022

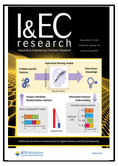

ACS Publications

https://doi.org/10.1021/acs.iecr.2c03214
Ind. Eng. Chem. Res. 2022, 61, 16972−16979

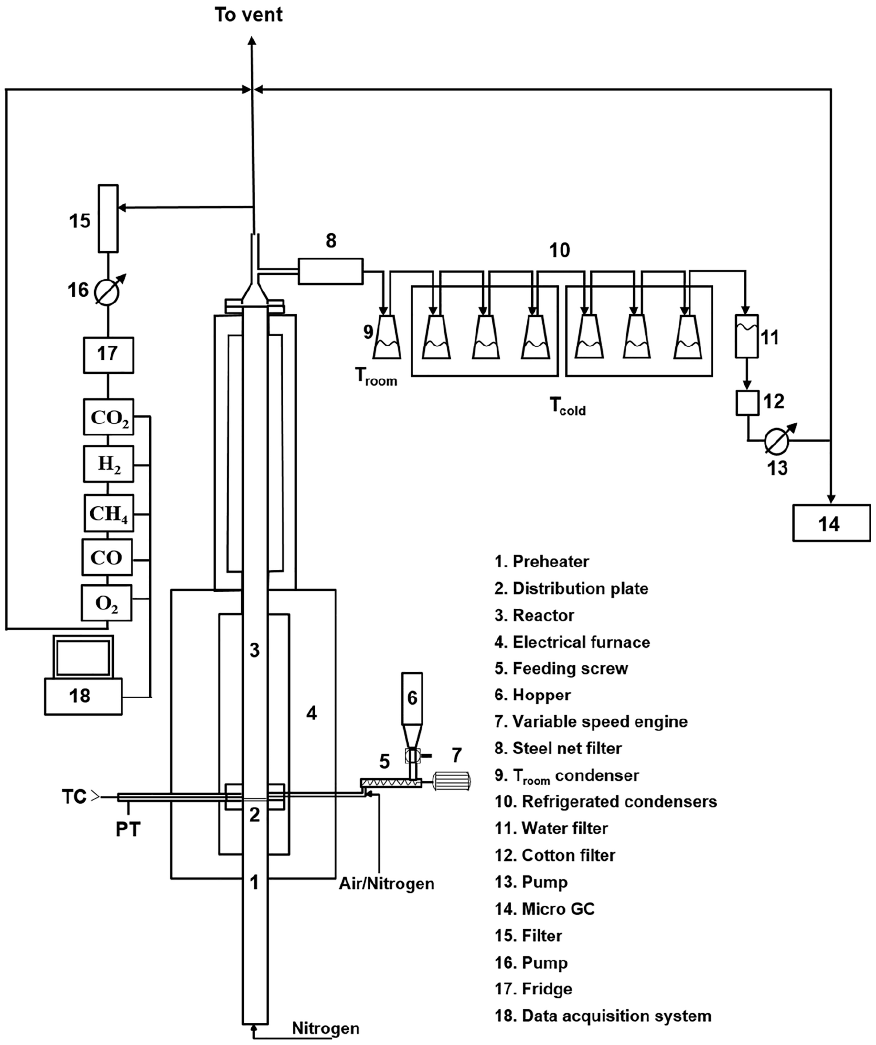

Figure 1. Scheme of the fluidized bed apparatus for gasification tests.

biochemical conversion routes such as anaerobic digestion (in the order of days/weeks), where the converted organic fraction does not exceed 60%.[4] While the direct combustion of several types of sludges is a common practice, gasification and pyrolysis processes are still limitedly explored for the valorization of this residue.[5]

Among the abovementioned thermal processes, the direct combustion of a tannery sludge suffers critical environmental issues that limit its applicability, as the full oxidizing conditions that are realized in the combustion chamber would unavoidably lead to the oxidation of Cr(III) (typically found in tannery sludges) to the more harmful Cr(VI) state.[6] Several studies have been carried out to limit undesired chromium release from sludge combustion, such as pretreatment with hydroxyapatite to reduce heavy-metal volatilization along incineration[7] or postcombustion stabilization of Cr-rich ashes through vitrification with SiO_2, Na_2O, and CaO.[8]

Gasification, instead, is an StE process carried out under partially oxidizing conditions and allows to produce syngas (that can be flexibly used as an energy source also in places/times different from those of production) together with the reduction of the amount of sludge to be landfilled and has the potential to reuse ashes (obtained as a coproduct, in the construction materials industry[9−11] or as adsorbents for fluid stream purification[12,13]), with an eye to the principles of circularity. Furthermore, the substoichiometric oxygen conditions adopted in gasification could reduce the production of Cr(VI). For example, a gasifier equipped with a multipoint hot-air injection system to treat leather solid waste was used, and only Cr(III) oxide was found in bottom ashes.[14] Similarly, it was demonstrated that the chromium species, obtained after gasification of tannery sludge in a downdraft reactor process, remain in the solid residue and mainly in their trivalent form.[3]

In this context, fluidized bed (FB) reactors are widely known to be appropriate as gasifiers due to the very good mass and heat transfer coefficients ensured by FB fluid dynamics and to the possibility of controlling emissions through proper design of the gasifier and its operating conditions.[15−17]

By also considering the relatively limited literature on this specific topic,[18] this research article reports on lab-scale FB gasification carried out on an industrial tannery sludge. After a complete chemical characterization of the material by a combination of techniques, gasification was carried out under two different reducing operating conditions, according to literature indications. Syngas, tar, and bottom and fly ash streams were analyzed, and their characteristics were critically discussed in relation to the parent sludge properties and the gasification conditions.

2. MATERIALS, EQUIPMENT, AND EXPERIMENTAL PROCEDURES

The raw material (an industrial tannery sludge coming from a plant located in southern Italy) was characterized by means of the following:

(i) proximate analysis (TGA701 LECO thermobalance, UNI 9903/ASTM D5142 standard procedures);
(ii) ultimate analysis (LECO CHN628 analyzer with the ASTM D5373 standard procedure for C, H, and N determination; LECO SC-144DR analyzer with the UNI 7584 standard procedure for S determination);
(iii) evaluation of the higher heating value (HHV), in a Parr 6200 calorimeter (ASTM D5865 standard procedure), followed by determination of the chlorine content by ionic chromatography (883 Basic IC plus Metrohm, UNI 9903 standard procedure);
(iv) determination of the content of Cr(total) and Cr(VI), according to a procedure developed by IRSA-CNR, through atomic absorption spectrometry (by dissolving 0.5 g of sludge with 10 mL of 65wt % HNO_3 and 5 mL of H_2O_2) and UV−visible spectrophotometry (Cr(VI) was solubilized in sulfuric acid, and its concentration was determined by a colorimetric reaction with diphenylcarbazide), respectively. The adopted spectrophotometers were an Agilent UV−vis Cary 5000 and an Agilent UV−vis Varian Cary 50.
(v) X-ray diffraction (XRD) analysis was carried out in a D8 Bruker diffractometer, by scanning the 5−60° 2θ range of diffraction angles at a velocity of 0.05° 2θ/s.

The bench-scale FB gasifier (electrically heated at a controlled temperature) is illustrated in Figure 1. It consisted of a stainless-steel (AISI 310) fluidization column (inner diameter = 41 mm; height = 1 m), with a distributor plate (made of a series of stainless-steel nets) that separates the gas inlet chamber/preheater (600 mm height) from the fluidization column. The reactor was equipped with a steel net filter, located downstream the reactor, for the capture of elutriated fines (fly ash stream). The material was fed at the bottom of the bed through a combination of pneumatic and mechanical conveying devices.

The operating conditions of the gasification tests (carried out at 850 °C) are illustrated in Table 1. The bed inert material was silica sand, 300−400 μm (inventory = 180 g). The fluidizing gas was composed by the sum of a stream of 300 NL/h of N_2 and a stream of 50 NL/h of air. This resulted in a fluidizing gas composed by 3% O_2 (rest N_2), with a fluidization velocity of 0.30 m/s (expressed at 850 °C; the minimum fluidization velocity for this system was 0.04 m/s). After sieving the sludge to a size finer than 1 mm, two tests were carried out: "test 1" and "test 2", with sludge flow rates of 99 and 63 g/h, respectively. Once the characteristics of the sludge were known, these two values resulted in air/fuel equivalence ratios (ER) of 15 and 24% of the stoichiometric value for tests 1 and 2, respectively, ensuring that operating conditions were well far from ER = 100% and able to favor the desired gasification (rather than combustion) kinetic patterns. These ER values were in line with literature reviews on the topic.[19] The total duration of each test, after reaching stationary conditions in the bench-scale apparatus, was 1 h. The gas obtained from the process, after filtration and water condensation, was sent to a system of online IR gas analyzers and to a condensation train (composed of one flask at room temperature and six flasks at −12 °C) to collect the produced tar compounds and then measured and analyzed by means of gas chromatography (Agilent 7890A) equipped with mass spectrometry (5975C-VLMSD) (GC−MS). The gasification tests were carried out under semibatch conditions: at the end of each test, the FB was cooled down in N_2 flux, and then, the bed material (sand + bottom ash) was withdrawn. Sand was separated by bottom ash through a combination of sieving and density-based procedures. Finally, bottom and fly ashes were characterized by proximate and ultimate analyses, and their chromium (Cr(total) and Cr(VI)) content was determined.

Table 1. Operating Conditions of FB Gasification Tests of Industrial Tannery Sludge

	test 1	test 2
bed inert material	silica sand, 300−400 μm, inventory = 180 g	
gasification temperature	850 °C	
minimum fluidization velocity	0.04 m/s (@850 °C)	
fluidizing gas	300 NL/h N_2 + 50 NL/h air (3% O_2; 97% N_2)	
fluidization velocity	0.30 m/s (@850 °C)	
flow rate of <1 mm sludge	99 g/h	63 g/h
air-to-fuel ER	0.15	0.24

3. RESULTS AND DISCUSSION

3.1. Properties of the Industrial Tannery Sludge.

Table 2 reports the main characteristics of the sludge. Moisture and volatiles accounted for, respectively, 18.46 and 50.13%, while an ash content of 31.41% was detected. A total C content of 33.61% was revealed by ultimate analysis (dry basis), together with 5.10% H, 2.44% N, and 4.07% S. The quite high C content is positive in view of the further energetic valorization process. Moreover, HHV = 14.90 MJ/kg for the sludge at hand, a value in line with data commonly reported for sludges and, more generally, biomasses. Finally, a Cl content of 0.35% was detected. Table 3 synoptically illustrates the contents of the main elements (including O, calculated by difference), along with those of ashes and moisture, both on a dry and wet basis.

Table 2. Results of the Analyses on the Industrial Tannery Sludge with Tests Carried Out in Triplicates (Standard Deviation Reported)

proximate analysis (% by weight)	
moisture	18.46 ± 0.26
volatiles	50.13 ± 0.05
fixed carbon	n.d.
ash	31.41 ± 0.30
ultimate analysis (% by weight; dry basis)	
C	33.61 ± 0.12
H	5.10 ± 0.16
N	2.44 ± 0.05
S	4.07 ± 0.02
HHV [MJ/kg] (dry basis) = 14.90 ± 0.26	

The concentration of Cr(total) in the parent sludge resulted in equal to 20.65 ± 0.05 g/kg (wet basis, corresponding to 25.32 ± 0.06 g/kg dry basis). No Cr(VI) was detected by UV−visible spectrophotometry. The detection limit of this technique was 2 mg/kg of Cr(VI); thus, if present, the Cr(VI) concentration in the tannery sludge was not higher than 2 ppm, and the concentration of Cr(total) substantially coincided with that of Cr(III).

Table 3. Synoptic List of Main Tannery Sludge Properties (Average % by Weight)

	dry basis	wet basis
C	33.61	27.41
H	5.10	4.16
N	2.44	1.99
S	4.07	3.32
Cl	0.35	0.29
ash	38.52	31.41
moisture		18.46
O (by difference)	15.91	12.96

Table 4. Main Outcomes of the FB Gasification Tests

	test 1 (ER = 0.15)	test 2 (ER = 0.24)
Syngas composition (dry and N_2-free basis)		
CO [% vol.]	35.49	27.05
H_2 [% vol.]	41.58	32.69
CH_4 [% vol.]	3.67	5.15
C_2H_4 [% vol.]	2.89	4.66
C_2H_6 [% vol.]	0.09	0.09
CO_2 [% vol.]	16.16	30.10
Total [% vol.]	99.88	99.74
SO_2 [ppm]	193	137
H_2/CO [vol./vol.]	1.17	1.21
CH_4/H_2 [vol./vol.]	0.09	0.16
HHV (dry and N_2-free basis) [MJ/N m^3]	13.1	12.6
LHV (dry and N_2-free basis) [MJ/N m^3]	12.0	11.6
tar concentration in syngas [g/N m^3]	26.4	22.3
elutriated stream flow rate (fly ash) [g/h]	7.57	4.24

Figure 2 reports the XRD spectrum for the dried sludge. The degree of crystallinity of the sample resulted in 7.90% only, to highlight its prevailing amorphous nature. Within the crystalline phase, we found the presence of Ca (as calcite $CaCO_3$), Si (as cristobalite SiO_2), S, and Cr (as eskolaite Cr_2O_3). The presence of the latter species was expected on the one hand due to the sludge nature; on the other hand, it is interesting to observe that Cr in eskolaite was present as Cr(III), to confirm the chromium analysis above discussed.

3.2. Outcomes of Fluidized Bed Gasification Tests.

Table 4 reports the main outcomes of the FB gasification tests. On a dry and N_2-free basis, for test 1 (ER = 0.15), syngas was mostly composed of CO (35.49% by vol.), H_2 (41.58%), CH_4 (3.67%), and C_2H_4 (2.89%), the rest being CO_2. H_2/CO and CH_4/H_2 ratios of 1.17 and 0.09, respectively, were obtained. The tar concentration in syngas was 26.4 g/N m^3, and a fly ash flow rate of 7.57 g/h was collected. For test 2 (less reducing conditions, ER = 0.24), syngas was mostly composed of CO (27.05% by vol.), H_2 (32.69%), CH_4 (5.15%), and C_2H_4 (4.66%), the rest being CO_2. H_2/CO and CH_4/H_2 ratios of 1.21 and 0.16, respectively, were obtained. The tar concentration in syngas was 22.3 g/N m^3, and a fly ash flow rate of 4.24 g/h was collected.

The more severe reducing conditions of test 1 allowed to obtain an amount of the two main gasification species (CO + H_2) of 77.07%, which is 22% more than what we observed during test 2 (CO + H_2 = 59.74%). Correspondingly, the CO_2 content obtained in the syngas from test 1 (16.16%) was far lower than what was observed in test 2 (CO_2 = 30.10%). It is here obviously recalled that CO_2 does not contribute to the syngas heating value and that its formation is favored by less reducing conditions as those experienced in test 2.

The evaluation of both the HHV and the lower heating value (LHV) of the syngas was carried out based on its chemical composition: in test 1, it had LHV = 12.0 and HHV = 13.1 MJ/N m^3, while values were lower in test 2 (LHV = 11.6 and HHV = 12.6 MJ/N m^3). They fall within the range reported by NETL-DOE, USA,[20] where data from industrial gasifiers to produce syngas as an energetic vector are reported (LHV = 8.3−13.0 MJ/N m^3 on a dry and N_2-free basis).

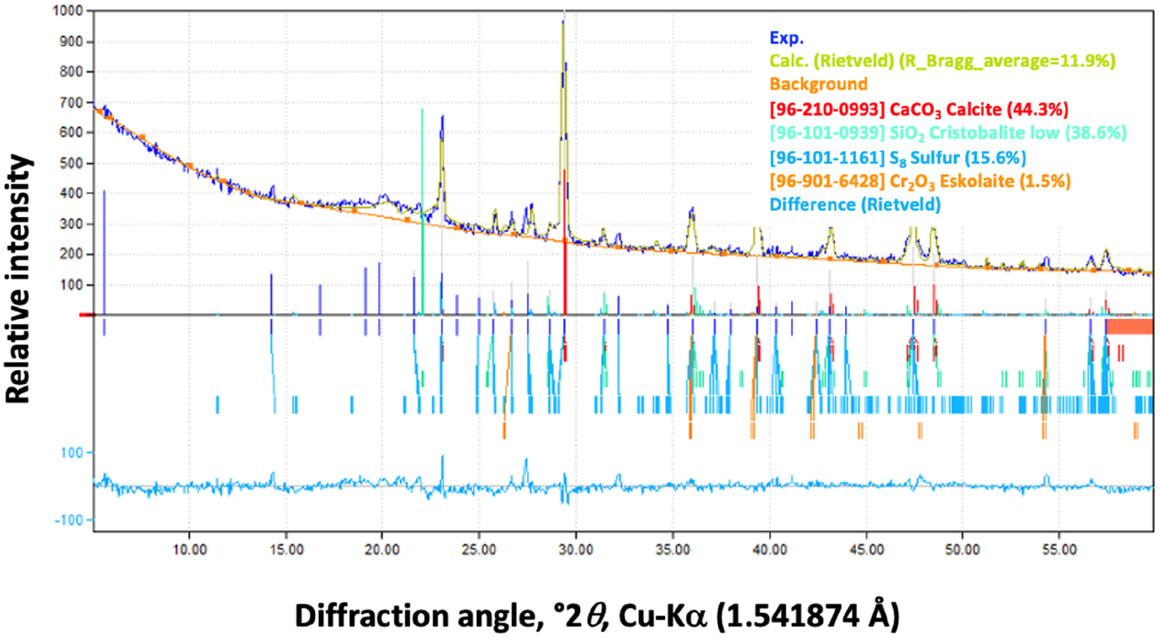

Figure 2. XRD spectrum for dried sludge (as received), with indication of the main identified peaks.

Table 5. GC−MS Results on the Characterization of Tar Compounds Collected during Gasification Test 1, at Room Temperature and at −12 °C[a]

retention time	peak-normalized area, %	compound	CAS no.	match quality
Test 1, tar collected at room temperature				
65.848	35.85	anthracene ($C_{14}H_{10}$)	120-12-7	95
39.402	13.20	naphthalene ($C_{10}H_8$)	91-20-3	95
64.776	12.74	dibenzothiophene ($C_{12}H_8S$)	132-65-0	97
66.212	5.97	phenanthrene ($C_{14}H_{10}$)	85-01-8	96
52.47	5.54	acenaphthylene ($C_{12}H_8$)	208-96-8	90
78.942	5.07	fluoranthene ($C_{16}H_{10}$)	206-44-0	94
48.485	4.43	biphenyl ($C_{12}H_{10}$)	92-52-4	95
57.826	4.43	fluorene ($C_{13}H_{10}$)	86-73-7	94
82.346	3.31	pyrene ($C_{16}H_{10}$)	129-00-0	94
55.015	2.98	dibenzofuran ($C_{12}H_8O$)	132-64-9	91
45.655	1.53	1-methylnaphthalene ($C_{11}H_{10}$)	90-12-0	94
44.826	1.16	2-methylnaphthalene ($C_{11}H_{10}$)	91-57-6	93
72.930	0.97	2-phenylnaphthalene ($C_{16}H_{12}$)	612-94-2	93
72.948	0.80	1-phenylnaphthalene ($C_{16}H_{12}$)	605-02-7	90
47.937	0.61	indole (C_8H_7N)	120-72-9	94
32.478	0.57	phenol (C_6H_6O)	108-95-2	87
13.994	0.48	pyridine (C_5H_5N)	110-86-1	94
67.685	0.37	dibenzo[*a*,*e*]cyclooctene ($C_{16}H_{12}$)	262-89-5	94
Test 1, tar collected at −12 °C (stage I)				
39.413	80.00	naphthalene ($C_{10}H_8$)	91-20-3	95
39.945	3.00	benzo[*c*]thiophene (C_8H_6S)	270-82-6	97
65.864	2.93	phenanthrene ($C_{14}H_{10}$)	85-01-8	96
52.470	1.90	acenaphthylene ($C_{12}H_8$)	208-96-8	90
13.956	1.89	pyridine (C_5H_5N)	110-86-1	97
32.474	1.71	phenol (C_6H_6O)	108-95-2	94
48.485	1.40	biphenyl ($C_{12}H_{10}$)	92-52-4	95
44.830	1.19	1-methylnaphthalene ($C_{11}H_{10}$)	90-12-0	95
64.788	0.90	dibenzothiophene ($C_{12}H_8S$)	132-65-0	96
55.022	0.87	dibenzofuran ($C_{12}H_8O$)	132-64-9	93
57.838	0.79	fluorene ($C_{13}H_{10}$)	86-73-7	90
29.584	0.78	aniline (C_6H_7N)	62-53-3	94
47.945	0.60	indole (C_8H_7N)	120-72-9	95
31.399	0.44	indene (C_9H_8)	95-13-6	91
8.734	0.36	benzene (C_6H_6)	71-43-2	94
66.238	0.34	anthracene ($C_{14}H_{10}$)	120-12-7	76
51.131	0.30	2-vinylnaphthalene ($C_{12}H_{10}$)	827-54-3	81
45.662	0.26	2-methylnaphthalene ($C_{11}H_{10}$)	91-57-6	97
42.761	0.14	quinoline (C_9H_7N)	91-22-5	94
29.798	0.12	benzonitrile (C_7H_5N)	100-47-0	87
42.712	0.07	isoquinoline (C_9H_7N)	119-65-3	81
Test 1, tar collected at −12 °C (stage II)				
8.742	54.40	benzene (C_6H_6)	71-43-2	90
6.178	45.60	2-methylfuran (C_5H_6O)	534-22-5	81

[a] Compounds are listed in order of relevance of the peak-normalized area. Database: NIST 11.

3.3. Tar Characterization. Tar concentration values listed in Table 4 are in line with values reported in the literature.[21] The detailed speciation of the tar compound content in the syngas from tests 1 and 2 is illustrated in Table 5/Figure 3 and Table 6/Figure 4, respectively. In both cases, tar species were mostly made up of polycyclic aromatic hydrocarbons (PAH), with the number of C atoms variable between 5 and 16, and in some cases also in the presence of heteroatoms (N, S, and O). More oxidizing conditions (test 2) determined a larger relative contribution of 2-, 3-, and 4-ring PAH not containing heteroatoms. Moreover, the following compounds were also identified:

- compounds with a simple structure (benzene);
- PAH without heteroatoms, having 2 (naphthalene, methylnaphthalene, indene, biphenyl, and vinylnaphthalene), 3 (anthracene, fluorene, phenanthrene, acenaphthylene, phenylnaphthalene, and methylanthracene), and 4 (fluoranthene and pyrene) rings;
- compounds containing N, with a simple structure (pyridine, aniline, and benzonitrile) or having 2 rings (indole and quinoline);
- compounds containing S, with 2 (benzothiophene) and 3 (dibenzothiophene and naphthothiophene) rings;
- compounds containing O, with a simple structure (phenol and methylfuran) or having 3 rings (dibenzofuran).

The chemical nature of the detected tar species is consistent with literature indications for sludges, at least from the qualitative viewpoint (a quantitative comparison cannot be performed, as data specifically referred to tannery sludge are hard to be found). For example, Phuphuakrat and colleagues[21] detected, as main tar compounds from sewage sludge fixed bed gasification, benzene, phenol, indene, and naphthalene. Among biomass tar species discussed by Pio et al.,[22] naphthalene, heterocyclic compounds, and two-/three-/four-ring aromatic hydrocarbons were present.

3.4. Bottom and Fly Ash Characterization with Chromium Speciation. Bottom ash from both FB gasification tests 1 and 2 was mostly composed by inorganic ash (Table 7), to confirm the almost complete conversion of volatiles and C under both ER values. As a matter of fact, from ultimate analysis, C contents not higher than 0.2% were observed. On the other hand (Table 8), the elutriated fly ash, having experienced a mean residence time in the FB gasifier that is much shorter than for the case of bottom ash, contained about 14−17% of volatiles and 3−4% of fixed carbon (i.e., the gasification burn-off degree for this stream is lower than 1).

In both bottom and fly ash, the concentration of the harmful Cr(VI) species was, as expected, higher when a higher ER value was adopted (9.6 vs 8.2 ppm in bottom ash, 7.1 vs 4.1 ppm in fly ash), but the gasifier operating conditions indeed guarantee that these values are 3−4 orders of magnitude lower than the

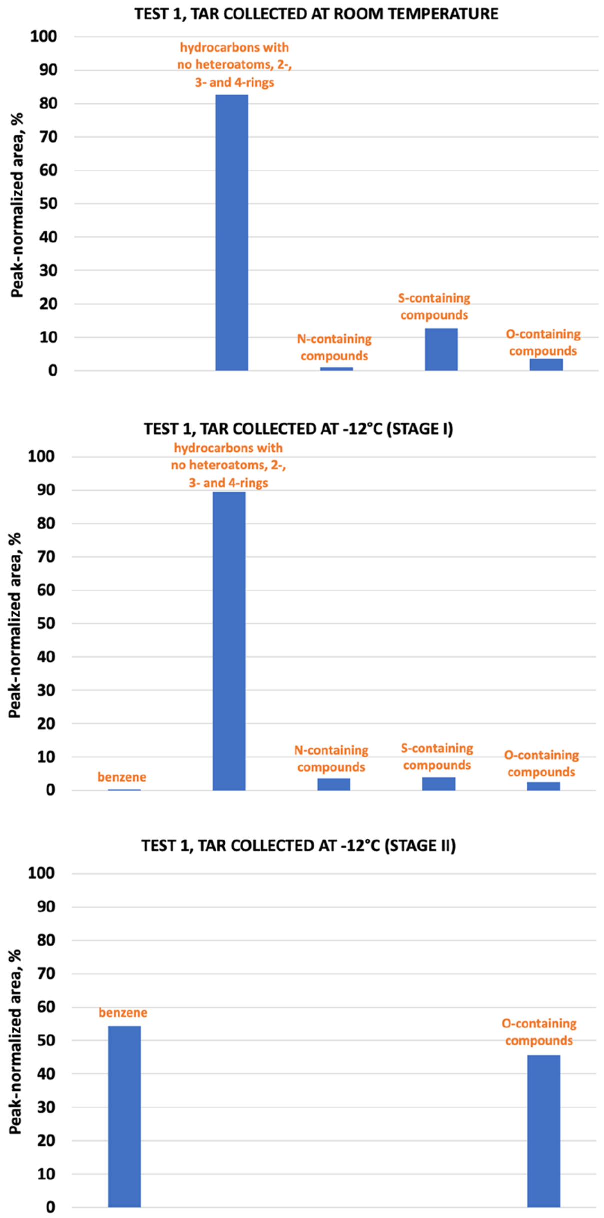

Figure 3. Speciation of tar collected from gasification test 1 based on the peak-normalized area.

Table 6. GC−MS Results on the Characterization of Tar Compounds Collected during Gasification Test 2, at Room Temperature and at −12 °C[a]

retention time	peak-normalized area, %	compound	CAS no.	match quality
		Test 2, tar collected at room temperature		
65.834	53.87	phenanthrene ($C_{14}H_{10}$)	85-01-8	96
64.761	12.30	dibenzothiophene ($C_{12}H_8S$)	132-65-0	97
66.205	8.95	anthracene ($C_{14}H_{10}$)	120-12-7	93
78.916	8.58	fluoranthene ($C_{16}H_{10}$)	206-44-0	96
82.316	4.87	pyrene ($C_{16}H_{10}$)	129-00-0	93
52.458	2.43	acenaphthylene ($C_{12}H_8$)	208-96-8	91
57.823	2.38	fluorene ($C_{13}H_{10}$)	86-73-7	93
72.911	2.31	2-phenylnaphthalene ($C_{16}H_{12}$)	612-94-2	92
48.466	1.38	biphenyl ($C_{12}H_{10}$)	92-52-4	94
55.004	1.22	dibenzofuran ($C_{12}H_8O$)	132-64-9	81
39.394	0.85	naphthalene ($C_{10}H_8$)	91-20-3	94
70.272	0.50	2-methylanthracene ($C_{15}H_{12}$)	613-12-7	83
51.109	0.35	2-vinylnaphthalene ($C_{12}H_{10}$)	827-54-3	86
		Test 2, tar collected at −12 °C (stage I)		
39.394	91.75	naphthalene ($C_{10}H_8$)	91-20-3	95
39.934	2.03	benzo[*c*]thiophene (C_8H_6S)	270-82-6	97
32.474	1.07	phenol (C_6H_6O)	108-95-2	91
65.860	0.95	phenanthrene ($C_{14}H_{10}$)	85-01-8	95
13.967	0.92	pyridine (C_5H_5N)	110-86-1	97
52.466	0.71	acenaphthylene ($C_{12}H_8$)	208-96-8	91
48.470	0.55	biphenyl ($C_{12}H_{10}$)	92-52-4	91
29.580	0.46	aniline (C_6H_7N)	62-53-3	93
44.815	0.44	1-methylnaphthalene ($C_{11}H_{10}$)	90-12-0	83
54.985	0.27	dibenzofuran ($C_{12}H_8O$)	132-64-9	76
8.730	0.24	benzene (C_6H_6)	71-43-2	94
47.937	0.21	indole (C_8H_7N)	120-72-9	76
31.372	0.17	3-ethynyltoluene (C_9H_8)	766-82-5	91
64.761	0.16	dibenzothiophene ($C_{12}H_8S$)	132-65-0	70
57.819	0.05	fluorene ($C_{13}H_{10}$)	86-73-7	90
		Test 2, tar collected at −12 °C (stage II)		
65.841	49.98	phenanthrene ($C_{14}H_{10}$)	85-01-8	94
8.738	13.64	benzene (C_6H_6)	71-43-2	94
6.174	10.44	2-methylfuran (C_5H_6O)	534-22-5	81
64.776	9.40	naphtho[1,2-*b*]thiophene ($C_{12}H_8S$)	234-41-3	81
52.447	8.75	acenaphthylene ($C_{12}H_8$)	208-96-8	74
66.205	4.33	9-methylidenefluorene ($C_{14}H_{10}$)	4425-82-5	76
52.477	3.45	biphenylene ($C_{12}H_8$)	259-79-0	70

[a] Compounds are listed in order of relevance of the peak-normalized area. Database: NIST 11.

concentration of total chromium, which remains in the preferred form of Cr(III) and tends to concentrate in elutriated fly rather than bottom ash. While the (although) limited oxygen presence in the FB gasifier was able to promote the chromium oxidation to Cr(VI), the degree of conversion in bottom ash was 0.069 (ER = 0.15) and 0.12% (ER = 0.24) only. The shorter mean residence time of fly ash in the gasifier has, in this respect, a positive consequence, i.e., chromium has less time to enter in contact with oxygen. As a matter of fact, the degree of chromium oxidation to Cr(VI) was 0.008 (ER = 0.15) and 0.013% (ER = 0.24), i.e., 1.6−1.7 times smaller than for bottom ash.

In the circular economy perspective, an interesting route lies on the possibility of chromium removal (in particular, in its trivalent state) from ashes in order to recirculate the metal in the tanning process. Contextually, possible options could include leaching with acid solutions or extraction with solvents followed by chemical precipitation for selective recovery of Cr in the form of basic chromium sulfate, a valuable product for the tanning process. Moreover, Cr present in the solid residue could represent a substitute for the chromite ore, which is a raw

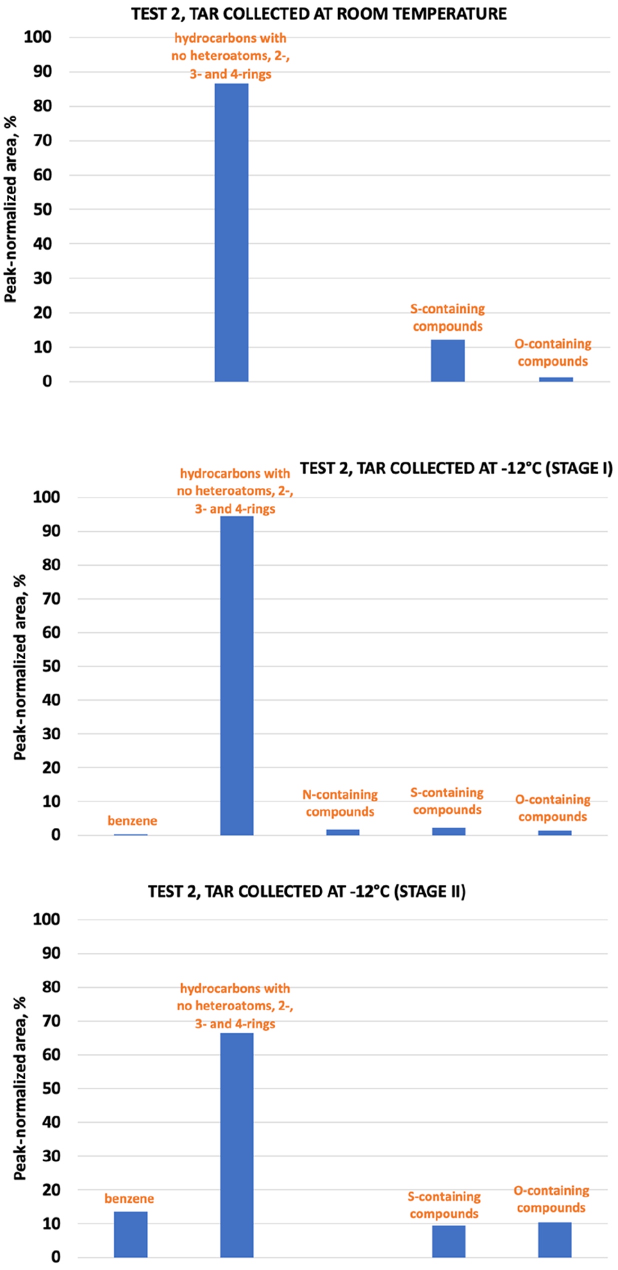

Figure 4. Speciation of tar collected from gasification test 2 based on the peak-normalized area.

Table 7. Results of the Analyses on Bottom Ash from FB Gasification of Tannery Sludge

proximate analysis (% by weight)		
	test 1 (ER = 0.15)	test 2 (ER = 0.24)
moisture	n.d.	n.d.
volatiles	n.d.	n.d.
fixed carbon	n.d.	n.d.
ash	100.00	100.00
ultimate analysis (% by weight; dry basis)		
	test 1 (ER = 0.15)	test 2 (ER = 0.24)
C	0.18	0.12
H	n.d.	n.d.
N	0.29	0.30
chromium speciation		
	test 1 (ER = 0.15)	test 2 (ER = 0.24)
Cr(total)	11.8 g/kg	8.0 g/kg
Cr(VI)	8.2 mg/kg	9.6 mg/kg
conversion to Cr(VI)	0.069%	0.120%

Table 8. Results of the Analyses on Fly Ash from FB Gasification of Tannery Sludge

proximate analysis (% by weight)		
	test 1 (ER = 0.15)	test 2 (ER = 0.24)
moisture	1.54	1.31
volatiles	13.84	17.10
fixed carbon	3.17	3.97
ash	81.45	77.62
ultimate analysis (% by weight; dry basis)		
	test 1 (ER = 0.15)	test 2 (ER = 0.24)
C	9.54	7.99
H	n.d.	n.d.
N	0.68	0.62
chromium speciation		
	test 1 (ER = 0.15)	test 2 (ER = 0.24)
Cr(total)	53.3 g/kg	56.4 g/kg
Cr(VI)	4.1 mg/kg	7.1 mg/kg
conversion to Cr(VI)	0.008%	0.013%

material essential to produce ferro-chromium, the substrate for the manufacture of stainless steel. In fact, chromium is the main element that provides the high corrosion resistance of stainless steel. To this end, the possibility of recycling Cr contained in the ash resulting from thermal processes on the leather residues was studied by reduction in carbon at a temperature of 1600 °C to produce a commercial high-carbon ferrochrome alloy.[23] This process is particularly suitable for tannery ashes that contain high concentrations of both chromium and iron, which also have a role in leather production.

4. CONCLUSIONS

In this preliminary research campaign, a tannery sludge of industrial origin was taken into consideration. With its 34% carbon content (dry basis), the material can be considered appropriate for energetic valorization. The selected process was the sludge gasification in a fluidized bed reactor, to produce syngas. Since the sludge came from the tannery industry, particularly relevant was its chromium content. In the parent material, we did not observe the harmful hexavalent Cr species. Under the best adopted operating conditions, a syngas with 42% H_2 (dry and N_2-free basis) and a lower heating value of 12 MJ/kg was obtained, with a limited tar concentration and the production of bottom ash whose gasification degree was, for all practical purposes, complete. The Cr(VI) concentration in bottom and fly ashes was not higher than 10 mg/kg, while the Cr(total) concentration was 3−4 orders of magnitude greater, showing the right choice of operating conditions that did not promote the oxidation of Cr(III) to Cr(VI) at a relevant extent. The evaluation of the energetic yield of the process, along with the investigation of possible recycle routes for gasification ash (f.i.: as an adsorbent material, or in the materials construction industry), will help to increase the circularity of the proposed process, with clear financial and environmental advantages accompanying the production of an energy vector from an industrial residue. Of course, the reuse of ashes should not end up into additional contaminations of water bodies. So, leaching of Cr(VI) needs to be carefully evaluated for a proper risk analysis and compliance with environmental regulations. To give examples, nowadays, the Italian limit for total chromium is 200 mg per kg of dry solid if the sludge is meant to be utilized in agriculture, and that for Cr(VI) is 2 (or 100) mg per kg of dry solid for agricultural use (or simple disposal). Stabilization of chromium in ashes by means of vitrification or encapsulation is a possible means to reduce the risk related to their reuse.

■ AUTHOR INFORMATION

Corresponding Author

Fabio Montagnaro − *Department of Chemical Sciences, University of Naples Federico II, 80126 Napoli, Italy*; Email: fabio.montagnaro@unina.it

Authors

Francesca Di Lauro − *Department of Chemical Sciences, University of Naples Federico II, 80126 Napoli, Italy*
Renata Migliaccio − *Institute of Sciences and Technologies for Sustainable Energy and Mobility (STEMS), National Research Council (CNR), 80125 Napoli, Italy*
Giovanna Ruoppolo − *Institute of Sciences and Technologies for Sustainable Energy and Mobility (STEMS), National Research Council (CNR), 80125 Napoli, Italy*
Marco Balsamo − *Department of Chemical Sciences, University of Naples Federico II, 80126 Napoli, Italy*; orcid.org/0000-0002-2063-8680
Edoardo Imperiale − *Italian Leather Research Institute (SSIP), 80078 Pozzuoli, Italy*
Daniela Caracciolo − *Italian Leather Research Institute (SSIP), 80078 Pozzuoli, Italy*
Massimo Urciuolo − *Institute of Sciences and Technologies for Sustainable Energy and Mobility (STEMS), National Research Council (CNR), 80125 Napoli, Italy*

Complete contact information is available at: https://pubs.acs.org/10.1021/acs.iecr.2c03214

Notes

The authors declare no competing financial interest.

■ ACKNOWLEDGMENTS

Authors thank Prof. R. Di Girolamo (University of Naples) for his help in XRD analysis. This work was carried out as part of the Italian national research project "Biofeedstock" PONARS01_00985.

■ REFERENCES

(1) UNIC. *Sustainability Report* 2020, https://unic.it/storage/Rapporto%20sostenibilità%202020/Report_Sostenibilità_2020_ENG_online.pdf (accessed July 7, 2022).

(2) Cieślik, B. M.; Namieśnik, J.; Konieczka, P. Review of sewage sludge management: standards, regulation and analytical methods. *J. Cleaner Prod.* **2015**, *90*, 1−15.

(3) Zhou, Y.; Chen, Z.; Gong, H.; Yang, Z. Chromium speciation in tannery sludge residues after different thermal decomposition processes. *J. Cleaner Prod.* **2021**, *314*, No. 128071.

(4) Oladejo, J.; Shi, K.; Luo, X.; Yang, G.; Wu, T. A review of sludge-to-energy recovery methods. *Energies* **2019**, *12*, 60.

(5) Eurostat, https://ec.europa.eu/eurostat/statistics-explained/index.php?title=File:Sewage_sludge_disposal_from_urban_wastewater_treatment,_by_type_of_treatment,_2015_(%25_of_total_mass)_V2.png&oldid=349285#filelinks (accessed July 7, 2022).

(6) Kavouras, P.; Pantazopoulou, E.; Varitis, S.; Vourlias, G.; Chrissafis, K.; Dimitrakopulos, G. P.; Mitrakas, M.; Zouboulis, A. I.; Karakostas, T.; Xenidis, A. Incineration of tannery sludge under oxic and anoxic conditions: Study of chromium speciation. *J. Hazard. Mater.* **2015**, *283*, 672−679.

(7) Tang, P.; Zhou, Y.; Xie, Z. Effects of hydroxyapatite addition on heavy metal volatility during tannery sludge incineration. *Environ. Sci. Pollut. Res.* **2013**, *20*, 4405−4413.

(8) Varitis, S.; Kavouras, P.; Pavlidou, E.; Pantazopoulou, E.; Vourlias, G.; Chrissafis, K.; Zouboulis, A. I.; Karakostas, T.; Komninou, P. Vitrification of incinerated tannery sludge in silicate matrices for chromium stabilization. *Waste Manage.* **2017**, *59*, 237−246.

(9) Kalpokaitė-Dičkuvienė, R.; Lukošiūtė, I.; Brinkienė, K.; Striūgas, N.; Baltušnikas, A.; Lukauskaitė, R.; Čėsnienė, J. Utilization of sewage sludge-biomass gasification residue in cement-based materials: effect of pozzolant type. *Environ. Technol.* **2018**, *39*, 2937−2950.

(10) Ferone, C.; Capasso, I.; Bonati, A.; Roviello, G.; Montagnaro, F.; Santoro, L.; Turco, R.; Cioffi, R. Sustainable management of water potabilization sludge by means of geopolymers production. *J. Cleaner Prod.* **2019**, *229*, 1−9.

(11) Zhang, W.; Wu, Y.; Huang, S.; Wu, S.; Gao, J. Study on physicochemical characteristics, solidification and utilisation of tannery sludge gasification ash. *J. Environ. Manage.* **2022**, *310*, No. 114584.

(12) Maneerung, T.; Li, X.; Li, C.; Dai, Y.; Wang, C. Integrated downdraft gasification with power generation system and gasification bottom ash reutilization for clean waste-to-energy and resource recovery system. *J. Cleaner Prod.* **2018**, *188*, 69−79.

(13) Ribeiro, P. B.; de Freitas, V. O.; Machry, K.; Muniz, A. R. C.; da Rosa, G. S. Evaluation of the potential of coal fly ash produced by gasification as hexavalent chromium adsorbent. *Environ. Sci. Pollut. Res.* **2019**, *26*, 28603−28613.

(14) Dudyński, M. Gasification of selected biomass waste for energy production and chemicals recovery. *Chem. Eng. Trans.* **2018**, *65*, 391−396.

(15) Scala, F. Ed., *Fluidized Bed Technologies for Near-Zero Emission Combustion and Gasification*, Woodhead Publishing: Oxford, 2013.

(16) Liu, Z.; Mayer, B. K.; Venkiteshwaran, K.; Seyedi, S.; Raju, A. S. K.; Zitomer, D.; McNamara, P. J. The state of technologies and research for energy recovery from municipal wastewater sludge and biosolids. *Curr. Opin. Environ. Sci. Health* **2020**, *14*, 31−36.

(17) Migliaccio, R.; Brachi, P.; Montagnaro, F.; Papa, S.; Tavano, A.; Montesarchio, P.; Ruoppolo, G.; Urciuolo, M. Sewage sludge gasification in a fluidized bed: experimental investigation and modeling. *Ind. Eng. Chem. Res.* **2021**, *60*, 5034−5047.

(18) Ongen, A.; Ozcan, H. K.; Arayici, S. An evaluation of tannery industry wastewater treatment sludge gasification by artificial neural network modeling. *J. Hazard. Mater.* **2013**, *263*, 361−366.

(19) Molino, A.; Larocca, V.; Chianese, S.; Musmarra, D. Biofuels production by biomass gasification: a review. *Energies* **2018**, *11*, 811.

(20) *NETL DOE*, https://www.netl.doe.gov/research/coal/energy-systems/gasification/gasifipedia/syngas-composition-igcc (accessed July 7, 2022).

(21) Phuphuakrat, T.; Nipattummakul, N.; Namioka, T.; Kerdsuwan, S.; Yoshikawa, K. Characterization of tar content in the syngas produced in a downdraft type fixed bed gasification system from dried sewage sludge. *Fuel* **2010**, *89*, 2278−2284.

(22) Pio, D. T.; Tarelho, L. A. C.; Pinto, P. C. R. Gasification-based biorefinery integration in the pulp and paper industry: A critical review. *Renewable Sustainable Energy Rev.* **2020**, *133*, No. 110210.

(23) Alves, C. R.; Keglevich de Buzin, P. J. W.; Heck, N. C.; Schneider, I. A. H. Utilization of ashes obtained from leather shaving incineration as a source of chromium for the production of HC-FeCr alloy. *Miner. Eng.* **2012**, *29*, 124−126.

Solar Energy 232 (2022) 471–482

Contents lists available at ScienceDirect

Solar Energy

journal homepage: www.elsevier.com/locate/solener

Dolomite-based binders manufactured using concentrated solar energy in a fluidised bed reactor

Milena Marroccoli [a], Neluta Ibris [a], Antonio Telesca [a], Claudio Tregambi [b,c,*], Roberto Solimene [c,*], Francesca Di Lauro [d], Odda Ruiz de Ballesteros [d], Piero Salatino [e], Fabio Montagnaro [d]

[a] *Scuola di Ingegneria, Università degli Studi della Basilicata, Viale dell'Ateneo Lucano 10, 85100 Potenza, Italy*
[b] *Dipartimento di Ingegneria, Università degli Studi del Sannio, Piazza Roma 21, 82100 Benevento, Italy*
[c] *Istituto di Scienze e Tecnologie per l'Energia e la Mobilità Sostenibili, Consiglio Nazionale delle Ricerche, Sede Secondaria, Piazzale V. Tecchio 80, 80125 Napoli, Italy*
[d] *Dipartimento di Scienze Chimiche, Università degli Studi di Napoli Federico II, Complesso Universitario di Monte Sant'Angelo, 80126 Napoli, Italy*
[e] *Dipartimento di Ingegneria Chimica, dei Materiali e della Produzione Industriale, Università degli Studi di Napoli Federico II, Piazzale V. Tecchio 80, 80125 Napoli, Italy*

ARTICLE INFO

Keywords:
Concentrated solar thermal energy
Directly irradiated fluidised bed reactor
Dolomite-based binders
Hydration
Low-CO_2 cements
Solar materials production

ABSTRACT

Dolomite-based binders are characterised by interesting technical and environmental features. For their synthesis, sources of both CaO and MgO are required. The idea developed in this work is to couple the synthesis of dolomite-based binders, starting from a natural dolomite, through the concept of concentrated solar energy (needed to drive the endothermal dolomite calcination process) in fluidised bed reactors. To this end, a fluidised bed system, where the concentrated solar radiation is mimicked by the use of Xe-lamps (short-arc), has been set up and operated. Natural dolomite (sieved in the 420–590 µm size range) was calcined at a nominal temperature of 850 °C, and bed temperature profiles during solar-driven calcination were investigated. Then, four binders were prepared by mixing slaked dolomite (obtained from the hydration of solar calcined dolomite) with either blast furnace slag or coal fly ash as supplementary cementitious materials. The binders were hydrated for curing times ranging from 7 to 56 days. X-ray fluorescence, X-ray diffraction and combined differential thermal and thermogravimetric analyses were employed as characterisation techniques both to analyse the chemical composition of starting materials and to investigate the evolution of the hydration in the four systems.

1. Introduction

Prior to the Industrial Revolution of the middle of 18th century, the mean concentration of atmospheric CO_2 was equal to about 280 ppm. Since then, consumption of fossil fuels (coal, in particular) and massive anthropogenic deforestation brought to a tremendous increase of this

---

Abbreviations: A, Anhydrite ($CaSO_4$) signal in XRD (AMCSD code 0020857); B, Brucite ($Mg(OH)_2$) signal in XRD (AMCSD code 0002433); BFS, Blast furnace slag; C, Calcite ($CaCO_3$) signal in XRD (AMCSD code 0000098)/DT-TG; CD, Calcined dolomite; CH, $Ca(OH)_2$ signal in DT-TG; CSH, Calcium silicate hydrates signal in DT-TG; CSP, Concentrating solar power; D, Dolomite ($CaMg(CO_3)_2$) signal in XRD (AMCSD code 0000906); DEP, Dehydration endothermal peak; DT-TG, Differential thermal-thermogravimetric; FA, Fly ash; FB, Fluidised bed; GGBFS, Ground granulated blast furnace slag; Gh, Hydrated gehlenite ($2CaO{\cdot}Al_2O_3{\cdot}SiO_2{\cdot}8H_2O$) signal in DT-TG; He, Hematite (Fe_2O_3) signal in XRD (AMCSD code 0000143); HSD/BFS3, Slaked dolomite and 30% by mass blast furnace slag hydrated sample; HSD/BFS5, Slaked dolomite and 50% by mass blast furnace slag hydrated sample; HSD/FA3, Slaked dolomite and 30% by mass fly ash hydrated sample; HSD/FA5, Slaked dolomite and 50% by mass fly ash hydrated sample; Ht, Hydrotalcite ($Mg_6Al_2(CO_3)(OH)_{16}{\cdot}4H_2O$) signal in XRD (AMCSD code 0014738)/DT-TG; ID, Internal diameter; IRC, Infrared camera; L, Lime (CaO) signal in XRD (AMCSD code 0008328); M, Mullite ($3Al_2O_3{\cdot}2SiO_2$) signal in XRD (AMCSD code 0001059); MBC, MgO-based cements; MC, $MgCO_3$ signal in DT-TG; MH, $Mg(OH)_2$ signal in DT-TG; P, Portlandite ($Ca(OH)_2$) signal in XRD (AMCSD code 0008415); PC, Portland cement; PC-Cli, Portland cement clinker; Pe, Periclase (MgO) signal in XRD (AMCSD code 0020752); Q, Quartz (SiO_2) signal in XRD (AMCSD code 0000789); RK, Rotary kiln; S, Siderite ($FeCO_3$) signal in XRD (AMCSD code 0017592); SCM, Supplementary cementitious materials; SD, Slaked dolomite; SD/BFS3, Mixture of slaked dolomite and 30% by mass blast furnace slag; SD/BFS5, Mixture of slaked dolomite and 50% by mass blast furnace slag; SD/FA3, Mixture of slaked dolomite and 30% by mass fly ash; SD/FA5, Mixture of slaked dolomite and 50% by mass fly ash; TWL, Total weight loss; XRD, X-ray diffraction; XRF, X-ray fluorescence.

* Corresponding authors.
E-mail addresses: claudio.tregambi@unisannio.it (C. Tregambi), roberto.solimene@cnr.it (R. Solimene).

https://doi.org/10.1016/j.solener.2022.01.007
Received 21 December 2020; Received in revised form 24 September 2021; Accepted 1 January 2022

value, reaching 300 ppm level at around year 1900 (Ekolu, 2020) and more than 410 ppm in September 2020 (ESRL, 2020). In 2019, after two years of increase, CO_2 emissions related to global energy production levelled at about 33 Gton; this trend was mainly related to a strong drop in emissions of CO_2 from the power field in developed Countries, thanks to the substitution of coal with natural gas, and a wider employment of renewable energies (IEA, 2019). In 2020, it has been estimated that global CO_2 emissions will decline by 8% (by about 2.6 Gton) principally as a result of the Covid-19 crisis (IEA, 2020a). In 2018 almost 65% of CO_2 emissions were related to industrial activities (power generation and other industries) (IEA, 2020b).

The production of cement consumes huge amounts of energy and raw materials, with a correspondingly high fuel consumption (generally fossil coal and pet coke); it accounts for roughly 7% of all CO_2 emitted in the atmosphere because of anthropogenic activities. Portland cement (PC, please refer to the provided list of abbreviations) represents the most broadly, worldwide employed, binder; it is produced by intergrinding PC clinker (PC-Cli) with about 5% of calcium sulphates (usually gypsum). PC-Cli is commonly obtained heating, in a rotary kiln at 1450–1500 °C, a mixture (raw meal) of limestone and clay (about 20% by mass). During the manufacturing process of 1 ton of PC, about 830 kg of CO_2 are released (Barcelo et al., 2014); this originates from both limestone calcination and fuel combustion (about 40% of the total CO_2 emissions) (Telesca et al., 2017; Xu et al., 2015).

The manufacture of low-CO_2 cements has been recognised as a way of cutting the carbon footprint from cement industry (Coppola et al., 2018a, 2018b; Gartner and Hirao, 2015; Gartner and Sui, 2018; Miller et al., 2018; Scrivener et al., 2018; Shi et al., 2011, 2019; Telesca et al., 2015, 2016; Wei et al., 2018). In this regard, MgO-based cements (MBC) represent a type of binders recognised as low-carbon alternatives to PC, in reason of the energy saving related to the lower temperatures required for their production. Moreover, these binders are also named “carbon–neutral” cements due to the ability of MgO to adsorb, during all its life-time, the atmospheric CO_2 in the same quantity as the one released during their production. These two interrelated features have pushed both cement producers and scientific community to a renewed interest in MBC (Dung et al., 2019; Harrison, 2008; Jia et al., 2017; Unluer and Al-Tabbaa, 2013; Walling and Provis, 2016). For the synthesis of MBC, “light-burned” MgO is obtained from magnesite ($MgCO_3$) calcination at temperatures generally ranging from 700 °C to 1000 °C (Walling and Provis, 2016); unfortunately, global magnesite reserves are limited and massive deposits are present only in a few Countries (e.g. Russia 22%, North Korea 24% and China 27%, this latter being the largest magnesite producer) (Yu et al., 2020). In this regard, dolomite ($CaMg(CO_3)_2$) can be considered as an abundant magnesium resource inasmuch as it is extensively diffused and benefits of larger deposits than magnesite. It is usually employed as a flux agent in metallurgy, a source of Mg in the production of glass, ceramic and construction materials (Hossain et al., 2011; Olszak-Humienik and Możejko, 1999). $CaMg(CO_3)_2$ is a natural rock-forming mineral composed of layers of calcium carbonate ($CaCO_3$) and magnesium carbonate ($MgCO_3$); its thermal decomposition has been extensively studied (Kristóf-Makó and Juhász, 1999) and consists in the following two steps reaction:

$$CaMg(CO_3)_2 \rightarrow CaCO_3 + MgO + CO_2, \text{ (I)}$$

$$CaCO_3 \rightarrow CaO + CO_2. \text{ (II)}$$

The formation of $CaCO_3$ and MgO occurs at about 550–600 °C (dolomite calcination Eq. (I)), while CaO forms from the decomposition of calcite at higher temperatures (650–700 °C, Eq. (II)); therefore, dolomite calcined at higher temperatures generates reactive MgO and CaO (Gunasekaran and Anbalagan, 2007).

Composite calcined dolomite (CD)-based binders can be obtained by mixing CD with proper supplementary cementitious materials (SCM) containing reactive silica and alumina (e.g. natural pozzolan, coal fly ash (FA), blast furnace slag (BFS)) (Giergiczny, 2019; Juenger et al., 2019; Li et al., 2020; Skibsted and Snellings, 2019). FA is a residue coming from the combustion of pulverised coal in electric power stations; it is mainly composed by silica, alumina, ferrous oxides and lime with various percentages of residual unburnt carbon. The chemical composition of FA depends on the kind of coal and regulates whether it is suitable to be used as component in various construction materials (e.g. inorganic binders, concrete). The American Society for Testing and Materials (ASTM C618) and the European Standard (EN 197-1) define two classes of FA, namely Class F and Class C. With respect to Class C, Class F fly ash features lower CaO and larger SiO_2 and Al_2O_3 amounts; consequently, Class F fly ash is regarded as a pozzolanic material, i.e. a siliceous, or a siliceous/aluminous, material able to react with both $Ca(OH)_2$ (portlandite) and $Mg(OH)_2$ (brucite) to form binding products (Giergiczny, 2019; Marinković and Dragaš, 2018; Xu and Shi, 2018). BFS is generated when iron ores are decomposed by coke in a blast furnace, at roughly 1800 °C. Molten iron represents the main product; the other constituents form a liquid slag which is water-quenched to produce a granulated slag (generally containing more than 95% of glassy phase). Granulated slag is milled to a fine powder, named ground granulated blast furnace slag (GGBFS); it is mainly employed as mineral additive in composite cements. GGBFS displays both cementitious characteristics (latent hydraulic activity) and pozzolanic behaviour (ability to react with $Ca(OH)_2$) (Giergiczny, 2019; Matthes et al., 2018; Yuksel, 2018).

Another way of limiting fuel consumption and thus saving CO_2 emissions related to cement production is the process integration with renewable energies. Use of solar energy through concentrating solar power (CSP) systems is widely investigated in current literature. CSP systems rely on focusing and concentration of solar energy onto a receiver, whence high temperature heat is produced and eventually exploited by thermodynamic cycles for power generation or by endothermal reactions for material processing (Purohit et al., 2021; Rosa, 2019). Calcination of metal carbonates is an appealing class of reactions for integration with CSP systems, as it claims for relevant amount of heat and thus allows the incorporation of a relevant share of renewable energy within the process. Calcination of limestone by concentrated solar energy was investigated since the eighties (Badie et al., 1980; Flamant et al., 1980; Salman and Khraishi, 1988) and nineties (Imhof, 1991, 1997, 2000a), and is still a hot research topic as new solar reactor/receiver paradigms are being developed and their integration within CSP systems is being assessed. Recently, Esence et al. (2020a, 2020b) developed an indirectly heated shallow cross-flow fluidised bed (FB) reactor for continuous thermal processing of minerals, and tested it at the solar furnace of 1 MW_{th} at Odeillo (France). Both limestone and dolomite calcination were scrutinised, achieving satisfying results upon careful optimisation of the front wall irradiation. Tregambi et al. (2020a, 2020b) developed instead a directly irradiated FB autothermal reactor for application to solar chemistry. It consists of a solar receiver plus chemical reactor integrated with a countercurrent solid–solid heat exchanger, which allows preheating of the inlet solid stream at the expense of the sensible heat of the product stream. A lab scale prototype was already tested (Tregambi et al., 2020b) and modelled (Padula et al., 2021) for solar calcination with promising results. Solar-driven calcination in conventional FB was also extensively investigated for application to CO_2 capture and sequestration (Di Lauro et al., 2021; Nikulshina et al., 2009; Tregambi et al., 2018a, 2019a) and thermochemical energy storage (Di Lauro et al., 2021; Tregambi et al., 2019a). Use of FB is frequently investigated in literature to perform solar-driven chemical processes, as they can simultaneously work as multiphase chemical reactors and effective solar receivers (Tregambi et al., 2021). Apart from FB, solar heated rotary kilns (RK) have also been widely investigated for calcination processes. RK feature high flexibility as regards chemical-physical properties of reactant streams (Alonso et al., 2017; Montagnaro et al., 2018). Abanades and André (2018) developed and tested a RK indirectly heated by concentrated solar radiation. According to their findings, rotation of the tube allowed uniform radial heating avoiding temperature gradients between the front and rear parts of the tube. Complete calcination of the limestone was obtained using air

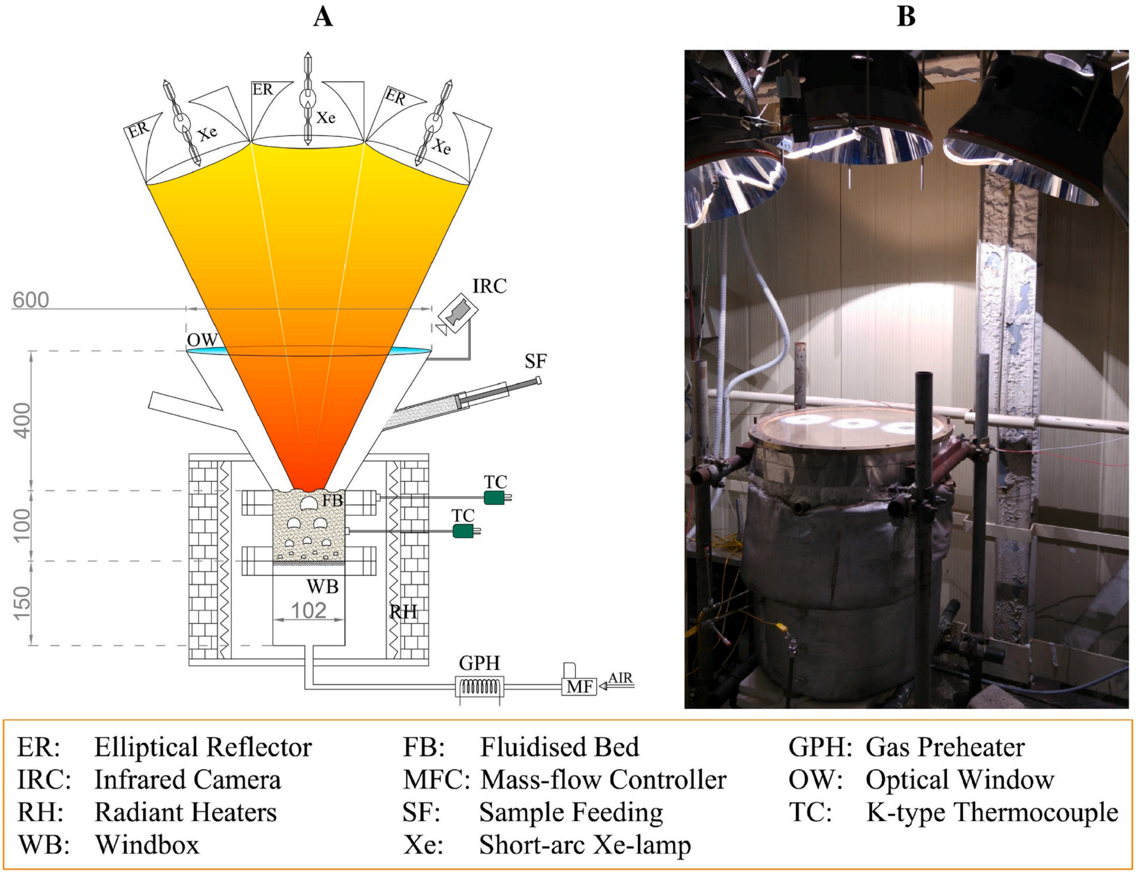

Fig. 1. (A) Sketch of the directly irradiated fluidised bed reactor used for dolomite calcination (quotes in mm); (B) Picture of the experimental rig.

as carrier gas, whereas partial calcination was achieved under a CO_2-rich gaseous atmosphere. Moumin et al. (2019) tested instead a directly irradiated rotary kiln for calcination of fine particles using both closed (i.e. by optical window) and open reactor configuration. Significant dust formation was observed, which could be easily handled in the open configuration. Calcination degree ranged between 24% and 99% according to different operating conditions.

Close to the topic of the present work, Meier and colleagues studied calcination of limestone for cement production using RK heated either directly (Meier et al., 2004) or indirectly (Meier et al., 2005a) with concentrated solar energy. Produced lime was characterised in terms or reactivity by mixing it with water and measuring the time needed to achieve a scheduled temperature value (60 °C) as a consequence of the exothermic hydration reaction. For tests performed in the 10 kW_{th} multitube RK, efficiency within 30–35% are documented, without accounting for possible heat recovery (Meier et al., 2006). First economic analyses for the process were also performed (Meier et al., 2005b), concluding that price of lime produced in a solar plant with a 25 MW_{th} capacity would be twice of that obtained by traditional heating strategies. A techno-economic analysis on the integration of concentrated solar energy within cement production plants was later performed also by González and Flamant (2014). No significant obstacles were identified as regard the integrated process. However, thermal losses must be within 45% to achieve a satisfactory return of the investment. Integration of solar energy within cement industry was proposed also by Imhof (2000b).

The present authors (Tregambi et al., 2018b) investigated limestone calcination for clinker production in a FB receiver/reactor with direct irradiation. Concentrated solar energy was simulated by means of #3 Xe-lamps (short-arc, 4 kW_e each), located within the foci of elliptical reflectors. At full power, the peak flux reached 3 MW/m^2, with a total power of 3.2 kW_{th}. Solar calcined lime was combined with clay in the formulation of Portland cement, and its reactivity was scrutinised with a focus on the influence of the harsher thermal history that materials may experience when processed in directly irradiated FB (Tregambi et al., 2016, 2018a, 2019b). Laboratory burnability and hydration behaviour tests successfully demonstrated the possibility of using solar calcined lime for the clinkerisation process. Fernández-González et al. (2018) investigated the use of concentrated solar power to carry out the synthesis of calcium aluminates to be then used as binders (high alumina refractory cements) or reagents in the metallurgical industry. Experiments were performed at a 1.5 kW_{th} solar furnace at PROMES-CNRS (Odeillo, France), by heating at very high temperature alumina and calcium carbonate within a crucible. The results proved the feasibility of the solar process to obtain the calcium aluminate compounds. Costa Oliveira et al. (2019) investigated the feasibility of producing Portland grey and white (i.e. with lower iron oxide content) cement clinker by means of direct irradiation of the raw materials. Experiments were performed at the solar platform of Almeria (Spain). Grey clinker was successfully produced, with chemical and mineralogical data comparable to those of conventional clinker, even though some crystal growth induced by overburn was noticed, as well as some heterogeneity in the sample arising from temperature gradients along the powder bed. Synthesis of white clinker was instead hindered by the whitish colour of the sample, which reduced the absorption of solar energy, preventing the achievement of the very high temperatures required to promote clinkerisation reactions. Tomatis et al. (2020) performed a life cycle analysis on the integration of solar energy in cement production for the calcination process, and stated that it would be possible to have lower impacts with respect to conventional calcination, in several categories (e.g. fossil fuels depletion, terrestrial ecotoxicity, climate change). The heliostat field is recognised as the more impactful component. They

Table 1
Mix design (g/100 g dolomite-based binder) of the investigated systems.

	SD/BFS3	SD/BFS5	SD/FA3	SD/FA5
SD	70	50	70	50
BFS	30	50	–	–
FA	–	–	30	50

Table 2
XRF chemical composition for starting materials, mass %.

	Raw dolomite	Solar CD	SD	BFS	FA
CaO	32.4	55.7	41.3	43.5	5.5
Al_2O_3	–	–	–	9.6	20.3
SiO_2	–	–	–	37.7	54.2
SO_3	–	–	–	1.0	2.0
Fe_2O_3	0.1	0.2	0.1	0.3	5.3
TiO_2	–	–	–	0.7	0.9
K_2O	–	–	–	0.3	1.9
MgO	20.5	35.1	30.7	6.3	2.5
Na_2O	–	–	–	0.3	1.1
MnO	–	–	–	0.2	–
P_2O_5	–	–	–	–	0.8
Loss on ignition @950 °C	46.6	8.2	27.1	–	4.4

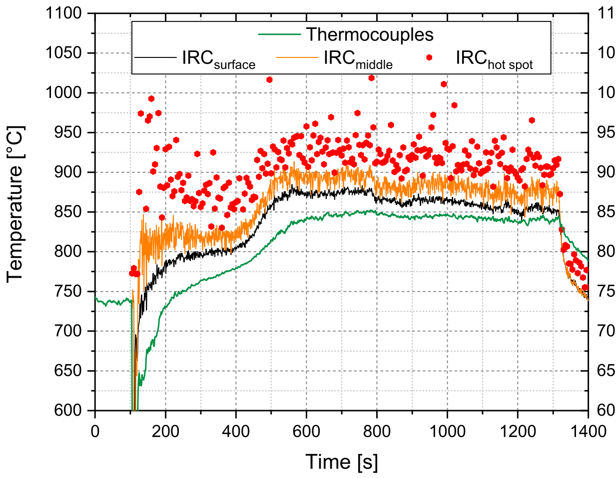

Fig. 2. In-bed and surface temperature profiles, and hot spot values, during solar-driven calcination of dolomite.

concluded that the exploitation of solar energy for calcination has the potential of contributing toward the decarbonisation targets settled for the cement industry. Moumin et al. (2020) performed instead a techno-economic analysis for the integration of a solar thermal calciner in the cement industry. They found that a maximum CO_2 reduction of 21% with respect to the overall plant emissions can be obtained for a 100% solarisation. However, this goal requires a very high value of solar multiple, making the investment unreasonable. For a CO_2 emission reduction within 14–17%, costs for the avoided emissions range within 118 and 74 €/ton. Importance of reactor efficiency, direct normal irradiation and solar multiple was pointed out.

Joining the different aspects presented in the prior art analysis, in this work the feasibility of utilising dolomite calcined in a FB reactor heated by concentrated solar simulated radiation for new green blended binders was investigated. Bed temperature profiles during solar-driven calcination of dolomite were scrutinised and reported, with the further aim of checking the possible negative effects of overtemperature peaks on MgO reactivity. CD was mixed with a largely overstoichiometric amount of water in order to control the strong exothermic reactions related to the formation of $Ca(OH)_2$ and $Mg(OH)_2$: a dry sample called “slaked dolomite (SD)” was obtained. Four SD-based binders were prepared by mixing SD with two different amounts (30% and 50% by mass, respectively) of BFS or FA; these binders were eventually hydrated for times up to 56 days. X-ray diffraction (XRD) and combined differential thermal (DT) and thermogravimetric (TG) analyses were employed as

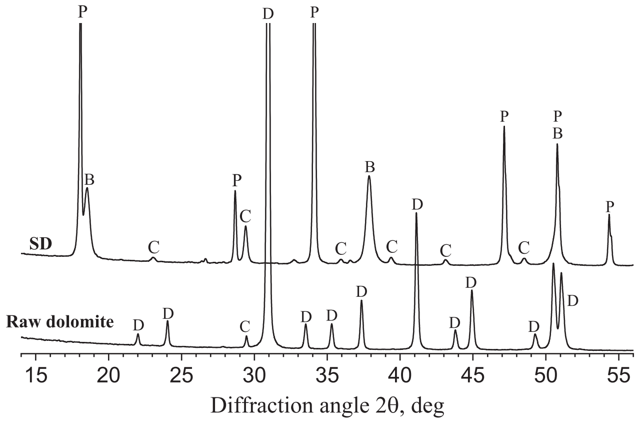

Fig. 4. XRD profiles of raw dolomite (bottom) and SD (top). Legend: B = brucite ($Mg(OH)_2$); C = calcite ($CaCO_3$); D = dolomite ($CaMg(CO_3)_2$); P = portlandite ($Ca(OH)_2$).

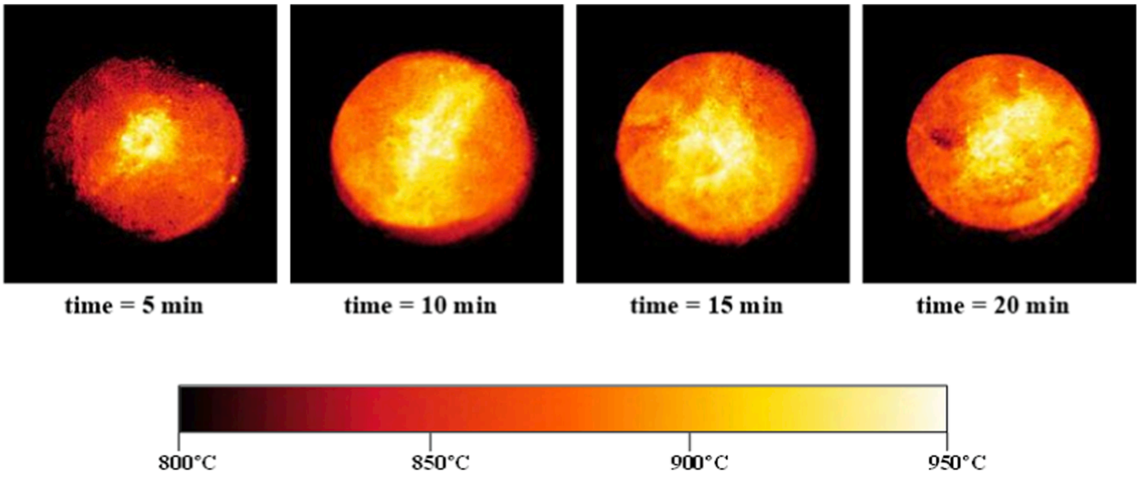
time = 5 min
time = 10 min
time = 15 min
time = 20 min

Fig. 3. Thermal pictures of the FB surface recorded with the infrared camera during solar-driven calcination of dolomite (up), and temperature scale in false colour (down).

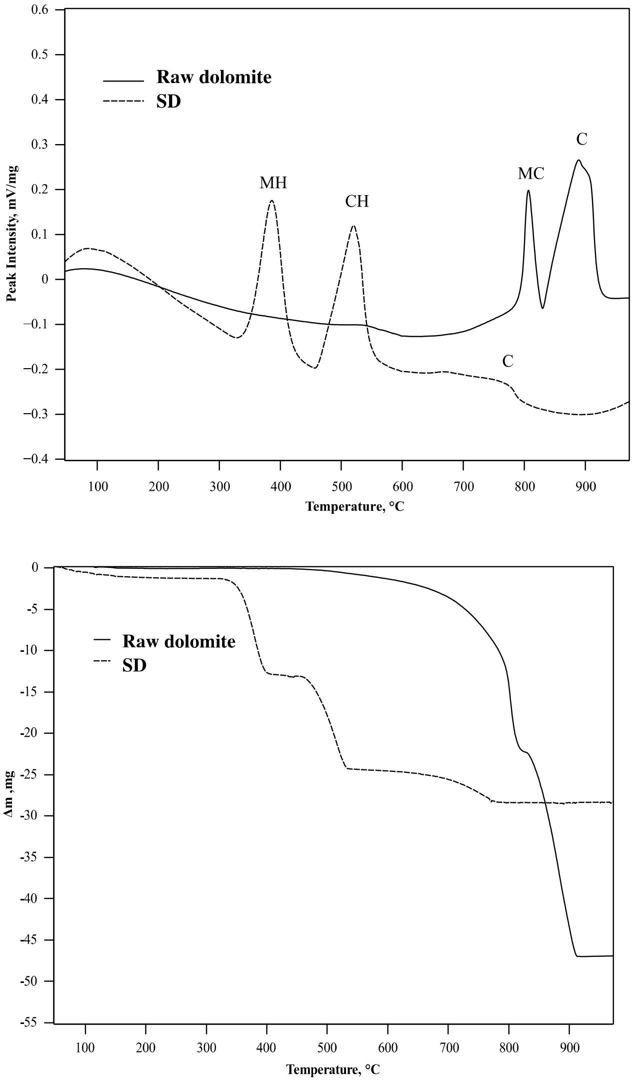

Fig. 5. DT (up)-TG (down) thermograms for raw dolomite and SD samples. Legend: C = calcium carbonate ($CaCO_3$); CH = calcium hydroxide ($Ca(OH)_2$); MC = magnesium carbonate ($MgCO_3$); MH = magnesium hydroxide ($Mg(OH)_2$). DT endo peaks up.

main characterisation techniques to investigate the evolution of the hydrating systems based on both CaO and MgO obtained from solar calcination.

The structure of this article is as follows. In Section 2, the experimental apparatus and techniques inherent to the solar-driven calcination (§2.1), and to the synthesis/characterisation of the Mg-based binders (§2.2), are presented. Section 3 reports on the results of the experimental campaign, with reference to both calcination of dolomite (§3.1) and characterisation of the manufactured Mg-based binders (§3.2).

2. Experimental

2.1. Solar calcination of dolomite in fluidised bed

Calcination of dolomite was carried out in a directly irradiated FB rig, 0.1 m ID, made of stainless steel (AISI 310). A technical sketch and a picture of the whole experimental rig are shown in Fig. 1. Starting from the bottom, the reactor features three different sections: i) the windbox, which extends for 0.15 m, and hosts at its upper extremity a stainless-steel porous grid (0.5 mm holes) serving as gas distributor; ii) the FB, 0.1 m height, containing the solid granular material; iii) the upper conical section (i.e. the freeboard), 0.4 m height with an internal cone angle of 32°, which promotes disengagement of the solid particles as the gas velocity is progressively reduced, while ensuring no limitation to the impinging radiative flux. A ceramic glass optical window (4 mm thickness, 0.9 transmittance in the spectral range 340–2350 μm) closes and seals the reactor environment, while allowing entrance of the concentrated solar radiation. Four 1″ tubes, 0.225 m long, are welded at middle height of the conical section and serve as gas discharge ports. Concentrated solar energy is mimicked by means of #3 dimmable Xe-lamps (short arc, 4 kW_e each), located within the foci of ellipsoidal reflectors (Optiforms E1585). A peak flux up to 3 MW/m^2 may be established on the reactor surface, with a total input power of 3.2 kW_{th}. The reactor is also equipped with radiant heaters (Watlow Ceramic Fiber Heaters, full power of 5 kW_{th} at 240 V) for speeding the initial heating up of the system, and with a resistive heater for gas preheating (Osram Sylvania Threaded Inline Heaters, full power of 1.6 kW at 170 V). An electronic mass flow controller sets the gaseous stream entering the reactor. Several thermocouples are located within the system for continuous temperature measurement: one at the outlet of the gas preheater, one at middle height inside the windbox, and two within the FB (one 0.05 m above the distribution grid and 0.05 m from the reactor wall; the other one 0.08 m above the distribution grid and 0.01 m from the reactor wall). Finally, an infrared camera (IRC) is used to map the temperature of the FB surface directly exposed to the concentrated solar radiation.

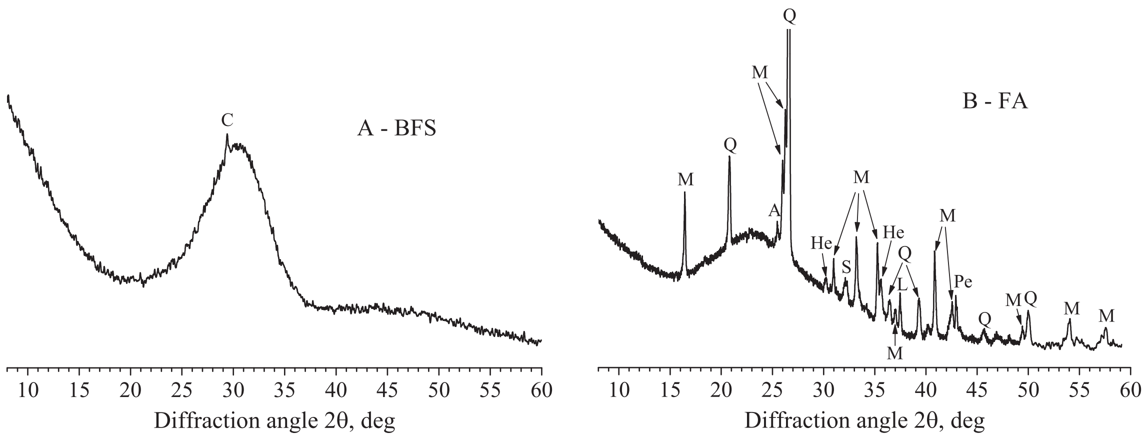

Fig. 6. BFS (A-left) and FA (B-right) XRD profiles. Legend: A = anhydrite ($CaSO_4$); C = calcite ($CaCO_3$); L = lime (CaO); M = mullite ($3Al_2O_3{\cdot}2SiO_2$); He = hematite (Fe_2O_3); Pe = periclase (MgO); Q = quartz (SiO_2); S = siderite ($FeCO_3$).

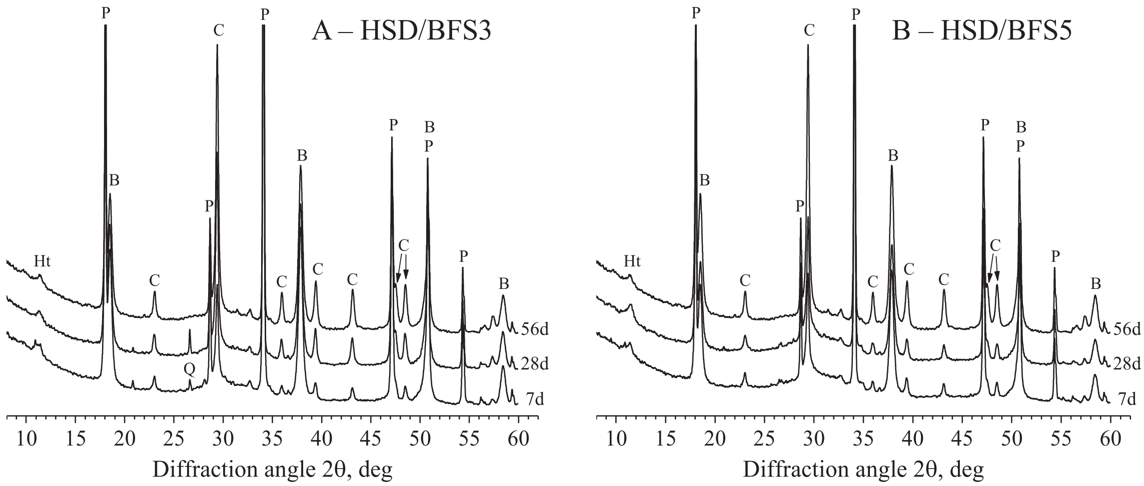

Fig. 7. HSD/BFS3 (A-left) and HSD/BFS5 (B-right) XRD profiles (binders hydrated at 20 °C for 7, 28 and 56 days). Legend: B = brucite ($Mg(OH)_2$); C = calcite ($CaCO_3$); Ht = hydrotalcite ($Mg_6Al_2(CO_3)(OH)_{16}\cdot 4H_2O$); P = portlandite ($Ca(OH)_2$); Q = quartz ($SiO_2$).

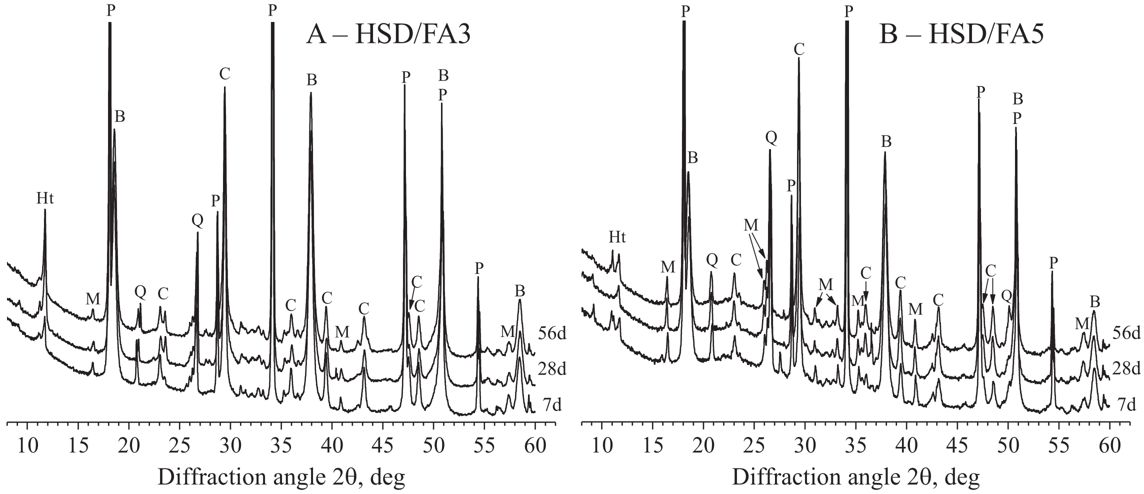

Fig. 8. HSD/FA3 (A-left) and HSD/FA5 (B-right) XRD profiles (binders hydrated at 20 °C for 7, 28 and 56 days). Legend: B = brucite ($Mg(OH)_2$); C = calcite ($CaCO_3$); Ht = hydrotalcite ($Mg_6Al_2(CO_3)(OH)_{16}\cdot 4H_2O$); M = mullite ($3Al_2O_3\cdot 2SiO_2$); P = portlandite ($Ca(OH)_2$); Q = quartz ($SiO_2$).

The raw dolomite was kindly supplied by Ca.ve. Dolomitica (Italy; see acknowledgement). Prior to its use, dust material in raw dolomite was removed by fluidising the sample at room temperature for 4 h. Dolomite calcination was performed using as bed inventory a mixture of inert sand, sieved within 850–1000 μm, and reactive dolomite, sieved within 420–590 μm. The sand acts as thermal flywheel, moderating possible strong temperature variations induced by the course of the chemical reaction. Its use is restricted to the lab scale tests, as it would not be required by an industrial application of this technology. Experimental tests were performed by referring to the following procedure. An inventory of 700 g of inert sand was loaded within the reactor and heated to about 750 °C exploiting both the radiative ovens and preheating of the fluidising gas, consisting of compressed ambient air. The air flow rate was always tuned to have a superficial gas velocity within the reactor of 0.6 m/s (about double the minimum fluidisation value of the sand). Once achieved the settled temperature, about 150 g of dolomite were added to the inventory of the FB. Simultaneously, the radiant heaters were turned off, while the simulator of concentrated solar energy powered on and tuned to establish a bulk bed temperature of about 850 °C. This temperature was already proven to be high enough to guarantee complete calcination of limestone under an air stream (Tregambi et al., 2019a). Solar calcination was prolonged for 20 min. In-bed temperature was continuously recorded with thermocouples and IRC. Once calcination was completed, the system was cooled down and the bed material discharged. Calcined dolomite was recovered by mechanical sieving, and will be sometimes also referred to as "solar" CD.

2.2. *Manufacture of Mg-based binders from solar calcined dolomite and industrial wastes*

2.2.1. *Materials, mixtures formulation and hydration experiments*

The light-burned solar CD was comminuted in a Fritsch Pulverisette 6 (FP6) laboratory planetary mill (100–650 rotations per minute, 500 mL grinding jar covered with silicon nitride) to pass through a sieve with 90 μm mesh grid. Afterwards, solar CD powder was hydrated with a largely overstoichiometric amount of water for 24 h to form dry SD, then gently crushed in an agate mortar to obtain a fine powder below 90 μm in size. Two different Italian SCM, namely a BFS (in accordance with EN 15167-1) and a low calcium FA (according to EN 450-1), were also employed.

Four binary dolomite-based binders were laboratory prepared (Table 1); they contained 30% or 50% by mass of BFS (SD/BFS3 and SD/BFS5, respectively) or FA (SD/FA3 and SD/FA5, respectively). Dolomite-based pastes (HSD/BFS3, HSD/BFS5, HSD/FA3, HSD/FA5)

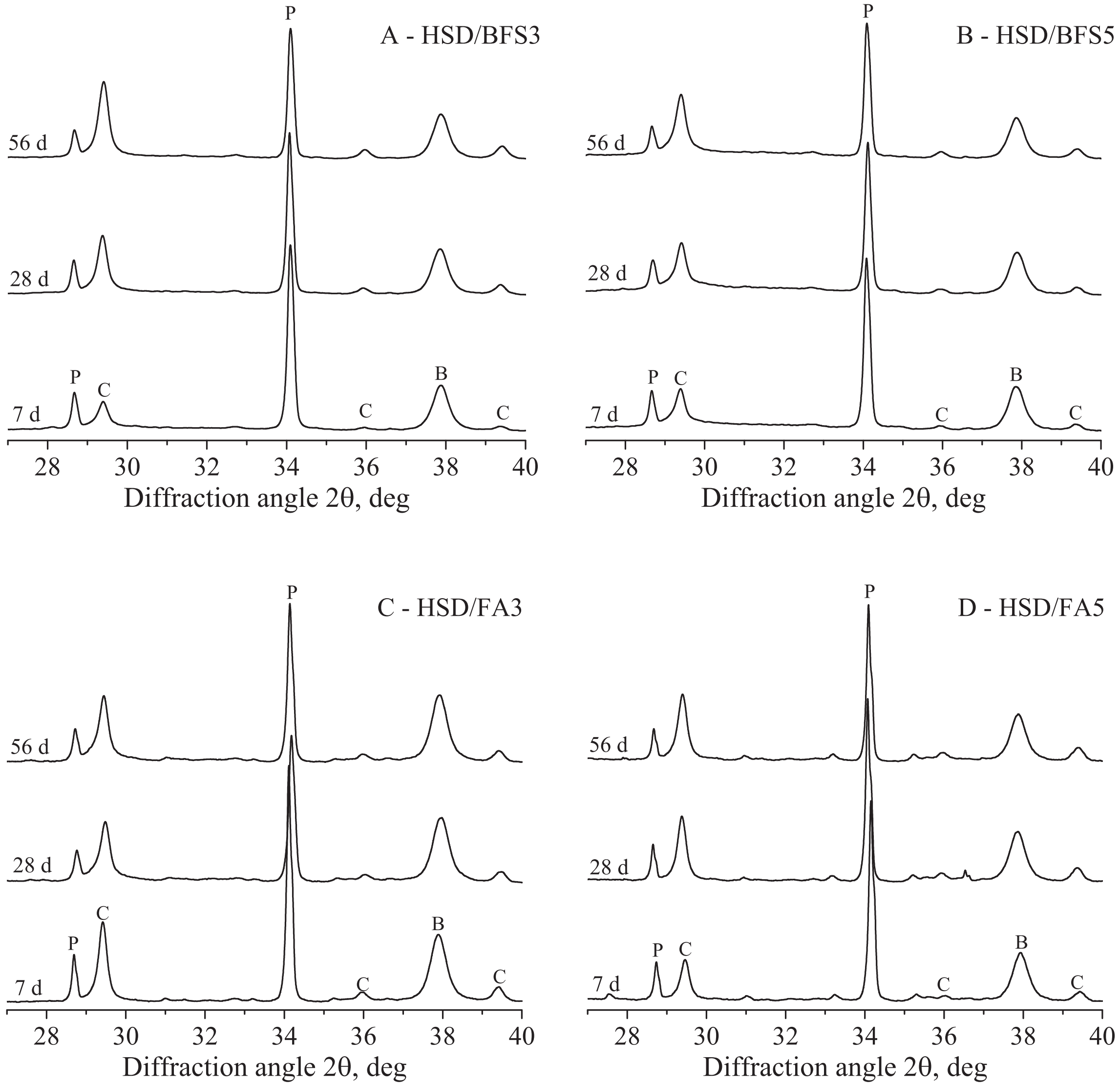

Fig. 9. HSD/BFS3 (A-up left), HSD/BFS5 (B-up right), HSD/FA3 (C-down left) and HSD/FA5 (D-down right) XRD profiles, zoom in the 2θ interval 27°–40° (binders hydrated at 20 °C for 7, 28 and 56 days). Legend: B = brucite ($Mg(OH)_2$); C = calcite ($CaCO_3$); P = portlandite ($Ca(OH)_2$).

were hydrated using a water/solid mass ratio equal to 0.50; the pastes were cast into plastic moulds (length of 15 mm, diameter of 30 mm), and located in a thermostatic heater (at 20 °C with a 95% relative humidity) for hydration times up to 56 days. At the end of each curing time, the moulds were pulverised. A solvent exchange method was employed in order to stop the hydration process: acetone first and later diethyl ether were added to the comminuted samples. They were finally stored in a desiccator equipped with silica gel and soda lime (to protect from H_2O and CO_2) before analyses.

2.2.2. *Characterisation techniques*

The chemical composition (Table 2) of the five starting materials (raw dolomite, CD, SD, BFS, FA), in terms of major oxides, was measured by using the X-ray fluorescence (XRF) BRUKER Explorer S4 spectroscope (1 kW of maximum power; LiF200, PET, OVO-55, OVO-B as analysed crystals). Table 2 also reports the values of loss on ignition for each material, evaluated at 950 °C. Data listed in Table 2 will be discussed in the Results section.

XRD analysis was employed for the evaluation of the mineralogical constituents of starting materials as well as hydration products of dolomite-based binders. XRD powder profiles were obtained with CuKα radiation using an Empyrean diffractometer by Malvern Panalytical with continuous scans of the 2θ angle (step = 0.013°, counting time 198.645 s). The diffraction profiles were analysed with the SIEVE+ software integrated into the PDF-4+ 2020 database of the ICDD "International Center for Diffraction Data" to search and identify the crystalline phases present in the samples. DT-TG analysis was performed using a Netzsch Tasc 414/3 running from 20 °C to 1000 °C at 10 °C/min in 150 μL alumina crucibles. The technique was applied for the components evaluation of analysed samples. DT analysis allowed the recognition of the following constituents (Taylor, 1997): (i) calcium silicate hydrates (dehydration endothermal peak (DEP) at 106 °C ± 8°C); (ii) hydrotalcite (DEP at 178 °C ± 6 °C); (iii) hydrated gehlenite (DEP at 240 °C ± 10 °C); (iv) magnesium hydroxide (419 °C ± 8 °C); (v) calcium hydroxide (DEP at 514 °C ± 8 °C); (vi) magnesium carbonate (DEP at 514 °C ± 8 °C) and (vii) calcium carbonates (DEP at 808 °C ± 14 °C). TG analysis allowed to quantitatively estimate $Mg(OH)_2$, $Ca(OH)_2$, $MgCO_3$ and $CaCO_3$ contents.

3. Results and discussion

3.1. *Calcination of dolomite in directly irradiated fluidised bed*

Fig. 2 shows the temperature profiles recorded during a typical

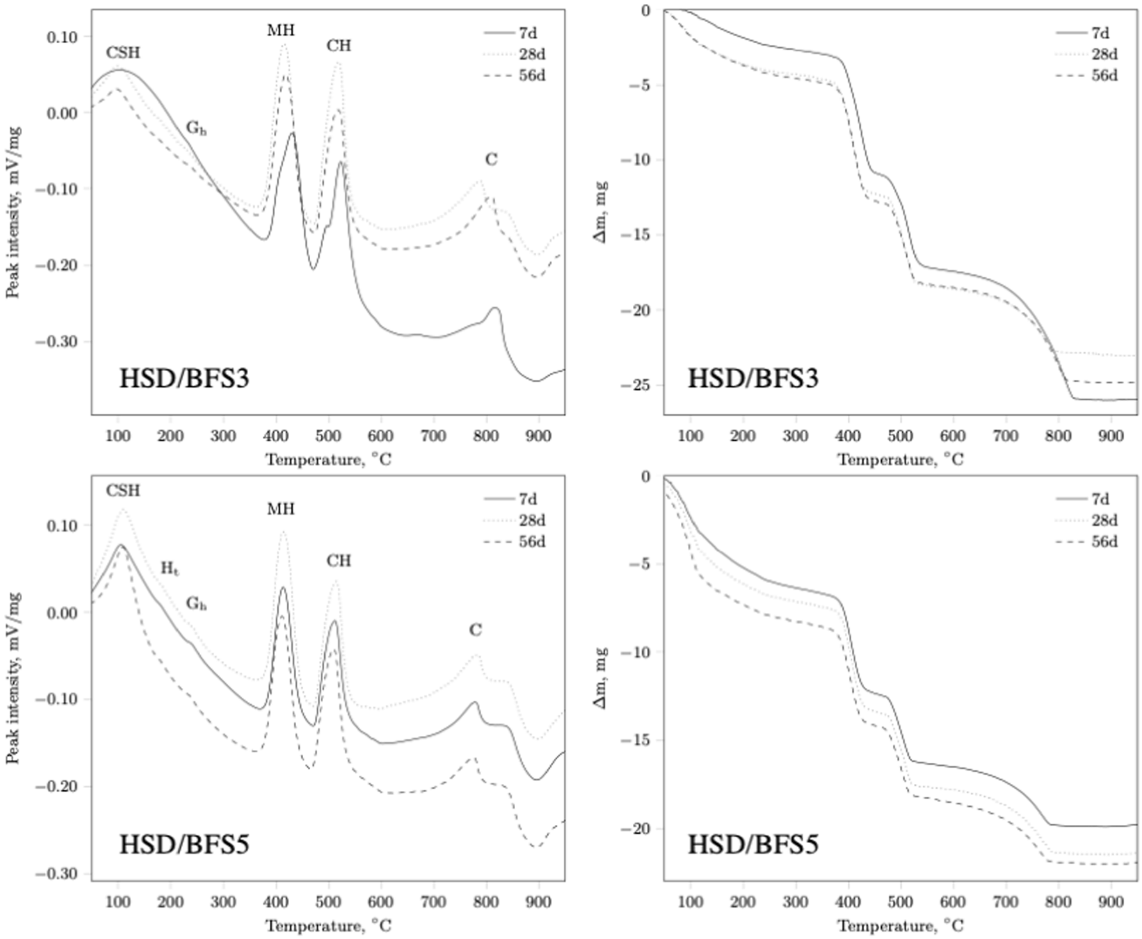

Fig. 10. DT (left)-TG (right) thermograms for HSD/BFS3 (up) and HSD/BFS5 (down) systems (binders hydrated at 20 °C for 7, 28 and 56 days). Legend: C = calcium carbonate ($CaCO_3$); CH = calcium hydroxide ($Ca(OH)_2$); CSH = calcium silicate hydrates ($3CaO\cdot 2SiO_2\cdot 3H_2O$); Gh = hydrated gehlenite ($2CaO\cdot Al_2O_3\cdot SiO_2\cdot 8H_2O$); Ht = hydrotalcite ($Mg_6Al_2(CO_3)(OH)_{16}\cdot 4H_2O$); MH = magnesium hydroxide ($Mg(OH)_2$). DT endo peaks up.

experiment of solar–driven calcination of dolomite in FB reactor. The green curve represents the average temperature value recorded by the thermocouples located in the upper part and at middle height of the FB. The black and orange curves represent the temperature values detected by IRC and refer, respectively, to the whole reactor surface and to a central circular region with a diameter of about 25 mm. Finally, the red hexagons refer to the maximum temperature value detected by the IRC in any point within the reactor surface (hot spots). The analysis of the chart shows an initial drop in temperature related to loading of the “cold” dolomite material within the system. Subsequently, the temperature rapidly increases because of the mixing with the hot sand within the reactor and because of the energy supplied by the simulator of concentrated solar energy. The temperature increase is partly slowed down during the 200–400 s time range, when probably most of the endothermal calcination reaction is occurring, withdrawing relevant amount of energy from the system (Tregambi et al., 2017). Temperature values recorded by the IRC show that the high concentrated solar radiation induces an overheating of the FB surface. Temperature values averaged in the 200–1200 s time range have been calculated. With respect to the values measured by thermocouples, the use of the IRC camera allowed to observe a mean overtemperature of about 27 °C when referring to the whole FB surface, and of 48 °C when referring only to the central region of the FB surface, where most of the concentrated radiation directly impinges. Data referring to the hot spots reveal that temperature can occasionally reach peaks of even 950 °C and higher. More into detail, hot spots values exceeding 1000 °C were detected only for 1% of the time during the 200–1200 s time range. As a consequence, the dolomite sample can be considered light-burned. Overheating of the center of the FB surface can be also appreciated by watching its thermal pictures, shown in Fig. 3 for different time instants during solar-driven calcination.

3.2. Characteristics of manufactured Mg-based binders starting from solar calcined dolomite

Data in Table 2 report a raw dolomite very rich in carbonate of calcium and magnesium (referred in terms of the corresponding oxides together with the associated loss on ignition following calcination at 950 °C). As a matter of fact, Fig. 4 (showing XRD profile of raw dolomite) witnesses the purity of the sample with the only detected crystalline peaks due to dolomite and small amount of calcite.

Furthermore, the solar calcination of dolomite was efficacious for obtaining a high degree of decarbonation, as inferred from the value of loss on ignition for solar CD in Table 2 (which is non-zero possibly due to uncontrolled atmospheric hydration of CaO and MgO, and residues of uncalcined material). Therefore, since the CO_2 emissions associated with the production of CD is equal to about 1.113 t_{CO2}/t_{CD}, 0.2 tons of which arising from fuel combustion and 0.913 tons of which related to material decomposition (Ecofys, 2009; Filkoski et al., 2018), it is possible to infer that the CO_2 saving associated with the use of the solar process is equal to about 18%.

Hydration of solar CD gave rise to slaked dolomite. The increase in the value of loss on ignition for SD (Table 2) is related to the hydration of CaO and MgO to the corresponding hydroxides. In fact, the XRD profile

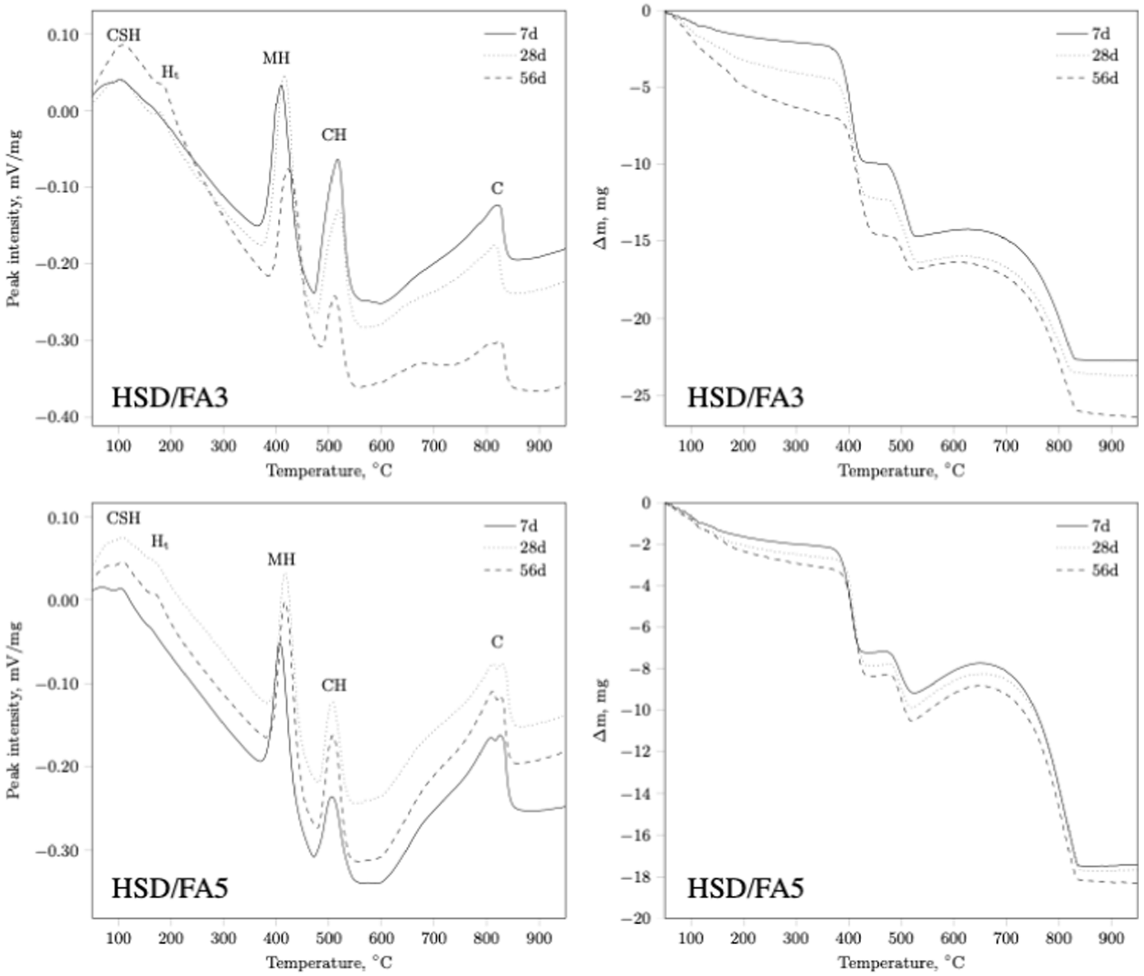

Fig. 11. DT (left)-TG (right) thermograms for HSD/FA3 (up) and HSD/FA5 (down) systems (binders hydrated at 20 °C for 7, 28 and 56 days). Legend: C = calcium carbonate ($CaCO_3$); CH = calcium hydroxide ($Ca(OH)_2$); CSH = calcium silicate hydrates ($3CaO{\cdot}2SiO_2{\cdot}3H_2O$); Ht = hydrotalcite ($Mg_6Al_2(CO_3)(OH)_{16}{\cdot}4H_2O$); MH = magnesium hydroxide ($Mg(OH)_2$). DT endo peaks up.

of SD (Fig. 4), apart from residues of calcite, shows large prevalence of portlandite and brucite. DT-TG analysis in Fig. 5 fully confirms the XRD results for raw and slaked dolomite; in fact, peaks for $MgCO_3$ and $CaCO_3$ are evident in the raw dolomite DT-thermogram while $Mg(OH)_2$, $Ca(OH)_2$ and $CaCO_3$ are well recognisable in the SD sample.

XRF data of Table 2 clearly indicate that the BFS sample is mainly composed of CaO and SiO_2, while Al_2O_3 (together with MgO) can be considered as a secondary component; moreover, the quality factor (Q_f=(CaO + MgO + Al_2O_3)/(SiO_2 + TiO_2)), the hydration modulus (H_m=(CaO + MgO + Al_2O_3)/(SiO_2)) and the coefficient of basicity (K_b=(CaO + MgO)/(SiO_2 + Al_2O_3)) values for BFS are equal to 1.55, 1.58 and 1.05, respectively. These results allow for the classification of the slag as both a good hydraulic (as its H_m is higher than 1.40) and neutral (as its $0.9 < K_b < 1.1$) material (Samui et al., 2020). The FA belongs to Class F, due to its high silico-aluminous fraction (74.5%) which largely prevails over the calcitic fraction (5.5%); in addition, its low loss on ignition value (4.4%) fulfils the minimal technical specifications reported in the EN 197–1 for fly ashes to be employed as SCM in blended cements.

Both SCM (i.e. BFS and FA) were analysed using XRD (Fig. 6). Apart from a very low intensity crystalline peak ascribed to calcite, the BFS sample is essentially amorphous, as indicated by the presence of a broad halo in the 2θ range 10°–35° in the diffraction profile of Fig. 6A, associated with the amorphous calcium-magnesium aluminosilicates that constitute the bulk material, as revealed by the oxide compositional analysis reported in Table 2. The XRD profile of Fig. 6B shows that mullite and quartz are the main crystalline phases for the FA sample, while periclase, lime, anhydrite, hematite and siderite are present as secondary components. The hump in the 2θ range 14°–37°, highlights the existence of a glassy fraction due to the presence of amorphous silicates responsible for the reactivity of the FA.

SD was mixed with BFS or FA to give SD/BFS and SD/FA samples, respectively, as in Table 1. SD/BFS and SD/FA systems were hydrated (to obtain HSD/BFS and HSD/FA samples, respectively) and the XRD profiles of the samples hydrated for 7, 28 and 56 days are reported in Figs. 7 and 8. The mineralogical analysis reveals the presence of magnesium aluminium carbonate hydroxide hydrate (namely hydrotalcite), deriving from the combination of Mg^{2+} and Al^{3+} with CO_3^{2-} (or also other available anions) in presence of water as well as of portlandite, brucite, calcite and quartz (Figs. 7 and 8). Mullite is only identified in the systems containing the FA (Fig. 8), as a result of the parent mullite content in FA (see Fig. 6B).

Some variances in the relative amounts of crystalline phases are observed depending on the curing time and the composition of the binder mixtures. The amount of hydrotalcite is higher in the HSD/FA and lower in the HSD/BFS systems, witnessing the higher reactivity of alumina in fly ash *vs.* alumina in blast furnace slag (moreover, FA has higher Al_2O_3 content than BFS). When comparing HSD/FA3 and HSD/FA5, the higher percentage of SD in HSD/FA3 brings about a larger magnesium content, able to develop more hydrotalcite (that, in this particular case, appears to increase with increasing curing time, see Fig. 8A). This effect is less evident for the HSD/BFS systems in which the

Table 3
Mass loss values, obtained from TG analysis, for the hydrated systems under investigation.

HSD/BFS3				
Curing period, days	Mass loss, wt%			
	Dehydration	Dehydroxylation	Decarbonation	TWL
7	2.94	14.21	3.61	20.76
28	4.63	13.74	4.65	23.02
56	4.85	13.43	6.40	24.68
HSD/BFS5				
Curing period, days	Mass loss, wt%			
	Dehydration	Dehydroxylation	Decarbonation	TWL
7	6.67	10.21	3.31	20.19
28	7.45	9.73	3.61	20.79
56	8.55	9.66	3.53	21.74
HSD/FA3				
Curing period, days	Mass loss, wt%			
	Dehydration	Dehydroxylation	Decarbonation	TWL
7	2.24	12.33	8.13	22.70
28	4.34	11.94	7.40	23.68
56	6.73	9.92	9.74	26.39
HSD/FA5				
Curing period, days	Mass loss, wt%			
	Dehydration	Dehydroxylation	Decarbonation	TWL
7	2.11	6.75	8.36	17.22
28	2.64	6.74	8.21	17.59
56	3.13	6.88	8.25	18.26

amount of hydrotalcite formed during the hydration process is quite low, regardless of the percentage of SD (Fig. 7). Fig. 9 helps in reading XRD profiles of Figs. 7 and 8 in the 2θ range 27°–40°, especially for calcite, portlandite and brucite main diffraction peaks. Regardless of the type or amount of SCM, the content of calcite appears to increase as curing time increases, portlandite decreases and brucite is mostly constant in all the binder systems.

Figs. 10 and 11 show the DT-TG results for all the hydrated samples. DT-TG analysis mainly confirms the XRD results. All DT curves are similar showing several endothermal peaks related to the presence of different phases, namely calcium silicate hydrates (CSH), magnesium and calcium hydroxides, calcium carbonate. In addition, an exothermal peak at 895 °C ± 5 °C, associated with the devitrification of slag (Singh and Garg, 2002), is observed in all the hydrated systems containing BFS. CSH are the main hydration products deriving from the reaction of calcium hydroxide (whose peak generally decreases with increasing curing time) with active silica in BFS or FA. CSH are also the favoured hydration products for ordinary Portland cements hydration process and are the main responsible for their technical properties. As expected, CSH, owing to their amorphous nature, are not recognised in the XRD profiles. DT-TG data confirmed XRD analysis and indicate that:

I) the peak of $Ca(OH)_2$ generally decreases with the increase of curing time for all the investigated systems (due to the progressive reaction to form CSH);
II) the peak of $Mg(OH)_2$ slightly reduces with the increase of curing times for all the investigated systems;
III) a tiny peak related to the formation of hydrotalcite was detected in all systems but HSD/BFS3;
IV) hydrated gehlenite is observed in the systems containing BFS;
V) one/two different endothermal peaks, associated with the decomposition of $CaCO_3$, mostly deriving from the combination of atmospheric CO_2 with $Ca(OH)_2$, are observed in all the systems.

Furthermore, from TG curves, it is observed that the total weight loss (TWL) of hydrated samples in the 20–950 °C interval can be ascribed to the following processes:

"low-temperature" dehydration of CSH, H_t and/or G_h (20–350 °C);

"medium-temperature" dehydroxylation of MH and CH (350–550 °C);

"high temperature" decarbonation of $CaCO_3$ phases (550–950 °C).

Table 3 reports the information retrieved from TG analyses. It can be substantiated that the formation of the favourite hydration products increases with curing times (see low-temperature dehydration loss values). Moreover, the extent of the dehydration loss (which is a direct measure of the formation of desired phases upon hydration) is, for the sample composed of slaked dolomite and blast furnace slag, higher when the fraction of BFS in the mixture is higher. This should be related to the silica content, necessary for the formation of CSH, present in BFS. On the contrary, the very low CaO amount in FA requires, in the mixtures composed of slaked dolomite and FA, a higher amount of the Ca-bearing SD for the production of CSH (fly ash is very rich in silica, indeed). This could explain why the dehydration loss for HSD/FA3 is higher (i.e., better) than for HSD/FA5. Altogether, the source of magnesium, arising from the solar calcination of natural dolomite, proves to be reactive for the formation, upon hydration of mixtures where SCM are present, of the desired binding phases.

4. Conclusions

The analysis of the fluidised bed temperature profiles during solar-driven calcination of dolomite allowed to determine the in-bed and surface temperature values, and the extent of hot spots, also relating them to the course of the calcination process. Mean overtemperature values, with respect to the nominal temperature of 850 °C, ranged between 27 °C and 48 °C. Hot spots exceeding the temperature value of 1000 °C were detected only for 1% of the time, meaning that the dolomite sample can be regarded as light–burned. In this work, we demonstrate that the solar-driven calcination process was satisfying in producing a reactive material for the formation of the desired binding phases upon hydration of dolomite-based binders; more in particular, the characterisation of the solar product confirmed the good extent of the calcination process. Furthermore, analyses on the two supplementary cementitious materials highlighted that, on the one hand, the blast furnace slag owns the characteristics of a proper hydraulic and neutral material and, on the other hand, the fly ash fulfils the technical requirements to be employed in blended cements. XRD on hydrated samples allowed to observe the formation of magnesium aluminium carbonate hydroxide hydrate (hydrotalcite), more relevant in the blends containing fly ash (that are richer in reactive alumina than blast furnace slag). The formation of the most important product of hydration, namely calcium silicate hydrates, was clearly demonstrated by DT-TG analyses. These compounds increase in concentration as long as the curing time increases; in this regard, particularly interesting appears the mixture composed of slaked dolomite and blast furnace slag (50/50 by weight), as this system shows the best relative proportions of calcium and silicon oxides: the dehydration loss varies from about 6.7% to 8.6% when curing time increases from 7 to 56 days (for comparison, in the 50/50 slaked dolomite/fly ash system, the range 2.1–3.1% has been observed). In conclusion, obtained results are promising for the synthesis of low-CO_2 dolomite-based binders starting from a material calcined in a fluidised bed reactor using solar energy as added value to foster the environmentally friendly character of the whole process.

Declaration of Competing Interest

The authors declare that they have no known competing financial interests or personal relationships that could have appeared to influence the work reported in this paper.

Acknowledgement

Ca.ve. Dolomitica S.r.l. (Ailano – Caserta, Italy) is gratefully acknowledged for providing samples of the dolomite sorbent used within the present experimental campaign.

References

Abanades, S., André, L., 2018. Design and demonstration of a high temperature solar-heated rotary tube reactor for continuous particles calcination. Appl. Energy 212, 1310–1320. https://doi.org/10.1016/j.apenergy.2018.01.019.

Alonso, E., Gallo, A., Roldán, M.I., Pérez-Rábago, C.A., Fuentealba, E., 2017. Use of rotary kilns for solar thermal applications: Review of developed studies and analysis of their potential. Sol. Energy 144, 90–104. https://doi.org/10.1016/j.solener.2017.01.004.

ASTM C618. Standard specification for coal fly ash and raw or calcined natural pozzolan for use in concrete.

Badie, J.M., Bonet, C., Faure, M., Flamant, G., Foro, R., Hernandez, D., 1980. 52 Decarbonation of calcite and phosphate rock in solar chemical reactors. Chem. Eng. Sci. 35 (1-2), 413–420. https://doi.org/10.1016/0009-2509(80)80114-X.

Barcelo, L., Kline, J., Walenta, G., Gartner, E., 2014. Cement and carbon emissions. Mater. Struct. 47, 1055–1065. https://doi.org/10.1617/s11527-013-0114-5.

Coppola, L., Bellezze, T., Belli, A., Bignozzi, M.C., Bolzoni, F., Brenna, A., Cabrini, M., Candamano, S., Cappai, M., Caputo, D., Carsana, M., Casnedi, L., Cioffi, R., Cocco, O., Coffetti, D., Colangelo, F., Coppola, B., Corinaldesi, V., Crea, F., Crotti, E., Daniele, V., De Gisi, S., Delogu, F., Diamanti, M.V., Di Maio, L., Di Mundo, R., Di Palma, L., Donnini, J., Farina, I., Ferone, C., Frontera, P., Gastaldi, M., Giosuè, C., Incarnato, L., Liguori, B., Lollini, F., Lorenzi, S., Manzi, S., Marino, O., Marroccoli, M., Mascolo, M.C., Mavilia, L., Mazzoli, A., Medici, F., Meloni, P., Merlonetti, G., Mobili, A., Notarnicola, M., Ormellese, M., Pastore, T., Pedeferri, M. P., Petrella, A., Pia, G., Redaelli, E., Roviello, G., Scarfato, P., Scoccia, G., Taglieri, G., Telesca, A., Tittarelli, F., Todaro, F., Vilardi, G., Yang, F., 2018a. Binders alternative to Portland cement and waste management for sustainable construction—part 1. J. Appl. Biomater. Funct. Mater. 16 (3), 186–202. https://doi.org/10.1177/2280800018782845.

Coppola, L., Bellezze, T., Belli, A., Bignozzi, M.C., Bolzoni, F., Brenna, A., Cabrini, M., Candamano, S., Cappai, M., Caputo, D., Carsana, M., Casnedi, L., Cioffi, R., Cocco, O., Coffetti, D., Colangelo, F., Coppola, B., Corinaldesi, V., Crea, F., Crotti, E., Daniele, V., De Gisi, S., Delogu, F., Diamanti, M.V., Di Maio, L., Di Mundo, R., Di Palma, L., Donnini, J., Farina, I., Ferone, C., Frontera, P., Gastaldi, M., Giosuè, C., Incarnato, L., Liguori, B., Lollini, F., Lorenzi, S., Manzi, S., Marino, O., Marroccoli, M., Mascolo, M.C., Mavilia, L., Mazzoli, A., Medici, F., Meloni, P., Merlonetti, G., Mobili, A., Notarnicola, M., Ormellese, M., Pastore, T., Pedeferri, M. P., Petrella, A., Pia, G., Redaelli, E., Roviello, G., Scarfato, P., Scoccia, G., Taglieri, G., Telesca, A., Tittarelli, F., Todaro, F., Vilardi, G., Yang, F., 2018b. Binders alternative to Portland cement and waste management for sustainable construction – Part 2. J. Appl. Biomater. Funct. Mater. 16 (4), 207–221. https://doi.org/10.1177/2280800018782852.

Costa Oliveira, F.A., Fernandes, J.C., Galindo, J., Rodríguez, J., Cañadas, I., Vermelhudo, V., Nunes, A., Rosa, L.G., 2019. Portland cement clinker production using concentrated solar energy – A proof-of-concept approach. Sol. Energy 183, 677–688. https://doi.org/10.1016/j.solener.2019.03.064.

Di Lauro, F., Tregambi, C., Montagnaro, F., Salatino, P., Chirone, R., Solimene, R., 2021. Improving the performance of calcium looping for solar thermochemical energy storage and CO_2 capture. Fuel 298, 120791. https://doi.org/10.1016/j.fuel.2021.120791.

Dung, N.T., Lesimple, A., Hay, R., Celik, K., Unluer, C., 2019. Formation of carbonate phases and their effect on the performance of reactive MgO cement formulations. Cem. Concr. Res. 125, 105894. https://doi.org/10.1016/j.cemconres.2019.105894.

Ecofys, Fraunhofer Institute for Systems and Innovation Research, Öko-Institut, 2009. Methodology for the free allocation of emission allowances in the EU ETS post 2012 - Sector report for the lime industry, Study Contract: 07.0307/2008/515770/ETU/C2.

Ekolu, S.O., 2020. Implications of global CO_2 emissions on natural carbonation and service lifespan of concrete infrastructures – Reliability analysis. Cem. Concr. Compos. 114, 103744. https://doi.org/10.1016/j.cemconcomp.2020.103744.

EN 15167-1. Ground granulated blast furnace slag for use in concrete, mortar and grout. definition, specifications and conformity criteria.

EN 197-1. Composition, specifications and conformity criteria for common cements.

EN 450-1. Fly ash for concrete – Part 1: definition, specifications and conformity criteria.

Esence, T., Benoit, H., Poncin, D., Tessonneaud, M., Flamant, G., 2020a. A shallow cross-flow fluidized-bed solar reactor for continuous calcination processes. Sol. Energy 196, 389–398. https://doi.org/10.1016/j.solener.2019.12.029.

Esence, T., Guillot, E., Tessonneaud, M., Sans, J.L., Flamant, G., 2020b. Solar calcination at pilot scale in a continuous flow multistage horizontal fluidized bed. Sol. Energy 207, 367–378. https://doi.org/10.1016/j.solener.2020.06.098.

ESRL, 2020. http://esrl.noaa.gov/gmd/ccgg/trends/. Last accessed: September 2020.

Fernández-González, D., Prazuch, J., Ruiz-Bustinza, I., González-Gasca, C., Piñuela-Noval, J., Verdeja, L.F., 2018. Solar synthesis of calcium aluminates. Sol. Energy 171, 658–666. https://doi.org/10.1016/j.solener.2018.07.012.

Filkoski, R., Petrovski, I., Gjurchinovski, Z., 2018. Energy optimisation of vertical shaft kiln operation in the process of dolomite calcination. Therm. Sci. 22 (5), 2123–2135. https://doi.org/10.2298/TSCI180125278F.

Flamant, G., Hernandez, D., Bonet, C., Traverse, J.-P., 1980. Experimental aspects of the thermochemical conversion of solar energy; Decarbonation of $CaCO_3$. Sol. Energy 24 (4), 385–395. https://doi.org/10.1016/0038-092X(80)90301-1.

Gartner, E., Hirao, H., 2015. A review of alternative approaches to the reduction of CO_2 emissions associated with the manufacture of the binder phase in concrete. Cem. Concr. Res. 78, 126–142. https://doi.org/10.1016/j.cemconres.2015.04.012.

Gartner, E., Sui, T., 2018. Alternative cement clinkers. Cem. Concr. Res. 114, 27–39. https://doi.org/10.1016/j.cemconres.2017.02.002.

Giergiczny, Z., 2019. Fly ash and slag. Cem. Concr. Res. 124, 105826. https://doi.org/10.1016/j.cemconres.2019.105826.

González, R.S., Flamant, G., 2014. Technical and Economic Feasibility Analysis of Using Concentrated Solar Thermal Technology in the Cement Production Process: Hybrid Approach—A Case Study. J. Sol. Energy Eng. 136 https://doi.org/10.1115/1.4026573.

Gunasekaran, S., Anbalagan, G., 2007. Thermal decomposition of natural dolomite. Bull. Mater. Sci. 30 (4), 339–344. https://doi.org/10.1007/s12034-007-0056-z.

Harrison, A.J.W., 2008. Reactive Magnesium Oxide Cements. Google Patents, United States of America.

Hossain, F.M., Dlugogorski, B.Z., Kennedy, E.M., Belova, I.V., Murch, G.E., 2011. First-principles study of the electronic, optical and bonding properties in dolomite. Comput. Mater. Sci. 50 (3), 1037–1042. https://doi.org/10.1016/j.commatsci.2010.10.044.

IEA, 2019. https://www.iea.org/articles/global-co2-emissions-in-2019. Last accessed: December 2020.

IEA, 2020a. https://www.iea.org/reports/global-energy-review-2020/global-energy-and-co2-emissions-in-2020. Last accessed: December 2020.

IEA, 2020b. CO_2 emissions from fuel combustion: overview 2020.

Imhof, A., 1991. The cyclone reactor - an atmospheric open solar reactor. Sol. Energy Mater. 24 (1-4), 733–741. https://doi.org/10.1016/0165-1633(91)90106-U.

Imhof, A., 1997. Decomposition of limestone in a solar reactor. Renew. Energy 10 (2-3), 239–246. https://doi.org/10.1016/0960-1481(96)00072-9.

Imhof, A., 2000a. Calcination of limestone in a solar reactor. ZKG Int. 53, 504–509.

Imhof, A., 2000b. Solar cement plants - An interesting challenge for business and science. ZKG Int. 53, 448–456.

Jia, Y., Wang, B., Wu, Z., Zhang, T., 2017. Effect of CaO on the reaction process of $MgO\text{-}SiO_2\text{-}H_2O$ cement pastes. Mater. Lett. 192, 48–51. https://doi.org/10.1016/j.matlet.2017.01.072.

Juenger, M.C.G., Snellings, R., Bernal, S.A., 2019. Supplementary cementitious materials: New sources, characterization, and performance insights. Cem. Concr. Res. 122, 257–273. https://doi.org/10.1016/j.cemconres.2019.05.008.

Kristóf-Makó, É., Juhász, A.Z., 1999. The effect of mechanical treatment on the crystal structure and thermal decomposition of dolomite. Thermochim. Acta 342 (1-2), 105–114. https://doi.org/10.1016/S0040-6031(99)00290-7.

Li, Y.-M., Wu, X.-Q., Wang, L.-J., Li, R.-Q., Huang, T.-Y., Wen, X.-Q., 2020. Comparative study on utilization of different types of municipal solid waste incineration bottom ash for clinker sintering. J. Mater. Cycles Waste Manag. 22 (6), 1828–1843. https://doi.org/10.1007/s10163-020-01067-6.

Marinković, S., Dragaš, J., 2018. 11 - Fly ash, in: Siddique, R., Cachim, P.B.T.-W. and S.C. M. in C. (Eds.), Woodhead Publishing Series in Civil and Structural Engineering. Woodhead Publishing, pp. 325–360. https://doi.org/10.1016/B978-0-08-102156-9.00011-0.

Matthes, W., Vollpracht, A., Villagrán, Y., Kamali-Bernard, S., Hooton, D., Gruyaert, E., Soutsos, M., De Belie, N., 2018. Ground Granulated Blast-Furnace Slag, in: De Belie, N., Soutsos, M., Gruyaert, E. (Eds.), Properties of Fresh and Hardened Concrete Containing Supplementary Cementitious Materials: State-of-the-Art Report of the RILEM Technical Committee 238-SCM, Working Group 4. Springer International Publishing, Cham, pp. 1–53. https://doi.org/10.1007/978-3-319-70606-1_1.

Meier, A., Bonaldi, E., Cella, G.M., Lipinski, W., Wuillemin, D., Palumbo, R., 2004. Design and experimental investigation of a horizontal rotary reactor for the solar thermal production of lime. Energy 29 (5-6), 811–821. https://doi.org/10.1016/S0360-5442(03)00187-7.

Meier, A., Bonaldi, E., Cella, G.M., Lipinski, W., 2005a. Multitube Rotary Kiln for the Industrial Solar Production of Lime. J. Sol. Energy Eng. 127, 386–395. https://doi.org/10.1115/1.1979517.

Meier, A., Gremaud, N., Steinfeld, A., 2005b. Economic evaluation of the industrial solar production of lime. Energy Convers. Manag. 46 (6), 905–926. https://doi.org/10.1016/j.enconman.2004.06.005.

Meier, A., Bonaldi, E., Cella, G.M., Lipinski, W., Wuillemin, D., 2006. Solar chemical reactor technology for industrial production of lime. Sol. Energy 80 (10), 1355–1362. https://doi.org/10.1016/j.solener.2005.05.017.

Miller, S.A., John, V.M., Pacca, S.A., Horvath, A., 2018. Carbon dioxide reduction potential in the global cement industry by 2050. Cem. Concr. Res. 114, 115–124. https://doi.org/10.1016/j.cemconres.2017.08.026.

Montagnaro, F., Tregambi, C., Salatino, P., Senneca, O., Solimene, R., 2018. Modelling oxy-pyrolysis of sewage sludge in a rotary kiln reactor. Fuel 231, 468–478. https://doi.org/10.1016/j.fuel.2018.05.094.

Moumin, G., Tescari, S., Sundarraj, P., de Oliveira, L., Roeb, M., Sattler, C., 2019. Solar treatment of cohesive particles in a directly irradiated rotary kiln. Sol. Energy 182, 480–490. https://doi.org/10.1016/j.solener.2019.01.093.

Moumin, G., Ryssel, M., Zhao, L., Markewitz, P., Sattler, C., Robinius, M., Stolten, D., 2020. CO_2 emission reduction in the cement industry by using a solar calciner. Renew. Energy 145, 1578–1596. https://doi.org/10.1016/j.renene.2019.07.045.

Nikulshina, V., Gebald, C., Steinfeld, A., 2009. CO_2 capture from atmospheric air via consecutive CaO-carbonation and $CaCO_3$-calcination cycles in a fluidized-bed solar reactor. Chem. Eng. J. 146 (2), 244–248. https://doi.org/10.1016/j.cej.2008.06.005.

Olszak-Humienik, M., Możejko, J., 1999. Kinetics of Thermal Decomposition of Dolomite. J. Therm. Anal. Calorim. 56, 829–833. https://doi.org/10.1023/A:1010174726982.

Padula, S., Tregambi, C., Solimene, R., Chirone, R., Troiano, M., Salatino, P., 2021. A novel fluidized bed "thermochemical battery" for energy storage in concentrated solar thermal technologies. Energy Convers. Manag. 236, 113994. https://doi.org/10.1016/j.enconman.2021.113994.

Purohit, S., Brooks, G., Rhamdhani, M.A., Pownceby, M.I., 2021. Evaluation of concentrated solar thermal energy for iron ore agglomeration. J. Clean. Prod. 317, 128313. https://doi.org/10.1016/j.jclepro.2021.128313.

Rosa, L.G., 2019. Solar heat for materials processing: A review on recent achievements and a prospect on future trends. ChemEngineering 3, 1–19. https://doi.org/10.3390/chemengineering3040083.

Salman, O.A., Khraishi, N., 1988. Thermal decomposition of limestone and gypsum by solar energy. Sol. Energy 41 (4), 305–308. https://doi.org/10.1016/0038-092X(88)90025-4.

Samui, P., Kim, D., Iyer, N., Chaudhary, S. (Eds.), 2020. New materials in civil engineering. Paperback ISBN: 9780128189610; eBook ISBN: 9780128190753. Imprint: Butterworth-Heinemann. Published Date: 23rd July 2020. Elsevier.

Scrivener, K.L., John, V.M., Gartner, E.M., 2018. Eco-efficient cements: Potential economically viable solutions for a low-CO_2 cement-based materials industry. Cem. Concr. Res. 114, 2–26. https://doi.org/10.1016/j.cemconres.2018.03.015.

Shi, C., Jiménez, A.F., Palomo, A., 2011. New cements for the 21st century: The pursuit of an alternative to Portland cement. Cem. Concr. Res. 41 (7), 750–763. https://doi.org/10.1016/j.cemconres.2011.03.016.

Shi, C., Qu, B., Provis, J.L., 2019. Recent progress in low-carbon binders. Cem. Concr. Res. 122, 227–250. https://doi.org/10.1016/j.cemconres.2019.05.009.

Singh, M., Garg, M., 2002. Calcium sulfate hemihydrate activated low heat sulfate resistant cement. Constr. Build. Mater. 16 (3), 181–186. https://doi.org/10.1016/S0950-0618(01)00026-5.

Skibsted, J., Snellings, R., 2019. Reactivity of supplementary cementitious materials (SCMs) in cement blends. Cem. Concr. Res. 124, 105799. https://doi.org/10.1016/j.cemconres.2019.105799.

Taylor, H.F.W., 1997. Cement Chemistry. Thomas Telford, London, U.K.

Telesca, A., Marroccoli, M., Tomasulo, M., Valenti, G.L., Dieter, H., Montagnaro, F., 2015. Calcium looping spent sorbent as a limestone replacement in the manufacture of portland and calcium sulfoaluminate cements. Environ. Sci. Technol. 49 (11), 6865–6871. https://doi.org/10.1021/acs.est.5b00394.

Telesca, A., Marroccoli, M., Tomasulo, M., Valenti, G.L., Dieter, H., Montagnaro, F., 2016. Low-CO_2 Cements from Fluidized Bed Process Wastes and Other Industrial By-Products. Combust. Sci. Technol. 188 (4-5), 492–503. https://doi.org/10.1080/00102202.2016.1138736.

Telesca, A., Marroccoli, M., Ibris, N., Lupiáñez, C., Díez, L.I., Romeo, L.M., Montagnaro, F., 2017. Use of oxyfuel combustion ash for the production of blended cements: A synergetic solution toward reduction of CO_2 emissions. Fuel Process. Technol. 156, 211–220. https://doi.org/10.1016/j.fuproc.2016.10.026.

Tomatis, M., Jeswani, H.K., Stamford, L., Azapagic, A., 2020. Assessing the environmental sustainability of an emerging energy technology: Solar thermal calcination for cement production. Sci. Total Environ. 742, 140510. https://doi.org/10.1016/j.scitotenv.2020.140510.

Tregambi, C., Chirone, R., Montagnaro, F., Salatino, P., Solimene, R., 2016. Heat transfer in directly irradiated fluidized beds. Sol. Energy 129, 85–100. https://doi.org/10.1016/j.solener.2016.01.057.

Tregambi, C., Montagnaro, F., Salatino, P., Solimene, R., 2017. Directly irradiated fluidized bed reactors for thermochemical processing and energy storage: Application to calcium looping. AIP Conf. Proc. 1850 https://doi.org/10.1063/1.4984456.

Tregambi, C., Salatino, P., Solimene, R., Montagnaro, F., 2018a. An experimental characterization of Calcium Looping integrated with concentrated solar power. Chem. Eng. J. 331, 794–802. https://doi.org/10.1016/j.cej.2017.08.068.

Tregambi, C., Solimene, R., Montagnaro, F., Salatino, P., Marroccoli, M., Ibris, N., Telesca, A., 2018b. Solar-driven production of lime for ordinary Portland cement formulation. Sol. Energy 173, 759–768. https://doi.org/10.1016/j.solener.2018.08.018.

Tregambi, C., Di Lauro, F., Montagnaro, F., Salatino, P., Solimene, R., 2019a. 110th Anniversary: Calcium Looping Coupled with Concentrated Solar Power for Carbon Capture and Thermochemical Energy Storage. Ind. Eng. Chem. Res. 58 (47), 21262–21272. https://doi.org/10.1021/acs.iecr.9b03083.

Tregambi, C., Montagnaro, F., Salatino, P., Solimene, R., 2019b. Solar-Driven Torrefaction of a Lignin-Rich Biomass Residue in a Directly Irradiated Fluidized Bed Reactor. Combust. Sci. Technol. 191 (9), 1609–1627. https://doi.org/10.1080/00102202.2019.1607847.

Tregambi, C., Bevilacqua, C., Troiano, M., Solimene, R., Salatino, P., 2020a. A novel autothermal fluidized bed reactor for concentrated solar thermal applications. Chem. Eng. J. 398, 125702. https://doi.org/10.1016/j.cej.2020.125702.

Tregambi, C., Padula, S., Galbusieri, M., Coppola, G., Montagnaro, F., Salatino, P., Troiano, M., Solimene, R., 2020b. Directly irradiated fluidized bed reactor for thermochemical energy storage and solar fuels production. Powder Technol. 366, 460–469. https://doi.org/10.1016/j.powtec.2020.02.045.

Tregambi, C., Troiano, M., Montagnaro, F., Solimene, R., Salatino, P., 2021. Fluidized Beds for Concentrated Solar Thermal Technologies – A Review. Front. Energy Res. 9, 618421 https://doi.org/10.3389/fenrg.2021.618421.

Unluer, C., Al-Tabbaa, A., 2013. Impact of hydrated magnesium carbonate additives on the carbonation of reactive MgO cements. Cem. Concr. Res. 54, 87–97. https://doi.org/10.1016/j.cemconres.2013.08.009.

Walling, S.A., Provis, J.L., 2016. Magnesia-Based Cements: A Journey of 150 Years, and Cements for the Future? Chem. Rev. 116 (7), 4170–4204. https://doi.org/10.1021/acs.chemrev.5b00463.

Wei, Z., Wang, B., Falzone, G., La Plante, E.C., Okoronkwo, M.U., She, Z., Oey, T., Balonis, M., Neithalath, N., Pilon, L., Sant, G., 2018. Clinkering-free cementation by fly ash carbonation. J. CO2 Util. 23, 117–127. https://doi.org/10.1016/j.jcou.2017.11.005.

Xu, D., Cui, Y., Li, H., Yang, K., Xu, W., Chen, Y., 2015. On the future of Chinese cement industry. Cem. Concr. Res. 78, 2–13. https://doi.org/10.1016/j.cemconres.2015.06.012.

Xu, G., Shi, X., 2018. Characteristics and applications of fly ash as a sustainable construction material: A state-of-the-art review. Resour. Conserv. Recycl. 136, 95–109. https://doi.org/10.1016/j.resconrec.2018.04.010.

Yu, J., Qian, J., Wang, F., Qin, J., Dai, X., You, C., Jia, X., 2020. Study of using dolomite ores as raw materials to produce magnesium phosphate cement. Constr. Build. Mater. 253, 119147. https://doi.org/10.1016/j.conbuildmat.2020.119147.

Yuksel, I., 2018. Blast-furnace slag. In: Siddique, R., Cachim, P. (Eds.), Waste and Supplementary Cementitious Materials in Concrete, Woodhead Publishing Series in Civil and Structural Engineering, 12. Woodhead Publishing, pp. 361–415. https://doi.org/10.1016/B978-0-08-102156-9.00012-2.

CHEMICAL ENGINEERING TRANSACTIONS
VOL. 92, 2022

A publication of
AIDIC
The Italian Association
of Chemical Engineering
Online at www.cetjournal.it

Guest Editors: Rubens Maciel Filho, Eliseo Ranzi, Leonardo Tognotti

ISBN 978-88-95608-90-7; **ISSN** 2283-9216

DOI: 10.3303/CET2292080

Hydrothermal Liquefaction Process to Obtain Sludge-Derived Bio-Fuels: Setup of the Experimental Apparatus and Preliminary Tests

Francesca Di Lauro[a], Marco Balsamo[a], Roberto Solimene[b,*], Piero Salatino[c], Fabio Montagnaro[a].

[a]Dipartimento di Scienze Chimiche, Università degli Studi di Napoli Federico II, Complesso Universitario di Monte Sant'Angelo, 80126 Napoli, Italy
[b]Istituto di Scienze e Tecnologie per l'Energia e la Mobilità Sostenibili, Consiglio Nazionale delle Ricerche, Piazzale V. Tecchio 80, 80125 Napoli, Italy
[c]Dipartimento di Ingegneria Chimica, dei Materiali e della Produzione Industriale, Università degli Studi di Napoli Federico II, Piazzale V. Tecchio 80, 80125 Napoli, Italy
roberto.solimene@stems.cnr.it

The increasing interest in renewable energies sources, alternative to traditional fossil fuels, is justified by both the growing energy demand and the necessity to reduce greenhouse gases emissions related to the power sector. In this context, the production of bio-oil (or bio-crude) as liquid fuel through the innovative hydrothermal liquefaction (HTL) process is of particular interest, especially when applied to biomass with high water content. In fact, water is in sub-critical state under typical HTL conditions and acts as solvent, catalyst, and reaction medium. Therefore, HTL allows to exploit the water content of biomass, thus avoiding the high energy demand of the dewatering step associated with other thermo-chemical processes (e.g., gasification, pyrolysis, etc.). For the HTL process performed in batch reactors, the minimisation of thermal transients is crucial to both obtain a high-yield bio-crude with more attractive energy properties and limit the formation of undesirable products. In this work, the setup of a lab-scale HTL apparatus was performed so to limit thermal transients, and some preliminary tests were carried out on a municipal sludge in order to evaluate the yield of the obtained bio-crude.

1. Introduction

According to International Energy Agency (IEA), in 2019, the world total energy supply reached 7.2×10^8 TJ and energy generation from fossil fuels accounted for 80.9% of the total world gross energy production compared to 19.1% represented by renewable sources (biofuels and nuclear, wind, solar, etc.). The use of biomass (e.g., lignocellulosic substrates, sludges, micro and macroalgae) in renewable fuels production technologies has been considered as a promising route to replace some of the fossil fuels. In addition, it is imperative to develop efficient waste-to-energy techniques to reduce the volumes and environmental impacts of different wastes commonly disposed of in landfills (e.g., sewage sludge, municipal and industrial solid waste), while valorising them as a sustainable and renewable fuel. For example, the municipal sewage sludge, which contains a large amount of proteins, carbohydrates and lipids (He et al. 2014), is abundantly produced from municipal and industrial wastewater treatment plants. However, the solid content in dewatered sewage sludge is typically in the range of 10–20$\%_{wt}$ and the energy content of the solid species is very low (higher heating value (HHV) of 10–25 MJ/kg on a dry basis (Malins et al. 2015)). Thus, it is necessary to convert the organic matrix into high-energy-content fuels, in particular liquid ones required for many applications such as in the transport sector (Gollakota et al. 2018). In the last decades, among the different biomass conversion technologies, the hydrothermal liquefaction (HTL) process is gaining increasing interest for the energetic valorisation of biomass via bio-oil production (Qian et al. 2017). HTL allows the conversion of wet biomass into liquid fuels by processing it in a hot, pressurised water environment (200–350 °C and 15–220 bar) to break down the biopolymeric structure and produce a liquid bio-oil as energy vector (Bach et al., 2016; Mujahid et al. 2020; Rizzo et al., 2020). Under typical HTL conditions,

Paper Received: 20 December 2021; Revised: 15 March 2022; Accepted: 19 April 2022
Please cite this article as: Di Lauro F., Balsamo M., Solimene R., Salatino P., Montagnaro F., 2022, Hydrothermal Liquefaction Process to Obtain Sludge-derived Bio-fuels: Setup of the Experimental Apparatus and Preliminary Tests, Chemical Engineering Transactions, 92, 475-480 DOI:10.3303/CET2292080

liquid water starts assuming the characteristics of a polar organic solvent, so allowing the organic molecules to take part, in water, in the desired chemical reactions (Basar et al. 2021). Moreover, ionic product is large enough to favour ionic reactions resulting in oil products (Wang et al. 2019). The main advantage of the HTL process is that it does not require preliminary procedures for drying the raw material, which is highly energy-intensive, as water under process conditions acts as a catalyst/reaction medium (Theegala and Midgett, 2012). Besides the target bio-oil, an aqueous phase, a bio-char and a gas phase are also produced (Rahman et al. 2021).

In the case of HTL applied to sewage sludge, the typical value for the energetic ratio (i.e., the ratio between HHV of the bio-crude and HHV of the starting material) is around 2.8, thus indicating that HTL is a process able to determine a significant energetic densification of the parent biomass (Castello et al. 2018).

In analogy with biomass pyrolysis, the heating rate of biomass during the HTL process and the quenching of the HTL products at the desired conditions are crucial to obtain a high-yield bio-crude with more attractive energy properties (Basar et al. 2021; Brand et al., 2014). This poses a huge challenge for HTL experimentation carried out in batch reactors. The minimisation of thermal transients has to be accomplished in reactors with volume sufficiently large to have feasible and reliable collection of HTL products for the needed qualitative and quantitative chemical and physical analysis. To this end, in this work a lab-scale plant consisting in a batch autoclave of 500 mL was setup and optimised so to limit thermal transients that could lead to the formation of undesired products. Preliminary analyses were also carried out in terms of water pressurisation/depressurisation during heating/cooling ramps emulating a typical cycle performed during a HTL test, so to verify the presence of water in the desired liquid state. Finally, preliminary HTL tests were performed on a municipal sewage sludge to evaluate the yield of both the target bio-crude and other by-products. The obtained results were compared with data present in literature.

2. Materials and Methods

In the following, the main properties of the sludge and the description of the experimental apparatus and operating conditions for HTL test and separation of the products is reported.

2.1 Feedstock

The municipal sludge used in this work was supplied from a wastewater treatment plant located in Milano, Italy. The main properties (Table 1) of the sludge are reported in a previous work of Cammarota et al. (2019). The sludge has a total C content of 34.6%, HHV=13.5 MJ/kg, and the most abundant elements are Fe (26710 ppm), Ca (13780 ppm) and P (14960 ppm). Prior to the HTL test, the biomass was dried in an oven at 105 °C, until no change in weight was observed.

Table 1: Main properties of the sludge used in this work (Cammarota et al. 2019).

Proximate analysis [$\%_{wt}$]		Ultimate analysis [$\%_{wt}$]		Main metal content [mg/kg]			
Moisture	12.1	C	34.6	Fe	26710	Mg	3597
Volatile matter	57.4	H	4.9	Ca	13780	Si	2544
Fixed carbon	9.3	N	5.9	P	14960	K	2019
Ash	21.2	S	0.8	Al	6932	Zn	586
HHV [MJ/kg]			13.5				

2.2 Experimental apparatus and procedures

The analysis of thermal transients along the process has been carried out in a nickel-chromium-molybdenum alloy (Hastelloy C-276) reactor (Figure 1). It consists of a 500 mL batch reactor (Parr Instruments, series PA 4575A) designed to operate at a maximum pressure and temperature of 345 bar and 500 °C, respectively. The reactor is equipped with: i) digital pressure transducer coupled with a needle valve for pressure measurement and control; ii) tubular electric heater coupled with thermocouples and PID system for temperature setting, measurement and heating rate control; iii) magnetic stirrer with maximum torque of 1.76 Nm and variable speed motor 1/8 hp, suitable for matrices with high viscosity as sludge (102–104 cP); iv) single loop cooling coil; v) inlet and outlet ports for gas injection and liquid/gas withdrawal; vi) gas sampling cylinder.

To limit to the formation of undesirable products along the HTL process, preliminary activities included the setup of the test facility in terms of pressurisation testing and water heating/cooling cycles. For this purpose, two configurations of the reactor were investigated: a "base system" where the heating of water was carried out only with the electric heater, and an "upgraded system" configuration where the heating has been carried out also with the support of a heating plate located on the bottom of the vessel, and by thermally insulating the top of the reactor with a layer of rock wool. For the heating/cooling test, the reactor was loaded with 300 mL of distilled water and pressurised at 30 bar. Then, it was heated to the temperature of 340 °C through tubular electric heater and the evolution of temperature and pressure was monitored over time.

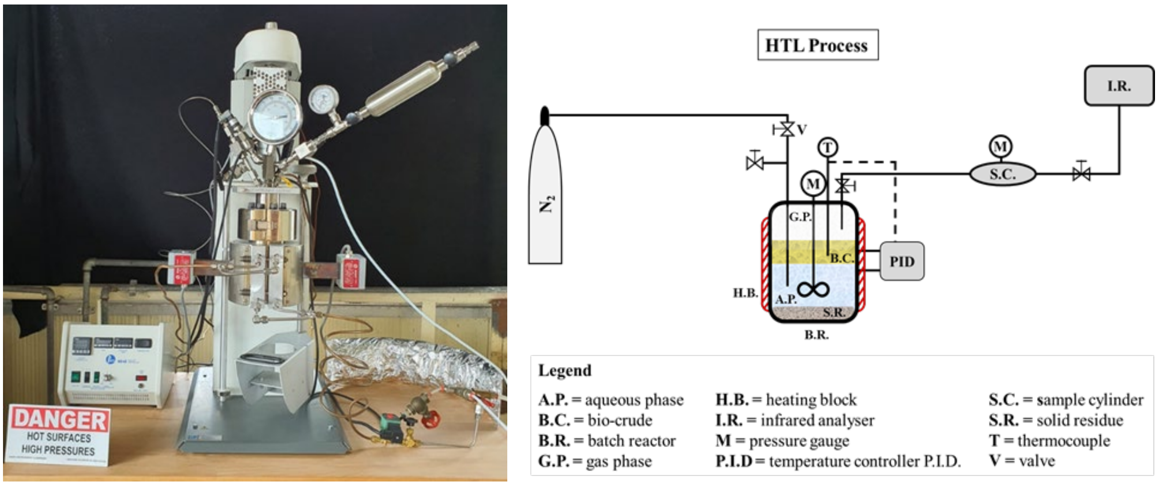

Figure 1: Batch autoclave reactor of 500 mL; picture (on the left) and layout (on the right) of the lab-scale apparatus.

For the HTL test, the reactor was loaded with 30 g (dry basis) of a municipal sludge together with 270 mL of distilled water so to obtain a slurry with a 10$\%_{wt}$ solid content, to reproduce the typical sewage sludge concentration value obtained downstream of wastewater treatment plants. Then, the reactor was purged four times with nitrogen at 5 bar to remove the oxygen present in the vessel.

The following stages are thereafter performed: a) first pressurization stage with N_2 fed by a gas cylinder at 30 bar; b) second pressurization stage at 200 bar by rapid heating of the system to the desired temperature level; c) running the HTL test at fixed time/temperature level (tested temperatures 300 and 350 °C – 20 min of isothermal stage); d) fast cooling of the reactor so to "freeze" chemical reactions, thus avoiding products re-distribution during thermal transients; e) depressurization of the reactor and sampling of the gas obtained from the HTL process. At the end of the test, liquid–solid phases separation was performed by coupling filtration, Soxhlet and liquid–liquid extraction with dichloromethane (DCM) and distillation.

2.3 Products separation procedures

Figure 2 depicts the scheme adopted for the separation and extraction of the hydrothermal liquefaction products. After the HTL test, the gas phase was vented to the atmosphere via a needle valve to restore ambient pressure and allowing reactor discharge. To minimise the use of solvents for environmental purposes, most of the liquid and solid phases were recovered from the vessel with a spatula. Then, 28 g of DCM was used to wash the wall of the reactor to maximise the products recovery. Subsequently, the recovered slurry was filtered on a Büchner under vacuum, and 30 g of DCM were used to wash the solid residue. After filtration, the solid phase was subjected to a Soxhlet extraction with DCM to recover the bio-oil from the solid pores and then dried at 105 °C in the oven for 24 h, while the liquid phase (a mixture of water and DCM) was separated into bio-crude and aqueous phase in a separating funnel. In fact, DCM has a low polarity and solubility in water, so allowing possible to solubilise organic compounds and obtain the extraction of bio-crude. Finally, the bio-oil fractions (also containing the liquid phase from Soxhlet extraction of the solid residue) are obtained by distillation vs. DCM under vacuum at 40 ºC, and subsequently weighed to estimate its yield. The solid and bio-crude yields Y were calculated according to equations (1) and (2), respectively:

$$Y_{Solid} = \frac{m_{solid,db}}{m_{biomass,db}} \cdot 100 \quad \text{Eq(1)}$$

$$Y_{Bio-crude} = \frac{m_{bio-crude}}{m_{biomass,dafb}} \cdot 100 \quad \text{Eq(2)}$$

where $m_{solid,db}$, $m_{bio\text{-}crude}$ and $m_{biomass,dafb}$ represent the mass of solid residue, bio-crude and starting biomass, respectively. The subscripts “*db*” and “*dafb*” refers to dry and dry ash-free basis, respectively.

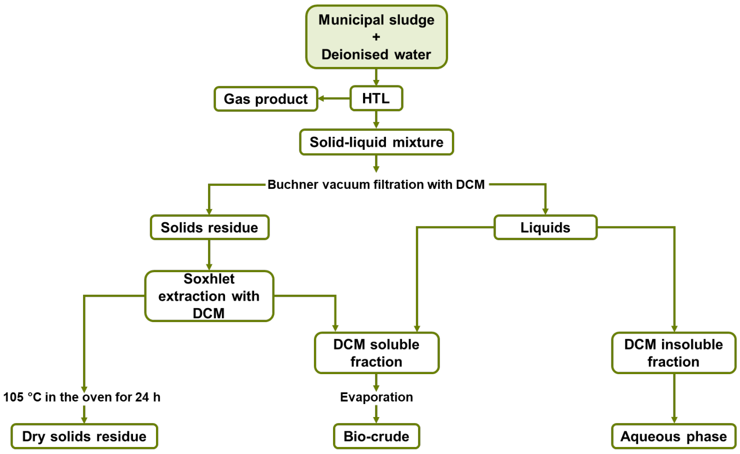

Figure 2: Experimental protocol for the separation of HTL products.

3. Results

In the following paragraphs the results of the setup of the HTL apparatus, together with the preliminary results of the HTL tests performed on the sludge, are reported.

3.1 Setup of HTL apparatus and heating/cooling rate for HTL system

The heating/cooling rate upon HTL tests must be as high as possible, to limit to the formation of undesirable products. Moreover, this rate affects the time-dependent evolution of phases produced along the isothermal stage of HTL. Figure 3 reports the experimental time-dependent thermal profiles obtained by heating the reactor from room temperature to the operating temperature of 340 °C, the latter chosen as a reference from a preliminary literature analysis (Di Lauro et al. 2020). The blue curve "base system" represents the temperature in the reactor when water is heated by only using the electric heating block of the system (co-axial with the reactor), while the orange curve "upgraded system" is obtained by heating the reactor also with the support of a 1000 W heating plate located on the bottom of the vessel and by thermally insulating the head of the reactor with a layer of rock wool. Two regions of interest are highlighted: the red one for temperature values between 200–280 °C, and the green one between 290–340 °C. During HTL test, the permanence of the system in the red region, over a period of 40–120 min, leads to the preferential formation of bio-char, while the temperature range highlighted by the green region leads to the preferential formation of bio-oil for characteristic reaction times of 15–30 min. Results show that, for the base system, a total heating time of 85 min is required: the system persists for about 25 min in the region of preferential bio-char formation and remains for 30 min in the range of temperatures characteristic of bio-oil formation, before reaching the desired final temperature of 340 °C. Overall, the mean heating rate is about 4 °C/min, value typical for HTL process carried out in reactors of similar size (see for example Brand et al. (2014) and Table 1 reported therein).

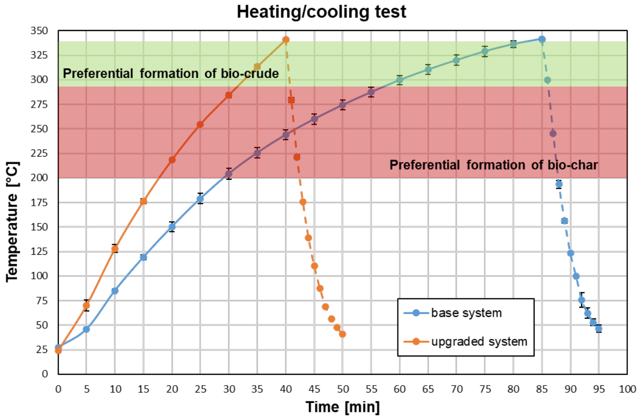

Figure 3: Performance of heating and cooling of HTL reactor, expressed as temperature-time plots. Tests carried out in triplicates.

From literature data, during HTL test, the permanence of the system in the red region over a period of 40–120 min leads to the preferential formation of bio-char, while the temperature range highlighted by the green region leads to the preferential formation of bio-oil for characteristic reaction times of 15–30 min. For the upgraded system, a significant amelioration of the heating rate is attained, about 8 °C/min, with the total heating time being practically halved with respect to the base system; the permanence in the region of preferential formation of bio-char is limited to 15 min. This result is encouraging for the minimisation of the course of the undesired reactions during the HTL tests in the upgraded configuration of the 500 mL batch reactor. For both systems, the cooling stage is very fast and in the order of 5 min with a mean cooling rate of about 30 °C/min.

3.2 Municipal sludge HTL test and yields of products

After the optimisation of the HTL reactor, the municipal sludge was used for preliminary hydrothermal liquefaction tests performed at 300 and 350 °C and 200 bar for 20 min, to verify the bio-oil and solid residue yield under the tested condition (Di Lauro et al. 2021). The pressure vs temperature curve during the thermal transient and the isothermal step, for the upgraded system during the municipal sludge HTL test, is reported in Figure 4 together with transient data obtained under unreactive conditions similar to those shown in Figure 3 (orange curve). It is worth to note that the evolution of pressure as a function of temperature during the HTL test can be almost overlapped to that under unreactive conditions up to the temperature of about 320 ºC. The subsequent increase in temperature, during the sludge HTL test, causes a sudden rise of pressure compared to that observed under unreactive conditions caused only by the change of temperature. It is very likely that this increase is associated with the onset of biomass decomposition reactions leading to the formation of gaseous products. This evidence confirms, as it is also reported in literature on HTL, that at lower temperatures the biomass fragments producing intermediate compounds prone to the formation of bio-oil, whereas at higher temperature secondary decomposition reactions and the Boudouard reaction starts to take place promoting the formation of gaseous species (Akhtar and Amin, 2011).

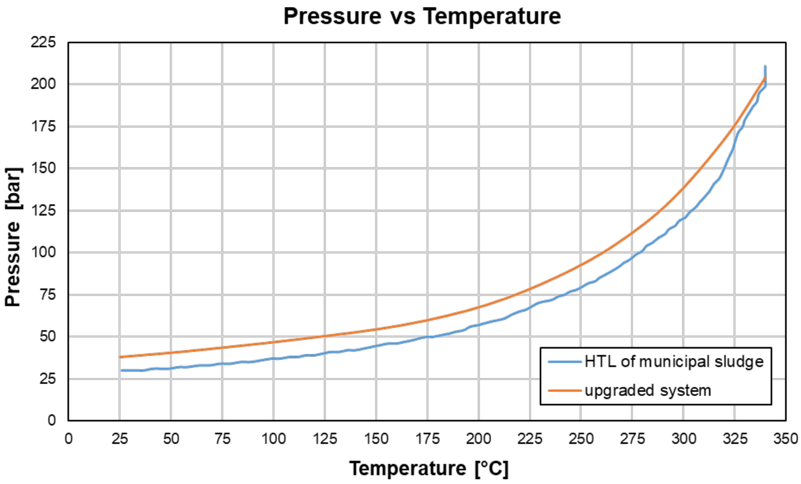

Figure 4: Evolution of pressure as a function of temperature, for the upgraded system during municipal sludge HTL test.

Results of the HTL runs showed that $Y_{Bio\text{-}crude}$ is 38.3% at 350 °C, a value approximately 10% greater than the figure obtained at the lower tested temperature (equal to 27.9%), thus testifying that the rise of temperature is beneficial in promoting the reaction pathways leading to the desired decomposition of organic molecules to produce the target bio-crude. These values for bio-crude fall within the range of values (at 300 °C 22–28%; at 350 °C 22–53% for 20–30min reaction time) reported in literature for HTL from sludge (Basar et al., 2021). Conversely, the increase of the HTL process temperature produces a reduction of Y_{Solid} that is 33.6% and 25.9% at 300 and 350 °C, respectively. In this context, it is highlighted that the inorganic fraction of the parent biomass, the char deriving from the HTL process and the unconverted organic matrix of the sludge all contribute to Y_{Solid}. These values are relatively nearby the ash yield on dry basis (24.1%), which can be calculated by proximate analysis. This indicates that probably the mean heating and cooling rates obtained with the upgraded system are sufficiently fast to limit the course of the undesired reactions leading to biochar formation and the fraction of the unconverted biomass. Further investigations will be carried out under different conditions of reaction time, heating rate and temperature to verify the effect of these variables on $Y_{Bio\text{-}crude}$.

4. Conclusions

In this work, a 500 mL lab-scale batch plant devoted to HTL tests was optimised to minimise thermal transients that could lead to the formation of undesirable products along the hydrothermal conversion process. A significant reduction of the thermal transient was attained with the use of a 1000 W heating plate placed at the bottom of the vessel, and by thermally insulating the top of the reactor with a layer of rock wool, with the total heating time being practically halved with respect to the base system (mean heating rate of 8 °C/min). For both systems, the cooling stage is very fast and in the order of 5 min (mean cooling rate of 30 °C/min). After the setup and optimisation of the experimental apparatus, preliminary tests of HTL were carried out on a municipal sludge, and a bio-crude yield of 38.3% was obtained at 350 °C in agreement with data present in literature. Future studies will focus on a more detailed study of the effect of operating conditions on bio-oil yield and quality.

Acknowledgments

This work has been carried out as part of the Italian national research project ‘Biofeedstock’ PONARS01_00985, in the framework of the MIUR PNR 2015-2020 programme.

References

https://www.iea.org/data-and-statistics/data-browser/?country=WORLD&fuel=Energy%20supply&indicator=TESbySource, accessed on February 2022.

Akhtar J., Amin N.A.S, 2011, A review on process conditions for optimum bio-oil yield in hydrothermal liquefaction of biomass, Renewable and Sustainable Energy Reviews, 15, 1615–1624.

Bach Q.V., Tran K.Q., Lystad K.Q., 2016, Fast hydrothermal liquefaction of macro-alga: characterization of products, Chemical Engineering Transactions, 50, 97–102.

Basar I.A., Liu H., Carrere H., Trably E., Eskicioglu C., 2021, A review on key design and operational parameters to optimize and develop hydrothermal liquefaction of biomass for biorefinery applications, Green Chemistry, 23, 1404–1446.

Brand S., Hardi F., Kim J., Suh D.J., 2014, Effect of heating rate on biomass liquefaction: differences between subcritical water and supercritical ethanol, Energy, 68, 420–427.

Cammarota A., Cammarota F., Chirone R., Ruoppolo G., Solimene R., Urciuolo M., 2019, Fluidized bed combustion of pelletized sewage sludge in a pilot scale reactor, Combustion Science and Technology, 191, 1661–1676.

Castello D., Pedersen T.H., Rosendahl L.A., 2018, Continuous hydrothermal liquefaction of biomass: A critical review, Energies, 11, 3165.

Di Lauro F., Balsamo M., Solimene R., Montagnaro F., Salatino P., 2020, Hydrothermal liquefaction for the production of energetic vectors from residual materials: literature analysis and characterisation of a tannery sludge, Proceedings of the 8th International Symposium on Energy from Biomass and Waste, Virtual Conference.

Di Lauro F., Balsamo M., Solimene R., Migliaccio R., Caracciolo D., Salatino P., Montagnaro F., 2021, Outline of a process for the hydrothermal liquefaction of a tannery sludge for biofuel production, Proceedings of the 10th European Combustion Meeting, 274, Naples, Italy.

Gollakota A.R.K., Kishore N., Gu S., 2018, A review on hydrothermal liquefaction of biomass, Renewable and Sustainable Energy Reviews, 81, 1378–1392

He C., Chen C.L., Giannis A., Yang Y.H., Wang J.Y., 2014, Hydrothermal gasification of sewage sludge and model compounds for renewable hydrogen production: A review, Renewable and Sustainable Energy Reviews, 39, 1127–1142.

Malins K., Kampars V., Brinks J., Neibolte I., Murnieks R., Kampare R., 2015, Bio-oil from thermo-chemical hydro-liquefaction of wet sewage sludge, Bioresource Technology 187, 23–29.

Mujahid R., Riaz A., Insyani R., Kim J., 2020, A centrifugation-first approach for recovering high-yield bio-oil with high calorific values in biomass liquefaction: A case study of sewage sludge, Fuel, 262, 116628.

Qian L., Wang S., Savage P.E., 2017, Hydrothermal liquefaction of sewage sludge under isothermal and fast conditions, Bioresource Technology, 232, 27–34.

Rahman T., Jahromi H., Roy P., Adhikari S., Hassani E., Oh T.S., 2021, Hydrothermal liquefaction of municipal sewage sludge: Effect of red mud catalyst in ethylene and inert ambiences, Energy Conversion and Management, 245, 114615.

Rizzo A.M., Dell’Orco S., Miliotti E., Chiaramonti D., 2020, Design, commissioning and start-up of a new hydrothermal liquefaction continuous pilot unit, Chemical Engineering Transactions, 80, 367–372.

Theegala C.S. and Midgett J.S., 2012, Hydrothermal liquefaction of separated dairy manure for production of bio-oils with simultaneous waste treatment, Bioresource Technology, 107, 456–463.

Wang L., Chang Y., Li A., 2019, Hydrothermal carbonization for energy-efficient processing of sewage sludge: A review, Renewable and Sustainable Energy Reviews, 108, 423–440.

Hydrothermal Liquefaction of a Sewage Sludge for the Production of Biofuels: Optimization of the Experimental Apparatus and Effect of Operating Parameters on the Process Performance

Francesca Di Lauro*
Dipartimento di Scienze Chimiche, Università degli Studi di Napoli Federico II, Complesso Universitario di Monte Sant'Angelo, 80126 Napoli, Italy
e-mail: francesca.dilauro2@unina.it

Marco Balsamo
Dipartimento di Scienze Chimiche, Università degli Studi di Napoli Federico II, Complesso Universitario di Monte Sant'Angelo, 80126 Napoli, Italy
e-mail: marco.balsamo@unina.it

Roberto Solimene
Istituto di Scienze e Tecnologie per l'Energia e la Mobilità Sostenibili, Consiglio Nazionale delle Ricerche, Piazzale V. Tecchio 80, 80125 Napoli, Italy
e-mail: roberto.solimene@stems.cnr.it

Piero Salatino
Dipartimento di Ingegneria Chimica, dei Materiali e della Produzione Industriale, Università degli Studi di Napoli Federico II, Piazzale V. Tecchio 80, 80125 Napoli, Italy
e-mail: piero.salatino@unina.it

Fabio Montagnaro
Dipartimento di Scienze Chimiche, Università degli Studi di Napoli Federico II, Complesso Universitario di Monte Sant'Angelo, 80126 Napoli, Italy
e-mail: fabio.montagnaro@unina.it

ABSTRACT

Hydrothermal liquefaction (HTL) process is an emerging technique for the conversion of wet biomass into liquid fuels by processing it in a hot, pressurized water environment (250–350 °C and 15–220 bar), for sufficient time to break down the solid bio-polymeric structure and produce a liquid bio-oil as energy vector. For HTL carried out in batch reactors, the minimization of thermal transients is crucial to obtain a high-yield bio-crude with more attractive energy properties. To this end, in this study a lab-scale plant consisting in a batch autoclave was optimized to limit thermal transients that could lead to the preferential formation of undesired co-products such as bio-char. The yield of the target bio-crude and other co-products was evaluated at different process times and temperatures, for HTL process applied to a sewage sludge. Additionally, the performances of different separation protocols for bio-crude recovery were investigated.

KEYWORDS

Hydrothermal liquefaction, Biomass-to-energy, Bio-fuels, Bio-crude, Sewage sludge, Energetic valorization, Thermochemical conversion.

INTRODUCTION

Energy production is one of the primary challenges of modern societies with a total world energy supply in 2020 exceeding 600000 PJ, mainly satisfied by fossil fuels [1]. The scientific research is focusing on the development of greener and sustainable technologies to meet the growing energy demand. Renewable energy sources include e.g. biomass, wastes, hydropower, wind, solar and geothermal. In the context of biomass exploitation for energy production, the main technologies for obtaining energy vectors are pyrolysis [2], torrefaction [3], gasification [4] or combustion [5]. The weak point of the abovementioned technologies lies in the energy-intensive drying stage required for biomasses with high moisture content [6]. In this context, hydrothermal liquefaction (HTL) represents a promising technology for the conversion of wet biomass, such as sewage sludge, into liquid fuels. HTL allows to treat high-water-content sludges (usually in the range of 80–90%$_{\mathrm{vol.}}$) in a process where the joint action of water and pressure determines the degradation of the starting bio-structure to produce unstable and reactive fragments that, in the same environment, can re-arrange themselves to give bio-liquids (termed as bio-crude or bio-oil) with energetic value, together with an aqueous phase, solid residue (bio-char) and gas as co-products [7]. Under typical HTL conditions (200–350 °C and 15–220 bar), liquid water starts assuming the characteristics of a polar organic solvent, so allowing the organic molecules to take part, in water, in the desired chemical reactions. Moreover, ionic product is large enough to favour ionic reactions resulting in oil products [8,9]. So, water acts as a catalyst, reaction medium and thermal flywheel in the HTL process [10].

HTL studies have been conducted on several biomass types also in mixtures of different organic substrates [11,12] and/or in presence of catalysts [13,14] to maximise the yield and quality of the bio-oil. However, most of the literature is based on HTL experiments performed in very small-scale batch reactors (generally a few mL), not allowing to properly assess the effect of thermal transients, which instead occur on larger scale systems, on products yields and quality [15–17]. In addition, small reaction volumes allow an effective extraction of bio-crude phase with the use of a low amount of an appropriate extraction solvent (such as dichloromethane, ethyl acetate, tetrahydrofuran, or petroleum ether) [18−20]. However, for scale-up purposes the quantity of extraction solvent should be minimized for both economic and environmental reasons. In this direction, centrifugation was recently proposed as an effective method for bio-crude recovery from HTL slurries [21].

In this work a lab-scale plant consisting in a 500 mL batch autoclave was optimized to limit thermal transients that could lead to the formation of undesired products [22]. To this end, sampling during heating ramps was carried out to assess the yield of products derived from HTL of sewage sludge, and verify the production of bio-oil during the transient heating. After the optimization of the experimental apparatus, the yield of the bio-oil produced with different separation methods and at different temperatures and isothermal reaction times was evaluated.

MATERIALS AND METHODS

Feedstock

The sewage sludge taken as a reference material for HTL tests was a municipal sludge deriving from a wastewater treatment plant located in Milano (Italy). Table 1 reports the main sludge properties in terms of proximate and ultimate analysis, higher heating value (*HHV*) and elements content, also reported in our previous work [22]. The sludge has a moisture and volatile matter content of 12.1% and 57.4%, respectively. The ash content is 21.2% and fixed carbon equals to 9.3%. The carbon is then to be sought in association with other species, and its total content is evidenced by ultimate analysis, where on dry basis the following values of composition were obtained: 34.6% (C), 4.9% (H), 5.9% (N), 0.8% (S). On a dry basis the higher heating value is 14.90 MJ/kg, a value in-line with data commonly reported for biomass and, in particular, for sludge. These results confirm the possibility of considering this sludge as an energy carrier in valorisation processes.

Table 1. Main properties of sewage sludge

Proximate analysis [%wt]		**Ultimate analysis [$\%_{wt}$]**		**Main elements content [mg/kg]**			
Moisture	12.1	**C**	34.6	**Fe**	26710	**Mg**	3597
Volatile matter	57.4	**H**	4.9	**Ca**	13780	**Si**	2544
Fixed carbon	9.3	**N**	5.9	**P**	14960	**K**	2019
Ash	21.2	**S**	0.8	**Al**	6932	**Zn**	586
HHV [MJ/kg]	13.5						

Hydrothermal liquefaction

The hydrothermal liquefaction process was performed in a 500 mL nickel-chromium-molybdenum alloy (Hastelloy C-276) batch reactor (Parr Instruments, series PA 4575A), designed to operate at a maximum pressure and temperature of 345 bar and 500 °C, respectively. The reactor is equipped with: i) digital pressure transducer coupled with a needle valve for pressure measurement and control; ii) tubular electric heater coupled with thermocouples and PID system for temperature setting, measurement; iii) magnetic stirrer with maximum torque of 1.76 Nm and variable speed motor 1/8 hp, suitable for matrices with high viscosity as sludge (102–104 cP); iv) single loop cooling coil; v) inlet and outlet ports for gas injection and liquid/gas withdrawal. To limit the formation of undesirable products along the HTL process, heating ramp was study in three configurations:

- Configuration A: experimental apparatus operated as described above;
- Configuration B: the heating stage was carried out also with the support of a 1000 W heating plate of 145 mm diameter located on the bottom of the vessel, and the top of the reactor was insulated with a layer of rock wool;
- Configuration C: with respect to B configuration, it was added a band heater (Watlow Series MI band) with a power of 1250 W coupled with a cylindrical steel block located between the reactor and the heating plate.

For HTL runs, the reactor was loaded with 30 g (on dry basis) of a sludge together with 270 mL of distilled water so to obtain a slurry with a 10$\%_{wt}$ solid content, so to reproduce the typical sewage sludge concentration value obtained downstream of wastewater treatment plants. Then, the reactor was purged four times with nitrogen at 5 bar to remove the oxygen present in the vessel, and the heating stage was started (the heating rate is a function of the configuration described above). It follows an isothermal stage and finally a fast cooling of the reactor so to "freeze" chemical reactions, thus avoiding products re-distribution during thermal transients. At the end of the HTL test the pressure difference between the starting and final stages allowed to estimate the gas yield (assuming that the produced gas is mainly composed by CO_2 [4]). Finally, the gas phase was vented to the atmosphere to restore ambient pressure and allow reactor discharge.

Products separation protocol

After the HTL test the liquid and solid phases were recovered from the vessel with a spatula, and 30 g of dichloromethane (DCM) were added to maximize the products recovery. Subsequently, the slurry was filtered on a Büchner under vacuum at 0.4 bar. After filtration, the solid phase was subjected to a Soxhlet extraction with DCM to recover the bio-oil from the solid pores, while the liquid phase was separated into bio-crude and aqueous phase according to two different separation techniques. The first one is liquid-liquid extraction performed with DCM in a separating funnel, followed by vacuum distillation for bio-oil recovery. In a different method, the water-bio-oil mixture was separated by centrifugation: the supernatant aqueous phase was taken by means of Pasteur pipettes, while the underlying bio-crude was recovered with the aid of 20 g of DCM and finally distilled under vacuum. After the separation processes the gas, solid residue and bio-crude yields (*Y)* were calculated according to equations (1–3), respectively:

$$Y_{gas} = \frac{m_{CO_2}}{m_{biomass,dafb}} \cdot 100 \tag{1}$$

$$Y_{solid\ residue} = \frac{m_{solid,db}}{m_{biomass,db}} \cdot 100 \tag{2}$$

$$Y_{bio-crude} = \frac{m_{bio-crude}}{m_{biomass,dafb}} \cdot 100 \tag{3}$$

where m_{CO_2}, $m_{solid,db}$, $m_{bio\text{-}crude}$ and $m_{biomass,dafb}$ represent the mass of gas, solid residue, bio-crude and starting biomass, respectively. The subscript "*db*" refers to dry basis, while "*dafb*" refers to free ash and dry basis. Finally, after each test, the bio-crude obtained was characterized by Mahler bomb calorimeter to measure its *HHV*, and consequently the energy recovery *ER* as the ratio of the higher heating value of the bio-crude and the starting sludge, multiplied by the mass yield of bio-crude.

RESULTS

Effect of reactor configuration on bio-crude yield

Figure 1 shows the time trend of the reactor temperature for the different configurations investigated, when 300 mL of distilled water were heated at a set point temperature of 350 °C. It can be observed that in configuration A, B and C the system requires, respectively, 90, 55 and 48 min to reach the temperature of 350 ºC. For all three systems, the cooling stage is very fast and in the order of 5 min.

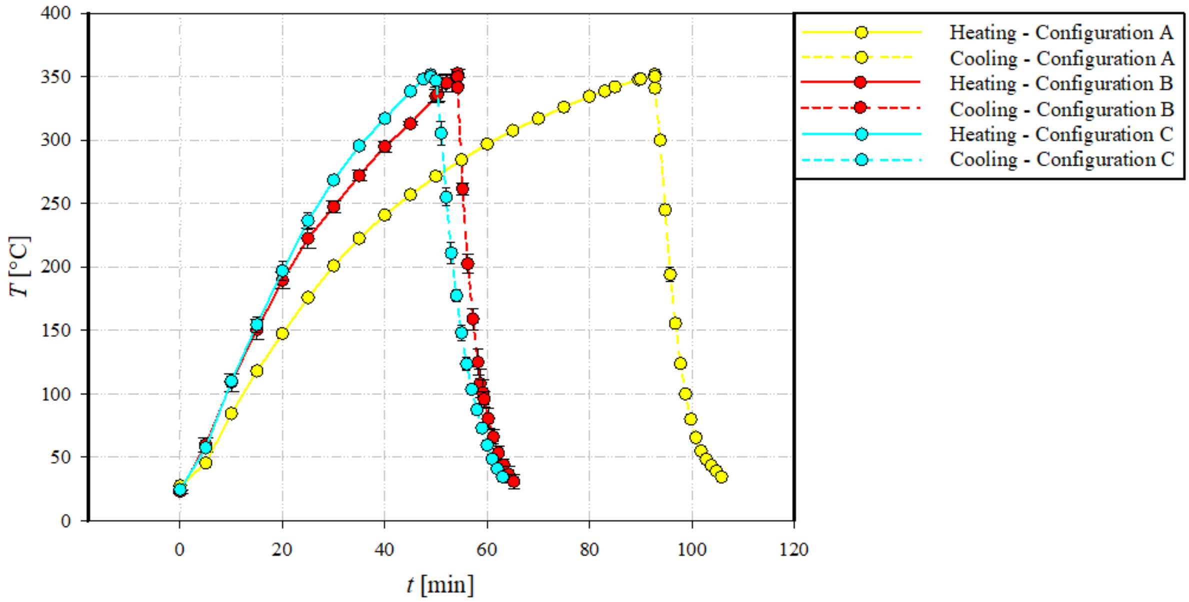

Figure 1. Heating/cooling test for configurations A, B and C using distilled water

Based on data obtained for the system with distilled water, HTL tests of the influence of the reactor configuration on the bio-oil yields were carried. In this study, configuration A was discarded due to the observed too long heating times. Figure 2 shows the yields of the bio-crude, solid and gaseous phases produced with a different heating ramp at temperatures of 300 and 350 °C and for an isothermal stage of 20 min. It is possible to observe that, for both temperatures, there are no relevant variations in the gas and solid yields when the heating rate changes, while this is not the case of bio-oil. In particular, for the tests carried out at 300 ºC (B-300-20 vs. C-300-20), an increase of $Y_{\text{bio-crude}}$ of 2% is observed for configuration C with respect to the B case; on the contrary, for the tests carried out at a temperature of 350 ºC, a decrease in the bio-crude yield for configuration C of about 10% can be noted. However, it is important to highlight that at 350 °C for configuration B, the reaction time in the non-isothermal stage, is greater than for configuration C, so the system is subjected to a reaction time that is globally higher (of about 8 min). In addition, comparing the higher heating value of the two bio-oils obtained in the tests at 350 °C and 20 minutes for the two configurations, for case C the *HHV* is 31.44 MJ/kg, a value 3.7% greater than that obtained for the configuration B.

Based on these results, configuration C was selected for a deeper experimental campaign to study the effect of temperature and time of the HTL process on yields and properties of the resulting phases.

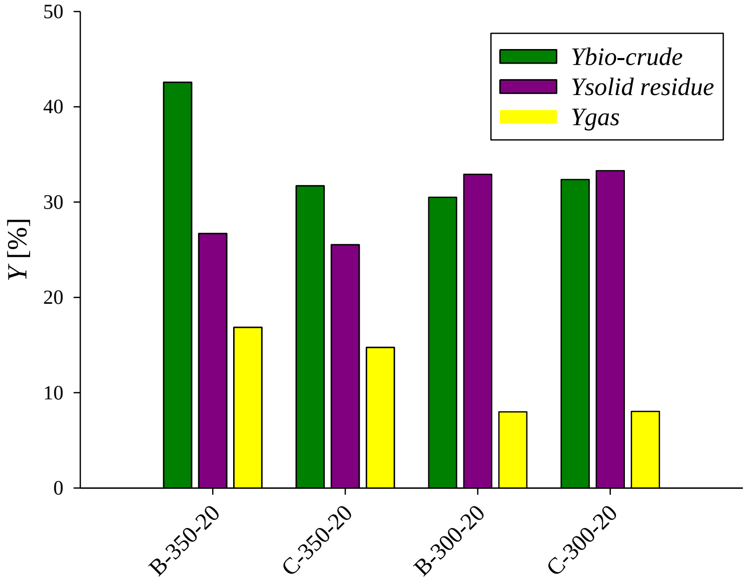

Figure 2. Yields of bio-crude, solid and gas phase for HTL tests performed for configurations B and C (temperatures of 300 and 350 °C, isothermal stage of 20 min)

Effect of separation protocol on bio-crude recovery

The second aspect investigated in this work was the method for the separation of bio-crude from the aqueous phase, namely liquid-liquid extraction and centrifugation. Figure 3 shows the yields of bio-crude, on a dry and ash-free basis, obtained from HTL tests under the same reaction conditions: "SF" refers to a separation by solvent extraction (DCM) in a separating funnel, while "Cen" refers to a separation obtained by centrifugation. The tests were conducted in duplicate at set point temperatures of 300 °C and 350 ºC and for a reaction time of the isothermal stage of 20 minute.

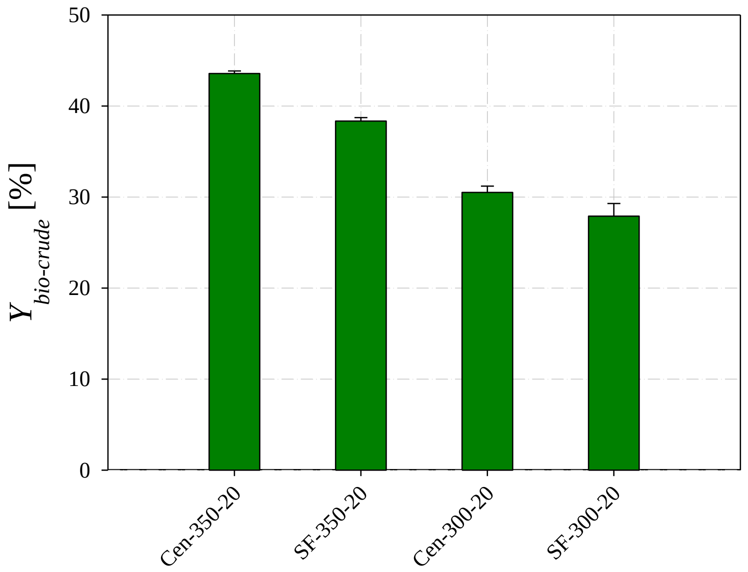

Figure 3. $Y_{bio\text{-}crude}$ under different liquid-liquid separation protocol at fixed reaction time/temperature. SF: Separatory funnel, Cen: centrifuge

It is noted that the yield of bio-oil, that is produced under identical reaction conditions, is different when different separation methods are used. For both temperatures the use of the centrifuge is more effective in the extraction of the bio-crude from the aqueous phase. In fact, the use of centrifugation led to a recovery of bio-oil of 3% and 6% greater than liquid-liquid extraction, at 300 °C and 350 °C, respectively. As an example, at 350 ºC the yield of bio-crude is 44% in the case of centrifugation vs. 38% in the case of extraction with DCM. Therefore, the use of centrifugation is a more effective method for bio-crude extraction and with an associated advantage of reduced environmental impact determined by the use of the halogenated DCM solvent.

Effect of reaction time/temperature on product distribution

HTL tests, for configuration C and using the centrifugation separation method, were conducted at two different temperatures of 300 °C and 350 ºC, and for different isothermal residence times, ranging from 0 (transient only) to 60 min. In addition, two HTL tests were carried out by stopping the heating of the system at temperatures levels of 250 °C and 275 °C to verify the possible products formation during thermal transients. Figure 4 shows the yields of bio-crude, solid residue and gas at different times parametric of the temperature. For the yield of bio-crude it is possible to identify a non-monotonic trend, with a maximum located at 30 min at 300 °C ($Y_{bio\text{-}crude}$ =35.20%) and at 10 min for a temperature of 350 °C (with a bio-crude yield of 43.21%). Higher temperatures coupled with low reaction times favour the distribution of products towards bio-oil formation. After 60 min $Y_{bio\text{-}crude}$ decreases at around 32% and 28%, for temperatures of 350 °C and 300 °C, respectively. From tests performed during the heating transient, it can be highlighted that even at 250 °C the formation of bio-crude is non-negligible with a value of 9.8% of $Y_{bio\text{-}crude}$. Y_{solid} decreases from 38% to 30% (300 °C), and from 32% to 23% (350 °C), between 0 and 30 min. The slight increase in the values of solid yield after 30 min is likely due to the decrease in $Y_{bio\text{-}crude}$. Finally, the yield of the gas phase does not follow a clear trend with the process time.

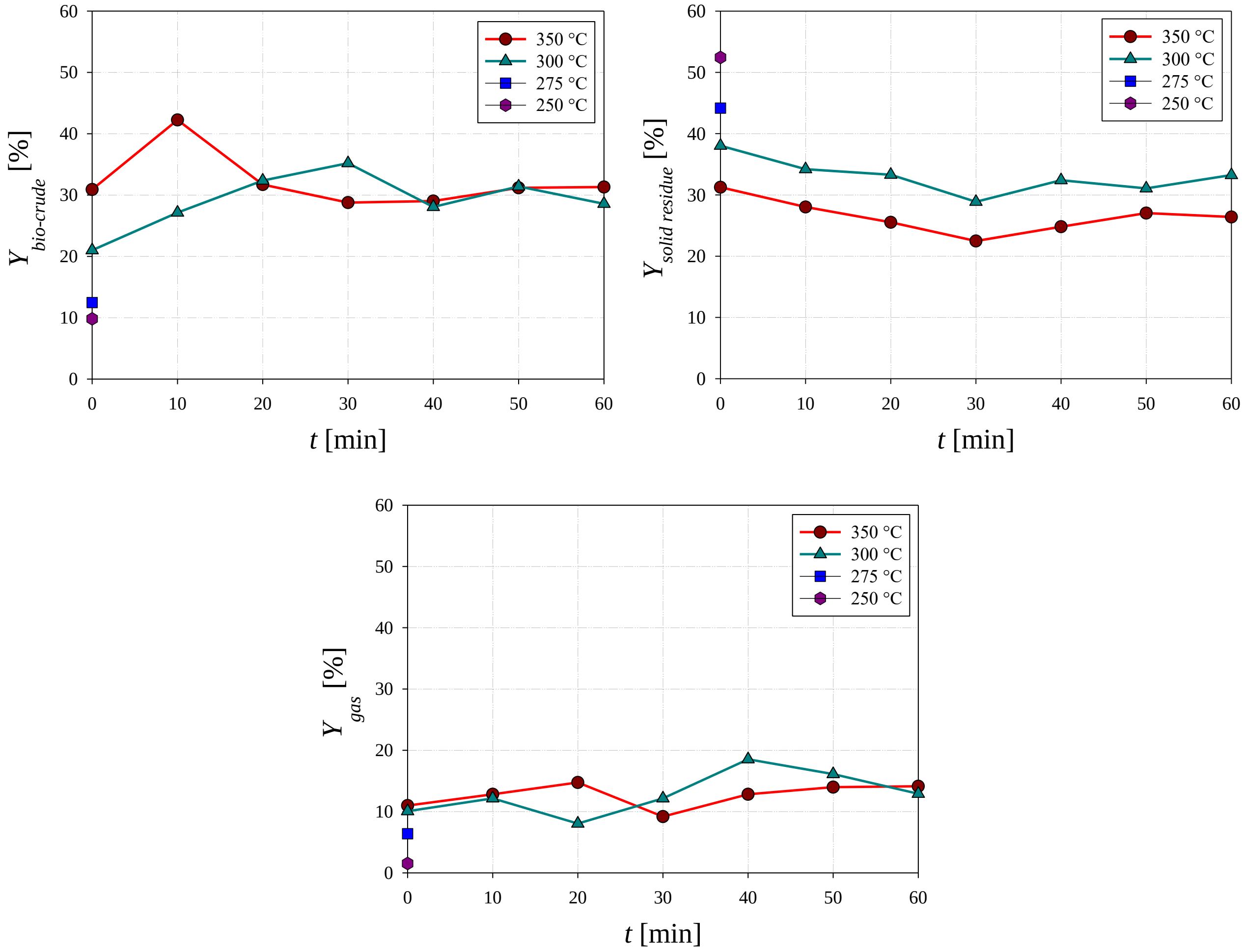

Figure 4. Yield of target bio-crude and other by-products at different temperature

Table 2 summarizes the bio-crude yield and energetic properties derived for the best operating conditions (350 °C–10 min and 300 °C–30 min). HHV values are very similar, so the difference in energy recovery outcomes is mainly determined by the greater value of bio-crude yield obtained at 350°C, with ER being about 78% and 25% greater than the value retrieved at the lowest operating temperature.

Table 2. Main property of bio-crude obtained for the best conditions of process.

Test	**$Y_{bio\text{-}crude}^{dafb}$ [%]**	**HHV [MJ/kg]**	**ER [%]**
Cen-300-30	36.07	28.81	62.34
Cen-350-10	43.21	30.04	77.87

CONCLUSIONS

In this work the energetic valorization of a sewage sludge for bio-crude production via HTL was investigated. The reactor was optimized to reduce thermal transients, and the effect of separation method, reaction time and temperature on products yield was assessed.

Results show that, the upgrades to the heating system allowed to attain an average heating rate of about 8 °C/min generally determining improved performances of the HTL process compared to configuration characterized by lower heating rates. Moreover, the centrifugation method was more effective with respect to liquid-liquid extraction with DCM, with a bio-crude recovery up to 5.2% greater. Moreover, the analysis of the effect of time and temperature on products yield has showed that at fixed process time a higher bio-crude yield was obtained at 350 °C with respect to 300 °C. At 10 min an optimal value of both $Y_{bio\text{-}crude}$ = 43% and energy recovery of 78% was derived (HHV=30 MJ/kg).

REFERENCES

1. International Energy Agency, Key World Energy Statistics 2021, WorldEnergyBalancesHighlights2021.xlsx (live.com).

2. Hu, Y., Attia, M., Tsabet, E., Mohaddespour, A., Munir, T. M., Fagar, S., Valorization of waste tire by pyrolysis and hydrothermal liquefaction: a mini-review, *Journal of Material Cycles and Waste Management*, Vol. 23, pp 1737–1750, 2021.

3. Tregambi, C., Montagnaro, F., Salatino, P., Solimene, R., Solar-Driven torrefaction of a lignin-rich biomass residue in a directly irradiated fluidized bed reactor, *Combustion Science and Technology*, Vol. 191, pp 1609–1627, 2019.

4. Migliaccio, R., Brachi, P., Montagnaro, F., Papa, S., Tavano, A., Montesarchio, P., Ruoppolo, G., Urciuolo, M., Sewage sludge gasification in a fluidized bed: Experimental investigation and modelling, *Industrial & Engineering Chemistry Research*, Vol. 60, pp 5034–5047, 2021.

5. Dong, H., Jiang, X., Lv, G., Wang, F., Huang, Q., Chi, Y., Yan, J., Yuan, W., Chen, X., Luo, W., Co-combustion of tannery sludge in a bench-scale fluidized-bed combustor: Gaseous emissions and Cr distribution and speciation, *Energy & Fuels*, Vol. 31, pp 11069–11077, 2017.

6. Haarlemmer, G., Simulation study of improved biomass drying efficiency for biomass gasification plants by integration of the water gas shift section in the drying process, *Biomass and Bioenergy*, Vol. 81, pp 129–136, 2015.

7. Fan, Y., Hornung, U., Dahmen, N., Hydrothermal liquefaction of sewage sludge for biofuel application: A review on fundamentals, current challenges and strategies, *Biomass and Bioenergy*, Vol. 165, 106570, 2022.

8. Wang, L., Chang, Y., Li, A., Hydrothermal carbonization for energy-efficient processing of sewage sludge: A review, *Renewable and Sustainable Energy Reviews*, Vol. 108, pp 423–440, 2019.

9. Basar, A. I., Liu, H., Carrere, H., Trably, E., Eskicioglu, C., A review on key design and operational parameters to optimize and develop hydrothermal liquefaction of biomass for biorefinery applications, *Green Chemistry*, Vol. 23, 1404, 2021.

10. Di Lauro, F., Balsamo, M., Solimene, R., Montagnaro, F., Salatino, P., Hydrothermal liquefaction for the production of energetic vectors from residual materials: literature analysis and characterisation of a tannery sludge, *Proceedings of the 8th International Symposium on Energy from Biomass and Waste*, 2020, Virtual Conference.

11. Huang, H., Chang, Y., Lai, F., Zhou, C., Pan, Z., Xiao, X., Wang, J., Zhou, C., Co-liquefaction of sewage sludge and rice straw/wood sawdust: The effect of process parameters on the yields/properties of bio-oil and biochar products, *Energy*, Vol. 173, pp 140–150, 2019.

12. Wang, J., Peng, X., Chen, X., Ma, X., Co-liquefaction of low-lipid microalgae and starch-rich biomass waste: The interaction effect on product distribution and composition, *Journal of Analytical and Applied Pyrolysis*, Vol. 139, pp 250–257, 2019.

13. Prestigiacomo, C., Proietto, F., Laudicina V. A., Siragusa, A., Scialdone, O., Galia, A., Catalytic hydrothermal liquefaction of municipal sludge assisted by formic acid for the production of next-generation fuels, *Energy*, Vol. 232, 121086, 2021.

14. Shah, A. A., Sharma, K., Haider, M. S., Toor, S. S., Rosendahl, L. A., Pedersen, T. H., Castello, D., The role of catalysts in biomass hydrothermal liquefaction and biocrude upgrading, *Processes*, Vol. 10, ~~pp~~ 207, 2022.

15. Prestigiacomo, C., Costa, P., Pinto, F., Schiavo, B., Siragusa, A., Scialdone, O., Galia, A., Sewage sludge as cheap alternative to microalgae as feedstock of catalytic hydrothermal liquefaction processes, *The Journal of Supercritical Fluids*, Vol. 143, pp 251–258, 2019.

16. de Caprariis, B., De Filippis, P., Petrullo A., Scarsella, M., Hydrothermal liquefaction of biomass: Influence of temperature an biomass composition on the bio-oil production, *Fuel*, Vol. 208, pp 618–625, 2017.

17. Faeth, J. L., Valdez, P. J., Savage, P. E., Fast hydrothermal liquefaction of nannochloropsis sp. to produce biocrude, *Energy Fuels*, Vol. 27, pp 1391–1398, 2013.

18. Mathanker, A., Das, S., Pudasainee, D., Khan, M., Kumar, A., Gupta, R., A review of hydrothermal liquefaction of biomass for biofuels production with a special focus on the effect of process parameters, co-solvents, and extraction solvents, *Energies*, Vol. 14, 4916, 2021.

19. Jablonsky, M., Skulcova, A., Malvis, A., Sima, J., Extraction of value-added components from food industry based and agroforest biowastes by deep eutectic solvents, *Journal of Biotechnology*, Vol. 282, pp 46–66, 2018.

20. Chand, R., Borugadda, V. B., Qiu, M., Dalai, A. K., Evaluating the potential for bio-fuel upgrading: A comprehensive analysis of bio-crude and bio-residue from hydrothermal liquefaction of agricultural biomass, *Applied Energy*, Vol. 254, pp 113679, 2019.

21. Mujahid, R., Riaz, A., Insyani, R., Kim, J., A centrifugation-first approach for recovering high-yield bio-oil with high calorific values in biomass liquefaction: A case study of sewage sludge, *Fuel*, Vol. 262, ~~pp~~ 116628, 2020.

22. Di Lauro, F., Balsamo, M., Solimene, R., Salatino, P., Montagnaro, F., Hydrothermal liquefaction process to obtain sludge-derived bio-fuels: Setup of the experimental apparatus and preliminary tests, *Chemical Engineering Transaction*, Vol. 92, pp 475–480, 2022.

Energetic valorisation of tannery sludge by gasification in fluidised bed

Massimo Urciuolo*, Renata Migliaccio*, Giovanna Ruoppolo*,
Francesca Di Lauro, Marco Balsamo**, Fabio Montagnaro**,**
Edoardo Imperiale*, Daniela Caracciolo*****
fabio.montagnaro@unina.it
*Istituto di Scienze e Tecnologie per l’Energia e la Mobilità Sostenibili,
Consiglio Nazionale delle Ricerche, Piazzale V. Tecchio 80, 80125 Napoli, Italy
**Dipartimento di Scienze Chimiche, Università degli Studi di Napoli Federico II,
Complesso Universitario di Monte Sant’Angelo, 80126 Napoli, Italy
***Stazione Sperimentale per l’Industria delle Pelli e delle Materie Concianti,
Comprensorio Adriano Olivetti, Via Campi Flegrei 34, 80078 Pozzuoli, Italy

Abstract

The present article deals with the valorisation of the organic content of tannery sludges to produce energy vectors. In this scenario, gasification is a viable option to obtain a flexible gaseous stream (syngas) of interesting energetic value, under operating conditions that do not favour the oxidation of Cr(III) (typically found in tannery sludges) to the more harmful Cr(VI) state. To this end, an industrial tannery sludge was characterised through proximate/ultimate analyses and determination of heating value, witnessing its capability to act as solid fuel in a gasification process, and metal analyses, showing its Cr(VI) content below the detection limit (2 ppm). The material has been submitted to gasification tests in a lab-scale Fluidised Bed (FB) reactor. The reactor, 41 mm ID and 1 m height, was electrically kept at the operating temperature of 850°C. The fluidisation velocity was 0.30 m/s at 850°C, i.e. 7.5 times the value of the minimum fluidisation velocity. The gasifying stream was composed by O_2 (3% vol.) diluted in N_2. The oxidant Equivalence Ratio (ER) ranged from 0.15 to 0.24, so to ensure sub-stoichiometric (i.e., reducing) conditions in the FB atmosphere. Under the most reducing operating conditions, it was possible to produce a syngas with lower heating value of 12.0 MJ/Nm^3 (dry and N_2 free basis). It contained, under these conditions, about 42% H_2, 36% CO and 4% CH_4, plus 16% CO_2 and other components. The tar produced from the process, fully characterised by Gas Chromatography-Mass Spectrometry (GC-MS), showed a favourably low concentration of about 25 g/Nm^3. FB bottom and fly ashes were analysed for their carbon and metal contents. In bottom ash, the total Cr concentration resulted in the range 8–12 g/kg, with Cr(VI) concentration between 8 and 10 ppm. In the elutriated stream, the total Cr concentration was about 55 g/kg, with Cr(VI) concentration between 4 and 7 ppm. The Cr(VI) concentration was higher when higher values of ER were used, but it resulted 3–4 orders of magnitude lower than the total Cr concentration, witnessing the appropriateness of the process for the production of a syngas with very limited oxidation of chromium in the solid residues.

Introduction

The Italian leather industry counts about 1,200 companies. Italy, in 2019, produced 128 million of m^2 of finished leathers for a production value of 4.9 billion euro, of which 3.6 billion euro accounts for export. The tannery districts are nowadays using advanced treatment plants, that are reaching high level of specialisation for tannery discharges [1]. The obtained sludge is rich in chromium (the removal of chromium by wastewater is greater than 99.4%). The huge volume of sludges generated by the leather industry, with a yearly global production of solid wastes deriving from the tanning process estimated to be on the order of 1 ton per ton of raw leather, poses economic and environmental issues associated with their landfilling, mainly due to the relevant amount of chemicals adopted in the tanning process (on average, 2 kg of chemicals are used to produce 1 m^2 of leather). In the circular economy perspective, the valorisation of the organic content of tannery sludge to produce energy vectors is a promising strategy to overcome the abovementioned issues (“Sludge-to-Energy (StE)” strategy) [2]. As a matter of fact, the direct combustion of a tannery sludge is not of particular interest, as the full oxidising conditions that are realised in the combustion chamber would unavoidably lead to the oxidation of Cr(III) (typically found in tannery sludges) to the more harmful Cr(VI) state. Gasification, instead, is a StE process carried out under partially oxidising conditions and allows to produce syngas (that can be flexibly used as energy source also in places/times different from those of production) together with the reduction of the amount of sludge to be landfilled, and the potential to reuse ashes in the construction materials industry (or as adsorbents for fluid streams purification), with an eye to the principles of circularity. In this context, fluidised bed reactors are widely known to be appropriate as gasifiers, due to the very good mass and heat transfer coefficients ensured by FB fluid-dynamics, and to the possibility of controlling emissions through a proper design of the gasifier and its operating conditions [3,4].

By also considering the relatively limited literature on this specific topic [5], this research article reports on lab-scale FB gasification carried out on an industrial tannery sludge. After a complete chemical characterisation of the material by a combination of techniques, gasification was carried out under two different operating conditions. Syngas, tar, bottom and fly ash streams were analysed, and their characteristics critically discussed with relation to the parent sludge properties and the gasification conditions.

Materials, equipment, and experimental procedures

The raw material (an industrial tannery sludge) was characterised by means of: (i) proximate analysis (TGA701 LECO thermobalance, UNI 9903/ASTM D5142 standard procedures); (ii) ultimate analysis (LECO CHN628 analyser with ASTM D5373 standard procedure for C, H, N determination; LECO SC-144DR analyser with UNI 7584 standard procedure for S determination); (iii) evaluation of the Higher Heating Value (HHV), in a Parr 6200 calorimeter (ASTM D5865 standard procedure), followed by determination of the chlorine content by ionic chromatography (883 Basic IC plus Metrohm, UNI 9903 standard procedure); (iv) determination of the content of Cr(total) and Cr(VI), according to a procedure developed by IRSA-CNR, through atomic absorption spectrometry and UV-visible spectrophotometry, respectively.

The bench-scale FB gasifier (electrically heated at a controlled temperature) is illustrated in Figure 1. It consists of a stainless-steel (AISI 310) fluidisation column (inner diameter=41 mm; height=1 m), with a distributor plate (made of a series of stainless-steel nets) that separates the gas inlet chamber/preheater (600 mm height) from the fluidisation column. The reactor is equipped with a steel net filter, located downstream the reactor, for the capture of elutriated fines (fly ash stream). The material is fed at the bottom of the bed through a combination of pneumatic and mechanical conveying devices.

The operating conditions of the gasification tests (carried out at 850°C) are illustrated in Table 1. The bed inert material is silica sand, 300–400 μm (inventory=180 g). The fluidising gas is composed by the sum of a stream of 300 NL/h of N_2 and a stream of 50 NL/h of air. This results in a fluidising gas composed by 3% O_2 (rest N_2), with a fluidisation velocity of 0.30 m/s (expressed at 850°C; the minimum fluidisation velocity for this system is 0.04 m/s). After having sieved the sludge to a size finer than 1 mm, two tests have been carried out: Test 1 and Test 2, with a sludge flow rate of 99 and 63 g/h, respectively. Once known the characteristics of the sludge, these two values result in air/fuel equivalence ratio ER=15% and 24% of the stoichiometric value for Test 1 and 2, respectively, so ensuring operating conditions well far from ER=100% and able to favour the desired gasification (rather than combustion) kinetic patterns.

The gas obtained from the process, after filtration and water condensation, is sent to a system of on-line IR gas analysers and to a condensation train (composed of one flask at room temperature and six flasks at –12°C) to collect the produced tar compounds, then measured and analysed by means of GC-MS techniques. The gasification tests were carried out under semi-batch conditions: at the end of each test, the FB is cooled down in N_2 flux and then the bed material (sand+bottom ash) is withdrawn. Sand is separated by bottom ash through a combination of sieving and density-based procedures. Finally, bottom and fly ashes were analysed by proximate, ultimate and Inductively Coupled Plasma-Mass Spectrometry (ICP-MS) analyses. The reader is referred to a previous work [6] for further details on the experimental apparatus and procedures.

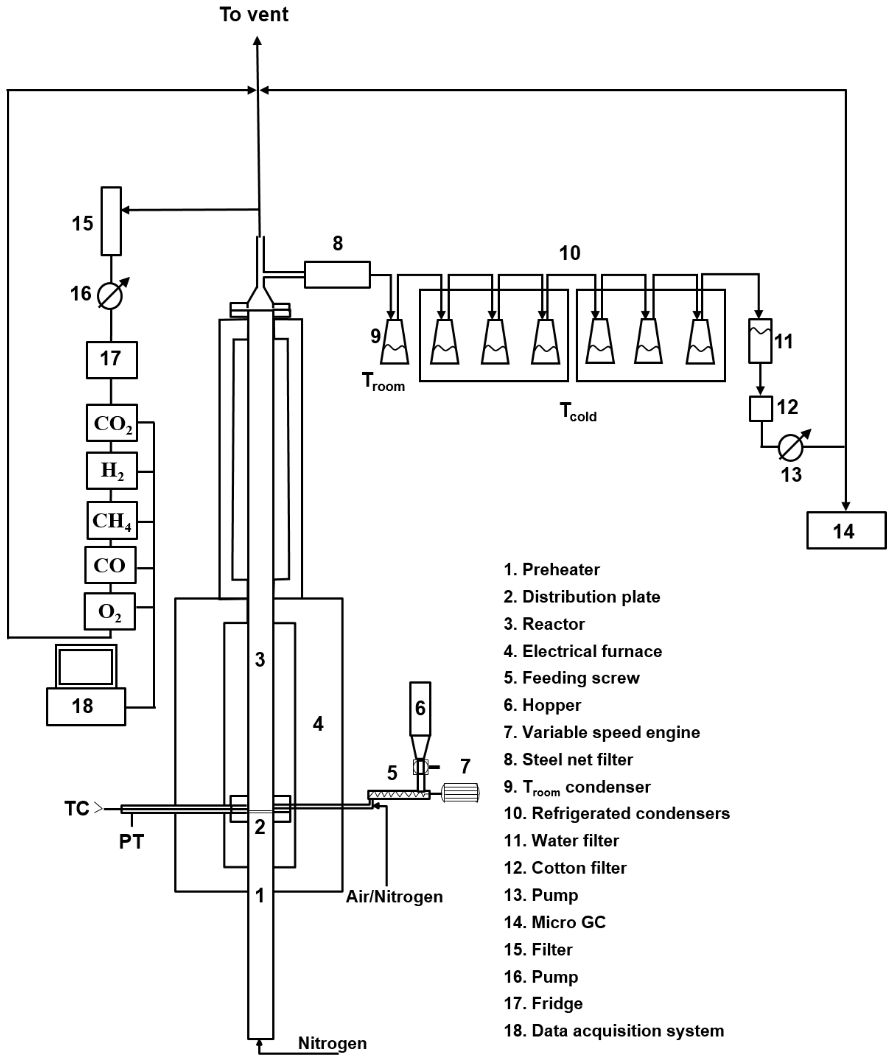

Figure 1. Scheme of the fluidised bed apparatus for gasification tests.

Table 1. Operating conditions of FB gasification tests of industrial tannery sludge.

	Test 1	**Test 2**
Bed inert material	Silica sand, 300–400 μm, inventory=180 g	
Flow rate of <1 mm sludge	99 g/h	63 g/h
Gasification temperature	850°C	
Minimum fluidisation velocity	0.04 m/s (@850°C)	
Fluidising gas	300 NL/h N_2 + 50 NL/h air (3% O_2; 97% N_2)	
Fluidisation velocity	0.30 m/s (@850°C)	
Air-to-fuel ER	0.15	0.24

Results and discussion

Properties of the industrial tannery sludge

Table 2 reports the main characteristics of the sludge. Moisture and volatiles account for, respectively, 18.46% and 50.13%, while an ash content of 31.41% was detected. No fixed C was observed by proximate analysis, but a total C content of 33.61% was revealed by ultimate analysis (dry basis), together with 5.10% of H, 2.44% of N and 4.07% of S. The quite high C content is positive in view of the further energetic valorisation process. Moreover, HHV=14.90 MJ/kg for the sludge at hand, a value that, at least as order of magnitude, is in line with data commonly reported for sludges and, more generally, biomasses. Finally, a low Cl content (0.35%) was detected. Table 3 synoptically reports the contents of the main elements (included O, calculated by difference), along with those of ashes and moisture, both on dry and wet basis. The concentration of Cr(total) in the parent sludge resulted equal to 20.65±0.05 g/kg (wet basis, corresponding to 25.32±0.06 g/kg dry basis). No Cr(VI) was detected by UV-visible spectrophotometry, with a detection limit of 2 mg/kg of Cr(VI). Thus, if present, Cr(VI) concentration in the tannery sludge was not higher than 2 ppm, and the concentration of Cr(total) substantially coincides with that of Cr(III).

Table 2. Results of the analyses on the industrial tannery sludge. Tests carried out in triplicates (standard deviation reported).

Proximate analysis (% by weight)	
Moisture	18.46±0.26
Volatiles	50.13±0.05
Fixed carbon	n.d.
Ash	31.41±0.30
Ultimate analysis (% by weight; dry basis)	
C	33.61±0.12
H	5.10±0.16
N	2.44±0.05
S	4.07±0.02
HHV [MJ/kg] (dry basis) = 14.90±0.26	

Table 3. Synoptic list of main tannery sludge properties (average % by weight).

	Dry basis	**Wet basis**
C	33.61	27.41
H	5.10	4.16
N	2.44	1.99
S	4.07	3.32
Cl	0.35	0.29
Ash	38.52	31.41
Moisture	–	18.46
O (by difference)	15.91	12.96

Outcomes of gasification tests

Table 4 reports the main outcomes of the FB gasification tests. On dry and N_2 free basis, for Test 1 (ER=0.15), syngas was mostly composed of CO (35.49% by vol.), H_2 (41.58%), CH_4 (3.67%) and C_2H_4 (2.89%), the rest being CO_2. H_2/CO and CH_4/H_2 ratios of 1.17 and 0.09, respectively, were obtained. Tar concentration in syngas was 26.4 g/Nm^3, and a fly ash flow rate of 7.57 g/h was collected. For Test 2 (less reducing conditions, ER=0.24), syngas was mostly composed of CO (27.05% by vol.), H_2 (32.69%), CH_4 (5.15%) and C_2H_4 (4.66%), the rest being CO_2. H_2/CO and CH_4/H_2 ratios of 1.21 and 0.16, respectively, were obtained. Tar concentration in syngas was 22.3 g/Nm^3, and a fly ash flow rate of 4.24 g/h was collected. The more severe reducing conditions of Test 1 allowed to obtain an amount of the two main gasification species (CO+H_2) of 77.07%, that is 22% more than what observed during Test 2 (CO+H_2=59.74%). Correspondingly, the CO_2 content obtained in the syngas from Test 1 (16.16%) was far lower than what observed in Test 2 (CO_2=30.10%). It is here obviously recalled that CO_2 does not contribute to the syngas heating value, and that its formation is favoured by less reducing conditions as those experienced in Test 2. The evaluation of both HHV and Lower Heating Value (LHV) of the syngas has been carried out based on its chemical composition: in Test 1, it is LHV=12.0 and HHV=13.1 MJ/Nm^3, while values are lower in Test 2 (LHV=11.6 and HHV=12.6 MJ/Nm^3). These values fall within the range reported by NETL-DOE, USA [7], where data from industrial gasifiers to produce syngas as energetic vector are reported (LHV=8.3–13.0 MJ/Nm^3 on dry and N_2 free basis). Finally, tar concentration also is in line with values reported in literature [8].

Table 4. Main outcomes of the FB gasification tests.

	Test 1 (ER=0.15)	Test 2 (ER=0.24)
Syngas composition (dry and N_2 free basis):		
CO [%vol.]	35.49	27.05
H_2 [%vol.]	41.58	32.69
CH_4 [%vol.]	3.67	5.15
C_2H_4 [%vol.]	2.89	4.66
C_2H_6 [%vol.]	0.09	0.09
CO_2 [%vol.]	16.16	30.10
Total [%vol.]	99.88	99.74
SO_2 [ppm]	193	137
H_2/CO [vol./vol.]	1.17	1.21
CH_4/H_2 [vol./vol.]	0.09	0.16
HHV (dry and N_2 free basis) [MJ/Nm^3]	13.1	12.6
LHV (dry and N_2 free basis) [MJ/Nm^3]	12.0	11.6
Tar concentration in syngas [g/Nm^3]	26.4	22.3
Elutriated stream flow rate (fly ash) [g/h]	7.57	4.24

Tar characterisation

While the detailed speciation of the tar compounds content in the syngas from Test 1 and 2 is not reported here for the sake of brevity, it is highlighted that, in both cases, tar species were mostly polycyclic aromatic hydrocarbons (with number of C atoms variable between 5 and 16), also in presence of heteroatoms (N, S, O). More, we found:

- Compounds with simple structure (benzene);
- Hydrocarbons with no heteroatoms, having 2 (naphthalene, methylnaphthalene, indene, biphenyl, vinylnaphthalene), 3 (anthracene, fluorene, phenanthrene, acenaphthylene, phenylnaphthalene, methylanthracene) and 4 (fluoranthene, pyrene) rings;
- Compounds containing N, with simple structure (pyridine, aniline, benzonitrile) or having 2 rings (indole, quinoline);
- Compounds containing S, with 2 (benzothiophene) and 3 (dibenzothiophene, naphthothiophene) rings;
- Compounds containing O, with simple structure (phenol, methylfuran) or having 3 rings (dibenzofuran).

Tar species condensed from syngas at room temperature were mostly rich in 2-, 3- and 4-rings hydrocarbons with no heteroatoms, and then rich in S-containing compounds. O- and N-containing tar species follow. The more complex species among those listed above, instead, enrich the tar condensed at –12°C.

Bottom and fly ash characterisation

Bottom ash from both FB gasification Test 1 and 2 was mostly composed by inorganic ash (Table 5), to confirm the almost complete conversion of volatiles and C under both ER values. On the other hand (Table 6), the elutriated fly ash, having experienced a mean residence time in the FB gasifier that is much lower than for the case of bottom ash, contained about 14–17% of volatiles and 3–4% of fixed carbon (i.e., the gasification burn-off degree for this stream is lower than 1). In both bottom and fly ash, the concentration of the harmful Cr(VI) species is, as expected, higher when a higher ER value was adopted (9.6 vs. 8.2 ppm in bottom ash, 7.1 vs. 4.1 ppm in fly ash), but the gasifier operating conditions indeed guarantee that these values are 3–4 orders of magnitude lower than the concentration of total chromium, that remains in the preferred form of Cr(III).

Table 5. Results of the analyses on bottom ash from FB gasification of tannery sludge.

Proximate analysis (% by weight)		
	Test 1 (ER=0.15)	**Test 2 (ER=0.24)**
Moisture	n.d.	n.d.
Volatiles	n.d.	n.d.
Fixed carbon	n.d.	n.d.
Ash	100.00	100.00
Ultimate analysis (% by weight; dry basis)		
	Test 1 (ER=0.15)	**Test 2 (ER=0.24)**
C	0.18	0.12
H	n.d.	n.d.
N	0.29	0.30
Chromium speciation		
Cr(total)	11.8 g/kg	8.0 g/kg
Cr(VI)	8.2 mg/kg	9.6 mg/kg

Table 6. Results of the analyses on fly ash from FB gasification of tannery sludge.

Proximate analysis (% by weight)		
	Test 1 (ER=0.15)	**Test 2 (ER=0.24)**
Moisture	1.54	1.31
Volatiles	13.84	17.10
Fixed carbon	3.17	3.97
Ash	81.45	77.62
Ultimate analysis (% by weight; dry basis)		
	Test 1 (ER=0.15)	**Test 2 (ER=0.24)**
C	9.54	7.99
H	n.d.	n.d.
N	0.68	0.62
Chromium speciation		
Cr(total)	53.3 g/kg	56.4 g/kg
Cr(VI)	4.1 mg/kg	7.1 mg/kg

Summary

In this preliminary research campaign, a tannery sludge of industrial origin was taken into consideration. With its 34% carbon content (dry basis), the material can be considered appropriate for energetic valorisation. The selected process was the sludge gasification in fluidised bed, to produce syngas. Since the sludge comes from the tannery industry, particularly relevant is its chromium content. In the parent material, we did not observe the harmful hexavalent Cr species. Under the best adopted operating conditions, a syngas with 42% H_2 (dry and N_2 free basis) and lower heating value of 12 MJ/kg was obtained, with limited tar concentration and the production of bottom ash whose gasification degree was, for all practical purposes, complete. Cr(VI) concentration in bottom and fly ashes was not higher than 10 mg/kg, while Cr(total) concentration was 3–4 orders of magnitude greater, witnessing the right choice of operating conditions that did not promote the oxidation of Cr(III) to Cr(VI) at a relevant extent. The evaluation of the energetic yield of the process, along with the investigation of possible recycle routes for gasification ash (f.i.: as adsorbent material, or in the materials construction industry), will help to increase the circularity of the proposed process, with clear financial and environmental advantages accompanying the production of an energy vector from an industrial residue.

References

[1] UNIC Sustainability Report 2020, https://unic.it/storage/Rapporto%20sostenibilità%202020/Report_Sostenibilità_2020_ENG_online.pdf

[2] Cieślik, B. M., Namieśnik, J., Konieczka, P., "Review of sewage sludge management: standards, regulation and analytical methods", *Journal of Cleaner Production, 90, 2015,* 1-15.

[3] Scala, F., Ed., *Fluidized Bed Technologies for Near-Zero Emission Combustion and Gasification*, Woodhead Publishing, 2013.

[4] Liu, Z., Mayer, B. K., Venkiteshwaran, K., Seyedi, S., Raju, A. S. K., Zitomer, D., McNamara P. J, "The state of technologies and research for energy recovery from municipal wastewater sludge and biosolids", *Current Opinion in Environmental Science & Health, 14, 2020*, 31-36.

[5] Ongen, A., Ozcan, H. K., Arayici, S., "An evaluation of tannery industry wastewater treatment sludge gasification by artificial neural network modeling", *Journal of Hazardous Materials, 263, 2013,* 361-366.

[6] Migliaccio, R., Brachi, P., Montagnaro, F., Papa, S., Tavano, A., Montesarchio, P., Ruoppolo, G., Urciuolo, M., "Sewage sludge gasification in a fluidized bed: experimental investigation and modeling", *Industrial & Engineering Chemistry Research, 60, 2021,* 5034-5047.

[7] https://www.netl.doe.gov/research/coal/energy-systems/gasification/gasifipedia/syngas-composition-igcc

[8] Phuphuakrat, T., Nipattummakul, N., Namioka, T., Kerdsuwan, S., Yoshikawa, K., "Characterization of tar content in the syngas produced in a downdraft type fixed bed gasification system from dried sewage sludge", *Fuel, 89, 2010,* 2278-2284.